Transactions of the ASME®

Journal of Turbomachinery

Published Quarterly by The American Society of Mechanical Engineers

VOLUME 122 • NUMBER 1 • JANUARY 2000

TECHNICAL PAPERS

Transactions of the ASME, Journal of Turbomachinery (ISSN 0889-504X) is published quarterly (Jan., Apr., July, Oct.) for $215.00 per year by The American Society of Mechanical Engineers, Three Park Avenue, New York, NY 10016. Periodicals postage paid at New York, NY and additional mailing offices. POSTMASTER: Send address changes to Transactions of the ASME, Journal of Turbomachinery, c/o THE AMERICAN SOCIETY OF MECHANICAL ENGINEERS, 22 Law Drive, Box 2300, Fairfield, NJ 07007-2300.
CHANGES OF ADDRESS must be received at Society headquarters seven weeks before they are to be effective. Please send old label and new address.
PRICES: To members, $40.00, annually; to nonmembers, $215.00.
To countries outside the United States and Canada, add $40.00 for surface postage and $60.00 for airmail postage.
STATEMENT from By-Laws. The Society shall not be responsible for statements or opinions advanced in papers or . . . printed in its publications (B7.1, Par. 3).

INDEXED by Applied Mechanics Reviews and Engineering Information, Inc.
Canadian Goods & Services Tax Registration #126148048

This journal is printed on acid-free paper, which exceeds the ANSI Z39.48-1992 specification for permanence of paper and library materials. ♾™
♻ 85% recycled content, including 10% post-consumer fibers.

TECHNICAL BRIEF

ANNOUNCEMENTS

Effects of Inlet Flow Field Conditions on the Performance of Centrifugal Compressor Diffusers: Part 1—Discrete-Passage Diffuser

V. G. Filipenco[1]

S. Deniz[2]

J. M. Johnston[3]

E. M. Greitzer

Gas Turbine Laboratory,
Massachusetts Institute of Technology,
Cambridge, MA 02139

N. A. Cumpsty
Whittle Laboratory,
Department of Engineering,
Cambridge University,
Cambridge CB3 ODY, United Kingdom

This is Part 1 of a two-part paper considering the performance of radial diffusers for use in a high-performance centrifugal compressor. Part 1 reports on discrete-passage diffusers (shown in Fig. 1) while Part 2 describes a test of a straight-channel diffuser designed for equivalent duty. Two builds of discrete-passage diffuser were tested, with 30 and 38 separate passages. Both the 30 and 38 passage diffusers investigated showed comparable range of unstalled operation and similar level of overall diffuser pressure recovery. The paper concentrates on the influence of inlet flow conditions on the pressure recovery and operating range of radial diffusers for centrifugal compressor stages. The flow conditions examined include diffuser inlet Mach number, flow angle, blockage, and axial flow nonuniformity. The investigation was carried out in a specially built test facility, designed to provide a controlled inlet flow field to the test diffusers. The facility can provide a wide range of diffuser inlet velocity profile distortion and skew with Mach numbers up to unity and flow angles of 63 to 75 deg from the radial direction. The consequences of different averaging methods for the inlet total pressure distributions, which are needed in the definition of diffuser pressure recovery coefficient for nonuniform diffuser inlet conditions, were also assessed. The overall diffuser pressure recovery coefficient, based on suitably averaged inlet total pressure, was found to correlate well with the momentum-averaged flow angle into the diffuser. Furthermore, the pressure recovery coefficient was found to be essentially independent of the axial distortion at diffuser inlet, and the Mach number, over the wide flow range (from maximum flow to the beginning of flow instabilities) investigated. It is thus shown that the generally accepted sensitivity of diffuser pressure recovery performance to inlet flow distortion and boundary layer blockage can be largely attributed to inappropriate quantification of the average dynamic pressure at diffuser inlet. Use of an inlet dynamic pressure based on availability or mass-averaging in combination with definition of inlet flow angle based on mass average of the radial and tangential velocity at diffuser inlet removes this sensitivity.

1 Introduction

1.1 Motivation and Scope. The radial diffuser plays an important role in establishing the overall efficiency and pressure rise of a centrifugal compressor stage. Depending on the design of the impeller and its matching to the diffuser, the diffuser can be the component limiting the operating range of the compressor between choke and stall. Radial diffusers can be grouped into two general classes: vaneless and vaned. High-performance centrifugal compressors (in, for example, aircraft engines) make use of vaned diffusers. These have a smaller exit radius for a given level of diffusion and generally a higher pressure recovery coefficient than the vaneless type, in spite of operating over a relatively narrower range of stable operation.

Part 1 of this paper is concerned with one special type of vaned diffuser, the discrete-passage diffuser, developed by General Electric Company. Its design is characterized by straight centerline passages, which are circular in cross section (and conical in form) from the diffuser inlet to the diffuser throat and then transition to a nearly rectangular cross section between the throat and diffuser exit (Fig. 1). Between the diffuser inlet and the throat, the intersection of the conical passages forms a quasi-vaneless space with highly swept back cusplike leading edges. The quasi-vaneless space is designed to diffuse supersonic inlet flow, and the throat area determines the maximum flow rate of the diffuser. Although discrete-passage diffusers are used in various centrifugal compressor applications, few data about their design and performance exist in the open literature.

Even though the impact of the diffuser is well known, the flow in diffusers of centrifugal turbomachines, which can be severely distorted in both space and time, is not sufficiently understood for many design and development purposes. The impact of vaned diffusers on performance and operating range of a centrifugal compressor stage can depend upon such parameters as Mach number, inlet flow angle, turbulence, blockage, and impeller exit flow nonuniformities. Still more important is the matching of diffuser to the impeller. Until recently the centrifugal compressor impeller and diffuser were considered separately in the design process and the influences of impeller exit flow and impeller–diffuser interaction were not taken into account. Furthermore, centrifugal compressor vaned diffuser design has been based on

[1] Current address: United Technologies Research Center, East Hartford, CT 06108.
[2] Current address: Praxair, Inc., Technology Center, Tonawanda, NY 14151.
[3] Current address: General Electric Aircraft, Fan & Compressor Aerodynamics, Lynn, MA 01910.

Contributed by the International Gas Turbine Institute and presented at the 43rd International Gas Turbine and Aeroengine Congress and Exhibition, Stockholm, Sweden, June 2–5, 1998. Manuscript received by the International Gas Turbine Institute February 1998. Paper No. 98-GT-473. Associate Technical Editor: R. E. Kielb.

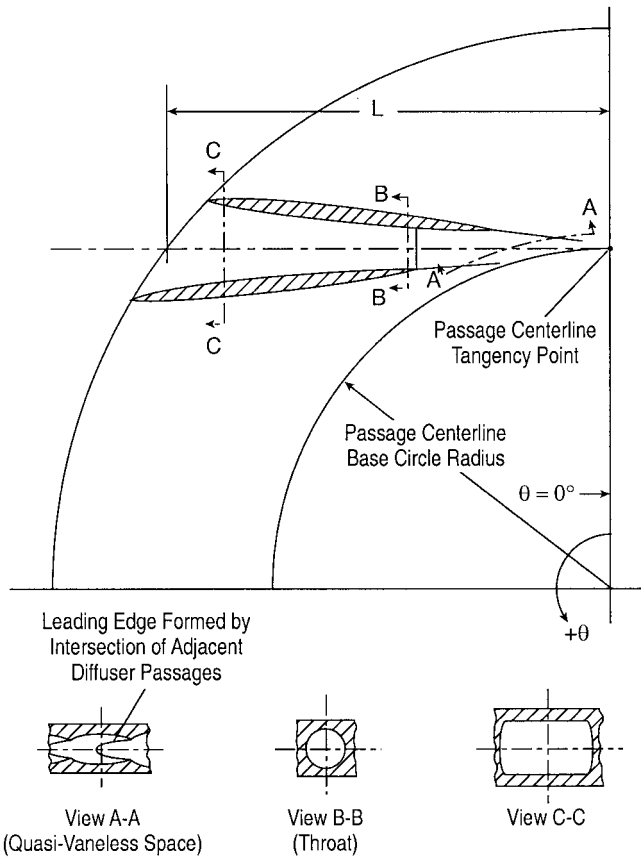

Fig. 1 Discrete-passage diffuser geometry schematic

data from single-channel diffuser investigations. The current state of the art employs empirical information to obtain a good diffuser–impeller combination. At present, the open literature does not show clear evidence for the relative merits of discrete-passage-type diffusers (the subject of Part 1) or straight-channel type diffusers (the subject of Part 2 (Deniz et al., 2000).

1.2 Background. The diffuser is one of the most comprehensively studied components of fluid mechanics. The extensive literature has been summarized by Japikse (1996, 1984). Most of the diffuser studies in the open literature have focused on single (individual) diffuser channels, with comparatively uniform inlet flows of a largely steady nature. Based on the work of many investigators, Japikse (1987) concluded that three fluid dynamic parameters must be known to specify the performance of a diffuser: the inlet blockage, the shape of the velocity profile entering the diffuser, and the turbulence scale and intensity at the diffuser inlet.

Blockage is the area equivalent to displacement thickness of a boundary layer in the diffuser inlet flow area. Based on the investigations for single-channel diffusers, diffuser pressure recovery decreases as inlet blockage increases. No general convention has been developed to specify the inlet velocity profile to a diffuser, although different inlet profiles, simple skewed and/or highly distorted, have been considered and reported in the open literature for single-channel diffusers. In most of the investigations, distorted mean-velocity inlet profiles decreased diffuser pressure recovery. The influence of the turbulence on the diffuser performance has scarcely been investigated in the open literature.

The situation is less well mapped and understood for centrifugal compressor diffusers. Some key points for vaned diffusers in centrifugal compressors can be summarized as follows:

1 The inlet conditions of a centrifugal compressor diffuser are determined by the impeller with highly distorted distributions in both axial (hub to shroud) and circumferential (blade to blade) directions, and vary with the impeller operating point. Knowledge about the influence of blockage or inlet velocity distribution for

Nomenclature

A = flow area
AR = area ratio (diffuser exit area over the area at the throat)
AS = aspect ratio = b/W_{th}
B = blockage, defined in Eq. (9)
Cp = pressure recovery coefficient, defined in Eq. (1)
Cp_ψ = pressure recovery coefficient based on availability-averaged diffuser inlet dynamic pressure, defined in Eq. (3)
Cp_a = pressure recovery coefficient based on the area-averaged diffuser inlet dynamic pressure
Cp_b = pressure recovery coefficient based on the diffuser inlet maximum total pressure
Cp_c = pressure recovery coefficient based on the area-averaged diffuser inlet absolute velocity and static density
L = length of the diffuser channel
LWR = length-to-width ratio of the diffuser channel = L/W_{th}
M = Mach number
N = impeller rotational speed (revolutions per minute)
P_s = static pressure
P_t = total pressure
$P_t\psi$ = availability-averaged total pressure, defined in Eq. (2)
Re = Reynolds number = Vb/ν
W_{th} = width of the diffuser throat
Z_b = number of impeller blades
Z_v = number of diffuser passages
b = diffuser depth
$\dot{m}$ = mass flow rate
r = radius or radial coordinate, orthogonal to x and θ
x = linear coordinate in the axial direction of the machine
α = flow angle, relative to the radial or meridional direction
α_n = flow angle nonuniformity, defined in Eq. (8)
β = wedge angle of diffuser vane
δ_m = displacement thickness at the diffuser inlet, defined in Eq. (10)
θ = angular coordinate, orthogonal to x and r, positive in rotor rotation direction
2θ = diffuser channel divergence angle
ζ = local linear coordinate normal to diffuser channel centerline
ν = kinematic viscosity
ξ = distance along diffuser channel centerline
ρ = density
σ_m = mass-flux deficit, defined in Eq. (10)

Subscripts

crit = critical
r = in radial direction or radial component
s = static
th = at diffuser throat
t = total condition or tangential component
θ = in θ direction (circumferential) or θ component
ψ = availability-averaged
0 = at impeller (swirl generator) inlet
1′ = at impeller (swirl generator) exit or same as vaneless space-inlet
1 = at diffuser inlet or same as vaneless space-exit
2 = at diffuser exit
3 = in main collector/plenum

single-channel diffusers is not directly applicable to centrifugal compressor diffusers.

2 Studies using a single diffuser channel do not give information on the flow mechanisms within the vaneless or quasi-vaneless spaces of a centrifugal compressor diffuser. Previous investigators have suggested that the flow phenomena in these regions are critical factors for stage stability (Hunziker and Gyarmathy, 1994) and pressure recovery (e.g., Elder and Gill, 1986; Inoue and Cumpsty, 1984).

3 Additional geometric parameters, compared to single diffuser channel flow, must be considered in the case of a centrifugal compressor diffuser. These include vaneless space radius ratio, vane number, geometry and sharpness of the vane leading edges, and the effect of downstream conditions.

Information concerning the overall performance of different types of vaned diffusers and diffuser subcomponents can be found in the open literature (e.g., Hunziker and Gyarmathy, 1994; Haupt et al., 1988; Clements, 1987; Japikse and Osborne, 1986; Stein and Rautenberg, 1985; Kano et al., 1982; Rodgers, 1982; Yoshinaga et al., 1980; Kenny, 1972). A distorted, nonuniform flow field was observed at the diffuser inlet in almost all of these investigations, but the influence of flow nonuniformities at the impeller exit on centrifugal compressor vaned diffuser performance and operating range has not been adequately investigated. The phenomenon of nonuniform flow leaving a centrifugal compressor impeller has been extensively considered in connection with both the study of the behavior of the impeller itself (jet-wake flow) and the behavior of vaneless diffuser.

Of particular relevance is a detailed experimental study of impeller exit flow and impeller–vaned diffuser interaction published by Krain (1981). Periodic flow unsteadiness was observed in the diffuser inlet region with temporal variations of inlet flow angle, of the order of 10–15 deg, and axial variations from hub to shroud, of the order of 20–25 deg. In a subsequent paper, Krain (1984) presented laser measurements downstream of the diffuser throat. Despite the large periodic unsteadiness at the impeller exit and nonuniform inlet conditions at diffuser inlet, levels of unsteadiness decreased rapidly downstream of the throat and the diffuser revealed a good overall pressure recovery. The CFD (Computational Fluid Dynamics) calculations on Krain's centrifugal compressor carried out by Dawes (1995) showed similar results with no significant influence of the unsteady, circumferential variation of the impeller exit flow on the vaned diffuser pressure recovery performance.

Two additional results covering the circumferential variation are worth noting. Inoue and Cumpsty (1984) focused on the influence of impeller exit flow unsteadiness and circumferential nonuniformity on the vaned diffuser performance. They found that the circumferential distortion from the impeller was attenuated very rapidly in the inlet region of the diffuser vanes and had only minor effects on the flow inside the vaned diffuser. Earlier Baghdadi (1976) compared the performance and stability of a radial wedge type diffuser (i.e., a straight-channel diffuser) using the vortex-nozzle swirling flow generator (having no moving parts and producing stationary wakes into the diffuser) tested by Baghdadi and McDonald (1975), with tests obtained with the same diffuser in actual centrifugal compressor stage. Diffuser performance and stability for the two cases were found to agree within the range of experimental accuracy. Since the vortex nozzle produced a circumferentially uniform flow, while the impeller produced a distorted jet-wake type flow at the diffuser inlet, it was concluded that the vaned diffuser performance is insensitive to the jet–wake structure of the impeller exit flow and the vaned diffusers were well able to cope with the flow nonuniformity and unsteadiness from the impeller. It was suggested that a combination of rapid mixing and the high frequency of the unsteadiness were responsible for the observed insensitivity of diffuser to the circumferential nonuniformities at the inlet.

Numerical methods for centrifugal compressor vaned diffuser design and detailed analysis of unsteady impeller–diffuser interaction are currently under development. Casey et al. (1995b), Dawes (1995), Dalbert et al. (1993), and Teipel et al. (1992) have reported on this. The calculations need to be compared with experimental data to verify their predictive value and there is a shortage of relevant data in the open literature, which could allow such a comparison, particularly including the influence of impeller exit flow nonuniformities on vaned diffuser performance and impeller–diffuser interaction.

1.3 Objectives. In Part 1 of this paper we examine the influence of diffuser inlet Mach number, flow angle, and axial flow nonuniformity on the performance and operating range of discrete-passage diffusers. Different methods of averaging the measured nonuniform flow field distributions at diffuser inlet to determine appropriate diffuser performance characterization parameters are considered in section 2. The experimental apparatus is described in section 3 and in section 4 the definitions of performance parameters are given. The experimental results are presented in section 5, followed by the summary and conclusions in section 6. The behavior of the straight-channel diffuser is addressed in Part 2. The experiments described here were made over a period of about eight years, beginning with the 30-passage discrete-passage diffuser. Over this time the procedure was altered and the ideas were modified. It was therefore not always possible to present some of the earlier data in the same way as that selected for the later data, in particular the method used for the straight-channel diffuser in Part 2.

2 Different Averaging Methods

In examining the effect of inlet nonuniformities, it is first necessary to define what is meant by diffuser performance. A number of different correlating parameters have been used to characterize diffuser behavior. Even for single-channel diffusers, many of the data in the open literature were not based on diffuser inlet (or impeller exit) traverses. This has resulted in ambiguous information on the diffuser inlet conditions. Static pressure is comparatively easy to measure in most diffuser configurations using wall-mounted static pressure taps, but to define the diffuser performance the inlet stagnation pressure distribution is needed. In some examples in the open literature, the inlet stagnation pressure is taken to be the value at the middle of the diffuser depth, while in others an averaged value is used, normally based on area or mass flow. In some cases the inlet stagnation pressure is estimated from compressor input power and flow rate. As pointed out by Klein (1981), there is often not enough information to compare one definition with another, limiting the generality of the available data. To establish definitive values of the pressure recovery for a diffuser, detailed measurements across the inlet, with suitable numerical averaging across the entire flow field are required.

The pressure recovery coefficient, Cp, defined as the static pressure rise through the diffuser divided by the inlet dynamic pressure, is the most frequently used diffuser performance parameter. This parameter indicates the fraction of the dynamic pressure at the inlet of the diffuser converted into static pressure by the diffuser:

$$Cp = \frac{P_{s2} - P_{s1}}{P_{t1} - P_{s1}} \tag{1}$$

In Eq. (1) P_{s1} and P_{s2} are mean values of static pressures at the diffuser inlet and exit. The static pressure at the diffuser inlet and exit is generally uniform enough so that the problem of defining the pressure recovery coefficient, Cp, is essentially a matter of assigning an appropriate value of total pressure, P_{t1}, for a nonuniform diffuser inlet flow.

Previous researchers have presented diffuser performance data based on various different definitions of the diffuser inlet dynamic pressure: area-averaged dynamic pressure (Al Mudhafar et al., 1982, and Bhinder et al., 1984; area-averaged velocity (Wolf and

Table 1 Facility dimensions summary

	Dimension
Impeller Exit Radius, $r_{1'}$	0.184 m
Impeller Axial Depth, b	9.0 mm
Vaneless Space Radius Ratio, $r_1/r_{1'}$	1.10
Number of Impeller Blades, Z_b	71
Impeller Blade Inlet Angle	−37.2 deg
Impeller Blade Exit Angle	64 deg

Johnston, 1969), mass-averaged dynamic pressure (Masuda et al., 1971), mass-averaged total pressure (Baghdadi, 1976), and dynamic pressure based on the potential core centerline total pressure (Runstadler et al., 1975, and Dutton et al., 1986). The extent of the test data from Runstadler et al. (1975) has caused the use of the centerline velocity to become the most widespread basis of defining the inlet dynamic pressure.

The different methods of specifying the diffuser inlet dynamic pressure make the interpretation, comparison, and generalization of the data of the different diffuser investigations difficult. Filipenco (1991) defined the pressure recovery coefficient in terms of availability-averaged inlet total pressure (Livesey and Hugh, 1966), based on addressing the following question: Given a nonuniform flow entering the diffuser, what is the maximum static pressure that could theoretically be attained without external work or heat interactions? This is the pressure that would be attained in a hypothetical ideal device through a reversible, adiabatic, zero work process that ends in a uniform zero-velocity state. Such a process conserves the net thermodynamic availability of the flow and an appropriate designation of the final total pressure attained is the "availability-averaged" total pressure, $P_{t\psi}$.

The availability-averaged total pressure, $P_{t\psi}$, at the diffuser inlet is defined as:

$$P_{t\psi 1} = \exp\left[\frac{\int_0^b \ln\left(P_{t1}\right)\rho_{s1}V_{r1}2\pi r_1 dx}{\int_0^b \rho_{s1}V_{r1}2\pi r_1 dx}\right] \tag{2}$$

and the availability-averaged pressure recovery coefficient is:

$$C_{p\psi} = \frac{P_{s2} - P_{s1}}{P_{t\psi 1} - P_{s1}} \tag{3}$$

with the denominator defined as the diffuser inlet availability-averaged dynamic pressure.

Among these different definitions of Cp (or diffuser inlet dynamic pressure) mentioned above, Cp_{ψ} is the most physically appropriate one to be used as a diffuser pressure recovery performance.

A closely similar, but more familiar, parameter is based on the mass-averaged total pressure at the diffuser inlet, $\hat{P}_{t1}$, defined as:

$$\hat{P}_{t1} = \frac{\int_0^b P_{t1}\rho_{s1}V_{r1}2\pi r_1 dx}{\int_0^b \rho_{s1}V_{r1}2\pi r_1 dx} \tag{4}$$

This can be substituted into Eq. (1) to define the mass-averaged pressure recovery coefficient.

For an ideal incompressible fluid, the availability-averaged total pressure is equal to the mass-averaged total pressure. In the present experiments, the diffuser inlet dynamic pressure based on the inlet mass-averaged total pressure was in the most extreme case 1.6 percent greater than the dynamic pressure based on the availability averaged total pressure. This variation is smaller than the scatter in most of the data, so that the mass-averaged pressure recovery coefficient is adequate as an appropriate measure. It will be shown that use of this parameter allows collapse of data at different levels of nonuniformity to a single curve.

3 Experimental Apparatus

3.1 Overall Test Facility Description. The experimental apparatus for radial diffuser investigations was designed to provide a controlled inlet flow to a centrifugal compressor diffuser. The diffuser inlet conditions accessible included Mach numbers greater than unity with high degree of swirl (flow angle 63–75 deg measured from radial direction). Control of the boundary layer properties on the hub and shroud was possible, giving inlet blockage up to $B = 0.35$ and diffuser inlet velocity profile axial distortion. The ranges cover those reported to be encountered at the diffuser inlet in actual centrifugal compressors by, for example, Hunziker and Gyarmathy (1994), Japikse and Osborne (1986), Mishina and Nishida (1984), and Kenny (1972). In these studies the blockage, B, at the centrifugal compressor impeller exit were calculated in a range from 0.10 to 0.37.

The facility consists of a specially designed impeller (swirl generator), which can deliver an axisymmetric, transonic flow into a test section in which different radial diffusers can be installed. Some salient facility dimensions are listed in Table 1. Downstream of the diffuser the flow exits to a plenum, followed by a throttle; a slave compressor downstream of the throttle valve can be activated to decrease diffuser back pressure if needed. The mass flow rate can be varied by the throttle valve and measured by a venturi-type flow meter located in the rig exit pipe, with a commercial flow straightener located ten pipe diameters upstream of the venturi. The overall facility scheme is shown in Fig. 2. The discrete-passage diffusers, which were supplied by General Electric Aircraft Engines, had at the inlet a span, b, (in the axial direction) of 9.0 mm and this was selected as the nominal span of the impeller and vaneless space.

To minimize the wakes of the impeller blades, the impeller (swirl generator) shown in Fig. 3 has 71 lightly loaded, high-solidity forward-leaning blades. The design is such as to produce a static pressure drop through the blade row. The impeller exit flow circumferential nonuniformity in static pressure does not exceed 2.0 percent of the average inlet dynamic pressure in the worst case and is considerably smaller than this in most situations. It was thus sufficient to measure diffuser inlet total pressure and flow angle axial distributions at only one circumferential location. The impeller speed could be varied to 6500 rpm and was measured by

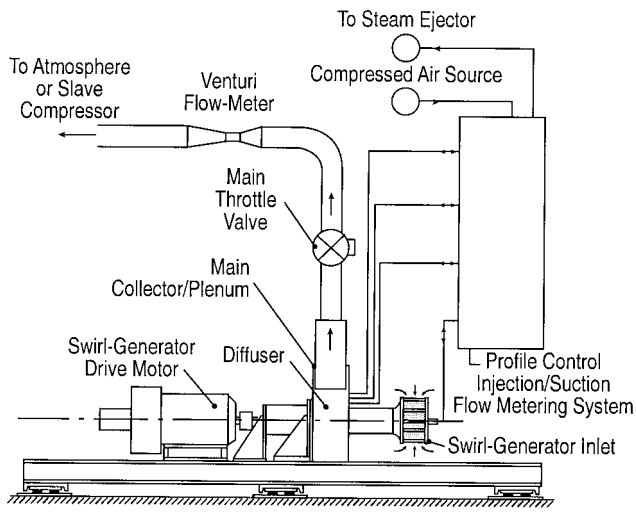

Fig. 2 Overall test facility schematic

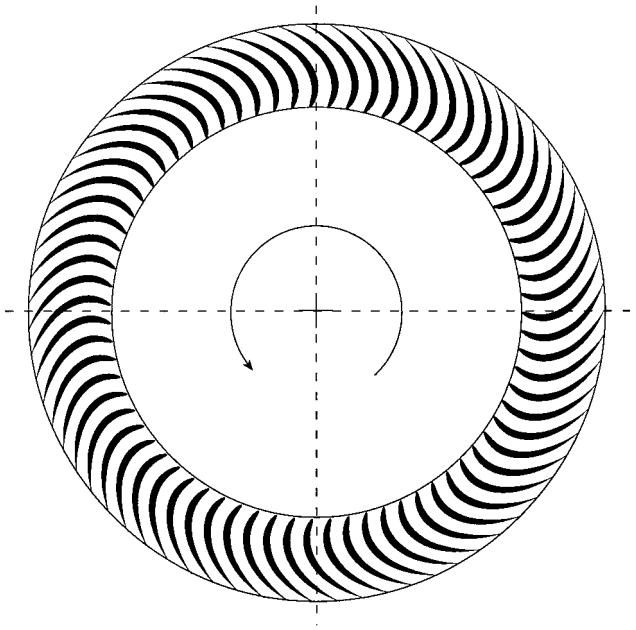

Fig. 3 Swirl generator blading. Blade number $Z_b = 71$.

means of a digital readout tachometer. No flow instabilities were encountered in the impeller over the operating range of interest.

The diffuser inlet boundary layer blockage and flow distortion are controlled using continuous circumferential slots immediately upstream and downstream of the impeller in the hub and shroud stationary walls. Each slot is independently connected to a flow control system through an array of passages and manifolds, so that air can either be injected or removed from the main flow. Figure 4 provides a schematic of the axial flow injection/suction slots and manifolds. Using a combination of injection and/or suction through these slots, a wide range of diffuser inlet blockage and axial velocity profile distortion may be obtained. The baseline (no air injection and/or suction) distributions of Mach number and flow angle at the diffuser inlet, which are almost symmetric about the axial centerline of the diffuser, are shown in Fig. 5. Figure 5 also shows examples of Mach number and flow angle distributions with injection and suction. Here, $x = 0$ corresponds to the wall on the same side of the labyrinth seal, which can be seen in Fig. 4.

Two discrete-passage diffusers of similar geometry but differing in the number of passages (30 and 38) were investigated. Both were originally designed to work with the same centrifugal compressor impeller in a turboshaft gas turbine engine by General Electric Aircraft Engines. The salient parameters of the discrete-passage test diffusers are listed in Table 2.

The test diffusers were mounted in the diffuser housing with a 1.10 radius ratio vaneless space between impeller exit and the diffuser inlet. Further details of construction and operation of the test facility are described by Filipenco (1991) and Johnston (1993).

3.2 Instrumentation. The test program includes wall static pressure measurements along the diffuser centerline, at the diffuser inlet and exit, and in the vaneless and quasi-vaneless spaces; temperature measurements at impeller inlet and diffuser exit, as well as total pressure, and flow angle measurements at the diffuser inlet.

To determine diffuser inlet Mach number and flow angle profiles, a rotatable cylindrical single-hole total-pressure/flow angle-probe axially spanning the inlet of the test diffuser was used at one circumferential position ($\theta = 0$ deg). A single hole probe was used to minimize probe diameter and thus the effect of the probe on the diffuser inlet flow field. The probe consisted of a 1-mm-dia stainless steel tube with a 0.23-mm-dia sensing hole radially drilled through one wall. With the probe positioned in a crossflow, the probe is rotated around its axis. For the expected 65–75 deg inlet flow angle range, the probe was rotated over a range of 40–115 deg in 5 deg steps. The maximum output pressure occurs when the sensing hole faces directly into the flow and determination of the flow angle, α, is made by finding the centroid of the measured total pressure versus flow angle curve. A second-order polynomial fit through a symmetric subset of the pressure reading versus probe-angle test data was used for this purpose. A fifth-order polynomial fit, which represents the pressure distribution more accurately, was then used to determine the total pressure. Flow angle and total pressure were measured at 15 axial points. Rated angular positioning linearity is to within 0.2 deg and the rated axial traverse positioning accuracy is to within 0.025 mm. All traverse/angle set points were approached from the same direction to avoid hysteresis error.

One diffuser channel was instrumented with an array of static pressure taps to measure the static pressure distribution on the different subcomponents of the diffuser. Since the quasi-vaneless space of the diffuser is considered to be important in determining diffuser performance and stability, additional static pressure taps were placed in the vaneless and quasi-vaneless spaces. The locations of the static pressure taps in one diffuser channel are shown in Part 2 (Fig. 2) for the straight-channel diffuser and they are similar to those of the discrete-passage diffusers. To measure the circumferential variation of the static pressure at the impeller exit, 10 taps were placed on each of the rear and front walls in the vaneless space at a radius of 1.05 impeller exit radii. Static pressure distribution at the diffuser exit was also measured with 5 taps placed on each of the rear and front walls. Measurements of the main plenum pressure and all steady-state pressures in the diffuser test rig, including the vaneless space, the quasi-vaneless space and diffuser channel, were carried out using of a single Druck-type PDCR-23D±5 psid pressure transducer, multiplexed to the various pressure taps by means of a Scanivalve. The rated combined

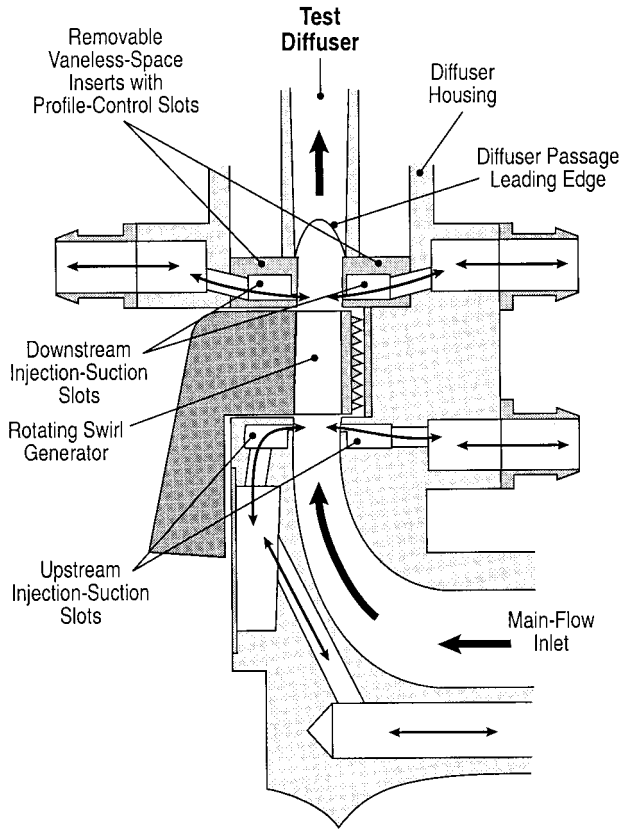

Fig. 4 Schematic of axial flow injection/suction system

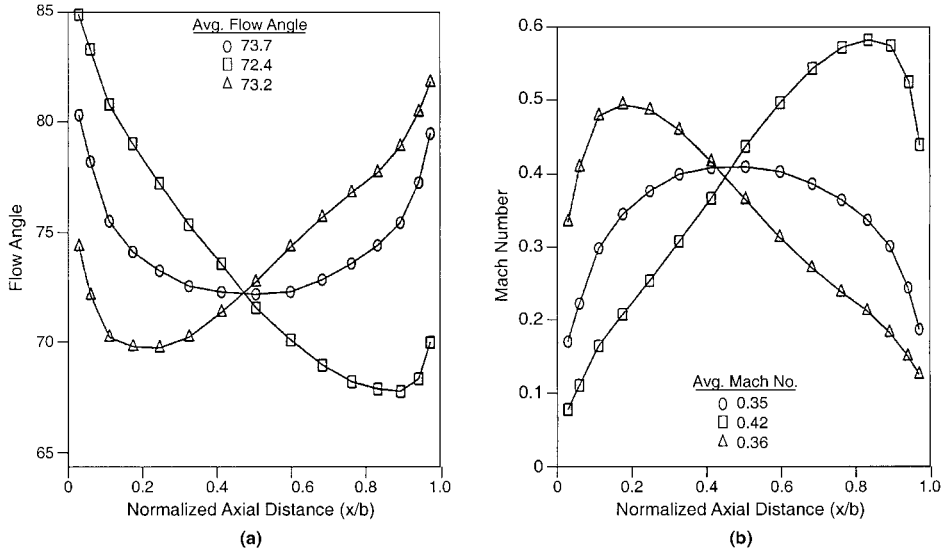

Fig. 5 Examples of the axial distribution of (*a*) flow angle, α, and (*b*) absolute Mach number, M, at discrete passage diffuser inlet: (○) no injection/suction, (△, ❑) with injection/suction

nonlinearity, hysteresis, and repeatability of this transducer is within ± 0.04 percent of full scale.

Temperature was measured at the test rig inlet (ambient temperature), at the exit of the test diffuser at diffuser axial midposition and at the exit of the venturi flow meter. The Mach number at diffuser exit is low, typically less than 0.20, so no recovery corrections were applied to the measured temperature at the diffuser exit. The flow between impeller exit and plenum is assumed adiabatic and uniform stagnation temperature. Calibrations of the temperature sensors gave an estimated overall accuracy to within ± 1 K, or less than 0.2 percent over the temperature range of the investigations.

Three Kulite high-frequency response pressure transducers were flush-mounted in the vaneless space and one Kulite high-frequency response pressure transducer was mounted in the plenum wall for the monitoring of rotating stall and surge.

Measured mass flow rate, $\dot{m}$, and impeller speed, N, were corrected to 101.3 kPa reference pressure and 288.15 K reference temperature.

4 Definition of Parameters

Station 0 denotes impeller inlet, station 1 diffuser inlet radius, station 2 diffuser exit radius, and station 3 the plenum after the diffuser exit, and station *th* denotes the throat of the diffuser. The axial direction is taken from the front wall where $x = 0$, to the rear wall where $x = b$. The flow angle, α, is defined as the angle from the radial direction. At each steady-state operating point, the values of the diffuser inlet total pressure profile and flow angle were measured at one tangential location ($\theta = 0$ deg) and at 15 axially distributed points. The gradients of the flow field parameters are larger near the diffuser walls than the center plane so that closer spacing was used in the former. Diffuser performance was assessed in terms of inlet parameters calculated from this traverse data.

Table 2 Dimensions of the two discrete-passage diffusers tested

	30 Passage Diffuser	38 Passage Diffuser
Inlet Radius, r_1	0.203 m	0.203 m
Inlet Width, b_1	0.009 m	0.009 m
Exit Radius, r_2	0.281 m	0.281 m
Diffuser Throat Diameter	0.013 m	0.011 m
Geometric Inlet Angle	69°	70.1°
Area Ratio, AR	4.29	4.37
Diffuser Length-to-Diameter Ratio, LDR	8.75	9.44

The Mach number profile at the diffuser inlet, $M_1(x)$, was determined from distribution of total pressure, $P_t(x)$, and inlet static pressure at that position. Using the Mach number distribution at the diffuser inlet, a mass-averaged inlet Mach number is calculated. To assess the data consistency, comparison was made between the measured mass flow rate using the venturi flow meter and the mass flow rate calculated from integration of the diffuser inlet traverse data. Agreement was within ± 5 percent, which was judged satisfactory.

It is necessary to have a consistent and reliable way of defining and determining the average inlet flow angle to the diffuser. The average diffuser inlet flow angle, α_1, is defined in terms of tangential and radial mass-averaged velocities at the diffuser inlet as:

$$\alpha_1 = \tan^{-1}\left[\frac{\hat{V}_{\theta 1}}{\hat{V}_{r1}}\right] \tag{5}$$

where

$$\hat{V}_{\theta 1} = \frac{\int_0^b \rho_1 V_{r1} V_{\theta 1} 2\pi r_1 dx}{\int_0^b \rho_1 V_{r1} 2\pi r_1 dx} \tag{6}$$

and

$$\hat{V}_{r1} = \frac{\int_0^b \rho_1 V_{r1} V_{r1} 2\pi r_1 dx}{\int_0^b \rho_1 V_{r1} 2\pi r_1 dx} \tag{7}$$

Since the mass-averaged tangential and radial velocities represent the tangential and radial momentum of the diffuser inlet flow, the average flow angle given by Eq. (5) is termed "momentum-averaged" flow angle, which is used in all the diagrams in the entire paper. Another way of defining inlet flow angle is by

mass-averaging of the measured inlet flow angle axial distribution. In the present experiments differences between the momentum-averaged and mass-averaged flow angles were smaller than 0.3 deg. This is small, but should not be dismissed as negligible, since the range of inlet flow angle between maximum flow rate and stall could be only 5 degrees.

Diffuser inlet flow angle nonuniformity, α_n, is defined as the root mean square (rms) deviation of the local flow angle, α, from the momentum-averaged value, $\hat{\alpha}$:

$$\alpha_n = \sqrt{\frac{1}{b}\int_0^b (\alpha - \hat{\alpha})^2 dx} \tag{8}$$

Based on information from single-channel diffuser investigations, blockage is generally considered to have an important effect on radial diffuser pressure recovery, with pressure recovery decreasing as inlet blockage increases. The diffuser inlet blockage is defined as:

$$B = 1 - \frac{A_{\text{effective}}}{A_{\text{geometric}}} \tag{9}$$

In Eq. (9), $A_{\text{geometric}}$ is the geometric area at the diffuser inlet radius and $A_{\text{effective}}$ is the area effectively used by the flow. $A_{\text{effective}}$ was calculated using the static pressure and the mass-averaged total pressure at the diffuser inlet.

In addition to the average diffuser inlet flow field quantities, various parameters were used to quantify the severity of the inlet flow field nonuniformity; inlet flow direction and blockage were referred to above. Detailed description and presentation of inlet flow field profiles in terms of distortion and skew parameters of mass, momentum, energy, and flow angle for the investigated discrete-passage diffusers can be found in Filipenco (1991) and Johnston (1993). For the investigations with discrete-passage diffusers the blockage at the diffuser inlet is quantified with the "mass-flux deficit," σ_m:

$$\sigma_m = \frac{\delta_m}{b} = \frac{\int_0^b [(\rho V_r)_{\max} - \rho V_r] 2\pi r_1 dx}{b(\rho V_r)_{\max} 2\pi r_1} \tag{10}$$

The parameter, δ_m, in Eq. (10) is essentially the displacement thickness at the diffuser inlet and gives the fraction of the mass flow "lost" relative to the mass flow that would have been attained if the profile were uniform with a value of velocity and flow angle corresponding to the local maximum value of mass-flux within the diffuser inlet. The mass-flux deficit values for 30 and 38 passage discrete-passage diffusers were 0.13–0.35 and 0.05–0.45, respectively. These ranges of mass-flux deficit, and skew achieved includes values above and below of those produced by typical centrifugal compressor impellers. The diffuser inlet Mach number investigated ranged from 0.1 up to 1.1. The Reynolds numbers (based on the diffuser inlet depth, b, and the inlet mass-averaged properties) were in the range of $1.2–9.2 \times 10^4$. The performance of the impeller was initially measured using a 1.20 radius ratio vaneless diffuser.

Using the data from the wall static pressure taps along the axial projection of the diffuser passage centerline, the static pressure coefficient along the diffuser centerline, $Cp(\xi/L)$, is defined as:

$$Cp(\xi/L) = \frac{P_s(\xi/L) - P_{s1}}{\hat{P}_{t1} - P_{s1}} \tag{11}$$

In Eq. (11), $\hat{P}_{t1}$ is "mass-averaged" diffuser inlet total pressure.

5 Results

A range of operating points along constant corrected speed lines were set up, from maximum flow rate to the onset of the flow instability in the diffuser, with various combinations of profile control slot injection/suction (including no injection/suction) to obtain a range of diffuser inlet Mach numbers, flow angles, profile distortions, and skew.

At each impeller corrected speed the minimum flow limit was marked by the breakdown of the axisymmetric flow regime in the impeller/diffuser; this was signaled by an audible blowdown of the plenum through the impeller inlet and also measured with high-frequency response pressure transducers.

5.1 Diffuser Inlet Flow Distributions. Diffuser inlet traverse data were obtained at corrected impeller speeds of 2000, 4000, and 6000 rpm, first with the inlet flow field as uniform as possible, generally without slot injection/ suction. The experiments were then repeated with progressively increased slot injection/ suction to produce increasingly skewed diffuser inlet profiles. Examples of diffuser inlet flow angle and Mach number axial profiles are shown in Fig. 5.

5.2 Diffuser Performance as a Function of Inlet Flow Angle, Distortion, and Mach Number. For the 30 passage discrete-passage diffuser, the overall diffuser pressure recovery coefficient, based on different averaging methods for the diffuser inlet flow field distributions, is plotted in Fig. 6(*a–d*) as a function of momentum-averaged flow angle at diffuser inlet (as defined by Eq. (5)). The curves, which are for constant corrected impeller speeds, go from maximum flow rate (on the left) to stall (on the right). Figure 6(*a–d*) contains all the operating points, with and without injection/suction (i.e., some with high blockage and high skew).

Availability-Averaged Pressure Recovery Coefficient. In Fig. 6(*a*), the diffuser overall pressure recovery coefficient, based on the availability-average of inlet stagnation pressure as defined by Eq. (3), correlates well with the momentum-averaged inlet flow angle over most of the diffuser operating range, except for the three leftmost points, which are caused by choking of the diffuser throat. These points will be discussed in section 5.4. The diffuser pressure recovery increases monotonically with increasing inlet flow angle, almost independent of inlet flow field axial distortion and diffuser inlet Mach number.

Mass-Averaged Pressure Recovery Coefficient. Although Fig. 6(*a*) is based on availability-averaged inlet dynamic pressure, the plots would be almost identical if the pressure recovery coefficient were based on mass-averaged inlet dynamic pressure. (As stated, the discrepancy between availability-averaged and mass-averaged inlet dynamic pressure was never greater than 1.6 percent, smaller than the scatter in the data).

Other Averaging Methods for Pressure Recovery Coefficient. For comparison, Figs. 6(*b*), 6(*c*), and 6(*d*) show same data as in Fig. 6(*a*), but plotted in terms of diffuser pressure recovery coefficient based on alternative definitions of the measured diffuser inlet total pressure, as mentioned before (see section 2). In Fig. 6(*b*), the discrete-passage diffuser overall pressure recovery coefficient, Cp_a, is based on the area-averaged dynamic pressure at inlet. In this case, insensitivity to Mach number is still observed but the increase in diffuser inlet flow field distortion, due to injection/suction, results in an increase in diffuser pressure recovery. Figure 6(*c*) shows the data plotted in terms of a pressure recovery coefficient, Cp_b, based on the peak value of the dynamic pressure at diffuser inlet. There is increased sensitivity of the diffuser pressure recovery to inlet conditions, with a decrease in pressure recovery as inlet flow field distortion increases. Figure 6(*d*) shows the diffuser pressure recovery coefficient, Cp_c, based on area-averaged velocity at diffuser inlet. A strong dependence of the diffuser pressure recovery performance on inlet flow field distortion is observed and an increase of diffuser inlet Mach number is seen to result in an increase of the diffuser pressure recovery coefficient.

Comparison of Figs. 6(*a)* through 6(*d*) shows that use of dif-

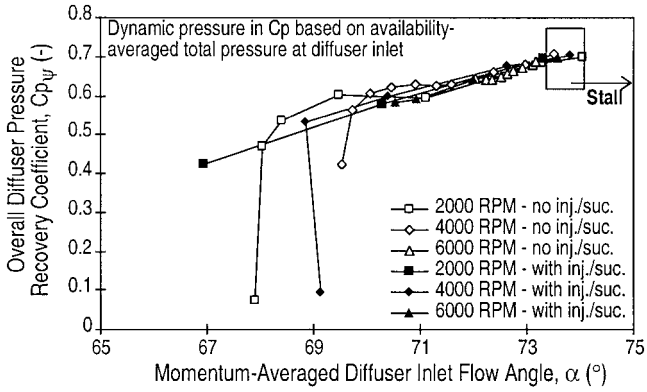

Fig. 6(*a*) Availability-averaged overall discrete-passage diffuser (30 passages) pressure recovery coefficient, Cp_ψ, versus momentum-averaged diffuser inlet flow angle, α.

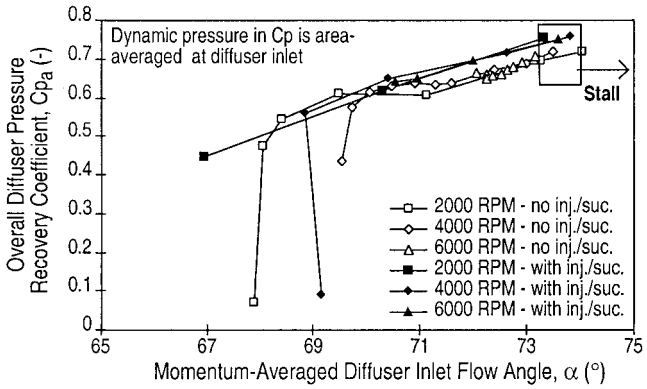

Fig. 6(*b*) Overall discrete-passage diffuser (30 passages) pressure recovery coefficient, Cp_a, based on the diffuser inlet area-averaged dynamic pressure versus momentum-averaged diffuser inlet flow angle, α.

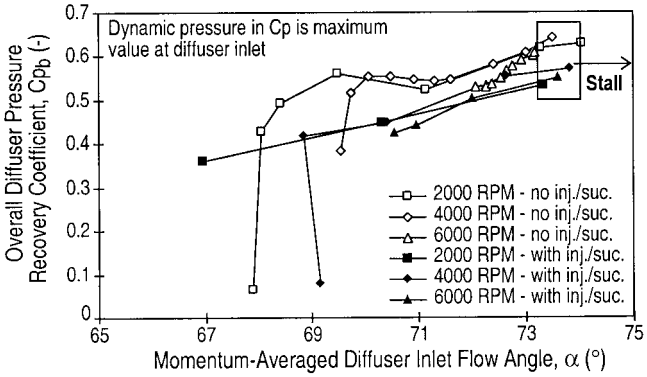

Fig. 6(*c*) Overall discrete-passage diffuser (30 passages) pressure recovery coefficient, Cp_b, based on the diffuser inlet local maximum total pressure versus momentum-averaged diffuser inlet flow angle, α.

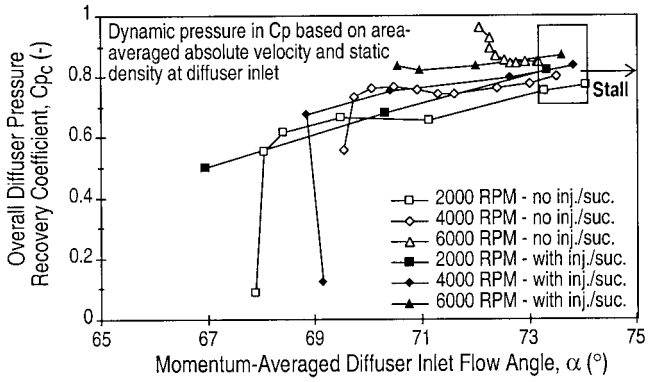

Fig. 6(*d*) Overall discrete-passage diffuser (30 passages) pressure recovery coefficient, Cp_c, based on the diffuser inlet area-averaged absolute velocity and static density versus momentum-averaged diffuser inlet flow angle, α.

ferent diffuser pressure recovery parameters that have been used by various investigators for correlating diffuser performance data can lead to different conclusions on the effect of inlet flow field distortion and Mach number on diffuser pressure recovery. The results show that when pressure recovery coefficient is based on availability and/or mass-averaged inlet total pressure the average flow angle at diffuser inlet is, overwhelmingly, the most important variable; inlet blockage, skew, and Mach number have only minor effects.

Figure 7 presents a summary plot of measurements for both the 30 and 38-passage diffusers and for three constant corrected impeller speeds. This plot contains data obtained using the pressure recovery coefficient based on the availability-averaged inlet total pressure with and without injection/suction at diffuser inlet. Both diffusers show the comparable level of pressure recovery and range of unstalled operation and both are similarly insensitive to inlet flow field distortion and Mach number.

5.3 Diffuser Stalling Condition. Stall of the discrete-passage diffuser occurs at a momentum-averaged flow angle ($\alpha_{crit} = 73.5 \pm 0.5$ deg) independent, to within experimental error, of the inlet flow field axial distortion and diffuser inlet Mach number. Using a total pressure/flow angle probe at diffuser inlet can change the stall onset of the diffuser and/or overall test rig and a test was therefore carried out at 4000 rpm with the 38-passage diffuser in which the total pressure/flow angle probe was removed. This was with no injection/suction, because with the total pressure/flow angle probe removed there is uncertainty in inlet conditions; comparisons without injection/suction are less subject to this uncertainty. The diffuser pressure recovery was found to be unaffected by the removal of the probe but rotating stall was found to occur at a mass flow 10 percent smaller than with the probe present, showing that the blockage due to even this small probe can have a noticeable effect on diffuser operating range. From this decrease in mass flow, one can estimate the change in inlet flow angle, assuming circumferential symmetry and an axial profile identical to that with the probe present. If this is done the stall point is increased by 0.45 deg compared to with the probe present.

5.4 Static Pressure Distribution in Diffuser Passage and in Quasi-Vaneless Space. The static pressure distributions along the axis of an individual diffuser passage (30-passage diffuser) are shown in Fig. 8 for two corrected impeller speeds, 2000 and 6000

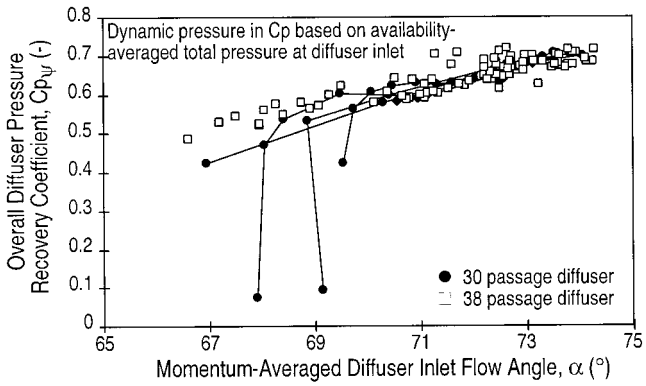

Fig. 7 Comparison of overall diffuser pressure recovery coefficient between 30 and 38 passage discrete-passage diffusers

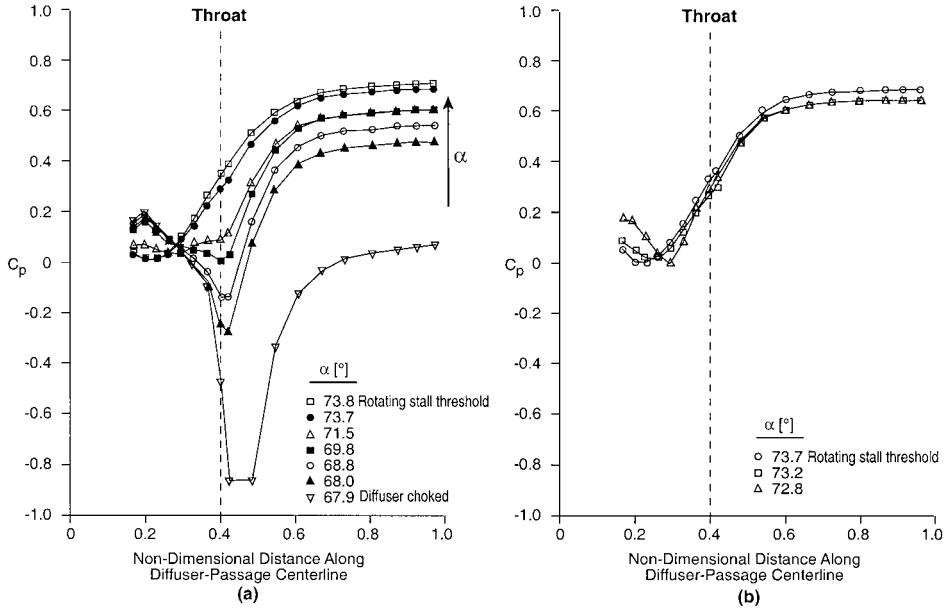

Fig. 8 Static pressure distribution along discrete passage diffuser passage centerline (30 passages) at (*a*) 2000 rpm, and (*b*) 6000 rpm, for flow angles from maximum flow rate to rotating stall threshold

rpm, for inlet flow angles from the minimum up to that just prior to stall. The static pressure in this figure is represented by the pressure coefficient defined in Eq. (11) with inlet dynamic pressure based on the mass-averaged total pressure. The maximum diffuser pressure recovery is achieved, for all corrected impeller speeds, at flow angles just prior to rotating stall. At this flow angle, over 90 percent of the overall static pressure rise occurs within the first 60 percent of the diffuser passage length. This trend of pressure rise is similar in most other operating points (flow angles) shown in Fig. 8 except for the choked condition.

For low flow angles, the diffuser pressure recovery upstream of the diffuser throat ($\xi/L = 0.40$) decreases at 2000 rpm and the overall diffuser pressure recovery is thus small (see also Fig. 6(*a*)). For these cases the diffuser inlet flow angle is less than the diffuser throat centerline angle and the flow must accelerate as it approaches the throat. The large static pressure drop upstream of the diffuser throat occurs at 2000 rpm for the lowest flow angle ($\alpha =$ 67.9 deg) because the velocity becomes sonic at the throat and the diffuser chokes.

The three points in Fig. 6(*a*) with the lowest pressure recovery values all have low diffuser inlet flow angles, and Mach numbers at the diffuser inlet, which were between 0.7 and 0.9. For flow angles smaller than the diffuser centerline angle the flow must accelerate up to the throat, and for these relatively high inlet Mach numbers this gives sonic velocity at the throat; one effect of choking the flow is much reduced pressure recovery. The combination of low flow angle and high inlet Mach number required the use of the downstream slave compressor, which was only used for the tests with the 30-passage discrete-passage diffuser. When the diffuser inlet Mach number was raised by increasing the rotational speed of the impeller, but without using the slave compressor, the inlet angle could not be brought down to the low values required to induce an acceleration into the throat. At higher impeller rotational speeds than those possible in these tests, choking would be induced without the need for low inlet angles, and the subsequent acceleration up to the diffuser throat, just as it can be for real compressor stages at sufficiently high impeller speeds. For the 38-passage discrete-passage and straight-channel diffusers, measurements with high Mach numbers at the diffuser inlet are all with the diffuser inlet flow angles equal to or greater than the throat centerline angle, so that the flow is decelerated as it approaches the throat; no choking at the throat is therefore observed.

When there is no suction or injection of flow between the impeller and the diffuser inlet, the average diffuser inlet flow angle is a function only of the impeller rotational speed and the overall pressure ratio across the machine. When injection or suction are applied in the vaneless space, an additional degree of freedom for determining diffuser inlet flow angle is introduced in our test rig. Some of the points in Figs. 6 and 7 for which the inlet flow angle was small were produced by using air injection with fairly high plenum back pressure. In these cases, a relatively small average flow angle at the diffuser inlet was obtained at a low average inlet Mach number and there was no choking of the diffuser.

The static pressure distribution in the quasi-vaneless space of the discrete-passage diffuser (as shown in detail by Filipenco, 1991) depends on the diffuser operating point (flow angle) rather than diffuser inlet Mach number, because the distributions are similar for all investigated corrected impeller speeds. There is a loading on the leading-edge cusps in the quasi-vaneless space with a consistent reversal of the loading from diffuser choke to stall over the range of diffuser inlet Mach numbers investigated. In addition, at any given operating point, there is a reversal of the loading across the leading edge cusps along the axial direction of the passage between the diffuser inlet and the throat. Near maximum flow rate (low flow angles), the pressure and suction surfaces of the leading edge cusps near the diffuser inlet are loaded so higher pressure is on the pressure surface, while near the throat the loading is reversed. At the near-stall point (high flow angles), the situation reverses, with higher pressure on the suction surface immediately at the diffuser inlet and opposite loading near the throat. This trend was found independent of inlet distortion.

It is hypothesized that mixing in the diffuser inlet region (e.g., in quasi-vaneless space and throat region) plays a major role in the observed insensitivity of the test diffuser performance to inlet flow field distortion. Filipenco (1991) has presented some basic calculations to support this. In the diffuser inlet region, the flow undergoes a transition from a nearly tangential swirling flow to a channel flow in the diffuser passage. The experimental investigations by Krain (1984) and Casey et al. (1995a) showed that the highly distorted impeller exit flow in both the circumferential and axial directions was almost wholly attenuated after the throat in channel part of the vaned diffuser, also indicating a rapid mixing process in the diffuser inlet region (in vaneless and quasi-vaneless spaces).

6 Summary and Conclusions

A test facility was developed for the study of centrifugal compressor diffuser performance over a wide range of diffuser inlet conditions. The facility allows for inlet Mach numbers up to unity with inlet flow angles of 63 to 75 deg from radial. Injection and/or suction in the vaneless space between the impeller exit and diffuser inlet allows the flow field entering the diffuser to be varied. The range of diffuser inlet blockage and axial flow nonuniformity achieved includes values above and below those produced by typical centrifugal compressor impellers.

Alternative definitions of diffuser overall pressure recovery coefficient for cases of nonuniform diffuser inlet conditions were examined and a definition of diffuser pressure recovery coefficient based on diffuser inlet availability-averaged total pressure was found to be most appropriate. The numerical results using availability averaging agreed closely (maximum 1.6 percent difference in inlet dynamic pressure) with the more widely used mass-averaged results. Pressure recovery coefficients based on mass-averaged inlet dynamic pressure will thus be adequate for most practical purposes and will be used for presenting results in Part 2 of this paper.

For both the discrete-passage diffusers investigated, the overall diffuser pressure recovery coefficient based on the availability-averaged (or the mass-averaged) diffuser inlet total pressure depends essentially on diffuser inlet momentum-averaged flow angle. The pressure recovery coefficient defined in this way is nearly independent of inlet flow field axial distortion and Mach number.

The pressure recovery performance of the two discrete-passage diffusers, tested with 30 and 38 passages, was virtually identical. For both diffusers, the stable, axisymmetric flow entered rotating stall at a critical value of momentum-averaged flow angle into the diffuser, independent of the diffuser inlet flow field distortion and Mach number.

The static pressure coefficient distribution in the quasi-vaneless space suggests that mixing in the diffuser inlet region plays an important role in the observed insensitivity of the pressure recovery performance to inlet flow field distortion.

Acknowledgments

Major funding for this work was provided by General Electric Aircraft Engines. Additional support was provided by the US Army Research Office under Grant DAAL 03-90-G-0138, Dr. T. Dologalski, Program Manager, and by the AFRAPT Program of the Air Force Office of Scientific Research. We are grateful to Dr. C. J. Russo for the initiation of this project, and to Dr. R. Markytan and the late Mr. L. King of General Electric for many helpful suggestions during the course of work.

References

Al-Mudhafar, M. M., Ilyas, M., and Bhinder, F. S., 1982, "Investigation of Flows in Rectangular Diffusers With Inlet Flow Distortion," ASME Paper No. 82-GT-67.

Baghdadi, S., and McDonald A. T., 1975, "Performance of Three Radial Vaned Diffusers With Swirling Transonic Flow," ASME *Journal of Fluids Engineering*, Vol. 97, pp. 155–173.

Baghdadi, S., 1976, "The Effect of Rotor Blade Wakes on Centrifugal Compressor Diffuser Performance—A Comparative Experiment," in: *Centrifugal Compressor and Pump Stability, and Surge*, ASME, pp. 121–138; ASME *Journal of Fluids Engineering*, Vol. 99, No. 1, 1977, pp. 45–52.

Bhinder, F. S., Al-Mudhafar, M. M., and Ilyas, M., 1984, "Further Data on the Performance of a Rectangular Diffuser in Distorted Inlet Flows," ASME Paper No. 84-GT-64.

Casey, M. V., Eisele, K., Zhang, Z., Gülich, J., and Schachenmann, A., 1995a, "Flow Analysis in a Pump Diffuser, Part 1: LDA and PTV Measurements of the Unsteady Flow," *Laser Anemometry*, ASME FED-Vol. 229, pp. 89–100.

Casey, M. V., Eisele, K., Muggli, F. A., Gülich, J., and Schachenmann, A., 1995b, "Flow Analysis in a Pump Diffuser, Part 2: Validation of a CFD Code for Steady Flow," *Numerical Simulations in Turbomachinery*, ASME FED-Vol. 227, pp. 135–143.

Clements, W. W., 1987, "A Theoretical and Experimental Study of Diffusion Levels in Centrifugal Compressor Stages," Dissertation, Faculty of Engineering, University of Belfast.

Dalbert, P., Gyarmathy, G., and Sebestyen, A., 1993, "Flow Phenomena in a Vaned Diffuser of a Centrifugal Stage" ASME Paper No. 93-GT-53.

Dawes, W. N., 1995, "A Simulation of the Unsteady Interaction of a Centrifugal Impeller With Its Vaned Diffuser: Flow Analysis," ASME JOURNAL OF TURBOMACHINERY, Vol. 117, pp. 213–222.

Deniz, S., Greitzer, E. M., and Cumpsty, N. A., 2000, "Effects of Inlet Flow Field Conditions on the Performance of Centrifugal Compressor Diffusers: Part 2 — Straight-Channel Diffuser," ASME JOURNAL OF TURBOMACHINERY, Vol. 122, this issue, pp. 11–21.

Dutton, J. C., Piemsomboon, P., and Jenkins, P. E., 1986, "Flowfield and Performance Measurements in a Vaned Radial Diffuser," ASME *Journal of Fluids Engineering*, Vol. 108, pp. 141–147.

Elder, R. L., and Gill, M. E., 1985, "A Discussion of the Factors Affecting Surge in Centrifugal Compressors," ASME *Journal of Engineering for Gas Turbines and Power*, Vol. 107, pp. 499–506.

Filipenco, V. G., 1991, "Experimental Investigation of Flow Distortion Effects on the Performance of Radial Discrete-Passage Diffusers," MIT GTL Report No. 206, Sept., Cambridge, Massachusetts, Dissertation.

Haupt, U., Seidel, U., Abdelhamid, A. N., and Rautenberg, M., 1988, "Unsteady Flow in a Centrifugal Compressor With Different Types of Vaned Diffusers," ASME JOURNAL OF TURBOMACHINERY, Vol. 110, No. 3, pp. 293–302.

Hunziker, R., and Gyarmathy, G., 1994, "The Operational Stability of a Centrifugal Compressor and Its Dependence on the Characteristics of the Subcomponents," ASME JOURNAL OF TURBOMACHINERY, Vol. 116, pp. 250–259

Inoue, M., and Cumpsty, N. A., 1984, "Experimental Study of Centrifugal Impeller Discharge Flow in Vaneless and Vaned Diffusers," ASME *Journal of Engineering for Gas Turbines and Power*, Vol. 106, pp. 455–467.

Japikse, D., 1984, "Turbomachinery Diffuser Design Technology," *The Design Technology Series* (DTS-1), Concepts ETI, Inc., Norwich, VT.

Japikse, D., and Osborne, C., 1986, "Optimization of Industrial Centrifugal Compressors; Part 6B: Studies in Component Performance—Eight Design Cases From 1972 to 1982," ASME Paper No. 86-GT-222.

Japikse, D., 1987, "The Technology of Centrifugal Compressors: A Design Approach and New Goals for Research," in: *Flow in Centrifugal Compressors*, Von Karman Institute, Lecture Notes.

Japikse, D., 1996, "Centrifugal Compressor Design and Performance," Concepts ETI, Inc., Norwich, VT.

Johnston, J. M., 1993, "Stall Onset Observations of a Discrete Passage Diffuser," MIT GTL Report No. 217, April, Cambridge, MA, M. Sc. Thesis.

Kano, F., Tazawa, N., and Fukao, Y., 1982, "Aerodynamic Performance of Large Centrifugal Compressors," ASME *Journal of Engineering for Power*, Vol. 104, No. 2.

Kenny, D. P., 1972, "A Comparison of the Predicted and Measured Performance of High Pressure Ratio Centrifugal Compressor Diffusers," ASME Paper No. 72-GT-54.

Klein, A., 1981, "Review: Effects of Inlet Conditions on Conical-Diffuser Performance," ASME *Journal of Fluids Engineering*, Vol. 103, pp. 250–257.

Krain, H., 1981, "A Study on Centrifugal Impeller and Diffuser Flow," ASME *Journal of Engineering for Power*, Vol. 103, pp. 1–10.

Krain, H., 1984, "Experimental Observation of the Flow in Impellers and Diffusers," in *Flow in Centrifugal Compressors*, Von Karman Institute for Fluid Dynamics, Lecture Series No. 1984-07.

Livesey, J. L., and Hugh, T., 1966, "Suitable Mean Values in One-Dimensional Gas Dynamics," *Journal Mechanical Engineering Science*, Vol. 8, No. 4, pp. 374–383.

Masuda, H., Ariga, I., and Watanabe, I., 1971, "On the Behavior of Uniform Shear Flow in Diffusers and Its Effects on Diffuser Performance," ASME *Journal of Engineering for Power*, pp. 377–385.

Mishina, H., and Nishida, H., 1984 "Effect of Relative Velocity Distribution on Efficiency and Exit Flow Angle," ASME Paper No. 83-GT-74.

Rodgers, C., 1982, "The Performance of Centrifugal Compressor Channel Diffusers," ASME Paper No. 82-GT-10.

Runstadler, P. W. J., Dolan, F. X., and Dean, R. C. J., 1975, "Diffuser Data Book," Technical Note TN-186, Creare, Inc., Hanover, NH.

Stein, W., and Rautenberg. M., 1985, "Flow Measurements in Two Cambered Vane Diffusers With Different Passage Widths," ASME Paper No. 85-GT-46.

Teipel, I., Wiedermann, A., and Evers, W., 1992, "Viscous Flows in Centrifugal Compressor Diffusers at Transonic Mach Numbers," ASME Paper No. 92-GT-48.

Wolf, S., and Johnston, J. P., 1969, "Effects of Nonuniform Inlet Velocity Profiles on Flow Regimes and Performance in Two-Dimensional Diffusers," ASME *Journal of Basic Engineering*, Vol. 91, pp. 462–474.

Yoshinaga, Y., Gyobu, I., Mishina, H., Koseki, F., and Hishida, N., 1980, "Aerodynamic Performance of a Centrifugal Compressor With Vaned Diffusers," ASME *Journal of Fluids Engineering*, Vol. 102, pp. 486–493.

Effects of Inlet Flow Field Conditions on the Performance of Centrifugal Compressor Diffusers: Part 2—Straight-Channel Diffuser

S. Deniz[1]

E. M. Greitzer

Gas Turbine Laboratory,
Massachusetts Institute of Technology,
Cambridge, MA 02139

N. A. Cumpsty
Whittle Laboratory,
Department of Engineering,
Cambridge University,
Cambridge CB3 ODY, United Kingdom

This is Part 2 of an examination of the influence of inlet flow conditions on the performance and operating range of centrifugal compressor vaned diffusers. The paper describes tests of a straight-channel type diffuser, sometimes called a wedge-vane diffuser, and compares the results with those from the discrete-passage diffusers described in Part 1. Effects of diffuser inlet Mach number, flow angle, blockage, and axial flow nonuniformity on diffuser pressure recovery and operating range are addressed. The straight-channel diffuser investigated has 30 vanes and was designed for the same aerodynamic duty as the discrete-passage diffuser described in Part 1. The ranges of the overall pressure recovery coefficients were 0.50–0.78 for the straight-channel diffuser and 0.50–0.70 for the discrete-passage diffuser, except when the diffuser was choked. In other words, the maximum pressure recovery of the straight-channel diffuser was found to be roughly 10 percent higher than that of the discrete-passage diffuser investigated. The two types of diffuser showed similar behavior regarding the dependence of pressure recovery on diffuser inlet flow angle and the insensitivity of the performance to inlet flow field axial distortion and Mach number. The operating range of the straight-channel diffuser, as for the discrete-passage diffusers, was limited by the onset of rotating stall at a fixed momentum-averaged flow angle into the diffuser, which was for the straight-channel diffuser, $\alpha_{crit} = 70 \pm 0.5$ deg. The background, nomenclature, and description of the facility and method are all given in Part 1.

1 Introduction

In Part 1 (Filipenco et al., 2000), we examined the influence of inlet flow field conditions on the performance of discrete-passage diffusers. In Part 2 we present the results of investigations of this topic for straight-channel diffusers as well as comparing the results for the two types of radial diffuser. The effects of diffuser inlet Mach number, flow angle, axial flow nonuniformity, and blockage on diffuser pressure recovery and onset of instability are addressed. The test facility, instrumentation, and parameters used are described in Part 1.

Straight-channel diffusers are used by a large number of turbomachinery companies. The configuration is both simple to manufacture and yields good performance (Krain, 1984; Kano et al., 1982; Rodgers, 1982). The starting point for the design of the straight-channel test diffuser is often a diffuser map (e.g., Reneau et al., 1967) for single-channel two-dimensional diffusers to select geometric diffuser parameters: diffuser channel divergence angle 2θ, area ratio AR, and length-to-width ratio LWR. Selected diffusers are often designed very close to the line of maximum pressure recovery and in the flow regime of no appreciable stall. According to the measurements by Yoshinaga et al. (1980), the optimal diffuser divergence angle for straight-channel type radial diffuser is in the range 8 to 10 deg.

To make direct use of single-channel diffuser performance data, the blockage at inlet should be given. Investigations for single channel diffusers had shown that diffuser pressure recovery decreases significantly as inlet blockage increases, for example Runstadler and Dean (1969) and Runstadler and Dolan (1973). The diffuser pressure recovery coefficient used by Runstadler is based on dynamic pressure calculated from the velocity at the center of the inlet section. For the same diffuser geometries that Runstadler used, Dong (1996) recalculated the pressure recovery coefficient based on mass-averaged total pressure at diffuser inlet and found that the dependence of pressure recovery on inlet blockage is much less (see for comparison Fig. 1). Recently Yaras (1996) also investigated the effects of inlet conditions on the flow in a fishtail curved diffuser and found that both the pressure recovery coefficient based on mass-averaged inlet total pressure and mass-averaged total pressure losses through the diffuser are observed to be relatively insensitive to variations in the diffuser inlet boundary layer.

For centrifugal compressor vaned diffusers, blockage should be defined at the diffuser throat, because the channel part of the centrifugal compressor vaned diffuser is geometrically similar to single-channel diffusers. There are almost never experimental data available at diffuser throat, but the throat blockage can be estimated (if it can be defined at diffuser inlet) by assuming isentropic flow from diffuser inlet to throat. It is also sometimes estimated from measurements of the diffuser pressure recovery from the diffuser inlet to the throat, adopting the approach first suggested by Kenny (1972), to derive a correlation between throat blockage and pressure rise. Calculation of throat blockage for the straight-channel diffuser tested here and performance comparisons with single channel diffuser data can be found in Deniz (1997).

The straight-channel diffuser investigated was designed to accept similar inlet conditions obtained in the discrete-passage diffuser tests described in Part 1. The overall inlet conditions for the

[1] Current address: Praxair, Inc., Technology Center, Tonawanda, NY 14151.

Contributed by the International Gas Turbine Institute and presented at the 43rd International Gas Turbine and Aeroengine Congress and Exhibition, Stockholm, Sweden, June 2–5, 1998. Manuscript received by the International Gas Turbine Institute February 1998. Paper No. 98-GT-474. Associate Technical Editor: R. E. Kielb.

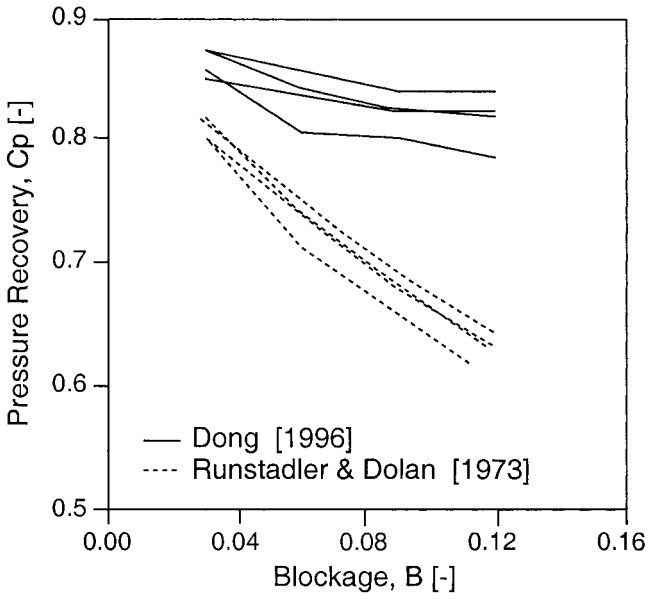

Fig. 1 Pressure recovery coefficient, *Cp*, as a function of inlet blockage, B_1, for single-channel diffusers with different area ratios and divergence angles; comparison of the data from Dong (1996) (*Cp* is based on mass-averaged diffuser inlet total pressure) and Runstadler and Dolan (1973) (*Cp* is based on diffuser inlet centerline total pressure)

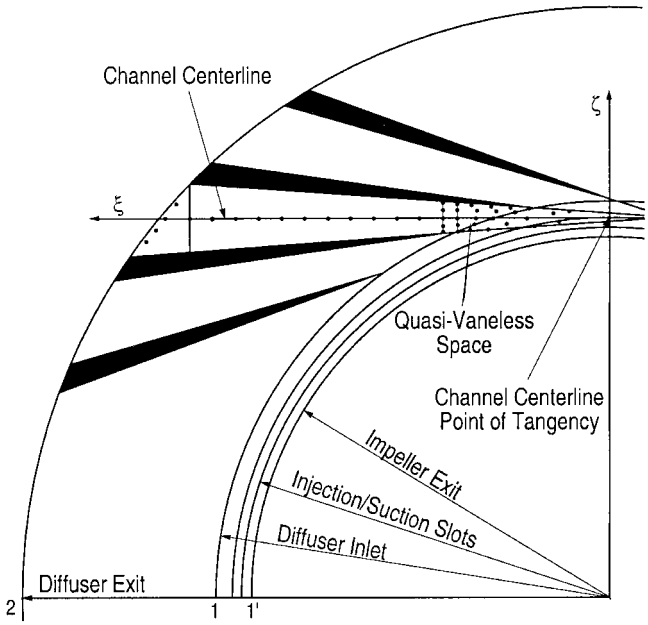

Fig. 2 Straight-channel diffuser geometry and static pressure tap locations

straight-channel diffuser design, i.e., the mean inlet flow angle, α, the number of vanes, the vaneless space radius ratio, the axial depth, b, and throat area, A_{th}, were therefore chosen to be similar to those of the discrete-passage diffuser. The main dimensions of the straight-channel diffuser and discrete-passage diffuser are given in Table 1. Figure 2 shows straight-channel diffuser geometry and the locations of channel centerline, vaneless, and quasi-vaneless space static pressure taps.

In Part 1 different definitions for averaging the nonuniform total pressure at inlet to the diffuser and the pressure recovery coefficient were described. Depending on the method used, the data can collapse into a narrow trend, or spread in a manner that is difficult to understand. The availability-averaged total pressure was selected as the most physically appropriate one to be used in defining the diffuser pressure recovery coefficient, but it was also found that mass-averaged total pressure gave similar values and is easier to use. In Part 1 the difference between availability and mass-averaged diffuser inlet dynamic total pressure was found to be no more than 1.6 percent and for the measurements in this part the difference is no more than 1 percent. The mass-averaged pressure recovery coefficient is sufficiently close to the availability-averaged pressure recovery coefficient so that it will be used throughout Part 2.

Table 1 Parameters for straight-channel and discrete-passage diffuser

	Straight-Channel Diffuser	Discrete-Passage Diffuser
Diffuser Channel Divergence Angle, 2θ	8 deg	
Area Ratio, AR	2.34	4.29
Length to Width Ratio, LWR	9.574	8.75
Number of Diffuser Channels, Z_v	30	30
Aspect Ratio, AS	0.643	
Diffuser Axial Width, b	9.0 mm	9.0 mm
b/r_1	0.044	0.044
$r_1/r_{1'}$	1.10	1.10
$r_2/r_{1'}$	1.64	1.52
Throat Area, A_{th}	0.00013 m^2	0.00013 m^2
Diffuser Centerline Design Angle	69 deg	69 deg
Wedge Angle of Diffuser Vane, β	4.0 deg	

The ranges of blockage, flow nonuniformity, and other parameters achieved include values above and below of those produced by typical centrifugal compressor impellers. They can be summarized for the straight-channel diffuser as follows:

- Diffuser inlet flow angle, α_1, 63–71 deg
- Diffuser inlet Mach number, M_1, 0.2–1.15
- Velocity profile axial-distortion (uniform and nonuniform profiles, inlet flow angle differences up to 45 deg between diffuser rear and front walls)
- Diffuser inlet blockage, B_1, 2–35 percent
- Diffuser inlet Reynolds number, Re_1, 0.4×10^5–2.5×10^5.

2 Results

2.1 Baseline Inlet Flow Field Data Without Air Injection/Suction. The results of four separate data sets are presented. The first data set or baseline (denoted with number I) was carried out without air injection/suction. The diffuser inlet flow angle and Mach number axial profiles were measured for every operating point. For the baseline case (no injection/suction) examples of axial distributions of flow angle and Mach number are shown in Figs. 3(*a*) and 3(*b*) for different corrected impeller speeds from 2000 to 6000 rpm and a constant atmosphere-to-plenum ratio. The profiles of flow angle and Mach number are fairly symmetric at diffuser inlet, although there is an influence of the labyrinth seal leakage shown in the flow angles near the front wall ($x/b = 0$). In Fig. 3(*b*), the diffuser inlet Mach number increases as impeller rotational speed increases and the maximum Mach number achieved at the diffuser inlet was 1.15.

For the baseline case (no injection/suction), the overall diffuser pressure recovery coefficient versus inlet flow angle is shown in Fig. 4. The figure includes all the different corrected impeller speeds examined and data from maximum flow rate to the onset of rotating stall. The pressure recovery coefficient is based on mass-averaged inlet total pressure and the inlet flow angle is the momentum-average. For all speeds the overall diffuser pressure recovery increases from 0.67 to 0.77 as the flow is reduced from maximum ($\alpha \approx 67$ deg) to the near-stall operating point ($\alpha \approx 70.5$ deg). (For constant impeller speed, lower mass flow rate implies

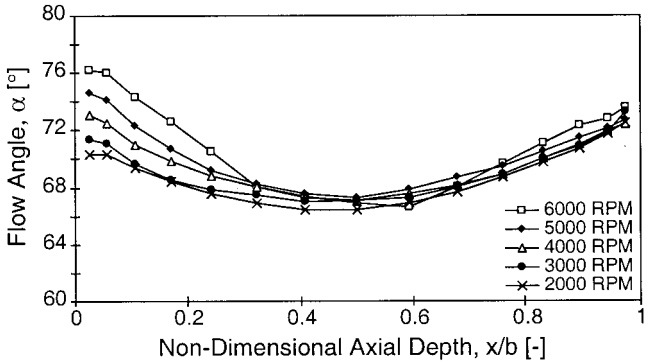

Fig. 3(*a*) Axial distributions of flow angle, α, at the straight-channel diffuser inlet for different corrected impeller speeds (no injection/suction)

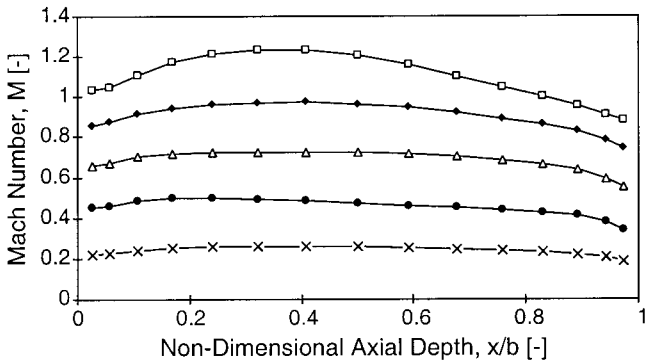

Fig. 3(*b*) Axial distributions of absolute Mach number, M, at the straight-channel diffuser inlet for different corrected impeller speeds (no injection/suction) (same legend as Fig. 3(*a*))

lower radial velocity and therefore increasing flow angle at the diffuser inlet.) Rotating stall appeared when α was between 70 and 70.5 deg for all impeller speeds investigated.

The effect of inlet Mach number on the mass-averaged overall diffuser pressure recovery coefficient is shown in Fig. 5. In this figure, the absolute Mach number at diffuser inlet varies from 0.2 to 1.15 and there is little influence on the mass-averaged overall diffuser pressure recovery coefficient. The observed insensitivity of diffuser pressure recovery on the diffuser inlet Mach number is in accordance with other vaned diffuser investigations, such as Krain (1984) (straight-channel diffuser), Hunziker (1993) (cambered-vane diffuser), and Japikse and Osborne (1986) (different vaned diffusers).

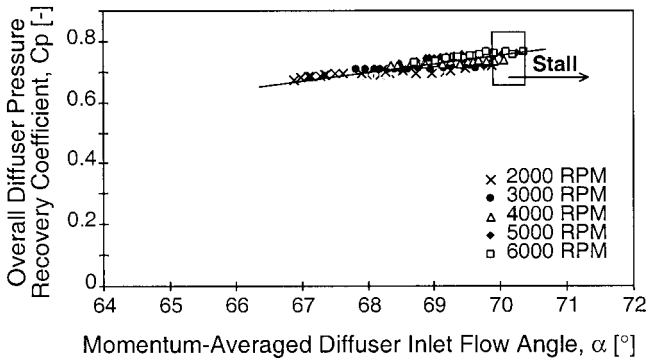

Fig. 4 Mass-averaged overall straight-channel diffuser pressure recovery coefficient, *Cp*, versus momentum averaged diffuser inlet flow angle, α, for different corrected impeller speeds (no/injection/suction)

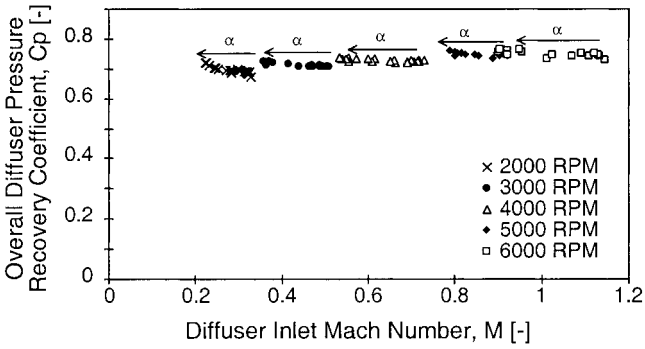

Fig. 5 Mass-averaged overall straight-channel diffuser pressure recovery coefficient, *Cp*, versus diffuser inlet Mach number, M, for different corrected impeller speeds (no injection/suction)

2.2 Influence of Inlet Flow Conditions (Data With Air Injection/Suction). Three series of experiments were undertaken with air injection/suction through the profile control slots in the vaneless space. The three data series are denoted with the numbers II, III, and IV in the legend of Figs. 6 and 7. Inlet conditions to the diffuser include low and high Mach numbers, symmetric and asymmetric profiles, with high and low distortions and blockage levels (see Fig. 6). In the legend of Fig. 6(*a*, *b*, *c*) the average value of the presented flow angle distribution is given together with the flow angle nonuniformity, α_n.

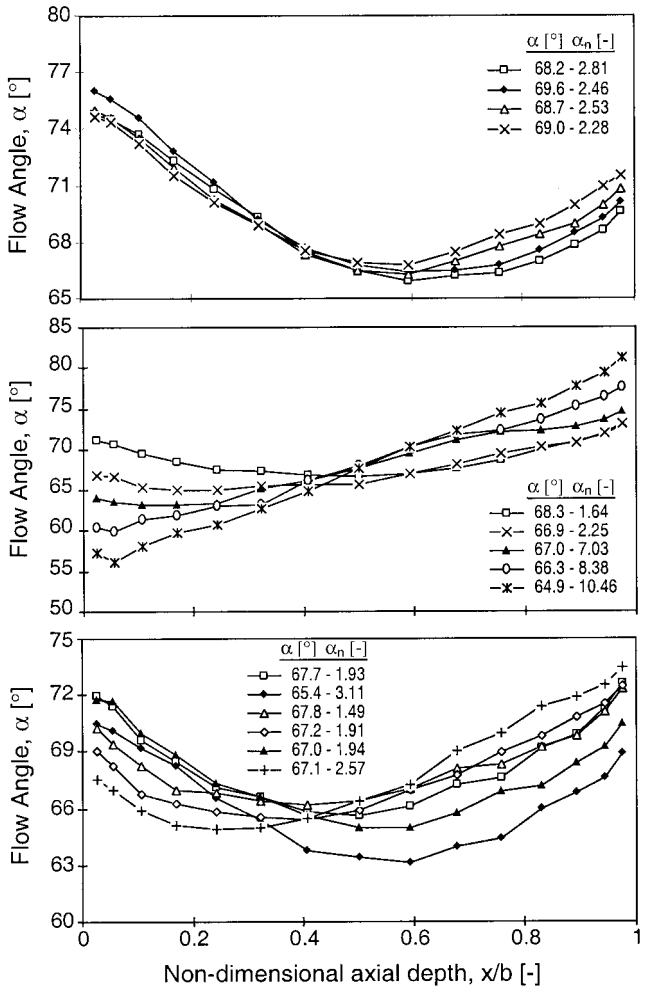

Fig. 6 Examples of flow angle, α, axial distribution at the straight-channel diffuser inlet (with injection/suction): (*a*) Series II, *N* = 5000 rpm, (*b*) Series III, *N* = 2000 rpm, (*c*) Series IV, *N* = 4000 rpm

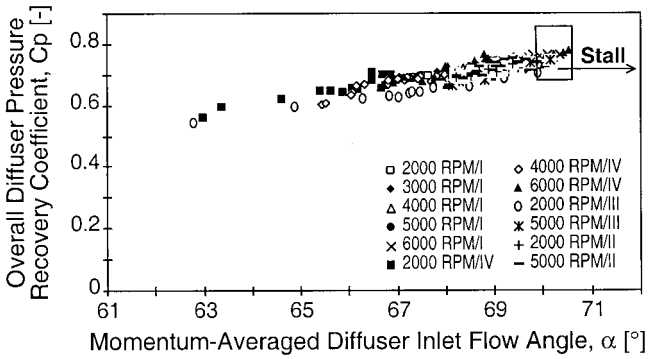

Fig. 7 Mass-averaged overall straight-channel diffuser pressure recovery coefficient, *Cp*, versus momentum averaged diffuser inlet flow angle, *α*, for different corrected impeller speeds and data series (I, II, III, IV) with and without injection/suction

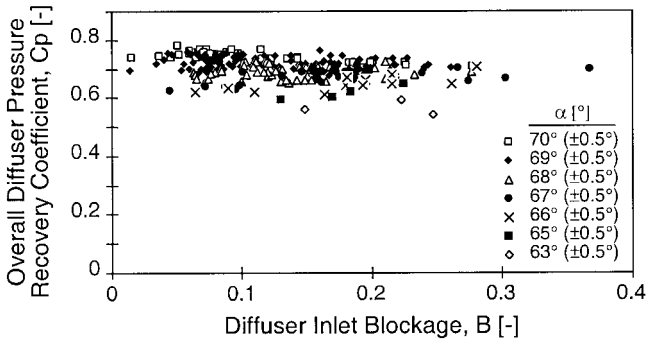

Fig. 8 Mass-averaged overall straight-channel diffuser pressure recovery coefficient, *Cp*, versus diffuser inlet blockage, *B*, with and without injection/suction

For data series II and III, two constant corrected impeller speeds were chosen, a low speed $N = 2000$ rpm (Mach number at diffuser inlet $M_1 \approx 0.2$ to 0.4) and a high speed $N = 5000$ rpm (Mach number at diffuser inlet $M_1 \approx 0.7$ to 1.0). For data series II, for a constant corrected impeller speed and throttle valve position, the applied injection and suction rates were at the same amount (maximum 10 percent of venturi mass flow rate), so that the venturi mass flow rate, $\dot{m}$, remained nearly constant with and without injection suction. The data series (II) thus did not have a high level of velocity nonuniformity at the diffuser inlet as seen in Fig. 6(*a*), where the difference of inlet flow angle between front and rear sides of the diffuser was smaller than 10 deg.

High levels of distortion at the diffuser inlet were obtained in data series III, where inlet distortion was varied from a symmetrical relatively flat distribution to an asymmetrical triangular distribution. Up to 45 deg difference of inlet flow angle between front and rear sides of the diffuser was achieved. Examples of the measured flow angle distributions are shown in Fig. 6(*b*).

Data series IV contains three different impeller speeds: 2000, 4000, and 6000 rpm. At the lowest speed the Mach number range at inlet to the diffuser is 0.2 to 0.4, while at the highest speed it is in the range 0.8 to 1.15. In the series IV data, asymmetric, distorted velocity profiles and also symmetric velocity profiles with different boundary layer blockage levels were applied at the diffuser inlet with both side injection or suction. Some examples of the measured flow angle distributions of series IV are shown in Fig. 6(*c*) for $N = 4000$ rpm. A full list of conditions is given in Deniz (1997).

Figure 7 shows mass-averaged overall pressure recovery coefficient for the straight-channel diffuser as a function of momentum-averaged flow angle into the diffuser for various impeller speeds, throttle valve positions, and inlet distortion parameter levels. The magnitude of the diffuser pressure recovery and operating range are essentially functions of inlet flow angle alone; the onset of rotating stall for the investigated straight-channel diffuser occurred at a momentum-averaged flow angle (70 ± 0.5 deg) independent of the inlet flow field distortion and Mach number. For all data series, with and without injection/suction, the maximum diffuser pressure recovery was achieved just before the rotating stall threshold.

As discussed in the introduction, the conventional view of diffuser performance puts great emphasis on the inlet blockage. Normally it is hard to know the magnitude of the blockage, but in these tests with the straight-channel diffuser it was measured. Figure 8 plots mass-averaged overall diffuser pressure recovery coefficient versus straight-channel diffuser inlet blockage. A slightly decreasing trend of the mass-averaged pressure recovery with increasing diffuser inlet blockage can be observed in Fig. 8. Note, however, that the lower pressure recovery coefficient values in Fig. 8 cannot be attributed to inlet blockage alone, because the points of lower pressure recovery are also points of lower inlet flow angle in Fig. 7.

The main trend of the Fig. 7 is that the performance of the vaned diffusers of centrifugal compressors can be correlated using one main parameter, the average inlet flow angle. For a given flow angle, mass-averaged overall diffuser pressure recovery coefficient is essentially independent of diffuser inlet conditions. To isolate the influence of parameters associated with the inlet flow field, the data in Figs. 7 and 8 are presented for constant flow angles in Figs. 9–11. Figures 9(*a*), 10(*a*), and 11(*a*) are for a high flow angle ($\alpha = 70$ deg) near to the rotating stall onset; Figs. 9(*b*), 10(*b*), and 11(*b*) are for the straight-channel diffuser metal angle ($\alpha = 69$ deg); and Figs. 9(*c*), 10(*c*), and 11(*c*) are for a lower flow angle ($\alpha = 67$ deg). In each of these the ordinate is the overall diffuser pressure recovery coefficient based on the mass-averaged inlet total pres-

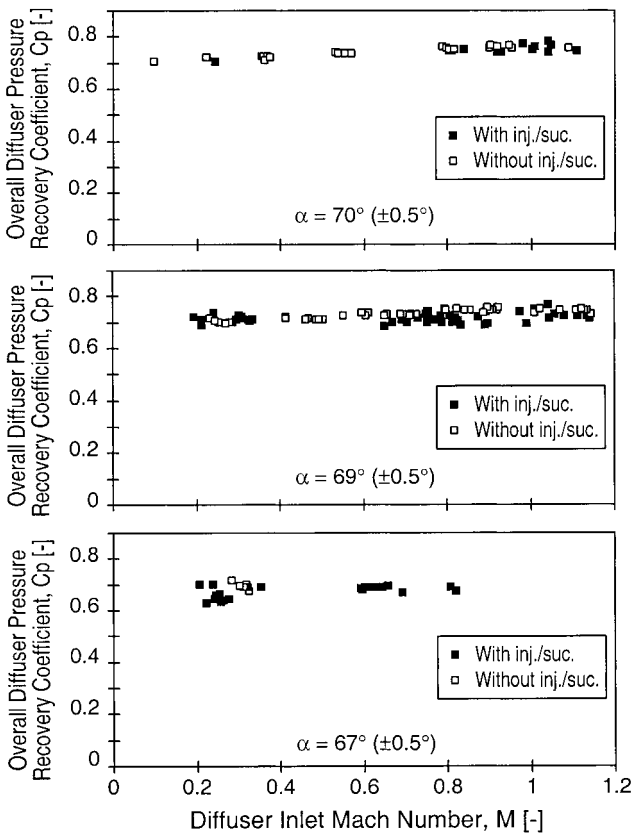

Fig. 9 Mass-averaged overall diffuser pressure recovery coefficient, *Cp*, versus diffuser inlet Mach number, M, represented for constant diffuser inlet flow angles

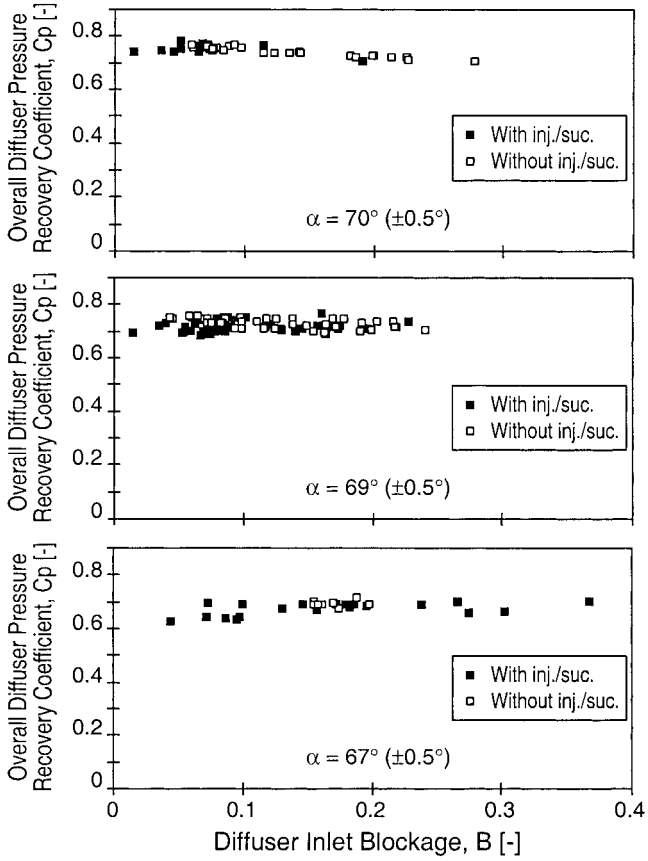

Fig. 10 Mass-averaged overall diffuser pressure recovery coefficient, *Cp*, versus diffuser inlet blockage, *B*, represented for constant diffuser inlet flow angles

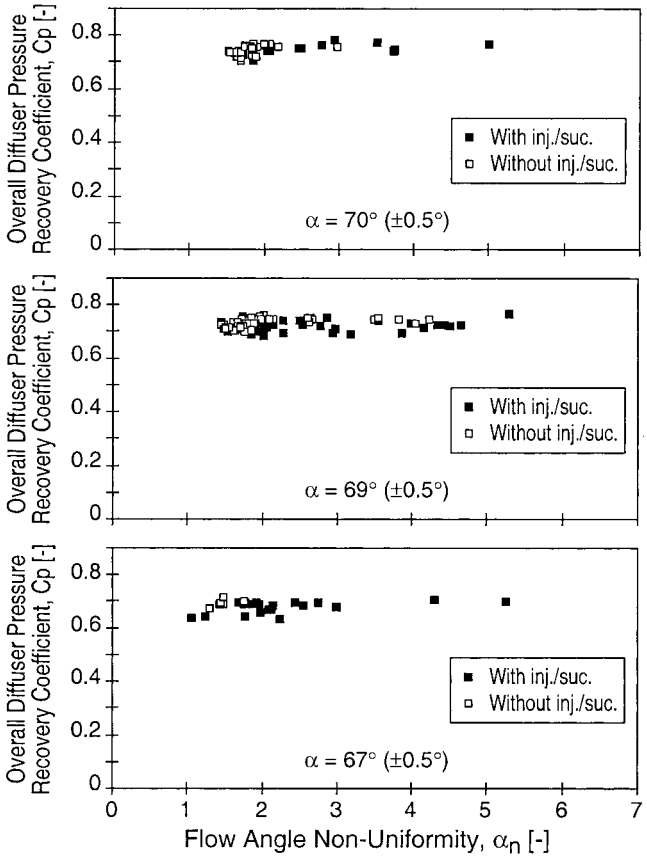

Fig. 11 Mass-averaged overall diffuser pressure recovery coefficient, *Cp*, versus diffuser inlet flow angle nonuniformity, α_n, represented for constant diffuser inlet flow angles

sure. Figure 9 has *inlet Mach number* as abscissa, Fig. 10 has *inlet blockage*, and Fig. 11 *flow angle nonuniformity*. (The axial variation in the velocity distribution at the diffuser inlet is expressed in term of the flow angle nonuniformity.) Figures 9–11 confirm that there is no significant dependence of mass-averaged pressure recovery on these parameters. This observation is also true for the other constant inlet flow angles; see Deniz (1997). The mass-averaged overall diffuser pressure recovery is overwhelmingly determined by the inlet flow angle.

An example of static pressure distribution along the centerline of one diffuser channel is plotted in Fig. 12 for experiments with injection/suction. This figure shows a constant speed ($N = 2000$ rpm) case with different inlet flow field distortion levels and flow angles. The average values of inlet flow angles are 63.0, 64.8, 68.4, 68.9, and 70.0 deg and there is significant difference in the pressure recovery between pressure rise curves of different flow angles. The slope of the pressure rise in the channel diffuser part is similar for all inlet flow angles, but the overall diffuser pressure recovery achieved is different. The reason for the different overall diffuser pressure recovery is the changes in pressure rise at the diffuser inlet region. In Fig. 12 the highest pressure recovery is for $\alpha = 70.0$ deg, which is close to the onset of rotating stall. Curves for flow angles 68.9 and 68.4 deg are near the diffuser inlet metal angle. For inlet flow angles equal or greater than the diffuser metal angle (70.0, 68.9, and 68.4 deg) there is a substantial fraction of the pressure rise, which occurs in the diffuser inlet region, in quasi-vaneless space after the leading edges and immediately upstream of the diffuser throat. In the channel part of the diffuser, the slope of the pressure rise decreases in the flow direction so lengthening of the diffuser is likely to produce small additional gains. More than 60 percent of the overall diffuser pressure static rise occurs within the first 30 percent of the diffuser channel length.

Decreasing the inlet flow angle to $\alpha = 64.8$ deg reduces the slope of the pressure rise in the diffuser inlet region, whilst decreasing the inlet flow angle further to $\alpha = 63.0$ deg results in a fall in static pressure in the diffuser inlet region (quasi-vaneless space), with an acceleration of flow until flow enters the channel part of the diffuser. The overall pressure recovery of the straight-channel diffuser is consequently low for $\alpha = 63.0$ deg, but this flow angle was only obtained at an inlet Mach number of about 0.3. Choking of the flow, which could be produced in the 30-passage discrete-passage diffuser at low diffuser inlet flow angle, was therefore not observed for the straight-channel diffuser. Unfortunately test data at the low diffuser inlet flow angle region (where the flow accelerates up to the diffuser throat) with high Mach numbers at diffuser inlet were not obtained for the straight-

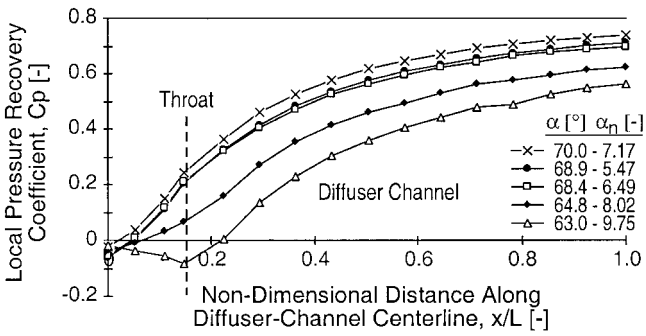

Fig. 12 Static pressure distribution along the centerline of a straight-channel diffuser channel for different flow angles at a constant impeller speed *N* = 2000 rpm (with injection/suction)

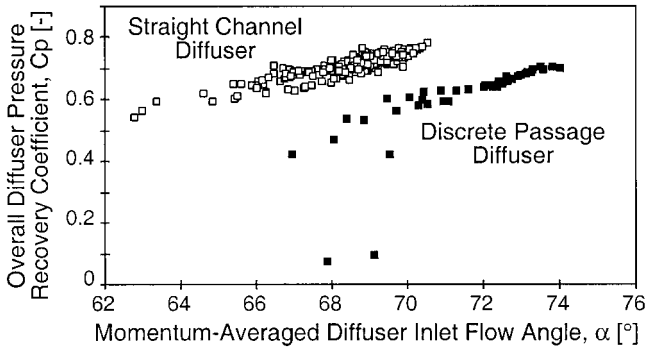

Fig. 13 Comparison of mass-averaged overall diffuser pressure recovery coefficient, *Cp*, for straight-channel and discrete-passage diffusers

channel diffuser investigations because the downstream slave compressor could not be used.

2.3 Comparison With Discrete-Passage Diffuser Results. The test results of the investigations with discrete-passage diffusers (see Part 1) showed that overall diffuser pressure recovery coefficient based on suitably averaged inlet stagnation pressure correlates well with an average inlet flow angle and is insensitive to axial distortions of the diffuser inlet flow field and Mach number. The results of the experiments with the straight-channel diffuser presented in Sections 2.1 and 2.2 show similar behavior.

The achieved overall diffuser pressure recovery levels of straight-channel and discrete-passage diffusers are compared in Fig. 13. The straight-channel diffuser tested here shows ~10 percent higher pressure recovery. At operating points near the design point, the pressure recovery coefficient (mass or availability-averaged) for the straight-channel diffuser is around 0.65–0.78 while for discrete-passage diffuser it is in the range of 0.60–0.70. The variation in the pressure recovery coefficient with inlet flow angle (momentum-averaged) is similar for both types of diffuser. Figure 13 shows that the critical inlet flow angle for the onset of rotating stall for the straight-channel diffuser and discrete-passage diffuser is 70 ± 0.5 deg and 73.5 ± 0.5 deg, respectively. The range of flow angles tolerated as operating range is about 5 deg for both designs but the operating range of the straight-channel diffuser is at smaller flow angles than that of the discrete-passage diffuser. Put differently, the straight-channel diffuser used for this experiment will accept a higher impeller mass flow. Perhaps surprisingly the optimum mass flows for the straight-channel diffuser and discrete-passage diffuser are not equal even when the geometric throat area and the inlet metal angle are the same.

3 Summary and Conclusions

An experimental investigation has been carried out on performance, operating range, and fluid dynamic phenomena of a straight-channel diffuser typical of high-performance centrifugal compressor stages. The influences of inlet flow field conditions, including Mach number, flow angle, fluid dynamic blockage, and flow nonuniformity in the axial direction on the pressure recovery and stability of a straight-channel diffuser were investigated on a centrifugal compressor diffuser test facility. The range of inlet conditions included Mach numbers from 0.2 to 1.15, flow angles from 63 to 71 deg, blockage levels from 3 to 35 percent, and high levels of axial flow field distortion, e.g., up to 45 deg flow angle difference between front and rear walls at the diffuser inlet.

The main conclusions of this investigation are as follows:

1 The pressure recovery coefficient for either discrete-passage or straight-channel diffusers is virtually a unique function of inlet flow angle. This requires a suitable average to be used for the inlet total pressure in calculating the pressure recovery coefficient and a suitable average flow direction to be used for the flow angle. It is then found that the dependence on Mach number (even at supersonic levels), blockage, and various inlet distortions is negligible.

2 It has been found that either an availability-averaged total pressure or a mass-averaged total pressure is satisfactory in correlating pressure recovery. The availability-average can be shown to be better theoretically, but in practice the mass-average is equally satisfactory.

3 The inlet flow direction should be based on the momentum-averaged flow angle.

4 The straight-channel diffuser investigated was found to give pressure recovery coefficients in the range 0.50–0.78 (proportional to inlet flow angle) whereas the discrete-passage diffuser investigated gave *Cp* values in the range 0.50–0.70, except when the diffuser was choked. When choking occurs, the diffuser pressure recovery decreased rapidly and the linear correlation between the inlet flow angle and diffuser pressure recovery coefficient was no longer valid.

5 The performance of the discrete-passage diffuser was essentially the same with 30 or 38 passages.

6 The onset of rotating stall was found in both types of diffuser to occur at a fixed value of inlet flow angle (based on the momentum-average). The actual magnitude of the critical angle depends on the type (and on the design) of diffuser. The presence of a total pressure/flow angle probe at diffuser inlet was found in one case examined to have caused stall at an diffuser inlet flow angle approximately 0.45 deg smaller.

7 The insensitivity of the diffuser performance to details of the flow such as Mach number, blockage, and velocity profile distortion suggests that a strong mixing process is at work in the quasi-vaneless space and throat region. What controls the performance are the overall mass flow, momentum, and energy of the flow entering the diffuser. By using suitable averages for inlet stagnation pressure and flow direction, it appears that most of the essential information has been included. This deserves further study. A paper demonstrating the importance of flow angle on radial diffuser performance by means of CFD will be published soon. This prospective paper will also be including a comparison between CFD predictions for the straight-channel diffuser and experimental results presented for the same diffuser in this paper.

8 It appears plausible to suggest that the approach to compressor diffuser performance estimation and design, which rests on the determination of blockage at the diffuser inlet or the throat, is unnecessary. This approach fails to take account of the mixing processes referred to in (7) above, which appear to be an important aspect in determining the overall diffusion capability.

Acknowledgments

This work was supported by the Kobe Steel Ltd. The program managers were Mr. Y. Fukao (present) and Dr. F. Kano (former). The comments, support, and helpful suggestions of these two individuals are greatly appreciated. Support for the first author was provided by the Swiss National Foundation for the Furtherance of Scientific Research and this support is gratefully acknowledged. We would like to express our appreciation to Mr. P.C. Tramm, Dr. D. Alverson, and Mr. D. Sagre of Allison Engine Company for providing invaluable recommendations concerning the design of the straight-channel diffuser.

References

Deniz, S., 1997, "Effects of Inlet Flow Field Conditions on the Performance of Centrifugal Compressor Diffusers," MIT Gas Turbine Laboratory Report #225, Mar., Cambridge, MA.

Dong, Y., 1996, private communication.

Filipenco, V. G., Deniz, S., Johnston, J. M., Greitzer, E. M., and Cumpsty, N. A., 2000, "Effects of Inlet Flow Field Conditions on the Performance of Centrifugal Compressor Diffusers: Part 1—Discrete-Passage Diffuser," ASME JOURNAL OF TURBOMACHINERY, Vol. 122, this issue, pp. 1–10.

Hunziker, R., 1993, "Einfluss der Diffusorgeometrie auf die Instabilliätsgrenze des Radialverdichters," Dissertation, ETH Zurich, Swiss Federal Institute of Technology, Switzerland, #10252.

Japikse, D., and Osborne, C., 1986, "Optimization of Industrial Centrifugal Compressors; Part 6B: Studies in Component Performance — Eight Design Cases From 1972 to 1982," ASME Paper No. 86-GT-222.

Kano, F., Tazawa, N., and Fukao, Y., 1982, "Aerodynamic Performance of Large Centrifugal Compressors," ASME *Journal of Engineering for Power*, Vol. 104, No. 2.

Kenny, D. P., 1972, "A Comparison of the Predicted and Measured Performance of High Pressure Ratio Centrifugal Compressor Diffusers," ASME Paper No. 72-GT-54.

Krain, H., 1984, "Experimental Observation of the Flow in Impellers and Diffusers," in: *Flow in Centrifugal Compressors*, Von Karman Institute for Fluid Dynamics, Lecture Series No. 1984-07.

Reneau, L. R., Johnston, J. P., and Kline, S. J., 1967, "Performance and Design of Straight, Two-Dimensional Diffusers," ASME *Journal of Basic Engineering*, Vol. 89, pp. 141–150.

Rodgers, C., 1982, "The Performance of Centrifugal Compressor Channel Diffusers," ASME Paper No. 82-GT-10.

Runstadler, P. W. J., and Dean, R. C. J., 1969, "Straight Channel Diffuser Performance at High Inlet Mach Numbers," ASME *Journal of Basic Engineering*, Vol. 91, pp. 397–422.

Runstadler, P. W., and Dolan, F. X., 1973, "Further Data of the Pressure Recovery Performance of Straight-Channel, Plane-Divergence Diffusers at High Subsonic Inlet Mach Numbers," ASME *Journal of Fluids Engineering*, Vol. 95.

Yaras, M. I., 1996, "Effects of Inlet Conditions on the Flow in a Fishtail Curved Diffuser With Strong Curvature," ASME *Journal of Fluids Engineering*, Vol. 118, pp. 772–778.

Yoshinaga, Y., Gyobu, I., Mishina, H., Koseki, F., and Hishida, N., 1980, "Aerodynamic Performance of a Centrifugal Compressor With Vaned Diffusers," ASME *Journal of Fluids Engineering*, Vol. 102, pp. 486–493.

DISCUSSION

J. J. Brasz[2]

1 A Comment About Diffuser Nomenclature

The names "discrete-passage diffuser" and "straight-channel diffuser" are not very accurate, since the so-called discrete-passage diffuser has straight channels and the so-called straight-channel diffuser has discrete passages. "Modified pipe diffuser" and "vane-island diffuser" would have been more appropriate names. However, in the discussion of the papers the nomenclature of the authors will be used.

2 Diffuser Inlet Blockage Has No Influence on Diffuser Pressure Recovery

The main conclusion of both papers is that diffuser inlet blockage has no influence on the pressure recovery of the diffuser and that the momentum-averaged diffuser inlet flow angle is the predominant variable controlling diffuser performance. This strong influence of the momentum-averaged inlet flow angle on the diffuser performance is to be expected. Vaned diffusers lose their pressure recovery capability at off-design conditions very quickly, more so than vaneless diffusers. The strong variation in C_p with inlet flow angle is due to change in velocity between the inlet of the vaneless section of the diffuser and the throat at the beginning of the vaned section of the diffuser. Diffuser inlet flow angle by itself is not a fundamental parameter. Figure 8(*a*) of the first paper [1] illustrates this. The section of the diffuser upstream of the throat shows a large variation in C_p (from $+0.4$ to -0.5 according to Fig. 8(*a*)) depending on the amount of deceleration or acceleration taking place between the inlet and the throat of the diffuser. The discrete-passage part of the diffuser (from throat to exit) seems to have more or less the same C_p as long as shock losses are neglected. The combined overall diffuser C_p, from vaneless diffuser inlet to vaned diffuser exit, varies—neglecting the diffuser choke point—from 0.45 to 0.70.

However, off-design performance deterioration of vaned diffusers is not directly related to, and should not be confused with, variations in diffuser design point pressure recovery. Studying both phenomena at the same time can obscure the results of the latter. Differences in diffuser peak efficiency as a function of changes in inlet blockage, Mach number, and Reynolds number are more subtle than the dramatic performance deterioration at off-design conditions. Closer inspection of the test results presented in both papers shows, besides the expected variation in C_p with inlet flow angle, a non-negligible variation in maximum C_p. Figure 7 of [1] shows at peak efficiency conditions for the same inlet flow angle a large (up to 15 percent) spread in pressure recovery for the 38-passage discrete-passage diffuser, potentially caused by Mach number, Reynolds number, and/or inlet blockage. Figure 4 of [2] indicates a 10 percent higher design pressure recovery coefficient for identical inlet flow angle at higher rpm, suggesting a Mach number effect. The top plot in Fig. 9 of [2] shows this correlation between C_p and inlet Mach number at optimum design conditions. It is this variation in C_p (and not the variation of diffuser performance as a function of inlet flow angle) that is of interest for the determination to what extent vaned diffuser performance is influenced by inlet blockage and/or Mach number. The conclusion of the papers that the pressure recovery is "nearly" independent of inlet flow axial distortion and Mach number is contradicted by the 10–15 percent difference in peak C_p shown by the test data. If "nearly" means "compared to extreme off-design conditions," the conclusion becomes somewhat true but not very meaningful.

Before contrasting the results from this study with previous work from Runstadler, two important differences should be kept in mind:

1. Runstadler dealt with diffuser throat blockage and not with blockage at the inlet of a vaneless diffuser.
2. The velocity profile corresponding to the blockage as experienced in the Runstadler experiments (symmetric solid core flow with boundary layer blockage) is very different from the skewness in the velocity profile, which resulted when blockage was introduced in the tests described in these papers. Runstadler mentions [6] that "asymmetric blockage distributions produce minor alterations in pressure recovery," which seems to be in line with the relative insensitivity to the diffuser inlet blockage found in the papers.

3 Mass-Averaging Versus Availability Averaging

Mass-averaging of the inlet total pressure traverse measurements seems intuitively more appropriate to determine the total pressure at the inlet of a diffuser than area-averaging or just using a centerline measurement. Availability-averaging as proposed in [1] is theoretically the correct method of determining the total pressure at diffuser inlet. Analysis of the test results apparently indicated that mass-averaging the total pressure traverse data gives total pressure values very close to but not identical to the ones obtained with availability-averaging. However, a difference of up to 1.6 percent in inlet dynamic pressure (and therefore in C_p) was still found when comparing C_p's based on mass-averaged total pressures versus availability-averaged total pressures. What is the physical reason for this difference and why did the authors use the mass-averaged total pressure in both papers when the theoretically correct availability-averaged total pressures are as readily available? If the availability-averaging concept is not used in the data analysis and the reason for differences in availability-averaging and mass-averaged total pressures is not well understood, this whole discussion about availability-averaging should be left out of the paper. The other averaging methods (based on area, centerline, or maximum velocity) can also be omitted since every compressor aerodynamicist will take mass-averaged quantities over area or centerline quantities.

4 Corrected Dependence of C_p on Inlet Blockage of the Data of Runstadler and Dolan

Figure 1 in [2] shows for the Runstadler and Dolan data [3] a much weaker dependence of pressure recovery on inlet blockage

[2] Carrier Corporation, Syracuse, NY 13221.

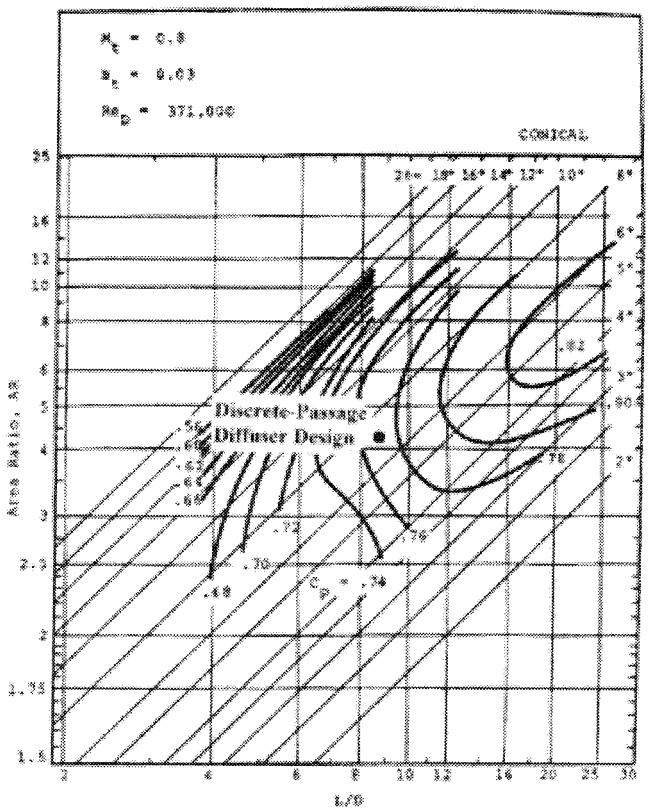

Fig. 14 Design point of the discrete passage diffuser (from [6] p. 87)

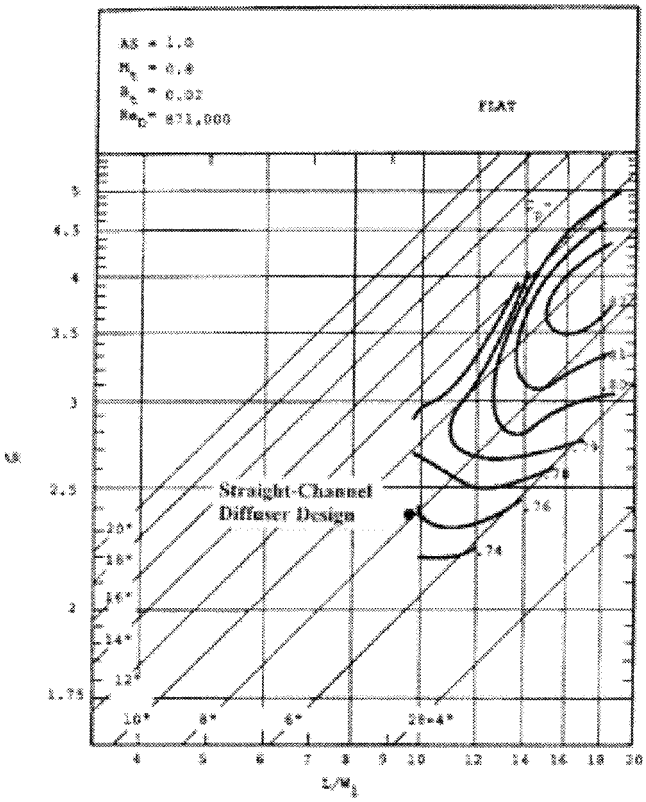

Fig. 15 Design point of the straight-channel diffuser(from [6] p. 60)

when using a mass-averaged diffuser inlet total pressure compared to a centerline diffuser inlet total pressure. In order to calculate a mass-averaged inlet total pressure for the Runstadler and Dolan data (which only contain a centerline total pressure), an assumption had to be made for the velocity profile in the boundary layer at the throat of the diffuser. It is not clear what velocity profile was assumed. Also, not only pressure recovery C_p, but also blockage B changes with diffuser inlet total pressure. It seems that in Fig. 1 the same blockage definition (based on centerline total pressure) was used for both the C_p based on centerline total pressure and C_p based on mass-averaged diffuser inlet total pressure. This is inconsistent. The blockage definition should use the same total pressure calculation method as the pressure recovery coefficient. If that were done, the pressure recovery coefficients based on mass-averaged diffuser inlet total pressure would become more dependent on blockage.

5 Straight-Channel Diffusers Have 10 Percent Higher C_p Than Discrete-Passage Diffusers

The dramatic difference in C_p between the discrete-passage diffuser and the straight-channel diffuser reported in these papers is in conflict with the literature and industrial design experience. The "discrete-passage diffuser" is essentially a pipe diffuser upstream of the throat and something between a vane-island diffuser and a pipe diffuser after its throat. When Rogers and Shapiro [4] tested the overall pressure recovery of a pipe diffuser and a vane-island diffuser, they found very similar C_p's with a slight advantage for the vane-island diffuser. Using the design data given in Table 1 of [2] and conical diffuser performance maps for the discrete-passage diffuser and the flat diffuser performance maps for the straight-channel diffuser, the diffuser data book [6] shows a slightly better performance for the discrete-passage diffuser. A C_p of 0.77 is found for the discrete-passage and a C_p of 0.76 for the straight-channel diffuser (see Figs. 14 and 15).

The predicted performance data refer to well-designed diffusers for given area and length over diameter/width ratios. Since it is highly unlikely that the tested discrete- passage diffusers, which were supplied by GE, were poorly designed, other explanations have to be pursued to explain the reported large difference in C_p. During the discussion of the paper at the Stockholm conference I could only explain this difference by a possible error in the static pressure measurement at the inlet of the diffuser since this measurement took place at only one circumferential location neglecting the well-known effect of circumferential distortion on static pressure due to the presence of downstream vanes. As a result the denominator of the definition of C_p could contain a higher or lower value than the average value, causing an artificially high or low C_p. The check for circumferential uniformity of static pressure was only carried out with a vaneless diffuser [5]. The emphasis of that test was to see whether the discharge piping caused any circumferential disturbance. The circumferential uniformity check was never repeated with either the discrete-passage diffuser or the straight-channel diffuser.

6 Difference in Surge and Choke Flow Compressors With Identical Impellers but Different Diffusers With the Same Throat Area

Figure 13 of [2] compares the mass-averaged overall diffuser pressure recovery coefficient for straight-channel and discrete-passage diffusers. The authors state: "Perhaps surprisingly the optimum mass flows for the straight channel diffuser and the discrete-passage diffuser are not equal even when the geometric throat area and the inlet metal angle are the same." This result is more bothering than surprising. A shift that large in operating range when using the same impeller and diffusers with the same throat area is hard to understand. Something in the experiments, either the measurements, the data processing, or the experimental setup, seems to have changed between the two passage diffuser and the straight-channel diffuser tests, carried out by three different investigators over a period of 10 years with periods of inactivity in between.

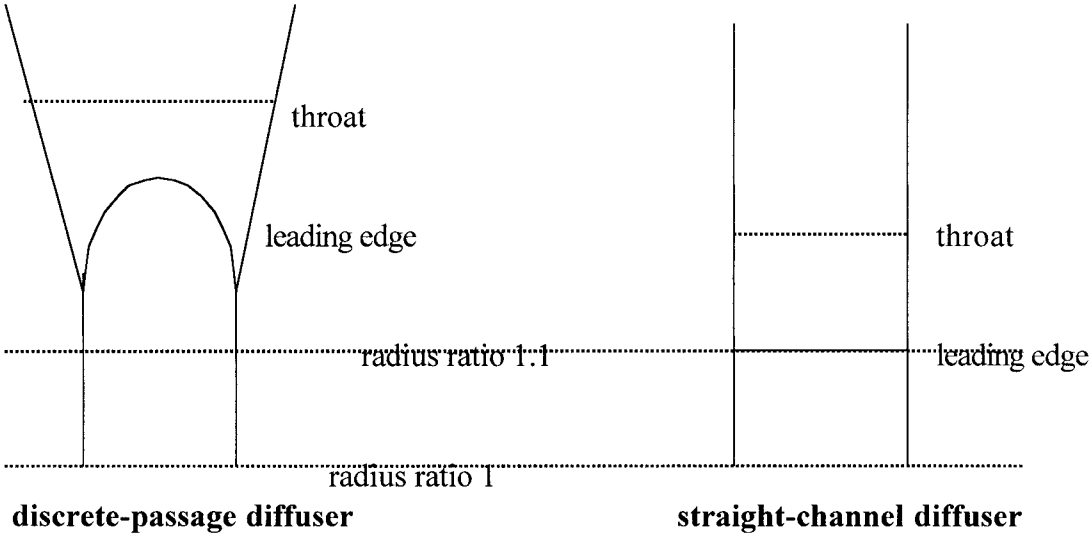

Fig. 16 Meridional view of discrete-passage and straight-channel diffuser illustrating the difference in diffuser leading edge and throat location

7 Difference in Throat Location for Straight-Channel and Discrete-Passage Diffuser

Comparing Fig. 8 of [1] with Fig. 12 of [2] shows a dramatic difference in the location of the throat area of both diffusers. The throat of the discrete-passage diffuser is at 40 percent and the throat of the straight-channel diffuser at 15 percent of the nondimensional distance along the diffuser-passage centerline. This seems strange, since given the same number of passages and the same tangency circle, the throat location of a discrete-passage or pipe diffuser should be very close to that of a straight-channel diffuser. Since Fig. 1 of [1] is only a schematic and not drawn to scale as Fig. 2 of [2] it is hard to understand where this difference comes from.

Further discussions with one of the authors [7] indicated another possible reason for the difference in C_p between the discrete-passage diffuser and the straight-channel diffuser. The leading edge of the straight-channel diffuser, which is the beginning of the semi-vaneless space, is located at a radius ratio of 1.1 of the impeller exit diameter. For the discrete-passage diffuser, the semi-vaneless space starts at a much larger radius (see Fig. 16). In other words, the gas passage length from impeller exit to diffuser throat is much longer for the discrete-passage diffuser than for the straight-channel diffuser. This would also mean that the two diffusers do not have identical tangency circles.

The additional blockage due to the longer gas passage in the vaneless and semi-vaneless diffuser of the discrete-passage diffuser could reduce choke flow and pressure recovery, although it is hard to believe that it would cause a 10 percent difference in diffuser C_p and the large change in choke and surge flow as shown in Fig. 13 of [2].

References

1 Filipenco, V. G., Deniz, S., Johnston, J. M., Greitzer, E. M., Cumpsty, N. A., "Effects of Inlet Flow Field Conditions on the Performance of Centrifugal Compressor Diffusers: Part 1—Discrete-Passage Diffuser," ASME Paper No. 98-GT-473, 1998; ASME JOURNAL OF TURBOMACHINERY, Vol. 122, 2000, this issue, pp. 1–10.

2 Deniz, S., Greitzer, E. M., and Cumpsty, N. A., "Effects of Inlet Flow Field Conditions on the Performance of Centrifugal Compressor Diffusers: Part 2—Straight-Channel Diffuser," ASME Paper No. 98-GT-474, 1998; ASME JOURNAL OF TURBOMACHINERY, Vol. 122, 2000, this issue, pp. 11–21.

3 Runstadler, P. W., and Dolan, F. X., "Further Data of the Pressure Recovery Performance of Straight-Channel, Plane Divergence Diffusers at High Subsonic Inlet Mach Numbers," ASME *Journal of Fluids Engineering*, Vol. 95, 1973.

4 Rogers, C., and Shapiro, L., "Design Considerations for High Pressure Ratio Centrifugal Compressors," ASME Paper No. 72-GT-91, 1972.

5 Filipenco, V.G., "Experimental Investigation of Flow Distortion Effects on the Performance of Radial Discrete-Passage Diffusers," GTL Report No. 206, Massachusetts Institute of Technology, Sept. 1991.

6 Runstadler, P. W., Dolan F. X., Dean, R. C., *Diffuser Data Book*, Creare Technical Note TN-186, Hanover, NH, May 1975.

7 Filipenco, F. G., personal communication, Aug. 1998.

Authors' Closure

The authors are grateful to Dr. Brasz for his careful, detailed, and extensive response to our papers. We will respond here to his main comments, where this seems appropriate or necessary and in doing this it is convenient to retain the numbering system used by Dr. Brasz. We also wish to point out that we attach such weight to his comments that we have also modified the papers as they will appear in the JOURNAL OF TURBOMACHINERY, and these now differ slightly from the papers presented at the IGTI Conference.

1 The names of diffuser types are rarely confusing to those familiar with the field. The term "discrete passage diffuser" was selected by General Electric Aircraft Engines and was used by the authors for consistency. The design of the discrete-passage diffuser is distinct from any other existing diffuser configuration, especially downstream of the throat.

2 We would disagree with Dr. Brasz that the main conclusion of our papers is that diffuser inlet blockage and skew have no influence on the pressure recovery. We would rather phrase the conclusion as follows: If one bases the pressure recovery coefficient on the mass-averaged (or availability-averaged) total pressure, the dependence on blockage and skew is mostly absorbed, and what remains is a strong dependence on momentum-averaged inlet flow angle.

We do not believe that we were confusing off-design and design-point performance. We would agree that there may be systematic variations in performance with, for example, Mach number, but these are small compared to that with inlet flow angle when pressure recovery coefficient is based on suitably averaged inlet quantities. We agree that the observed variations in the overall diffuser pressure recovery coefficient for the investigated diffusers are not completely negligible as far as overall compressor pressure rise and efficiency are concerned. But given the large range of inlet conditions over which this scatter is seen, the variations in diffuser pressure recovery are relatively small. The inlet flow angle flow angle was varied by up to 45 deg over the diffuser width and the inlet blockage was varied from 2 to 35 percent. With this range in inlet conditions, the spread in the

mass-averaged diffuser pressure recovery coefficient (or in other words the width of the scatter band of the pressure recovery coefficient after taking out the effect of the momentum-averaged inlet flow angle) was ± 3.8 percent for the 30-passage discrete-passage diffuser, ± 7.6 percent for the 38-passage discrete-passage diffuser and ± 6.8 percent for the straight-channel-diffuser. (For the 30-passage discrete-passage diffuser, the choke points were not included in this spread.) Further, the scatter does not show any trend or correlation with the level of inlet flow nonuniformity or blockage, as can be seen from the constant inlet flow angle presentations in Figs. 9, 10, and 11 of Part 2.

The evidence shown in our papers, and by Dong, is that pressure recovery depends primarily on the average dynamic pressure at inlet. It is fundamental to our thinking that the use of pressure recovery coefficients in which the inlet dynamic pressure is based on conditions on the centerline of the channel is misleading whenever the flow is highly nonuniform, as it is at inlet to the diffusers of a centrifugal compressor. The evidence that average dynamic pressure is what is important suggests that strong mixing processes are at work in the inlet region that make average conditions appropriate and the maximum conditions near the center largely irrelevant. If mass-averaged or availability-averaged dynamic pressure is used to determine pressure recovery coefficient, only small effects due to blockage, Mach number or skew remain.

3 The availability-averaged dynamic pressure at diffuser inlet was used at the beginning for the tests on the discrete-passage diffusers, this being the theoretically most appropriate average. The pressure recovery coefficient based on this value compares the diffuser pressure recovery to the best possible that could be achieved, using any arbitrary hypothetical device. Later it was recognized that many people found availability-averaging confusing, while the difference in pressure recovery coefficient using this from one using the mass-averaged dynamic pressure was small, certainly no more than the scatter in the data. As a result it was decided to use the mass-averaged pressure recovery coefficient in later experiments and presentations.

The difference between availability-averaged and mass-averaged dynamic or total pressure depends mainly on the ratio of the total pressures, but also on thermodynamic properties of the working fluid. In the case of an incompressible flow, for example, the availability-averaged dynamic or total pressure is in fact *exactly* equal to the corresponding mass-averaged value. In the present case, assuming that the working fluid (air) behaves as a perfect gas, the ratio of the availability-averaged total pressure, to that of the mass-averaged value is the ratio of Eqs. (2) and (4) in Part 1.

We agree that averaging methods based on area, centerline, or maximum velocity should not be regarded as proper candidates for presenting compressor diffuser data. Nevertheless, since they are the basis of much of the diffuser data available in the open literature, which informs our thinking on such matters, the present data was used to show just how inappropriate they are.

4 Dong's conclusions regarding the influence of inlet blockage on single-channel diffuser pressure recovery are primarily based on data. The estimation of the pressure recovery coefficient based on average conditions is possible using information given in an appendix to Runstadler and Dolan (1973). Contrary to what Dr. Brasz writes, it is not self-evident that the same calculation method for inlet total pressure should be used to calculate pressure recovery coefficient and the blockage, nor is it obvious that if this been done the dependence on blockage would have been greater.

5 In light of Dr. Brasz's comments, it seems to us unfortunate that the original papers gave as a firm conclusion that the straight-channel diffuser had a substantially higher pressure recovery coefficient than the discrete-passage diffuser. We have modified the papers to appear in the JOURNAL to reflect this. Although this is what we measured for the specific cases examined, the comparison of performance level for different types of diffusers was not the object of the research. Rather, it was to see how inlet flow conditions affected performance of different types of diffusers. With tests for just two discrete-passage diffusers and one straight-channel diffuser, there is no way of being sure that the design goals for each had been met, or that the designs specifically match one another, so there is insufficient evidence for a firm conclusion of relative merit for the different types of diffuser. The publications we have seen (Klassen, 1973; Rodgers and Sapiro, 1972; Sakai et al., 1997) are not very clear on the relative merits of different types of diffuser, although they show a slight advantage for the straight-channel type.

As mentioned in the papers, the discrete-passage diffuser designs were supplied to us by GE Aircraft Engines with little information on their history or on the intent and details of their design. The straight-channel diffuser was designed at the MIT Gas Turbine Laboratory to accept similar inlet conditions obtained in the discrete-passage diffuser tests. This design was modified based on recommendations provided by Allison Engine Company. Its main geometric parameters are selected to be in the flow regime of no appreciable stall and close to the line of maximum pressure recovery according to the diffuser map by Reneau et al. (1967).

Although the channel geometry of the discrete-passage diffuser is nearly rectangular, the cross section at the throat is circular, and this makes a comparison of the discrete-passage diffuser channel geometry with the single-channel diffuser maps (conical or flat channel) difficult. It is possible to compare the area ratio and nondimensional length of the channel part of the discrete-passage diffusers to single-channel flat or straight-wall diffuser geometries and their performance maps (Reneau et al., 1967, for example). From this the divergence angle of the discrete passage diffusers in the rectangular cross-sectional part would appear to be too large, corresponding to the large transitory stall region with low diffuser pressure recovery. A comparison of the discrete-passage diffuser channel using the inlet and outlet areas with the conical diffuser maps of Runstadler et al. (1975) gives high Cp values, as shown in Fig. 1 of Brasz's comments. It may also be mentioned that the measurements for the discrete-passage diffusers show a much smaller pressure rise in the channel part than for the equivalent straight-channel diffuser, again suggesting that the divergence angle has been set too large and the diffusers channel part might be in the transitory stall regime.

The paper was not sufficiently explicit about the definition of measured static pressure used at the inlet in finding the pressure recovery coefficient, and we are grateful to Dr. Brasz for giving us the opportunity to explain this. For the straight channel diffuser, measurements from five taps in the leading edge region of one diffuser channel were averaged to obtain the inlet static pressure. The local variation of the static pressure at the inlet of one diffuser channel can be calculated for the straight-channel diffuser. The difference in static pressure between the average of five static pressure taps and one tap at midspan was less than 15 percent at the diffuser channel inlet. More relevantly, the influence of this nonuniformity in inlet static pressure on the diffuser pressure recovery coefficient is less than 2.5 percent because inlet static pressure is used in calculating the numerator and the denominator of the Cp. We have examined the specific point raised and found that if the tap at midpitch had been used by itself, the error would be less than 2 percent for 95 percent of data points with the straight-channel diffuser. In the discrete-passage diffuser tests, the pressure recovery results shown in Fig. 6(a) are based on a single static pressure measurement from a static pressure probe located at the diffuser inlet, at midpitch of a passage. In addition, Cp can be calculated using available data from three static pressure taps, which were located in the quasi-vaneless space within the pitch of one passage. If the measurements from any one of these taps is used, the variation in overall Cp, in the worst case, was found to be 2.8 percent of that obtained using the single static pressure measurement at mid-pitch, corresponding to a variation in Cp from 0.69 to 0.71.

Toward the end of his comment No. 5, Dr. Brasz states that the check for circumferential uniformity of static pressure was only carried out with a vaneless diffuser, with the emphasis on seeing whether the discharge piping caused any circumferential disturbance. In fact the circumferential variation of the static pressure at the diffuser inlet (using static pressure taps at both front and rear walls in the vaneless-space) as well as at the diffuser exit were measured for the straight-channel diffuser, as was mentioned in the papers.

6 The flow angle range shown for the two diffuser configurations in Fig. 13 of Part 2 should not be interpreted as a direct indication of mass-flow range, since the mass-flow and diffuser inlet flow angle can be varied independently in this facility using a combination of rotor speed, injection/suction through the profile control slots, and main plenum pressure.

We do not have a firm explanation for the difference in optimum inlet flow angle for the discrete-passage and the straight-channel diffusers; essentially the straight-channel diffuser operates best at smaller inlet flow angles (measured from radial). The throat is reached only after the flow has passed a considerable fraction of the diffuser length along the suction surface of a vane, and in the case of the discrete-passage diffuser, the throat extends over a significant fraction of the diffuser length in the flow direction (this point is raised by Dr. Brasz in his point No. 7). It seems that a single area (at the throat) and a single metal direction at inlet are inadequate as a description of the diffuser. Given the method of manufacture and assembly, it is implausible that the discrepancy in optimum flow angle results from the passage of time between the start of tests on the discrete-passage diffuser and the completion of the tests on the straight-channel diffuser. It would be useful to carry out computations of the flow in the two types of diffuser to see whether the difference is confirmed, as well as to provide its explanation.

The cases that showed choking result from the way the test facility was used to obtain some of the data points in the first set of experiments and, as explained in the paper, should be discounted as a phenomenon created by the test facility. The first set of experiments on discrete-passage diffusers used a downstream compressor to produce subatmospheric conditions downstream of the diffuser and this allowed enough flow to be drawn through the diffuser to choke it, while the combination of rotor speed with side wall suction and injection still produced the relatively large measured swirl.

References

Klassen, H. A., 1973, "Performance of a Low-Pressure Ratio Centrifugal Compressor With Four Diffuser Designs," NASA TN D-7237, Mar.

Rodgers, C., and Sapiro, L., 1972, "Design Considerations for High Pressure Ratio Centrifugal Compressors," ASME Paper No. 72-GT-91.

Sakai, T., Tohbe, Y., Fujii, T., and Tatsumi, T., 1997, "Development of a High Pressure Ratio Centrifugal Compressor for 300 kW-Class Ceramic Gas Turbine," ASME Paper No. 97-GT-480.

D. Hagelstein
Institute of Turbomachinery,
University of Hannover,
Hannover, Germany

K. Hillewaert
Von Karman Institute for Fluid Dynamics (VKI),
Rhode Saint Genèse, Belgium

R. A. Van den Braembussche
Von Karman Institute for Fluid Dynamics (VKI),
Rhode Saint Genèse, Belgium

A. Engeda
Michigan State University,
East Lansing, MI 48109

R. Keiper
Kühnle, Kopp & Kausch AG (KKK),
Frankenthal, Germany

M. Rautenberg
Institute of Turbomachinery,
University of Hannover,
Hannover, Germany

Experimental and Numerical Investigation of the Flow in a Centrifugal Compressor Volute

This paper presents the experimental and numerical investigation of an outward volute of rectangular cross section. The investigation is carried out at the level of stage performance, volute performance, and detailed flow field study at selected peripheral positions for various operating points. The objective of the investigation was to gain further knowledge about the flow structure and loss mechanism in the volute. Simultaneously with the experimental investigation, a numerical simulation of the flow in the volute was carried out. A three-dimensional Euler code was used in which a wall friction term and a tuned artificial dissipation term account for viscous effects. A reasonable agreement between the experimental and numerical results is observed. As a result a good and detailed knowledge about the pressure recovery and loss mechanism in the volute is obtained.

Introduction

The primary function of a centrifugal compressor volute is to serve as the transition from the impeller and diffuser to the pipe system. Depending on the particular configuration, the losses in volutes, especially at off-design can be significantly high, which leads to poor stage efficiency and reduction of operating range.

It is well known that the collecting volute of a centrifugal compressor, operating at off-design conditions, produces a peripheral pressure distortion. This pressure distortion intensively acts back on the impeller exit, when a vaneless diffuser is chosen (cf. Hagelstein et al., 1997) and leads to a periodic throttling of the impeller flow. This results in a cyclic acceleration and deceleration of the fluid inside each impeller channel. As a result the inlet flow angle and thus the incidence angle vary periodically, which is the reason for a decrease of impeller efficiency and operating range. The varying force that acts on the impeller blades can cause impeller failure, especially when high inlet pressures are considered (cf. Sorokes et al., 1998, and Borer et al., 1997).

Several simplified one- or two-dimensional models exist that predict the peripheral pressure distortion caused by the volute (e.g., Iversen et al., 1960; Kurokawa, 1980; Badie et al., 1992). However, measurements of Van den Braembussche and Hände (1990), Ayder and Van den Braembussche (1991), and Ayder (1993) clearly show the fully three-dimensional nature of the volute flow. The secondary flow inside the volute has a major influence on pressure distortion and on the distribution of the through flow velocities. This implies that a reliable prediction method must consider the three-dimensional character of the flow. Van den Braembussche et al. (1999) present an analytical quasi-one-dimensional prediction method, which takes into consideration the three dimensionality of the flow. A reasonable correspondence of the pressure distributions and the losses with the experimental results obtained at the large centrifugal compressor test stand of the Institute of Turbomachinery in Hannover could be found.

Ayder and Van den Braembussche (1994) used a steady three-dimensional Euler method for the calculation of the diffuser and volute flow of a compressor with elliptic volute. They introduced an artificial dissipation term in their calculations in order to limit the flow quantities in the vortex core to finite values. Generally good agreements with measurement results were obtained. The calculated total pressure distributions were a little less accurate. Hillewaert and Van den Braembussche (1999) coupled the volute calculation method with the three-dimensional unsteady, inviscid impeller calculation method developed by Fatsis (1995). This model was applied to the compressor geometry investigated in this paper and a good agreement with the results measured at the diffuser exit was obtained.

There are quite few measurement results available of the flow inside the volute. The works of Van den Braembussche and Hände (1990), Ayder and Van den Braembussche (1991, 1994), and Ayder (1993) give a good insight in the flow behavior inside the volute at nominal and off-design operating points. Nevertheless, we are far from fully understanding the flow phenomena and loss mechanisms inside the volute and further empirical data are necessary to improve the existing flow models further.

Hence measurement results are presented in this paper, which were obtained at the large centrifugal compressor test stand of the Institute of Turbomachinery in Hannover. Detailed measurements were carried out at the diffuser exit and at several peripheral positions in the volute and in the exit pipe diffuser, respectively. The results are compared with those obtained using the calculation method of Ayder (1993).

Contributed by the International Gas Turbine Institute and presented at the 44th International Gas Turbine and Aeroengine Congress and Exhibition, Indianapolis, Indiana, June 7–10, 1999. Manuscript received by the International Gas Turbine Institute February 1999. Paper No. 99-GT-79. Review Chair: D. C. Wisler.

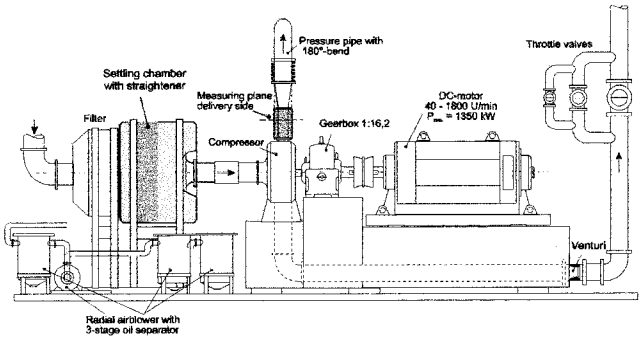

Fig. 1 Centrifugal compressor test stand

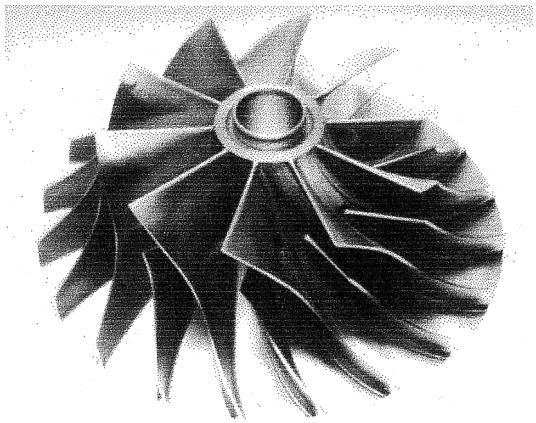

Fig. 2 Unshrouded 60 deg backswept impeller with 20 blades (every second one splittered)

Compressor Test Facility

Figure 1 shows the test loop schematically. Atmospheric air is sucked into the compressor through the suction chamber, which has a fine filter and a flow straightener. The inlet temperature T_K and static pressure p_K are measured in the suction chamber. On the discharge side the compressor outlet total temperature, static and total pressures, and the mass flow are measured. The mass flow is measured with a venturi. The three parallel arranged throttle valves shown on the discharge side of the piping allow an accurate and fine control of the mass flow rate.

The test compressor is driven by a 1.35 MW DC motor whose speed can be varied from 40–1800 rpm. The motor and the compressor are connected through a gearbox with 1:16.2 gear ratio. The compressor testing, control, and measurement are all fully automated and conducted from an isolated control room.

Figure 2 shows the unshrouded impeller used for the tests. It has 20 blades with every second one splittered. The blade outlet angle is 60 deg measured from the tangential direction. The impeller diameter is 400 mm.

Figure 3 shows a meridional and front view of the external volute. The term "external" means that the whole volute channel is situated at larger radii than the diffuser exit. The impeller and the volute are connected through a vaneless diffuser with a radius ratio of 1.5. The diffuser width is pinched from $b_2 = 26.5$ mm to $b_3 = 20.5$ mm. The volute cross section was made rectangular purely from cost considerations. The volute was designed for circumferentially constant static pressure distribution.

Figure 4 shows a photo of the test compressor shroud wall, which shows the inner volute radius to be the same as the diffuser outlet radius. The rectangular volute cross section is also shown to be continued up to the compressor outlet flange.

Experimental Results and Discussion

Stage Performance. Figure 5 shows the complete performance map for the compressor tested with an external volute. Total pressure ratio and efficiency are presented as a function of reduced mass flow rate over a range of speeds from $Mu_2 = 0.62$ to $Mu_2 = 1.11$. Stage performance measurements were carried out at planes K and 8 as shown in the figure. Since the diffuser used is a vaneless one, a wide operational range between surge and choke is seen. Detailed flow measurements were carried out near the diffuser exit at $\lambda = 1.4$ and at $Mu_2 = 0.86$ in the volute for three flow rates near surge ($m/m_{des} = 0.40$), at best efficiency point ($m/m_{des} = 1.0$) and near choke ($m/m_{des} = 1.35$). These operating points are marked by circles in the compressor map.

Volute/Component Performance. As already indicated, the volute was designed for a circumferentially constant static pressure distribution. Figure 6 shows the circumferential static pressure distribution for $Mu_2 = 0.86$ at diffuser exit ($\lambda = 1.45$) for mass flow rates, ranging from near choke to surge. The static pressure tappings were located in the hub wall. For the design point mass flow rate ($m/m_{des} = 1.0$) an almost constant static pressure distribution is seen. Near choke flow, the pressure falls continuously from the tongue ($\theta = 0$ deg) to volute outlet ($\theta = 360$ deg). This is because the large amount of mass flow leads to flow acceleration in the circumferential direction which in turn causes the pressure fall. Near surge flow, the pressure is seen to rise from the tongue region to about $\theta = 200$ deg. This is due to the fact that the volute is too big for the low mass flow, which leads to flow diffusion. Between $\theta = 200$ deg and the volute outlet the pressure tends to level off indicating flow separation and end of the diffusion.

As shown in Fig. 6, the off-design operation of the compressor results in a nonuniform pressure distribution at the diffuser exit due to the volute. This nonuniform pressure distribution extends upstream to the impeller inlet and hence influences the flow through the impeller. The flow in each impeller channel thus experiences a periodic throttling due to the stationary circumferential nonuniform pressure distribution. Jiang et al. (1996) and Hagelstein et al. (1997) have reported this throttling effect to be the cause of blade vibration. One further consequence of this effect is a circumferntial variation of the flow leaving the impeller. Figure

Nomenclature

b = diffuser width
Cp = static pressure coefficient
Mu = circumferential Mach number
m = mass flow rate
n = rotational speed
p = pressure
R = radius
V = flow velocity
α = tangential flow angle
θ = circumferential angle
λ = radius ratio $= R/R_2$
π = pressure ratio
ω = total pressure loss coefficient

Subscripts

des = design
K = settling chamber
opt = optimum
r = radial
t = tangential
2 = impeller outlet
3 = diffuser outlet
8 = compressor discharge plane

Superscripts

0 = total average
$\bar{}$ = average

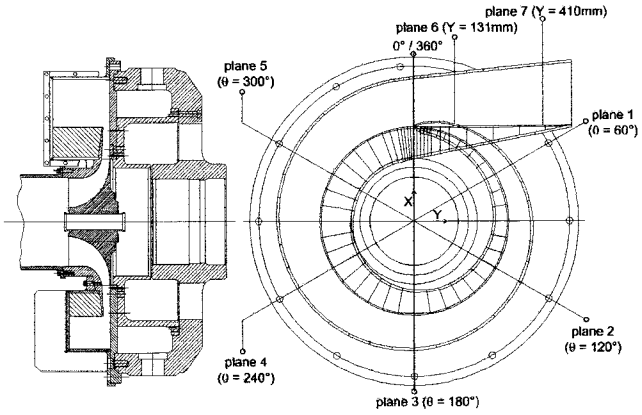

Fig. 3 Cross-sectional view of the centrifugal compressor with external volute (including planes for probe measurements inside the volute)

7 shows the circumferential distribution of total pressure, flow angle, and total temperature near the diffuser exit for the three operating points mentioned in Fig. 5. These measurements have been obtained by means of three different types of probe, namely total temperature probes, Cobra probes and Kiel probes, which were traversed axially one after the other. The estimated uncertainty in the probe measurements is ± 1.5 deg for the flow angle. The diagrams show spanwise mass-averaged values. It was shown that near or at best efficiency point the circumferential distribution of static pressure tended to be uniform and hence had very little or no effect on the impeller flow. Therefore at this operating point, the circumferential distribution of total pressure, flow angle, and total temperature is unaffected and also remains uniform, which suggests a rotational symmetric flow pattern.

At or near choke flow, the circumferential drop in the static pressure is also directly reflected in the total pressure. The impeller has a negative slope throughout the operational range. A lower static pressure at impeller exit tends to push the operating point to higher mass flow and hence also to lower total pressure. With the circumferential increase in mass flow rate, the flow angle increases in the vicinity of the volute exit. At the same time and in the same trend the energy transfer (total enthalpy) circumferentially decreases, which is seen in the total temperature.

At or near surge flow, the reverse effect is observed. The total pressure is seen to increase due to the increase in the throttling

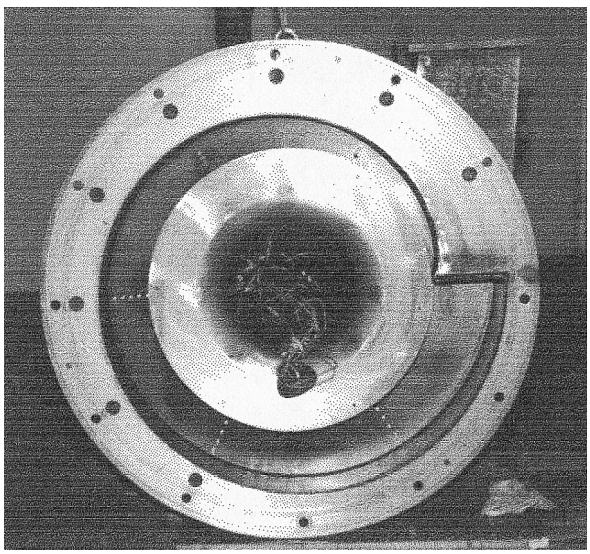

Fig. 4 Compressor shroud wall with external volute of rectangular cross section

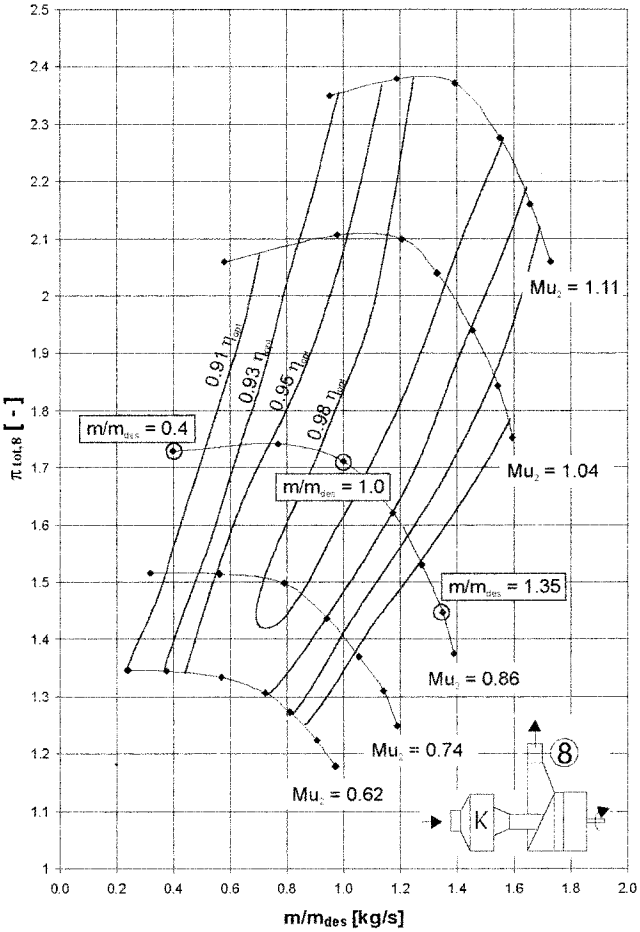

Fig. 5 Compressor map

effect circumferentially. At the same time the flow angle falls and the energy transfer increases gently. For this operating point, it is interesting to note that the minimum value of the total temperature and pressure is found at about $\theta = 120$ deg, which corresponds to a position behind the tongue. This is due to the impeller response to the perturbation of the tongue, which is transmitted along a streamline to the diffuser exit and results in the shown phase shift. This phase shift cannot be seen at high mass flow, because there the impeller discharge flow has a very high flow angle. Thus the impeller response will manifest itself closer to the peripheral position of the static pressure perturbation of the tongue.

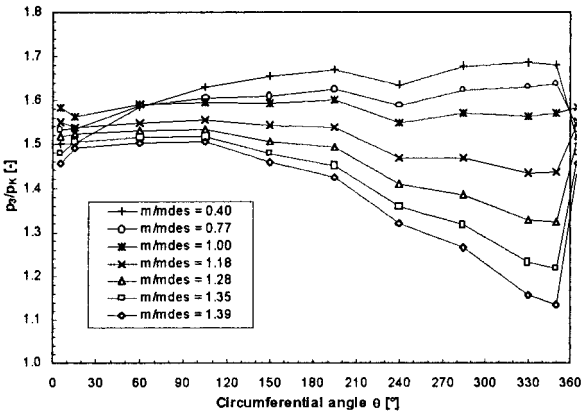

Fig. 6 Circumferential pressure distribution at diffuser exit ($\lambda = 1.45$) for $Mu_2 = 0.86$

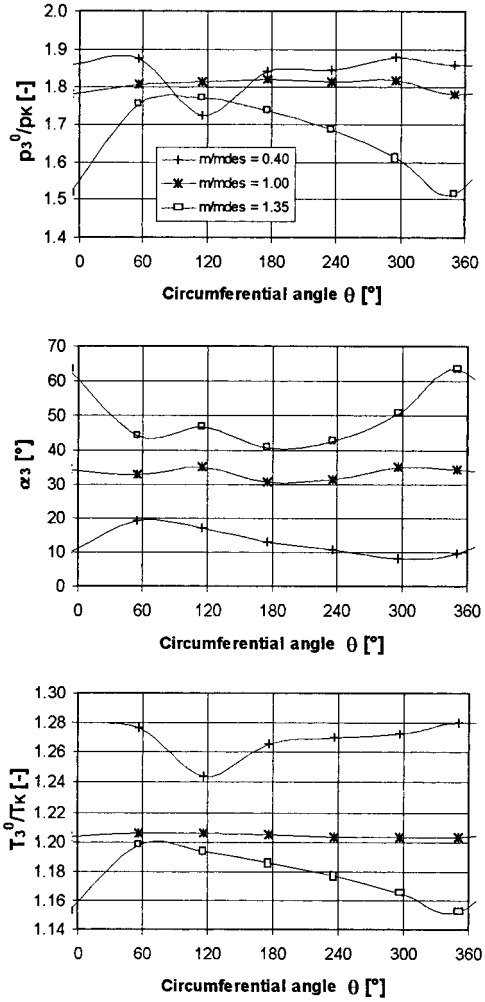

Fig. 7 Circumferential distribution of total pressure, flow angle, and total temperature at λ = 1.4

Experimental Flow Field Study. To understand the flow mechanism in the volute, flow field measurements were carried out using pneumatic five-hole probes (United Sensor DA-187) at seven cross-sectional planes. Figure 3 shows the location of these planes. The first five planes are located 60 deg apart circumferentially, whereas planes 6 and 7 are located in the volute exit diffuser leading to the flange. For planes 2 to 7 axial traverse of the flow was carried out for five radial positions. In plane 1 traverses have been made at only three radial positions for reasons of space restrictions. Measurements have been made at about 18 axial position for each traverse.

The flow field measurements at a particular mass flow ($m/m_{des} = 1.35$) are presented in Figs. 8(*a*) to 8(*d*). Figure 8(*a*) shows the measured distribution of swirl velocity in vector form for the seven volute planes. The strong vortex flow pattern is clearly seen for this operating point and its center is also clearly seen to coincide with the center of the cross section. The rotational velocity of this vortex flow increases from near zero at the center to a higher value radially out. From the center to some radial distance the gradient is high; thereafter it is moderate. In contrast to this, Ayder (1993) observed a more or less linear distribution of the swirl velocity in a volute with elliptical cross section, whereas the current cross section is rectangular. In the case of a rectangular cross section, the secondary corner flows are suspected to affect the flow mixing process in the volute. These secondary vortex flows in the corners are known to exist but are small and difficult to measure or quantify, by means of probe traverses.

Figure 8(*b*) shows the distribution of the pressure coefficient:

$$Cp = \frac{P - \bar{P}_3}{\bar{P}_3^0 - \bar{P}_3} \tag{1}$$

in the planes. The pressure distribution in any cross section is mostly determined by the vortical nature of the flow. The strong vortex flow induces a centrifugal effect, which results in an increasing pressure gradient radially out. In the vortex center, the pressure can sink to a lower value depending on the pressure at diffuser outlet. A negative *Cp* refers to a pressure inside the volute that is lower than the average pressure at diffuser exit. As can be seen, there are large areas inside the volute with negative values of *Cp*, indicating a pressure drop from diffuser outlet to the volute center. The conservation of angular momentum and the centrifugal forces caused by the tangential velocity V_t should lead to a radially increasing pressure. However, this effect is overlaid by the strong secondary vortex, which causes a remarkable pressure difference from the volute center to the walls. While the pressure at the volute walls is mainly determined by the diffuser discharge flow, the pressure at the volute center is a function of the swirl velocities. At this operating point with high swirl velocities inside the volute, this results in a loss of static pressure that was originally recovered in the radial diffuser.

A comparison of planes 1 to 6 shows clearly that the pressure falls in the peripheral direction, which corresponds well to the measured pressure distribution presented in Fig. 6.

The high swirl velocity at the volute wall and mostly the high velocity gradient in the vortex center are all sources of high loss. The distribution of the loss coefficient ω is shown in Fig. 8(*c*):

$$\omega = \frac{\bar{P}_3^0 - P^0}{\bar{P}_3^0 - \bar{P}_3} \tag{2}$$

A small fluid particle rotating in the outer region of the vortex requires kinetic energy to maintain its motion. After the dissipation of kinetic energy, this part is no longer able to rotate on an external flow path. It thus moves toward the area of low pressure, in this case toward the main vortex center. This leads to a separation of parts with high kinetic energy in the outer area and parts with low kinetic energy in the vortex center. This in turn is the cause of the high increase of the loss coefficient in the volute center. The above-mentioned separation process is supported by the rigid body vortex distribution, which is approximately maintained from planes 1 to 4. This distribution is accompanied by low shear stresses and low turbulent mixing. The large flow angles between $240 < \theta < 360$ deg lead to an increase of V_{r3}, which in turn is the cause for the different swirl distribution in plane 5. Here we can no longer speak of a rigid body vortex because there is a highly nonlinear variation of swirl velocity across the measurement section. The result is an intense turbulent mixing process, which disturbs the well-established loss distributions convected from the upstream planes. This is seen by the more uniform loss distribution in plane 5 and the decrease of loss coefficient (increase of total pressure) in the vortex core.

The loss coefficients in measurement plane 1 to 4 are negative, because the loss coefficient compares the local total pressure loss to the average inlet total pressure. The local total pressure, however, depends on the total pressure on the same streamline at the impeller exit. Due to the circumferential pressure distortion at the volute off-design operation, the total pressure can be higher than the average value used in the loss calculation.

Figure 8(*d*) shows the distribution of the throughflow velocity. Maximum values were measured near the vortex core. But near the volute wall the throughflow velocities were also high (as are the swirl velocities), which leads to wall friction losses that should not be neglected. At this high mass flow the incidence at the tongue is rather high. The flow simulation predicts large flow separation in the exit pipe diffuser near the hub wall. The probe measurements in plane 6 and 7 could not resolve this separation but show a highly disturbed exit diffuser flow for this operating point.

Since these kinds of measurement are extremely costly and time

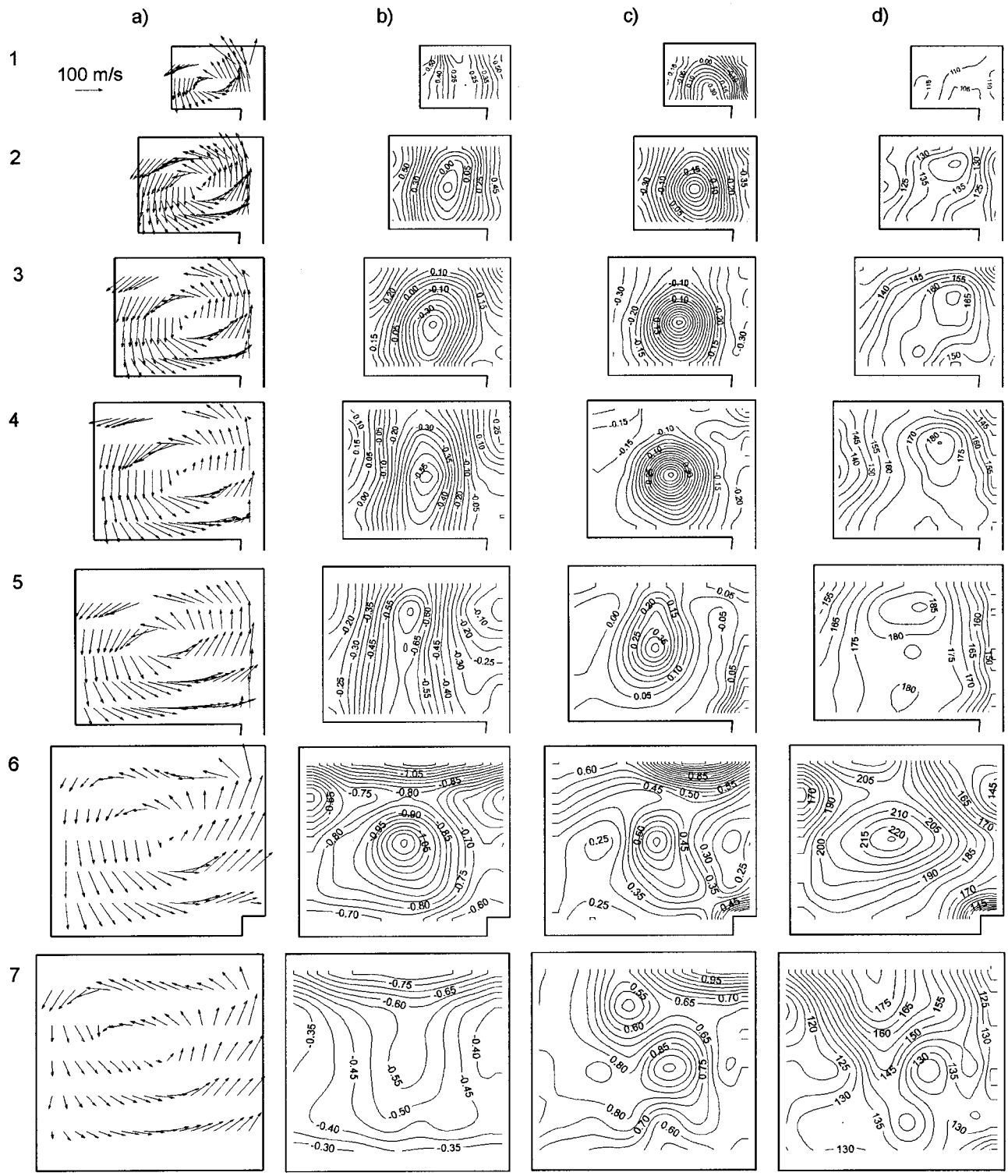

Fig. 8 Results of the flow field measurements in planes 1 to 7 ($m/m_{des} = 1.35$, $Mu_2 = 0.86$): (*a*) swirl velocity V_{swirl}; (*b*) pressure recovery coefficient *Cp*; (*c*) total pressure loss coefficient ω; (*d*) throughflow velocity V_t

consuming, it is desired to apply a calculation method that allows a more convenient investigation of a given volute geometry. The model presented by Ayder (1993) is applied here and comparisons to the experimental results are made.

Flow Simulation

Numerical Procedure. Since the influence of the boundary layers is manifested internally as a viscous loss, it is not necessary to carry out a thorough and detailed account of it. For certain flow cases, instead of using a time and cost-intensive full three-dimensional Navier–Stokes solution, it seems appropriate to use an Euler solution with a second-order viscosity term to account for wall friction effects and internal shear. Such calculations applied to volutes are known to offer good agreement between measurements and calculations, as shown by Ayder and Van den Braembussche (1994) and Hillewaert et al. (1998).

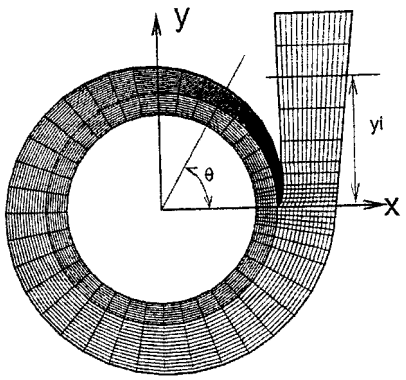

Fig. 9 Grid of compressor volute

In the current work, the Euler equations in conservative form have been solved using a finite volume approach. The octagonal volumes were determined by rectangular elements at various radial cross sections of the volute. Figure 9 shows the grid used in the present work. To be able to maintain the same number of elements in each cross section, a structured grid was used, which also allows comparable accuracy. A meridional view of the grid at $\theta = 270$ deg is shown in Fig. 10. The equations have been solved by means of the time-stepping scheme presented by Jameson et al. (1981). The influence of wall friction is included by body forces in the momentum equation (cf. Denton, 1986). A description of the numerical procedure is presented in detail by Ayder (1993).

Results of the Flow Simulation. The volute is designed for circumferentially constant static pressure. Apart from this operating point, the circumferential variation of total pressure and temperature and for a fully three-dimensional calculation also the two flow angles are needed. The circumferential variation of the static pressure is a result of this calculation and will be compared to the measured values. The required values of total pressure and temperature and flow angle are known from the measurement and have been imposed at the volute inlet. This was done by a linear interpolation between the measured locations. Because of local backflow at low flow rate, it was not possible to define "inlet" values here. Therefore, the grid was extended to the diffuser inlet, and circumferentially uniform values were imposed. Except for a small region near the volute tongue, this assumption corresponds well to the measurements.

A comparison of measured and calculated pressure distribution at diffuser exit is given in Fig. 11. For all three operating points a satisfactory correspondence between measured and calculated values can be seen. At design mass flow ($m/m_{des} = 1.0$) a slight circumferential decrease of static pressure is calculated, while an almost constant static pressure was measured. A somewhat higher discrepancy is seen at high mass flow ($m/m_{des} = 1.35$). Here, the measured pressure drop with increasing values of θ is smaller than

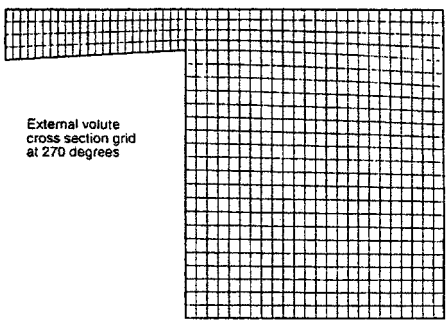

Fig. 10 External volute cross section grid at $\theta = 270$ deg

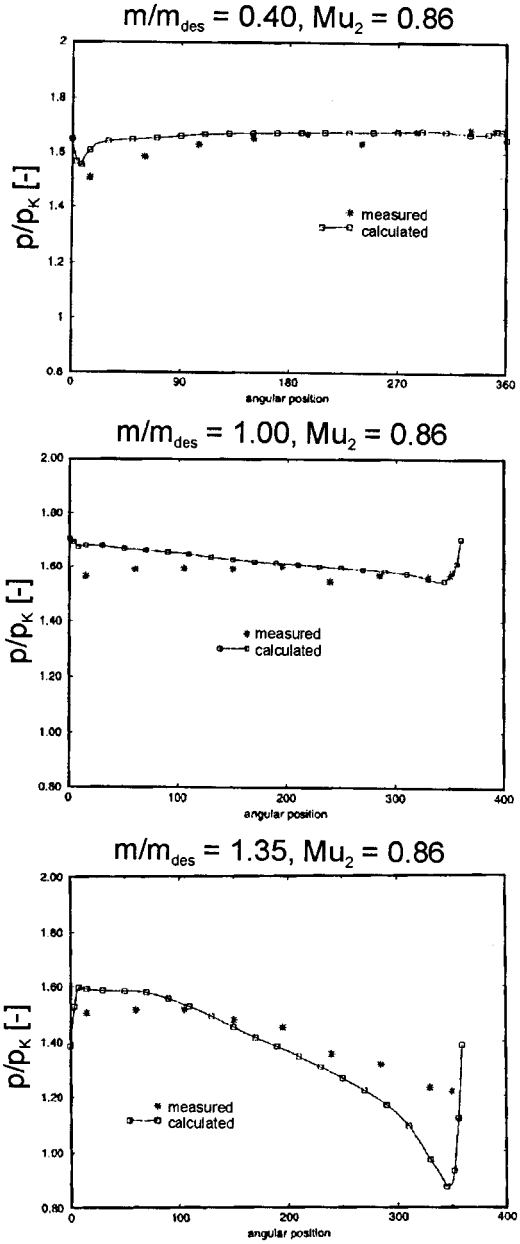

Fig. 11 Comparison of measured and calculated pressure distribution at diffuser exit ($\lambda = 1.45$)

the calculated variation. From this comparison we can conclude that the accuracy of the prediction of the circumferential pressure distribution is better at lower flow rate, which leads to the assumption that the intensity of the swirl is a source of inaccuracy in the calculation.

Since it is not possible to carry out a comparison between measured and calculated data at all measurement sections for all operating points, the following comparison is limited to measurement plane 3. This reveals sufficient information about the accuracy of the calculation method.

The swirl and throughflow velocities and the Cp and ω values in plane 3 are shown in Fig. 12 for the nominal operating point ($m/m_{des} = 1.0$). Measured and computed distributions of the swirl velocity correspond very well. The deviation is somewhat larger for the throughflow velocity. The calculation shows higher values near the center, while the measurements show an almost uniform distribution. However, for reasons of continuity the average values are almost equal. The agreement for static pressure rise and total pressure loss in section 3 is quite good. Both measurement and

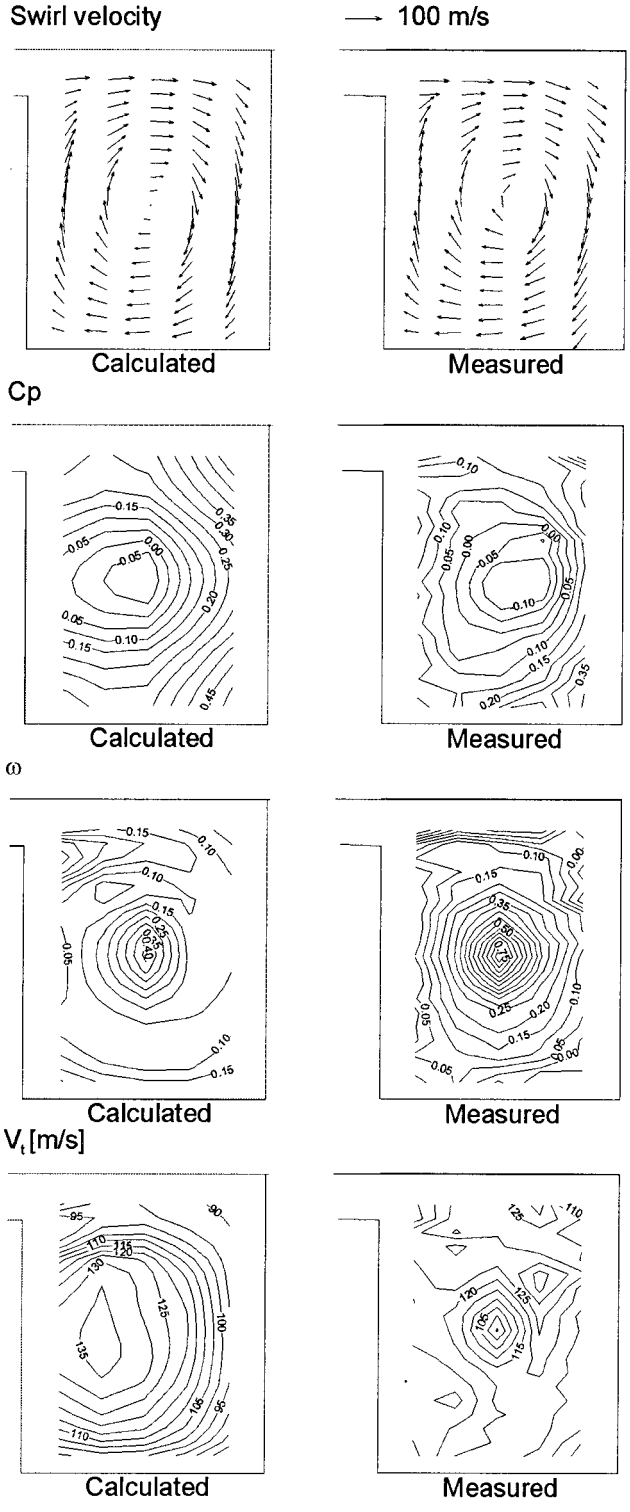

Fig. 12 Comparison of measured and calculated flow field in plane 3 for nominal operating point (m/m_{opt} = 1.0)

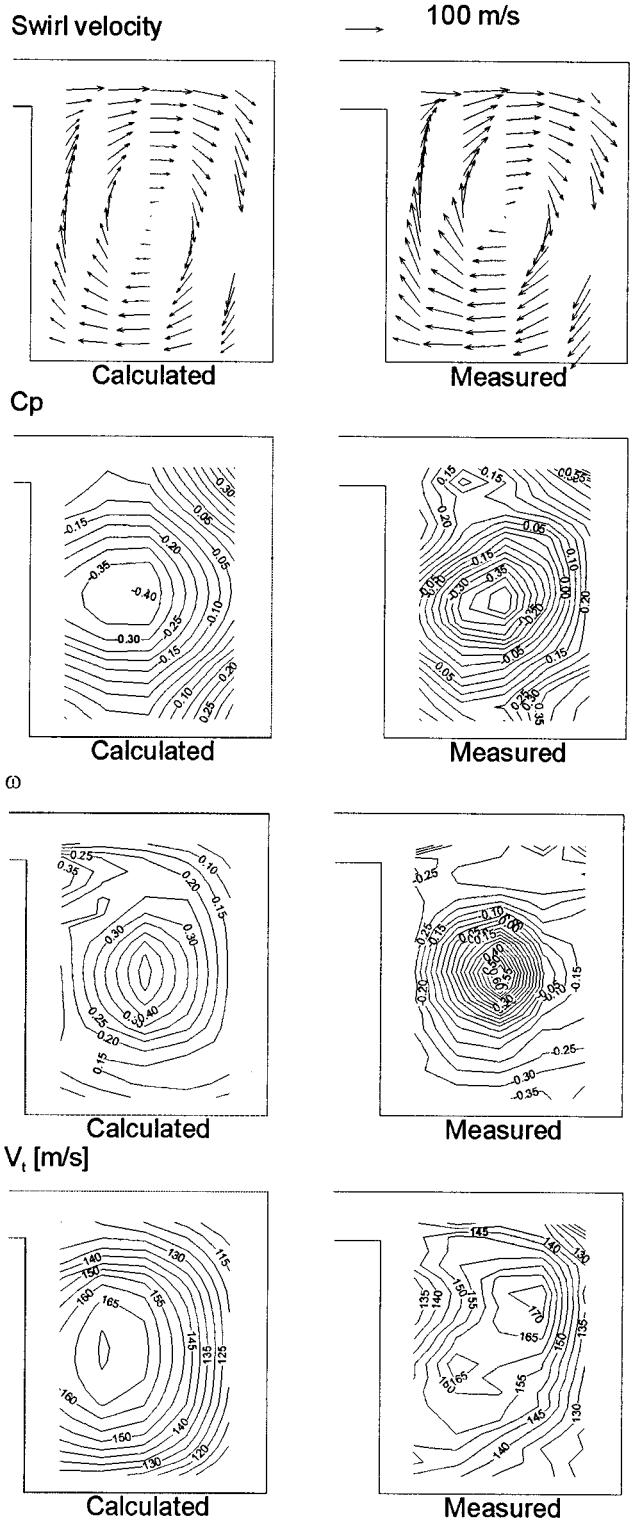

Fig. 13 Comparison of measured and calculated flow field in plane 3 near choke flow (m/m_{opt} = 1.35)

calculation show a negative *Cp* in the vortex center, indicating a pressure decrease from the diffuser outlet.

The calculated losses are less concentrated in the vortex center with a lower level of the maximum. Thus, the mechanism of separation of areas with higher and those with lower loss is not fully covered by the calculation method. This leads to a lower accuracy of the prediction of global losses by the numerical method. However, except for the loss concentration in the vortex center, local loss distributions are well predicted.

The swirl and throughflow velocities in Fig. 13 are characteristic for a volute operating at maximum mass flow. As mentioned before, the flow at the diffuser exit results in a forced vortex-type secondary flow inside the volute with an increase of swirl velocity from the volute center to the volute walls and a maximum throughflow velocity in the vortex core. The measured throughflow velocities are slightly more disturbed, but correspond well with the calculations. A satisfactory agreement between measured and cal-

culated values is also visible for the static pressure rise and the loss coefficient in plane 3. Again the concentration of pressure loss in the center is higher in the measurement than in the calculation.

Measured and calculated values of swirl and throughflow velocities at minimum mass flow for plane 3 are given in Fig. 14. The swirl velocity distribution is similar but the vortex core is not exactly at the same position. The measurement indicates a counterotating vortex at the shroud wall of the volute, which is not seen in the calculated flow field. However, this does not have a significant influence on the through flow velocity. For this operating point the values of the throughflow velocity are minimum in the vortex center. The pressure rise and especially the losses are well predicted in section 3.

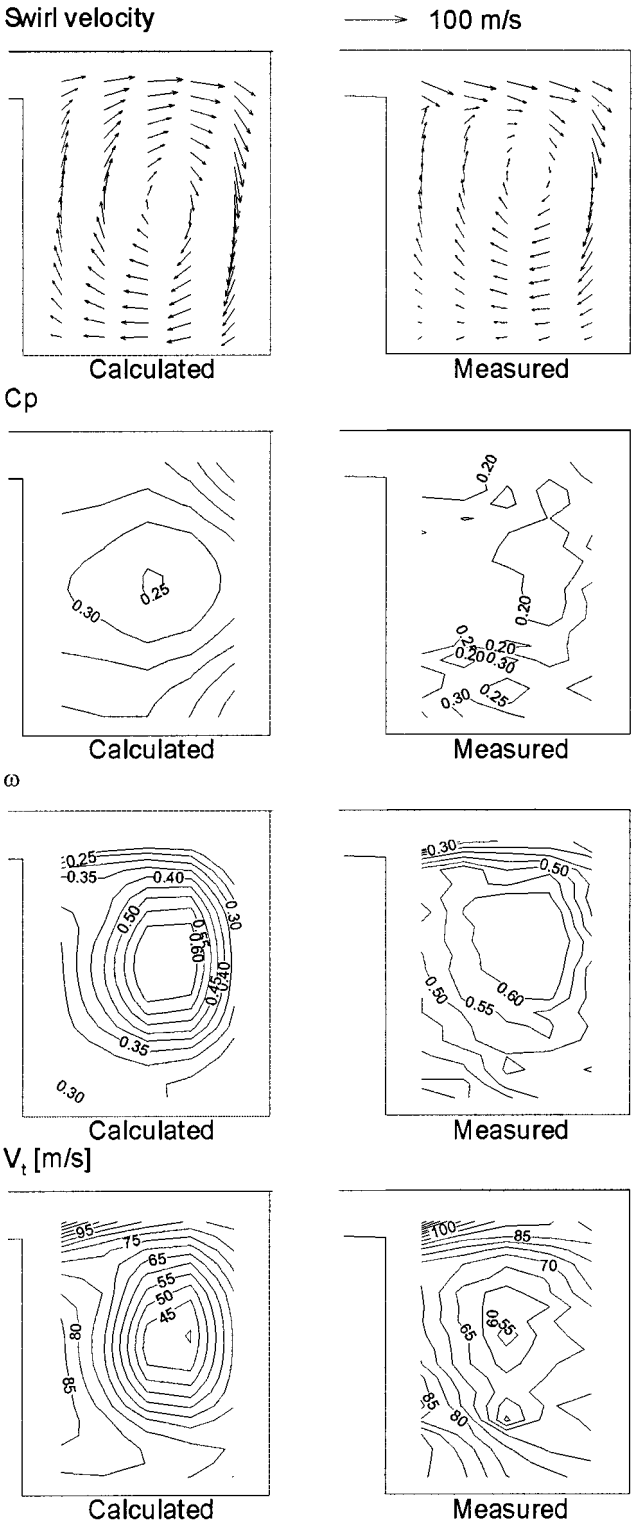

Fig. 14 Comparison of measured and calculated flow field in plane 3 near surge (m/m_{opt} = 0.4)

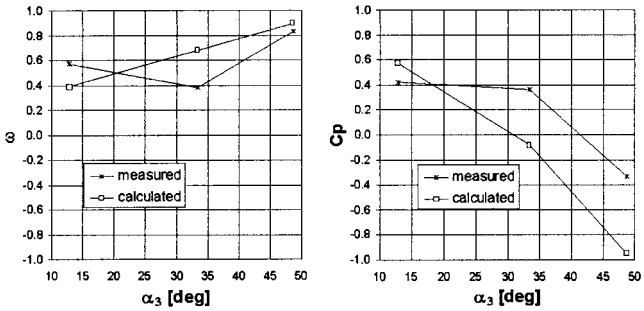

Fig. 15 Comparison of measured and calculated global volute performance (pressure recovery and total pressure loss)

The comparisons have shown that the three-dimensional flow model provides a good description of the flow field inside the volute. Some discrepancies can be seen near the vortex center, where the measurements show more concentrated values of *Cp* and ω (especially at medium and high mass flow rates). It is our belief that the use of a finer grid would lead to a better resolution of the pressure and loss distribution in the area of high gradients, i.e., in the vortex center. However, the grid has not been refined in order not to increase the calculation time too much.

Global Component Performance. It is of major importance for the designer to gain accurate knowledge of the global characteristics of the volute. Figure 15 shows a comparison of measured and calculated global loss and pressure rise coefficients plotted versus flow angle at diffuser exit.

At high mass flow, the losses are about twice the value of the design point. This confirms the assumption that the kinetic energy of the vortex is totally dissipated. The losses at minimum mass flow are underestimated, since the model is not able to calculate correctly the losses originating from the flow separation, which could be observed in the exit diffuser.

On the right hand plot of Fig. 15 it can be seen that at high mass flow, the static pressure decreases from volute inlet to the exit of the pipe diffuser. This is not only due to the fact that the volute is too small but to a large extent results from the high losses. The overprediction of the losses results in a corresponding underprediction of the static pressure rise.

One can conclude that the Euler method correctly predicts the tendency of the losses and the pressure rise. If one considers the complexity of the flow and the small computation time (if compared to a full Navier–Stokes computation), the accuracy can be considered to be satisfying. The calculation method is a valuable tool to predict the optimum operating point and local flow phenomena, such as the flow in the tongue region. It is less accurate to predict the volute performance.

Conclusions

Flow measurements at the diffuser exit and inside the external volute of a centrifugal compressor have been reported. It is shown how the circumferential pressure distortion at off-design operation influences the impeller discharge flow and consequently leads to a circumferential variation of impeller operating point with a variation of total pressure, temperature and flow angle.

Detailed flow measurements inside the volute gave further insight in the three-dimensional structure of the volute flow and may serve as a source to further improve existing models for the volute flow.

Comparisons of the measured and calculated flow fields in the

external volute clearly show that the three-dimensional Euler method with a correction for friction effects provides a quite accurate description of the flow. Local loss as well as static pressure rise distributions are calculated with sufficient accuracy. The method can therefore be used to lay out an optimum geometry and for the study of flow details, e.g., the flow in the tongue region.

The calculations give a correct trend for the overall performance except at low mass flow where flow separation was not predicted.

Acknowledgments

The authors wish to thank the members of the Forschungsvereinigung Verbrennungskraftmaschinen (FVV) for the financial support of this study, the numerous fruitful discussions, and for allowing the publication of this document.

References

Ayder, E., and Van den Braembussche, R. A., 1991, "Experimental Study of the Swirling Flow in the Internal Volute of a Centrifugal Compressor," ASME Paper No. 91-GT-7.

Ayder, E., 1993, "Experimental and Numerical Analysis of the Flow in Centrifugal Compressor and Pump Volutes," Ph. D. thesis, VKI.

Ayder, E., and Van den Braembussche, R. A., 1994, "Numerical Analysis of the Three-Dimensional Swirling Flow in Centrifugal Compressor Volutes," ASME JOURNAL OF TURBOMACHINERY, Vol. 116, pp. 462–468.

Badie, R., Jonker, J. B., and Van Essen, T. G., 1992, "Calculation on the Time-Dependent Potential Flow in a Centrifugal Pump," ASME Paper No. 92-GT-151.

Borer, C., Sorokes, J., McMahon, T., and Abraham, E., 1997, "An Assessment of the Forces Acting Upon a Centrifugal Impeller Using Full Load, Full Pressure Hydrocarbon Testing," *Proc. Texas A&M Turbomachinery Symposium.*

Denton, J. D., 1986, "The Use of Distributed Body Force to Simulate Viscous Effects in 3D Flow Calculations," ASME Paper No. 86-GT-144.

Fatsis, A., 1995, "Numerical Study of the 3D Unsteady Flow and Forces in Centrifugal Impellers with Outlet Pressure Distortion," Ph. D. thesis, Universiteit Gent, Fakulteit van de toegepaste Wetenschappen, in samenwerking met Von Karman Institute for Fluid Dynamics, 1995.

Hagelstein, D., Van den Braembussche, R. A., Keiper, R., and Rautenberg, M., 1997, "Experimental Investigation of the Circumferential Static Pressure Distortion in Centrifugal Compressor Stages," ASME Paper No. 97-GT-50.

Hillewaert, K., and Van den Braembussche, R. A., 1999, "Numerical Simulation of Impeller–Volute Interaction in Centrifugal Compressors," ASME JOURNAL OF TURBOMACHINERY, Vol. 121, pp. 603–608.

Iversen, H. W., Rolling, R. E., and Carlson, J. J., 1960, "Volute Pressure Distribution, Radial Force on the Impeller, and Volute Mixing Losses of a Radial Flow Centrifugal Pump," ASME *Journal of Engineering for Power*, Vol. 82, No. 1, pp. 136–144.

Jameson, A., Schmidt, W., and Turkel, E., 1981, "Numerical Solutions of the Euler Equations by a Finite Volume Method Using Runge–Kutta Time Stepping Schemes," AIAA Paper No. 81-1259.

Jiang, Z., Seidel, U., Shao, Z., and Rautenberg, M., 1996, "Diffuser, Circumferential Pressure Field and Blade Vibration in a Centrifugal Compressor," *Proc. 3rd ISAIF*, Beijing, China.

Kurokava, J., 1980, "Theoretical Determination of the Flow Characteristics in Volutes," *Proc. IAHR-AIRH Symposium 1980*, Tokyo, Japan.

Rautenberg, M., Van den Braembussche, R. A., et al., 1998, "Strömungsvorgänge in spiralförmigen Sammelräumen für Radialverdichterstufen," *FVV-Abschlußbericht*, Heft 659, Frankfurt/Main, Germany.

Sorokes, J. M., Borer, C. J., and Koch, J. M., 1998, "Investigation of the Circumferential Static-Pressure Non-Uniformity Caused by a Centrifugal Compressor Discharge Volute," ASME Paper No. 98-GT-326.

Van den Braembussche, R. A., and Hände, B. M., 1990, "Experimental and Theoretical Study of the Swirling Flow in Centrifugal Compressor Volutes," ASME JOURNAL OF TURBOMACHINERY, Vol. 112, pp. 38–43.

Van den Braembussche, R. A., Ayder, E., Hagelstein, D., Rautenberg, M., and Keiper, R., 1999, "Improved Model for the Design and Analysis of Centrifugal Compressor Volutes," ASME JOURNAL OF TURBOMACHINERY, Vol. 121, pp. 619–725.

DISCUSSION

N. A. Cumpsty[1]

I became aware of the small amount of published material on compressor volutes when I tried to provide some coverage of this topic in my book *Compressor Aerodynamics* (Cumpsty, 1989). I therefore warmly welcome this significant contribution, combining experiment and numerical treatment.

One of the issues I was forced to address in *Compressor Aerodynamics* is the difference between the optimum operating condition and the design condition. In the design condition the static pressure is normally taken to be uniform around the diffuser exit; this is primarily because it makes the design easy, with the impeller, diffuser, and volute all amenable to simple independent analysis. Uniform conditions also minimize noise and vibration. Nevertheless, uniform static pressure will not in general be the condition for maximum pressure rise of the stage at a given speed, since the volute static pressure field can decelerate the flow. The radial geometry makes it hard to visualize the processes in a simple way, but one can imagine the volute unwrapped to represent one enormous vane downstream of an axial rotor. In this case, some pressure rise would be achieved by having the vane loaded and the circumferential pressure nonuniform.

One of the things that makes the diffuser volute combination so hard to analyze is the radically different geometry of the impeller, the diffuser, and the volute. The length scale of the volute is one circumference so, adopting the simple-minded unwrapping to an axial geometry of the paragraph above, the effect of the volute can be felt a long way upstream, certainly to the inlet of the impeller. A proper calculation therefore needs to include unsteady effects in the impeller and to calculate the impeller, diffuser, and volute together. This is something that should now be entirely possible and an approximate implementation was reported by Hillewaert and Van den Braembussche (1999). The calculations reported in the present paper are very different from this, of course, with measured (time-averaged) total pressure and temperature and measured flow angle imposed at volute inlet. This allows a steady calculation to be performed, but omits what might be regarded as the most interesting part of the problem. Given that stagnation conditions are specified at volute inlet, the agreement shown in Fig. 11 is disappointing and seems less good than in the paper reporting a one-dimensional method applied to the same date (Van den Braembussche et al., 1999).

In the present paper it is suggested that the intensity of swirl is the cause of the inaccuracy in the prediction. Would the authors care to expand on the reasons for assuming this and why it should be so? Taking this further, the authors state that the high loss at high mass flow rates (twice the value at design point) confirms the assumption that the kinetic energy of the vortex is totally dissipated. This may be so, but the agreement in Fig. 15 between calculations and measurement is not very satisfactory. Would the authors be able to interrogate the results of their calculations at high flow rates to estimate how much energy is involved in the vortex to establish whether this is the primary cause of the increased loss?

Authors' Closure

There are more references on volute flow and impeller response to distortions than one would conclude from a first look at the literature. However, most of them are about pumps and do not provide relevant information. The research we started some 10 years ago, about which more information can be found in the references of this paper, aimed for a better understanding of the flow structure and the loss mechanisms in volutes.

The optimum operating point of a compressor depends on its application. Compressors operating at very high pressure level have their optimum point at constant circumferential pressure in order to limit the radial force on the shaft (Fatsis et al., 1997) and to avoid a reduction of the stable operating range.

In case one aims for maximum efficiency, the optimum point will depend on the trade-off between a possible gain in the volute pressure rise and the extra losses due to the unsteady impeller flow resulting from the circumferential pressure variation. One considers here the static pressure distribution at constant radius and not the one resulting from an increase in radius between the diffuser

[1]University of Cambridge, Department of Engineering, Whittle Laboratory, Madingley Rd., Cambridge, CB3 0DY, United Kingdom.

exit and the volute outer wall. There is very little information available about these extra impeller losses. Abramian and Howard (1994) experimentally proved for a centrifugal pump that a volute circumferential pressure distortion leads to a decrease of impeller efficiency. One can therefore conclude that the point of maximum stage efficiency will not be far from the point of circumferentially constant outlet pressure.

Calculating the impeller, diffuser, and volute together with an unsteady three-dimensional viscous flow solver is indeed the best approach, because of the strong interaction between the components. However, this requires a huge amount of computer effort. Periodicity occurs only every 360 deg so that the numerical domain cannot be limited to a few pitches of the rotor and stator, as is commonly done in axial compressor or turbine stage calculations.

Results presented in the literature have been obtained after some simplifications have been introduced. Flathers et al. (1996) made steady three-dimensional Navier–Stokes calculations with outlet distortion (frozen rotor model). Hillewaert et al. (1999) made unsteady Euler calculations with corrections for viscosity. The present paper, comparing experiments and calculations of the volute flow with specified inlet boundary conditions, intends to verify the accuracy of the latter model and to complement the measurements with more detailed information.

Indeed, the agreement of Fig. 11 is not as good as one would wish: first, because the inlet conditions are available only at six circumferential positions. This is insufficient to describe accurately the large circumferential distortion that occurs near choking mass flow. Second, by the way the inlet conditions have been specified in present calculations. Although theoretically correct, they amplify the calculation errors. Any underestimation of the static pressure in the second half of the volute, because of a small overestimation of the upstream volute losses, results in a local increase of the radial velocity component. This local increase of the mass flux also increases the swirl intensity and hence the local flow blockage and losses in the volute. The result is a further decrease of the local static pressure. The total mass flow being imposed this requires a decrease of the mass flux and hence an increase of the pressure in the first part of the volute. This mechanism is responsible for the overly large pressure drop along the volute circumference and overly high volute losses. The same problem also occurred in the one-dimensional approach described by Van den Braembussche et al. (1999) but to a smaller extent, because of the stronger coupling of the volute with the impeller flow. Specifying the volute inlet flow angle is a last source of errors. A local increase of the radial velocity component thus results in a proportional increase of the tangential velocity. This is opposite to what happens at the exit of a backward leaned impeller.

The larger circumferential variation of the radial velocity results in an even larger increase of the swirl kinetic energy because the latter one is proportional to the circumferential integration of Vr^3. This error on the incoming swirl kinetic energy is the main cause of the discrepancies in the volute losses and static pressure rise observed in Fig. 15.

Except for an increase of radius in the downstream diffuser or the installation of three-dimensional vanes inside the volute, there is no mechanism to recuperate the kinetic energy related to the swirl resulting form the diffuser exit radial velocity (Japikse, 1982; Weber and Koronowski, 1986). This is also experimentally confirmed by the total pressure loss contours shown in the present paper and by Ayder et al. (1993, 1994). 55 percent of the volute inlet kinetic energy near choking mass flow is due to the diffuser outlet radial velocity component. It reduces to 10 percent at the exit measurement plane and it was observed to disappear completely farther downstream. The swirl velocity is responsible for 68 percent of the total volute losses at maximum mass flow. The first step to improving the performance is therefore by reducing the diffuser exit radial velocity.

References

Abramian, M., and Howard, J. H. G., 1994, "Experimental investigation of the steady and unsteady relative flow in a model centrifugal impeller passage," ASME JOURNAL OF TURBOMACHINERY, Vol. 116, pp. 269–279.

Flathers, B., and Bache, G. E., 1999, "Aerodynamically induced radial forces in a centrifugal gas compressor—Part 2: Computational investigation," ASME *Journal of Engineering for Gas Turbines and Power*, Vol. 121, pp. 725–734.

Fatsis, A., Pierret, S., and Van den Braembussche, R. A., 1997, "3D Unsteady Flow and Forces in Centrifugal Impellers With Circumferential Distortion of the Outlet Static Pressure," ASME JOURNAL OF TURBOMACHINERY, Vol. 119, pp. 94–100.

Japikse, D., 1982, "Advanced diffusion levels in turbocharger compressors and component matching," *Proc. 1st Intl. Conf. on Turbocharging and Turbochargers*, London.

Weber, C. R., and Koronowski, M. E., 1986, "Meanline performance prediction of volutes in centrifugal compressors," ASME Paper No. 86-GT-216.

Stall Inception in the Compressor System of a Turbofan Engine

Bernd Höss

Dirk Leinhos

Leonhard Fottner
Institut für Strahlantriebe,
Universität der Bundeswehr München,
D-85577 Neubiberg, Germany

Compressor flow instabilities have been the subject of a great number of investigations during the past decade. While most of this research work was done on isolated test-rig compressors, this paper presents stall inception measurements in the compressor system of a two-spool turbofan engine at various power settings. Several analyzing techniques such as temporal low-pass and band-pass filtering, temporal and spatial Fourier transforms including power-spectral-density calculations of the spatial coefficients, and a wavelet analyzing technique are applied. For the low-pressure compressor three different types of stall inception processes were observed depending on the rotor speed. At low speed, stall originates from spike-type precursors, while long wavy pressure fluctuations corresponding to modal waves were observed prior to stall at midspeed for undistorted inlet flow. At high speed, the rotor shaft unbalancing dominates the stall inception process as an external forcing function. In the case of distorted inlet flow spike-type stall inception behavior dominates throughout the speed range. While filtering and the Fourier spectra give a good insight into the physical background of the stall inception process (but with a very short warning time), the wavelet transform indicates the approach of the stalling process a few hundred rotor revolutions in advance independently of the type of precursor. Setting up a reliable stall avoidance control based on this analysis scheme seems to be promising.

Motivation and Objective

Increasing the overall efficiency while improving engine handling is a desired but a very challenging task for any control unit since safe operation of the engine has to be guaranteed for all flight and engine conditions as well. These demands affect particularly the choice of the steady-state compressor working line with a sufficient surge margin. Especially inlet distortions combined with a rapid engine acceleration lead to a great decrease in surge margin. In the case of exceeding the compressor stability limit, flow separation within the compressor occurs, leading to one of the two instability modes: rotating stall or surge. Both conditions are very adverse as they result not only in a sharp thrust loss but also in very high mechanical stresses. Often the engine has to be shut down to recover.

In order to put the compressor working line closer to its stability limit, a future control system has to be capable to detect the incipient flow instability by parameter identification in real time (not necessarily by computation) and start any flow stabilizing action either by dethrottling and therefore unloading the compressor ("stall avoidance") or by actively modifying, locally or globally, the damping behavior of the oscillatory system ("active control").

The first investigations on the topic of compressor flow separations concentrated on the flow structure of a fully developed stall cell. Detailed flow measurements in low-speed compressors by Day and Cumpsty (1978), Das and Jiang (1984), and Poensgen and Gallus (1996) showed that a stall cell is a highly active zone of three-dimensional flow. Common to these measurements is a very high circumferential velocity component in front of the stall cell.

From the viewpoint of any inflight control system, the pre-stall and stall formation process is of particular interest, as any stabilizing action has to take place during these periods to be effective at a reasonable expense. For this reason further investigations concentrated hereon. Two different mechanisms of stall inception could be identified independently of the fully developed instability mode due to the fact that surging is always preceeded by the formation of rotating stall very rapidly growing circumferentially (as reported by Day, 1993b). On one hand, so-called modal waves predicted by the theoretical post-stall compression model of Moore and Greitzer (1986) as initial rotating velocity disturbances of long length scale at the compressor circumference become underdamped with the compressor working close to its stability limit and finally lead to stall. These type of precursors were experimentally supported by the work of McDougall et al. (1990) carried out on a single-stage, low-speed compressor and later confirmed by Garnier et al. (1991) and subsequently by Hoying (1993), Tryfonidis et al. (1995), and recently by Day et al. (1999) also for high-speed compressors. These experiments show that stall inception via modal waves plays a dominant role for many compressors at least in a limited speed range. In the paper of Day et al. (1999) the only experimental confirmation known to the authors for the existence of modal waves in a compressor installed in an engine has been stated for the single-spool VIPER engine but only within a very narrow speed range. On the other hand, short length scale disturbances—so called spikes—localized within only a few rotor passages and rapidly growing from the first detection to fully developed stall have been first reported by Day (1993a) for two low-speed compressors. Later investigations showed that some compressors only exhibit these spike-type precursors, i.e., Escuret and Garnier (1996) and Lawless et al. (1993), but most compressors might reveal both precursor types, depending on the stage matching, and therefore on the rotor speed, according to Camp and Day (1998).

No further stall precursor studies in a full-scale aeroengine were performed besides the above-mentioned investigation of Day et al. (1999) preceded by research of Wilson and Freeman (1994) and Day and Freeman (1994) with the same VIPER engine and a further investigation done by Gallops et al. (1993) with two bypass engines but with a conventional, low-frequency instrumentation.

A very critical point on the way to successful flow stabilization

Contributed by the International Gas Turbine Institute and presented at the 43rd International Gas Turbine and Aeroengine Congress and Exhibition, Stockholm, Sweden, June 2–5, 1998. Manuscript received by the International Gas Turbine Institute February 1998. Paper No. 98-GT-475. Associate Technical Editor: R. E. Kielb.

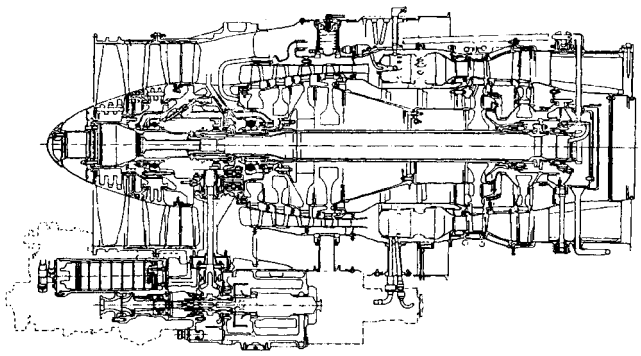

Fig. 1 LARZAC 04 C5 test engine

Table 1 Performance data LARZAC 04 C5 at design speed and sea level conditions

n_{LPC}	17500 rpm
n_{HPC}	22561 rpm
Π_{LPC}	2.26
Π_{HPC}	4.6
TET	1403 K
μ	1.13
mass flow rate	27.64 kg/s
F	13 kN
$N_{LPC,\,rotor}$ $1^{st}/2^{nd}$	23 / 29
$r_{tip,LPC,\,1^{st}\,rotor}$	0.229 m
$r_{hub,LPC,\,1^{st}\,rotor}$	0.097 m

based on computer-aided controlling is not only the type of precursor but also the obtained pre-warning time prior to stall formation. This depends very strongly on the parameter identification technique. Applying simple thresholding of the time domain signals results usually in a very short warning time of only a few rotor revolutions (rotor revs.) (McDougall et al., 1990; Escuret and Garnier, 1996). Tryfonidis et al. (1995) demonstrated a more sophisticated analyzing technique by calculating the power spectral density and the traveling wave energy of the spatial Fourier coefficients. Doing this, warning times of a few hundred rotor revolutions were obtained.

In this paper stall inception measurements mainly from the low-pressure compressor of the two-spool aeroengine LARZAC 04 are presented and analyzed in time and frequency domain with several analyzing techniques.

The results of these analyses are compared with each other regarding the physical background of the stall inception process as well as the obtained pre-warning time.

Experimental Facility, Instrumentation, and Data Acquisition

Test Engine. The tests were carried out with the twin-spool turbofan engine LARZAC 04 C5 (Fig. 1). It consists of a two-stage low-pressure compressor (LPC), a four-stage high-pressure compressor (HPC), an annular combustion chamber, and single-stage high and low pressure turbines. The core and bypass flow expand unmixed through separate nozzles. Two bleed valves after the second stage of the HPC reduce HPC compressor blade loading at part-speed up to 80 percent HPC rotor speed.

Performance parameters at design speed and sea level static conditions are listed in Table 1. The engine was designed in the late 60's by the GRTS (Groupement Turbomeca-Snecma) and is on duty in the ALPHA JET trainer aircraft.

Throttling Devices. One common way to throttle a compressor in an engine installation is either overfueling ("fuel-spikes") or rapid and repeated power setting changes, thereby evoking nonequilibrium conditions (heat transfer, tip clearances). While the first method also leads to turbine overheating, both methods cause compressor flow separation during transients, in a manner that is very hard to reproduce and that is unfavorable for stall inception investigations.

In order to overcome these limitations, external devices consisting of two mechanical and one pneumatic throttling device were built. The mechanical devices reduce the nozzle areas by either moving a parabolic body of revolution axially into the core nozzle (Fig. 2) or by closing an aperture in order to reduce the secondary nozzle area (Fig. 3). Therefore, the two compressors can be throttled stationary and independently of each other. With the pneumatic throttling device, overpressured air can be blown into the HPC's exit plane, thus increasing air mass flow rate through the combustion chamber and the turbines. This allows HPC throttling also at high speeds causing HPC surging.

Instrumentation. The instrumentation of the LARZAC test engine can be classified into a low and a high-frequency part according to the sensor frequency response.

The low-frequency or conventional part is described in detail by Höss and Fottner (1997) and is shown in Fig. 4. With the measured quantities it is possible to determine the stationary and low-frequency component performance behavior by gas path analysis. The high-frequency instrumentation consists of miniature pressure transducers.

Figure 5 shows the various instrumentation positions within the compressor system. Each compressor is equipped with five wall-static pressure transducers in front of the first stage. While they are equally spaced in front of the LPC, this was not possible in front of the HPC due to constructive restraints. With this, circumferentially distributed pressure fluctuations can be resolved spatially in the case of a sine-fluctuation up to the second order. In most cases when modal waves were observed the first two spatial harmonics dominate the inception process.

Another wall-static pressure transducer is located in front of the second-stage rotor of the LPC. In conjunction with the total pressure probe facing axially or circumferentially at the same axial position and the traversable total pressure probe within the second stator, it is possible to compare the suitability of the measuring quantities for early detection of stall precursors. The abovementioned measurements by Day and Cumpsty (1978) and Das

Nomenclature

a = wavelet parameter of dilation or compression
a_k = Fourier coefficients
b = wavelet parameter of translation in time
$c_{a,b}$ = wavelet coefficients
F = thrust
HPC = high-pressure compressor
LPC = low-pressure compressor
n = rotor speed
N = number of blades
r = radius
T_0 = time of period
TET = turbine entry temperature
μ = bypass ratio
Π = pressure ratio
ϕ = flow coefficient
Ψ = pressure rise coefficient
$\Psi_{a,b}$ = wavelet function

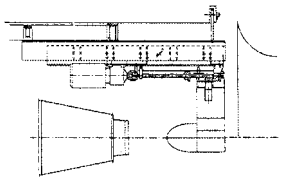

Fig. 2 Core throttle

and Jiang (1984) showed very high amplitude variations of the total pressure signal, especially of the circumferential total pressure. Further total pressure probes—partly traversable—are located in front of and behind the compressors and in the second stator of the HPC in order to localize the radial and axial position and extension of the stall.

The reference-volume of the sensors is built as either a vented or a sealed gage. The vented gage sensors have the advantage that the pressure within the reference volume can be adapted to the pressure level of the flow. Therefore smaller sensor ranges with a higher resolution can be used.

Data Acquisition and Control Unit. The data acquisition system is mainly the system described by Herpel and Fottner (1993). It consists of a device for measuring low-frequency signals of up to 96 channels with an overall sampling rate of 100 kHz and a resolution of 16 bit.

The high-frequency signals are digitized with a sampling rate of 32.8 kHz and 13 bit resolution for each channel with an analog low-pass filter of 12.8 kHz. This frequency spectrum is by far sufficient for resolving pressure fluctuations occurring during stall inception. Due to data transfer and storage, the system is limited to a simultaneous eight channel input.

Beside this data acquisition system, a control unit based on a Pentium PC and a DSP data acquisition card was established. This system is capable of controlling the positions of the power lever, the mechanical throttling devices and the pneumatic throttle simultaneously and synchronously. Up to eight further input signals (i.e., signals of the miniature pressure transducers) can be monitored by an averaging and a gradient technique and by a Fast Fourier-Transform. In case of stall or surge, the throttling can be reliably interrupted by the control unit within a few milliseconds.

Analyzing Techniques

In the case of the high-frequency pressure signals, several analysis techniques were used and the results compared to each other. Aliasing of the signal due to undersampling was avoided by analog or digital filtering.

The signals are analyzed in the time domain by low-pass and band-pass filtering with various filter steepnesses, in the temporal frequency domain by a Fourier and a wavelet transform and the circumferentially distributed wall-static pressure signals at LPC inlet also by a spatial Fourier transform. Additionally, the power spectral density is calculated with the spatial Fourier coefficients as input data.

Time Domain. The signals are analyzed in the time domain by a digital single band, nonrecursive FIR filter in low-pass and band-pass configuration. This filter is linear in phase. The frequency response and the filter steepness, respectively, can be chosen arbitrarily.

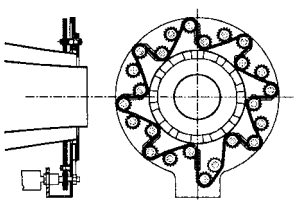

Fig. 3 Bypass throttle

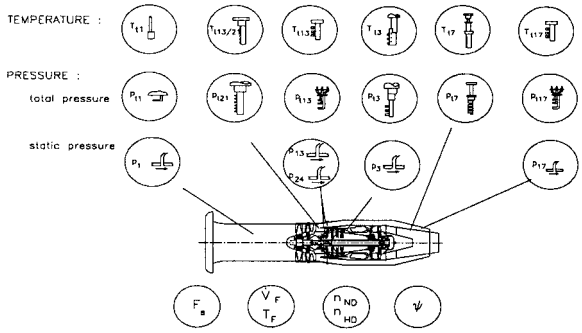

Fig. 4 Low-frequency instrumentation positions

Fourier Transform. According to the theory of continuous Fourier transform, a given continuous, periodic function $x(t)$ can be described by a sum of sine waves. Using Eq. (1) (Table 2) the function $x(t)$ can be written as shown in Eq. (3) with $\omega_0 = 2\pi/T_0$ and a_k as the Fourier coefficients as given in Eq. (2). A discrete, finite function can be transformed analogously by replacing the integrals by sums.

The temporal frequency spectra of the miniature pressure transducer signals were determined using a Fast-Fourier-Transform algorithm. Thereby, the window size can be varied from 64 (about 2 ms in time) to 65,536 (2 s in time) measured data points. While smaller time windows result in a coarse frequency spectrum, larger windows wash out or broaden nonperiodic or fast changing (growing in amplitude or changing frequency) signals within the frequency spectrum. Usually a time window of 0.125 s (4096 samples) was used. Different weightings of the time-window borders showed no remarkable effect on the results.

Additionally, the circumferentially distributed wall-static pressure signals at the LPC inlet are spatially Fourier transformed by replacing the time variable t in Eq. (2) with the circumferential position of the sensor. Therefore, long-wavelength rotating disturbances can be identified by a constant phase speed. This analyzing technique was first demonstrated by McDougall et al. (1990) and later in greater detail by Garnier et al. (1991).

Power Spectral Density and Traveling Wave Energy. Further information about flow phenomena in the circumferential direction can be extracted from a series of pressure signals by computing the power spectral density (PSD) of the temporal development of their spatial Fourier coefficients.

While the spatial Fourier transform yields amplitude and phase over time, the PSD gives the development of the power of separate

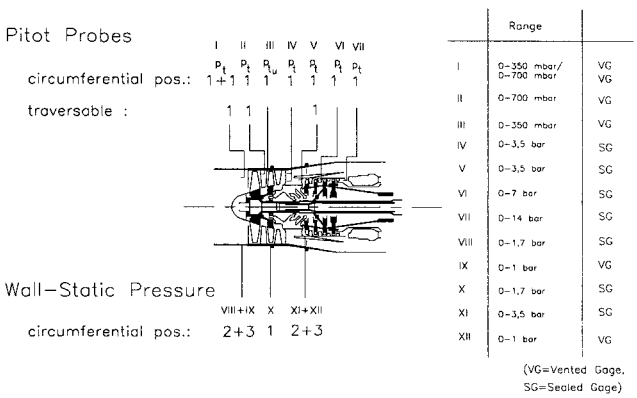

Fig. 5 Positions of miniature pressure transducers

Table 2 Basic equations of continuous Fourier and wavelet transform

	Continuous Fourier Transform	Continuous Wavelet Transform
basic idea	each continuous and periodic function x(t) can be described by a sum of sine waves	each continuous and periodic function x(t) can be described by a sum of wavelets
basis function	$\exp(j\varphi) = \cos\varphi + j\sin\varphi$ (1)	´mother´ wavelet ψ (in general arbitrary)
coefficients	$a_k = \frac{1}{T_0}\int x(t)\exp(j\omega_0 kt)\,dt$ (2)	$c_{a,b} = \frac{1}{\sqrt{a}}\int x(t)\,\psi\left(\frac{t-b}{a}\right)dt$ (4)
inverse transform	$x(t) = \sum_{k=-\infty}^{k=+\infty} a_k \exp(j\omega_0 kt)$ (3)	$x(t) = \frac{1}{K_\psi}\iint c(a,b)\,\frac{1}{\sqrt{a}}\,\psi\left(\frac{t-b}{a}\right)\frac{da\cdot db}{a^2}$ (5) with K_ψ = constant

frequencies as a function of time without the phase information. This method was first used by Garnier et al. (1991) for analyzing pre-stall data and consequently developed into the calculation of traveling wave energy (TWE) by Tryfonidis et al. (1995).

The TWE is obtained by overlaying the negative half of the PSD spectrum with the positive and integrating the resulting differences for a desired bandwidth for every step in time. Since standing wave phenomena yield symmetric PSD's with respect to zero frequency, they do not contribute to the TWE. Therefore, the TWE accumulates the energy content of any traveling disturbance that lasts for a certain period of time.

Since the magnitude of traveling wave energy is related to the stability of the system in cases where the compressor exhibits stall inception via a modal wave, plotting the TWE for a time prior to stall and thresholding it can be used as a stall warning indication.

Wavelet Transform. The wavelet analysis is a relatively new signal processing tool developed in the late 80's, and is mainly used for data compression and image processing, but also for other applications.

The transform process is very similar to the Fourier transform. Both operations are linear and transform the input signal to a different domain. As basis functions the Fourier transform uses sine and cosine waves while the wavelet transform uses so called wavelets. The definition of a wavelet is given by its "mother" function ψ as

$$\psi_{a,b}(t) = \frac{1}{\sqrt{a}}\,\psi\left(\frac{t-b}{a}\right) \tag{6}$$

with a as parameter of dilation or compression and b as translation in time. This means that a wavelet can be dilated in its frequency and located in time. The "mother" wavelets can principally be chosen arbitrarily but have to fulfill certain mathematical restrictions that are not discussed here and can be found in detail in Strang and Nguyen (1996) or Chan (1995).

Corresponding to the Fourier coefficients (Eq. (2)) the wavelet coefficients, representing the magnitude of a wavelet at a time, can be determined according to Eq. (4).

The great advantage of the wavelet transform is illustrated in Fig. 6. While for all frequencies within the Fourier transform the same time window is used (in this case a simple square window) and therefore the maximum resolution is restricted by this windowing, the wavelet transform uses a dyadic time resolution with frequency.

Therefore this analyzing technique seems to be much more appropriate to resolve low-pressure fluctuations as they occur during compressor stall onset at least via the spike-type inception process. First investigations in order to recognize precursors by means of wavelet transform were done by Liao and Chen (1996).

In contrast to their investigations, we chose the "Daubechies" wavelet (see Daubechies, 1988) as the "mother" wavelet (Fig. 7). The very hard to interpret phase information was neglected. A typical magnitude plot is shown in Fig. 8. The levels correspond to the wavelet frequency according to: $2^{\text{Level}} = f$.

Due to the chosen wavelet, a sine wave is represented best by the level corresponding to the doubled frequency.

In order to quantify the results of the magnitude plots of the wavelet transform, a further statistical feature was integrated within the analyzing procedure. For each level the amplitude range is divided into zones. For a window (in this case the length was set to 0.1 s) sliding in time the amplitudes within each zone are counted. This results in a frequency vector for each time window (here frequency means how often an amplitude appears within a certain time window). The frequency of the lowest amplitude zone is set to zero. In order to reduce the large amount of resulting data, the sum of the amplitudes and the sum of the elements of the frequency vector are multiplied. This leads to a similar result as if summing up all amplitudes of one level within a time window, but the method described is not as susceptible to singular events.

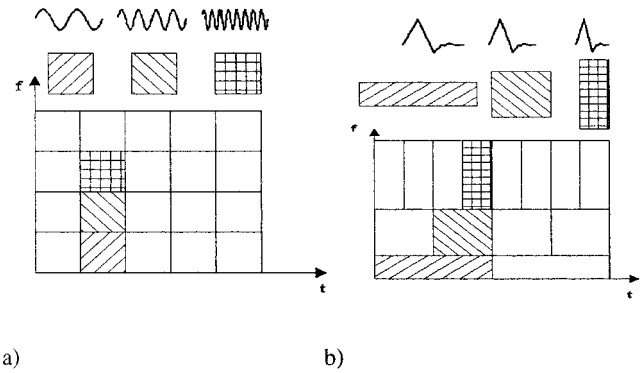

Fig. 6 Time-frequency resolution for (*a*) Fourier transform and (*b*) wavelet transform

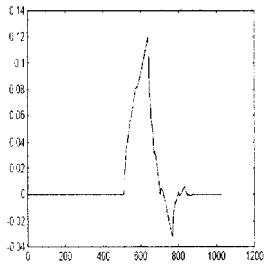

Fig. 7 Daubechies wavelet

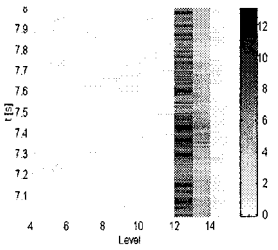

Fig. 8 Magnitude plot of wavelet transform

LPC Measurement Results

In order to throttle the low-pressure compressor, the bypass aperture was closed step by step until the compressor stalled. To guarantee equilibrium conditions in order to determine the stationary compressor characteristics, there was a certain waiting time between each throttling step and taking of the data. After stall recovery, the last throttling steps were repeated, but this time the aperture was closed not stepwise but continuously. No remarkable differences either of the stalling point within the compressor characteristics or in the stalling process could be detected, so this throttling can be assumed to be quasi-steady in terms of stall inception. Even for higher throttling rates, and also for a combined throttling with core and bypass throttle, the stalling behavior remained unchanged.

Compressor Performance. The low-pressure compressor characteristic was determined by gas path analysis of the measured low-frequency data. The steady compressor characteristics are shown in Fig. 9. The measured working points are marked by circles, while the dethrottled characteristics starting from the steady working line to higher mass flow rates are extrapolated. The closing of the bleed valves between about 55 and 58 percent of the corresponding LPC rotor speed results in a slight dethrottling of the LPC. One remarkable feature of the compressor characteristics is the very flat progression of the upper speedlines. A reason for this progression might be the unusual trend of the total-to-static pressure rise stage characteristics as shown in Fig. 10. While for stage 2 the gradient is always negative indicating stable compressor flow, it tends to be positive for stage 1 for all speedlines and all throttling rates. According to Stenning (1980) and his two-dimensional stability analysis, the flow becomes unstable with a gradient equal to zero. Nevertheless, the compressor flow as a whole is stable most probably due to stabilizing effects of the second stage. The values in Fig. 10 rather show a trend than being precise due to the broad spreading of the measured high-frequency data with which these stage characteristics were calculated.

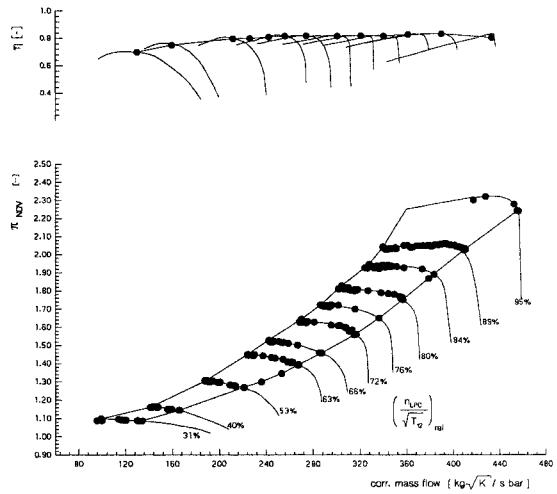

Fig. 9 LP compressor characteristics

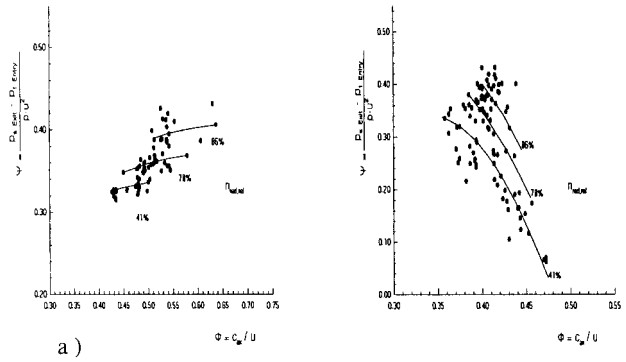

Fig. 10 LPC stage characteristics: (*a*) Stage 1, (*b*) Stage 2

Stall Inception With Clean Inlet Flow

Low-Pass Filtered Time Domain Signals. Figure 11 shows the stall inception for three speed lines in the time domain. The data was low-pass filtered with 1000 Hz and a smooth filter steepness. These three speed-lines of 54, 78, and 90 percent corrected LPC rotor speed are representative for the whole speed range with 54 percent representing the low-speed range, which extends from idle to about 70 percent, with 78 percent representing the mid-speed up to about 84 percent and with 90 percent representing the high-speed range. The upper plots are arranged to show the axial extension within the LPC showing the sensor signals of the static pressure in front of the first rotor (331 deg at the circumference in the direction of rotation), the total pressure within the first stator (22 deg), the wall-static pressure in front of the second rotor (34 deg), and the total pressure near the hub (295 deg) behind the second stator. (The term "total" for the "total-pressure" probes is only valid in the case of stable flow facing the head of the probes. In case of instability the probe does not sense the stagnation pressure any more, but nevertheless this term is used for these pressure probes). The lower plots show the signals of the circumferentially distributed static pressure transducers in front of the first stage.

For all speed settings, stall occurs first within the first rotor. Taking the information of the stage characteristics (Fig. 10) into account, this appears to be sensible as the first stage is heavily loaded for all speeds. No remarkable precursors are detectable in these time domain plots except for the lowest speeds where a self-recoverable, one-cell, part-span stall (similar to the front-end-stall reported by Day et al., 1999) was observed before deep stalling. With higher shaft speeds, stall develops faster from the first visible spikes to fully developed stall (from about 10 rotor revolutions at 54 percent to about 3 rotor revolutions at 90 percent). At 90 percent there are intensive pressure fluctuations with rotor frequency visible already long before stall inception. These fluctuations are damped out again and therefore they are not directly triggering stall inception. The reason for these fluctuations might be a permanent blade stall fixed to one blade. This explanation is supported by the sharp, spike-type signal patterns. Generally the total pressure probe in the first stator detects the first spike with the biggest amplitude or even one rotor revolution earlier than the other sensors but also with higher noise.

At rotor speeds higher than 74 percent the stalling of the LPC causes the HPC to surge as shown in the $p_{tLPC,exit}$ trace (please note the larger time scale). This surging is shown in the total pressure traces of the sensor behind the LPC and it always starts with an overpressured spike in this signal caused by the HPC blowdown. This type of interaction due to LPC stall is known as rotating inlet distortion for the HPC.

Temporal Fourier Transform. This description of an almost identical stall inception process for all speed settings changes

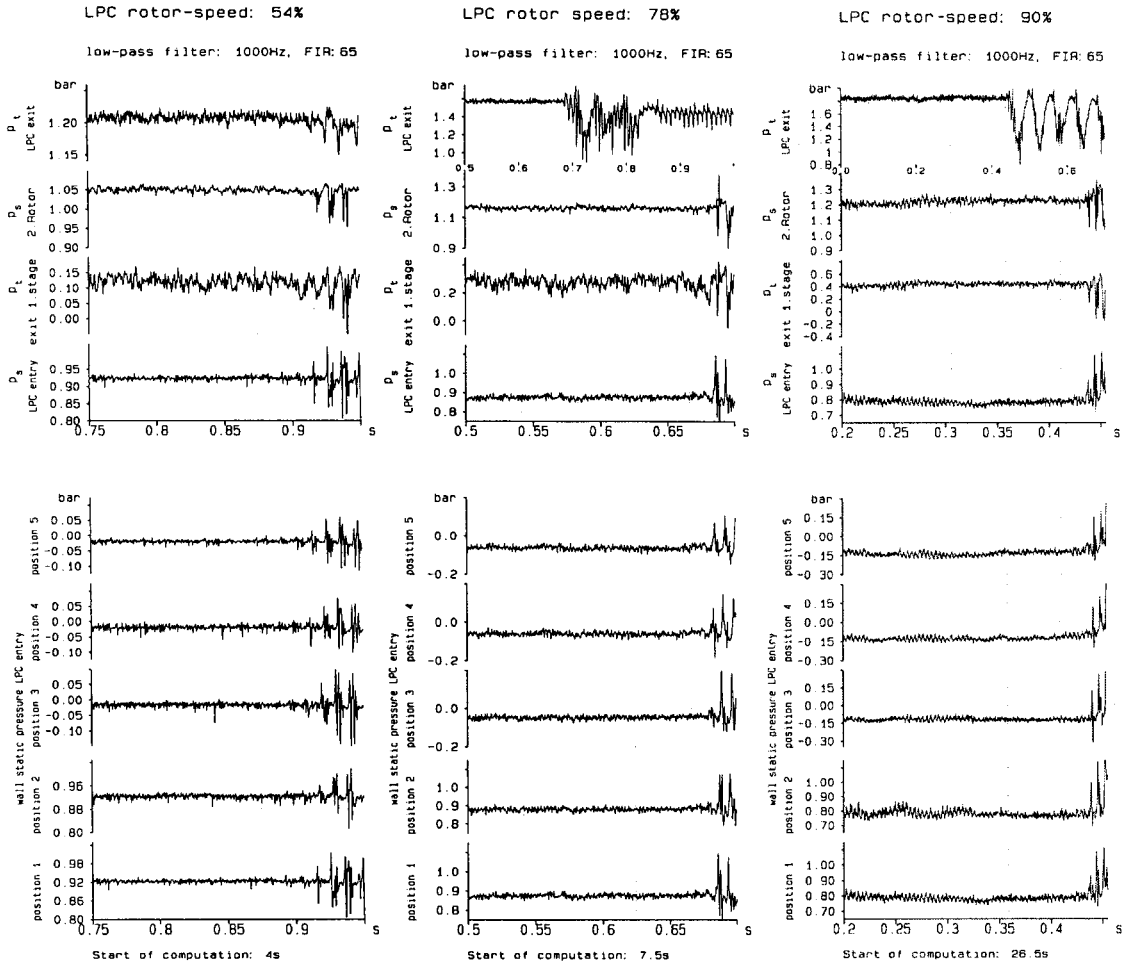

Fig. 11 Pressure signals during stall inception at (*a*) 54 percent of these LPC rotor speed, (*b*) 78 percent rotor speed, (*c*) 90 percent rotor speed

abruptly when taking the temporal Fourier transform into consideration. The Fourier spectra of the signals of the same static pressure probe at inlet is shown in Fig. 12 for the three speeds. While at 54 percent only the shaft frequencies and the main hum can be identified with a slight broadening when approaching the stall onset point, there are further frequencies visible at 78 percent corresponding rotor speed. The first additional frequency that is very slight and hard to detect is at 144 Hz. Usually this would not have been noticed. Easier to detect are the peaks at 288 Hz. There are further frequency peaks visible in the higher frequency range, one at 832 Hz, another one at 1057 Hz, and even a higher one with the same frequency step. This step is exactly the LPC rotor frequency, but these high frequencies are no multiples of any rotor frequency. The amplitudes of these frequencies grow, partly exponentially (especially for the higher speeds), until stall occurs. Up to now no final explanation has been found for these frequencies, but this phenomenon is discussed in greater detail later in this report.

At 90 percent speed the picture is pretty much the same as at 78 percent. A highly fluctuating amplitude of low order can be identified weakly at about 200 Hz. Other clearly visible frequencies are the shaft speeds with the second harmonic of the HP shaft and those higher frequencies described above. The LP shaft frequency and the first-order frequency shift rise dramatically in amplitude just before stall inception.

Band-Pass Filtered Time Domain Signals. In order to be able to judge if and, if yes, which of these frequencies develop into rotating stall, a huge amount of band pass filtering was performed. In Fig. 12 only those data sets are shown that fit best the earliest detectable oscillations in the time domain leading directly to stall. Presenting only the results, at 54 percent speed no prestall frequency could be identified until the first visible spikes appeared. At 78 percent speed the 144 Hz frequency fits best, slowing down to stall with about 125 Hz. At 90 percent the LPC rotor frequency clearly dominates and develops very rapidly into fully developed rotating stall within one rotor revolution.

Spatial Fourier Transform. As a further analyzing technique, the spatial Fourier transform as a transform not of time but of space of the circumferentially distributed static pressure signals at LPC inlet was performed (Fig. 13).

At low speed (54 percent) there is no incitement visible either in the amplitude or in the phase of the first and the second Fourier coefficients. The amplitude never reveals any striking and dramatic changes during the pre-stall phase in our data sets. Generally it rises slightly at least for one coefficient just before stall inception. When stall inception occurs, it rises very quickly, representing the growing process of the stall cell within a few rotor revs.

The phase of the Fourier coefficients behaves differently. For the speed lines at mid- and high-speed zones of constant changing phases and phase velocities can be recognized. This was also observed by McDougall et al. (1990), Garnier et al. (1991), and others and was interpreted as an established, long-wavelength disturbance running around the circumference at a fixed rotational frequency.

At 78 percent corresponding rotor speed there is a zone of constant phase angle velocity visible about four rotor revolu-

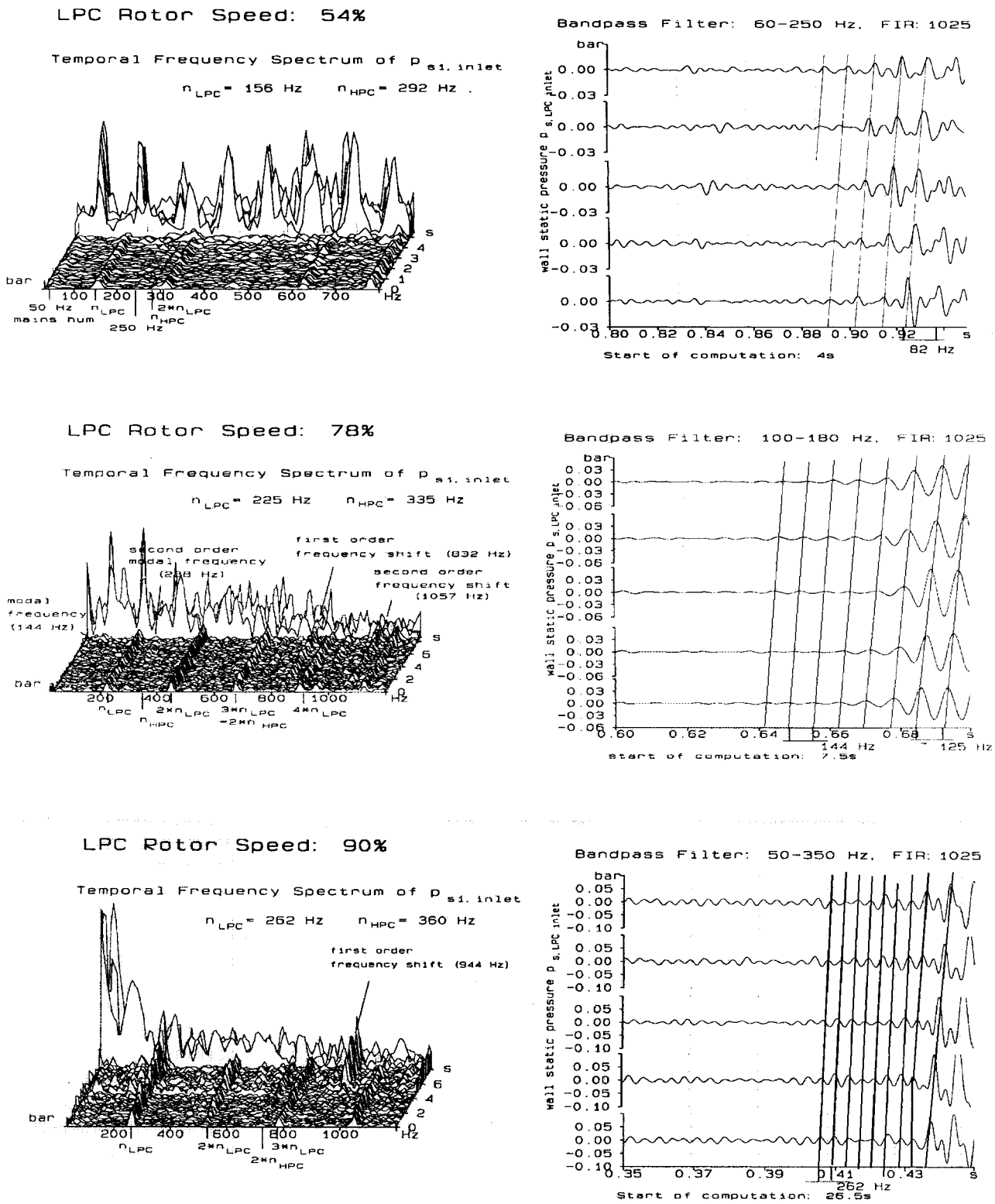

Fig. 12 Temporal Fourier spectrum and band-pass filtered time domain signals at 54, 78, and 90 percent corresponding rotor speed

tions just before stall within the first Fourier coefficient. The phase angle velocity amounts to 144 Hz. The smooth transient to stall indicates that the stall cell grows out of this rotating wave. This frequency was already found within the temporal Fourier frequency spectrum and within the band-pass filtered time domain signal.

In agreement with the interpretations of McDougall et al. (1990), Garnier et al. (1991), Day (1993a), Tryfonidis et al. (1995), and many other authors based on the theoretical model of Moore and Greitzer (1986) this observed frequency is due to an incompressible modal wave, which grows as an eigenmode of the oscillatory system from infinitely small values to rotating stall. Further periods of constant phase angle velocities can be found within the phase of the second Fourier coefficient. There the phase angle velocity amounts to 225 Hz, which is the LP rotor frequency. This frequency appears several times before the stall inception in a

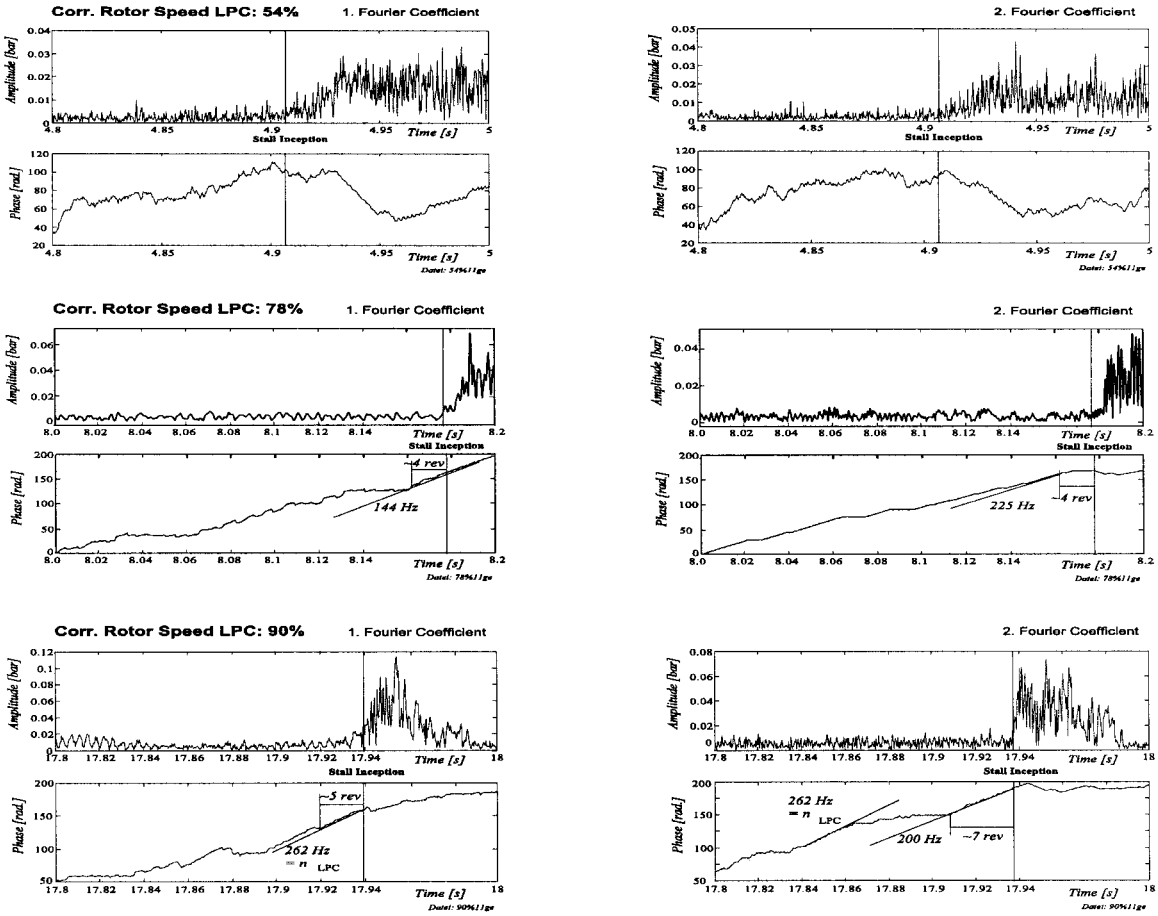

Fig. 13 Spatial Fourier coefficients at 54, 78, and 90 percent corresponding rotor speed

steplike manner, but disappears completely at about four revolutions before stall inception.

At higher rotor speeds (90 percent) the stall inception behavior is dominated by the LP rotor frequency. This can be observed within the first Fourier coefficient for about five revolutions immediately prior to stall inception but also during several periods before. Within the second Fourier coefficient, the rotor frequency is also visible, but here a constant phase velocity at a frequency of ~200 Hz exists for the same five rotor revolutions immediately prior to stall inception. This 200 Hz signal was already found within the temporal Fourier spectrum but only very weak and highly unsteady in its frequency and moreover only visible in two out of the five circumferential pressure signals. Therefore, it seems very unlikely that stall onset is triggered by this frequency. The abrupt disruptions of the phase velocity after stall inception are due to the onset of HPC surging.

Power Spectral Density and Traveling Wave Energy. An additional analysis was carried out by calculating the power spectral density (PSD) of the previously computed spatial Fourier coefficients and the temporal development of the traveling wave energy (TWE). Using these methods confirms the type of stall inception as proposed by the spatial and temporal FFT alone, while the TWE gives an earlier notice of stall inception throughout the speed range. The PSD's and TWE's of the first and second Fourier coefficients for 54, 78, and 90 percent corrected speed are shown in Fig. 14. The PSD of the first coefficient at 54 percent corrected speed from −1.2 to 1.2 times rotor speed is plotted in the upper left corner. No significant rise of any particular frequency up to the point where a stall cell emerges at about 56 percent corrected speed can be observed. This is typical for a spike-type stall inception rather than that of a modal wave growing into stall and supports what was concluded from the inspection of the phase plot in Fig. 13. Due to shaft unbalancing the rotor frequency is dominant. The TWE of these spectra during a period of 3 seconds prior to stall is depicted below. Though there is no particular dominating eigenmode, the TWE increases in a rather wavy form until the onset of stall, where it grows excessively. For this particular set of data, a warning time of roughly 0.25 seconds (40 rotor revolutions) before stall can be defined. This example gives a good impression of the capabilities of the TWE. Because of its integrating character not only modal waves, but all traveling disturbances that exist over a certain period of time contribute to the TWE. The PSD of the second Fourier coefficient at this speed is presented in the upper right corner. There is some activity in the pre-stall phase, but eventually a disturbance at 56 percent corrected speed (same as for the first coefficient) becomes unstable first. The TWE of the second Fourier coefficient (below) does not reveal a steady rise before stall. It wiggles around a constant value. A very sharp drop, which is generated by the negative constant phase velocity phenomena shown in Fig. 13, marks the stall onset.

Since stall at 78 percent corrected rotor speed is triggered by a modal wave at 144 Hz (0.64 of corrected rotor speed) (Fig. 12), the rotor frequency is left out in the figures at this speed for easier detection of the important frequencies. The steadily increasing value for the PSD of the 1st Fourier coefficient at 64 percent corresponding rotor speed (Fig. 14, middle) clearly exhibits a smooth transition from inception to fully developed stall. This can be expected for stall inception via a modal wave. Looking at the PSD of the second coefficient supports the existence of a single modal wave, since no other signal is growing during the stall inception phase. A peak can be recognized for fully developed stall at around 64 percent rotor speed indicating the established rotating

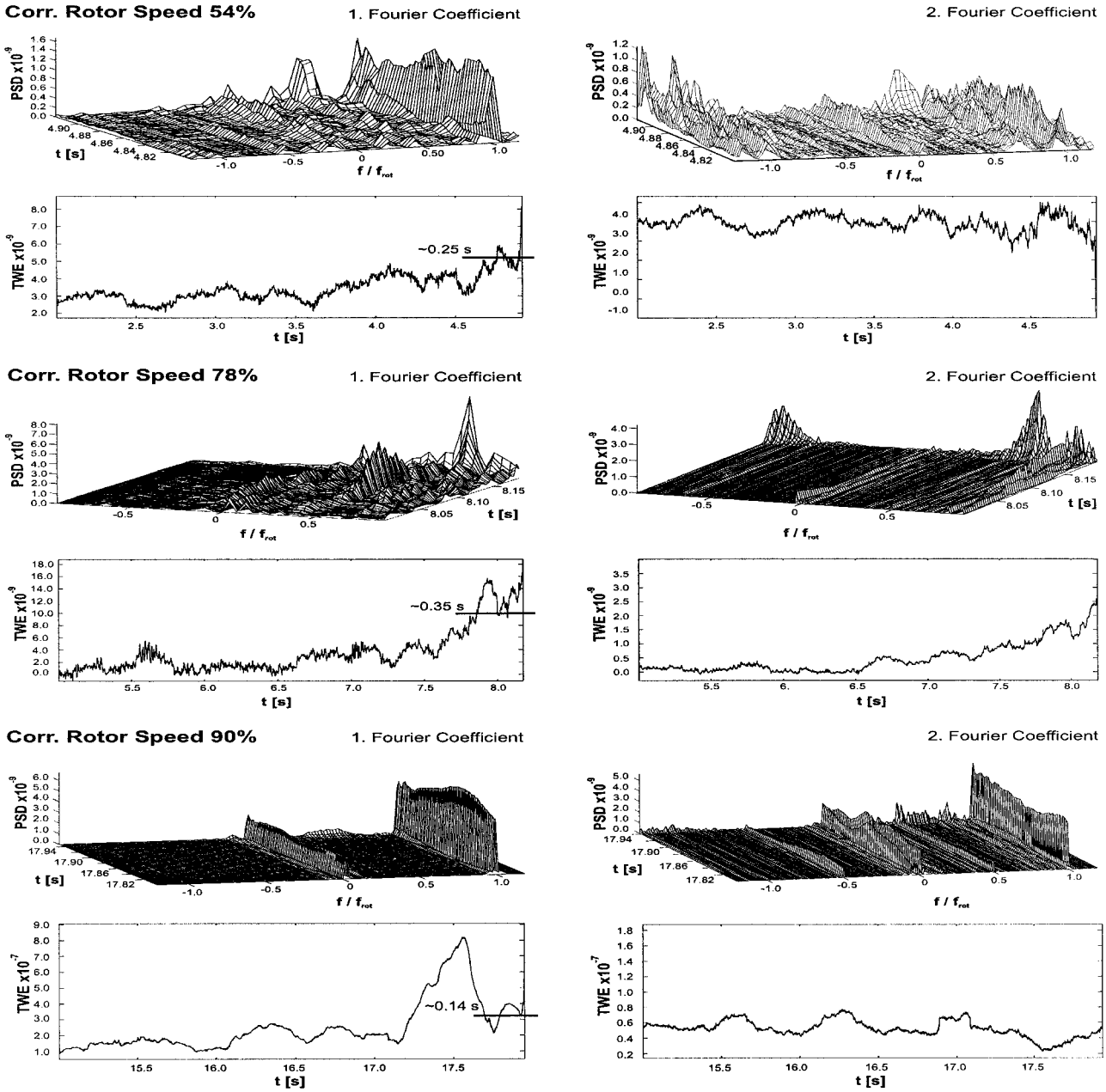

Fig. 14 PSD and TWE of the spatial Fourier coefficients at 54, 78, and 90 percent corresponding rotor speed

stall cell. Conservatively thresholding the TWE of the first coefficient, gives a warning time of approximately 0.35 seconds (75 rotor revolutions). A similar observation can be made for the TWE of the second Fourier coefficient.

The PSD of the spatial Fourier coefficients at 90 percent speed are shown at the bottom of Fig. 14. One can clearly see that the rotor frequency dominates both PSD spectra. This is consistent with the results of the temporal Fourier transform (Fig. 12). The phenomenon, detected in the phase plot of the second coefficient (Fig. 13, bottom) at 200 Hz, also exists in the PSD. It seems to be a modal wave, but its magnitude is negligible compared to the rotor frequency and does not go unstable first. Since the signal at ± 50 percent rotor frequency can be interpreted as a standing wave, it does not contribute to the TWE. The drastic increase of the PSD for both coefficients at 50 percent rotor frequency at 17.94 seconds already indicates a rotating stall cell, which develops and slows down within one revolution starting from the disturbance at 100 percent rotor frequency. The TWE of the first coefficient shows a strong increase when approaching stall approximately 0.14 seconds (37 rotor revolutions) before the stall cell is fully developed. From inspection of the time trace at around 17.5 seconds (not shown here) one can see that the peak in the TWE is generated by the blade stall mentioned before, which disappears again. This behavior demonstrates the difficulty of defining and thresholding a fixed value of TWE in a real engine environment. The TWE of the second coefficient does not give any additional information.

Wavelet Transform. The results of the wavelet transform of the inlet static pressure signal of one sensor for each speed line is shown in Fig. 15. The magnitude plots show great amplitudes at very high levels corresponding to the rotor blade passages at any time within the pre-stall phase. While at 54 percent speed the amplitude distribution grows continuously from very high levels to lower levels until stall onset occurs, this behavior is less pronounced at higher speeds where the lower levels show a greater amplification. After the onset of stall the lower levels predominate

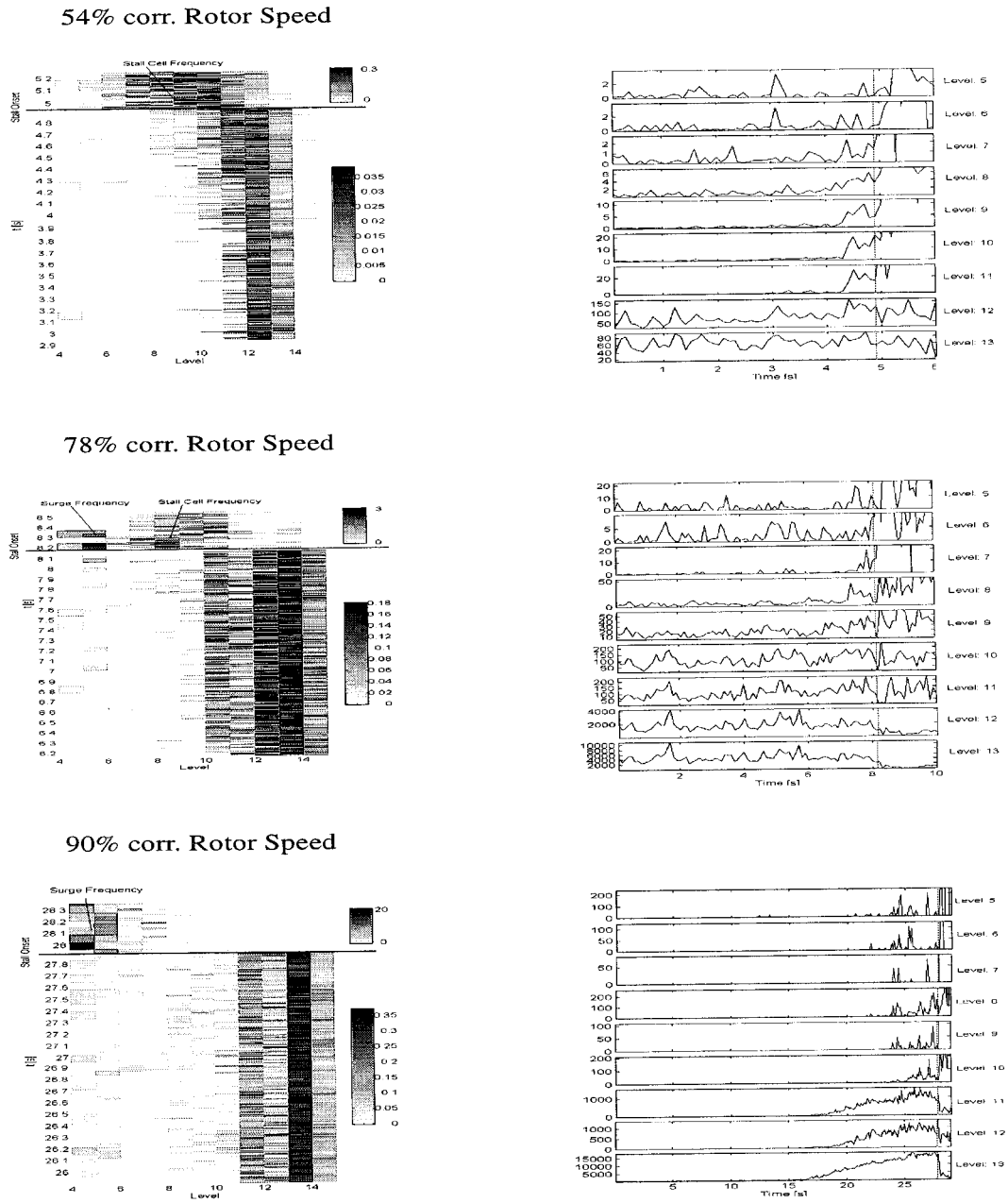

Fig. 15 Wavelet transform and statistical evaluation of the amplitude variations

according to the stall cell and surge frequencies. (The levels correspond to the number of bisectioning the time window, so the signal frequency is 2^{Level}). In order to quantify this signal behavior, the above-described statistical analysis for each level was performed with the results plotted on the right hand side of Fig. 15. The scaling of the *y* axis results from summing up the amplitudes, but in this case it is somewhat arbitrarily since only the relative development of the curves themselves is of interest. Starting with 54 percent speed it is clearly visible that levels 8, 9, 10, 11, and 12 rise while approaching the surge line with a pre-warning time of about half a second (about 80–100 rotor revolutions). Level 8 corresponds to the rotor frequency whereas level 12 is slightly above the rotor passage frequency.

At 78 percent speed this increase in amplitude is clearly found within levels 7, 8, and 9 (level 8 corresponds to a sine-wave frequency of about half the rotor frequency) with about 1 second warning time (200 rotor revolutions) whereas the levels corresponding to the rotor passage frequency (levels 12 and 13) decrease. A similar behavior occurs at 90 percent speed with the center of increase indicating stall inception at levels 8, 9, and 10 corresponding to the rotor frequency with a pre-warning time of about 1.5 second (400 rotor revolutions). This time the compressor was not throttled only the last few steps of the speed line until stall, but continuously all the way from the steady working point until stall occurs, resulting in a long measurement time of 30 seconds. The statistics of the wavelet transform show a dramatic but continuous increase in the amplitude-frequency distribution within levels 11, 12, and 13 already 10 seconds prior to stall inception. Just before stall inception, these levels decrease. With these levels corresponding to fluctuations of a very high frequency (i.e., rotor passage frequency) they are more of a general measure for the damping of the compressor flow than to be for the physical origin of stall (in contrast to the above-discussed stalling behavior at 54 percent).

The result of the statistical analysis of the wavelet transform was almost identical, independent of the sensor's position, except for the total pressure probe behind the LPC with the weakest signal. This is due to the axial and radial position of the

origin of the stalling process within the first rotor at the tip of the blades.

Discussion on High-Frequency Signal Content. As shown in Fig. 12 an additional, unexpected frequency appeared in the temporal Fourier transform for data sets starting at about 74 percent LPC rotor speed up to full speed. The frequency was always located between the third harmonics of the LP and HP rotor frequencies. A further frequency was visible at a frequency step corresponding to the LP rotor speed above the first one. These frequencies are no multiples of any lower orders.

Analyzing the unfiltered data (except the analog filtering with 12.8 kHz) with the spatial Fourier transform showed also a clear dominance of this frequency within phase propagation. This is shown in Fig. 16 for 86 percent rotor speed. The filtered data were low-pass filtered before transformed.

This result sustains the existence of a high-frequency rotating disturbance. On the other hand the propagation velocity of these frequencies are too high to rotate on a self-supporting base. An explanation could be the interaction within the pressure oscillations caused by the LP and HP shafts, with the LP shaft dominating. Yet it is not clear whether these interactions play any role within the stall inception process as they rise almost exponentially for higher rotor speeds just before stall inception. This will be the subject of further investigations.

Stall Inception With Inlet Distortion. To investigate the effect of inlet distortion on the stall onset process, several types of inlet distortions were generated by mounting a pressure gauze or a delta wing into the bellmouth inlet (for details see Bernhard and Fottner, 1993). With these devices, either pressure distortions of various extends, twin-swirl distortions, or combinations of them were generated.

Shown in Fig. 17 is the low-pass filtered time domain signal of the circumferentially distributed wall static pressure sensors at LPC inlet with a 90 deg gauze mounted at 84 percent rotor speed. This gauze was mounted covering the pressure sensor positions 4 and 5 with position 1 being the first sensor behind the pressure gauze in terms of rotor rotation.

It is obvious that the sensor at position 1 is affected most strongly by this pressure distortion. This is also visible within the temporal Fourier transform showing a broad-band noise due to local flow separations that originate at the exit (circumferentially in rotor rotation) of the pressure gauze. These pressure fluctuations are usually damped out at sensor positions 2 and 3, disappearing completely at position 4 and 5, where the pressure gauze was mounted. Stall originates from a local spike-type flow separation of a sufficient large extension surviving the damping within the undistorted section. This stall inception behavior is consistent with the measurements of Wilson and Freeman (1994) and Day et al. (1999) and can be explained by a local unloading of the first stage when entering the distorted section and an additional loading at the exit. This is most probably because of the turning of the undistorted flow at the section boarders inwards to the distorted section and therefore changing the stage loading locally. These spike-type stall precursors are observed for the whole speed range in case of total pressure inlet distortion and also for swirl distortion. Modal waves were not observed neither in the time domain nor in the temporal Fourier or wavelet transform. With the statistical evaluation of the wavelet transform for sensor 1 stall inception is announced by a gradual increase in amplitude-frequency distribution of the levels 9 and 10 already two seconds in advance, as shown in Fig. 18.

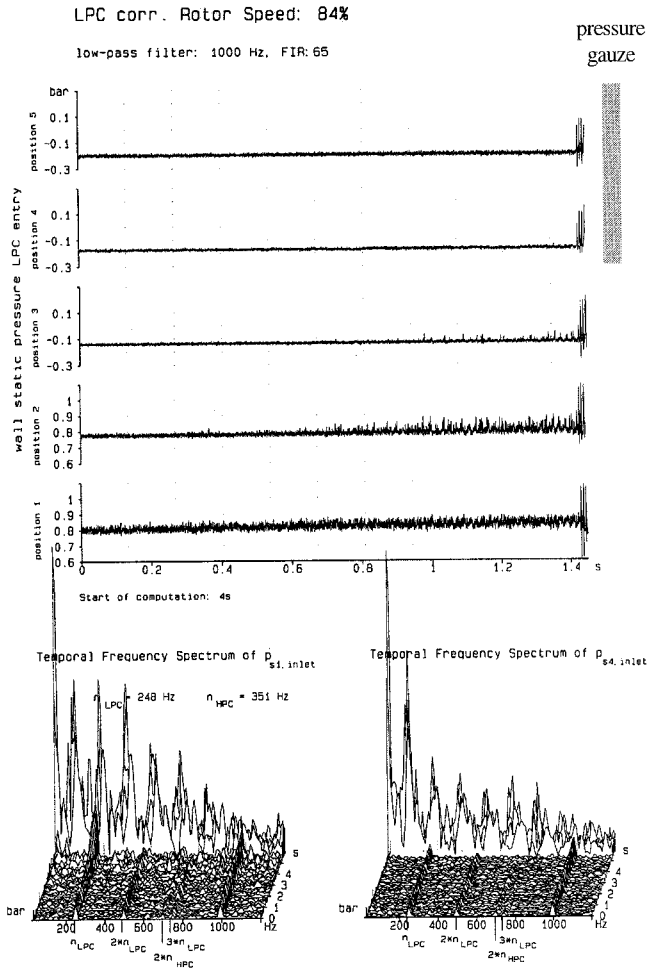

Fig. 17 Low-pass filtered pressure signals and temporal Fourier transform at 84 percent rotor speed with 90 deg total pressure inlet distortion

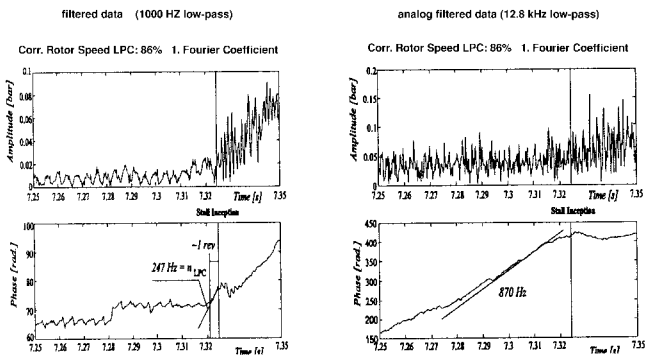

Fig. 16 Spatial Fourier transform of low-pass filtered and unfiltered data at 86 percent rotor speed

Discussion of LPC Measurements

The high-frequency data measured before and during stall inception were analyzed with various techniques. The results led to a congruent picture of the stall inception process within the LPC of the LARZAC engine and showed also the advantages and limitations of each analyzing technique regarding the physical background of the inception process and the obtainable stall warning times.

While at low speeds the compressor flow becomes unstable in a spike-type manner, it reveals a modal wave precursor behavior at midspeeds for undistorted inlet flow. This low- and mid-speed behavior is also observed within other high-speed compressors and the VIPER engine as recently described by Day et al. (1999).

A further flow disturbance that determines stall inception at high-speed settings is the shaft order perturbation due to rotor imbalance, a nonideal casing or blades, etc. Regarding the results

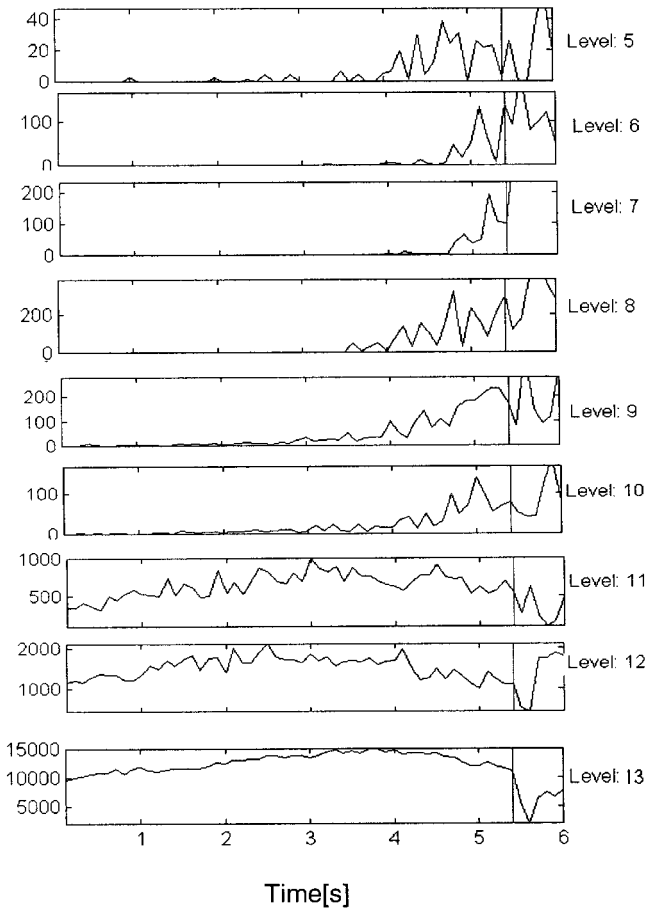

Fig. 18 Statistical evaluation of wavelet transform coefficient for static pressure signal at LPC inlet with total pressure inlet flow distortion

in time and frequency domain, it is very likely that stall develops from these perturbations. Also Day et al. (1999) assumed that it might be possible that shaft order perturbations play a role within the stall inception process. Tryfonidis et al. (1995) supposed that external forcing functions as, i.e., rotor shaft perturbations could excite a nonlinear response of the system. It is also possible that according to the linear stability model by Hendricks et al. (1993) applied by Tryfonidis et al. (1995) finally a compressible mode of the oscillatory system excited by the shaft perturbations becomes unstable. Independent of the analytical identification of system modes, the influence reported herein of shaft order perturbations on the stall inception process is very important for any controlling system either in order to prevent stall by fast dethrottling actions or by active flow stabilization.

Higher frequencies observed within the temporal and spatial Fourier transform most probably indicate an interaction between two forcing functions (LPC and HPC rotor imbalance) resulting in a nonlinear system response. This is the subject of further investigations.

The assumptions of Camp and Day (1998) cannot be supported by these measurements. Although the stage matching is adverse for all speeds regarding the stage characteristics of the first stage, the compressor reveals modal-wave-type behavior for undistorted inlet flow. Camp supposed that an even stage matching is a required condition for the growing process of modal waves.

In case of distorted inlet flow, spike-type stall inception behavior dominates for the whole speed range. Modal waves were not observed any more. Therefore the approach of stall inception was indicated already a long time in advance, at least right behind the most deprived sections, due to a continuously increasing broadband noise representing local flow separations. These fluctuations were damped out again within the other sections until stall occurs. For a total pressure distorted inlet flow generated by a gauze this most deprived section is at the exit (in terms of rotor rotation) of the gauze due to the local increase in blade loading. The reason for this local increase in blade loading is the turning of the undistorted streamlines inward at the distorted section. On the other hand, the flow is stabilized at the entrance of the distorted section by locally unloading the stage.

From the viewpoint of a stall avoidance control system, this local loading and unloading of the stage could be used for indicating the surge margin. In conjunction with a statistical evaluation of an appropriate analyzing tool (e.g., wavelet) this would rather be a measure for the damping of the flow than for the flow structure. This statistical evaluation based on the results of the wavelet transform for clean inlet flow was demonstrated. Even though different types of stall inception patterns have been recognized, the wavelet analyzing technique was able to indicate the surge line approach at all speeds with sufficient warning time to allow any effective control action. Due to the coarse resolution, these signs were represented in different levels, but generally centered around the level representing the stall phenomenon. This result is very encouraging from the view of any stall avoidance control system, as with only one analyzing tool and data from one sensor, by simply thresholding the sum of the amplitudes within certain levels, stall inception can be identified.

Conclusions and Summary

Stall inception behavior has been the subject of numerous investigations with isolated compressors on test-rigs or numerical simulations. Only very few full-scale engine tests were performed to verify these results and investigate component interactions on stall inception in an engine installation.

In order to investigate this stall inception behavior of the compressor system of the two-spool turbofan engine LARZAC 04, this engine has been equipped with extended low-frequency and high-frequency instrumentation. The experimental setup including the instrumentation, throttling devices, and the data acquisition system have been introduced. Various analyzing techniques in the time domain, temporal and spatial Fourier frequency domain, PSD and TWE of the spatial Fourier coefficients, and a wavelet transform have been presented. Data from LPC measurements with and without inlet distortion have been analyzed and discussed.

Three different types of stall precursor for undistorted inlet flow have been identified. While the spike-type behavior at low-speed and modal waves at mid-speed were already known from compressor test-rig data, these investigations show that forcing functions as they exist in an engine installation as, i.e., the rotor shaft imbalance play an important role in the stall inception process, at least at higher speeds. Any controlling unit has to be able to control not only some oscillatory incompressible and compressible eigenmodes, but also external and internal forcing functions. Therefore extending the stable range of an on-duty aeroengine compressor at all speed settings is a much more challenging task than it was supposed to be regarding only the measurements from low-speed compressors.

On the other hand an active stall avoidance control with sufficient stall warning time for all speeds is possible in a reliable and fairly simple manner regarding the results of the wavelet transform and the extended statistical evaluation.

Acknowledgments

This work was supported by the DFG. This support is gratefully acknowledged.

References

Bernhard, D., and Fottner, L., 1993, "Einfluß kombinierter Drall- und Totaldruck-Eintrittstörungen auf das Stabilitätsverhalten von Turbostrahltriebwerken," *DGLR Jahrestagung*, DGLR-JT93-047.

Camp, T. R., and Day, I. J., 1998, "A Study of Spike and Modal Stall Phenomena

in a Low-Speed Axial Compressor," ASME JOURNAL OF TURBOMACHINERY, Vol. 120, pp. 393–401.

Chan, Y. T., 1995, *Wavelet Basics* Kluwer Academic Publishers.

Das, D. K., and Jiang, H. K., 1984, "An Experimental Study of Rotating Stall in a Multistage Axial-Flow Compressor," ASME *Journal of Engineering for Gas Turbines and Power*, Vol. 106.

Daubechies, I., 1988, "Orthonormal Bases of Compactly Supported Wavelets," *Comm. Pure Appl. Math.*, Vol. 41, pp. 906–966.

Day, I. J., and Cumpsty, N. A., 1978, "The Measurement and Interpretation of Flow Within Rotating Stall Cells in Axial Compressors," *Journal Mechanical Engineering Science*, Vol. 20.

Day, I. J., 1993a, "Stall Inception in Axial Flow Compressors" ASME JOURNAL OF TURBOMACHINERY, Vol. 115, pp. 7–9.

Day, I. J., 1993b, "Active Suppression of Rotating Stall and Surge in Axial Compressors," ASME JOURNAL OF TURBOMACHINERY, Vol. 115, pp. 40–47.

Day, I. J., and Freeman, C., 1994, "The Unstable Behavior of Low and High Speed Compressors" ASME JOURNAL OF TURBOMACHINERY, Vol. 116, No. 2.

Day, I. J., Breuer, T., Escuret, J., Cherrett, M., and Wilson, A., 1999, "Stall Inception and the Prospects for Active Control in Four High-Speed Compressors," ASME JOURNAL OF TURBOMACHINERY, Vol. 121, pp. 18–27.

Escuret, J. F., and Garnier, V., 1996, "Stall Inception Measurements in a High-Speed Multistage Compressor," ASME JOURNAL OF TURBOMACHINERY, Vol. 118, pp. 690–696.

Gallops, G. W., Roadinger, T. J., and French, J. V., 1993, "Stall Testing and Analysis of Two Mixed Flow Turbofans," ASME Paper No. 93-GT-62.

Garnier, V. H., Epstein, A. H., and Greitzer, E. M., 1991, "Rotating Waves as a Stall Inception Indication in Axial Compressors," ASME JOURNAL OF TURBOMACHINERY, Vol. 113.

Hendricks, G. J., Bonnaure, L. P., Longley, J. P., Greitzer, E. M., and Epstein, A. H., 1993, "Analysis of Rotating Stall Onset in High-Speed Axial Flow Compressors," AIAA Paper No. 93-2233.

Herpel, Th., and Fottner, L., 1993, "A System for Monitoring, Measurement and Analysis of Transient Performance and Stall Phenomena of Gas Turbine Engines," ICIASF '93 Record, IEEE Publication 93 CH3199-7.

Höss, B., and Fottner, L., 1997, "Experimental Setup, Measurement and Analysis of the Onset of Compressor Flow Instabilities in an Aeroengine," ICIASF '97 Record, IEEE Publication 1997.

Hoying, D. A., 1993, "Stall Inception in a Multistage High Speed Axial Compressor," AIAA Paper No. 93-2386.

Lawless, P. B., Kim, K. H., and Fleeter, S., 1993, "Spatial Domain Characterization of Abrupt Rotating Stall Initiation in an Axial Flow Compressor," Paper No. AIAA-93-2238.

Liao, S., and Chen, J., 1996, "Time-Frequency Analysis of Compressor Rotating Stall by Means of Wavelet Transform," ASME Paper No. 96-GT-57.

McDougall, N. M., Cumpsty, N. A., and Hynes, T. P., 1990, "Stall Inception in Axial Compressors," ASME JOURNAL OF TURBOMACHINERY, Vol. 112.

Moore, F. K., and Greitzer, E. M., 1986, "A Theory of Post-Stall Transients in Axial Compression Systems: Part I—Development of Equations; Part II—Application," ASME *Journal of Engineering for Gas Turbines and Power*, Vol. 108.

Poensgen, C. A., and Gallus, H. E., 1996, "Rotating Stall in a Single-Stage Axial Flow Compressor," ASME JOURNAL OF TURBOMACHINERY, Vol. 118, pp. 189–196.

Stenning, A. H., 1980, "Rotating Stall and Surge," ASME *Journal of Fluids Engineering*, Vol. 102.

Strang, G., and Nguyen, T., 1996, *Wavelets and Filter Banks*, Wellesley-Cambridge Press.

Tryfonidis, M., Etchevers, O., Paduano, J. D., Epstein, A. H., and Hendricks, G. J., 1995, "Prestall Behavior of Several High-Speed Compressors," ASME JOURNAL OF TURBOMACHINERY, Vol. 117, pp. 62–80.

Wilson, A. G., and Freeman, C., 1994, "Stall Inception and Development in an Axial Flow Aero-Engine," ASME JOURNAL OF TURBOMACHINERY, Vol. 116, No. 2.

Propagation of Multiple Short-Length-Scale Stall Cells in an Axial Compressor Rotor

M. Inoue

M. Kuroumaru

T. Tanino

M. Furukawa

Department of Energy and Mechanical Engineering, Kyushu University, Fukuoka, Japan

Evolution and structure of multiple stall cells with short-length-scale in an axial compressor rotor have been investigated experimentally. In a low-speed research compressor rotor tested, a short-length-scale stall cell appeared at first, but did not grow rapidly in size, unlike a so-called "spike-type stall inception" observed in many multistage compressors. Alternatively, the number of cells increased to a certain stable state (a mild stall state) under a fixed throttle condition. In the mild stall state the multiple stall cells, the size of which was on the same order of the inception cell (a few blade spacings), were rotating at 72 percent of rotor speed and at intervals of 4.8 blade spacings. With further throttling, a long-length-scale wave appeared overlapping the multiple short-length-scale waves, then developed to a deep stall state with a large cell. In order to capture the short-length-scale cells in the mild stall state, a so-called "double phase-locked averaging technique" has been developed, by which the flow field can be measured phase locked to both the rotor and the stall cell rotation. Then, time-dependent ensemble averages of the three-dimensional velocity components upstream and downstream of the rotor have been obtained with a slanted hot-wire, and the pressure distributions on the casing wall with high-response pressure transducers. By a physically plausible explanation for the experimental results, a model for the flow mechanism of the short-length-scale stall cell has been presented. The distinctive feature of the stall cell structure is on the separation vortex bubble with a leg traveling ahead of the rotor, with changing the blade in turn on which the vortex leg stands.

Introduction

It is said there are two types of stall inception in axial compressors. The first one is characterized by long-length-scale disturbances (Garnier et al., 1991) for which two-dimensional linearized stability analyses are available (Moore and Greitzer, 1986; Weigl et al., 1998). The second one is characterized by a short-length-scale disturbance known as a "spike" (McDougall et al., 1990). Sometimes, these inception types are coupled (Day, 1993). Recently, Day et al. (1999) investigated the stall inception for several European aeroengine-type compressors, and found a new type of high-frequency stall inception in two compressors operating at full speed. From the experimental results of low-speed compressor testing at the Whittle Laboratory, in which multiple part-span stall cells rotated at 82 percent of rotor speed and at intervals of five blade spacings, they thought that the high-frequency waves resulted from multiple part-span stall cells. Multiple wave disturbances due to part-span stall cells were also reported in the low-speed compressor test rig by Mathioudakis and Breugelmans (1985). Silkowski (1995) observed them in a low-speed four-stage compressor test rig with a mismatched stage condition, and mentioned that the short-length-scale disturbances (spike) appeared and disappeared sporadically near the stall condition at first, then the number of the spikes increased as the flow rate decreased, and finally multiple spikes appeared at intervals of 4.5 blade spacings rotating at roughly 70 percent of rotor speed at a lower flow rate.

In a low-speed compressor test rig at Kyushu University, a similar phenomenon has occurred in evolution of rotating stall. In this paper, the formation process of the multiple part-span cells with short-length-scale and the process of coalescing into a big rotating stall cell are presented first, based on the measurement data by pressure transducers mounted on the casing wall near the rotor leading edge. Second, a so-called "double phase-locked averaging" (DPLA) technique is proposed to capture the short-length-scale stall cell by a slanted hot-wire and high-response pressure transducers, with which three-dimensional flow fields before and behind the rotor and the casing wall pressure distribution can be obtained synchronously with both the rotor and the cell rotation. Last, a flow mechanism of the short-length-scale stall cell is discussed based on the time-dependent ensemble averages of the three-dimensional velocity components upstream and downstream of the rotor and the casing wall pressure distributions.

Experimental Facility and Instrumentation

A schematic view of the test section of the low-speed research compressor is shown in Fig. 1. It consists of a 449-mm-dia rotor with hub/tip ratio of 0.7, two cantilevered stators upstream and downstream of the rotor, and inlet and outlet guide vanes. The rotor comprises 24 blades designed for a constant whirl angle of absolute inlet flow and 50 percent reaction at midspan. The two stators consisting of 22 blades are geometrically identical, and the inlet guide vanes are designed for the same exit flow angle distribution as the rotor in order to simulate the middle stage of a compressor. The gap between the rotor and the stator is about a half of the blade height, which is considerably larger than the actual compressor stages to make a survey of the flow field. The compressor stage has the flow rate coefficient of $\phi = 0.5$, and the pressure coefficient of $\psi = 0.4335$ at the design point. The blade profile used is from the NACA 65 series for the rotor, two stators, and outlet guide vanes, and from the NACA 63 series for the inlet guide vanes. The blade tip clearance is 0.5 mm (0.75 percent of blade height) for the rotor and stators. Additional information for the bladings is shown in Table 1.

The stage performance was evaluated for a combination of the rotor and the downstream stator. The total pressure rise of the stage was obtained from the pressure difference between the inlet and

Contributed by the International Gas Turbine Institute and presented at the 44th International Gas Turbine and Aeroengine Congress and Exhibition, Indianapolis, Indiana, June 7–10, 1999. Manuscript received by the International Gas Turbine Institute February 1999. Paper No. 99-GT-97. Review Chair: D. C. Wisler.

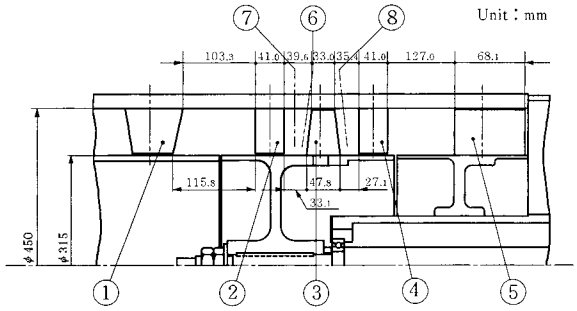

1	I.G.V.	5	O.G.V.
2	Stator 1	6	Measurement Location S1
3	Rotor	7	Measurement Location S2
4	Stator 2	8	Measurement Location S3

Fig. 1 Schematic view of test section

Table 1 Design specifications of rotor and stator

Rotor

	r/r_t	β_1	β_2	σ	Cl_0	γ	τ
Tip	1.000	57.2	45.6	0.850	0.909	48.9	6.0
	0.925	53.3	38.2	0.919	1.045	43.2	8.0
Mid	0.850	48.8	29.0	1.000	1.215	36.2	10.0
	0.775	43.5	18.0	1.097	1.415	27.7	12.0
Hub	0.700	37.4	5.5	1.214	1.618	17.9	14.0

Stator

	r/r_t	α_1	α_2	σ	Cl_0	γ	τ
Tip	1.000	48.3	29.0	0.779	1.360	35.7	10.0
	0.925	48.4	29.0	0.842	1.331	35.9	10.0
Mid	0.850	48.7	29.0	0.917	1.307	36.2	10.0
	0.775	49.2	29.0	1.005	1.289	36.4	10.0
Hub	0.700	49.8	29.0	1.113	1.278	36.5	10.0

* isolated airfoil lift coefficient of NACA65 profile camber line at zero angle of attack in potential flow

α_1 : inlet flow angle
α_2 : exit flow angle
β_1 : inlet flow angle
β_2 : exit flow angle
σ : solidity
Cl_0 : lift coefficient *
γ : stagger
τ : maximum thickness (%)

outlet chamber by subtracting the aerodynamic losses of other elements, which had been obtained in a preliminary experiment without the rotor and the downstream stator. The flow rate was measured by a flow nozzle connecting with outlet chamber (see Inoue et al., 1993).

A single slanted hot-wire and a five-hole pressure probe are used to survey internal flows in the radial direction upstream and downstream of the rotor, and both in the radial and circumferential direction downstream of the stators.

For measuring the casing wall pressure distribution, 14 high-response pressure transducers (Kulite XCS-062) are mounted on the casing wall to cover the measuring points from 24.6 mm upstream of the rotor leading edge to 20.4 mm downstream of the rotor trailing edge in the axial direction. One of the pressure transducers near the rotor leading edge is used to detect rotating stall inception of the rotor and to observe a transient phenomenon of the stall cell development. A trigger pulse of the stall inception is taken by setting a threshold level for the low-pass filtered (LPF) signal of the pressure sensor for which the blade passing frequency has been removed. Another pressure sensor is located at 90 deg apart in the circumferential direction to measure the number of stall cells and their rotating speed.

Evolution of Multiple Short-Length-Scale Stall Cells

Pressure-Rise Characteristics of the Compressor Stage. Figure 2 shows the pressure-rise characteristics of the compressor stage tested. The pressure coefficient ψ is the maximum at the flow rate coefficient of $\phi = 0.380$. With throttling from $\phi = 0.380$ to 0.346 the pressure coefficient is reduced, but in this flow range no signal indicating stall inception is observed in the LPF output of the pressure sensor on the casing wall near the rotor leading edge. The cause of the pressure reduction was examined by flow surveys downstream of the rotor and the stator using the five-hole pressure probe. The averaged total pressure at the rotor exit increases from $\phi = 0.400$ to 0.355 (the figure omitted). But, as shown in Fig. 3, which shows the total pressure distributions at the downstream stator exit for $\phi = 0.400$ and 0.355, a corner stall grows noticeably between a cantilevered stator blade and the casing wall at $\phi =$ 0.355. The pressure reduction is mainly caused by growth of this stator corner stall. Stall inception of the rotor is detected at $\phi = 0.346$, from where the flow rate decreases by itself (without throttling) to $\phi = 0.332$ in around 100 rotations of the rotor, and the pressure drops from $\psi = 0.516$ to 0.470. As the flow rate decreases from $\phi = 0.332$ to 0.295 by closing the throttle carefully, the pressure is reduced gradually to $\psi = 0.428$, and then, jumps to $\psi = 0.335$ at $\phi = 0.264$. In this paper, the flow ranges from $\phi = 0.346$ to 0.332, $\phi = 0.332$ to 0.295, and $\phi = 0.295$ to 0.264 are designated as the flow ranges A, B, and C, respectively, for convenience of the following discussion.

Time Evolution of Casing Wall Pressure Trace. Figure 4 shows a time evolution of the casing wall pressure trace with the low-pass filter near the rotor leading edge in the flow range A. The output of LPF pressure is shown versus time. For each horizontal line, the short and long vertical lines stand for blade passing and rotor rotations respectively, and n is a number for rotor rotation corresponding to the left vertical line. Immediately after the stall inception is detected in the LPF pressure signal, a spiky wave is generated in a rotor rotation with rapid increase followed by rapid decrease in the pressure. Similar wave shapes appear at intervals of 1.36 times of a rotor rotation. Then, the second spiky wave appears next to the first one, and the number of waves increases at unequal intervals with time. Finally, the similar shapes of wave stand in at intervals of about 0.27 times of a rotor rotation. In the flow range B, they keep to be at the same intervals of about 0.27 (the figure is omitted).

An LPF pressure trace in the flow range C is shown in Fig. 5. It is clearly seen that the short-length-scale waves and a long-length-scale wave are overlapping each other, and turn into a big wave due to a deep stall cell.

Cross-Correlation Function of Two Pressure Signals. In order to examine the number and rotating speed of the stall cells, the LPF pressure signals have been analyzed by a cross-correlation function. Figure 6(*a*) shows the LPF pressure traces for two pressure sensors located 90 deg apart in the circumferential direction, and a cross-correlation function of the two signals, when short-length-scale waves exist at intervals of 1.36 times of a rotor rotation. From this figure, it is estimated that one cell rotates at 73.4 percent of the rotor speed.

Nomenclature

C_p = pressure coefficient
LPF = low-pass filtered
p' = deviation of pressure from ensemble average
p_{oi} = stagnation pressure in inlet chamber
p_w = casing wall pressure
r = radius
r_t = radius of blade tip
T_p = stall cell location relative to a blade spacing
u_t = blade tip speed
Δ = an increment of gray scale in the figures
ρ = density
ϕ = flow rate coefficient (the mean axial velocity divided by u_t)
ψ = pressure coefficient (the total pressure rise divided by $\rho u_t^2/2$)

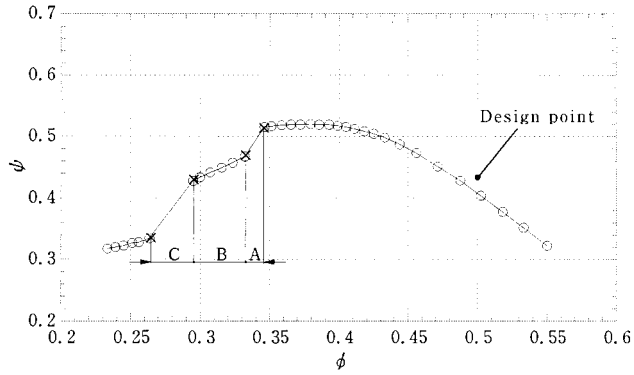

Fig. 2 Stage performance of compressor stage tested

If the cells are rotating at nearly constant speed, the number of the cells must be increasing with time until it attains the final condition of range A. Then, pieces of the pressure trace where the number of cells are expected to be 2, 3, 4, and 5 have been analyzed by the cross-correlation function, respectively. The results are shown in Figs. 6(*b*)–(*e*). From the interval of two large peaks, it is found that the rotating speed of the cell decreases a little with the number of cells, and is 72.2 percent of the rotor rotation when five cells exist. In the cross-correlation functions of Figs. 6(*b*), 6(*c*), and 6(*d*), the number of small peaks between two large peaks are 2, 3, and 4, respectively. This fact seems to be as if the number of the cells was one more than what had been expected from the LPF pressure traces. This is because the cells stand in at unequal intervals as will be shown by the wavelet analysis described later. It should be noted that the number of cells estimated only by the cross-correlation function may be incorrect when they are at unequal intervals.

In range B, the LPF pressure traces and the cross-correlation function of two pressure signals are similar to Fig. 6(*e*), but the corresponding two large peaks are indistinguishable from other peaks in the cross-correlation function (the figure is omitted). Figure 7 shows the LPF pressure traces and the cross-correlation function in range C. From this figure, the rotating speed of a large cell is estimated to be 29.3 percent of a rotor rotation.

Wavelet Analysis. The size and the interval of the stall cells are examined by the wavelet transform, which is useful to get local information on disturbances (Farge, 1992).

The wavelet transform of a pressure signal $p(t)$ is defined by

$$W(a, b) = \frac{1}{\sqrt{a}} \int \Psi(T) p(t) dt$$

where $\Psi(T)$ is a wavelet function, a is the scaling parameter, b implies translation, and $T(t - b)/a$. When an appropriate function is chosen as $\Psi(T)$, a large value of $W(a, b)$ implies that the disturbance with scale a exists locally around b.

In the present study,

$$\Psi(T) = -\sin(2T) \exp(-T^2)$$

was used since a wave form of this wavelet is similar to the spiky LPF pressure signal observed in Fig. 4.

Figure 8 shows the contour map of $W(a, b)$ in the flow range A. The abscissa is $b/\Delta t$ and the ordinate is a logarithmic scale of $a/\Delta t$ in the opposite direction, where Δt corresponds to 1/120 of a rotor rotation. One cell appears in the first line of the figure, and the second one is generated in the second line. Just after the third cell is generated, the intervals are irregular, as shown in the third line, but a space appears to every three cells in which the fourth cell is generated as shown in the fourth line. In several rotations after the fourth cell is generated, a space appears to every four cells to generate the fifth one. The condition of five cells is so stable as to keep it through flow range B (the figure is omitted). In ranges A and B, the maximum values of $W(a, b)$ are located at $a/\Delta t \approx 10$. This means that the size of a cell is on the order of two blade spacings since the rotor has 24 blades ($a \approx 10\Delta t = 1/12$ of a rotor rotation).

Figure 9 shows the result of the wavelet analysis in range C. It is clearly seen that a large-scale disturbance appears overlapping the five small disturbances in the first line of the figure, and develops as the small ones disappear. The scale of the large disturbance is on the order of a rotor rotation. This means a single large stall cell is generated in range C.

Additional Discussion. Recently, Camp and Day (1998) proposed a simple model to explain the occurrence of long-length-scale or spike-type stall inception in a given situation. According to their model, if the peak of the overall pressure characteristic is reached before the critical value of rotor incidence is exceeded anywhere in the compressor, then long-length-scale oscillations will occur, while, if the critical rotor tip incidence is exceeded before the peak of the overall pressure characteristic is reached, then spikes will appear in the overloaded rotor.

In the low-speed compressor stage used in this study, however, the type of stall inception did not conform to their model. A spike appeared at the beginning of the flow range A beyond the peak of the stage characteristic as shown in Fig. 2. Between the peak and the appearance of the spike, no long-length-scale wave was observed. The spike did not grow rapidly in size, unlike a so-called "spike-type stall inception." Alternatively, the number of cells increased under a fixed throttle condition, and reached five in a certain flow range, keeping the size and rotating speed.

In the present compressor stage test rig, another rotor and stator, which have swept endbend blades and the same design point, were tested. They were designated as the CEF rotor and the CEF stator

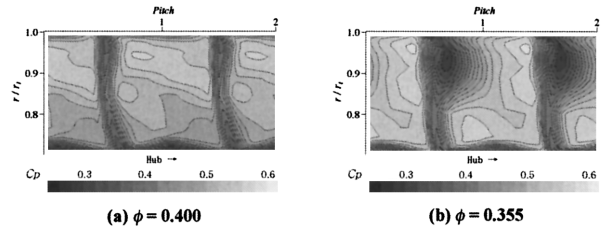

Fig. 3 Total pressure distribution downstream of stator

Fig. 4 Low-pass filtered pressure trace near rotor leading edge in flow range A

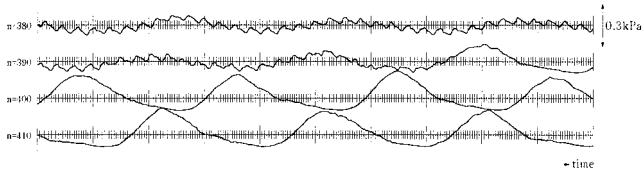

Fig. 5 Low-pass filtered pressure trace near rotor leading edge in flow range C

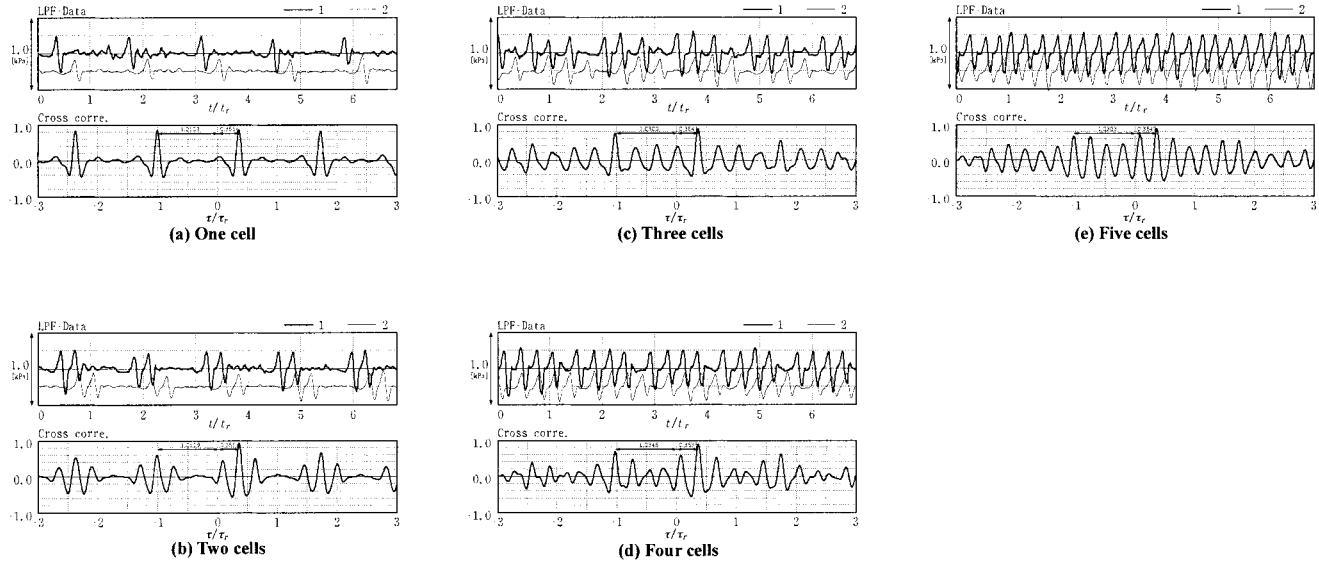

Fig. 6 Traces and cross-correlation function of two pressure signals in flow range A

(Inoue et al., 1997). In every combination of the rotor and stator (e.g., a combination of the CEF rotor and the baseline stator), the situation was similar for the development of rotating stall cells. However, the time in which the number of cells increased from one to five varied depending on the combination of the rotor and stator. When the development of the corner stall in the stator (see Fig. 3(*b*)) was suppressed by using the CEF stator, the number of cells increased so rapidly that the cross-correlation analysis could not made for each cell number. It happened very rarely that six cells appeared in the flow range B. When the stall inception was delayed by using the CEF rotor and CEF stator, flow range B was very narrow. The evolution of the rotating stall is very sensitive to the blading geometry. Under a certain condition, a short-length-scale cell may grow rapidly in size without increasing the number of cells. Under a different condition, a long-length-scale wave may appear suddenly without a stable condition of range B. Further investigation will be necessary on this point.

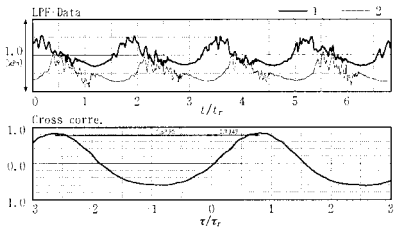

Fig. 7 Traces and cross-correlation function of two pressure signals in flow range C

Structure of Short-Length-Scale Stall Cell

Double Phase-Locked Averaging Technique. The size, the pressure wave pattern, and the rotating speed of a short-length-scale cell near stall inception are almost the same as those of the multiple stall cells in flow range B. Therefore, structure of the cells is considered to be identical at the stall inception and in the range B. The structure of short-length-scale stall cell at stall inception will be found if the structure of the cells can be captured in the stable condition of range B.

So far, flow structure of a rotating stall cell was measured by phase-locking data acquisition techniques with the cell rotation (Das and Jiang, 1984; Poensgen and Gallus, 1996; Palomba et al., 1998). These techniques are available for a long-length-scale stall cell, since blade geometry has a secondary effect for the cell structure. For capturing the short-length-scale stall cell, however, it is necessary to acquire the data synchronously with both the rotor and the cell rotation because the cell size is on the order of

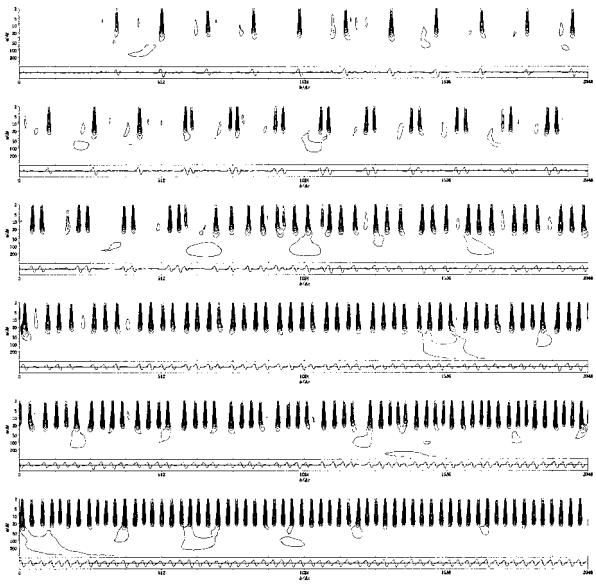

Fig. 8 Result of wavelet analysis in flow range A

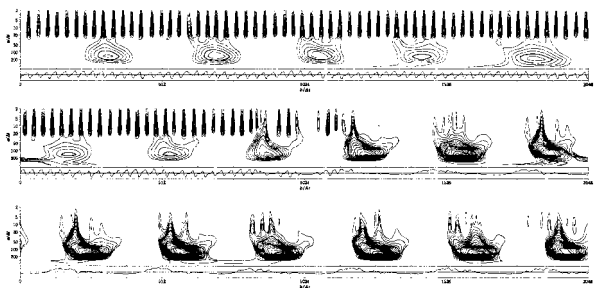

Fig. 9 Result of wavelet analysis in flow range C

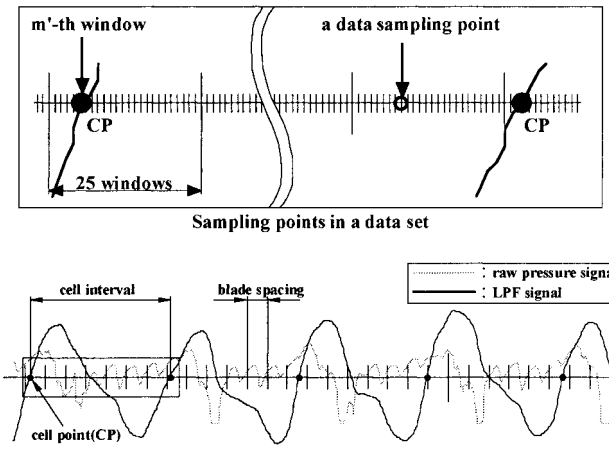

Fig. 10 Illustration of reference location of stall cell

a blade spacing length-scale. In this study, the following data-sampling and averaging technique is developed to get time-dependent ensemble averages.

The data acquisition is made upstream and downstream of the rotor by hot-wire surveys, and on the casing wall by 14 Kulite pressure sensors. At each location, the sensor signals for 600 circumferential sampling points per one rotor rotation are acquired during a sufficient number of the rotor rotations by a sampling system phase-locked to the rotor. Thus, 25 data sampling points are included in a blade spacing since the number of blades is 24 ($600/24 = 25$).

The location of the stall cell relative to a blade is determined by using these data sampling points and the LPF pressure signal on the casing wall near the rotor leading edge. Namely, a blade spacing is divided into 25 windows by these points, as illustrated in the upper part of Fig. 10. The reference point of the cell (cell point) is taken at a point where the LPF pressure signal crosses the zero line from negative to positive as illustrated in the lower part of Fig. 10. The interval between one cell point and the next cell point corresponds to a period of the cell traveling. A set of data is composed by the data acquired at each sampling point in a cell interval. When the front cell point of the data set is located in the m'-th window ($m' = 1, 2, \ldots, 25$), the data set is registered in the m'-th data group. All the data belonging to the same data group are averaged at each sampling point. However, one should notice that this averaged data set would not constitute a velocity or a pressure distribution synchronous with the cell rotation, because the rotational speed of the cell is different from the rotor speed. As the data are acquired at a fixed location synchronously with the rotor rotation, the time delay between the cell point and a data sampling point causes a relative location of the stall cell to shift. Therefore, the location of the cell point for each data sampling point should be modified. Such a modification is made by assuming that the cell point would travel at a constant speed. Then, the averaged data at each sampling point for the m'-th data group are rearranged for the m-th data group ($m = 1, 2, \ldots, 25$) in which the cell point is located in the m-th window at the moment of the data acquisition. The averaged data set in the m-th data group constitutes the time-dependent ensemble-averaged distribution at the moment when the cell point crosses in the m-th window. In the present paper, the location of cell relative to a blade is represented by $T_p = (m - 1)/25$.

The present authors call this sampling and averaging technique the "double phase-locked averaging (DPLA) technique." The DPLA technique is applied to flow surveys of velocity vectors upstream and downstream of the rotor by using a single slanted hot-wire. The hot-wire sensor used is a tungsten filament of 5-μm diameter, 1-mm effective length, and 45-deg slanting angle. The axis of the hot-wire probe is rotated at intervals of 30 deg for 12

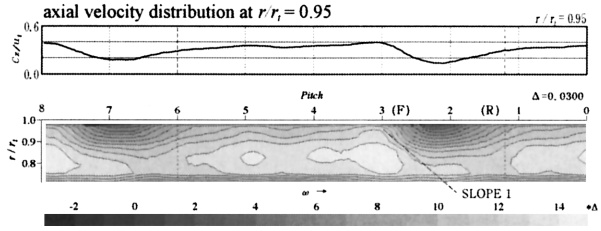

Fig. 11 Axial velocity distributions 25.6 mm upstream of the rotor at $T_p = 0.2$

orientations of the sensor. At each sensor orientation, the DPLA is made. Since a reverse flow exists in the stall cell, an appropriate set of the 8 ensemble averages of the hot-wire signal is chosen from the 12 averages to evaluate three components of a velocity vector. Namely, three components of the flow velocity are determined from the 8 ensemble averages by solving calibration equations of the hot-wire with the least-mean-square method (Kuroumaru et al., 1982). The DPLA technique is applied also to the casing wall pressure measurement.

Flow Field Upstream of the Rotor. Figures 11 and 12 show the contour maps of the axial velocity component 25.6 mm (77.7 percent of the axial blade chord) upstream of the rotor leading edge at $T_p = 0.2$ and 0.8. The top horizontal line represents the casing wall on which the numbers are marked backward to identify the blade spacings. The bottom line represents the hub wall surface, and the rotor blades rotate from left to right. The axial velocity component normalized by the blade tip speed is indicated by the gray scale. The symbol Δ stands for amount of increase in each gray scale, and the normalized axial velocity is evaluated by multiplying Δ by the number marked on the scale bar at the bottom of the figure. The cross-sectional average of the axial velocity corresponds nearly to 10 on the scale bar, since the measurements were conducted at the flow rate coefficient of about $\phi = 0.31$. The vertical dotted line is the reference position of a stall cell. The circumferential distance normalized by the blade spacing between the dotted line and the identification number on the right hand side of it is identical to T_p.

It can be seen in Fig. 11 that the axial velocity deficit regions appear over two blade spacings in the outer half of the annular flow passage, and they travel to the left at about 28 percent of the rotor rotation in the relative frame to the rotor. This fact means the short-length-scale stall cells of part-span type are rotating from left to right at 72 percent speed in the stationary frame. In this paper, the terms of "front" (F) and "rear" (R) are used on the basis of the relative frame. That is, the left-hand side of the cell in the figure is the front side. The effect of the stall cell is considerably large even at a distance from the rotor by about 78 percent of the axial chord length, and the minimum axial velocity becomes nearly zero in the cell. The axial velocity near the casing is slightly high at the front of the cell. This phenomenon is consistent with the velocity trace of a spike-type disturbance measured by Day (1993) and Silkowski (1995), in which abrupt decrease followed by slight increase in velocity occurs in a few blade spacing. On the top of Fig. 11, the velocity trace at $r/r_t = 0.95$ are shown for reference.

A large region of high axial velocity is located at the front and hub side of the stall cell. The shapes of the low and high-velocity

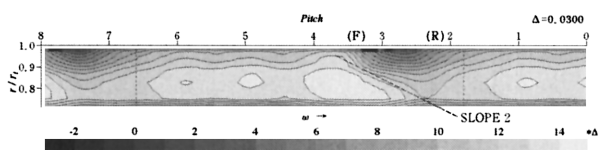

Fig. 12 Axial velocity distributions 25.6 mm upstream of the rotor at $T_p = 0.8$

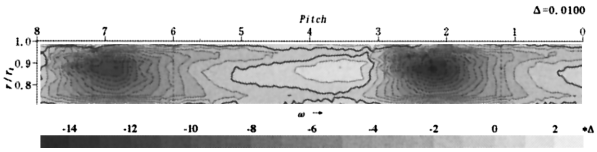

Fig. 13 Radial velocity distribution 25.6 mm upstream of the rotor at $T_p = 0.2$

regions vary with the relative cell location T_p. Looking at the front of the right-hand side cell in the figure, the slope of the contour lines between the low and high-velocity regions is steeper at $T_p = 0.2$ than at $T_p = 0.8$ (compare Slopes 1 and 2). Another high-velocity region is located near the circumferential position of 5 (refer to the number marked on the top horizontal line on the figure). This region does not travel in the relative frame because this is caused by a potential effect of the unstalled blade.

Figures 13 and 14 show the contour maps of the radial and relative tangential velocity components upstream of the rotor at $T_p = 0.2$. The figures are represented in the same manner as Fig. 11. The velocity components are normalized by the blade tip speed. The relative tangential velocity is taken as positive when it is in the opposite direction of the rotor rotation. In Fig. 13, the downward flow regions extend from the casing to hub in the same circumferential position of the axial velocity deficit regions. A region of slightly high upward flow exists at the front of the downward flow region. In Fig. 14, the regions of high tangential velocity are located at the front of the axial velocity deficit regions. The shapes of contour lines both for the radial and tangential velocity components change little with the relative cell location T_p (figures are omitted).

The three-dimensional feature of the flow field can be made clearer when the secondary flow velocity vector is defined by a component normal to the averaged exit flow angle in an unstalled flow region at each radial location. Figure 15 shows the secondary flow velocity vectors upstream of the rotor. They proceed to the left and downward direction near the stall cell, that is, from the axial velocity deficit region to the high axial velocity region.

Flow Field Downstream of the Rotor. Figures 16(*a*)–(*d*) show the contour maps of the normalized three velocity components and the secondary flow velocity vectors 8 mm downstream of the rotor trailing edge at $T_p = 0.2$. One can clearly distinguish the part-span stall cells from the unstalled blade wakes in these figures. Comparing the unstalled blade wakes between the fourth and sixth blade spacing (refer to the number marked on the top horizontal line on the figure), the wake is thicker as the stall cell approaches, because of increase in the angle of attack. In the stall cell, the axial velocity deficit region with a strong reverse flow appears in the casing side and the increment in axial velocity occurs in the hub side to satisfy continuity. Looking at the right-hand side cell, the low-energy fluid is discharged from the suction corner in the third spacing, while from the pressure corner in the

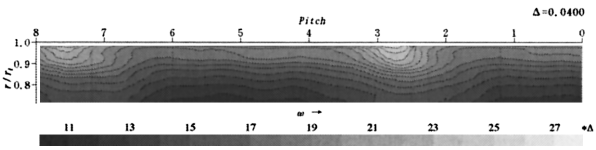

Fig. 14 Tangential velocity distribution 25.6 mm upstream of the rotor at $T_p = 0.2$

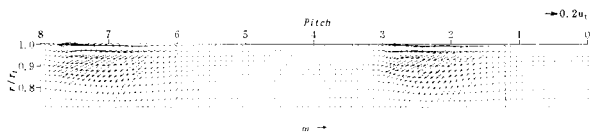

Fig. 15 Secondary flow vector 25.6 mm upstream of the rotor at $T_p = 0.2$

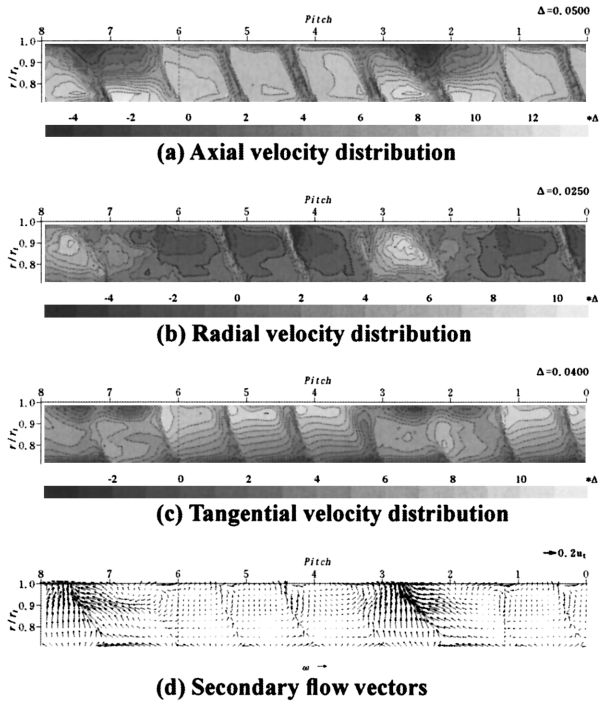

Fig. 16 Flow field 8 mm downstream of the rotor at $T_p = 0.2$

second spacing. Both low-energy fluids join with each other and make a big triangle reverse flow region as shown by a thick solid line (Fig. 16(*a*)). The radially outward flow occupies almost the third spacing. For the second spacing, however, the radial velocity component is not as high as that in the third spacing (Fig. 16(*b*)). The relative tangential velocity is extremely low near the tip of the stall region, and a considerably high tangential velocity region appears along the pressure surface side (Fig. 16(*c*)). In Fig. 16(*d*), the secondary flow vectors proceed toward the reverse flow region. A counterclockwise and a clockwise circulating flow are observed in front and rear of the reverse flow region, respectively.

Comparing Fig. 16(*a*) with Fig. 11, the axial velocity deficit regions upstream and downstream of the rotor are located almost at the same circumferential position. This phenomenon is similar to what was observed in the long-length-scale stall cell by many researchers (Das and Jiang, 1984; Poensgen and Gallus, 1996; Palomba et al., 1998).

As T_p increases, the stall cell travels from right to left, changing in shape as if it penetrated the blade wakes. The contour maps of the three velocity components and the secondary flow velocity vectors at $T_p = 0.8$ are shown in Figs. 17(*a*)–(*d*). It is found from Figs. 17(*a*) and 17(*c*) that the flow in the second spacing is recovering and the stall in the third spacing develops. The axial flow deficit region moves to the fourth spacing, and develops from the suction corner. The reverse flow region has two peaks: One is in the third spacing and another is at the fourth blade suction corner. The radially outward flow region for the fourth spacing is larger than that for the third spacing, although the axial velocity deficit region for the fourth spacing is considerably smaller (Fig. 17(*b*)). A clockwise circulating flow is observed again at the rear of the cell in the secondary flow map (Fig. 17(*d*)).

Casing Wall Pressure. Figure 18 shows the variation of the ensemble-averaged pressure distributions on the casing wall with T_p. The casing wall pressure p_w is represented by the pressure coefficient C_p defined as

$$C_p = (p_w - p_{oi})/(\rho u_t^2/2)$$

where p_{oi} and ρ are the pressure and the air density of the inlet chamber, and u_t is the blade tip speed. The arrows U and D

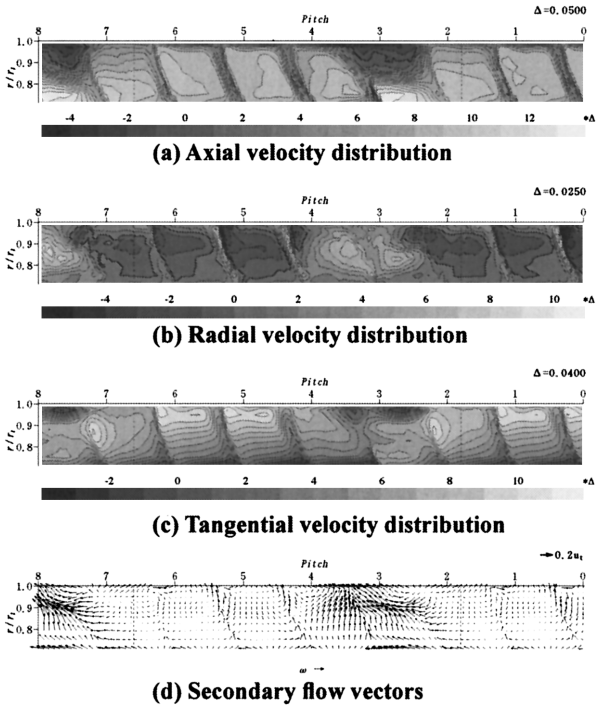

Fig. 17 Flow field 8 mm downstream of the rotor at $T_p = 0.8$

indicate the axial locations of the hot-wire surveys upstream and downstream of the rotor, respectively.

The most distinctive feature of the casing wall pressure is the behavior of a bubble-like extremely low-pressure region traveling ahead of the rotor from right to left. The bubble seems to have a leg that stands on the blade suction surface of the third blade at $T_p = 0.0$, and on the fourth blade suction surface at $T_p = 0.8$ (refer to the number marked on the bottom horizontal line on the figure). Comparing the pressure distribution at $T_p = 0.2$ (or $T_p = 0.8$) with Fig. 11 and Fig. 16(*a*) (or Fig. 12 and Fig. 17(*a*)), the

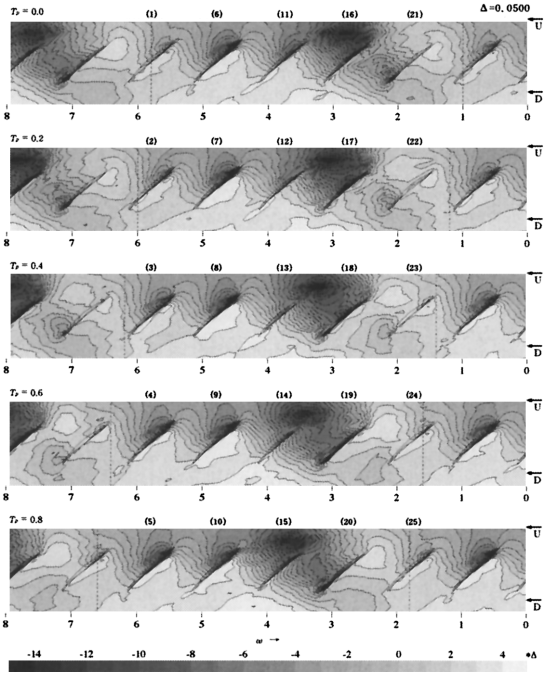

Fig. 18 Variation of ensemble-averaged pressure distributions on the casing

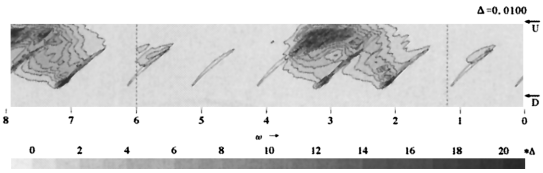

Fig. 19 Pressure fluctuation on the casing wall at $T_p = 0.2$

circumferential location of this bubble shifts by nearly one blade spacing in front of the axial velocity deficit regions. That is, this bubble precedes the axial velocity deficit regions upstream and downstream of the rotor. On the right-hand side of the bubble, a considerably high-pressure region appears and the pressure hardly rises from inlet to exit of the (stalled) blade passage.

When looking at the blades in sequence of the number in parentheses marked in Fig. 18, one can see variation of the pressure distribution around a blade while the stall cell is traveling on a blade spacing. As the stall cell approaches from the right, a low-pressure region grows gradually on the suction surface near the leading edge due to increase in the angle-of-attack (see the blades from (1) to (10) in order). Then, this low-pressure region is linked to the low-pressure bubble traveling ahead of the rotor, and merges in it to form a leg of the bubble (see from (11) to (15)). As the low-pressure bubble travels toward the left-hand side blade, the low-pressure leg is stretched and moved toward the trailing edge with increasing the pressure level (see from (16) to (19)). Finally, it separates from the low-pressure bubble and flows to the rotor exit (see from (20) to (23)). At $T_p = 0.6$ to 0.8, a comparatively low-pressure region is discharged downstream of the rotor between the second and third blades, and a part of the low-pressure region is discharged from the third blade trailing edge. These two comparatively low-pressure regions are corresponding to the two peaks of reverse flow region in Fig. 17(*a*). Then they are linked together downstream of the second blade at $T_p = 0.0$ and 0.2, which corresponds to the triangle reverse flow region in Fig. 16(*a*).

The pressure fluctuation has been evaluated by $\overline{p'^2}/(\rho u_t^2/2)^2$ where p' is the deviation from the ensemble averaged pressure at each measuring position. Figure 19 shows the distribution of pressure fluctuation on the casing wall at $T_p = 0.2$. It is extremely high in the low-pressure bubble ahead of the rotor, and considerably high in the low-pressure region inside the blade passage where the stall cell exists.

Flow Model for Short-Length-Scale Stall Cell. A flow mechanism of the short-length-scale cell has been investigated, by making animations for the velocity distributions upstream and downstream of the rotor and the pressure distribution on the casing wall, at intervals of $T_p = 0.04$. From observation of these animations, the low-pressure bubble traveling ahead of the rotor seems to be a key for the stall cell structure. According to the two-dimensional numerical simulation of the long-length-scale full-span stall by Saxer-Felici et al. (1999), a strong vortex bubble forming ahead of the rotor makes such a low pressure region. Hoying et al. (1999) also found a similar shape of vortex ahead of the rotor when they captured a short-length-scale stall of part-span type in their three-dimensional numerical simulation, and they thought it was the tip clearance vortex moving upstream of the rotor leading edge. Referring to the results of these two simulations, the low-pressure bubble shown in Fig. 18 must be a vortex.

In our experiment, however, behavior of the tip clearance vortex for the unstalled blades cannot be captured clearly in the casing wall pressure distribution (Fig. 18), the axial velocity distribution (Figs. 16 and 17(*a*)) and the secondary flow velocity vectors (Figs. 16 and 17(*d*)) behind the rotor, because the tip clearance is considerably small (0.75 percent of blade span, and 1 percent of tip chord length).

A physically plausible explanation is that the low-pressure bubble would be caused by a separation vortex moving upstream of

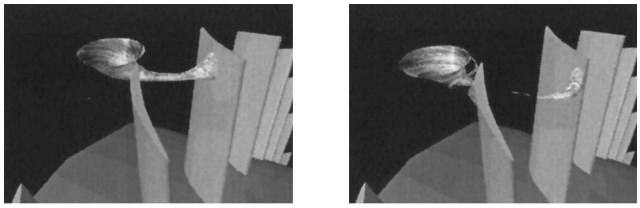

(a) (b)

Fig. 20 Illustrations for the flow mechanism of short-length-scale stall cell

the rotor. According to the vortex theory, bound vortices are distributed on an unstalled blade surface, which make a blade circulation (lift force). When leading edge separation occurs, a separation vortex is released from the blade surface to reduce the blade circulation. In the case of part-span stall, the separation vortex is only in the casing side. Its circulation may be on the order of blade circulation, if most of the blade circulation near the tip is lost due to stall. On the other hand, all the vortex lines are attached to the blade surface in the hub side where separation has not occurred yet. According to continuity of the vortex lines, they must separate somewhere from the blade suction surface to be linked to the separation vortex near the casing. That is, the vortex core consisting of these separated vortex lines spans from the blade suction surface to the casing wall. A spiral focus-type of separation will occur both on the suction surface and casing wall. The casing-side end of the vortex core moves ahead of the rotor to form the low-pressure bubble with a strong circulation. It travels in the circumferential direction due to interaction with the blades.

The behavior of this vortex is illustrated in Figs. 20(*a*) and 20(*b*). The flow model presented in this illustration is consistent with the experimental results mentioned in the previous sections.

In Fig. 18, the pressure is much lower at the low-pressure bubble than in the blade passage, because the end of the separation vortex attaches itself to the casing wall, while another end is attached to the suction surface at a distant from the casing. As the separation vortex is considered to behave violently, likewise a tornado, the ensemble-averaged low-pressure region is considerably wide ahead of the rotor and in the blade passage. The extremely high level of pressure fluctuation in the low-pressure bubble and the considerably high fluctuation level in the blade passage in Fig. 19 support this.

As the vortex bubble with a leg travels in the circumferential direction, the vortex leg is stretched and finally broken. This behavior corresponds to the variation of pressure distributions around the blades from (16) to (21) in Fig. 18. The broken vortex leg flows downstream and is discharged as low-energy fluids downstream of the rotor, which corresponds to the pressure distributions around the blades from (22) to (25). On the suction surface of the blade located in the left-hand side of the vortex bubble, a local separation will occur near the leading edge due to increase in the angle of attack, from where vortex lines are released in the flow. As the vortex bubble approaches the blade, the released vortex lines are swallowed into the bubble. The separation grows to a large focus-type separation, and the new vortex leg is generated. This behavior corresponds well to the variation of pressure distributions around the blades from (11) to (16) in Fig. 18.

The velocity distributions 8 mm downstream of the rotor in Figs. 16 and 17 can be explained by the present model. The reverse flow near the casing and the radial outward flow are induced by the vortex. At $T_p = 0.2$, the vortical flow just discharging from the second blade suction surface causes a strong reverse flow at the suction corner and a strong outward flow in the third blade spacing in Figs. 16(*a*) and 16(*b*). The vortical flow, which is discharged from the passage between the second and third blades and is linked to the former vortical flow, has a slight effect on the radial flow velocity, partly because of location of the vortex center and partly because of decay. The slight effect can be seen in the clockwise secondary flow at the rear of the cell in Fig. 16(*d*). At $T_p = 0.8$ (Fig. 17), the effect of the vortical flow is large on the axial velocity, but small on the radial velocity in the third blade spacing, because the vortex center is located near the measuring plane. The reverse flow at the suction corner and the outward flow along the suction side of the fourth blade spacing are induced by the vortical flow at the trailing edge of the third blade. The reverse flow region has two peaks, since the two vortical flows have not been linked to each other yet.

The velocity distributions 25.6 mm upstream of the rotor shown in Figs. 11–15 can be also explained by the present model. The separation vortex is inclined as illustrated in Fig. 20. The induced velocity of the inclined vortex leg is related to the locations of the axial velocity deficit region and the high axial velocity region in Figs. 11 and 12. That is, the separation vortex is located nearly parallel to the axial velocity contour lines in front of the axial velocity deficit region. The slope of the contour lines between the axial velocity deficit region and the high axial velocity region in Fig. 12 is more gradual than in Fig. 11, since the vortex is more stretched at $T_p = 0.8$, as conjectured from Fig. 18. The large axial velocity deficit is mainly due to the blockage effect of the low-energy fluid with vortical structure in the blade passage. The effect of the induced velocity of the separation vortex appears also in the regions of high tangential velocity shown in Fig. 14, and can be seen more clearly in the secondary flow vectors shown in Fig. 15.

The flow mechanism of the short-length-scale demonstrated above can be understand more clearly by observing the animations for the velocity distributions upstream and downstream of the rotor and the pressure distribution on the casing wall. The distinctive feature of the stall cell structure is on the low-pressure bubble consisting of the separation vortex, which travels ahead of the rotor. The elimination of this bubble should be a key for the active control of the spike-type rotating stall.

Conclusions

In the low-speed compressor test rig in Kyushu University, the multiple short-length-scale stall cells appeared in a certain flow range. Then, formation and evolution of the multiple stall cells were investigated by the use of the cross-correlation function and the wavelet analysis for the casing wall pressure near the rotor leading edge. A short length-scale stall cell appeared at first, but did not grow rapidly in size. Alternatively, the number of cells increased to a certain stable state (a mild stall state) under a fixed throttle condition. In the mild stall state, the number of cells was five, the size was on the same order as the inception cell (a few blade spacings) and the rotating speed was nearly 72 percent of rotor speed. With further throttling, the multiple short-length-scale stall cells turned into a long-length-scale wave overlapping the five short-length-scale waves, then developed to a deep stall state with one large cell rotating nearly at 29 percent of rotor speed.

The size, the wave form, and the rotating speed of the stall cell were almost the same as what appeared at the stall inception. They were also similar to those of the spike-type stall inception which had been reported in many literatures.

Then, time-dependent averages of the three-dimensional flow upstream and downstream of the rotor and the pressure distributions on the casing wall were obtained by the double phase-locked averaging technique, in which the outputs of a slanted hot-wire and high-response pressure transducers were averaged phase-locked to both the rotor and the cell rotation. The distinctive feature of the flow field was shown on the pressure distribution on the casing wall, that is an extremely low-pressure bubble with a leg traveling ahead of the rotor. The leg was linked to a blade suction surface while changing the blade in turn as the pressure bubble traveled.

A model for the flow mechanism of the short-length-scale stall cell has been presented based on the experimental results of the variation of the pressure distributions, which is summarized by:

- The separation vortex bubble with a leg standing on the blade surface travels ahead of the rotor in the circumferential direction.
- As it travels, the vortex leg stretches, breaks down, and finally discharges to the rotor exit, resulting in reverse flow regions near the casing downstream of the rotor.
- At the same time, a local separation occurs on the suction surface of the adjacent blade, from where the separated vortex lines are swallowed into the vortex bubble to generate a new vortex leg.

This model reveals the behavior of the three-dimensional velocity distributions measured upstream and downstream of the rotor. In concluding, the authors hope that further experiments or numerical simulations could be made to support the present model.

Acknowledgments

The authors are extremely grateful to Toshiba Co. for financial support of this experimental research work, and to Messrs. Maeda and Nakamura for helping the experimental work. They also appreciate the reviewers who recommended that we combine two papers concerning the evolution of multiple stall cells and the structure of short-length-scale cells.

References

Camp, T. R., and Day, I. J., 1998, "A Study of Spike and Modal Stall Phenomena in a Low-Speed Axial Compressors," ASME JOURNAL OF TURBOMACHINERY, Vol. 120, pp. 393–401.

Das, D. K., and Jiang, H. K., 1984, "An Experimental Study of Rotating Stall in a Multistage Axial-Flow Compressor," ASME *Journal of Engineering for Gas Turbines and Power*, Vol. 106, No. 3, pp. 542–551.

Day, I. J., 1993, "Stall Inception in Axial Flow Compressors," ASME JOURNAL OF TURBOMACHINERY, Vol. 115, pp. 1–9.

Day, I. J., Breuer, T., Escuret, J., Cherrett, M., and Wilson, A., 1999, "Stall Inception and the Prospects for Active Control in Four High-Speed Compressors," ASME JOURNAL OF TURBOMACHINERY, Vol. 121, pp. 18–27.

Farge, M., 1992, "Wavelet Transforms and Their Applications to Turbulence," *Annual Review of Fluid Mechanics*, Vol. 24, pp. 395–457.

Garnier, V. H., Epstein, A. H., and Greitzer, E. M., 1991, "Rotating Waves as a Stall Inception Indication in Axial Compressors," ASME JOURNAL OF TURBOMACHINERY, Vol. 113, pp. 290–301.

Hoying, D. A., Tan, C. S., Huu Duc Vo, and Greitzer, E. M., 1999, "Role of Blade Passage Flow Structures in Axial Compressor Rotating Stall Inception," ASME JOURNAL OF TURBOMACHINERY, Vol. 121, pp. 735–742.

Inoue, M., Kuroumaru, M., and Ando, Y., 1993, "Pressure Fluctuation on Casing Wall of Isolated Axial Compressor Rotors at Low Flow Rate," ASME JOURNAL OF TURBOMACHINERY, Vol. 115, pp. 19–27.

Inoue, M., Kuroumaru, M., Furukawa, M., Kinoue, Y., Tanino, T., Maeda, S., and Okuno, K., 1997, "Controlled-Endwall-Flow Blading for Multistage Axial Compressor Rotor," ASME Paper No. 97-GT-248.

Kuroumaru, M., Inoue, M., Higaki, T., Abd-Elkhalek, F. A., and Ikui, T., 1982, "Measurements of Three-Dimensional Flow Field Behind an Impeller by Means of Periodic Multi-Sampling of a Slanted Hot-Wire," *Bulletin of the JSME*, Vol. 25, No. 209, pp. 1674–1681.

Mathioudakis, K., and Breugelmans, F. A. E., 1985, "Development of Small Rotating Stall in a Single Stage Axial Compressor," ASME Paper No. 85-GT-227.

McDougall, N. M., Cumpsty, N. A., and Hynes, T. P., 1990, "Stall Inception in Axial Compressors," ASME JOURNAL OF TURBOMACHINERY, Vol. 112, pp. 116–125.

Moore, F. K., and Greitzer, E. M., 1986, "A Theory of Post-Stall Transients in Axial Compression Systems: Part I, II," ASME *Journal of Engineering for Gas Turbines and Power*, Vol. 108, pp. 68–76; 231–239.

Palomba, C., Puddu, P., and Nurzia, F., 1998, "3D Flow Field Measurement Around a Rotating Stall Cell," ASME Paper No. 98-GT-594.

Poensgen, C. A., and Gallus, H. E., 1996, "Rotating Stall in a Single-Stage Axial Flow Compressor," ASME JOURNAL OF TURBOMACHINERY, Vol. 118, No. 2, pp. 189–196.

Saxer-Felici, H. M., Saxer, A., Inderbitzin, A., and Gyarmathy, G., 1999, "Prediction and Measurement of Rotating Stall Cells in an Axial Compressor," ASME JOURNAL OF TURBOMACHINERY, Vol. 121, pp. 365–375.

Silkowski, P. D., 1995, "Measurements of Rotor Stalling in a Matched and a Mismatched Multistage Compressor," GTL Report, No. 221, Gas Turbine Laboratory, Massachusetts Institute of Technology.

Weigl, H. J., Paduano, J. D., Frechette, L. G., Epstein, A. H., and Greitzer, E. M., 1998, "Active Stabilization of Rotating Stall and Surge in a Transonic Single Axial Compressor," ASME JOURNAL OF TURBOMACHINERY, Vol. 120, pp. 625–636.

DISCUSSION

N. A. Cumpsty[1]

This is an interesting paper describing carefully obtained results of part-span stall with a new interpretation of the consequences of stall in terms of bound circulation and vortices. This new interpretation is highly original and the authors are to be congratulated on it. The attachment of the vortex to the endwall seems to bear some relation to an endwall flow feature found here in Cambridge during the spike inception process, which I hope we will describe in a future paper.

My principal point in writing is to emphasize something I think could easily be overlooked. The spikes, which are one route to compressor stall, are not the same or even similar to part-span stall cells. By beginning the introduction to the paper with reference to spike inception, the impression could be created that there is some link. Either spike or modal-stall inception leads to a change to a different flow regime, but whether this results in part-span stall, full-span stall, or surge depends on other factors. Among the factors affecting the outcome are the presence of other blade rows nearby, the presence of a nearby throttle or screen, the inertia of the air in the system, and the compliance of the air in the system.

Spikes resemble part-span stall cells in the sense that they occupy only a small part of the circumference, but in most other respects they are very different. For example:

1 spikes are transient events that either grow into stall cells or disappear within less than one rotor revolution;
2 spikes extend in the spanwise direction for a distance of only a few tip-clearance heights, whereas part-span stall cells occupy a substantial fraction of the span;
3 the disturbance caused by the spike is local to the tip of the blade affected and in our experience is not detectable one chord upstream or at the trailing edge of the blade row.

Spikes occur when the tip region of the rotor is, in some sense, overloaded. As Day and Camp (1998) showed, this can be correlated with local incidence for a given rotor. Spike stall is normal when the total-to-static pressure rise characteristic of the stage still has a marked negative gradient, whereas modal stall is the normal route when the characteristic is nearly flat. It would appear that in the experiments described in this paper, the total-to-static pressure rise characteristic at stall was almost flat and the mechanism of stall almost certainly involved modes. One can just detect the prestall modes at the start of the trace shown in Fig. 4. The vanes and stators upstream of the rotor act like a throttle and encourage the formation of the multiple part-span cells, whose effect decays in the axial direction more rapidly than for a single full-span stall cell.

In the second paragraph of the section "Additional discussion," it is stated that inception found in their experiments did not confirm to the Camp and Day (1998) model. This is just as it should be, since Fig. 4 seems to show long-wavelength small-amplitude oscillations (i.e., modes) prior to the formation of the stall cells.

In summary, I would like to suggest that the compressor used for this paper becomes unstable by the growth of long-wavelength "Moore and Greitzer" modes. Perhaps it is the presence of the accelerating blade row ahead of the rotor that suppresses the single-cell, full-span stall cells. Instead the instability leads to part-span cells, whose effect does not propagate as far upstream as a full-span cells. The number of cells increases as the mass flow is reduced by throttling until the cells begin to coalesce, so that for flows below about $\phi = 0.29$ a single cell is formed.

Authors' Closure

We are grateful to Professor Cumpsty for his useful discussion for this paper.

[1] University of Cambridge, Department of Engineering, Whittle Laboratory, Madingley Rd., Cambridge CB3 0DY, United Kingdom.

It is correct that this paper describes occurrence of the short-length-scale part-span stall cell with tornado-like structure, but does not describe the results of an ordinary part-span stall cell with relatively long length-scale, as reported by Tanaka and Murata (1972), Poensgen and Gallus (1996), and Palomba et al. (1998).

As to the introduction, we must call attention to the high-frequency stall inception that occurs in multistage compressors occasionally. It seems to result from the multiple short-length-scale part-span stall cells with tornado-like structure, in which a vortex spans from a blade suction surface to a casing wall ahead of the rotor. The vortex ends traveling ahead of the rotor cause the high-frequency spiky pressure waves on the casing wall.

A spike at stall inception is a transient event, and is not the same as the short-length-scale stall cell because the latter is in a developed state (or somewhat stable state). But, in our opinion, a spiky wave appearing at the spike inception has structure similar to that appearing at the onset of the multiple short length-scale part span stall cell. That is, the spiky wave pattern both in the spike and the short-length-scale stall cells is caused by the vortex bubble traveling ahead of the rotor at $70 \sim 80$ percent of rotor speed.

In our experiment the transient event was quite different from the spike-type inception, since the spiky wave never grew rapidly. However:

1 a first spiky wave disappeared within one rotor revolution sometimes;
2 although the vortex immersed its leg near midspan in the developed state, the vortex leg might be located near the tip at the onset; and
3 the spiky wave could be detected only on the region of a low-pressure bubble, and never downstream of the rotor.

Furthermore, our model is consistent with the fact that the spiky wave occurs when the tip region of the rotor is overloaded, because the vortex traveling ahead of the rotor resulted from the separation vortex.

The reason for the flat characteristics of the stage is that the corner stall (Fig. 3) developed in the downstream stator before the appearance of a spiky wave. However, we could not find a modal wave after the corner stall was developed. The small-amplitude disturbance shown at the beginning of the pressure trace in Fig. 4 is too small to capture by the wavelet analysis clearly as shown in Fig. 8. We do not understand why the modal wave disturbance was suppressed in our experiment until $\phi = 0.295$. Probably, the stability of the whole system (but not the stability of a local stage) or the geometry of other blade rows may affect this, as Prof. Cumpsty pointed out.

Reference

Tanaka, S., and Murata, S., 1972, "On the Partial Flow Rate Performance of Axial Compressor and Rotating Stall," *Bulletin of JSME*, Vol. 18, No. 117, pp. 256–263.

Modeling Shrouded Stator Cavity Flows in Axial-Flow Compressors

S. R. Wellborn

I. Tolchinsky

Rolls-Royce Allison,
Indianapolis, IN 46206

T. H. Okiishi
Iowa State University,
Ames, IA 50011

Experiments and computational analyses were completed to understand the nature of shrouded stator cavity flows. From this understanding, a one-dimensional model of the flow through shrouded stator cavities was developed. This model estimates the leakage mass flow, temperature rise, and angular momentum increase through the cavity, given geometry parameters and the flow conditions at the interface between the cavity and primary flow path. This cavity model consists of two components, one that estimates the flow characteristics through the labyrinth seals and the other that predicts the transfer of momentum due to windage. A description of the one-dimensional model is given. The incorporation and use of the one-dimensional model in a multistage compressor primary flow analysis tool is described. The combination of this model and the primary flow solver was used to reliably simulate the significant impact on performance of the increase of hub seal leakage in a twelve-stage axial-flow compressor. Observed higher temperatures of the hub region fluid, different stage matching, and lower overall efficiencies and core flow than expected could be correctly linked to increased hub seal clearance with this new technique. The importance of including these leakage flows in compressor simulations is shown.

Introduction

Over the years, experience has confirmed that shrouded stator cavity flows can have a significant effect on the performance of multistage axial-flow compressors. For example, Wellborn and Okiishi (1996) illustrated this with the results of their experiments that confirmed the consistent degradation of compressor performance with seal clearance increase. Similar observations have been reported by Jefferson and Turner (1958), Wisler (1988), LeJambre et al. (1998), and Heidegger et al. (1996).

The ability to predict this impact of shrouded hub seal leakage on compressor performance is an emerging competence. Extension of fully three-dimensional, viscous, and unsteady computations into the hub cavity and seal tooth regions of flow is not yet routinely practical nor may it even be necessary for design purposes. An engineering approximation that couples a simple model of hub cavity flow with a reliable computation of the main compressor flow would be attractive if it worked, because it could be widely used in product design and development.

In this paper, the development and validation of such a leakage model/multistage compressor flow code combination are described. This technique was used to reliably simulate the significant impact on performance of the increase of hub seal leakage in a twelve-stage axial-flow compressor. Observed higher temperatures of the hub region fluid, different stage matching patterns, and lower overall efficiencies and flow than expected could be correctly linked to increased hub seal clearance with this new technique.

The major contributions of this paper are:

- The presentation of an effective simplified model of shrouded stator cavity flows for axial flow compressors
- Confirmation that a simplified model of the cavity flow combined with an established primary flow solver can predict the impact of increased seal clearance on engine compressor performance.

Contributed by the International Gas Turbine Institute and presented at the 44th International Gas Turbine and Aeroengine Congress and Exhibition, Indianapolis, Indiana, June 7–10, 1999. Manuscript received by the International Gas Turbine Institute February 1999. Paper No. 99-GT-75. Review Chair: D. C. Wisler.

Case Study

We begin this paper by describing a case study in which the correct CFD prediction of compressor performance, stage matching, and primary flow path properties was dependent upon the correct modeling of hub leakage flows. The compressor, a 12-stage machine, was designed with the same philosophy as past compressors. Major design features included variable geometry stators for the first five vane rows and bleed extraction. The compressor contained a nearly constant mean-line radius in the front stages, but transitioned to a constant hub radius in the rear stages. To minimize manufacturing cost, rear stage vanes were constructed from stamped strip stock and some rotor wheels were common. All stators were shrouded with cavity volumes approximately the same size as those in past compressors. Multiple knife seals were used with abradable material on the inner surface of the inner band to retard flow through the cavity.

Testing of the compressor rig began. Following the initial seal-run-in operation and mechanical check out of the rig, the team suspended testing and disassembled the compressor; therefore, only limited aerodynamic performance data exist for the first build. Shortly after, the compressor was reassembled and placed back onto the test stand. Time constraints prohibited the refurbishing of the abradable material on the inner band seals and the outer case above the rotors. Time constraints also prohibited the measurement of worn abradable material on the case and inner band between build 1 tear-down and build 2 build-up.

Once testing of build 2 began, three things were immediately noticed for operation at design speed. First, near the operating line, flow dropped nearly 2.2 percent and the efficiency was reduced over 1 point between build 1 and build 2. Second, the compressor stages matched differently between the two builds, as illustrated in Fig. 1. Figure 1(*a*) sketches the variation in pressure rise values when the compressor was throttled from the choke to the stall side of the operating line for build 1. Figure 1(*b*) shows the trend for build 2. As depicted, for build 1 the rear of the machine loaded when flow was decreased, the pivot point being the first stage. For build 2, when flow was decreased, most of the rear half remained unthrottled, while the front of the compressor loaded. Third, measured temperatures throughout the front-stage hubs were consid-

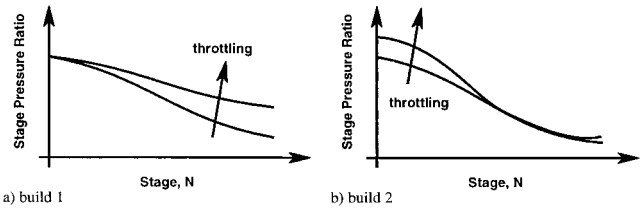

Fig. 1 Variation in stage matching between builds 1 and 2 of the compressor

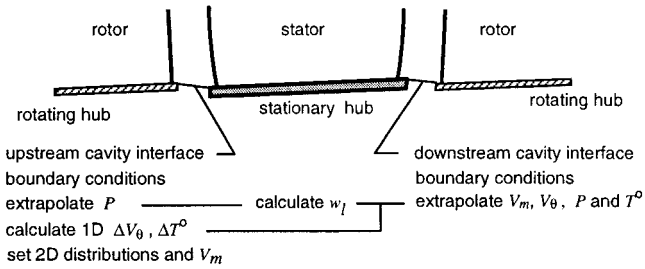

Fig. 2 Schematic of shrouded stator cavity flow model

erably higher than design intent for build 2. This was somewhat evident with build 1, but not to the extent seen with build 2. These changes in flow, efficiency, matching, and hub temperatures caused concern since the blading was not altered between the builds.

While the testing of build 2 continued, an attempt was made to determine the cause of the observed difference between design intent, build 1, and build 2 performance data. To do this, computer simulations of the compressor flow were undertaken. The tool used to perform these calculations was a combination of a one-dimensional leakage flow model and a multistage compressor analysis and design tool. From these simulations, it became clear that a cause of the different build 2 performance was that seal-tooth clearances had been increased above nominal running values between builds. The development, application, and results of this combined simulation tool are presented to prove seal-tooth clearance increase influenced the compressor performance and to demonstrate, in a generic sense, the impact of shrouded stator leakage flows on multistage compressor performance.

Cavity Flow Model Development

Data presented by Wellborn and Okiishi (1996), Heidegger et al. (1996), and more recently Ozturk et al. (1998) show that the flow in shrouded stator cavities can be quite complex with axial, radial, and circumferential variations along with unsteady fluctuations tied to the the rotor passing frequency. These complexities are in addition to other expected cavity flow characteristics such as leakage due to seal-tooth clearance, temperature increase due to windage, and tangential velocity change due to momentum transfer. Data from these studies also suggest the cavity flow becomes more axisymmetric as immersion into the cavity increases. Therefore, one way to include cavity flows in a multistage simulation would be to directly compute the outermost portion of the cavity, for example, from the inner radius of the inner band to hub radius. The influence of the rest of the cavity on the power stream flow could be easily included by a simple one-dimensional model. This could lead to reliable solutions, since the complexities of prescribing circumferential and axial variations at the cavity/power stream interface would be avoided. Unfortunately, this method could not be easily implemented, since the current version of the multistage analysis tool used does not support multiblock capability, and thus another approach was taken. The flow through the entire cavity under the hub platform was modeled and its influence on the power stream was included by imposing boundary conditions at the cavity/power stream interface. This procedure is illustrated in Fig. 2. Some flow variables were extrapolated from the main flow field, while others were predicted by a model of the cavity flow.

This less direct approach led to the need to have the correct specification of flow properties at the cavity/power stream interface. Studies were undertaken to determine which flow parameters, at the upstream interface, most influenced the flow field of a moderately loaded stator. These studies showed that the stator power stream flow field was most sensitive to the one-dimensional cavity flow parameters of leakage massflow, tangential velocity, and injection temperature at the upstream cavity interface. Slightly less important was the meridional injection angle. Of much less importance were spatial variations (axial and circumferential) of leakage flow. In addition, a second study showed that the downstream cavity flow could be approximated by simple axisymmetric mass extraction. Therefore, a shrouded stator seal cavity flow model was developed to predict the most important one-dimensional variables given cavity geometry parameters and flow conditions at the cavity/power stream interfaces.

The one-dimensional model was based on the representative straight-through seal-tooth geometry shown in Fig. 3. The shrouded stator cavity consists of the open region between the rotor drum and the stator inner band. Not shown but also included in the model are provisions to include stepped-tooth seals. Both types of seals are commonly used in compressors. Within the cavity, flow is assumed to be driven from the downstream cavity to the upstream cavity by the pressure differential across the stator. Therefore, a positive net flux of flow will enter the main flow path upstream of the stator leading edge.

The model consists of two components. The first estimates the flow characteristics through the labyrinth seals in which the knife-to-knife approach developed by Chupp et al. (1986) and Tipton et al. (1986) was used. The second component estimates the change in total temperature and tangential momentum through the cavity with a model similar to that proposed by McGreehan and Ko (1989). The contribution of this work is the coupling of these two components together and the link of the model with the multistage

Nomenclature

A = area
C_f = skin friction coefficient
C_p = specific heat at constant pressure
g_c = gravitational constant
M = moment
N = stage number
P = pressure
P_{rise} = stage pressure rise
R = gas constant
Re_θ = rotational Reynolds number
r = radius
T = temperature
V_m = meridional velocity
V_θ = tangential velocity
w_l = leakage massflow
ϵ = seal-tooth clearance
μ = viscosity
ρ = density
τ = shear stress
Φ = nondimensional leakage massflow rate
Ω = rotational speed

Subscripts and Superscripts

c = core or average value
in = inlet condition
out = outlet condition
o = total condition
r = rotor
s = stator
ϵ = clearance

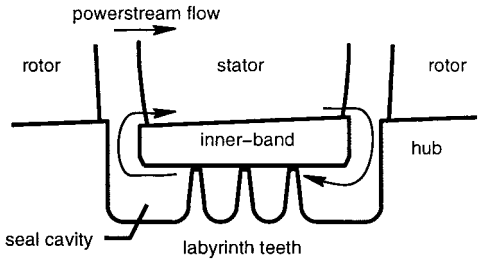

Fig. 3 Representative straight-through seal cavity

flow solver developed by Adamczyk et al. (1986). For completeness, brief descriptions of the primary flow solver, both one-dimensional model components and how they were coupled, are presented.

APNASA Design and Analysis Tool. The model equations presented by Adamczyk (1985) have the capability of simulating the blade row interaction effects associated with multistage turbomachinery. These equations have been incorporated into a practical tool, APNASA, for solving multistage flow fields. The average-passage analysis approach solves multistage flows using a steady reduced form of the three-dimensional Navier–Stokes equations for which the effects of neighboring blade rows are represented by axisymmetric blockages, body forces, and deterministic stresses. An iterative numerical solution procedure is employed in which the governing equations for each row are first solved using a cell-centered time-marching Runge–Kutta scheme. The body forces and deterministic stresses representing other blade rows are sequentially updated after each iteration. Multiple sweeps through the turbomachine component are required to achieve convergence. Reynolds averaged turbulence is approximated with either an algebraic (Baldwin–Lomax) or a two-equation (k–ϵ) turbulence model. Additional information on the development of APNASA and the average passage equations can be found in Celestina et al. (1986), Mulac and Adamczyk (1992), Shabbir et al. (1996), and Adamczyk et al. (1998).

Seal-Tooth Leakage. A wealth of information concerning labyrinth seal-teeth leakage characteristics is available. Thorough reviews of these characteristic were given by both Mahler (1972) and Ludwig (1978). Past studies (Stocker et al., 1977; Chupp et al., 1986; Tipton et al., 1986; Wisler, 1988) have pointed out the aerodynamic and geometric parameters that most affect the non-dimensional leakage mass-flow rate (Eq. (1)) through seal-teeth. Table 1 indicates that the most important aerodynamic parameter that affects leakage flow is the pressure differential across a tooth; however, the axial Reynolds number and knife tip speed do play moderate roles. Important geometric parameters along with observations of their influence on the leakage massflow rate are listed in Table 2. Figure 4 illustrates some of the geometric parameters listed in Table 2.

$$\Phi = \frac{w_l \sqrt{RT^o_{\text{in}}}}{\sqrt{g_c}\, P^o_{\text{in}} A_\epsilon} \tag{1}$$

Table 1 Aerodynamic parameters affecting the performance of labyrinth seals (Tipton et al., 1986)

Parameter	Function	Influence
Pressure ratio	P_{out} / P_{in}	Strong
Axial Reynolds number	$w_l \epsilon / A_\epsilon \mu_{in}$	Moderate
Knife tip speed	$V_\theta / \sqrt{g_c R T_{in}}$	Moderate
Rotational Reynolds number	$P_{in} \Omega^2 / \mu_{in} R T_{in}$	Weak
Taylor number	$(P_{in} V_\theta \epsilon / \mu_{in} R T_{in}) \sqrt{\epsilon / r_\epsilon}$	Weak

Table 2 Geometric parameters affecting the performance of labyrinth seals (Tipton et al., 1986)

Parameter	Function / Symbol	Influence: Straight	Influence: Stepped
Number of knifes	K_n	Strong	Strong
Knife angle	K_θ	Moderate	Moderate
Knife tip thickness	K_t / ϵ	Moderate	Moderate
Knife tip sharpness	K_r / ϵ	Moderate	Moderate
Knife tapper	K_β	Weak	Weak
Knife pitch	K_p / ϵ	Moderate	Weak
Knife height	K_h / ϵ	Weak	Weak
Land surface roughness	$L_e / 2\epsilon$	Moderate	Weak
Land porosity	$L_p / 2\epsilon$	Moderate	Weak

Many models for predicting massflow leakage rates through seal-teeth have been developed. One successful model is the knife-to-knife flow analysis approach, in which the flow through multiple seal-teeth is modeled as a series of adiabatic throttles. One-dimensional flow parameters at the knife throats are interconnected through total pressure loss calculations across each seal-tooth. Carry-over effects and individual tooth discharge coefficients are also imposed. To include aerodynamic and geometric influences on the leakage characteristics of the seal-teeth, empirical correlations, drawn from well-documented studies, are utilized. A previously developed knife-to-knife flow analysis algorithm (Tipton et al., 1986) was utilized for the current one-dimensional cavity flow model. This method includes the influence of those aerodynamic and geometric parameters listed in Tables 1 and 2 on leakage. Originally the code predicted seal-tooth leakage within 10 percent of measured leakage for a variety of seal-teeth geometries. Some modifications to the code were made in order to simplify the program. These revisions to the coding did not alter prediction accuracies.

Windage. Although the leakage characteristics of labyrinth seals are well documented, the influence of windage on cavity discharge flow properties has been reported to a much lesser extent. McGreehan and Ko (1989) presented a method that predicts the seal power dissipation over a range of desired design parameters. A momentum balance similar to theirs was utilized to predict the temperature rise and tangential velocity increase through the cavity in the current one-dimensional cavity model. Moments acting on a control volume are balanced by the change in angular momentum of the fluid passing through the control volume:

$$M_r + M_s = w_l r_c \Delta V_\theta \tag{2}$$

The rotor and stator moments are

$$M_r = \tau_r \int_r r_r dA_r = C_{f_r} \tfrac{1}{2} \rho \Omega^2 r_r^2 \int_r r_r dA_r$$

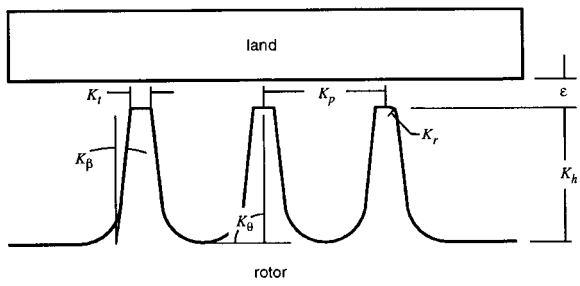

Fig. 4 Schematic of seal-teeth geometric parameters

$$M_s = \tau_s \int_s r_s dA_s = C_{f_s} \tfrac{1}{2} \rho \Omega^2 r_s^2 \int_s r_s dA_s$$

and

$$r_c = \frac{r_{\text{out}} + r_{\text{in}}}{2}.$$

Rotor and stator skin friction coefficients can be chosen to match measured data. Those given by McGreehan and Ko (1989) are

$$C_{f_r} = 0.042\left(1 - \frac{V_{\theta_c}}{r_c \Omega}\right)^{1.35} \text{Re}^{-0.2}$$

$$C_{f_s} = 0.063\left(\frac{V_{\theta_c}}{r_c \Omega}\right)^{1.87} \text{Re}^{-0.2}.$$

Here the average core velocity is assumed as

$$V_{\theta_c} = \frac{V_{\theta_{\text{out}}} + V_{\theta_{\text{in}}}}{2}.$$

Noting that the change in tangential velocity is

$$\Delta V_\theta = V_{\theta_{\text{out}}} - V_{\theta_{\text{in}}},$$

the angular momentum equation can be expressed as:

$$\tfrac{1}{2} \rho \Omega^2 \left[C_{f_r} r_r^2 \int_r r_r dA_r + C_{f_s} r_s^2 \int_s r_s dA_s \right] = w_l r_c (V_{\theta_{\text{out}}} - V_{\theta_{\text{in}}}) \quad (3)$$

Equation (3) is solved for $V_{\theta_{\text{out}}}$ by the bisection method consecutively for each zone in the shrouded stator cavity. The incoming tangential velocity is known from either the primary flow or a previous zone. The massflow is taken from the seal-tooth leakage prediction. Once the momentum balance is applied for the current zone, the total temperature rise is calculated from:

$$T^o_{\text{out}} = T^o_{\text{in}} + \frac{M_r \Omega}{C_p w_l} \quad (4)$$

Model Coupling Procedures. Equations (1), (3), and (4) are interdependent. For example, Eq. (1) requires the total temperature at the inlet of the first seal-tooth, however; the total temperature can change depending on the power dissipation in the downstream cavity. Both Eqs. (3) and (4) require the leakage massflow. Because of this, an iterative approach was taken to obtain the seal cavity conditions. The procedure to couple these models together is outlined below. Although the procedure is iterative, convergence was usually achieved within three cycles:

- Collect inlet and exit flow properties from the power stream cavity interfaces (as determined from primary flow solver).
- Apply the knife-to-knife model to estimate the seal-tooth leakage across the labyrinth seals (Eq. (2)).
- Using the estimated leakage, predict the temperature rise and increase in tangential velocity through the cavity from Eqs. (3) and (4).
- Check convergence of the predicted upstream temperature. If the difference is greater than 1 deg, then use the updated temperatures and tangential velocities to re-estimate the seal-tooth leakage (return to step 2).
- If the difference between old and new upstream temperature is less than 1 deg convergence has been achieved.

A validation of this one-dimensional model was performed to assess its accuracy. This study covered a range of low-speed and high-speed cavity configurations. Results suggest that the model was able to predict the seal-tooth leakage flow rate to within 10 percent of the data base. The increases in tangential velocity and total temperature were predicted to within 15 percent for most configurations.

The one-dimensional model was never put directly into APNASA. Instead the model was run outside the primary flow solver. Interface parameters were updated at certain intervals during the iteration of the powerstream flow, typically every 50 iterations. For the upstream interface, the total temperature, tangential velocity, and the flux of momentum normal to the cell face (provided by the model) were specified through the input deck, along with the meridional flow angle. For the downstream interface, proper values were extrapolated to the phantom cells while maintaining the prescribed local massflow out of the power stream. Both interfaces had constant leakage distributions across their axial and circumferential extents. The calculation of the entire compressor was considered converged when both overall performance parameters and cavity flow parameters changed negligibly (0.2 and 5 percent, respectively) with iteration.

Cavity Flow Model Application and Importance

Confirmation of the importance of modeling shrouded stator cavity flows in multistage CFD simulations is now reviewed. It is shown that the inclusion of seal cavity flows enabled accurate simulation of the rematching, hot hub, and overall performance degradation problems observed in going from build 1 to build 2 of the case study compressor.

Rear Block Loading Levels and Rematching. To help determine what caused the changes in rear stage loading between builds 1 and 2, two numerical experiments were completed. First, rotor tip clearance values were increased from design intent to double that amount, while seal-clearance values were kept nominal. Second, shrouded stator seal-tooth clearance values were increased from the design intent to double and triple that amount while rotor tip clearance values remained at their nominal values. Since wear could have occurred at both the case and shroud, both experiments were performed to determine which clearance increase, rotor tip or labyrinth seal, had the biggest impact on stage matching and the spanwise distribution of flow properties.

For these simulations, only the flow through the last six stages (plus stator 6) was computed. Mesh density and distributions were identical for all configurations. Inlet total pressure and temperature conditions were taken from the build 1 measured data. Inlet flow angles were acquired from a match of the test data. The discharge static pressure was set to obtain an operating condition near the operating line for each simulation.

Comparison of data from the double rotor tip clearance simulation with the nominal tip clearance simulation showed that for this compressor, only slight changes in stage matching occurred when rotor tip clearances were doubled. This is shown in Fig. 5. Here, predicted and measured differences in pressure rise are given for stages 7–12. The filled circles denote the difference in measured pressure rise between build 2 and build 1 near the operating line. The open circles represent the difference in predicted pressure rise between the double and nominal tip clearance simulations. Both data sets are presented as a percentage of the design pressure rise. Rig data clearly indicate that stages 7 and 8 pumped more in build 2, while stages 9–11 had at least 5 percent less pressure rise for build 2. Simulation data show levels far below the magnitude observed in the rig test. Additional simulations with larger tip clearance values were not attempted because of this rather modest change in stage matching with tip clearance variation and also because the simulation data showed that increasing tip clearance did not alter the spanwise distributions of total pressure and temperature near the hub.

Data from simulations for shrouded stator seal clearances being increasingly opened suggest a different effect both on stage matching and spanwise distributions of data. Stage pressure rise values are given in Fig. 6. As before, the predicted and measured differ-

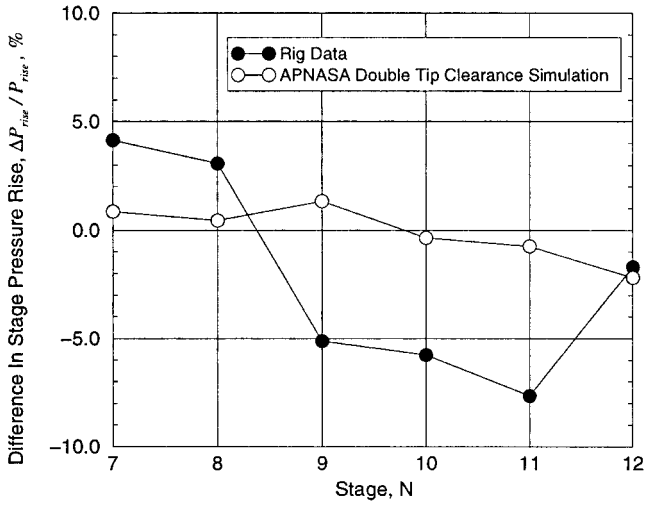

Fig. 5 Predicted and measured differences in pressure rise for stages 7–12. The filled circles denote the difference in pressure rise between build 2 and build 1. The open circles represent the difference in pressure rise between the double and nominal tip clearance simulation.

ences in pressure rise are for stages 7–12. The filled circles denote the difference in pressure rise between build 2 and build 1 (the same as in Fig. 5). The open circles represent the difference in pressure rise between the double and nominal seal clearance simulations. The open triangles represent the difference in pressure rise between the triple and nominal seal clearance simulations. As before, all data sets are presented as a percentage of the design pressure rise. Doubling the seal clearances rematched the stages to a level similar to that seen when tip clearances were doubled; however, unlike with tip clearance variations, changes in the spanwise profiles near the hub occurred. This prompted the triple clearance simulation. Data from this simulation began to look similar to the measured data between builds. For this simulation pressure rise differences were near −5 percent for stages 9–12, while those for stages 7 and 8 were increased. Predicted stage 7 levels overshoot the measured difference by 5 percent. We attribute this to the fact that in the simulations, inlet conditions into stator 6 were not changed, even though between builds they were different. Also note that the stage 12 predicted pressure rise difference was larger than measured. This observation will be discussed later.

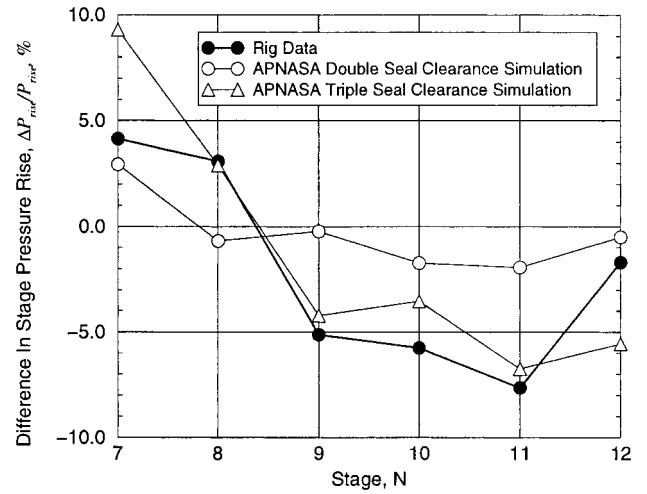

Fig. 6 Predicted and measured differences in pressure rise for stages 7–12. The filled circles denote the difference between build 2 and build 1. The open circles represent the difference between the double and nominal seal clearance simulation, while the open triangles represent the difference between the triple and nominal seal clearance simulation.

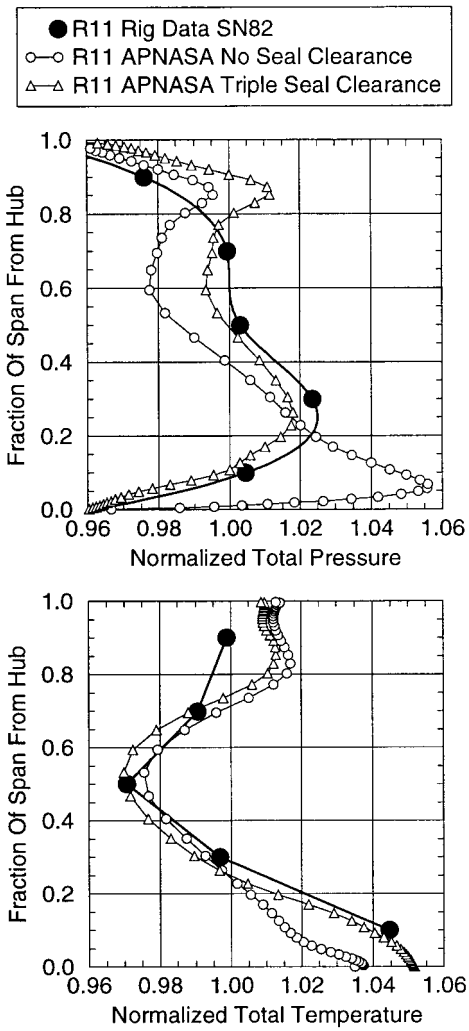

Fig. 7 Normalized distributions of rotor 11 discharge total pressure and total temperature

The triple seal clearance simulation not only helped explain the difference in matching between builds 1 and 2, but it also improved the prediction of spanwise distributions of total pressure and temperature, especially near the hub. Figure 7 shows the normalized distributions of total pressure and total temperature for rotor 11 discharge. Filled circles represent measured rig data, open circles represent data from the simulation with no seal leakage, while open triangles denote data for the simulation with triple seal clearances. The increase in seal-tooth clearance generally stiffened the pressure profile but more importantly caused a reduction in hub total pressure as in the measurements. Furthermore, the hub temperature increased to a level observed in the measurements when seal-tooth clearances were tripled.

The close match of the triple seal clearance simulation data to measured data suggest that a large amount of wear on the inner band occurred toward the end of the first build test. Because of this, when the testing of build 2 was completed, a detailed evaluation of cold build clearances was performed. These data, corrected for the cold-to-hot transformation, are shown in Fig. 8. Here the estimated average hot running seal clearances are given for each stage. Actual numbers have been nondimensionalized by the nominal clearance values; therefore, on the vertical axis the numbers 2, 3, and 4 refer to double, triple, and quadruple the nominal clearance. As depicted, measurements indicate that stages 6–9 clearances were near triple the nominal

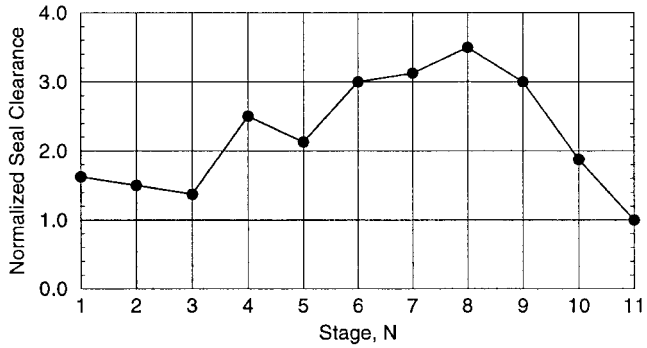

Fig. 8 Measured levels of seal-tooth clearance from the tear-down of build 2

clearance, the level predicted by the APNASA simulations, while stage 10 was double and stage 11 was close to the nominal value. We propose that the reason for the stage 12 miss in predicted pressure rise values (stated earlier) was due to this nominal clearance value for stage 11. These clearance measurements confirmed that the simple model developed was able to correctly include the influence of shrouded stator cavity flows in a multistage compressor simulation.

Front Block Hot Hubs. The success realized with the rear stage simulations prompted another series of numerical experiments. In question were the hot hubs measured in the front half of the compressor. As previously mentioned, build 2 hub probes measured temperatures higher than design intent. This hot hub was partially seen in build 1 but not to the extent observed in build 2. Since seal clearance measurements were acquired for all stages, the one-dimensional seal cavity flow model/APNASA combination was used to determine whether the hot hub measured in the rig could be simulated.

Two simulations were performed: the first with nominal rotor tip clearances and no seal-tooth leakage; the second with nominal rotor tip clearances and seal-teeth clearance set to those measured after the build 2 tear-down. Also included in the second simulation was hot gas ingestion into the primary flow path at the hub just upstream of rotor 1. This hot fluid came from downstream bleed holes in the rotor drum that supplied pressure to an oil sump. A path existed between the sump and the power stream flow path just aft of the inlet guide vane, and although a number of mechanical seals were in place to retard this flow, a small amount of leakage occurred (less than one third of the amount of nominal rear stage seal-tooth leakage).

The setup for these simulations consisted of the first five stages and inlet guide vane of the compressor. As before, inlet total pressure and temperature conditions were taken from the measured build 1 data, while flow angles were acquired from a data match of the measurements. The stator 5 discharge static pressure was set to obtain an operating condition near the operating line for each simulation. It must be mentioned that a considerable amount of time was spent adjusting leakage flow parameters associated with hot gas ingestion in order to match rotor 1 discharge flow. The details of this study are beyond the scope of this paper; however, hot gas ingestion did influence the performance of rotor 1 and possibly downstream stages.

The impact of including cavity flows and hot gas ingestion upstream of rotor 1 on the near hub temperature is illustrated in Fig. 9. Here the differences in temperature from design intent are shown for stages 1–5. Filled circles represent design intent data, which are identically zero since the design intent was used as the basis. Filled squares denote the differences between measured build 2 temperatures and design intent. Open circles represent the APNASA simulation with no shrouded cavity flows. Note that these data are very near design intent. Finally, open squares denote data for the APNASA simulation with the influence of shrouded stator cavity flows included through the implementation of the cavity model along with the influence of hot gas ingestion upstream of rotor 1. As seen, the simulation results quite accurately mimic the trends of increased temperatures through the first five stages as observed in the build 2 rig data. Because of these results we attributed the measured hot hubs in build 2 to the open seal clearances and ingestion of hot gas ahead of rotor 1, rather than inefficient blading.

Impact on Overall Performance. The use of APNASA coupled with the cavity flow model gave us better insight into why build 2 behaved so much differently from build 1 and design intent. Although the previous two studies were performed separately by breaking up the compressor into two separate analysis regions, the changes in overall performance (flow and efficiency) were estimated from the combination of the two studies. These estimates lead us to believe that flow should be reduced by about 1.6 percent and efficiency by 0.8 point when shrouded stator cavity flows are included to the level consistent with the measured clearances. These values are slightly below the measured differences of 2.2 percent in flow and 1 point in efficiency between builds 1 and 2.

Since the validity of the assumptions imposed for these estimates could be questioned, one final simulation was performed in which the entire compressor flow (all twelve stages) was simulated with and without shrouded stator leakage. This was somewhat of an academic exercise, but was useful as a benchmark of the analysis tool for future designs. The results of this simulation suggested the compressor should pull 1.2 percent less flow and run 0.7 points less efficient with seal leakage. These values are comparable to the values estimated above.

Conclusions

A simple one-dimensional model of seal cavity flows was developed and coupled with a multistage analysis and design tool. This technique was used to reliably simulate the significant impact on performance of the increase of hub seal leakage in a twelve stage axial-flow compressor. Observed higher temperatures of the hub region fluid, different stage matching patterns, and lower

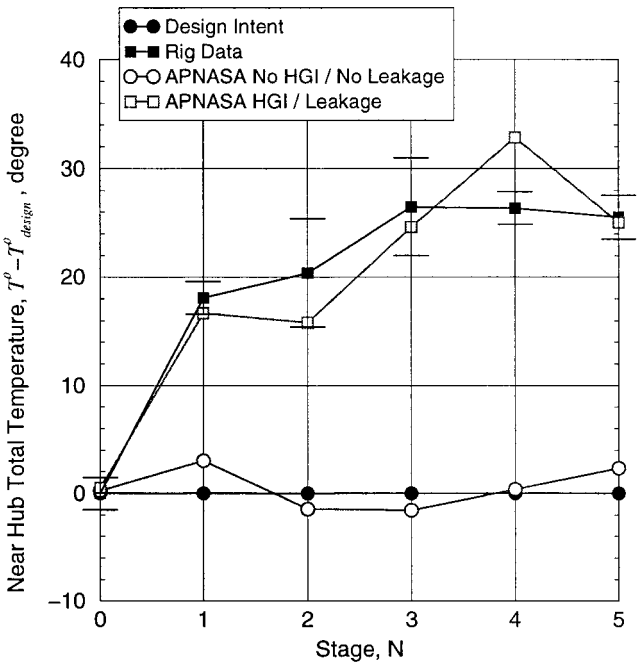

Fig. 9 Measured and predicted hub total temperature data given as a difference from design intent

overall efficiencies and flow than expected could be correctly linked to increased hub seal clearance. The simple leakage model and flow code combination success in simulating observed compressor performance is very encouraging and has been proven to be a useful design and analysis tool.

Acknowledgments

The research reported in this paper owes its existence to the efforts of many. The NASA Lewis Research Center, Cleveland, Ohio, sponsored much of this work under Contract NAS3-27725 (A. Strazisar, contract monitor). NAS computer time, used for some of the simulations, was appreciated. Sincere gratitude is also offered to the many individuals who have contributed to this work through their thoughtful discussion. These include at Rolls-Royce Allison: Dick Alverson, Robert Delaney, Dale Elliott, Mark Gritton, Ed Hall, Nathan Heidegger, and John Rathman, and at NASA Lewis Research Center: John Adamczyk, Aamir Shabbir, and Anthony Strazisar. Finally, we thank Rolls-Royce Allison for permission to publish this paper.

References

Adamczyk, J. J., 1985, "Model Equation for Simulating Flows in Multistage Turbomachinery," ASME Paper No. 85-GT-220.

Adamczyk, J. J., Mulac, R. A., and Celestina, M. L., 1986, "A Model for Closing the Inviscid Form of the Average-Passage Equation System," ASME JOURNAL OF TURBOMACHINERY, Vol. 108, pp. 180–186.

Adamczyk, J. J., Hathaway, M. D., Shabbir, A., and Wellborn, S. R., 1998, "Numerical Simulation of Multi-Stage Turbomachinery Flows," presented at AGARD Applied Vehicle Technology Panel Symposium on Design Principles and Methods for Aircraft Gas Turbine Engines, Toulouse, France, May 11–15.

Celestina, M. L., Mulac, R. A., and Adamczyk, J. J., 1986, "A Numerical Simulation of the Inviscid Flow Through a Counterrotating Propeller," ASME JOURNAL OF TURBOMACHINERY, Vol. 108, pp. 187–194.

Chupp, R. E., Holle, G. F., and Scott, T. E., 1986, "Labyrinth Seal Analysis, Vol. IV—User Manual for the Labyrinth Seal Design Model," Allison Gas Turbine, Division of General Motors Corporation, Indianapolis, IN, Jan. (also AFWAL-TR-85-2103 Vol. IV).

Heidegger, N. J., Hall, E. J., and Delaney, R. A., 1996, "Parameterized Study of High-Speed Compressor Seal Cavity Flow," AIAA Paper No. 96-2807.

Jefferson, J. L., and Turner, R. C., 1958, "Some Shrouding and Tip Clearance Effects in Axial Flow Compressors," *International Ship Building Progress*, Vol. 5, pp. 78–101.

LeJambre, C. R., Zacharias, R. M., Biederman, B. P., Gleixner, A. J., and Yetka, C. J., 1998, "Development and Application of a Multistage Navier–Stokes Flow Solver, Part II: Application to a High-Pressure Compressor Design," ASME JOURNAL OF TURBOMACHINERY, Vol. 120, pp. 215–223.

Ludwig, L., 1978, "Gas Path Sealing in Turbine Engines," *Seal Technology in Gas Turbine Engines*, AGARD, AGARD Publications, Neuilly Sur Seine France, Apr. (also NASA TM 73890).

McGreehan, W. F., and Ko, S. H., 1989, "Power Dissipation in Smooth and Honeycomb Labyrinth Seals," ASME Paper No. 89-GT-220.

Mahler, F. H., 1972, "Advanced Seal Technology," Pratt and Whitney Aircraft Division Tech. Rep. PWA-4372, Feb. (also AFAPL TR-72-8).

Mulac, R. A., and Adamczyk, J. J., 1992, "The Numerical Simulation of a High-Speed Axial Flow Compressor," ASME JOURNAL OF TURBOMACHINERY, Vol. 114, pp. 517–527.

Ozturk, H. K., Childs, P. R. N., Turner, A. B., Hannis, J. M., and Turner, J. R., 1998, "A Three-Dimensional Computational Study of Windage Heating Within an Axial Compressor Stator Well," ASME Paper No. 98-GT-119.

Shabbir, A., Zhu, J., and Celestina, M. L., 1996, "Assessment of Three Turbulence Models in a Compressor Rotor," ASME Paper No. 96-GT-198.

Stocker, H. L., Cox, D. M., and Holle, G. F., 1977, "Aerodynamic Performance of Conventional and Advanced Design Labyrinth Seals With Solid-Smooth, Abradable, and Honeycomb Lands," NASA CR-135307, Nov.

Tipton, D. L., Scott, T. E., and Vogel, R. E., 1986, "Labyrinth Seal Analysis. Vol. III—Analytical and Experimental Development of a Design Model for Labyrinth Seals," Allison Gas Turbine, Division of General Motors Corporation, Indianapolis, IN, Jan. (also AFWAL-TR-85-2103 Volume IV).

Wellborn, S. R., and Okiishi, T. H., 1996, "Effects of Shrouded Stator Cavity Flows on Multistage Axial Compressor Aerodynamic Performance," NASA CR 198536, Oct.

Wellborn, S. R., and Okiishi, T. H., 1999, "The Influence of Shrouded Stator Cavity Flows on Multistage Compressor Performance," ASME JOURNAL OF TURBOMACHINERY, Vol. 122, pp. 486–497.

Wisler, D. C., 1988, *Advanced Compressor and Fan Systems*, GE Aircraft Engines, Cincinnati, OH (also 1986 Lecture to ASME Turbomachinery Institute, Ames, IA).

Deterministic Stress Modeling of Hot Gas Segregation in a Turbine

J. Busby
United Technologies Research Center,
411 Silver Lane,
East Hartford, CT 06108

D. Sondak
Boston University,
Boston, MA 02215

B. Staubach
Pratt & Whitney,
East Hartford, CT 06108

R. Davis
United Technologies Research Center,
411 Silver Lane,
East Hartford, CT 06108

Simulation of unsteady viscous turbomachinery flowfields is presently impractical as a design tool due to the long run times required. Designers rely predominantly on steady-state simulations, but these simulations do not account for some of the important unsteady flow physics. Unsteady flow effects can be modeled as source terms in the steady flow equations. These source terms, referred to as Lumped Deterministic Stresses (LDS), can be used to drive steady flow solution procedures to reproduce the time-average of an unsteady flow solution. The goal of this work is to investigate the feasibility of using inviscid lumped deterministic stresses to model unsteady combustion hot streak migration effects on the turbine blade tip and outer air seal heat loads. The LDS model is obtained from an unsteady inviscid calculation. The inviscid LDS model is then used with a steady viscous computation to simulate the time-averaged viscous solution. The feasibility of the inviscid LDS model is demonstrated on a single-stage, three-dimensional, vane-blade turbine with a hot streak entering the vane passage at midpitch and midspan. The steady viscous solution with the LDS model is compared to the time-averaged viscous, steady viscous, and time-averaged inviscid computations. The LDS model reproduces the time-averaged viscous temperature distribution on the outer air seal to within 2.3 percent, while the steady viscous has an error of 8.4 percent, and the time-averaged inviscid calculation has an error of 17.2 percent. The solution using the LDS model is obtained at a cost in CPU time that is 26 percent of that required for a time-averaged viscous computation.

Introduction

Experimental data taken from gas turbine combustors indicate that the flow exiting the combustor has both circumferential and radial temperature gradients. These temperature gradients have a significant impact on the wall temperature of the first-stage rotor. A combustor hot streak, which can typically have temperatures twice the free-stream stagnation temperature, has a greater streamwise velocity than the surrounding fluid and therefore a larger positive incidence angle to the rotor as compared to the free stream. Due to this rotor incidence variation through the hot streak and the slow convection speed on the pressure side of the rotor, the hot streak typically accumulates on the rotor pressure surface. As a result, the time-averaged rotor-relative stagnation temperature is larger on the pressure surface than on the suction side. The secondary flow in the rotor passage also causes the hot fluid on the pressure side to spread from midspan toward the hub and tip endwalls, resulting in the heating of the outer air seal.

In the absence of total pressure nonuniformities, the temperature gradients due to the hot streak have minimal impact on the pressure distribution in the rotor. Thus, steady-state computations are typically used to compute the pressure distribution through the first stage of the turbine. For a steady-state computation, the tangential components of the hot streak at the exit of the stator are flux-averaged and only the radial variation in the rotor frame is retained. Many authors have shown that the tangential variations in the hot streak are of prime importance in establishing the hot streak migration path through the blade passage [1–4]. By mixing out the tangential variation at the rotor inlet, the steady-state computations do not model the temperature segregation in the blade passage or produce the correct temperature distributions on the blade surface.

Previously, the only way to model the hot streak migration through the rotor correctly was with three-dimensional, time-accurate, viscous computations. However, three-dimensional, unsteady, viscous computations are too computationally intensive and time consuming to be integrated into the design process. A more desirable approach is to include the time-averaged, unsteady effects into a steady computation via an unsteady model. For this work, the lumped deterministic stresses associated with an unsteady, inviscid calculation are used to model the time-averaged, unsteady effects in a steady, viscous calculation. Since the migration and segregation of the hot streak in the rotor are predominantly convective in nature, the inviscid LDS field should provide a reasonable model for the time-averaged temperature distribution in the rotor passage. Although unsteady, inviscid calculations are more computationally expensive than steady inviscid or viscous computations, they require significantly less computational resources than unsteady viscous computations.

Computational Model

Since deterministic stresses are analogous to turbulent stresses, decomposing velocities into mean and fluctuating components and applying the decomposed velocities to the Navier–Stokes equations is a natural starting point for modeling the deterministic stresses. Consider the two-dimensional Navier–Stokes equations:

$$\frac{\partial Q}{\partial t}+\frac{\partial E}{\partial x}+\frac{\partial F}{\partial y}-\mathrm{Re}^{-1}\left(\frac{\partial E_v}{\partial x}+\frac{\partial F_v}{\partial y}\right)=0 \tag{1}$$

where Q is the vector of conserved variables, E and F are the convection fluxes, and the diffusion fluxes, E_v and F_v, are given by

$$E_v=\begin{bmatrix}0\\ \tau_{xx}\\ \tau_{xy}\\ e_5^v\end{bmatrix} \quad F_v=\begin{bmatrix}0\\ \tau_{xy}\\ \tau_{yy}\\ f_5^v\end{bmatrix} \tag{2}$$

Contributed by the International Gas Turbine Institute and presented at the 44th International Gas Turbine and Aeroengine Congress and Exhibition, Indianapolis, Indiana, June 7–10, 1999. Manuscript received by the International Gas Turbine Institute February 1999. Paper No. 99-GT-76. Review Chair: D. C. Wisler.

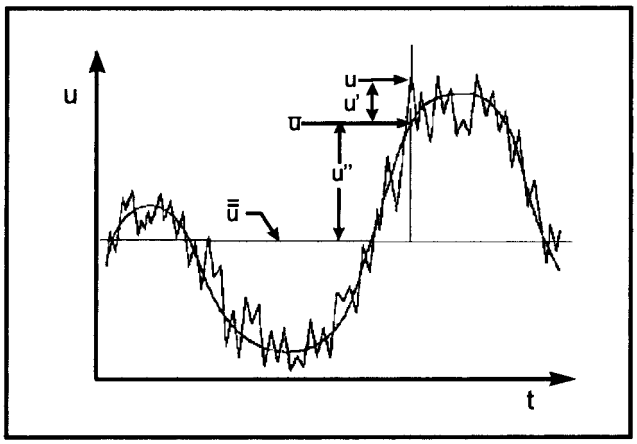

Fig. 1 Unsteady velocity decomposition

where

$$e_5^u = u\tau_{xx} + v\tau_{xy} + q_x \tag{3}$$

$$f_5^v = u\tau_{xy} + v\tau_{yy} + q_y \tag{4}$$

In conventional Reynolds decompositions, velocities are decomposed into mean and fluctuating components, and the stresses τ_{ij} in these equations represent the sum of molecular stresses and turbulent stresses. In the theory of deterministic stresses [5], the velocity fluctuations are considered to have a random (turbulent) component and a deterministic component. The deterministic fluctuations occur on larger space and time scales than the random fluctuations, and are a result of phenomena such as wake passing and rotor-stator potential interaction. In [5], the flowfield is further decomposed into an "average passage" and deviations from the average passage, but the average-passage analysis is not employed in the present study.

The velocity is first decomposed into a "deterministic" velocity $\bar{u}$ and a stochastic fluctuation u',

$$u_j = \bar{u}_j + u_j' \tag{5}$$

The deterministic velocity is further decomposed into a mean value and a deterministic fluctuation,

$$\bar{u}_j = \bar{\bar{u}}_j + u_j'' \tag{6}$$

This decomposition is illustrated in Fig. 1. The value of $\bar{\bar{u}}$ is constant, since it is averaged over all time scales. The smooth curve represents temporal variation of the deterministic velocity $\bar{u}$, which has a relatively large time scale, and the jagged line represents the instantaneous velocity, u.

The decompositions in Eqs. (5) and (6) may be interpreted as using mass-weighted averaging (Favre averaging) or Reynolds averaging. Here, the Navier–Stokes equations are mass-averaged in the conventional manner using Eq. (5). The velocity is then further decomposed according to Eq. (6), and the resulting equation is Reynolds averaged. A combination of mass-weighted averaging and Reynolds averaging is employed because this yields a more convenient form of the equations as compared with using either averaging technique alone. These averaging procedures yield two "additional" stress terms,

$$R_{ij} = \overline{\rho u_i' u_j'} + \overline{\rho u_i'' u_j''} \tag{7}$$

where the first term on the right-hand side is the conventional Reynolds stress and the second term on the right-hand side is the deterministic stress. The total stress, τ_{ij}, therefore has three components: the molecular stress, the turbulent stress and the deterministic stress:

$$\tau_{ij} = \tau_{ij}^m + \tau_{ij}^t + \tau_{ij}^d \tag{8}$$

An analogous decomposition is also applicable to the heat transfer rate, q_i.

Each diffusion flux in Eq. (2) can be decomposed into three components in accordance with Eq. (8). Rewriting Eq. (1) with this decomposition and explicitly indicating the functional dependence of the fluxes on $\bar{Q}$, Q', and Q'', yields

$$\frac{\partial \bar{Q}}{\partial t} + \frac{\partial E(\bar{Q})}{\partial x} + \frac{\partial F(\bar{Q})}{\partial y} - \mathrm{Re}^{-1}\left\{ \frac{\partial}{\partial x}\left[E_v^m(\bar{Q}) + E_v^t(\bar{Q}, Q') + E_v^d(\bar{Q}, Q'')\right] + \frac{\partial}{\partial y}\left[F_v^m(\bar{Q}) + F_v^t(\bar{Q}, Q') + F_v^d(\bar{Q}, Q'')\right]\right\} = 0 \tag{9}$$

Now, define an operator $R(\bar{Q}, Q')$

$$R(\bar{Q}, Q') \equiv \frac{\partial E(\bar{Q})}{\partial x} + \frac{\partial F(\bar{Q})}{\partial y} - \mathrm{Re}^{-1}\left\{ \frac{\partial}{\partial x}\left[E_v^m(\bar{Q}) + E_v^t(\bar{Q}, Q')\right] + \frac{\partial}{\partial y}\left[F_v^m(\bar{Q}) + F_v^t(\bar{Q}, Q')\right]\right\} \tag{10}$$

Note that this operator does not include the time term or the deterministic stress terms. The sum of the deterministic stress terms in both coordinate directions is defined as

$$D(\bar{Q}, Q'') \equiv -\mathrm{Re}^{-1}\left(\frac{\partial E_v^d(\bar{Q}, Q'')}{\partial x} + \frac{\partial F_v^d(\bar{Q}, Q'')}{\partial y}\right) \tag{11}$$

Applying Eqs. (10) and (11) to Eq. (9) yields

$$\frac{\partial \bar{Q}}{\partial t} + R(\bar{Q}, Q') + D(\bar{Q}, Q'') = 0 \tag{12}$$

Let Q_s represent a steady-state solution (without deterministic stresses), and let Q_{ta} represent the time-average of an unsteady solution. Since the numerical approximation of R is driven toward zero for a steady-state solution,

$$R(\bar{Q}_s, Q_s') = 0$$

The time-average of an unsteady solution will not be identical (in general) to the steady-state solution due to the existence of the deterministic stresses. Averaging a periodic flow over one period results in $\partial Q_{ta}/\partial t = 0$ and the deterministic stress term, D, is given by

$$D = -R(\bar{Q}_{ta}, Q_{ta}')$$

Since the "residual" of the Navier–Stokes solver is the numerical approximation of R, one method of computing D is to initialize the flow solver with Q_{ta} and to compute the residual. This, of course, is not a practical method for deducing the deterministic stresses, since the goal is to solve for Q_{ta} without incurring the expense of an unsteady computation, but it is a convenient method for extracting the D field as an aid toward developing a useful model for D. If D could be successfully modeled, it could be input to the solver as a source term and convergence to a steady state would then result in the solution for Q_{ta} without performing an unsteady simulation.

Some unsteady effects are inviscid, such as vane–blade potential interaction, and other unsteady effects are viscous, such as wake shedding. A method for computing the LDS model without performing an unsteady, viscous simulation is to use an unsteady, *inviscid* simulation instead. The resulting LDS field is interpolated onto the viscous grid, and the viscous simulation is converged to a steady state. This will capture some of the unsteady effects, with the advantage that the cost of the inviscid simulation is significantly less than that for a viscous simulation. Also, the procedure

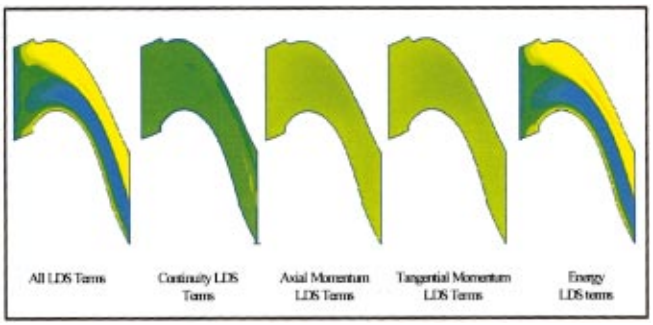

Fig. 2 Relative total temperature distributions resulting from the addition of each component LDS term

used to compute the LDS model can be used in conjunction with any flow solution procedure.

Flow Solution

The time-dependent, Reynolds-averaged, Navier–Stokes equations are solved with an implicit dual time-step approach coupled with a Lax–Wendroff/multiple-grid procedure [4, 6–9]. For the steady computations, only the Lax–Wendroff/multiple-grid procedure is used. The scheme uses central differences for the spatial derivatives with second- and fourth-order smoothing for stability. The algorithm is second-order accurate in time and space. The Baldwin–Lomax [10] turbulence model is used to compute the turbulent viscosity.

No-slip and adiabatic wall conditions are used on all solid boundaries. Giles' [11] two-dimensional, steady, nonreflecting, free-stream boundary conditions are used at the downstream free-stream boundary. At the inter-blade-row boundaries where the computational grid sectors move relative to each other, the pseudo-time-rate change of the primary variables are interpolated from the adjacent blade row and added to the time-rate changes computed from the Lax–Wendroff treatment. The pressure rise is prescribed by fixing the average exit static pressure and inlet total pressure.

Results

The three-dimensional, unsteady, hot streak migration through the first stage of a multiple-stage, high-pressure turbine is examined. The relative Mach numbers at the vane and blade exit are 0.77 and 0.76, respectively. The core of the hot streak is located at midspan and midpassage with a temperature ratio of 1.86.

The inviscid LDS field, computed from a time-averaged, unsteady inviscid solution, is interpolated onto a viscous grid and applied to a steady viscous solution. The temperature distribution on the blades, outer air seal, and through the passage is presented to demonstrate the capabilities of the inviscid LDS model.

For hot streak simulations, the LDS field associated with the energy equation dominates the unsteady flow. The effect of the individual components (i.e., continuity, axial and tangential momentum, and energy) of the LDS model on the relative total temperature distribution in the blade sector are shown in Fig. 2. The relative total temperature distribution obtained from a steady viscous solution with all of the LDS components is shown on the left. Addition of the LDS terms from the continuity, axial, and tangential momentum equations produces a minimal change in the total temperature distribution. The LDS terms from the energy equation produce nearly all of the temperature segregation in the solution. However, other viscous simulations that did not contain hot streaks [12] showed that the LDS field associated with the other equations may dominate the flow. Thus, all of the LDS terms are used in the inviscid LDS model.

The inviscid LDS model is used to simulate the hot streak migration through a single, vane-blade, turbine stage. The inviscid and viscous grid distributions are shown in Fig. 3. The LDS field

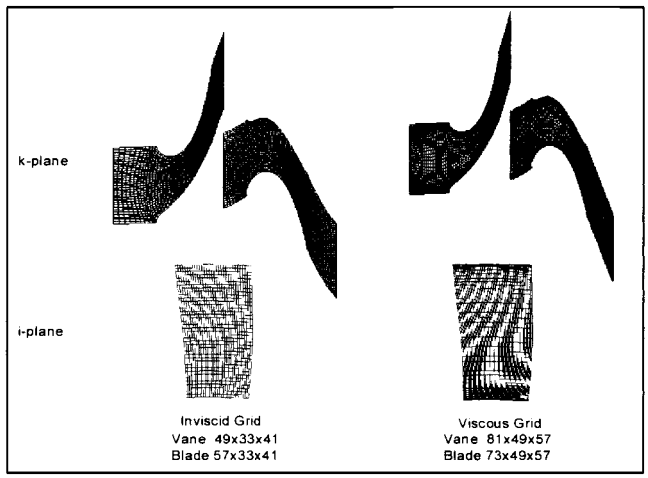

Fig. 3 Inviscid and viscous grid distributions

is computed from the time-averaged solution obtained with the inviscid grid. The unsteady computations are based on 15 cycles (one blade passing one vane). For the unsteady inviscid and viscous solutions, 200 iterations per global cycle are used. The time-history of the axial force on the blade for the unsteady, inviscid, and viscous computations is shown in Fig. 4.

Since the grid densities differ for the inviscid and viscous grids, the LDS model obtained from the inviscid solution does not map directly onto the viscous grid. Therefore, a three-dimensional interpolation of the inviscid LDS field onto the viscous grid must be performed. The inviscid LDS model is then applied to the corresponding steady viscous solution.

The convergence of the steady viscous calculation with inviscid LDS model is shown in Fig. 5, along with the convergence for the steady viscous calculation. The steady solution with the inviscid LDS model requires more iterations to converge, but converges to nearly the same level as the steady viscous computation. The convergence of the calculation with the inviscid LDS model shows that the additional source term does not cause instabilities in the solution process.

The relative total temperature distributions on the blade at three spanwise locations are shown in Fig. 6. The results from the steady viscous solution with the inviscid LDS model are compared to the time-averaged and steady viscous solutions as well as the time-averaged inviscid solution. The inviscid LDS model produces surface temperatures very close to the time-averaged viscous values. Near the endwalls, the inviscid LDS model predicts the same heat loads as the time-averaged viscous solution, but near midspan,

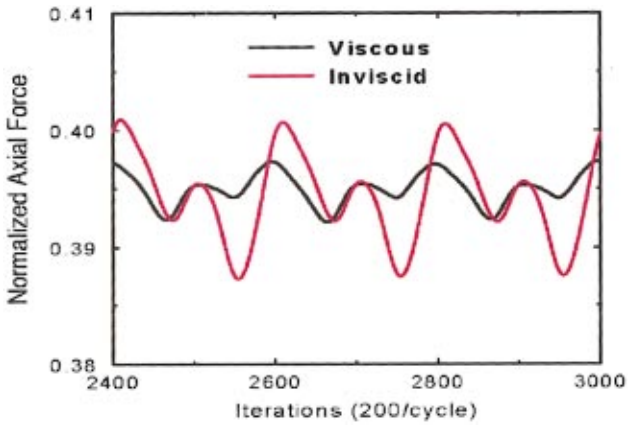

Fig. 4 Time-history of the unsteady loads on the blade

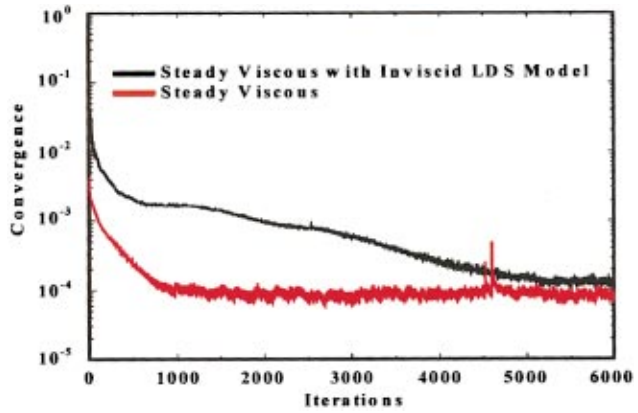

Fig. 5 Convergence history for the steady three-dimensional viscous solution with inviscid LDS model

the heat load predicted with the inviscid LDS model is less than that of the time-averaged viscous solution. The reason for the discrepancy at midspan is addressed in the following paragraphs. However, the inviscid LDS model improves the overall prediction of the heat loads on the blade tremendously over that produced by the unsteady, time-averaged Euler solution or the steady viscous solution, especially in the mid-span region.

Contours of relative total temperature on the rotor pressure and suction surfaces (see Fig. 7) indicate that the hot streak predicted with the inviscid LDS model has less spreading of the core region on the *pressure* surface than that of the time-averaged viscous solution, but matches the time-averaged viscous solution extremely well on the *suction* side of the blade. Blade-to-blade cuts of the relative total temperature contours at the *leading edge* of the blade (see Fig. 8) indicate that the inviscid LDS model reproduces the time-averaged viscous temperature segregation near the leading edge that is not produced by the *steady* viscous solution. In Fig. 9, blade-to-blade cuts near *midchord* show that the core of the hot streak predicted with the LDS model is similar to that predicted with the time-averaged viscous flow, while the steady computation does not produce a core flow at all. However, the core of the hot streak predicted with the LDS model breaks apart near its lower edge with some of the core migrating to the pressure surface and some remaining just off of the pressure surface, resulting in a smaller section of the pressure side of the blade heating up (see Fig. 7, also). The time-averaged viscous solution indicates that the core remains concentrated and all of it migrates to the pressure side of the blade, resulting in a larger area of the pressure side of the blade heating up. It is believed that unsteady, viscous effects on the blade play a role in the spreading of the core on the pressure side of the blade. These unsteady effects would not be captured by the inviscid LDS model. Near the trailing edge (see Fig. 10), the behavior of the core hot streak is similar to that at midchord: The core produced with the LDS model is less concentrated than that of the time-averaged viscous computation, resulting in a smaller area of the blade surface heating up.

The ultimate goal of this work is to predict the effect of the hot streak on the time-averaged temperature distribution on the outer air seal with a steady computation. The circumferentially averaged relative total temperatures on the outer air seal for the steady and time-averaged viscous solutions, time-averaged inviscid and steady viscous with the inviscid LDS model are shown in Fig. 11. The steady viscous computation predicts cooler temperatures in the leading edge region than the time-averaged viscous computation, while the time-averaged, inviscid solution captures the heating at the leading edge, but cools rapidly. The inviscid LDS model does a good job of predicting the time-averaged viscous temperature level as well as the location where the outer air seal begins to heat up. The steady viscous solution with the inviscid LDS model reproduces the time-averaged viscous total temperature distribution on the outer air seal (on average) to within 2.3 percent, while the steady viscous solution has an average error of 8.4 percent, and the time-averaged inviscid solution has an average error of 17.2 percent.

The steady viscous solution with the LDS model is significantly less expensive to compute than the unsteady viscous solution. The computational costs for the inviscid, viscous and LDS solutions are shown in Table 1. The CPU times for the steady computations are based on 6000 iterations, while those for the unsteady computations are based on 15 cycles (one blade passing one vane). For the unsteady inviscid and viscous solutions, 200 iterations per global cycle are used. The viscous

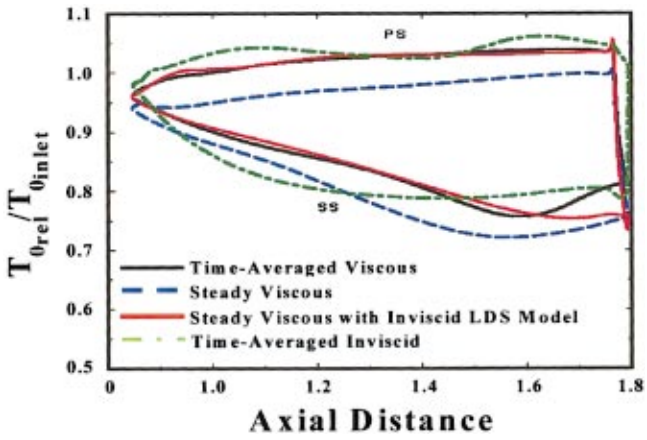

Fig. 6(*a*) 20 percent span

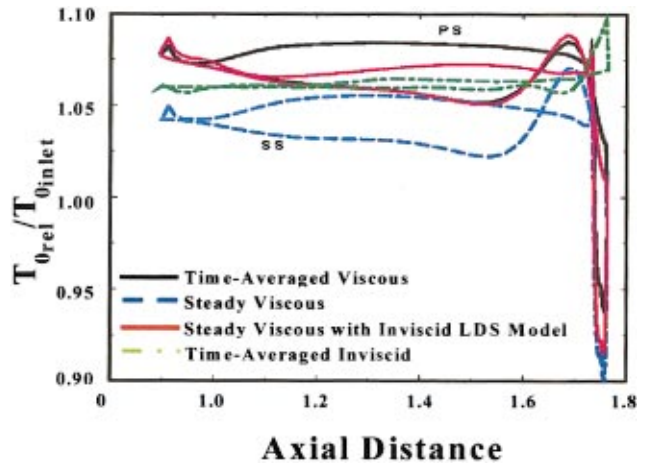

Fig. 6(*b*) 50 percent span

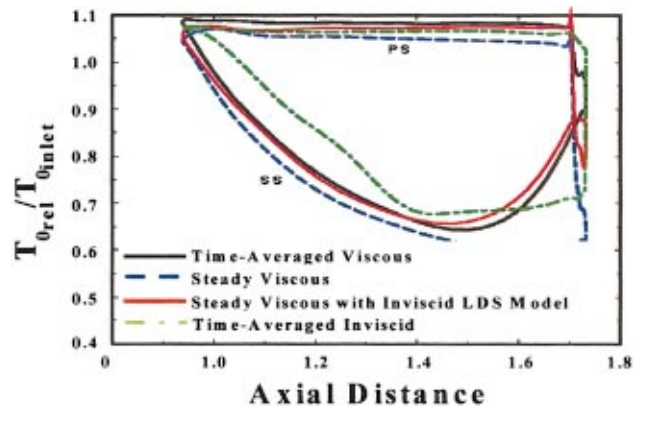

Fig. 6(*c*) 80 percent span

Fig. 6 Time-averaged relative total temperature distribution on blade

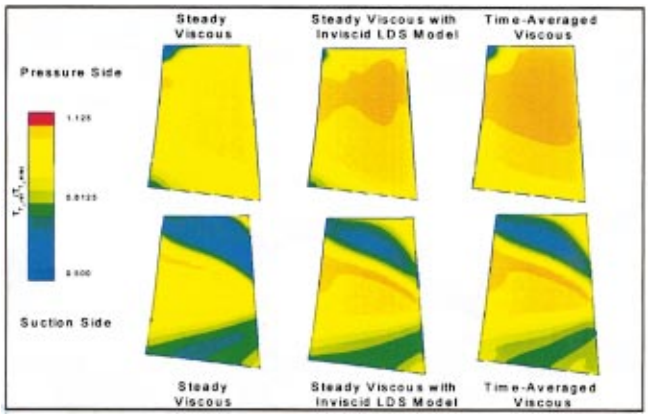

Fig. 7 Relative total temperature contours on the rotor surface

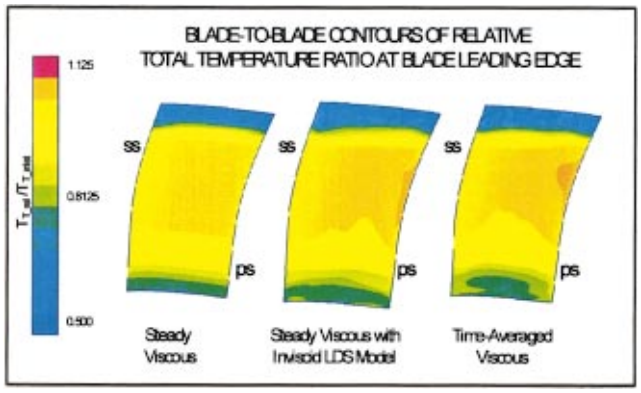

Fig. 8 Relative total temperature segregation at rotor leading edge

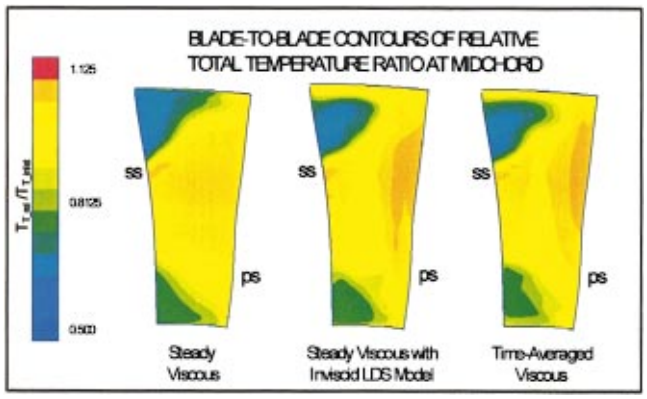

Fig. 9 Relative total temperature segregation at rotor midchord

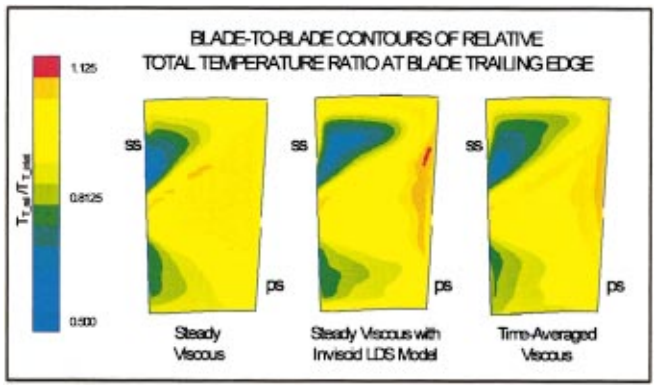

Fig. 10 Relative total temperature segregation at rotor trailing edge

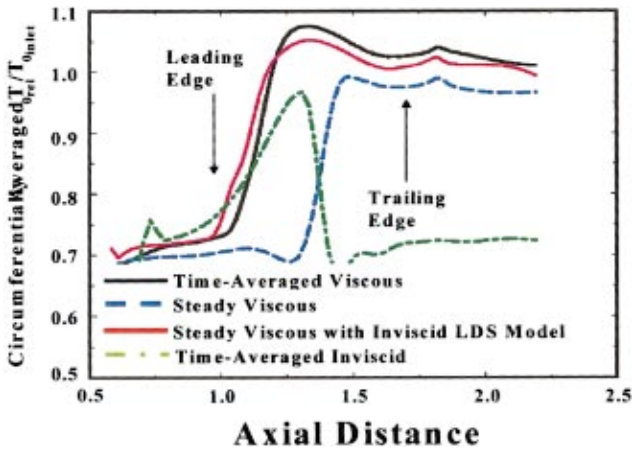

Fig. 11 Circumferentially averaged, relative total temperature on outer air seal

computations require more inner iterations to reduce the error in the packed regions of the grid near solid surfaces. The CPU requirements for the steady viscous computations with inviscid LDS model are only 26 percent of those for the unsteady viscous computations.

Conclusions

The results presented in this paper indicate that the inviscid LDS model is a viable option for predicting the time-averaged flow characteristics of a hot streak migrating through a turbine stage and the temperature increase on the outer air seal caused by the hot streak. The inviscid LDS model does not exactly reproduce the segregation and spreading of the hot streak core that is predicted by the time-averaged viscous flow; however, it does a much better job than that of the steady viscous or unsteady inviscid approaches. This deficiency may be due to the lack of viscous effects in the inviscid LDS model. Further work is required to incorporate viscous effects into the inviscid LDS model and to examine in detail the LDS field associated with the viscous regions. This could be achieved by comparing the LDS field from a viscous solution with that from an inviscid solution. Performing a parametric study of the application of the LDS models for various hot streak profiles may also indicate the driving mechanism behind the differences in the LDS solution and the time-averaged solution.

The success of the LDS model comes at the relatively low cost of the inviscid solutions. Another approach that may be even less costly is to develop a new inter-blade-row boundary condition that

Table 1 Three-dimensional CPU requirements

	Total Grid Points	STEADY (CPU sec.)	UNSTEADY (CPU sec.)	TOTAL (CPU sec.)	% Savings over Unsteady N-S
Inviscid Grid	143,418	68,668	169,546	238,514	86%
Viscous Grid	430,122	205,942	1,525,449	1,731,391	0%
Viscous+Inviscid LDS	430,122	444,456*	N/A	444,456	74%

*CPU=Steady Inviscid+Unsteady Inviscid + Steady Viscous

includes the unsteady effects as a source term, similar to the implementation of the LDS model. An analytical description of the source term may also be derived from the lumped deterministic stress terms.

Acknowledgments

This work was performed with support from NASA Lewis Research Center and funded by the High Performance Computing and Communication Program (HPCCP). The authors appreciate the guidance and support of the NASA Lewis technical monitor, Mr. Joseph Veres. In addition, the authors would like to acknowledge the technical support of Dr. Om Sharma and Dr. Ron-Ho Ni of Pratt & Whitney. Finally, the second author in this effort, Dr. Doug Sondak, is now located at Boston University in the Office of Information Technology.

References

1 Saxer, A. P., and Felici, H. M., "Numerical Analysis of Three-Dimensional Unsteady Hot Streak Migration and Shock Interaction in a Turbine Stage," ASME JOURNAL OF TURBOMACHINERY, Vol. 118, 1996, pp. 268–277.

2 Dorney, D. J., Davis, R. L., and Edwards, D. E., "Unsteady Analysis of Hot Streak Migration in a Turbine Stage," *Journal of Propulsion and Power*, Vol. 8, No. 2, Mar.–Apr. 1992, pp. 520–529.

3 Rai, M. M., and Dring, R. P., "Navier–Stokes Analyses of the Redistribution of Inlet Temperature Distortions in a Turbine," *Journal of Propulsion and Power*, Vol. 6, May–June 1990.

4 Takahashi, R., and Ni, R. H., "Unsteady Hot Streak Simulation Through 1-$\frac{1}{2}$ Stage Turbine," AIAA Paper No. 91-3382, 1991.

5 Adamczyk, J. J., "Model Equation for Simulating Flows in Multistage Turbomachinery," ASME Paper No. 85-GT-226, 1985.

6 Davis, R. L., Shang, T., Buteau, J., and Ni, R. H., "Prediction of 3-D Unsteady Flow in Multi-stage Turbomachinery Using an Implicit Dual Time-Step Approach," AIAA Paper No. 96-2565, 1996.

7 Ni, R. H., "A Multiple Grid Scheme for Solving the Euler Equations," *AIAA Journal*, Vol. 20, No. 11, 1981, pp. 1565–1571.

8 Ni, R. H., and Bogoian, J. C., "Predictions of 3-D Multi-Stage Turbine Flow Fields Using a Multiple-Grid Euler Solver," AIAA Paper No. 89-0203, 1989.

9 Ni, R. H., and Sharma, O. P., "Using a 3-D Euler Flow Simulation to Assess Effects of Periodic Unsteady Flow Through Turbines," AIAA Paper No. 90-2357, 1990.

10 Baldwin, B. S., and Lomax, H., "Thin Layer Approximation and Algebraic Model for Separated Turbulent Flows," AIAA Paper No. 78-257, 1978.

11 Giles, M., "Nonreflecting Boundary Conditions for Euler Equation Calculations," *AIAA Journal*, Vol. 28, No. 12, 1990, pp. 2050–2058.

12 Sondak, D. L., Dorney, D. J., and Davis, R. L., "Modeling Turbomachinery Unsteadiness With Lumped Deterministic Stresses," AIAA Paper No. 96-2570, 1996.

Turbomachinery Wakes: Differential Work and Mixing Losses

M. G. Rose

N. W. Harvey

Turbine Systems,
Rolls-Royce plc,
Derby, United Kingdom

In this paper the mixing of stator wakes in turbomachinery is considered. An extension is made to the existing model of Denton (1993), which addresses the effects of acceleration before mixing. Denton showed that if a total pressure wake was accelerated, mixing loss diminished, and vice versa. Here a total temperature wake is shown to exhibit a reverse trend. An attempt is also made to understand better the work transfer process between a stator wake and a rotor. The paper concentrates on axial turbines, but a brief look at compressors is included. It is argued that the free-stream work is not the same as the wake work, and the concept of "Differential Work" is introduced. A simple steady velocity triangle based model is proposed to give an estimate of the ratio of wake work to free-stream work (μ, see later). The model is compared to an unsteady CFD result to offer some verification of the assumptions. It is concluded that the rotodynamic work process tends to reduce total pressure wake depths in turbines and compressors and therefore mixing losses. The mixing loss due to total temperature wakes is less strongly affected by the differential work process.

Introduction

Turbomachinery designers have a wealth of analytical and computational tools available to them today. One can simply run two-dimensional or three-dimensional unsteady CFD codes to predict the nature of the wake–rotor interaction. Physically plausible and reasonably accurate results are routinely generated; turbine design is being influenced by such results. The problem with such predictions is that they don't explain to the designer *why* the flow field does what it does. There is a need for relatively straightforward "thought models" to help the designer understand the origins of loss occurring in unsteady flows and improve the design. The papers of Denton and Cumpsty (1987) and Denton (1993) are among the most important in trying to provide such understanding. Indeed Denton (1993) suggests that "a good physical understanding of the [origins of loss] may be more valuable than a quantitative prediction."

This paper is an attempt to extract a strand of fundamental understanding from the physics of unsteady interaction in two areas:

1 Wake mixing loss in steady flow when the wake has total temperature as well as total pressure deficits relative to the free stream and undergoes acceleration prior to mixing.
2 The interaction of stator wakes with downstream rotors and how this affects the subsequent mixing loss.

It should also be noted that this paper presents very idealized analyses. However, the result is to highlight the processes of differential work extraction between the free stream and wakes through a blade passage, and to show this has a significant effect on loss generation from subsequent mixing of the wakes.

Denton and Cumpsty (1987) make clear the importance of entropy generation as the correct way to gage the loss generation in a turbomachine. The topic of the mixing losses due to wakes is addressed and an algebraic expression given for the losses as a narrow wake mixes out at constant area in an incompressible flow. A simple theoretical model is presented of an acceleration or diffusion process prior to the mixing out of the distortion. The paper shows that acceleration before mixing reduces loss and diffusion greatly increases the mixing loss. The results of a compressible numerical approach are reported to be similar trends with greater loss at higher Mach numbers.

Wakes With Temperature and Pressure Profiles. Denton (1993) presents an extension to the ideas in Denton and Cumpsty (1987) with the more generalized mixing of both total temperature and total pressure are considered in compressible flow. It is shown, at a Mach number of 0.5, that a "square" wake with a velocity defect causes more mixing loss if the flow is diffused before mixing and less if accelerated.

In gas turbines, the HP NGV's are heavily film cooled using perhaps 10 percent of the core massflow at about half the free-stream temperature. This type of cooling tends to result in a wake of low temperature with a modest total pressure deficit. The coldness of the wake will also be exacerbated by the energy transfer processes in the von Karman vortex shedding process at the trailing edge. This phenomenon has been investigated experimentally and computationally by Carscallen et al. (1999).

Hartsel (1972) considered the mixing losses associated with turbine film cooling. He produced a simple calculation procedure to predict the losses of total pressure due to mixing. The entropy rise directly due to the temperature changes was neglected.

Wake Rotor Interaction. The wakes from one blade row interact unsteadily with the next while mixing out. Many papers have been published on this topic. Studies have been made in linear cascades with bar passing, see Banieghbal et al. (1995); rotating machines, see Schröder (1991) and Walraevens and Gallus (1995); and experiment against numerical prediction, see Moss et al. (1997). In Hodson and Dawes (1998) a good picture is given of the nature of this interaction in turbines. The wakes arrive at negative incidence onto the aerofoils and tend to slip toward the suction side as they negotiate the blade row known as "the negative jet effect." The significance of the unsteady work terms due to variations in static pressure is brought out and the idea of "energy separation" introduced. The paper concludes that energy separation is much more significant than the negative jet effect.

In compressors, wakes tend to arrive at positive incidence into both rotors and stators, e.g., Kerrebrock and Mikolajczak (1970). In compressor stators a mechanism has been identified that reduces

Contributed by the International Gas Turbine Institute and presented at the 44th International Gas Turbine and Aeroengine Congress and Exhibition, Indianapolis, Indiana, June 7–10, 1999. Manuscript received by the International Gas Turbine Institute February 1999. Paper No. 99-GT-25. Review Chair: D. C. Wisler.

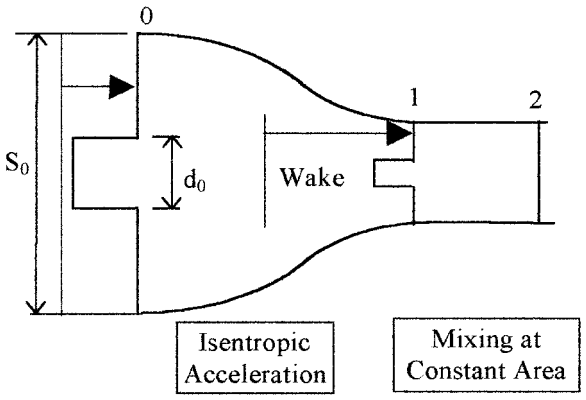

Fig. 1 Simple wake mixing model with acceleration before mixing (Denton, 1993)

subsequent mixing loss; this is known as wake stretching, e.g., Van Zante et al. (1997). Incoming compressor rotor wakes are stretched as the free stream diffuses through the stators. The authors point out that this stretching motion makes the wakes less deep and leads to a reduction in the subsequent mixing loss. Valkov and Tan (1999) address the recovery of energy in tip leakage vortices as they negotiate compressor stators; the energy is recovered in a similar way to the wake stretching effect.

Steady Wake Mixing With Temperature and Pressure Deficits

A simple mixing process is considered (Fig. 1); the flow is two dimensional, in that a wake of finite width is considered. As in Denton (1993), an acceleration is considered before mixing. This nonphysical assumption is made to help understand the fundamentals. The fluid enters with a square wake of width d while the width of the whole flow is S. The wake has total temperature T_{ow} and total pressure P_{ow}, the equivalents for the free stream are T_{of} and P_{of}.

Acceleration in a zero work, adiabatic and isentropic fashion to static pressure P_1 is assumed. Simple compressible flow expressions are used to give conditions at 1. The static pressure gives the Mach number, which gives the static temperature and hence the density and velocity. The continuity equation, per unit depth (Eq. (1)) can be used to give the wake width d_1 after the acceleration and also the width of the passage S_1.

$$\rho_{w0} V_{w0} d_0 = \rho_{w1} V_{w1} d_1$$

$$\rho_{f0} V_{f0} (S_0 - d_0) = \rho_{f1} V_{f1} (S_1 - d_1) \quad (1)$$

Mixing is assumed to be carried out at constant area; no friction with the bounding walls is allowed, mass; momentum, and energy are all conserved. The mixing calculation is one dimensional, in that only streamwise momentum is considered. See Appendix 1 for the algebra. The resulting equation is a quadratic in the mixed out exit velocity V_2. There are two roots to the equations, subsonic and supersonic, as explained by Denton (1993).

A simple spread sheet was used to perform the calculations. First the mixing losses *without* prior acceleration are considered. Three different cases were used, and all had a free-stream Mach number of 0.808 and a wake massflow fraction of 10 percent.

1 A wake of reduced total pressure (80 percent of free stream) but of uniform total temperature. This gave an entropy flux rise of 337 W/K. Mixing starting from the inlet conditions, with no premixing acceleration.
2 A cold streak (60 percent of free-stream T_o) with no total pressure deficit. This gave an entropy flux rise of 2984 W/K, nearly ten times the size of that for case (1) above.
3 Combined total pressure and total temperature deficits (80 percent P_o and 60 percent T_o). The mixing loss for this case with no prior acceleration is 2 percent lower than that for case (2), with the total temperature defect alone. This is because if one reduces the total pressure of the wake its Mach number also falls and its static temperature rises. Mixing involves heat transfer to the wake. The static temperature of the wake is nearer to the free-stream so there is less heat transfer and less entropy rise. Denton (1993) shows this, the impact of total temperature and total pressure on mixing at Mach 0.5 (his Fig. 6). In this diagram there is a slight left right tilt to the contours; the total pressure deficit can both increase and decrease the overall loss if a total temperature difference exists.

In the next section the variation of the mixing loss with premixing acceleration is considered. Figure 2 shows some typical results for the three cases considered. In this figure the mixing loss *relative* to the no-acceleration point (pressure ratio = 1.0) is plotted. This is to cope with the different scale of mixing loss between the cases. In each case the inlet free-stream Mach number is 0.808 and the wake mass flow is 10 percent of the free-stream value. There is some numerical inaccuracy in the spreadsheet that causes difficulties close to sonic conditions (the descriminant becomes negative). Where this occurs the points are omitted and the curves simply joined up from the supersonic to the subsonic regimes. The three cases are considered:

1 A wake of reduced total pressure (80 percent of free stream) but of uniform total temperature (indicated as $P_{ow}/P_{of} = 0.8$

Nomenclature

a = constant in quadratic: squared term
b = constant in quadratic: linear term
c = constant in quadratic
Cp = specific heat constant pressure, kJ/kgK
d = wake width, m
H = enthalpy, kJ
J = constant used and defined in Appendix 2
K = constants in mixing calc. solution
L = constant used and defined in Appendix 2
M = Mach number
P = pressure, Pa
R = gas constant, kJ/kgK
s = specific entropy, J/kgK
S = pitch of stator, m
T = temperature, K
U = blade speed, m/s
V = velocity, m/s
W = watts
α = absolute whirl angle, deg
β = relative whirl angle, deg
γ = ratio of specific heats
δ = depth of control volume, m
Δ = change in
ρ = gas density, kg/m^3
μ = ratio of wake work to free-stream work
ω = rotational speed, rad/s

Subscripts

o = stagnation conditions
0 = wake prior to acceleration
1 = wake after acceleration, rotor inlet conditions and wake before mixing
2 = mixed-out state, rotor exit state, and relative wake before mixing
3 = mixed-out relative conditions
r = rotor relative conditions
w = wake conditions
f = free-stream conditions
ax = axial momentum equation constant
ang = angular momentum equation constant
c = continuity equation constant
e = energy equation constant
θ = circumferential component
rat = ratio relative exit to absolute inlet

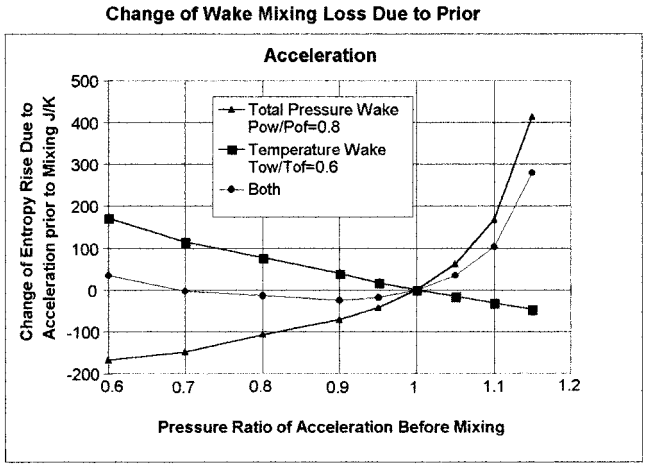

Fig. 2 Effect of acceleration on mixing loss

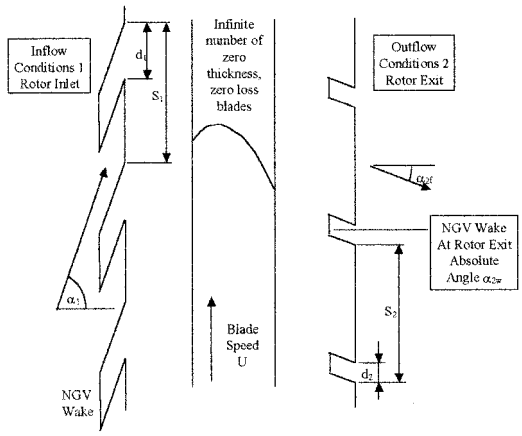

Fig. 3 Simple differential work extraction model

on Fig. 2). The entropy rise increases strongly if diffusion occurs before mixing and reduces slightly if acceleration occurs. Denton (1993) explains this is because the velocity deficit of the wake is reduced if the two streams are accelerated.

2 A cold streak (60 percent of free stream) with no total pressure deficit (identified as $T_{ow}/T_{of} = 0.6$). If the cold streak is accelerated, the resulting mixing loss increases, diffusion causes a reduction of loss, the reverse of 1. Shapiro (1953) has an expression showing the dependence of mixing loss on Mach number; higher Mach number gives higher loss. The difference in velocity between the cold streak and the free stream increases with acceleration, giving rise to more mixing loss.

3 Combined total pressure and total temperature deficits (identified as "both" in Fig. 2). The sensitivity to premixing acceleration or diffusion is reduced. If the flow is accelerated there is little change in the mixing loss. Diffusion still causes increased mixing losses but less than for the total pressure deficit alone.

The conclusion from this section must be that in an HP turbine it is not adequate to consider the effects of total pressure wakes alone. If these wakes are cold, the mixing loss may be much higher, and the sensitivity of this loss to acceleration or diffusion may be quite different.

Mixing of Wakes After Passing Through a Rotor

It might be hoped that the model of the previous section could be used to determine the effect of the rotor on the NGV wake mixing loss. To do this requires the answer to the question "Does the rotor diffuse or accelerate the flow?"

However, acceleration is a *zero work*, isentropic, adiabatic process and a turbine rotor cannot be represented in this way. There are huge work terms present in the rotor of the HP turbine. The total temperature may drop by 20 percent and the total pressure may drop below half its inlet value. Instead one has to consider a *high work*, isentropic, adiabatic process; this is carried out below.

It is well known that wakes arrive at negative incidence in a turbine, e.g., Hodson and Dawes (1998); and positive incidence in a compressor rotor, e.g., Kerrebrock and Mikolajczak (1970). The incidence is indicative of reduced inlet angular momentum. The Euler work equation tells us that there will be different work done by, or to, the wake when compared to the free stream. Since the work terms are very large, it is quite conceivable that they could transform the nature of the wake and the subsequent mixing losses.

Methodology. A simple approach is made, in which unsteadiness is ignored. A turbine rotor with an infinite number of zero thickness, zero loss blades is considered (Fig. 3). Such a rotor can be considered steady because there are no circumferential gradients of static pressure. One can effectively consider the two streams, wake and free stream, as independent. This does create a geometric problem, however: the two streams arrive at different relative inlet angles so the rotor has to change inlet angle. This problem is alleviated if one considers the rotor to have zero axial length, which is close to the classical actuator disk model.

In this section a simple velocity triangle calculation is used for the wakes and the free stream. A standard two-dimensional mixing calculation is then used to predict the mixing loss of the wakes. In the following sections the behavior of the velocity triangle model is checked by making comparisons with three-dimensional CFD results, both steady and unsteady. The model is then used to look at the effects of rotor work extraction on the mixing losses in an HP turbine and a stage of a core compressor.

Figure 3 shows the model; flow is from left to right, is two-dimensional, lossless, and of constant thickness. At inlet the NGV wakes are represented as a series of "square" wakes. They are of width d_1 and the pitch of the NGV's is S_1, all the fluid is traveling at angle α_1. The wake total pressure is P_{ow1} and total temperature is T_{ow1}, while the corresponding values for the free stream are P_{of1} and T_{of1}. At rotor exit the NGV wakes are shown, unmixed, they have a different absolute flow angle to the free stream. The static pressures are assumed to be uniform across the inlet and exit planes.

Figure 4 is a classical turbine velocity triangle. ABC is the free-stream rotor inlet triangle with absolute inlet angle α_1. DCB is the free-stream rotor exit triangle with relative exit angle β_2. To simplify the diagram the axial velocity is the same at inlet and exit and radius is constant. The blade speed vector is nondimensionalized and plotted as unity length. In this way the vector AD becomes the free-stream stage loading coefficient $\Delta H/U^2$.

The velocity triangles for the wakes are overlaid on Fig. 4. It is assumed that the wakes leave the NGVs at the free-stream angle $\alpha 1$, and leave the rotor at the same relative angle as the free stream,

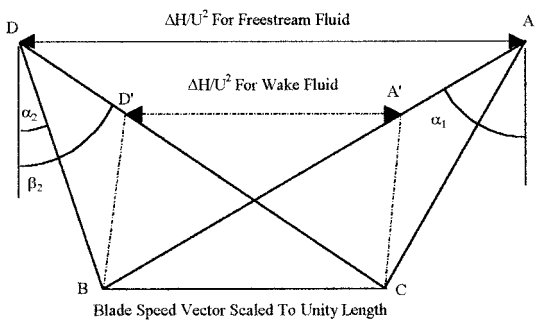

Fig. 4 Classical turbomachinery velocity triangles for free stream and wake

Table 1 HP turbine case

$P_1 = 2.17$ MPa	$\alpha_1 = 77.3$ deg	$M_{1f} = 0.947$
$T_{1f} = 1590.5$ K	U = 487.3 m/s	$P_2 = 1.43$ Mpa
$\gamma = 1.2868$	R = 287.24	$\beta_2 = 70.4$ deg

β_2. This latter assumption is verified against an unsteady three-dimensional CFD solution in a subsequent section. The wake inlet velocity triangle is A′BC, with the wake of course having a lower velocity than the free stream. The wake arrives onto the rotor with negative incidence. The wake exit velocity triangle is D′CB. The resulting vector A′D′ is the stage loading coefficient for the wake fluid. Given these assumptions, the work done by the wake is reduced compared to the work done by the free stream.

A "Differential Work Coefficient" is introduced here to express the ratio between the work done by the wake and the work done by the free stream μ.

$$\mu = \frac{\Delta U V_{\theta w}}{\Delta U V_{\theta f}} \tag{2}$$

In a spread sheet simple trigonomic expressions and compressible flow equations were used to look at how the differential work coefficient μ behaves. The process is described in Appendix 2.

Typical Results: Differential Work Extraction Between Wake and Free Stream. Here a prediction of the way in which the differential work coefficient μ varies for an HP turbine is made. Table 1 gives the input parameters for the case chosen.

Figure 5 presents a contour plot of μ as the total pressure and temperature of the wake are varied for this case. Encouragingly, the equal work line, $\mu = 1.0$, passes through the unity pressure and temperature ratio point. The coefficient μ has a low value if the wake is both cold and of low total pressure. Also, the trend in μ is monotonic for both total pressure and total temperature. However, the sensitivity of μ to total pressure is a function of the total temperature. It should be noted that in these calculations the incidence of the wake onto the rotor varied between -140 and $+14$ deg. For the very large values of negative incidence the behavior of the aerofoil will be very different from the simple assumptions made. Because of this, values of μ below 0.7 and results for wake-to-free stream total pressure ratios below 0.8 may be misleading.

Verification of Simple Wake Model Using CFD

The simple model was checked and, to a limited extent, verified by comparing it to two different three-dimensional CFD calculations, one steady and one time resolved, both for HP turbines.

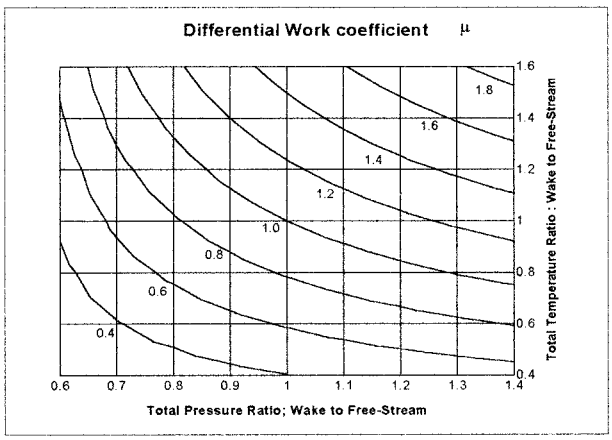

Fig. 5 Variation of differential work coefficient μ as wake total temperature and total pressure are varied for an HP turbine example

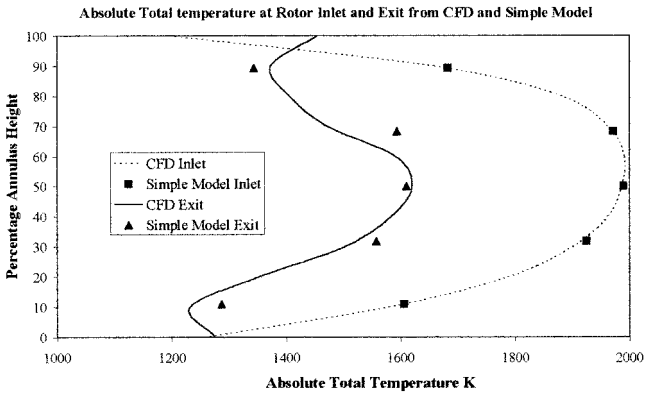

Fig. 6 Absolute total temperature rotor inlet and exit

Comparison With Three-Dimensional Steady CFD. The first case is a steady three-dimensional prediction made with the Rolls-Royce version of the Dawes Code known as JA63; see Gwilliam and Kingston (1998). This single-row steady solution is for an HP turbine blade with a strong parabolic distribution of total temperature at rotor inlet (Fig. 6). The circumferentially meaned peak value at about 55 percent annulus height is just less than 2000 K; the endwalls are at about 1200 K. Figure 7 shows the corresponding inlet total pressure profile. The velocity triangle model was applied at five radial sections of the rotor, and these are indicated in Figs. 6 and 7, showing the inlet stagnation boundary conditions for the velocity triangle calculations. The CFD also provided the other input conditions: inlet Mach number, inlet absolute whirl angle, exit static pressure, and exit relative whirl angle. Upstream and downstream planes were chosen for the calculations such that the effects of the rotor potential field were negligible.

The exit stagnation conditions calculated by CFD and the velocity triangle method are also shown in Figs. 6 and 7. The total temperatures agree to about ± 100 K. This is a wide error margin when compared to the temperature drop due to work of around 400 K. The total pressure is within about 2 percent of the CFD calculation.

At first sight the alignment of the velocity triangle predictions and the CFD, in terms of radial profiles, is surprising. But it should be noted the velocity triangle calculation has the benefit of the relative exit angle and exit static pressure as computed by the CFD code. These to no small extent define the work done by the streamlines. The velocity triangle approach lacks loss, mixing, three dimensionality, and radius change. Radial mixing in turbines or "spanwise transport" as addressed by Lewis (1993) is ignored. However, the CFD code does include many of the mechanisms of

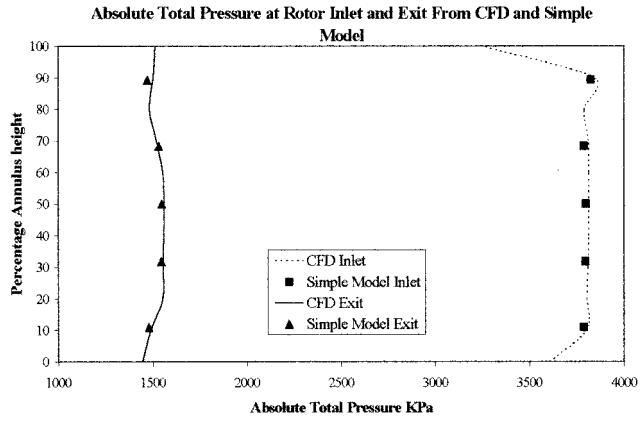

Fig. 7 Absolute total pressure rotor inlet and exit

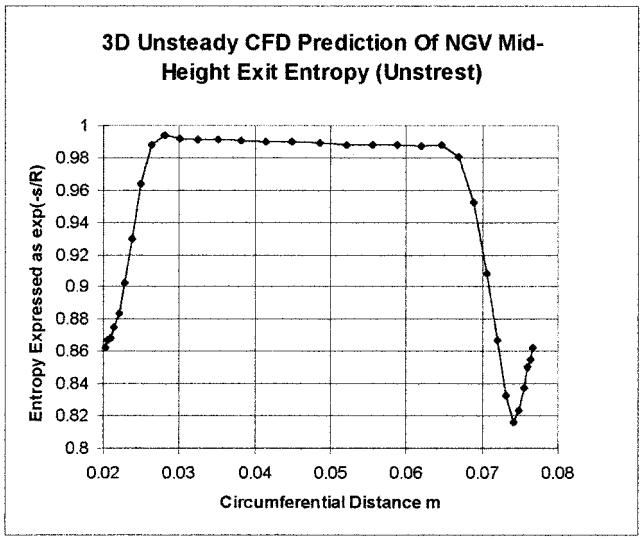

Fig. 8 NGV midheight exit entropy distribution from UNSTREST

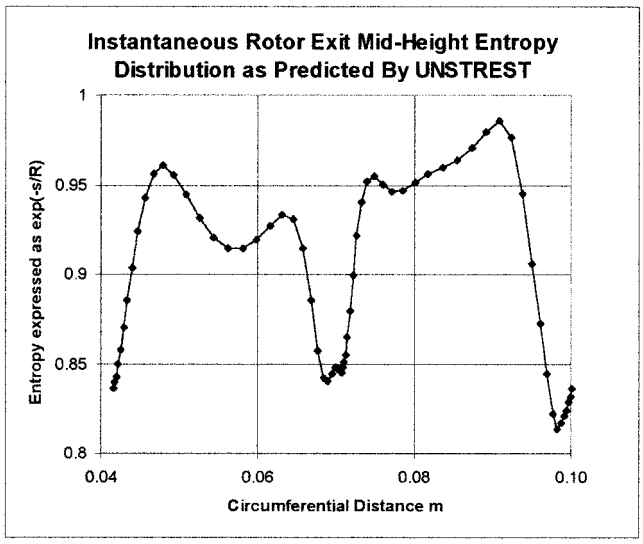

Fig. 9 Midheight entropy at rotor exit instantaneous picture from UNSTREST solution

spanwise transport: Reynolds stresses, radial skewing of boundary layers and radial migration of vortices and wakes. The exit angle distribution taken from the CFD will have conveyed some effects of spanwise transport to the model. In the model, work is the only thing accounted for; clearly it is the work that dominates the rotor flow field.

However, the method has been verified and the relative impact of work, loss, and secondary flows has been illustrated. The three-dimensional Navier–Stokes Solver and a trivial velocity triangle approach agree very closely.

Comparison With Unsteady Three-Dimensional CFD. A further attempt was made to verify the velocity triangle model against an unsteady three-dimensional prediction for an HP turbine. The aim is not to demonstrate great accuracy, but to show reasonable trends. The code used originates from Denton (1997). Known as UNSTREST, it has been developed by Rolls-Royce and is in regular design use. The code is a multirow solver using a structured **H**-mesh and a numerical scheme due to Ni. In this calculation there were two rotors for each vane.

As with the steady CFD calculation, values are taken from the unsteady solution to provide boundary conditions for the simple model at NGV exit and rotor exit. A comparison is made between the model and a single snap shot of the unsteady three-dimensional calculation near midheight. This approach can be criticized because we cannot be sure the fluid at inlet in the snap shot will reach the conditions seen at exit. Properly one ought to track the same fluid particles through the rotor in time. However, here we have assumed that the fluid at inlet will experience the same exit conditions, in due course.

Figure 8 shows the midheight entropy distribution at NGV exit, in which the wake can be clearly seen. The entropy was used as a marker to differentiate between the free stream and the wake. Fluid with a value of $\exp(-s/R)$ 5 percent or more below the free-stream value was regarded as wake. Having differentiated the two flows, the mass meaned inlet values for the two were computed at this location.

Figure 9 shows a calculated instantaneous entropy distribution at the midheight of the rotor exit. The rotor wakes can clearly be seen but it is difficult to differentiate the NGV wake fluid from the rest. Noting that the passage on the left has higher entropy fluid (lower $\exp(-s/R)$ than that on the right (which is closer to the NGV free-stream value), it was decided to regard the former passage as wake and the latter as free stream. The turning points in the entropy distribution were identified and the flow split up into rotor wakes, NGV wake, and the free stream. Again mass flux weighted means of the variables were evaluated for each stream.

Table 2 summarizes the results of the two calculations in terms of the effect on the NGV wake of passing through the rotor. The differential work coefficient μ determined from the UNSTREST results is 0.915, compared to 0.878 from the simple model, a remarkably small difference of only 4 percent. The velocity triangle model correctly determines the trend of reducing the wake total pressure deficit and increasing its temperature. However, the simple model underestimates the pressure rectification of the wake in UNSTREST by about 30 percent while the rise in temperature of the almost isothermal inlet wake is overestimated by the model by 24 percent.

The key assumption of a common rotor relative exit angle β_2 for the wake and free stream was checked in the UNSTREST solution. The angles were found to be within 2 deg of each other: 73.82 deg in the free stream, 71.39 deg in the NGV wake, and 72.35 deg mean angle. There appears to be slightly less turning in the wake fluid, whereas one would expect the wake to be overturned in line with the negative jet effect.

Of course this process is not wholly rigorous. It is difficult to identify the wake because of wake bending and also mixing between the streams is well underway at rotor exit. The assumption made, that one passage is wake and the other is free stream, is clearly not accurate. This will numerically augment the apparent mixing in the CFD.

However, the trend that can be derived from the unsteady calculation agrees with the simple model. In both, the wake is found to do less work and the two values of μ are close. In both, the total pressure deficit of the wake has been profoundly reduced,

Table 2 Comparison of simple model to unsteady CFD values

Percentage Wake Defect		Inlet	Exit	Differential Work Coefficient
UNSTREST 3D Unsteady CFD	Total Pressure	-12.8	+2.6	0.915
	Total Temperature	-0.21	+1.9	
Simple Velocity Triangle Model	Total Pressure	-11.9	-1.1	0.878
	Total Temperature	-0.22	+2.4	

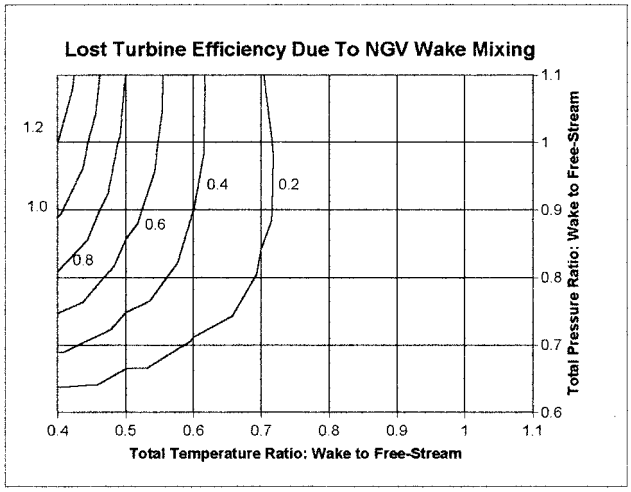

Fig. 10 Lost turbine efficiency due to NGV wake mixing loss predicted from simple model

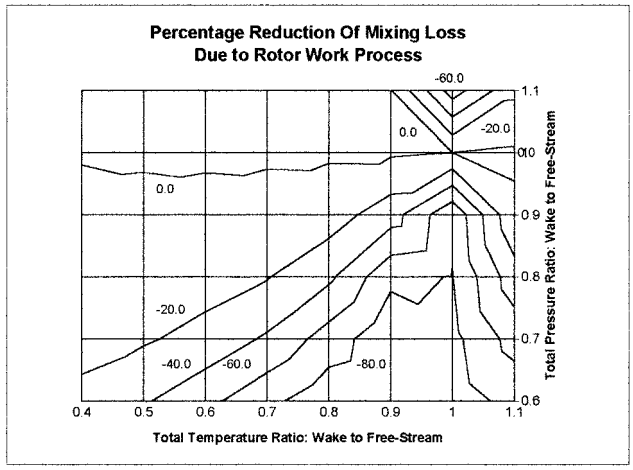

Fig. 11 Percentage change in entropy rise due to mixing with and without rotor work

and in both, the wake emerges slightly hot relative to the free stream, having entered approximately isothermally. We have a total pressure defect at rotor inlet creating a total temperature excess at rotor exit: an effect just due to its lower work.

Application of the Model to Understand Stator Wake Mixing Losses

The simple velocity triangle model has been verified for turbines by comparison with CFD results. One can conclude, for this narrow range of validity, that the approach is not wildly in error. The first verification showed that if the relative angle and static pressure at exit are known then the work is well predicted, as is the exit total pressure. The second shows that for one case the assumptions stand up reasonably well. First among these is the neglect of any unsteady effects and the assumption of a common relative exit angle. In the rest of this section the model is used to make predictions of the variation of mixing loss after a rotor, first for turbines, then compressors.

Turbine Case. At rotor exit the NGV wake is assumed to mix out at constant area with no boundary friction and no heat transfer. This mixing sum is like the one already described in Appendix 1, but it is two-dimensional in order to accommodate the whirling nature of the flow.

To perform the mixing sum, one needs to know the width of the wake at rotor exit. The differential work extraction process will have led to a redistribution between the streams. In Appendix 3 the expressions to calculate the wake width at rotor exit are given.

Appendix 4 gives the detail of the required two-dimensional mixing calculation. An example is given below of how the wake mixing loss varies for an HP turbine as the total temperature and total pressure of the NGV wake are varied. The mixing loss is expressed as a reduction of the turbine stage efficiency (otherwise 100 percent in this hypothetical case). Figure 10 shows the result. Table 3, below, gives the fixed boundary conditions of this example.

In Fig. 10 the lost turbine efficiency is quite modest over much of the graph. For wake temperatures above 80 percent of the free-stream value and also for wakes that are cold and of low total pressure, the loss is less than 0.1 percent of stage efficiency. These losses seem low relative to the losses predicted by Hartsel (1972). This is because this paper only addresses the mixing out of the NGV wake; the mixing of coolant jets introduced at an angle to the mainstream flow is not considered. The differential work process has also had an effect to reduce loss. However, substantial losses are predicted for cold wakes with near to free stream total pressure. Losses of in excess of 1 percent are predicted for cold streaks at the free-stream total pressure and below 45 percent of the free-stream total temperature. This high loss region is primarily due to the mixing losses associated with cold streaks, not due to the differential work extraction process itself.

Table 3 HP turbine wake mixing loss data

$\alpha_1 = 77.26°$	$P_1 = 2.17$ MPa	$M_{1f} = 0.95$
$T_{1f} = 1590.5$ K	$P_2 = 1.43$ Mpa	$S = 0.07$ m
$R = 287.2417$	$\gamma = 1.2868$	$U = 487.25$ m/s
$d_1 = 0.007$ m		

To understand the effects of differential work extraction, a comparison is made to a case with no work extraction. In this case mixing is assumed to occur at the NGV exit conditions. Figure 11 shows the percentage reduction of mixing loss due to the work process across the rotor. The work process has a profound effect on the mixing loss. For the isothermal wake, the work extraction process almost eradicates the mixing loss due to the total pressure wake. Reductions of between 70 and 90 percent are predicted.

For a cold streak at the free-stream total pressure, the work extraction process has very little effect (Fig. 11). Slight increases of loss are predicted due to the rotor expansion process of only between 0.5 and 2 percent.

For regions in Fig. 11 where both total pressure and total temperature differences exist, large reductions of mixing loss are generally found. These reductions vary from nearly 100 percent for deep total pressure wakes, which are slightly cool down to about 10 percent for wakes of 80 percent of the total pressure and 60 percent of the total temperature of the free stream.

Compressor Case. Thus far this paper has concentrated on turbines; but the mechanisms described are relevant to almost all turbomachinery. Here a brief look at a single stage of a multistage compressor is made in order to see how differential work may affect wake mixing in that environment. Table 4 gives a list of the characteristics of the compressor stage.

Figure 12 is a velocity triangle diagram for the compressor case; the same symbols are used as in Fig. 4. Based on Fig. 12, one would expect higher wake work than free-stream work. Figure 13 shows the variation of the differential work coefficient μ as a stator wake flows into the rotor of the compressor. All the previous assumptions are still used, except that the requirement for constant streamtube height across the rotor is relaxed to allow for annulus contraction. The assumption of a common rotor relative exit angle may be less applicable in the compressor case. The mixing sum

Table 4 Core compressor stage data

$\alpha_1 = -37.2°$	$P_1 = 78$ KPa	$M_{1f} = 0.6089$
$T_{1f} = 268$ K	$P_2 = 95$ KPa	$S = 0.07$ m
$R = 287$	$\gamma = 1.4$	$U = -333.2$ m/s
$d_1 = 0.007$ m	$\beta_2 = -37.2°$	

still assumes constant streamtube height. The wake at inlet is 10 percent of the stator pitch, while its massflow varies as the wake to free-stream total pressure ratio is altered. As can be seen (Fig. 13) μ is above unity if the wake is below the free-stream total pressure. This will tend to bring the wake up to the free-stream value. If the wake is a high total pressure stream, μ falls below unity and the rotor work process tends to bring the wake toward the free stream again.

The percentage reduction in wake mixing loss due to the compressor rotor is shown in Fig. 14. The reduction in mixing loss is very strong (-88 percent) and insensitive to the wake total pressure ratio. In both Figs. 13 and 14 the curves turn up at the lowest total pressure ratios (0.786). This effect is due to the stalling of the wakes; the static pressure at inlet is held constant and as the total pressure falls the wake loses velocity. Associated with this is very high positive incidence onto the blading; as with the turbine, the model becomes unreliable at the extremes.

A very brief inspection of the impact of temperature distortion on the compressor was made. Only a small range was considered ± 10 percent and very little variation resulted. The differential work coefficient μ did behave as one would expect: more work on cold wakes, but the changes were not significant.

The wake stretching papers referred to earlier set out to explain

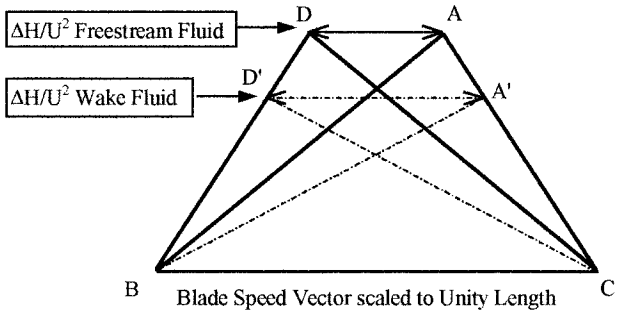

Fig. 12 Velocity triangles for compressor case wake and free stream

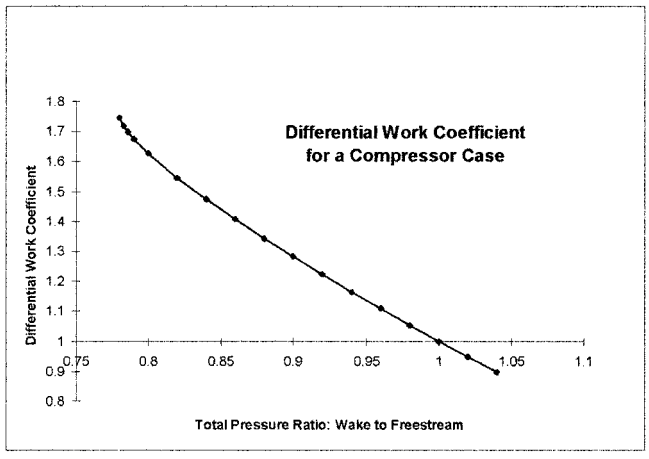

Fig. 13 Variation of μ as the total pressure of the stator wakes is varied

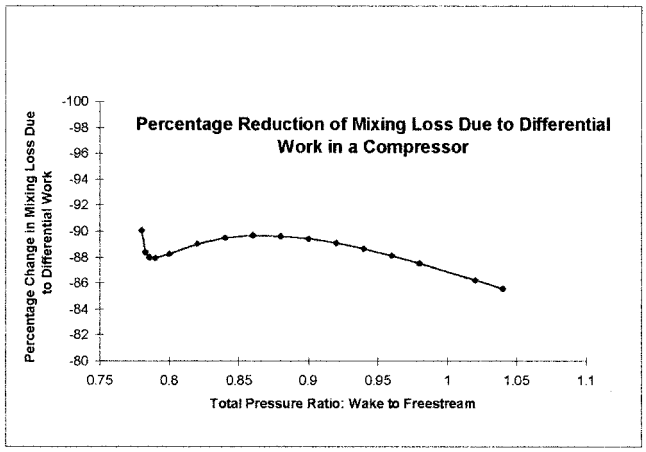

Fig. 14 Change in the stator wake mixing loss due to differential work extraction for a multistage compressor stage

reduced mixing losses in stators. This work addresses reduced mixing losses in rotors. The current authors suspect that these two mechanisms are really the same. If one were to consider the changes in rotor relative total temperature as the wake negotiates the stator, a similar mechanism would be found.

Discussion. This work suggests that in both compressors and turbines, the differential work process between free stream and wake tends to reduce subsequent mixing losses. The wake is rectified by the rotordynamic work process.

This process has been present in turbomachinery throughout its history. It does not, therefore, immediately offer a root for performance improvement. However, what is offered is an understanding or thought process, which should help understand the predictions and measurements made in real machines.

Conclusions

The HP nozzle guide vane wakes of modern gas turbines may generate significant mixing losses, if they are much cooler than the free stream. This trend was shown by previous authors.

If cold wakes are accelerated before they mix out, the large mixing losses are increased. If diffusion occurs before mixing, there is a modest loss reduction. This effect is the reverse of the trends observed for total pressure wakes reported by Denton (1993).

Combined total temperature and total pressure wakes tend to have slightly less loss than the total temperature effect alone would give. The sensitivity of such combined wakes to acceleration or diffusion is reduced compared to the two effects independently applied.

The rotor work extraction process differentiates between the wakes and the free stream. In a turbine, less work is extracted if the wake is of low total pressure, or low total temperature. In a compressor more work is done on the wake if it is of low total pressure. This reduces the stator wake mixing losses quite considerably in both types of machine.

A very simple, steady velocity triangle approach has been verified for turbine blades across a very narrow range of application, against three-dimensional steady and unsteady CFD.

A differential work coefficient μ is defined, being the ratio of the wake work to the free-stream work. μ varies across a wide range and within the limitations of the proposed model can be as low as 0.7 or as high as 2.

Mixing calculations have been performed after the rotor to see what effect the differential work extraction may have on the mixing losses in an HP turbine and in a single stage of a multistage compressor. In the turbine the effect of the rotor work extraction process on the NGV total pressure wakes is predicted to have a

profound effect on the subsequent mixing loss, substantially reducing it. This result is also found in the compressor. For pure cold streaks the differential work extraction process has very little effect. For combined wakes of low total temperature and pressure the differential work tends to reduce the mixing loss over a range between 10 and 80 percent.

The predicted reduction in mixing loss due to differential work extraction must have been present in turbomachinery throughout history, but has been a substantially unknown mechanism. Its effect has been to improve efficiencies by relatively small amounts. It may also be one of the reasons why an almost wholly steady flow approach to the design of turbomachinery blading (at least until recently) has been so successful.

These conclusions provide an encouragement to reconsider the best way to cool HP NGVs. Currently large-scale film cooling is used, taking perhaps 10 percent of core mass flow as coolant. This tends to give a wide, cold wake with little total pressure loss. It looks likely that a more internally cooled NGV, using less coolant and with a warmer wake of more reduced total pressure, may incur a substantially reduced mixing loss through the rotor, and therefore higher turbine efficiency.

Acknowledgments

The authors would like to acknowledge the permission granted by Rolls-Royce plc to publish this paper.

References

Banieghbal, M. R., Curtis, E. M., Denton, J. D., Hodson, H. P., Huntsman, I., Schulte, V., Harvey, N. W., and Steele, A. B., 1995, "Wake Passing in LP Turbine Blades," AGARD PEP 85th Sym., CP-571.

Carscallen, W. E., Currie, T. C., Hogg, S. I., and Gostelow, J. P., 1999, "Measurement and Computation of Energy Separation in the Vortical Wake Flow of a Turbine Nozzle Cascade," ASME JOURNAL OF TURBOMACHINERY, Vol. 121, pp. 703–708.

Denton, J. D., and Cumpsty, N. A., 1987, "Loss Mechanisms in Turbomachines," I. Mech. E C260/87.

Denton, J. D., 1993, "Loss Mechanisms in Turbomachines," ASME JOURNAL OF TURBOMACHINERY, Vol. 115, pp. 621–656.

Denton, J. D., 1997, "UNSTREST Code," private communication.

Gwilliam, N. J., and Kingston, T. R., 1998, "Advanced Computational Fluid Dynamics in the Design of Military Turbines," R.T.O. Symposium "Design Principles and Methods for Gas Turbine Engines," Toulouse, May, Paper No. 32.

Hartsel, J. E., 1972, "Prediction of Effects of Mass-Transfer Cooling on the Blade-Row Efficiency of Turbine Aerofoils," AIAA 10th ASM, San Diego, Jan.

Hodson, H. P., and Dawes, W. N., 1998, "On the Interpretation of Measured Profile Losses in Unsteady Wake-Turbine Blade Interaction Studies," ASME JOURNAL OF TURBOMACHINERY, Vol. 120, pp. 276–284.

Kerrebrock, J. L., and Mikolajczak, A. A., 1970, "Intra Stator Transport of Rotor Wakes and its Effect on Compressor Performance," ASME *Journal of Engineering for Power*, Vol. 92, pp. 359–368.

Lewis, K. L., 1993, "The Aerodynamics of Shrouded Multistage Turbines," PhD. Thesis Cambridge University, Nov.

Moss, R. W., Ainsworth, R. W., Sheldrake, C. D., and Miller, R., 1997, "The Unsteady Pressure Field Over a Turbine Blade Surface: Visualization and Interpretation of Experimental Data," ASME Paper No. 97-GT-474.

Shapiro, A. H., 1953, *The Dynamics and Thermodynamics of Compressible Fluid Flow*, Wiley.

Schröder, Th., 1991, "Investigations of Blade Row Interaction and Boundary Layer Transition Phenomena in a Multistage Aero Engine Low-Pressure Turbine by Measurements With Hot-Film Probes and Surface Mounted Hot-Film Gauges," Von Karman Institute for Fluid Dynamics, LS 1991-06.

Valkov, T. V., and Tan, C. S., 1999, "Effect of Upstream Rotor Vortical Disturbances on the Time-Averaged Performance of Axial Compressor Stators: Part 2—Rotor Tip Vortex/Streamwise Vortex-Stator Blade Interactions," ASME JOURNAL OF TURBOMACHINERY, Vol. 121, pp. 387–397.

Van Zante, D. E., Adamczyk, J. J., Strasizar, A. J., and Okiishi, T. H., 1997, "Wake Recovery Performance Benefit in a High-Speed Axial Compressor," ASME Paper No. 97-GT-535.

Walraevens, R. E., and Gallus, H. E., 1995, "Stator–Rotor–Stator Interaction in an Axial Flow Turbine and Its Influence on Loss Mechanisms," AGARD PEP 85th Sym., CP-571.

APPENDIX 1

One-Dimensional Wake Mixing Sum

In this appendix, an algebraic expression is derived for the mixing losses as a simple "square" wake undergoes compressible mixing. In Fig. A1, station 1 is the flow inlet, a wake of width d with different total pressure and temperature to the free stream is prescribed. The mixing process is assumed to produce at exit station 2 a uniform flowfield. It is assumed that there is no friction between the fluid and the bounding surfaces. The area available to the total flow is constant, width S and depth δ. The flow is assumed to be steady and the fluid has constant properties.

In order to find the mixed-out conditions at 2 one needs to use the conservation of mass, momentum, and energy and the equation of state for a perfect gas is also required. Equation (A1.1) represents the conservation of mass; the equation has been divided through by $S\delta$ to simplify it. It also defines the variable K_c, which is used to facilitate solution:

$$\rho_2 V_2 = \rho_{w1} V_{w1} \frac{d}{S} + \rho_{f1} V_{f1}\left(1 - \frac{d}{S}\right) = K_c \qquad \text{(A1.1)}$$

Conservation of momentum is expressed in Eq. (A1.2). Again it has been divided through by $S\delta$ and it also defines the variable K_{ax} for later use:

$$\rho_2 V_2^2 + P_2 = \rho_{w1} V_{w1}^2 \frac{d}{S} + \rho_{f1} V_{f1}^2\left(1 - \frac{d}{S}\right) + P_1 = K_{ax} \qquad \text{(A1.2)}$$

The conservation of energy is expressed in Eq. (A1.3). As above the whole has been divided through by $S\delta$ and the variable K_e is introduced to facilitate solution:

$$\rho_2 V_2\left(CpT_2 + \frac{V_2^2}{2}\right) = \rho_{w1} V_{w1} \frac{d}{S}\left(CpT_{w1} + \frac{V_{w1}^2}{2}\right) + \rho_{f1} V_{f1}\left(1 - \frac{d}{S}\right)\left(CpT_{f1} + \frac{V_{f1}^2}{2}\right) = K_e \qquad \text{(A1.3)}$$

Below an outline is given of the solution procedure adopted. First Eq. (A1.1) is substituted into Eq. (A1.2) giving Eq. (A1.4):

$$V_2 K_c + P_2 = K_{ax} \qquad \text{(A1.4)}$$

Equation (A1.1) can also be substituted into Eq. (A1.3) as seen below:

$$K_c\left(CpT_2 + \frac{V_2^2}{2}\right) = K_e \qquad \text{(A1.5)}$$

The static temperature at mixed-out exit T_2 can be replaced using the equation of state $P = \rho RT$ leading to the following:

$$K_c\left(\frac{\gamma P_2}{\rho_2(\gamma - 1)} + \frac{V_2^2}{2}\right) = K_e \qquad \text{(A1.6)}$$

Static pressure P_2 can be substituted for using Eq. (A1.4) and density ρ_2 can be substituted for using Eq. (A1.1). This leads to

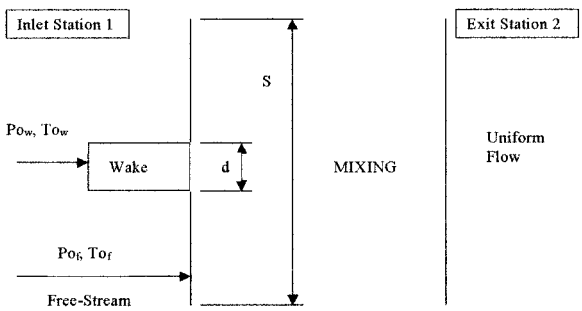

Fig. A1 One-dimensional compressible wake mixing sum

quadratic equation in V_2, the mixed-out exit velocity, which can be solved using the familiar quadratic root formula:

$$aV_2^2 + bV_2 + c = 0$$

where

$$a = -\frac{K_c}{2}\frac{\gamma+1}{\gamma-1}; \quad b = \frac{\gamma}{\gamma-1}K_{ax}; \quad c = -K_e \quad \text{(A1.7)}$$

APPENDIX 2

Evaluation of Differential Work Coefficient μ

Below the process followed to evaluate the differential work coefficient is outlined, step by step.

(*i*) From known inlet total pressure and static pressure compute inlet Mach number, for both wake and free stream:

$$\mathrm{M}_1 = \sqrt{\frac{2}{\gamma-1}\left[\left(\frac{P_o}{P}\right)_1^{(\gamma-1)/\gamma} - 1\right]} \quad \text{(A2.1)}$$

(*ii*) From the Mach numbers compute the total to static temperature ratios. Then using the input total temperatures compute the static temperatures:

$$\left(\frac{T_o}{T}\right)_1 = \left[1 + \frac{\gamma-1}{2}\mathrm{M}_1^2\right] \quad \text{(A2.2)}$$

(*iii*) Use Mach numbers and static temperatures to compute the absolute velocities for wake and free stream:

$$V_1 = \mathrm{M}_1\sqrt{\gamma R T_1} \quad \text{(A2.3)}$$

(*iv*) Compute the relative inlet velocities:

$$V_{r1}^2 = U^2 - 2UV_1\sin\alpha_1 + V_1^2 \quad \text{(A2.4)}$$

(*v*) Compute the relative total temperature for each stream at 1:

$$T_{or1} = T_1 + \frac{1}{2Cp}V_{r1}^2 \quad \text{(A2.5)}$$

(*vi*) Compute the relative total pressure for each stream at 1:

$$\left(\frac{P_{or}}{P}\right)_1 = \left(\frac{T_{or}}{T}\right)^{\gamma/(\gamma-1)} \quad \text{(A2.6)}$$

(*vii*) Isentropic flow with no radius change is assumed so the relative total pressure at rotor exit is the same as that at rotor inlet. This is true for both streams:

$$P_{or1f} = P_{or2f} \quad \text{and} \quad P_{or1w} = P_{or2w} \quad \text{(A2.7)}$$

(*viii*) The exit static pressure is an input parameter P_2 and is the same for both streams. The relative total to static pressure ratios are calculated and via Eq. (A2.1) the exit relative Mach numbers are computed.

(*ix*) The static temperature at exit can now be computed using Eq. (A2.2) and the relative total temperature at rotor exit is the same as the inlet value given adiabatic flow and no radius change.

(*x*) Now the relative exit velocity for each stream can be computed using Eq. (A2.3).

(*xi*) The absolute whirl velocity at rotor exit for both streams is given by:

$$V_{\theta 2} = V_{r2}\sin\beta_2 - U \quad \text{(A2.8)}$$

(*xii*) Finally the Euler work equation is used to give the work of each stream and their ratio μ; see Eq. (2).

APPENDIX 3

Wake Width After Rotor and Global Continuity

The wake width at rotor exit can be evaluated from the continuity equations below; first for the freestream and then for the wake:

$$V_{f1}\rho_{f1}(S-d_1)\delta\cos\alpha_1 = V_{rf2}\rho_{f2}(S-d_2)\delta\cos\beta_2$$

$$V_{w1}\rho_{w1}d_1\delta\cos\alpha_1 = V_{rw2}\rho_{w2}d_2\delta\cos\beta_2 \quad \text{(A3.1)}$$

where V is velocity, ρ is density, S is NGV pitch, δ is the thickness of the domain, d is the width of the wake, α is the absolute whirl angle, β is the relative whirl angle and the subscripts have the following significance: 1 is rotor inlet, 2 is rotor exit *f* refers to the free stream and *w* refers to the wake, *r* stands for relative conditions. Both flows are isentropic; they span the same range of static pressure; therefore:

$$\frac{\rho_{f1}}{\rho_{f2}} = \frac{\rho_{w1}}{\rho_{w2}} \quad \text{(A3.2)}$$

One can write

$$\frac{V_{rf2}}{V_{f1}}\left(\frac{S-d_2}{S-d_1}\right) = \frac{V_{rw2}}{V_{w1}}\frac{d_2}{d_1} \quad \text{(A3.3)}$$

or

$$d_2 = \frac{S}{\dfrac{V_{\mathrm{ratw}}}{V_{\mathrm{ratf}}}\left(\dfrac{S-d_1}{d_1}\right) + 1} \quad \text{(A3.4)}$$

$$\text{where:} \quad V_{\mathrm{ratw}} = \frac{V_{rw2}}{V_{w1}} \quad \text{and} \quad V_{\mathrm{ratf}} = \frac{V_{rf2}}{V_{f1}}$$

Equation (A3.4) gives the wake width at rotor exit; the equation is independent of the joint relative exit angle β_2 so that continuity has not yet been globally satisfied. The chosen boundary conditions for the simple spread sheet calculation are not mutually compatible. Specified are relative exit angle, static pressure, constant stream tube height, and exit relative total pressure and temperature. These last two are effectively specified through the full prescription of the inlet velocity triangle and the assumption of zero loss. These boundary conditions fix an exit mass flow, which in general may not be the same as the inlet one. To proceed it is necessary to relax one of the boundary conditions. It is chosen here to adjust the relative exit angle to satisfy the continuity equation across the rotor. The other boundary conditions remain unaltered. Equations (A3.1) for the free stream and wake are added together and solved for the relative exit angle β_2 (Eq. (A3.5)). In practice only small movements of the relative exit angle were required. The result was then fed back into the calculation, no iteration was required to satisfy all the expressions.

$$\cos\beta_2 = \cos\alpha_1\frac{V_{f1}\rho_{f1}(S-d_1) + V_{w1}\rho_{w1}d_1}{V_{f2r}\rho_{f2}(S-d_2) + V_{w2r}\rho_{w2}d_2} \quad \text{(A3.5)}$$

APPENDIX 4

Two-Dimensional Compressible Wake Mixing

This appendix gives a way of calculating the losses generated as a two-dimensional inclined wake mixes out at constant area. The flow is steady and of constant properties. The assumption of steady flow is applicable here because of the assumption of an infinite number of rotors. This situation is very much like the one de-

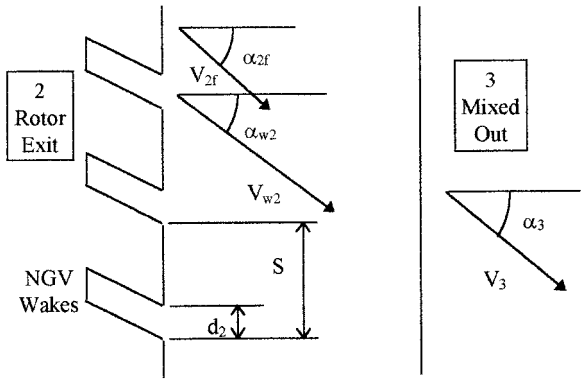

Fig. A2 Two-dimensional compressible wake mixing sum

scribed in Appendix 1. The only differences are that in this case both axial and whirl momentum must be considered.

Figure A2 shows the control volume. The flow enters at station 2 (rotor exit) the two streams of fluid are traveling at different absolute whirl angles (α_{2f} for the free stream and α_{2w} for the wake). The wakes are of width d_2 and they are pitched a distance S apart. The wakes have different total pressure and temperature to the free stream, static pressure is assumed uniform at both stations. At station 3 the flow has mixed out to a common absolute flow angle α_3.

The continuity of mass flow is expressed by Eq. (A4.1) below; the whole has been divided through by $S\delta$ and the variable K_c is introduced to facilitate solution:

$$\rho_3 V_3 \cos \alpha_3 = \rho_{f2} V_{f2} \cos \alpha_{f2}\left(1 - \frac{d_2}{S}\right) + \rho_{w2} V_{w2} \cos \alpha_{w2} \frac{d_2}{S} = K_c \quad \text{(A4.1)}$$

There are two momentum expressions to be considered here first momentum in the circumferential direction or "whirl" direction is considered. The equation for circumferential momentum is given below. It has been divided through by $Sr\delta$ where r is the (constant) radius and a variable K_{ang} is defined for later use:

$$\cos \alpha_3 \sin \alpha_3 V_3^2 \rho_3 = K_{\text{ang}} = \rho_{w2} V_{w2}^2 \sin 2\alpha_{w2} \frac{d_2}{2S} + \frac{\rho_{f2} V_{f2}^2}{2} \sin 2\alpha_{f2}\left(1 - \frac{d_2}{S}\right) \quad \text{(A4.2)}$$

A similar treatment of the axial momentum equation is given below:

$$\cos^2 \alpha_3 V_3^2 \rho_3 + P_3 = K_{ax} = \rho_{w2} V_{w2}^2 \cos^2 \alpha_{w2} \frac{d_2}{S} + \rho_{f2} V_{f2}^2 \cos^2 \alpha_{f2}\left(1 - \frac{d_2}{S}\right) + P_2 \quad \text{(A4.3)}$$

For this case the energy equation is:

$$\rho_3 V_3 \cos \alpha_3 \left(CpT_3 + \frac{V_3^2}{2}\right) = \left(1 - \frac{d_2}{S}\right) V_{f2} \cos \alpha_{2f} \rho_{f2} \left(CpT_{f2} + \frac{V_{f2}^2}{2}\right) + \frac{d_2}{S} V_{w2} \cos \alpha_{2w} \rho_{w2} \left(CpT_{w2} + \frac{V_{w2}^2}{2}\right) = K_e \quad \text{(A4.4)}$$

The solution procedure is similar to the previous one-dimensional mixing sum. The resulting equation is a quadratic in $\sin^2 \alpha_3$. An outline of the algebra is given below.

First Eqs. (A2.1) and (A2.2) are combined to remove the post-mixing density ρ_3.

$$V_3 \sin \alpha_3 = \frac{K_{\text{ang}}}{K_c} \quad \text{(A4.5)}$$

Then Eqs. (A2.1) and (A2.3) are combined to again remove the density ρ_3:

$$P_3 = K_{ax} - K_c V_3 \cos \alpha_3 \quad \text{(A4.6)}$$

Equation (A2.1) is used again to remove the density from Eq. (A2.4), giving:

$$K_c \left(CpT_3 + \frac{V_3^2}{2}\right) = K_e \quad \text{(A4.7)}$$

In this equation the mixed-out temperature T_3 can be replaced by the static pressure and density from the equation of state $P = \rho RT$. The mixed-out density can be again substituted for using Eq. (A2.1) giving:

$$\frac{\gamma}{\gamma - 1} \frac{P_3 V_3 \cos \alpha_3}{K_c} + \frac{V_3^2}{2} = \frac{K_e}{K_c} \quad \text{(A4.8)}$$

In this expression the mixed-out static pressure P_3 can be replaced using Eq. (A2.6) and the mixed-out exit velocity V_3 can be substituted using Eq. (A4.5). After algebraic manipulation this is now the required quadratic in $\sin^2 \alpha_3$:

$$a \sin^4 \alpha_3 + b \sin^2 \alpha_3 + c = 0 \quad \text{(A4.9)}$$

where:

$$a = J^2 + \frac{K_{ax}^2}{K_{\text{ang}}^2}; \quad b = 2JL - \frac{K_{ax}^2}{K_{\text{ang}}^2}; \quad c = L^2; \quad L = \frac{\gamma + 1}{2\gamma}; \quad J = \frac{K_e K_c}{K_{\text{ang}}^2}\left(\frac{\gamma - 1}{\gamma}\right) - 1$$

A solution is obtained using the classic quadratic root equation.

Prediction of Transitional Heat Transfer Characteristics of Wake-Affected Boundary Layers

K. Kim

M. E. Crawford

Mechanical Engineering Department,
The University of Texas at Austin,
Austin, TX 78712

The presence of wake-passing in the gas turbine environment significantly modifies the heat transfer characteristics on the downstream blade surface by causing wake-induced transition. In this study, time-dependent boundary layer calculations were carried out using a model for wake-induced transition based on a prescribed time-dependent intermittent function. The model is determined from the well-known turbulent spot propagation theory in a time–space diagram and from experimental evidence in the ensemble-averaged sense. Time-averaged heat transfer distributions are evaluated and compared with experimental results for different flow and wake-generating conditions over a flat plate. Comparison showed that the present time-dependent calculations yield more accurate results than existing steady superposition models.

Introduction

Periodic wake-passing from upstream blade rows in the gas turbine flowfield can strongly influence the boundary layer and heat transfer characteristics on the surfaces of the downstream blades. This form of flow unsteadiness, which is caused by the relative motion of adjacent blade rows, affects the unique transition process on the blade surface, which is known as wake-induced transition. Since the optimal blade design relies heavily on accurate heat transfer analysis of the blade surface, it is important to predict the unsteady boundary layer development due to the wake-induced transition.

A number of the measurements on wake-affected boundary layers have been conducted recently in laboratory simulations using rotating wake generators (Pfeil and Herbst, 1979; Pfeil et al., 1983; Dullenkopf et al., 1991; Liu and Rodi, 1991; Orth, 1993; Funazaki et al., 1997; Chakka and Schobeiri, 1999) and in a turbine-compressor environment (Halstead et al., 1997). The experimental results showed that the unsteady wakes produce an incident flow that has two distinctive characteristics: a free-stream velocity defect, and its associated high turbulence during the wake-passing. Orth (1993) and Halstead et al. (1997) concluded that the high turbulence of the incoming wakes, rather than the level of free-stream velocity defect, is primarily responsible for initiating the wake-induced transition.

Figure 1 shows the general concept of wake-induced transition. While the wakes pass over the surface approximately at the speed of the free stream, high turbulence in the wakes penetrates into the laminar boundary layer and initiates turbulent strips or spanwise coalescence of turbulent spots. These turbulent strips convect downstream and grow, due to different propagation speeds of their leading and trailing edges. The passing wakes appear only to trigger or initiate the starting location of the turbulent strips, and the wakes do not affect the turbulent strips during their downstream development. This has been described by Orth (1993), and his experimental evidence backs up the separate treatment of these two flow phenomena by ignoring the interaction between the free-stream velocity defect and the turbulent strips, downstream of initiation. Thus, only the effect of strong turbulence in the periodic wake passing is considered in the model of wake-induced transition developed herein, while the effect of periodic free-stream velocity defect from the wakes is neglected.

The literature contains several different approaches for predicting the transitional boundary layers due to wake-passing. For time-averaged results, time-averaged intermittency models were proposed by Mayle and Dullenkopf (1990, 1991), Hodson et al. (1992), and Funazaki (1996). In contrast, time-accurate calculations have been carried out by Tran and Taulbee (1992), Cho et al. (1993), and Fan and Lakshminarayana (1996) by solving the unsteady boundary layer equations or the Navier–Stokes equations in conjunction with low-Reynolds-number k–ϵ models.

Recently, Kim and Crawford (1998) introduced a model for wake-induced transition that reproduces the time-accurate development of the wake-affected boundary layer. They used an unsteady boundary layer scheme and a simple engineering model for the wake-induced transition based on the theory of turbulent spots. Their computational results were compared with various measured time-resolved and time-averaged boundary layer profiles and parameters. In the present paper, transition model is revised based on the measurements of the ensemble-averaged intermittency by Chakka and Schobeiri (1999), and the transitional heat transfer characteristics in the wake-affected boundary layers are predicted and compared with the measured data and the predicted results of the time-averaged superposition model.

Model for Wake-Induced Transition

To compute periodically unsteady transitional boundary layers, a conventional eddy viscosity formulation (Hodson et al., 1992) is adopted to estimate the effective viscosity:

$$\nu_{\text{eff}}(x, y, t) = \nu_{\text{lam}} + \Gamma(x, t)\nu_{\text{turb}}(x, y, t) \tag{1}$$

where ν_{lam} is the molecular viscosity, and ν_{turb} is the turbulent eddy viscosity. The transitional function $\Gamma(x, t)$ is considered in an ensemble-averaged sense, and thus it is different from the conventional steady state intermittency or instantaneous intermittency. In the experimental work by Chakka and Schobeiri (1999), they measured the ensemble-averaged intermittency as

$$\tilde{\gamma} = \frac{1}{N}\sum_{j=1}^{N} I_{ij}(t_i) \tag{2}$$

where the index i represents the phase-locked time (or fixed angle) with respect to the wake-passing period, and N is the number of wake-passing periods used in the evaluation. I is the instantaneous

Contributed by the International Gas Turbine Institute and presented at the 44th International Gas Turbine and Aeroengine Congress and Exhibition, Indianapolis, Indiana, June 7–10, 1999. Manuscript received by the International Gas Turbine Institute February 1999. Paper No. 99-GT-45. Review Chair: D. C. Wisler.

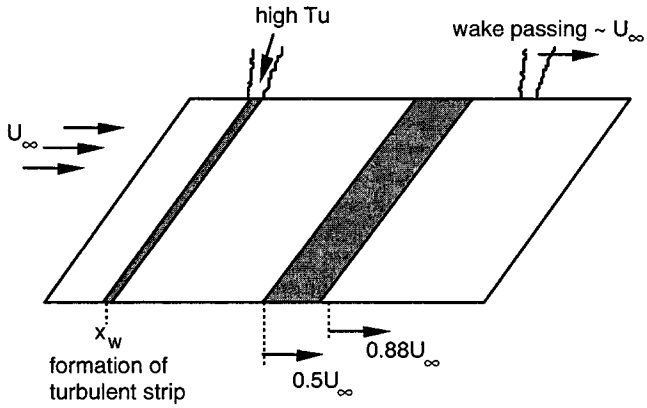

Fig. 1 Development of turbulent strips on the wake-affected surface

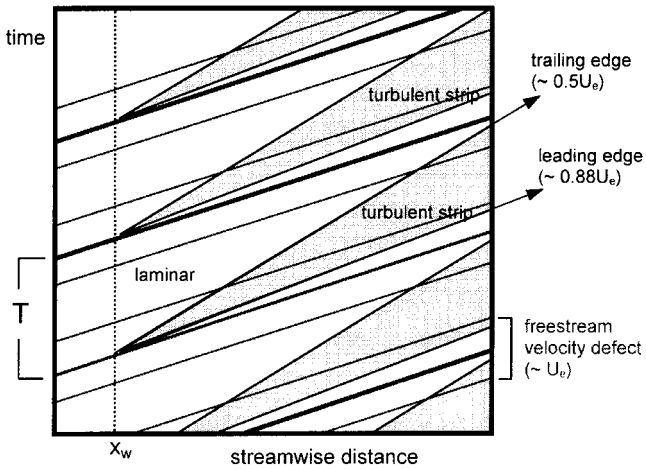

Fig. 2 Convection of turbulent strips and free-stream velocity defect due to the wake-passing

intermittency, which appears as the random step function with 0 (laminar) and 1 (turbulent). $\tilde{\gamma}$ is identical to the present transitional function, $\Gamma(x, t)$. The first possibility for the determination of $\Gamma(x, t)$ can be derived from the propagation process of the turbulent strips as shown in Fig. 2, following the qualitative description of wake-induced transition by Pfeil et al. (1983). The idea for the model is simply to switch on and off the turbulent viscosity term in Eq. (1) while following the locus of the turbulent strips. For example, at some location x, the $\Gamma(x, t)$ abruptly switches on with a periodicity of T (Fig. 2) and switches off in a step function manner as depicted in Fig. 3. This switch is somewhat unrealistically abrupt at the interface of the turbulent strip with the undisturbed laminar flow because it implies a sudden variation of the effective viscosity. Computationally, the switch tends to cause numerical difficulty at the interface and, in turn, leads to an unrealistic time-resolved response of the boundary layer.

For more realistic prediction of turbulent strip behavior, the intermittent function $\Gamma(x, t)$ is determined using the observation of experiments. Chakka and Schobeiri (1999) measured the ensemble-averaged intermittency in a similar case of wake-passing on a curved plate. Their results showed that the ensemble-averaged intermittency is a Gaussian distribution in which a normalized shape is conserved downstream. This idea is modeled as

$$\Gamma(x, t) = \exp\left(-\pi \left(\frac{t/T - x/(a_c U_e T)}{\tau/T} \right)^2 \right) \tag{3}$$

where T is the wake-passing period, and τ is the time duration for the turbulent strip, as defined by

$$\tau = \int_{-\infty}^{\infty} \Gamma(x, t)\, dt \tag{4}$$

In reality, τ in Eq. (3) can be approximated using the classical theory of turbulent spot propagation:

$$\tau = \left(\frac{1}{a_{TE}} - \frac{1}{a_{LE}} \right) \frac{(x - x_w)}{U_e} \tag{5}$$

where a_{LE} and a_{TE} are the ratios of propagation velocities for the leading edge and trailing edge of the turbulent spot, respectively, to the free-stream velocity:

$$U_{LE} = a_{LE} U_e \quad \text{and} \quad U_{TE} = a_{TE} U_e \tag{6}$$

$\Gamma(x, t)$ becomes traveling function in the streamwise direction with a center convecting velocity of $a_c U_e$, which can easily be determined from the propagation velocity of the leading ($a_{LE} U_e$) and trailing ($a_{TE} U_e$) edges of the turbulent strip.

For a given wake-passing frequency (or wake period), the in-

Nomenclature

a, b, w = constants for the model of free-stream velocity defect
a_c = ratio of traveling velocity of the center of turbulent strip to the local free-stream velocity
a_{LE}, a_{TE} = ratios of propagation velocity of leading and trailing edges of turbulent strip to the local free-stream velocity
f = wake-passing frequency
H = shape factor = δ^*/θ
L = characteristic length
Re = Reynolds number
S = reduced wake-passing frequency = fL/U_∞
St = Stanton number
T = wake-passing period = $1/f$
t = time
Tu = turbulence level
$\bar{U}, \tilde{U}$ = time-mean and ensemble-averaged velocity
$U_e(x)$ = undisturbed steady free-stream velocity at the boundary layer edge
$U_{et}(x, t)$ = wake-disturbed unsteady free-stream velocity = $U_e(x) W(x, t)$
U_∞ = inlet velocity
$\tilde{u}$ = periodic fluctuation of ensemble-averaged velocity = $\tilde{U} - \bar{U}$
u_d^* = normalized velocity defect = $(\tilde{U} - U_{\text{lam}})/U_e$
$\tilde{u}_{\text{rms}}$ = rms velocity of periodic fluctuation
$W(x, t)$ = relative fluctuation function for free-stream velocity defect
x = streamwise distance
x_w = onset of wake-induced transition
y = normal distance from the wall
δ^* = displacement thickness
θ = momentum thickness
$\Gamma(x, t)$ = time-dependent intermittent (or transitional) function
$\bar{\gamma}$ = Stanton number based time-averaged intermittency
ν = kinematic viscosity
τ = duration of turbulent strip

Subscripts

e = free-stream
L, lam = laminar
T, turb = turbulent
m = time-mean
s = steady
w = wake
tot = total

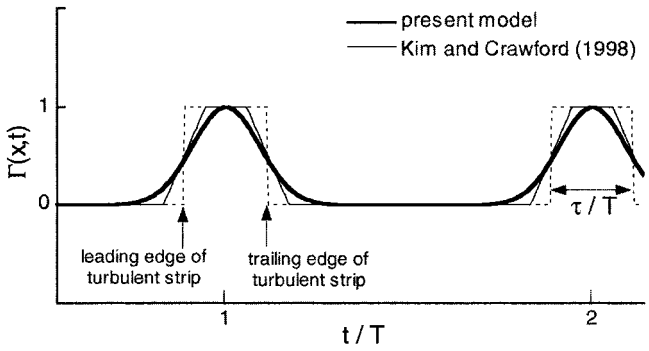

Fig. 3 Intermittent function for the transition model as a function of time

termittent function for the trajectories of the turbulent strips that successively move in the time-space domain is prescribed using Fig. 2 with propagation velocities set to be 88 percent (a_{LE}) of local free-stream velocity for the leading edge and 50 percent (a_{TE}) for the trailing edge in the computations. In reality, the propagation speed of the turbulent spots or strip will be influenced by the existence of pressure gradients. However, pressure dependence is not considered, since the adverse pressure gradient is not important in the predicted measurements considered herein. Figure 3 shows the present model of the intermittent function in the form of a Gaussian distribution, along with the older trapezoidal shaped model used by Kim and Crawford (1998).

Determination of the onset for the transition presents a challenge, because no reliable theory is available for the wake-disturbed boundary layer. An existing empirical correlation for steady transition developed by Abu-Ghannam and Shaw (1980) is utilized in the present simulations. In their model, the momentum Reynolds number at the start of transition is expressed as

$$\mathrm{Re}_{\theta,s} = 163 + \exp(6.91 - Tu) \tag{7}$$

where Tu is the free-stream turbulence level in units of percent of free-stream velocity. Assuming that the strip formation occurs at the point of maximum turbulence level in the wakes, and that its maximum turbulence level is sufficiently high, the transition onset, x_w, can be estimated to be the leading term, $\mathrm{Re}_{\theta,s} = 163$, even if the turbulence level in the wakes is not precisely known. This is the primary reason that the above correlation was selected over the one by Mayle (1991), even though Mayle's correlation seems to be more accurate in case the free-stream turbulence level is known. We should note that Chakka and Schobeiri (1999) found a dependence of the transition onset on the wake-passing frequency.

Even though the free-stream velocity defect in the wakes is not considered a significant factor, and thus excluded from the transition model, the free-stream velocity defect is easily included in the boundary conditions for a more realistic prediction. The free-stream velocity gradient is expressed using the unsteady Bernoulli equation as

$$-\frac{1}{\rho}\frac{dP}{dx} = \frac{\partial U_{et}}{\partial t} + U_{et}\frac{\partial U_{et}}{\partial x} \tag{8}$$

To include the free-stream velocity defect in the time-resolved calculations, the unsteady free-stream velocity is modeled to be $U_{et}(x, t) = U_e(x)W(x, t)$, where $U_e(x)$ is an undisturbed steady freestream velocity and $W(x, t)$ is a relative free-stream time-dependent part. $W(x, t)$ is modeled from free-stream experimental data using a Gaussian distribution,

$$W(x, t) = 1 - a \cdot \exp\left(-\left(\frac{t/T - x/(U_e T)}{w/2}\right)^2\right) + b \tag{9}$$

where the constant w is the width of the velocity defect, and the constants a and b account for the maximum amplitude of the velocity defect in the free stream. These three constants were approximated from the free stream measurements. Alternatively, external flowfield computations, i.e., Euler solutions, may provide the time-dependent boundary conditions.

The convection paths for the maximum (and leading and trailing edges) of the free-stream velocity defects are also illustrated in Fig. 2, in addition to the turbulent strip propagation paths. For simplicity, it is assumed that the location of the formation of the turbulent strips (x_w) occurs at a streamwise location that coincides with the line of maximum velocity defect. Since the convection speed is different for the free-stream velocity defect inside the wakes and for the turbulent strip, they separate from each other and a traveling velocity defect may eventually catch a neighboring turbulent strip.

In order to implement these models, a time-dependent boundary layer scheme described by Cebeci and Platzer (1989) has been implemented for the time-resolved calculations of periodic boundary layer flow. The two-dimensional incompressible time-dependent boundary layer equations are numerically solved by the Keller-box method. The algebraic eddy viscosity turbulence model developed by Cebeci and Smith (1974) is used for the estimation of turbulent viscosity. In their formulation, turbulent viscosity in the inner and outer layers of the boundary layer is given as

$$\nu_{\mathrm{turb}} = \begin{cases} (0.4y(1 - \exp(-y/A))^2\left|\dfrac{\partial U}{\partial y}\right| & \text{for the inner layer} \\ 0.0168\displaystyle\int_0^\infty (U_e - U)dy & \text{for the outer layer} \end{cases} \tag{10}$$

In Eq. (10), $A = 26\nu_{\mathrm{lam}}U_\tau^{-1}N$ and $N = (1 - 11.8p^+)^{-1/2}$ where U_τ is the wall friction velocity and $p^+ = (\nu_{\mathrm{lam}}U_e/U_\tau^3)(dU_e/dx)$. Note that the turbulent viscosity is determined using the computed instantaneous boundary layer velocity profile in the time-dependent calculations.

Steady laminar boundary layer velocity profiles are used to start the time-marching calculation. After starting the computation, several wake-passing periods are calculated to overcome the transient response due to these arbitrary velocity profiles at the initial time and to reach the converged periodicity. The required number of periods increases as frequency rises. In the case of a moderate reduced frequency ($S = fL/U_\infty$ based on the characteristic length of flow, L) of unity, less than six cycles were found to be sufficient. The time-dependent boundary layer code was qualified first by extensive comparison with open-literature examples of oscillating laminar and turbulent flows (Kim, 1998), while the only one case of the benchmark tests are listed herein. Parikh et al. (1981) measured turbulent boundary layer responses in a water tunnel with a harmonic oscillation of the free stream described by

$$U_e(t) = \begin{cases} U_0, & x < x_0 \\ U_0 - \dfrac{a(x - x_0)}{L}(1 - \cos\,\omega t), & x_0 < x < x_0 + L \end{cases} \tag{11}$$

where the amplitude parameter of the free stream, a/U_0, was 0.05, and L is the length (0.6 m) of flow deceleration zone. The free-stream velocity remains steady and spatially constant from the leading edge to the location x_0, and the time-mean velocity decreases linearly in the test section length where the sinusoidal oscillation occurs. Measurements were carried out using four different oscillation frequencies (0.01, 0.25, 0.5, and 2.0 Hz) at $(x - x_0) = 0.568$ m, where $x_0 = 2$ m. Time variation of the normalized displacement thickness of the boundary layer is presented in Fig. 4(*a*), where the time-mean thickness is used for normalization. The predicted values are in excellent agreement with the measurements both for the amplitude and phase angle of the variation. In Fig. 4(*b*), predicted friction coefficients, normalized by their time-mean values, are compared with measurements. Agreement is generally

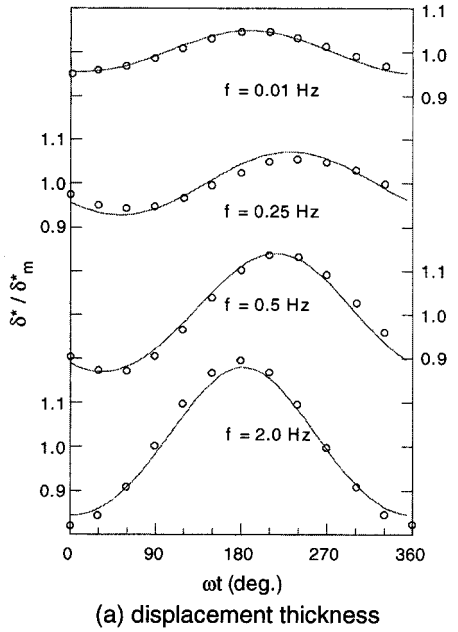

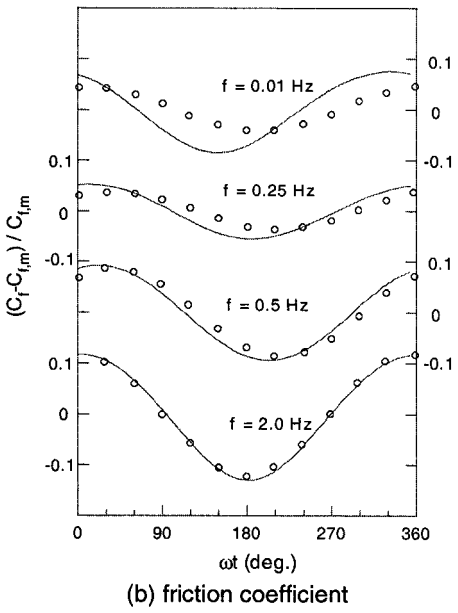

Fig. 4 Time-dependent variation of displacement thickness and friction coefficient in oscillating turbulent boundary layer: Symbols show the measurements by Parikh et al. (1981); solid lines show the computations.

good, although the computation overpredicted the amplitude of the lowest frequency case of $f = 0.01$ Hz, and the phase angle is shifted. However, as the frequency increases, the computation shows excellent agreement. In addition, the comparison shows that the time-resolved surface quantities such as friction coefficient are more difficult to predict than the time-resolved boundary layer integral parameters.

Grid dependence of the computations in space and time were thoroughly checked by performing calculations with grid systems of much finer resolution, and the convergence of periodicity was checked by comparing the calculations with the ones in which the wake-passing periods were doubled.

Results and Discussion

Prediction of the Time-Resolved Boundary Layer Development. Liu and Rodi (1991) conducted extensive hot-wire measurements in the boundary layer developing along a plate subjected

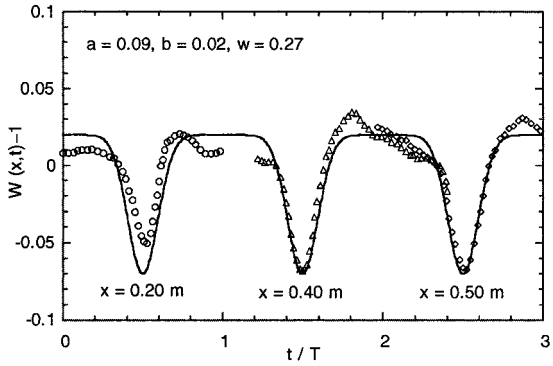

Fig. 5 Modeled free-stream velocity defects for case 3 using Gaussian distribution; symbols show the measurements at $y = 15$ mm by Liu and Rodi (1991).

to periodic wake-passing, and they reported a wide variety of time-resolved measurement data for the wake-affected boundary layer development and transition process. Periodic wakes were created using the squirrel-cage type wake generator in front of the test plate, and the free-stream velocity was almost constant at 15.5 m/s. In the case of no wake, the free-stream turbulence level is so low (0.3 percent) that the entire surface length of the plate (0.5 m) remained laminar. Liu and Rodi (1991) created four cases of different wake-passing frequency: case 2 (20 Hz), case 3 (40 Hz), case 4 (60 Hz), and case 5 (120 Hz). However, only the calculations for case 3 are presented in this paper. Transition onset was determined to be 0.075 m from the leading edge by using the correlation by Abu-Ghannam and Shaw (1980). As described earlier, the effect of free-stream velocity defect was included in the calculation using the measurement data set at $y = 15$ mm, as shown in Fig. 5. Calculations were carried out with and without the inclusion of free-stream velocity defect in order to appreciate the effect of free-stream velocity defect on the boundary layer development.

Figure 6 presents the calculated time-resolved boundary layer parameters at three streamwise locations, and the agreement with the measurement data is good in all three locations. These results show the temporal switching between the laminar and turbulent states during the wake-passing and turbulent strip propagation.

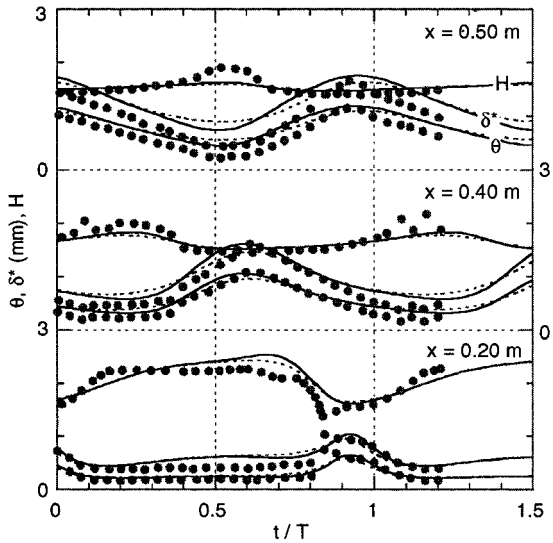

Fig. 6 Time-resolved variation of boundary layer parameters for case 3 of the measurements by Liu and Rodi (1991); symbols show the measurements; solid lines show the predictions with free-stream velocity defect and dotted lines without free-stream velocity defect.

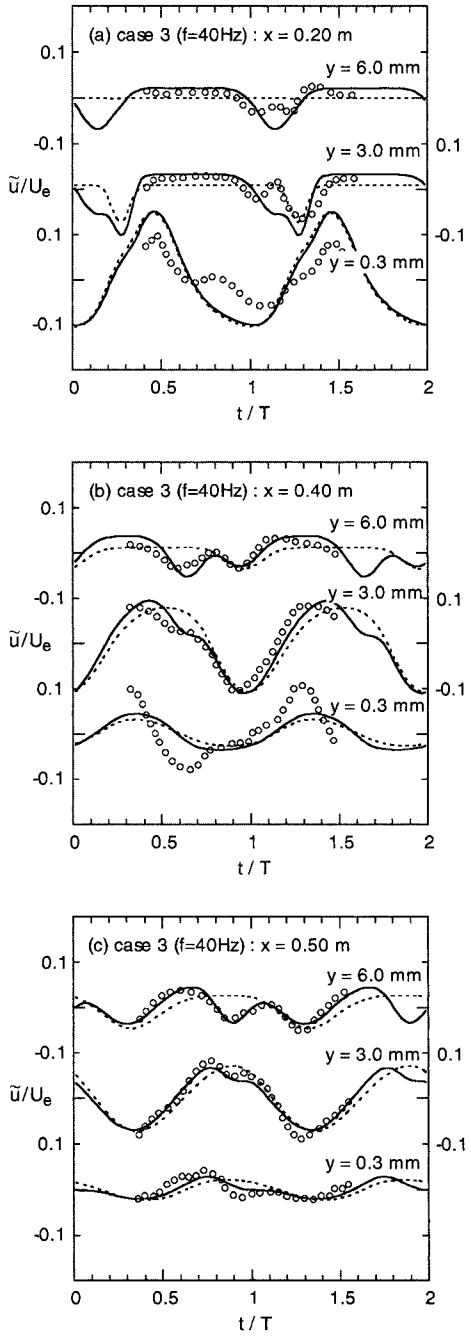

Fig. 7 Periodic fluctuation of ensemble-averaged boundary layer velocity for case 3 of the measurements by Liu and Rodi (1991); symbols show the measurements; solid lines show the predictions with free-stream velocity defect and dotted lines without free-stream velocity defect.

Note that the predicted results have the same phase for all three locations, and this trend shows that the convection path of the turbulent strips is different from the one of the passing wakes.

Periodic fluctuations ($\tilde{u}$) of the ensemble-averaged boundary layer velocity are shown in Fig. 7 for three normal distances, and the calculated ensemble-averaged velocity traces agree well with the corresponding measurement data. Note that $\tilde{u}$ is defined as the difference between the ensemble-averaged velocity ($\tilde{U}$) and the time-mean velocity ($\bar{U}$). Comparison between the results of computation with and without the free-stream velocity defect shows the two contributions to the ensemble-averaged velocity fluctuation, namely the unsteady transition process and the free-stream velocity defect. Predicted near-wall velocity traces ($y = 0.3$ mm) at $x = 0.2$ and 0.4 m show significant discrepancy with the

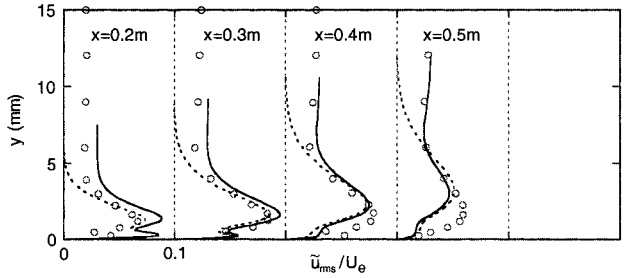

Fig. 8 Profiles of rms velocity of periodic fluctuation for case 3 of the measurements by Liu and Rodi (1991); symbols show the measurements; solid lines show the predictions with free-stream velocity defect and dotted lines without free-stream velocity defect.

measurements, although the predictions at $x = 0.5$ m show excellent agreement. It is not clear whether that discrepancy is caused by the deeper penetration of wake disturbances that move at the speed of free stream or the possible effect of secondary wakes from the returning bars. Both effects are excluded from the model in the present approach.

In Fig. 8, the rms profiles of the periodic fluctuation component ($\tilde{u}$) are compared with the measurements. In the upstream region closer to the transition onset, the rms profiles for both the measurements and the calculations show the two local maxima near the surface due to the periodic transition. As the transition proceeds, the maxima grow continuously, and they decrease as the turbulent strips merge.

Figure 9 presents the contours of the velocity defect at the streamwise location of $x = 0.2$ and 0.5 m. Note that the velocity defect represents the level of disturbed boundary layer velocity, and it is defined as $u_d^* = (\tilde{U} - U_{\text{lam}})/U_e$, where U_{lam} is from the undisturbed laminar profile for the case of no wake-passing. These contours represent the time history of the disturbed flow at a fixed streamwise location. In Fig. 9(a), the negative contours of round-edged triangular shape ($t/T = 0.1 \sim 0.4$) show the duration of the turbulent strip and the temporal transition to turbulent status. After the turbulent strip passes, the negative contours immediately disappear, but the positive contours, which are confined to the near-wall region during the convection of the strips, last longer. This

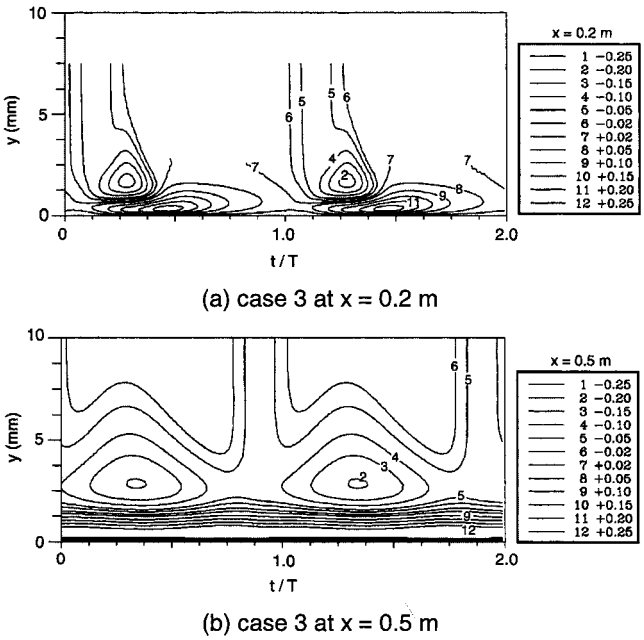

Fig. 9 Predicted velocity defect contours for case 3 of the measurements by Liu and Rodi (1991)

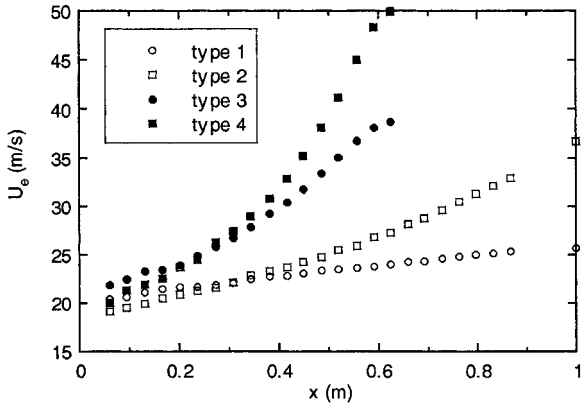

Fig. 10 Free-stream velocity distributions from the measurements by Funazaki et al. (1997)

time period ($t/T = 0.4 \sim 0.9$) can be interpreted as the existence of the becalmed region behind the turbulent strips. As the strips grow while convecting downstream, they terminate the becalmed region of the preceding strips and begin to merge with each other, as shown in Fig. 9(*b*).

Complete results of the calculations with detailed discussion for the other cases of the measurements are described in Kim and Crawford (1998) for a slightly different intermittent function model. However, the difference is found to be minor when compared with the present results.

Prediction of the Heat Transfer Measurements. The effects of the periodic wake-passing on boundary layer transition and heat transfer on a flat plate were studied experimentally by Funazaki et al. (1997). The test Reynolds number was 1.3×10^6, based on the inlet flow velocity (20 m/s) and the length of a flat plate ($L = 1$ m), and the inlet free-stream turbulence level without wake-passing was about 0.5 percent. Using a flow accelerating device and varying the inclination angle, four types of favorable pressure gradient flow cases (types 1 to 4) were generated and used for heat transfer measurements as well as the case of zero pressure gradient (type 0). Figure 10 shows the velocity distributions for the cases with favorable pressure gradient.

Figure 11 shows the steady boundary layer calculations for three cases without periodic wakes and the results agree well with the measurements. Note that all predictions of no-wake transition were performed using the length transition model of $\gamma_s = 1 - \exp(-5\eta^3)$ where $\eta = (x - x_S)/(x_E - x_S)$. The start ($x_S$) and

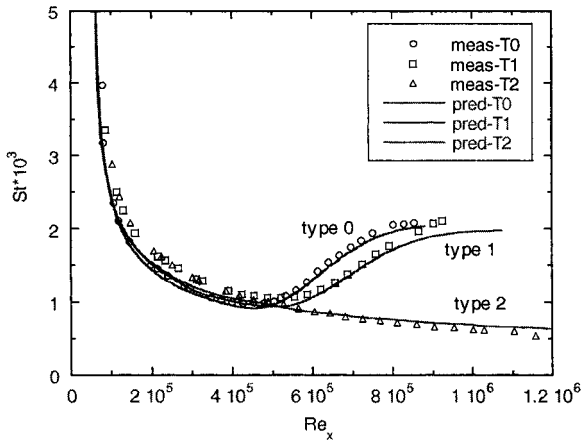

Fig. 11 Stanton number variations for the cases of no wakes: symbols show the measurements by Funazaki et al. (1997); solid lines show the steady boundary layer predictions.

end (x_E) of transition are determined using Eq. (7) and the correlation $\mathrm{Re}_{\theta E} = 2.667\ \mathrm{Re}_{\theta S}$ (Abu-Ghannam and Shaw, 1980).

The free-stream turbulence is set to be 1.4 percent, which is higher than the reported value of 0.5 percent. The experimental unheated starting length of 45 mm from the leading edge was taken into account for all the heat transfer predictions. Compared with the zero pressure gradient case ($T0$), transition is delayed in the flow of type 1 ($T1$), and is completely suppressed in the flow of type 2 ($T2$) over the entire length of the measurement plate by the presence of the stronger favorable pressure gradient.

Wake-Passing Cases of Normal Rotation. Funazaki et al. (1997) used a wake generator of the spoke-wheel type to simulate periodic wake-passing over the test plate. There is no effect of secondary wakes with the spoke-wheel type wake-generator, but the cylindrical bars on the wheel should be long enough to ensure the two-dimensional flow over the test plate, in contrast to the squirrel-cage-type wake generator used by Liu and Rodi (1991). By changing the rotation of the spoke-wheel, there were two types of wake-passing created: (*a*) normal rotation (wake generating bars in front of the plate move toward the measurement plate); and (*b*) reverse rotation (bars move away from the measurement plate). In the measurements, time-averaged heat transfer of the wake-disturbed plate for each type of flow was recorded for three cases of wake-passing by changing the number of bars on the spoke-wheel. As a result, the corresponding reduced wake-passing frequencies ($S = fL/U_\infty$) were 1.88, 2.83, and 5.65, based on the inlet flow velocity and the plate length.

Predictions of the wake-affected heat transfer characteristics were carried out using two approaches. The first approach used a steady-flow method involving superposition of a fully laminar Stanton number (St_L) distribution and a fully turbulent Stanton number (St_T) distribution, obtained without the presence of the wakes. For this approach, superposition (Mayle, 1991) leads to

$$\overline{\mathrm{St}} = \overline{\mathrm{St}}_L + \bar{\gamma}_w(\mathrm{St}_T - \mathrm{St}_L) \tag{12}$$

where $\bar{\gamma}_w$ is a superposition function that contains the wake-passing effect.

From the theory of turbulent spot propagation and the time–space diagram of Pfeil et al. (1983) in Fig. 2, Funazaki (1996) proposed

$$\bar{\gamma}_w = \left(\frac{1}{a_{TE}} - \frac{1}{a_{LE}}\right) S\left(\frac{x - x_w}{L}\right) = \left(\frac{1}{a_{TE}} - \frac{1}{a_{LE}}\right)\left(\frac{x - x_w}{U_\infty T}\right) \tag{13}$$

Experimental values of a_{TE} and a_{LE} from various measurements of turbulent spots are about 0.5 and 0.88, respectively. This simple model implies that the propagation and the growth of the turbulent strips are independent of the movement of the wakes outside the boundary layer, and that the time-averaged transition process can be estimated without the detailed knowledge of the wake propagation.

The effect of pressure gradient cannot be accounted for in the simple model such as Eq. (13). Thus, a new formulation was presented to include the streamwise variation of local free-stream velocity (Hodson et al., 1992; Funazaki et al., 1997):

$$\bar{\gamma}_w = \left(\frac{1}{a_{TE}} - \frac{1}{a_{LE}}\right) \int_{x_w}^{x} \frac{f}{U_e}\, dx = \left(\frac{1}{a_{TE}} - \frac{1}{a_{LE}}\right) \int_{x_w}^{x} \frac{1}{U_e T}\, dx \tag{14}$$

where f is the wake-passing frequency ($f = 1/T$).

For the second approach, time-resolved boundary layer calculations were performed for the periodic boundary layer development due to wake-passing for each type of the flow. Time-dependent variation of the intermittent function (not to be confused with the superposition intermittency function in the first approach) was prescribed in the formulation of the turbulent viscosity, similar to that carried out for the measurements of Liu and Rodi (1991). The wake effect on the free-stream velocity was neglected in the

present calculations, because the measurements did not provide sufficient information. However, this would not significantly affect the time-averaged results, since free-stream fluctuation is only a minor factor for the transition process. For all the predictions, transition onset was determined from the correlation of starting location by Abu-Ghannam and Shaw (1980), and the resulting starting locations of transition from the leading edge of the test plate in meters are 0.0492 (type 0), 0.0498 (type 1), 0.0524 (type 2), 0.0519 (type 3), and 0.0537 (type 4). Steady transition due to the background turbulence was ignored, and the related issue on multimode transition will be discussed later.

The heat transfer results from the predictions using the time-averaged steady superposition model (Eq. (13)) and the time-averaged results of the time-resolved computation are presented in Fig. 12 for three cases at three reduced wake-passing frequencies and compared with the measurements. When the pressure gradient is zero or mildly favorable, the steady model from Eq. (13) shows reasonable prediction of time-averaged heat transfer, but the prediction using the steady model starts to deviate from the measurements when the favorable pressure gradient becomes significant. In contrast, the time-averaged results from the time-resolved calculation provide good agreement for all three types of flow. However, significant underprediction occurs at $S = 5.65$ for the flow of type 0, and this indicates that the transition onset is earlier than predicted by the correlation. Assigning an earlier onset will yield better results. Generally speaking, computational results for the time-averaged heat transfer on the surface show that the prediction is less favorable in the early region around $\mathrm{Re}_x = 2 \times 10^5$ where the turbulent strips start to develop. A possible explanation is that the interaction between the newly formed turbulent strips and the passing wakes containing high disturbance is intense, unlike the present assumption of no interaction between them.

Funazaki et al. (1997) reported only the time-averaged intermittency distribution without providing the corresponding heat transfer results for their higher acceleration cases: types 3 and 4, as shown in Fig. 13. To compare the experimental results with the time-dependent calculations, the time-resolved heat transfer is averaged and inserted into the rearranged superposition Eq. (12) to yield a calculating equation for the time-averaged intermittency distribution:

$$\bar{\gamma}_w = \frac{\overline{\mathrm{St}} - \mathrm{St}_L}{\mathrm{St}_T - \mathrm{St}_L} \tag{15}$$

These results are plotted in Fig. 13, and they compare very accurately with the measurements. The results from the steady superposition models are also plotted in Fig. 13, showing a significant disagreement for large x.

For type 0 and 1 flows, steady transition due to the background turbulence occurs in the case of no wake-passing, and the slight underprediction of the time-resolved computations near the trailing edge of the plate at $S = 1.88$ could be attributed to a multimode transition associated with the steady transition between the wakes. Mayle and Dullenkopf (1990) assumed that the production of steady and wake-induced transitions are independent of each other, and proposed the following superposition for the multimode transition:

$$\bar{\gamma}_{\mathrm{tot}} = 1 - (1 - \bar{\gamma}_w)(1 - \gamma_s) \tag{16}$$

where γ_s is the intermittency distribution when the wake-passing is absent in steady boundary layers. Preliminary testing of Eq. (16) with both time-averaged intermittency models produced a significant overprediction (not presented in the paper). First of all, the presence of wake-passing modifies the flow before the region of steady transition and forces the wake-affected flow to have a flow history that is different from the no wake-passing case. Thus, even if the assumption that permits independent existence of two modes of transition is valid, superposition in Eq. (16) using information from the no wake-passing case would lead to incorrect results.

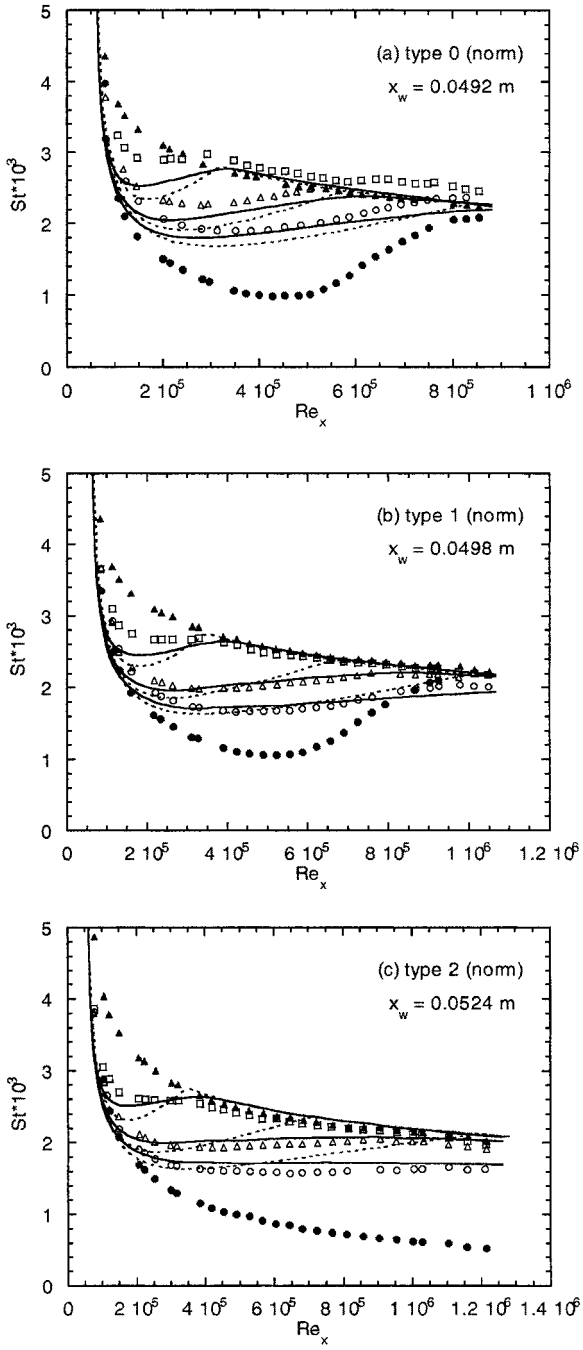

Fig. 12 Time-averaged Stanton number distributions for the cases of normal rotation; symbols show the measurements of Funazaki et al. (1997) (●: no wake, ○: $S = 1.88$, △: $S = 2.83$, □: $S = 5.65$, and ▲: fully turbulent); solid lines are the corresponding time-resolved predictions for the cases of wake-passing; dotted lines are the predictions of the steady superposition model for the corresponding wake-passing cases (Eq. (13)).

Second, the two modes of transition are not independent, and thus they should influence each other. The activity of the becalmed region, which is excluded in the analytic models, may play the role of stabilizing the surrounding flow and suppressing the effect of background turbulence to trigger the transition between the turbulent strips, until the becalmed region is terminated by the following wakes or the surrounding turbulent flow. For the flows of types 2, 3, and 4, steady transition does not appear because of the large favorable pressure gradient, eliminating the opportunity of multimode transition.

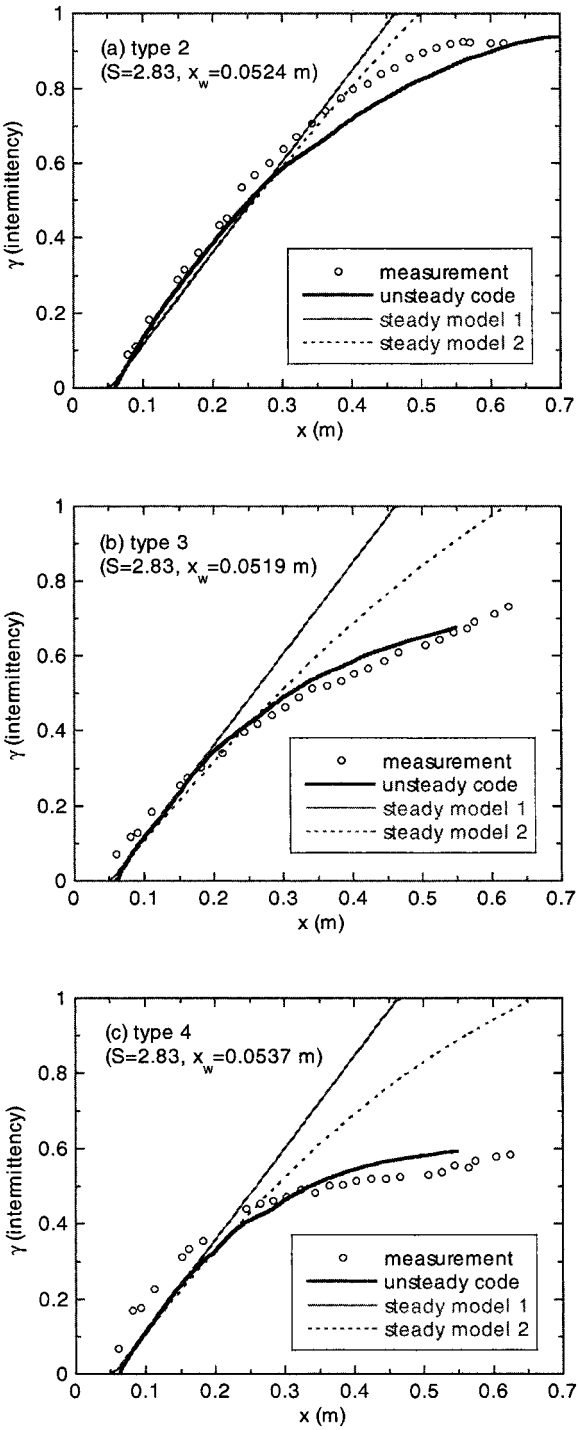

Fig. 13 Comparison of predicted time-averaged intermittency factor with the measurements (Funazaki et al., 1997) for high acceleration cases

Wake-Passing Cases of Reverse Rotation. Funazaki et al. (1997) also conducted heat transfer measurements for reverse rotation of the wake-generating bars, with the rest of flow conditions remaining the same. Compared with the results from normal rotation of the bars, time-averaged heat transfer was significantly reduced in the cases of the reverse rotation on the same test surface, according to the measurements. It indicates that the flow mechanism associated with the influence of wake-passing is quite different from the normal rotation of moving bars. Figure 14 illustrates the flowfield created by the different rotation of wake-generating bars. The flow pattern for the normal rotation case is on the upper surface, and the reverse rotation case can be considered

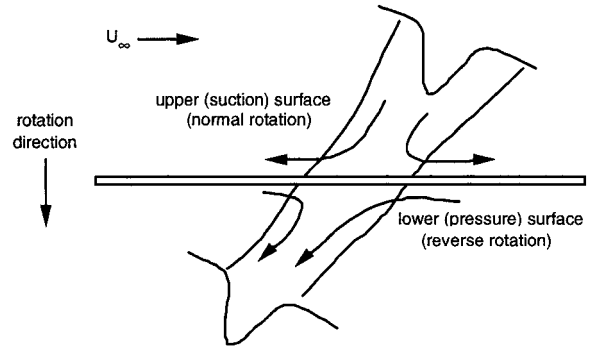

Fig. 14 Wake and surface interaction for normal and reverse rotations of wake-passing (adapted from Binder et al., 1985)

as the flow on the lower surface or the pressure side of a turbine blade. After the cutting of wakes by the test plate, a flow toward the upper or suction surface (test surface with normal rotation) results in accumulation of flow inside the wake. In contrast, flow leaving the lower or pressure surface (test surface with reverse rotation) causes the wake to be diminished (Binder et al., 1985). Funazaki and Kitazawa (1997) also state that the wake-induced turbulent region in the reverse rotation case was reduced by the effect of the negative jet away from the plate surface.

Funazaki and Kitazawa (1997) measured the time-resolved turbulent intensity for the cases of zero-pressure gradient and $S = 2.83$ using both rotational directions. From the observation of their measured turbulence intensity at $y = 0.2$ mm, reverse rotation produces a much weaker effect on the boundary layer than normal rotation in both strength and duration of turbulent fluctuations. Quantitatively comparing the two experimental cases, the duration of turbulent fluctuation near the surface was reduced by approximately 25 percent for the reverse rotation case. Therefore, the intermittent function for reverse rotation was modified, yielding the duration of turbulent strip, τ, in the intermittent function to be 75 percent of that for normal rotation case:

$$\left(\frac{\tau}{T}\right)_{\text{reverse}} = 0.75\left(\frac{\tau}{T}\right)_{\text{normal}} \tag{17}$$

In the time-resolved prediction for the reverse rotation case, a modified distribution of the intermittent function was used, but with the same location of transition onset for each type of flow. The time-mean results from the predictions are shown in Fig. 15, along with the measured data. Although the intermittent function for the reverse rotation case is rather arbitrarily determined and calibrated using the experimental observation, predicted time-mean heat transfer results agree well with the experimental data. There is a slight overprediction in the flow of type 2 in Fig. 15(*c*), but the prediction can be improved by shifting forward the transition onset.

Time-resolved variations of the boundary layer parameters from unsteady boundary layer computations are compared with the measurements by Funazaki and Kitazawa (1997) in Fig. 16. Despite some discrepancies with the measurements, boundary layer parameters are well predicted for cases of either normal or reverse rotation. Wake-affected variations of displacement and momentum thicknesses show the distinct characteristics of these cases. In normal rotation, both thicknesses increase rapidly with the arrival of the turbulent strip and decrease gradually toward the trailing edge of the strip. However, the reverse rotation case shows an almost symmetric increase and decrease during the passage of the turbulent strips, but with narrower duration. However, both cases do not show major difference in the variation of boundary layer integral parameters, although the wake-passing due to normal rotation has a larger impact on the laminar boundary layer, as shown in the comparison of the time-averaged heat transfer of Figs. 12 and 15.

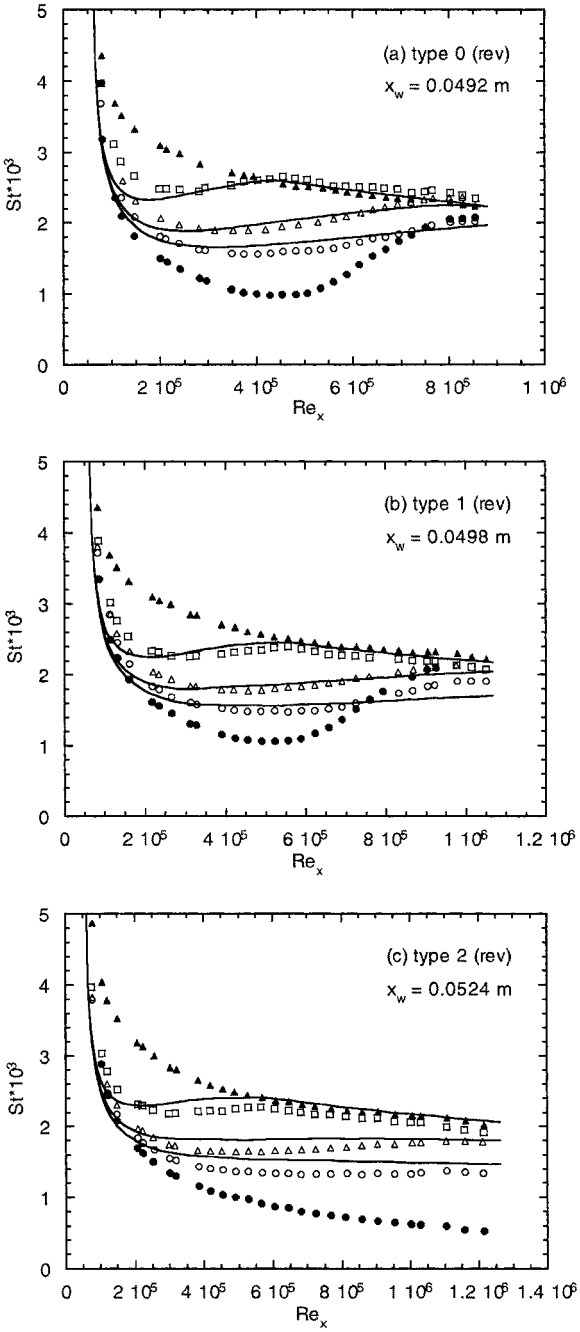

Fig. 15 Time-averaged Stanton number distributions for the cases of reverse rotation: symbols show the measurements of Funazaki et al. (1997) (●: no wake, ○: $S = 1.88$, △: $S = 2.83$, □: $S = 5.65$, and ▲: fully turbulent); solid lines show the corresponding time-resolved predictions for the cases of wake-passing.

Conclusions

A simple model for the evolution of wake-induced transition is proposed to simulate the time-resolved variation of wake-affected boundary layer development. The model is based on the classical theory of the turbulent spot propagation and experimental observation. In the process of transition, it is assumed that there is no interaction between the turbulent strips and the wakes after the high turbulence in the wakes initiates the turbulent strip at an earlier location. The ensemble-averaged intermittent function was modeled using Gaussian distribution and the linear propagation theory of turbulent spots. Comparison with the measurement data showed the capability of model to capture the details of ensemble-averaged variation of wake-affected boundary layer flow.

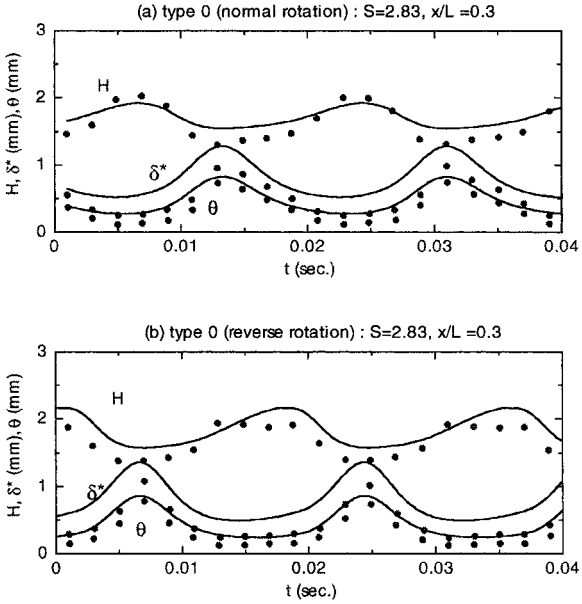

Fig. 16 Time-resolved variations of the boundary layer parameters: (*a*) normal rotation and (*b*) reverse rotation; symbols show the measurements by Funazaki and Kitazawa (1997); solid lines show the time-resolved predictions.

Heat transfer measurements under zero and favorable pressure gradients were calculated at several reduced wake-passing frequencies, and the estimated time-averaged results show that the present method provides more accurate predictions than a time-averaged superposition model, especially when the effect of pressure gradient is significant. The reverse rotation cases of wake-generating bars were also considered. The duration time of the intermittent function was set to be 75 percent of the one for the normal rotation, yielding good agreement with the measurements.

References

Abu-Ghannam, B. J., and Shaw, R., 1980, "Natural Transition of Boundary Layers—The Effects of Turbulence, Pressure Gradient, and Flow History," *Journal of Mechanical Engineering Science*, Vol. 22, No. 5, pp. 213–228.

Binder, A., Forster, W., Kruse, H., and Rogge, H., 1985, "An Experimental Investigation Into the Effect of Wakes on the Unsteady Turbine Rotor Flow," ASME *Journal of Engineering for Gas Turbines and Power*, Vol. 107, pp. 458–466.

Cebeci, T., and Platzer, M. F., 1989, "A General Method for Unsteady Heat Transfer on Turbine Blades," NASA CR 4206.

Cebeci, T., and Smith, A. M. O., 1974, *Analysis of Turbulent Boundary Layers*, Academic Press, New York.

Chakka, P., and Schobeiri, M. T., 1999, "Modeling Unsteady Boundary Layer Transition on a Curved Plate Under Periodic Unsteady Conditions: Aerodynamics and Heat Transfer Investigations," ASME JOURNAL OF TURBOMACHINERY, Vol. 121, pp. 88–97.

Cho, N.-H., Liu, X., Rodi, W., and Schönung, B., 1993, "Calculation of Wake-Induced Unsteady Flow in a Turbine Cascade," ASME JOURNAL OF TURBOMACHINERY, Vol. 115, pp. 675–686.

Dullenkopf, K., Schulz, A., and Wittig, S., 1991, "The Effect of Incident Wake Conditions on the Mean Heat Transfer of an Airfoil," ASME JOURNAL OF TURBOMACHINERY, Vol. 113, pp. 412–418.

Fan, S., and Lakshminarayana, B., 1996, "Computation and Simulation of Wake-Generated Unsteady Pressure and Boundary Layers in Cascades: Part 1—Description of the Approach and Validation," ASME JOURNAL OF TURBOMACHINERY, Vol. 118, pp. 96–108.

Funazaki, K., 1996, "Unsteady Boundary Layers on a Flat Plate Disturbed by Periodic Wakes: Part 1—Measurement of Wake-Affected Heat Transfer and Wake-Induced Transition Model," ASME JOURNAL OF TURBOMACHINERY, Vol. 118, pp. 327–336.

Funazaki, K., and Kitazawa, T., 1997, "Boundary Layers Transition Induced by Periodic Wake Passage (Measurements of the Boundary Layer by Hot-Wire Anemometry)," *Bulletin of GTSJ*, p. 26; also private communication with K. Funazaki.

Funazaki, K., Kitazawa, T., Koizumi, K., and Tadashi, T., 1997, "Studies on Wake-Disturbed Boundary Layers Under the Influences of Favorable Pressure Gradient and Free-Stream Turbulence: Part 1—Experimental Setup and Discussions on Transition Model," ASME Paper No. 97-GT-451.

Halstead, D. E., Wisler, D. C., Okiishi, T. H., Walker, G. J., Hodson, H. P., and Shin, H.-W., 1997, "Boundary Layer Development in Axial Compressors and Tur-

bines: Part 1 of 4: Composite Picture," ASME JOURNAL OF TURBOMACHINERY, Vol. 119, pp. 114–127.

Hodson, H. P., Addison, J. S., and Shepherdson, C. A., 1992, "Models for Unsteady Wake-Induced Transition in Axial Turbomachines," *Journal de Physique III*, Vol. 2, pp. 545–574.

Kim, K., 1998, "Computation of Wake-Passing Effects on Turbine Blade Boundary Layers," Ph.D. Dissertation, The University of Texas at Austin, Austin, TX.

Kim, K., and Crawford, M. E., 1998, "Prediction of Unsteady Wake-Passing Effects on Boundary Layer Development," *Heat Transfer in Turbomachinery*, ASME HTD-Vol. 361/PID-Vol. 3, p. 399.

Liu, X., and Rodi, W., 1991, "Experiments on Transitional Boundary Layers With Wake-Induced Unsteadiness," *Journal of Fluid Mechanics*, Vol. 231, pp. 229–256.

Mayle, R. E., 1991, "The Role of Laminar–Turbulent Transition in Gas Turbine Engines," ASME JOURNAL OF TURBOMACHINERY, Vol. 113, pp. 509–537.

Mayle, R. E., and Dullenkopf, K., 1990, "A Theory for Wake-Induced Transition," ASME JOURNAL OF TURBOMACHINERY, Vol. 112, pp. 188–195.

Mayle, R. E., and Dullenkopf, K., 1991, "More on the Turbulent-Strip Theory for Wake-Induced Transition," ASME JOURNAL OF TURBOMACHINERY, Vol. 113, pp. 428–432.

Orth, U., 1993, "Unsteady Boundary-Layer Transition in Flow Periodically Disturbed by Wakes," ASME JOURNAL OF TURBOMACHINERY, Vol. 115, pp. 707–713.

Parikh, P. G., Reynolds, W. C., and Jayaraman, R., 1981, "On the Behavior of an Unsteady Turbulent Boundary Layer," presented at the Symposium on Numerical and Physical Aspects of Aerodynamic Flows, Long Beach, CA, Jan. 19–21.

Pfeil, H., and Herbst, R., 1979, "Transition Procedure of Instationary Boundary Layers," ASME Paper No. 79-GT-128.

Pfeil, H., Herbst, R., and Schröder, T., 1983, "Investigation of the Laminar–Turbulent Transition of Boundary Layers Disturbed by Wakes," ASME JOURNAL OF TURBOMACHINERY, Vol. 105, pp. 130–137.

Tran, L. T., and Taulbee, D. B., 1992, "Prediction of Unsteady Rotor-Surface Pressure and Heat Transfer From Wake Passings," ASME JOURNAL OF TURBOMACHINERY, Vol. 114, pp. 807–817.

The Origin of Turbulent Spots

M. W. Johnson

A. Dris

Department of Engineering,
The University of Liverpool,
Liverpool L69 3GH, United Kingdom

It has been suggested that a turbulent spot is formed when a transient separation occurs in the laminar boundary layer and this criterion has been successfully used by Johnson and Ercan (1996, 1997) to predict bypass transition for boundary layers subjected to a wide range of free-stream turbulence levels and streamwise pressure gradients. In the current paper experimental results are presented that support the premise that the formation of turbulent spots is associated with transient separation. Near-wall hot-wire signals in laminar and transitional boundary layers are analyzed statistically to produce probability distributions for signal level and trough frequency. In the laminar period the signal level is normally distributed, but during the inter-turbulent periods in the transitional boundary layer, the distribution is truncated at the lower end, i.e., the lowest velocity periods in the signal disappear, suggesting that these are replaced during transition by the turbulent periods. The number of these events (troughs) also correlates with the number of turbulent spots during early transition. A linear perturbation theory is also used in the paper to compute the streamlines through a turbulent spot and its associated calmed region. The results indicate that a hairpin vortex dominates the flow and entrains a low-momentum fluid stream from upstream with a high-momentum stream from downstream and then ejects the combined stream into the turbulent spot. The hairpin can only exist if a local separation occurs beneath its nose and the current results suggest that this separation is induced when the instantaneous velocity in the near-wall signal drops below 50 percent of the mean.

Introduction

The turbulent spot can be considered as the "building block" of a turbulent flow. In the transition of a laminar boundary layer to a turbulent one, the turbulent spot plays a pivotal role. The first appearance of turbulent spots determines the start of transition location and the subsequent growth of the spots dictates the length of the transition region prior to a fully turbulent boundary layer being achieved. Emmons (1951) first recognized the intermittent nature of transitional flow and the role of the turbulent spot in the transition process. Narasimha (1957) measured the variation in intermittency through transition and showed that this was most accurately represented by a "concentrated breakdown" model, i.e., a model in which all the turbulent spots are initiated at the same streamwise location and the increase in intermittency through transition results purely from the growth in size of these spots. More recently, with the availability of more accurate measurement techniques for intermittency, the validity of this model has been challenged. Johnson and Fasihfar (1994) showed that a concentrated breakdown model did not give a good prediction of the evolution of spot statistics through transition and that a "distributed breakdown" model, i.e., one where spots are initiated at different streamwise locations resulted in improved prediction.

Johnson (1994) and Johnson and Ercan (1996, 1997) and more recently Mayle and Schultz (1997) and Mayle et al. (1998) have shown that the pretransitional boundary layer near wall velocity fluctuations, induced primarily by pressure fluctuations associated with the free-stream turbulence, grow more or less linearly in the streamwise direction. These fluctuations are of long wavelength (greater than 15 to 20 boundary layer thicknesses), but can be many times greater in amplitude (typically 20 to 100) in the near-wall region than in the free-stream. When these fluctuations reach some critical level (approximately a local turbulence level of 23 percent according to Johnson (1994)) significant numbers of turbulent spots are induced and transition commences. Natural transition induced through Tollmien–Schlichting waves also commences when the waves reach a similar critical amplitude. T–S waves possess a shorter wavelength (typically 2 to 3 δ) and also grow exponentially once the critical boundary layer Reynolds number is exceeded. However, it would appear that the criterion for the amplitude of fluctuation that induces a turbulent spot is common to both modes of transition.

The structure of turbulent spots has been studied extensively through both experiment (e.g., Cantwell et al. (1978); Seifert and Wygnanski (1994); Gostelow et al. (1995) and numerically (Bertolotti et al. (1992)); however, the mechanism leading to the initiation of the spot and turbulence production is not clear. Various mechanisms for the generation of turbulence in a boundary layer have been proposed. Sirovich and Karlsson (1997) believe that turbulent bursts are generated by the interaction of spanwise vorticity and oblique waves induced by the low frequency unsteadiness. On the other hand, Smith et al. (1991) attribute the turbulent bursts directly to the spanwise vorticity, produced through the unsteadiness, which induces transient separation of the boundary layer flow. This mechanism has also been proposed by one of the current authors (Johnson, 1994).

The objective of the current paper is to investigate through both experiment and theory the process of turbulent spot initiation.

Theoretical Model for Spot Initiation

Johnson (1994) considered the effect of the fluctuating pressure field resulting from free-stream turbulence on the near-wall velocity profile within the laminar boundary layer. Experimental observations (Johnson and Ercan, 1996) of the near-wall velocity fluctuations within laminar boundary layers show that the dominant wavelengths are much greater than the boundary layer thickness. Similar results have since been obtained theoretically by Mayle and Schultz (1997). If this is the case, it is reasonable to assume that the effect of the pressure field close to the wall is restricted to two dimensions (i.e., the x–y plane) and that there will be negligible phase shift over short distances from the wall. Experimental observations also indicate that near the wall the turbulence level is constant and hence as the mean velocity is proportional to y, it follows that the instantaneous velocity must also be proportional to y. With the assumptions so far made, a streamline in the near wall region will be as shown in Fig. 1. In the unperturbed flow, the streamline at a height y from the wall will carry fluid at a velocity u. When the flow is perturbed by a local reduction in pressure,

Contributed by the International Gas Turbine Institute and presented at the 44th International Gas Turbine and Aeroengine Congress and Exhibition, Indianapolis, Indiana, June 7–10, 1999. Manuscript received by the International Gas Turbine Institute February 1999. Paper No. 99-GT-32. Review Chair: D. C. Wisler.

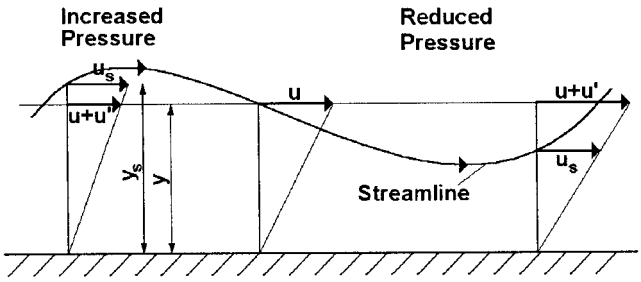

Fig. 1 Near-wall streamlines perturbed through the pressure field induced by the free-stream turbulence

however, the fluid will accelerate and will also move closer to the wall (to satisfy 2-d continuity). Conversely, when the pressure increases, the streamline will move away from the surface. Along a streamline, assuming that the perturbation is time invariant and viscosity can be neglected,

$$p_0(y) = p(x, y_s) + \tfrac{1}{2}\rho u_s^2, \tag{1}$$

where the pressure field is assumed to be a function only of the free-stream perturbations and not the local conditions and u_s is the velocity of fluid on the streamline at a height y_s above the wall. Continuity also requires that

$$uy = u_s y_s \tag{2}$$

Now with a general waveform $w(x)$ for the perturbing pressure field

$$\frac{1}{\rho}p(x, y_s) = a y_s^2 w(x) = a\left(\frac{uy}{u_s}\right)^2 w(x) \tag{3}$$

where a is a constant. Hence from Eq. (1),

$$\frac{u^2}{2} = a\left(\frac{uy}{u_s}\right)^2 w(x) + \frac{u_s^2}{2} \tag{4}$$

and so, taking the root of this quadratic, which meets the requirement that $u_s = u$ when $w(x) = 0$,

$$\left(\frac{u_s}{u}\right)^2 = \frac{1}{2} + \sqrt{\frac{1}{4} - \frac{2ay^2 w(x)}{u^2}} \tag{5}$$

However, the velocity $u + u'$ measured at the fixed height y is given by

$$u + u' = \frac{y u_s}{y_s} = \frac{u_s^2}{u} \tag{6}$$

and hence

$$\frac{u'}{u} = -\frac{1}{2} + \sqrt{\frac{1}{4} - \frac{2p(x, y)}{\rho u^2}\left(\frac{u_s}{u}\right)^2} \tag{7}$$

This relation indicates that the minimum value of the measured velocity $u + u'$ is $\frac{1}{2}u$ when $p(x, y) = \frac{1}{4}\rho u^2$. If $p(x, y)$ exceeds this value, the streamline no longer has an equilibrium position and an instability occurs. In fact, as the streamline is deflected outward, the local pressure increases, decelerating the fluid on the streamline still further, resulting in further deflection of the streamline from the wall, until ultimately the fluid stalls and flow separation results. This simple model therefore predicts that when a pressure perturbation induces the near-wall velocity to drop below 50 percent of the unperturbed local velocity, an instability arises, which results in local separation of the flow. It is the normal velocity v' associated with this separation that is believed to initiate the turbulent spot.

Experimental Work

The experimental measurements were made in the boundary layer wind tunnel in the Department of Engineering at the University of Liverpool. A detailed description can be found in Fasihfar (1992). The flat plate has a length and width of 1.2 m and 0.7 m, respectively and a flow velocity of 30 m/s, which was constant along the plate, was used for all the current experiments. A turbulence generating grid, placed 0.75 m upstream of the plate leading edge, induced a free-stream turbulence level of 1 percent at the plate leading edge. A Dantec 55C01 anemometer and 55P15 probe were used for the boundary layer measurements. The signal was digitized over a sample length of 15 seconds using a sampling frequency of 10 kHz. The signals were linearized using a digital "look-up" calibration table. At each of 12 streamwise x locations, a boundary layer traverse consisting of 50 measurement points was made in order that the boundary layer integral parameters could be evaluated. One of the near-wall measurement points, which lay at approximately $y/\delta = 0.1$, was selected for the signal analysis. The turbulent and inter-turbulent periods and hence the intermittency were determined using the method of Fasihfar and Johnson (1992), whereby the signal was high pass filtered to remove the low-frequency laminar fluctuations. The turbulent periods were then defined as those periods when the signal amplitude exceeded a specified threshold value. Full details, including the choice of the filter setting and threshold are given in Fasihfar and Johnson (1992). In the current work, the unfiltered signal was then analyzed in the turbulent and inter-turbulent periods to evaluate probability distributions for signal level and trough frequency.

Experimental Results

Boundary Layer Development. Figure 2 shows the boundary layer development along the plate. Laminar flow is maintained up to $\mathrm{Re}_x = 900{,}000$, at which point the intermittency starts to increase, indicating that transition has commenced. In the current work transition is not fully completed at the last measurement station. The near-wall local turbulence level increases approximately linearly through the laminar layer to a value close to 23 percent at start of transition, as discussed by Fasihfar and Johnson (1992), and reaches a peak at 40 percent in the transition period

Nomenclature

a = constant in Eq. (3)
p = instantaneous static pressure
p_o = time invariant total pressure on a streamline
Re = $U\delta/\nu$ = boundary layer thickness Reynolds number
Re_x = Ux/ν = Reynolds number based on streamwise distance
Re_θ = $U\theta/\nu$ = boundary layer momentum thickness Reynolds number
t = time
T = Ut/δ = dimensionless time
u = time-averaged local velocity
$\bar{u}_{\mathrm{lam}}$ = time-averaged inter-turbulent period velocity
$\bar{u}_{\mathrm{tur}}$ = time-averaged turbulent period velocity
u' = fluctuating velocity
u_i = $u + u'$ = instantaneous velocity
u_s = velocity on a streamline
U = free-stream velocity
v' = normal fluctuating velocity
$w(x)$ = waveform
x, y, z = streamwise, normal, and spanwise coordinates
X, Y, Z = $x/\delta, y/\delta, z/\delta$ = dimensionless coordinates
y_s = normal distance from wall to streamline
δ = boundary layer thickness
ρ = fluid density

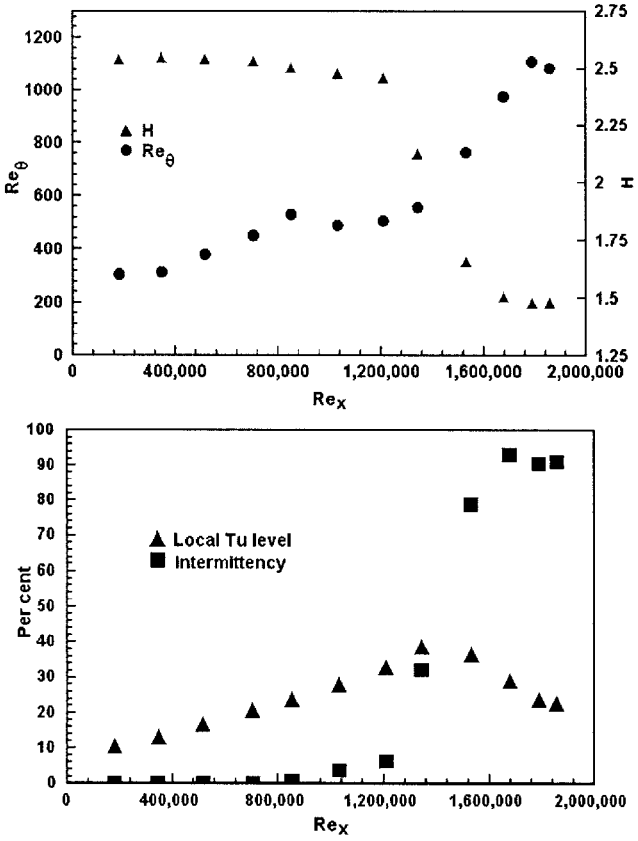

Fig. 2 Boundary layer development

before decreasing to a level of about 25 percent as the end of transition is approached. The reason for the peak at midtransition is primarily because of the difference in the mean velocities in the turbulent and inter-turbulent periods, and the local turbulence levels within each period considered separately are considerably lower, as discussed by Fasihfar and Johnson (1992).

Signal Level Probability. The significance of the pretransitional development of the near-wall velocity fluctuations in the triggering of turbulent spots has been recognized for a number of years (Johnson (1994) and Mayle and Schultz (1997)). The mechanism through which the spots are induced has not clearly been identified, however, and it was with this objective in mind, that the near-wall hot-wire signals at $y/\delta = 0.1$ were analyzed to try to identify those parts of the signal responsible for inducing spots. The distribution of occurrence level for each sample (Fig. 3) was determined by first nondimensionalizing the instantaneous velocities with the inter-turbulent mean velocity. The range of observed instantaneous velocities between the minimum and maximum value was then divided into approximately 25 equal subranges or bins. The sample, which consisted of 150,000 instantaneous velocity measurements, was then analyzed to determine the proportion of the total sample time spent in each subrange. The results were then divided by the bin size, such that the choice of the number of bins did not affect the computed probability. The spread of observed values increases necessarily as the rms fluctuation level increases with distance downstream, as shown in Fig. 3. The probability curve is almost symmetric in the laminar period up to $Re_x = 900{,}000$, but at the first measurement station within the transition region, $Re_x = 1{,}030{,}000$, the symmetry is lost. Although there is a significant probability that the velocity will exceed 150 percent of the local mean, the probability is almost negligible that it will be below 50 percent. The loss of the low-velocity events also increases the inter-turbulent mean $\bar{u}_{lam}$, which results in the most probable signal level $u_i/\bar{u}_{lam}$ reducing from 1 to 0.9 and hence the whole distribution curve is shifted to the left. This asymmetry becomes greater as the transition proceeds with very low probabilities below 50 percent of the local inter-turbulent mean velocity at any streamwise location. This observation therefore lends strong experimental support to the suggestion by Johnson and Ercan (1996, 1997) that turbulent spots are induced when the near-wall instantaneous velocity drops below 50 percent of the mean, in that it is these parts of the signal which apparently vanish from the inter-turbulent periods. Beyond $Re_x = 1{,}340{,}000$, a second peak resulting from the turbulent periods, which are associated with a higher mean velocity, develops at a $u_i/\bar{u}_{lam} > 1$. This peak becomes dominant as the end of transition is approached and also adopts a normal distribution profile about a mean level of $\bar{u}_{tur}/\bar{u}_{lam}$.

Trough Frequency. The trough frequency is defined as the frequency at which minima occur in the signal. In the present work, the distribution of the trough depths is computed within the laminar or inter-turbulent period as the frequency with which minima occur within each bin. This frequency is then divided by the bin size to remove the effect of the number of bins chosen. Frequency distributions for the troughs (Fig. 4) again show that the instantaneous velocity rarely drops below 50 percent of the mean even though significant frequencies are detected over 200 percent of the mean. The total trough rate in the inter-turbulent period (Fig. 5) remains constant at about 800 Hz as the boundary layer develops.

If each time the instantaneous velocity drops below the 50 percent threshold, a turbulent spot is induced, the number of observed threshold events should be equal to the number of spots induced. Figure 5 shows that during the early part of transition, the spot rate (= number of turbulent periods/sample time) is indeed approximately equal to the rate at which troughs disappear into the

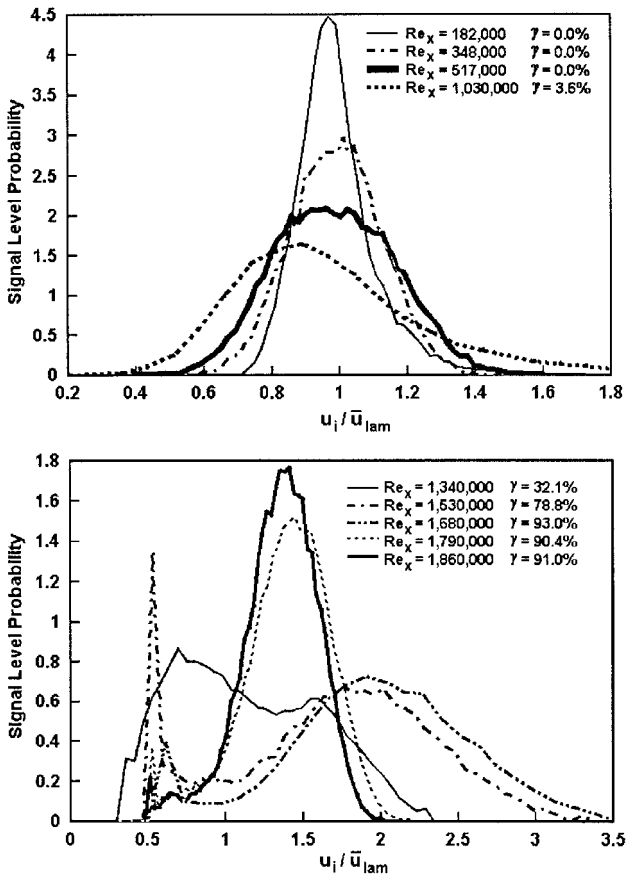

Fig. 3 Signal level probabilities

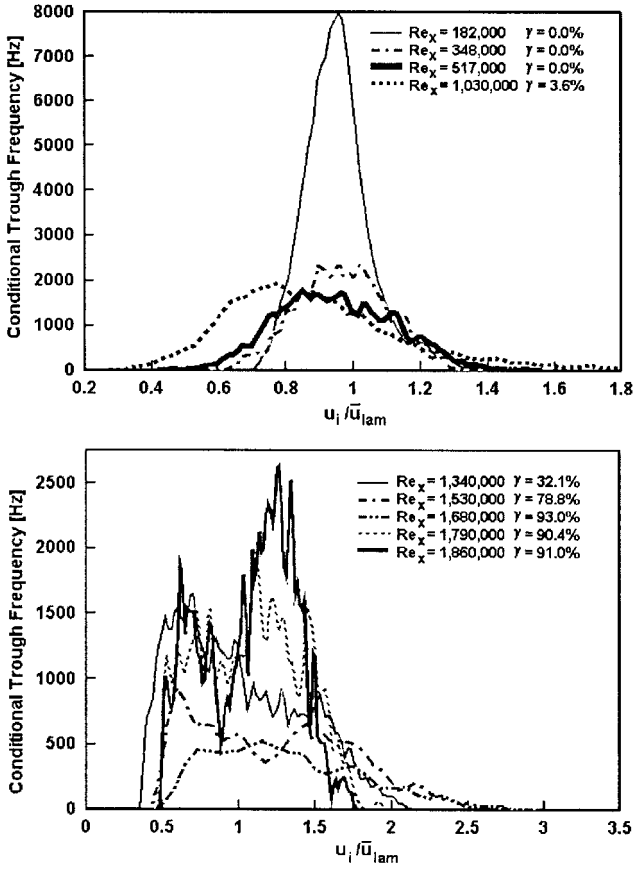

Fig. 4 Trough frequency distributions

turbulent period (= intermittency × trough rate). This is not the case farther downstream, however, as the number of observed spots will be less than the total number induced as the spots will be less than the total number induced as the spots will begin to merge with their neighbors as they grow in size. Nevertheless, the result shown in the figure confirms that the induction of a spot is associated with the disappearance of a trough in the near-wall velocity signal.

Concentrated or Distributed Breakdown. Whatever the criterion for the induction of turbulent spots, for concentrated breakdown to occur, the criterion can only be satisfied over a very short streamwise distance (Narasimha, 1957). This would seem to neglect the statistical nature of the free-stream turbulence responsible for inducing bypass transition. Consider, for example, a steady flow over a flat plate, but suppose that the free-stream turbulence level varies with time. Assuming the variation is made fairly slowly, we would expect the transition location to move downstream as the turbulence level is decreased and to move upstream as it is increased. This is not dissimilar from a wake-induced transition experiment (e.g., Halstead et al., 1995) where periods of high free-stream turbulence in the wakes result in large diversions upstream in the transition location. This is an extreme example of what happens when we have a nominally constant free-stream turbulence level. If the turbulence level were measured over periods of only a few wavelengths, then its magnitude would be found to vary considerably, because of its statistical nature. This variation would thus lead to a variation in the location at which turbulent spots are generated and hence to a "distributed breakdown." In the case of natural transition the amplitude of the Tollmien–Schlichting waves also varies with time, but they grow very rapidly in the streamwise direction and hence a large number of spots will be induced over a relatively short streamwise distance and thus can be modeled approximately as concentrated breakdown. However, for bypass transition the growth in amplitude is approximately linear and hence the spot initiation sites will have a significant streamwise distribution. This effect is apparent in most measured intermittencies (e.g., Gostelow and Walker, 1991) where the intermittency consistently exceeds the Narasimha concentrated breakdown model value by between 2 and 5 percent in the early transition period, but is accurately modeled by a distributed breakdown model (Johnson and Ercan, 1997). In the current experiments occasional spots (at a frequencies less than 1 Hz and which result in intermittencies less than 0.01 percent) were observed at measurement stations in the laminar boundary layer $Re_x < 900{,}000$. These very early turbulent spots have a negligible effect on the time mean boundary layer parameters and are generally ignored by researchers, but their existence is evidence of occasional extraordinary low troughs in the near-wall velocity signal, which induce occasional turbulent spots in the laminar boundary layer.

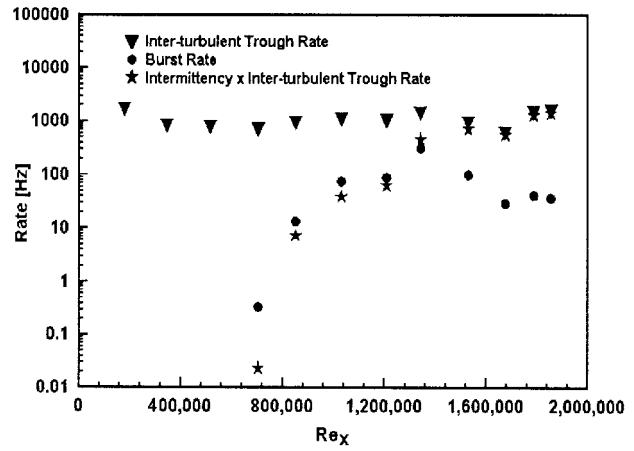

Fig. 5 Minima and burst rates along the plate

Theoretical Work

The theoretical results described in the current paper were obtained using the method described by Johnson (1998a, 1999), which is similar to the method of Li and Widnall (1989). A steady nondeveloping boundary layer flow is perturbed by a fully three-dimensional viscid linear perturbation. The method is therefore only strictly accurate for small linear perturbations and turbulence, which results from nonlinear perturbations, is not predicted. Nevertheless, Johnson (1998b) showed that the geometric development of the linear perturbation region was very similar to that of the measured (and hence nonlinear) development of a turbulent spot and its associated calmed region.

Figure 6 shows the streamlines through the perturbed region at $T = Ut/\delta = 60$ for $\mathrm{Re} = 4000$ ($\mathrm{Re}_\theta = 470$) as seen by an observer travelling at 50 percent of the free-stream velocity (approximately the average velocity of the perturbation region). It should be noted therefore that fluid with a velocity less than $0.5\,U$ (i.e., $Y < 0.25$) is seen by this moving observer to approach the perturbed region from the front, whereas fluid with a greater velocity ($Y > 0.25$) is seen to approach from the rear. The Y axis in the figure has been scaled by a factor of 5 and streamlines originating from each Y level are staggered by $\Delta Y = 1$ for clarity. In the figure all the streamlines originating above $Y = 0.1$ travel around the core of a hairpin vortex at $X = 30$. The streamlines beneath this level pass beneath the nose of the hairpin vortex and are deflected along its legs around the calmed region, which is bounded by the vortex. These streamlines are in fact within the viscous sublayer ($Y = 0.1$ corresponds to $y^+ = 9$ at this Reynolds number). The streamlines originating at $Y = 0.2$ are turned by the hairpin vortex through 180 deg to move away from the surface to mix with fluid carried

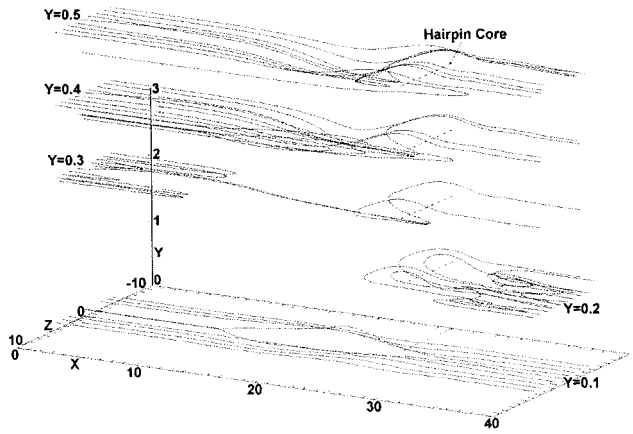

Fig. 6 Streamlines through the perturbed region

by streamlines originating behind the perturbed region at $Y > 0.25$. The streamlines originating from $Y = 0.4$ and 0.5 dip toward the wall through the calmed region to replace the fluid ejected by the hairpin ($Y = 0.2$ streamlines). This results in an increase in the boundary layer momentum in the calmed region and hence a local thinning of the boundary layer. The streamlines from $Y = 0.4$ and 0.5 pass through the calmed region to a point below the nose of the hairpin vortex. At this point, the fluid slows rapidly because of the increasing shear due to the wall below and the hairpin vortex above. The fluid is then entrained by the hairpin and is ejected forward along a similar path to the streamlines originating from $Y = 0.2$. The fact that the fluid streams originating from upstream ($Y = 0.2$) and downstream ($Y = 0.4$ and $Y = 0.5$) have significantly different energy levels will lead to high local shear rates as the two streams mix out in the hairpin vortex and forward of it following ejection and this leads to the turbulence, which identifies this region as the turbulent spot.

In the current work, the region where the high-momentum stream from downstream (streamlines from $Y = 0.3$, 0.4, and 0.5) meets the low-momentum stream from upstream (streamlines from $Y = 0.1$ and 0.2), is of particular interest. Where these two streams meet, the high-momentum stream bifurcates with one part continuing to the spot and the remainder turning through 180 deg into the calmed region. The bifurcation occurs along a line between the calmed region and the hairpin vortex, which forms an open loop. The front of the loop lies beneath the nose of the hairpin vortex and travels with it (i.e., at approximately 50 percent free-stream velocity); however, the legs of the loop trail behind the nose and end on the wall at separation points. It is therefore a necessary condition, for the establishment of the hairpin and the turbulent spot and its associated calmed region, that the boundary layer is perturbed sufficiently to induce a local separation of the flow.

The hairpin vortex and bifurcation point have also been observed in experiments (e.g., Cantwell et al., 1978).

Conclusions

1 A simple analytical model is presented, which suggests that the pressure fluctuations induced by the free-stream turbulence perturb the near-wall velocity in the laminar layer. If the instantaneous velocity is reduced to 50 percent of the unperturbed velocity, transient separation occurs and a turbulent spot is initiated.

2 Probabilities for the near-wall signal level in the laminar and inter-turbulent periods show that instantaneous velocities below approximately 50 percent of the mean are negligibly small even though velocities in excess of 200 percent are present. This observation appears to confirm that occurrences of instantaneous velocities below this threshold are responsible for the initiation of turbulent spots. This hypothesis is also supported by the fact that the occurrence rate of such events (troughs) is approximately equal to the burst rate within the early transition period. In mid and late transition, merging of spots occurs and hence the burst rate becomes lower than the trough rate.

3 A linear perturbation model is used to predict the streamlines through a turbulent spot and its associated calmed region. The results show that the hairpin vortex is responsible for sustaining the turbulent spot and that the vortex depends on the existence of a local separation of the flow. The separation is induced when the local instantaneous velocity drops below 50 percent of the mean.

References

Bertolotti, F. P., Herbert, Th., and Spalart, P. R., 1992, "Linear and Non-linear Stability of the Blasiuis Boundary Layer," *Jnl. of Fluid Mechanics*, Vol. 242, pp. 441–474.

Cantwell, B., Coles, D., and Dimotakis, P., 1978, "Structure and entrainment in the plane of symmetry of a turbulent spot," *Jnl. of Fluid Mechanics*, Vol. 87, pp. 641–672.

Emmons, H. W., 1951, "The Laminar Turbulent Transition in a Boundary Layer—Part 1," *Jnl. of Aero. Sciences*, Vol. 18, pp. 490–498.

Fasihfar, A., 1992, "Mechanisms of boundary layer transition," Ph.D. thesis, University of Liverpool.

Fasihfar, A., and Johnson, M. W., 1992, "An improved boundary layer transition correlation," ASME Paper No. 92-GT-245.

Gostelow, J. P., Melwani, N., and Walker, G. J., 1995, "Effects of Streamwise Pressure Gradient on Turbulent Spot Development," ASME JOURNAL OF TURBOMACHINERY, Vol. 118, pp. 737–743.

Gostelow, J. P., and Walker, G. J., 1991, "Similarity behavior in transitional boundary layers over a range of adverse pressure gradients and turbulence levels," ASME JOURNAL OF TURBOMACHINERY, Vol. 113, pp. 617–625.

Halstead, D. E., Wisler, D. C., Okiishi, T. H., Walker, G. J., Hodson, H. P., and Shin, H.-W., 1997, "Boundary layer development in axial compressors and turbines. Part 4. Computations and Analyses," ASME JOURNAL OF TURBOMACHINERY, Vol. 119, pp. 128–139.

Johnson, M. W., 1994, "A bypass transition model for boundary layers," ASME JOURNAL OF TURBOMACHINERY, Vol. 116, pp. 759–764.

Johnson, M. W., and Fasihfar, A., 1994, "Properties of turbulent bursts in transitional boundary layers," *Int. Jnl. of Heat and Fluid Flow*, Vol. 15, No. 4, pp. 283–290.

Johnson, M. W., and Ercan, A. H., 1996, "A boundary layer transition model," ASME Paper No. 96-GT-444.

Johnson, M. W., and Ercan, A. H., 1997, "Predicting bypass transition: A physical model versus empirical correlations," ASME Paper No. 97-GT-475.

Johnson, M. W., 1998a, "The structure of turbulent spots," submitted for journal publication.

Johnson, M. W., 1998b, "Turbulent spot characteristics in boundary layers subjected to streamwise pressure gradient," ASME Paper No. 98-GT-124.

Johnson, M. W., 1999, "Prediction of turbulent spot growth rates," ASME Paper No. 99-GT-31.

Li, F., and Widnall, S. E., 1989, "Wave patterns in plane Poiseuille flow created by concentrated disturbances," *Jnl. of Fluid Mechanics*, Vol. 208, pp. 639–656.

Mayle, R. E., and Schultz, A., 1997, "The path to predicting bypass transition," ASME JOURNAL OF TURBOMACHINERY, Vol. 119, pp. 405–411.

Mayle, R. E., Dullenkopf, K., and Schultz, A., 1998, "The turbulence that matters," ASME JOURNAL OF TURBOMACHINERY, Vol. 120, pp. 402–409.

Mayle, R. E., 1999, "A theory for predicting the turbulent spot production rate," ASME JOURNAL OF TURBOMACHINERY, Vol. 121, pp. 588–593.

Narasimha, R., 1957, "On the Distribution of Intermittency in the Transition Region of a Boundary Layer," *J. of Aero. Sciences*, Vol. 24, pp. 711–712.

Seifert, A., and Wygnanski, I. J., 1994, "On Turbulent Spots in a Laminar Boundary Layer subjected to Self-Similar Adverse Pressure Gradient," *Jnl. of Fluid Mechanics*, Vol. 296, pp. 185–209.

Sirovich, L., and Karlson, S., 1997, "Turbulent drag reduction by passive mechanisms," *Nature*, Vol. 388, pp. 753–755.

Smith, C. R., Walker, J. D. A., Haidari, A. H., and Sobrun, U., 1991, *Phil. Trans. R. Soc. Lond. A336*, pp. 131–175.

Three-Dimensional Unsteady Flow for an Oscillating Turbine Blade and the Influence of Tip Leakage

D. L. Bell[1]

L. He

School of Engineering,
University of Durham,
Durham, DH1 3LE, United Kingdom

The results of two investigations, concerning the aerodynamic response of a turbine blade oscillating in a three-dimensional bending mode, are presented in this paper. The first is an experimental and computational study, designed to produce detailed three-dimensional test cases for aeroelastic applications and examine the ability of a three-dimensional time-marching Euler method to predict the relevant unsteady aerodynamics. Extensive blade surface unsteady pressure measurements were obtained over a range of reduced frequency from a test facility with clearly defined boundary conditions (Bell and He, 1997). The test data indicate a significant three-dimensional effect, whereby the amplitude of the unsteady pressure response at different spanwise locations is largely insensitive to the local bending amplitude. The computational results, which are the first to be supported by detailed three-dimensional test data, demonstrate the ability of the inviscid method to capture the three-dimensional behavior exhibited by the experimental measurements and a good level of quantitative agreement is achieved throughout the range of reduced frequency. Additional computational solutions, obtained through application of the strip methodology, reveal inadequacies in the conventional quasi-three-dimensional approach to the prediction of oscillating blade flows. The issue of linearity is also considered, and both experimental and computational results indicate a linear behavior of the unsteady aerodynamics. The second, an experimental investigation, addresses the influence of tip leakage upon the unsteady aerodynamic response of an oscillating turbine blade. Results are provided for three settings of tip clearance. The steady flow measurements show marked increases in the size and strength of the tip leakage vortex for the larger settings of tip clearance and deviations are present in the blade loading toward the tip section. The changes in tip clearance also caused distinct trends in the amplitude of the unsteady pressure at 90 percent span, which are observed to correspond with localized regions where the tip leakage flow had a discernible impact on the steady flow blade loading characteristic. The existence of these trends in the unsteady pressure response warrants further investigation into the influence of tip leakage on the local unsteady flow and aerodynamic damping.

Introduction

A significant effort has been made in recent years to develop computational methods for the prediction of unsteady flows around oscillating turbomachinery blades, aimed at accurately determining flutter stability margins under practical working conditions. The state-of-the-art computational methods largely consist of two kinds of approach: nonlinear time marching methods such as those presented by He and Denton (1994) and Gerolymos (1993), and time-linearized methods, for instance Hall and Lorence (1993). Both approaches have been developed into fully three-dimensional methods, which can be applied to the complex three-dimensional blade geometries that characterize the modern turbomachine. It is unfortunate then, although not unexpected, that published experimental programs have not similarly progressed to provide three-dimensional test cases. The absence of three-dimensional test data not only poses the obvious validation difficulty, but more crucially it limits our understanding. This has detrimental repercussions, because the understanding gained from experimental investigations plays an important role in the development of such prediction methods.

It is notable that blading types most susceptible to flutter are often typified by high aspect ratios, unshrouded tip sections, and significant tip clearances. Now, while the deleterious steady flow nature of tip leakage is well documented, e.g., as reported by Sjolander in a recent VKI lecture series (1997), the influence of these secondary flows on blade flutter is by comparison unexplored. The omission of such work takes on increasing importance when it is realized that the contribution to aerodynamic damping is usually disproportionately weighted toward the tip section, due to the relatively high amplitudes of vibration there. It is also common to find high aerodynamic loading at blade tip sections and the influence of changes in blade loading, induced by tip leakage, on the aeroelastic response is unknown.

Research has been undertaken, in two parts, to address the issues raised. First, detailed and reliable three-dimensional test data for a turbine blade oscillating in bending mode are presented, and the ability of a three-dimensional time-marching Euler method to capture the relevant unsteady aerodynamics examined. The measurements and predictions, which encompass a range of reduced frequency, are also studied in order to assess the linearity of the test configuration. Following this, the influence of tip clearance upon the unsteady pressure response of the oscillating turbine

[1] Current address: ALSTOM Energy Ltd. Steam Turbines, Newbold Road, Rugby, Warwickshire, CV21 2NH, United Kingdom.

Contributed by the International Gas Turbine Institute and presented at the 43rd International Gas Turbine and Aeroengine Congress and Exhibition, Stockholm, Sweden, June 2–5, 1998. Manuscript received by the International Gas Turbine Institute February 1998. Paper No. 98-GT-571. Associate Technical Editor: R. E. Kielb.

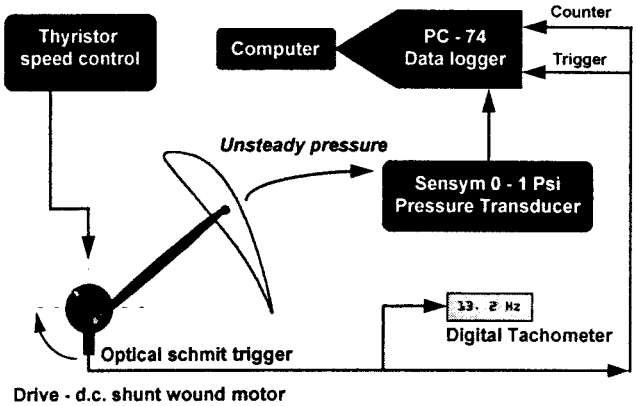

Fig. 1 Schematic of data acquisition hardware

blade is experimentally investigated. Steady flow measurements of the tip leakage vortex along with both steady and unsteady blade pressure distributions are provided and the results discussed. To the authors' knowledge, this is the first work to address the influence of tip clearance upon the local unsteady aerodynamics of oscillating turbomachinery blades.

Low-Speed Test Facility

Here the test facility is described in brief. A more detailed specification is provided by Bell and He (1997).

Description. A low-speed test facility, which employed a single prismatic turbine blade (chord: 0.2 m), was used to generate the test data. At the working section the turbine blade was mounted in a profiled duct. The profiled sidewalls were specified by the adjacent blades in cascade, with plane sections extending one axial chord up and downstream of the blade. The working section was located in the exhaust of a low-speed wind tunnel and the tunnel boundary layers were bled, in order to provide uniform inlet flow conditions.

The blade was driven at a sinusoidal rate by a single bar crank mechanism (Fig. 1), and a three-dimensional bending mode was enforced by hinging the blade at root and driving the tip section. This provided a linear variation in bending amplitude along the blade span. Specification of the bending mode and other operational parameters are given in Table 1.

Instrumentation, Data Acquisition, and Reduction. The low speed and scale of the test facility meant that realistic reduced frequencies were reproduced with low frequencies of blade vibration (4 to 21 Hz). This enabled the unsteady pressure signals from the blade surface to be recorded with externally mounted pressure transducers. The use of outboard pressure transducers is an important feature of this test facility, because it significantly reduces the cost for a suitable pressure transducer when compared to the relatively expensive surface mounted kind. Furthermore, it allows a single pressure transducer to measure the unsteady pressure for all positions on the blade surface instrumented with a static tapping. That is provided that all unsteady pressure signals can be synchronized.

Table 1 Operational conditions

Experiment Conditions	
Nominal deflection	40.3°
Typical reference velocity, V_{ref}	33.4 m/s
Bending mode direction	35.5° *(to axial)*
Bending amplitude at tip, B_C	0.055 chord
Bending amplitude at hub	0.006 chord
Reynolds number, Re	4.5×10^5
Reduced frequency, k	0.15, 0.25, 0.50, 0.75

The blade was extensively instrumented at five spanwise sections: 10 (near hub), 30, 50, 70, and 90 percent span, with 10 tappings on the pressure and suction surface at each section. Five calibrated Sensym 142C01D pressure transducers were used to monitor the unsteady pressure response, therefore 20 sets of measurements were required to cover the full blade surface. The unsteady voltage output from the transducers was discretized and recorded by a PC-mounted Amplicon PC-74 data-logging card, and data acquisition was triggered by an optical schmitt trigger, which referenced a fixed phase in the blade motion. A schematic representation of this hardware is provided in Fig. 1.

Figure 2 demonstrates that despite the relatively low amplitude of unsteady pressure signals, the sensitivity of the pressure transducers and data-logger was able to resolve them with sufficient clarity. This figure also illustrates the process of noise reduction, whereby the unsteady pressure signals were ensemble-averaged over 40 periods. Following this, the unsteady pressures were reduced into their harmonic components using a Fourier Series. The final harmonic components were then corrected for phase shift and attenuation along the tube lengths that separated the blade surface tapping points and the transducers; see Bell and He (1997).

The test facility was also equipped with traverse gear, to enable five-hole probe measurements of stagnation pressure and flow angle at inlet to the test section and an axial plane 75 percent chord downstream of the blade. The downstream measurements provided information regarding the development of the tip leakage vortex.

Experimental Error and Repeatability

Further to previous publications of results obtained from the low-speed test facility (Bell and He, 1997, 1998), a more rigorous evaluation of experimental error and repeatability in the measurement of unsteady pressure has been performed. This work, which is summarized below, is described in detail by Bell (1999).

To enable a quantitative assessment of experimental error and repeatability, 40 unsteady pressure measurements were acquired

Nomenclature

B_C = bending amplitude at tip, nondimensionalized with chord
B_L = local bending amplitude, nondimensionalized with chord
C = blade chord, m
Cp = steady pressure coefficient = $(P - P_2)/(\bar{P}_{01} - \bar{P}_2)$
$|Cp_n|$ = amplitude of the nth harmonic pressure coefficient = $|\tilde{P}_n|/(\bar{P}_{01} - \bar{P}_2)B_C$
dA = projected blade surface area (unit span), normal to the direction of bending, m
h = blade span, m
k = reduced frequency, based on chord and reference velocity
S = pitch, m
V_{ref} = reference velocity = $\sqrt{2(\bar{P}_{01} - \bar{P}_2)/\rho}$, ms^{-1}
x = chordwise position, m
Y = stagnation pressure loss, Pa
$\bar{Y}$ = pitch-averaged loss coefficient = $\int_S YV_x dy/((\bar{P}_{01} - \bar{P}_2)\int_S V_x dy)$
z = radial position, m
$\bar{\alpha}$ = pitch-averaged exit flow angle = $\tan^{-1}[S\int_S V_y V_x dy/(\int_S V_x dy)^2]$
ϕ_n = phase angle of the nth harmonic pressure response, deg
τ = tip clearance/gap, m
ξ = coefficient of aerodynamic damping = $(1/h)\int_h \int_C ((-\pi B_L|Cp_1| \times \sin\phi_1)/CB_C)dAdz$

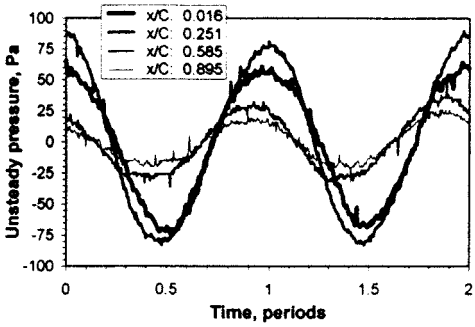

(i). Sample raw pressure traces

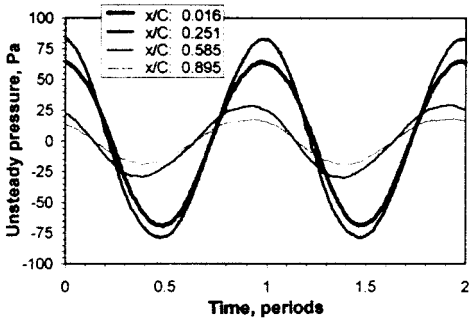

(ii). Sample ensemble-averaged pressure response (40 periods)

Fig. 2 Data acquisition and reduction; sample results at 70 percent span, suction surface (*k*: 0.25)

from five surface tappings (selected to provide a representative range of unsteady pressure amplitude) under identical operating conditions. In the measurement of each unsteady pressure signal, the experimental procedure outlined in the previous section was followed. This included the process of ensemble-averaging and the correction for phase shift and attenuation of pressure signals within the tapping tubes. From the statistical sample of 200 unsteady pressure measurements, the deviation from mean values were determined for both amplitude ($|Cp_1|$) and phase angle (ϕ_1) of the first harmonic pressure. The results demonstrated an excellent level of repeatability, which accounts for the contribution of random error, with all deviations in the measurement of phase angle falling within the range ± 4 deg and within ± 0.06 for the nondimensional amplitude of first harmonic pressure. The corresponding standard deviation was 0.93 deg in measurement of phase angle (ϕ_1) and 0.018 in the measurement of pressure amplitude ($|Cp_1|$).

In order to estimate an overall level of experimental error in the measurement of unsteady pressure, it was also necessary to consider the accuracy of the correction imposed for the phase shift and attenuation of pressure signals within the tapping tubes, which is described in the preceding work (Bell and He, 1997). This correction relied upon the specification of phase shift and attenuation coefficients for the tapping tubes at each test case reduced frequency. These coefficients were experimentally determined through a least-squares "best-fit" to calibration test data, which comprised measurements of $|Cp_1|$ and ϕ_1 for various lengths of tapping tube. During the calibration procedure, the deviation of measurements from the least-squares best-fit was recorded, to enable an estimation of accuracy to be made. The standard deviation in calibration measurements was 2.45 deg in phase angle and 0.042 in $|Cp_1|$. This also demonstrates a good level of accuracy, which combined with the results described above allows an overall error band to be confidently established that envelopes the standard deviation of measurements. This error band was conservatively estimated as ± 6 deg in the measurement of the true phase angle (ϕ_1) and ± 0.1 in the measurement of the true pressure amplitude ($|Cp_1|$). This represents a high level of accuracy for type of experimental work undertaken.

Numerical Method

The experimental test cases were numerically simulated by an extended three-dimensional time-marching Euler method. In this method the flow is governed by the unsteady three-dimensional inviscid Euler equations. The equations were discretized in space by a cell-vertex finite volume scheme (Denton, 1983), and temporally integrated with the explicit five-step Runge–Kutta method. The second and fourth-order adaptive smoothing proposed by Jameson et al. (1981) was adopted in the streamwise direction, with simple second-order smoothing in the circumferential and radial directions. The scheme was applied to an **h**-type mesh with a zonal moving grid to accommodate the motion of the blade.

In order to model the experimental working section, a single passage computational domain was extended to encompass two blade passages. This domain was a geometric reproduction of the experimental test section, which included the sidewalls. The mesh used for both steady and unsteady computations comprised 81 nodes in the axial direction, 54 circumferentially, and 11 in the radial direction. The mesh was refined in the axial and circumferential directions to resolve the leading and trailing edge regions, and a single-node cusp was attached to the trailing edge. Downstream of the trailing edge, the side and endwalls of the computational domain were linearly contracted to obtain a corrected mass flow in the inviscid calculations. The extent of the contraction was determined by measurements of displacement thickness performed at the downstream traverse plane in the test section. At the downstream boundary each endwall had been contracted by 0.75 percent chord in the radial direction, and each sidewall by 3.0 percent chord in the circumferential direction. A tip clearance was not, however, included in the computational domain.

The inlet boundary was specified by uniform inlet flow conditions previously obtained from the test facility (Bell and He, 1997), while the downstream boundary was set by a fixed back pressure condition. The reflecting downstream boundary condition was adopted, because the test facility exhausted to atmosphere.

To obtain a converged solution from the time-marching method, computations were performed at an artificially high Mach number. The exit Mach number for the computations was in the region of 0.3, compared to 0.1 in the test facility. This should not, however, introduce significant compressibility effects into the computations. Reduced frequency was matched for each unsteady test case.

Experimental and Numerical Results

Steady Flow Results. Figure 3 demonstrates reasonable agreement between the predicted and measured steady flow blade pressure distribution. The results shown here, taken at midspan, are representative of the full blade surface, at least between 10 and 90 percent span. Previous measurements from the test facility (Bell and He, 1997) indicated negligible three-dimensional effects in terms of the steady blade pressure distribution. Equally, without the inclusion of tip clearance, there was no source of three-dimensional effects in the inviscid steady flow computations given the uniform inlet conditions.

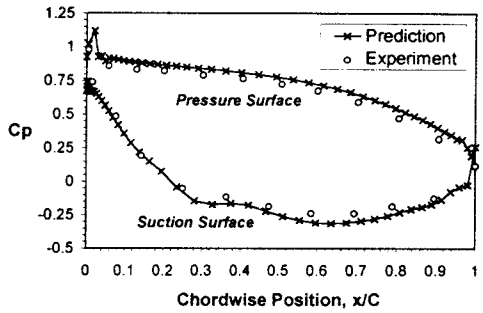

Fig. 3 Predicted and measured blade pressure distribution

Table 2 Numerical test for linearity (k: 0.75)

Bending Amplitude, B_C	0.0275 C	0.0165 C	0.0055 C
Aerodynamic damping, ξ	5.13	5.13	5.21

The steady flow solution obtained from the three-dimensional Euler solver was found to deteriorate quite markedly when the contraction of the computational domain downstream of the trailing edge was omitted. Although this is largely due to the blockage from the contraction setting a more realistic mass flow, the way in which the contraction was applied also helped to relieve the diffusion toward the trailing edge of the blade suction surface.

Linearity. Before the experimental and numerical results are discussed, the linearity of the test configurations is examined. This is of general interest in terms of the unsteady flow physics and has implications for the use of time-linearized numerical schemes. Moreover, it was important to ascertain the extent of linearity for the purposes of this investigation, because the unsteady calculations were performed at half the experimental bending amplitude. This situation was imposed due to difficulties in obtaining a converged solution for the full bending amplitude. This is thought to be associated with the direction of bending and large amplitude at the tip, causing excessive distortion of the **h**-type zonal mesh.

Numerical and experimental tests were performed in order to assess linearity. Numerical test cases were calculated for three different bending amplitudes at a reduced frequency of 0.75, and experimental measurements were taken at both the normal bending amplitude and a reduced value (used for numerical calculations), at a reduced frequency of 0.50.

The numerical test for linearity, Table 2, shows the inviscid aerodynamic response to the blade motion to be linear. Aerodynamic damping is identical for the two highest bending amplitudes tested, and only deviated very slightly for the low amplitude ($0.0055C$), where the effect of machine error is more appreciable. This test alone is not sufficient to prove linearity, however, because viscous effects were neglected by the numerical model.

The experimental measurements, presented in Fig. 4, also demonstrate quite linear behavior. The amplitude of the first harmonic pressure response for the suction surface (Fig. 4(i)) is almost identical for both bending amplitudes tested, and the same case was found for the pressure surface. The phase angle also shows excellent agreement for the whole pressure surface and from the leading edge to midchord on the suction surface. Aft of 60 percent chord on the suction surface, the phase measurements tend to deviate beyond the envelope of experimental error (specified as 6 deg standard deviation), most notably toward the hub section (10 percent span). The most likely explanation for this apparent nonlinear activity is considered to be the unsteady behavior of an intermittent external leakage flow, which is thought to have entered the test section through a faulty gland at the hub of the suction surface. It should be noted, however, that within this region of nonlinear activity, the amplitude of the unsteady pressure response, and the contribution from the deviation in phase toward the aerodynamic damping, is relatively small.

Predicted and Measured Unsteady Pressure Response. Experimental measurements were performed at four reduced frequencies, as specified in Table 1. Figure 5 shows the measurements and numerical prediction obtained for a reduced frequency of 0.25. The results presented here are in the form of the first harmonic pressure response and in order to preserve clarity they are provided for just three spanwise sections; 10 percent span (near hub); midspan; and 90 percent span (near tip).

Figure 5(i) shows the predicted and measured amplitude of the first harmonic pressure response, (k: 0.25). A consistent three-dimensional feature of the experimental measurements, represented in this figure, is an insensitivity in the amplitude of unsteady pressure to the local bending amplitude. While the bending amplitude at 90 percent span is around five times that found at 10 percent span, the variation in $|Cp_1|$ is not nearly as severe. Indeed, the amplitude of unsteady pressure measured on the pressure surface is almost identical along blade span. This figure also shows that the inviscid numerical scheme achieves good qualitative and quantitative agreement with the measured amplitude of unsteady pressure, and the insensitivity to local bending amplitude is captured. To demonstrate further the three-dimensional nature of the experimental measurements of unsteady pressure amplitude, and the capability of the three-dimensional Euler method, a prediction from a quasi-three-dimensional version of the numerical method is included. A quasi-three-dimensional prediction, also at k: 0.25, of the amplitude of the first harmonic pressure for the suction surface is shown in Fig. 6. This figure clearly shows the insensitivity of the experimental measurements of $|Cp_1|$ to the local bending amplitude, and the inability of the quasi-three-dimensional strip method to capture this behavior.

The predicted phase angle of the first harmonic pressure response, Fig. 5(ii), also demonstrates good agreement with the experimental measurements for all spanwise locations on the pressure surface. However, the prediction of phase for the suction surface does not display quite the same level of agreement. From the leading edge to around 40 percent chord there is reasonable agreement between prediction and measurement; however, farther downstream the agreement tends to deteriorate. The predicted unsteady pressure response of the suction surface is led by that at the trailing edge, whereas for the experiment the phase at the trailing edge lags the response at midchord. For inviscid flow, the unsteady lift, and therefore blade pressure distribution are heavily influenced by the condition of flow at the trailing edge. Information propagates upstream from the trailing edge and manifests in the phase lead of the unsteady response from this position, as demonstrated by the numerical solutions and the response measured for the pressure surface. Due to the relatively strong viscous diffusion of the suction surface in the test facility, however, the pressure toward the trailing edge could be sensitive to information

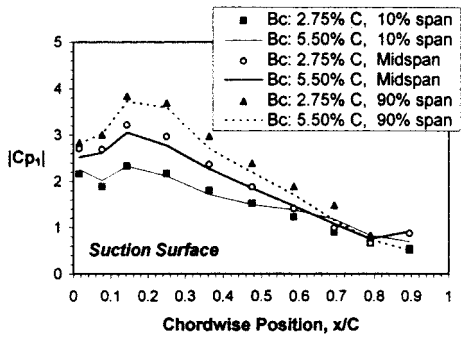

(i). Amplitude, suction surface

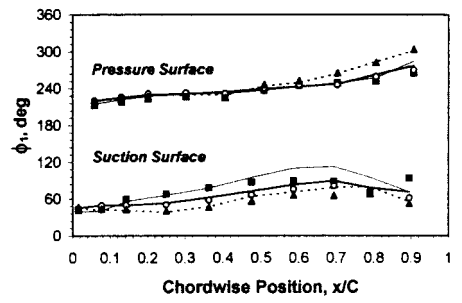

(ii). Phase Angle

Fig. 4 Experimental test for linearity, k: 0.50; first harmonic pressure response at two bending amplitudes (lines denote measurements obtained at the normal bending amplitude, and symbols those obtained at the reduced bending amplitude)

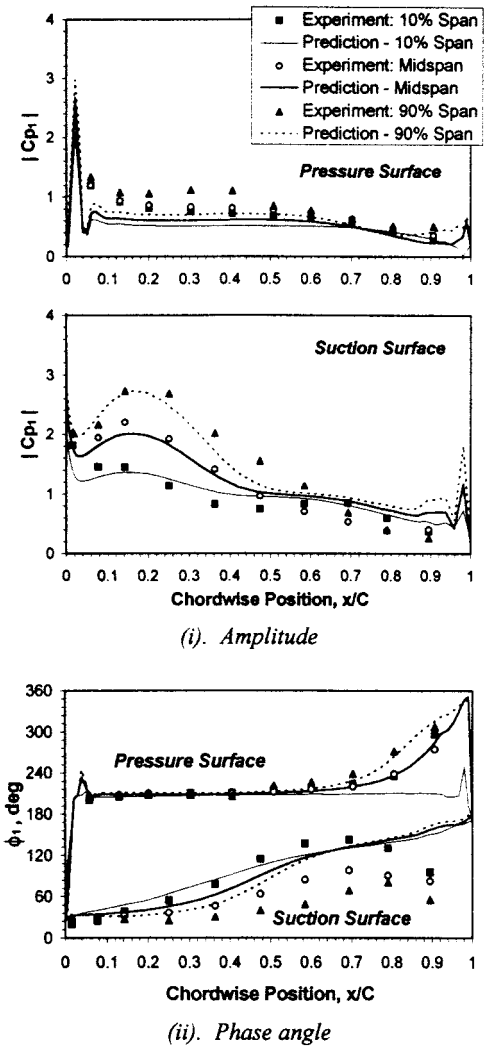

Fig. 5 Predicted and measured first harmonic pressure response (reduced frequency: 0.25)

convected from upstream, since this will determine the behavior of the relatively thick boundary layer found here. It is notable, however, that these discrepancies occur in regions where the amplitude of the unsteady response and consequent contribution to aerodynamic damping is relatively low.

The high level of agreement between the predicted and measured first harmonic pressure response and the qualitative trends observed are typical of the full range of reduced frequency tested. Furthermore, the predictions are a strong indication that the unsteady flow in the test facility is dominated by inviscid mechanisms.

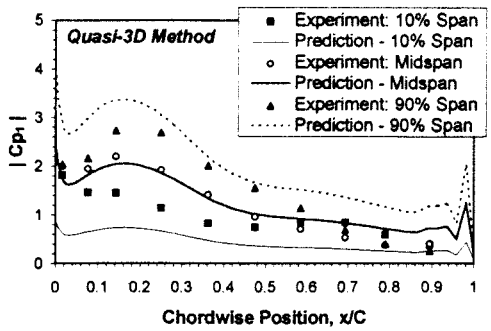

Fig. 6 Quasi-three-dimensional prediction of $|Cp_1|$ — suction surface, k: 0.25

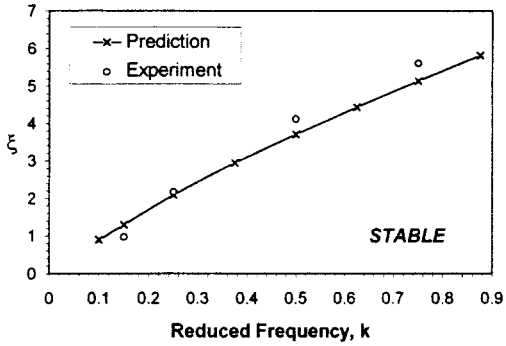

Fig. 7 Predicted and measured variation in aerodynamic damping with reduced frequency

One of the most important features of numerical predictions of the kind presented is the ability to determine aerodynamic damping accurately and so predict stability margins. The numerical solution consistently picks up the increases in both phase and amplitude as the reduced frequency is increased. This is reflected by a favorable comparison between the predicted and measured variation in aerodynamic damping with reduced frequency, as shown in Fig. 7.

Tip Leakage Effects

It is significant that the numerical predictions were conducted without an inclusion of tip clearance, while the experimental test configuration had a tip gap of 0.5 percent chord (to accommodate the blade motion). Despite this, very good agreement was achieved for the unsteady blade surface pressure for all spanwise positions between 10 and 90 percent span. This suggested that the tip clearance flow did not significantly influence the unsteady pressure response of the blade. However, it was also notable from previous work (Bell and He, 1997) that the tip clearance did not influence the measured steady flow blade surface pressure distribution. Consequently, it is not clear how a more significant tip leakage flow, with a marked effect on the steady flow blade loading, would influence the unsteady aerodynamics. Attention must also be given to the tip endwall passage vortex. There are two points to make here: The first is that under circumstances of low turning, the tip leakage flow is usually the dominant secondary flow structure (Sjolander, 1997). The second is that the presence of secondary flow mechanisms (which generate the passage vortex) is both inevitable and realistic for any experimental investigation performed in the endwall region.

To assess the influence of tip leakage upon the unsteady aerodynamic response of the oscillating turbine blade, an experimental investigation has been undertaken. Here, measurements of steady flow and unsteady pressure are compared over a range of tip clearance.

Experimental Setup. The experimental test facility provided a suitable environment for investigating the effect of tip leakage flow on both the steady and unsteady aerodynamic response. The unsteady pressure measurement procedure, previously described, enabled extensive instrumentation of the blade surface, which allowed the local influence of tip leakage to be readily identified. Furthermore, the downstream five-hole probe traverse provided an indication of the strength of the tip clearance flow through measurement of the tip leakage vortex.

Three settings of tip clearance, ranging from 0.5 to 1.5 percent chord, were investigated and measurements were taken at the free-stream flow conditions previously shown in Table 1. The different tip gaps, specified in Table 3, were set by the use of precise spacers in the blade mounting. At each setting of tip

Table 3 Summary of tip clearances

τ (m)	τ/C	τ/h
0.001	0.005	0.005
0.002	0.010	0.010
0.003	0.015	0.015
All clearances +/- 0.1 mm		

clearance, steady flow blade surface pressure measurements were recorded and a downstream five-hole probe traverse performed. In addition, unsteady pressure was measured over the full blade surface at four reduced frequencies, which are also specified in Table 1.

The previous experimental configuration had uniform inlet flow conditions, and the tunnel boundary layers were bled. However, to produce a more realistic aerodynamic environment, a thickened tip endwall boundary layer was adopted for this investigation. The pitch-averaged inlet stagnation pressure profile, recorded one axial chord length upstream of the blade, is shown in Fig. 8.

Steady Flow Results. A detailed appraisal of tip leakage flows is beyond the scope of the present work. The purpose here is to provide the aerodynamic background for the unsteady experiments and identify features of the steady flow that may influence the unsteady aerodynamic response of the oscillating turbine blade. Steady flow measurements obtained for each of the three tip clearances are presented in Figs. 9–11.

In Fig. 9, the changes in blade loading due to the tip clearance are apparent through the comparison of pressure distributions at three spanwise sections, 10 percent span (near the hub), midspan, and 90 percent span (near the tip). Significant variations in spanwise loading are evident at the 90 percent span location and the extent of this variation changes with increasing tip clearance. An unloading of the suction surface can be observed between 10 and 60 percent chord, at the 90 percent span location, which increases with tip gap. In addition, a consistent increase in suction can be observed for the two larger clearances between 70 percent chord and the trailing edge on the suction surface. These trends in blade loading are consistent with results presented by Sjolander (1997), in a review of recent advances in secondary and tip clearance flows in axial turbines. Sjolander provides an explanation of these loading effects, which is reinforced by the visualization of spanwise flows in a turbine cascade test. As the flow enters the blade passage, it is deflected away from the tip on the suction surface, causing the reduction in loading observed. Farther downstream, however, the tip leakage vortex rolls up along the suction surface and induces flow toward the tip. The high velocities associated

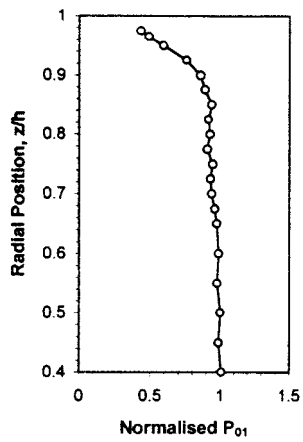

Fig. 8 Inlet total pressure profile in pitch-averaged form

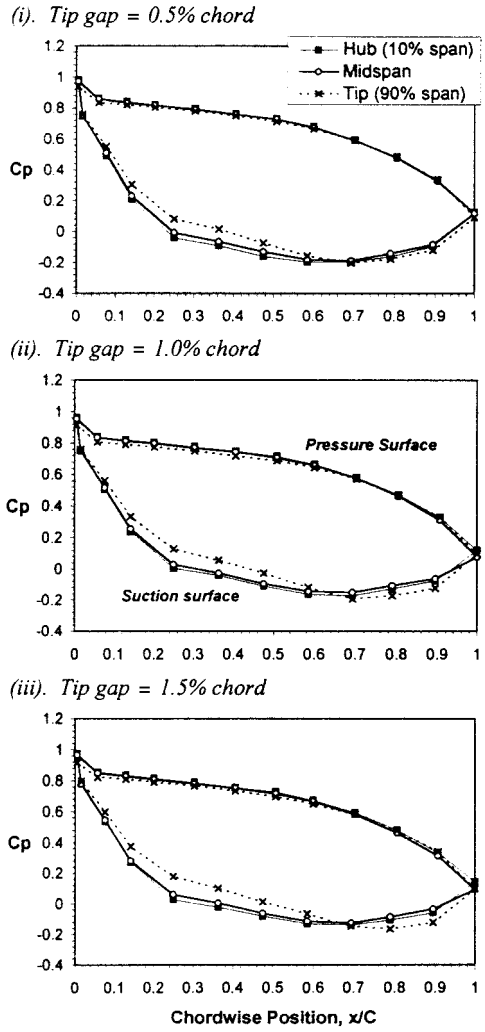

Fig. 9 Variation in blade pressure distribution with tip gap

with the vortex and the induced flow causes a reduction in pressure toward the trailing edge of the suction surface, i.e., an increase in suction.

In contrast, the pressure surface loading is largely unaffected by

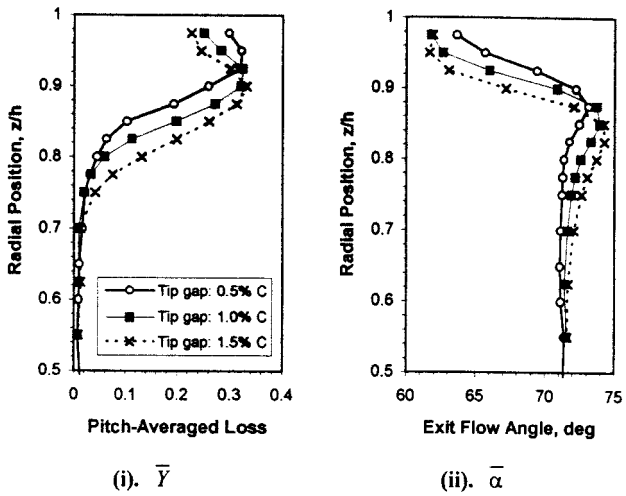

Fig. 10 Pitch-averaged measurements of loss ($\bar{Y}$), and exit flow angle ($\bar{\alpha}$), 75 percent chord downstream

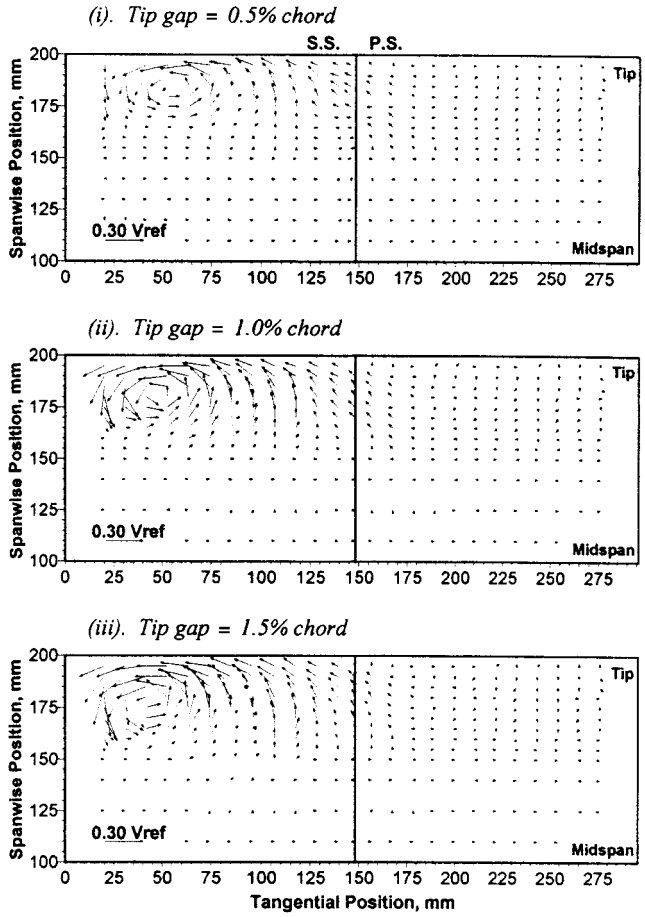

Fig. 11 Secondary velocity vectors

(Exit traverse plane, 75% C downstream)

the tip leakage, at least up to the 90 percent span location. It is recognized, however, that significant changes in loading can be expected much nearer the tip, which are dependent upon tip clearance. The comparative insensitivity of the pressure surface loading to tip leakage is also a typical feature of these endwall flows (Sjolander, 1997). Therefore, the present test facility provides a suitable aerodynamic environment for investigating the influence of tip leakage flow on the unsteady pressure response of an oscillating turbine blade.

The five-hole probe measurements taken 75 percent chord downstream of the blade are presented in Figs. 10 and 11. These show the relative strength of the tip leakage vortex, the associated loss and deficit in exit flow angle. The spanwise distribution of loss and exit flow angle, Fig. 10,[2] also exhibit quite typical features of a tip leakage flow. The loss core, associated with the tip leakage vortex, subtends a greater radial distance as the tip gap is increased and the peak loss increases slightly. Characteristic underturning is also evident toward the tip endwall, and once again the radial extent of this adverse effect increases with tip gap. It is also notable, however, that the peak in overturning, which occurs further away from the endwall, also increases in size and magnitude as the tip clearance rises. The secondary velocity vectors, shown in Fig. 11, clearly demonstrate the existence of the tip leakage vortex. As the tip clearance is increased, it is apparent that the vortex increases considerably in both size and strength. In all cases, the associated underturning causes the vortex to migrate away from the suction surface position; however, the center of the vortex is farther away from both the suction surface and endwall for the higher tip clearances. Furthermore, the absence of a passage vortex in Fig. 11 demonstrates that the secondary flow is dominated by the tip leakage vortex for this case of moderate turning and loading.

It can be concluded from the results presented in this section that the three tip clearances generate distinct and different tip leakage flows, and so provide suitable cases for the unsteady experiment.

Unsteady Pressure Measurements. The unsteady blade surface pressure measurements obtained at each setting of tip clearance and over a range of reduced frequency are presented and discussed here.

The volume of data generated by the series of unsteady experiments meant that it was easiest to compare results obtained for each tip clearance through consideration of aerodynamic damping. Figure 12 shows the variation in aerodynamic damping over the range of reduced frequency for each tip clearance. The figure shows the aerodynamic damping to be unaffected by the different tip leakage flows. Equally, comparisons of local damping, evaluated at each spanwise location, did not demonstrate any discernible trend in the unsteady aerodynamic response over the range of tip gap investigated.

Although it is often the aim of investigations of this nature to evaluate global parameters such as aerodynamic damping, comparisons of these quantities can often be misleading. Indeed, in this case it was found upon inspection of the first harmonic pressure response that a change in tip gap did in fact influence the unsteady pressure response.

Figure 13 shows the amplitude, and Fig. 14 the phase angle, of the first harmonic pressure response recorded at 90 percent span for the extreme settings of tip gap (0.5 and 1.5 percent chord). Although results are arbitrarily presented for just two reduced frequencies (0.25 and 0.75), the trends observed for these cases are typical of the full range of reduced frequency tested. Differences in the amplitude of the first harmonic pressure response of the suction surface are evident at 90 percent span for the different settings of tip clearance (Fig. 13), which extend beyond the envelope of standard deviation for $|Cp_1|$ (0.1). It can be seen in this figure that as the tip clearance increases, the amplitude of the unsteady pressure consistently decreases for all measurement positions between the leading edge and 30 percent chord on the suction surface. While in contrast, aft of 60 percent chord, the amplitude of unsteady pressure can be observed to increase with tip gap. The amplitude of unsteady pressure recorded for the pressure surface is, however, seemingly unaffected by the change in tip clearance. Differences are also present in the phase angle of the first harmonic pressure response for the suction surface, with a more rapid reduction in phase angle observed toward the trailing edge as the tip clearance is increased. Although this variation is in excess of the specified standard deviation (6 deg), the maximum change in phase angle remains below 15 deg.

It is notable, and thought significant, that the trends in amplitude of unsteady pressure with tip clearance are in correspondence with

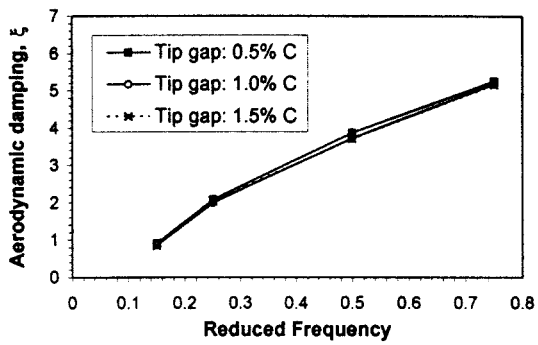

Fig. 12 Variation in aerodynamic damping with tip gap

[2] The spanwise distributions of loss and exit flow angle are the result of pitch-averaged measurements from the left hand passage, as viewed in Fig. 11.

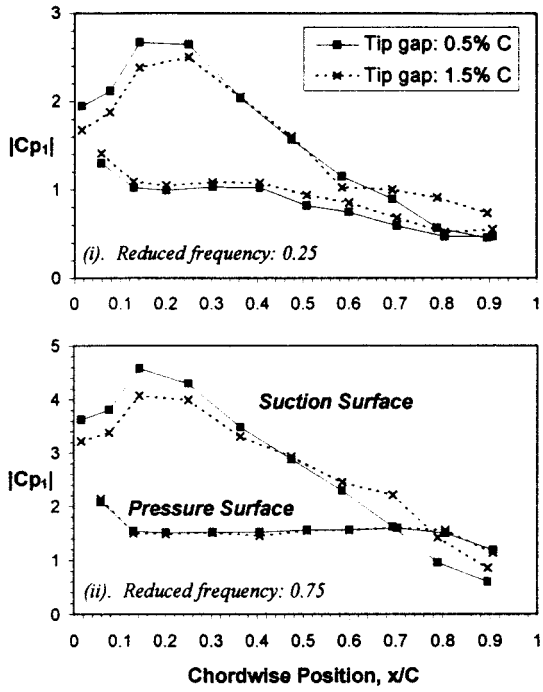

Fig. 13 Variation in amplitude of first harmonic pressure at tip section (90 percent span) with tip clearance – *k*: 0.25 and 0.75

the changes observed in steady flow blade loading. The slight increases in unloading observed for the suction surface with increasing tip gap coincide with the reduction in $|Cp_1|$. The increases in suction observed toward the trailing edge of the suction surface for increasing tip gap coincide with the increases in amplitude of unsteady pressure.

It is recognized that the trends in amplitude of the unsteady pressure response, observed for the changes in tip gap, do not represent substantial changes in the unsteady aerodynamic response. However, the consistent nature of results throughout the range of reduced frequency supports the presumption that these trends are true aerodynamic effects of the variation in tip clearance. Furthermore, the fact that effects have been observed at a considerable radial distance from the blade tip (90 percent span) gives rise to conjecture that the influence of tip leakage on the unsteady aerodynamic response will be considerably more significant nearer the tip section. In any case, further research, with more detailed instrumentation of the tip section, is required if the influence of tip leakage on blade flutter is to be clearly identified.

Finally, it is important to realise that the thickness of the blade used in this investigation (maximum thickness: 17.5 percent chord) is not particularly representative of a tip section. Normal tip sections tend to be much thinner and consequently the pressure gradient that drives the tip leakage flow is likely to be higher. Therefore one might also expect the influence of tip leakage, on both the steady and unsteady blade loading, to be more significant in realistic circumstances.

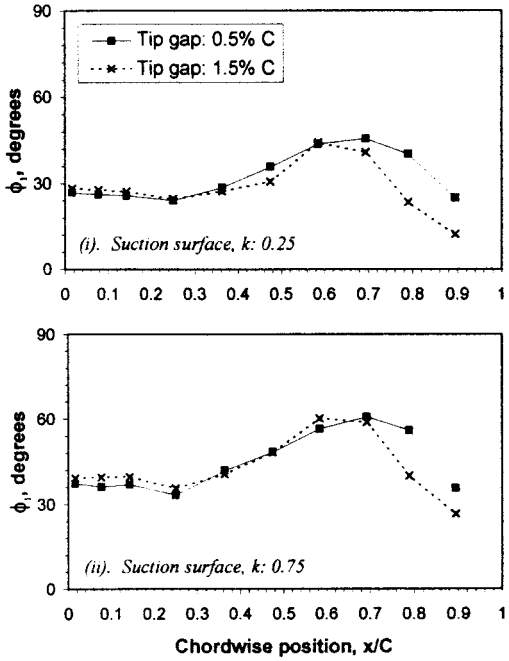

Fig. 14 Variation in phase of first harmonic pressure at tip section (90 percent span) with tip clearance – *k*: 0.25 and 0.75

Concluding Remarks

The results of two investigations, concerning the aerodynamic response of a turbine blade oscillating in a three-dimensional bending mode, have been presented. First, detailed and reliable three-dimensional test cases were provided for a range of reduced frequency, and the predictive capability of a three-dimensional time-marching Euler method was examined. The principal findings of this study are as follows:

- *Three-dimensional effects:* The test data exhibits a significant three-dimensional effect. The amplitude of the unsteady pressure response at different spanwise locations on the blade surface is largely insensitive to the local bending amplitude.
- *CFD predictions:* An extended three-dimensional time-marching Euler method demonstrated very good agreement with the test data for the full range of reduced frequency tested. The insensitivity to local bending amplitude was also captured by this method, while a quasi-three-dimensional version of this numerical method proved unable to predict this behavior. Discrepancies were, however, observed in the prediction of phase angle toward the trailing edge of the suction surface. This has been attributed to unsteady viscous effects in the test facility, induced by relatively strong diffusion toward the trailing edge of the suction surface.
- *Linearity:* Experimental and numerical tests for linearity demonstrated a predominantly linear behavior of the unsteady aerodynamics.

In addition, the influence of tip leakage on the local unsteady aerodynamic response of an oscillating turbine blade has been examined for the first time. Experimental measurements were presented for three settings of tip clearance over a range of reduced frequency, and the following observations made:

- *Influence of tip leakage:* The results showed a consistent variation in the amplitude of the unsteady pressure response at 90 percent span for changes in tip gap. This observation was apparent throughout the full range of reduced frequency tested, and was noted to correspond with localized regions where the tip leakage flow had a discernible impact on the steady flow blade loading characteristic. It is the authors' opinion that the apparent influence of tip leakage on the unsteady pressure response, at considerable distance from the blade tip (90 percent span), warrants further investigation into the local unsteady flow.

Acknowledgments

The research was performed at the School of Engineering, University of Durham, under the sponsorship of ALSTOM Energy

Limited. The authors would like to thank Drs. B. Haller and P. Walker of ALSTOM Energy for their technical support.

References

Bell, D. L., and He, L., 1997, "Three Dimensional Unsteady Pressure Measurements for an Oscillating Turbine Blade," ASME Paper No. 97-GT-105.

Bell, D. L., and He, L., 1998, "Three Dimensional Unsteady Flow Around a Turbine Blade Oscillating in Bending Mode—An Experimental and Computational Study," *Proc. 8th ISUAAT*, Stockholm, Sweden.

Bell, D. L., 1999, "Three Dimensional Unsteady Flow for an Oscillating Turbine Blade," Ph.D. Thesis, University of Durham, U.K.

Denton, J. D., 1983, "An Improved Time-Marching Method for Turbomachinery Flow Calculations," ASME *Journal of Engineering for Gas Turbines and Power*, Vol. 105, pp. 514–524.

Gerolymos, G. A., 1994, "Advances in the Numerical Integration of the Three-Dimensional Euler Equations in Vibrating Cascades," ASME JOURNAL OF TURBOMACHINERY, Vol. 115, pp. 781–790.

Hall, K. C., and Lorence, C. B., 1993, "Calculation of Three-Dimensional Unsteady Flows in Turbomachinery Using the Linearized Harmonic Euler Equations," ASME JOURNAL OF TURBOMACHINERY, Vol. 115, pp. 800–809.

He, L., and Denton, J. D., 1994, "Three Dimensional Time-Marching Inviscid and Viscous Solutions for Unsteady Flows Around Vibrating Blades," ASME JOURNAL OF TURBOMACHINERY, Vol. 116, pp. 469–476.

Jameson, A., Schmidt, W., and Turkel, E., 1981, "Numerical Solutions of the Euler Equations by Finite Volume Method Using the Runge–Kutta Timestepping Scheme," AIAA Paper No. 81-1259.

Sjolander, S. A., 1997, "Physics of Tip Clearance Flows I & II," VKI Lecture Series 1997–01 on Secondary and Tip-Clearance Flows in Axial Flow Turbomachines, Von Karman Institute for Fluid Dynamics, Belgium.

A Detailed Analysis of Film-Cooling Physics: Part I—Streamwise Injection With Cylindrical Holes

D. K. Walters

J. H. Leylek

Department of Mechanical Engineering,
Clemson University,
Clemson, SC 29634

A previously documented systematic computational methodology is implemented and applied to a jet-in-crossflow problem in order to document all of the pertinent flow physics associated with a film-cooling flowfield. Numerical results are compared to experimental data for the case of a row of three-dimensional, inclined jets with length-to-diameter ratios similar to a realistic film-cooling application. A novel vorticity-based approach is included in the analysis of the flow physics. Particular attention has been paid to the downstream coolant structures and to the source and influence of counterrotating vortices in the crossflow region. It is shown that the vorticity in the boundary layers within the film hole is primarily responsible for this secondary motion. Important aspects of the study include: (1) a systematic treatment of the key numerical issues, including accurate computational modeling of the physical problem, exact geometry and high-quality grid generation techniques, higher-order numerical discretization, and accurate evaluation of turbulence model performance; (2) vorticity-based analysis and documentation of the physical mechanisms of jet–crossflow interaction and their influence on film-cooling performance; (3) a comparison of computational results to experimental data; and (4) comparison of results using a two-layer model near-wall treatment versus generalized wall functions. Solution of the steady, time-averaged Navier–Stokes equations were obtained for all cases using an unstructured/adaptive grid, fully explicit, time-marching code with multigrid, local time stepping, and residual smoothing acceleration techniques. For the case using the two-layer model, the solution was obtained with an implicit, pressure-correction solver with multigrid. The three-dimensional test case was examined for two different film-hole length-to-diameter ratios of 1.75 and 3.5, and three different blowing ratios, from 0.5 to 2.0. All of the simulations had a density ratio of 2.0, and an injection angle of 35 deg. An improved understanding of the flow physics has provided insight into future advances to film-cooling configuration design. In addition, the advantages and disadvantages of the two-layer turbulence model are highlighted for this class of problems.

1 Introduction

Film cooling is commonly used in modern gas turbines to prevent hot-section components from failing at elevated temperatures. Increasingly, designers are trying to extract greater cooling performance from less coolant air, particularly in next-generation high-efficiency gas turbines. To make significant advances in cooling technology requires a fundamental understanding of the physical mechanisms involved in film-cooling flowfields. At the same time, designers need a truly predictive design tool that allows relatively quick turnaround times without the "build 'em and bust 'em" approach that is currently used. Computational fluid dynamics presents the designer with the potential for an effective, fast, and accurate method of achieving these goals.

A previously documented paper (Walters and Leylek, 1997) presented the results of a computational simulation of a three-dimensional jet-in-crossflow problem. A systematic computational methodology was adopted to ensure the most accurate results possible with the available tools. The case simulated was of a row of streamwise injected jets, with relatively short L/D ratios (3.5 and 1.75). The paper was primarily concerned with the downstream surface results, in the form of adiabatic effectiveness. The current study examines in detail the physical mechanisms associated with three-dimensional jet-in-crossflow problems, using the same case examined in Walters and Leylek above. The underlying flow physics found in film-cooling applications are documented using traditional as well as more novel vorticity-based analyses, which proved to be highly illuminating. The influence of physical mechanisms on film-cooling performance is highlighted. Additionally, the performance of the k–ϵ turbulence model with near-wall treatment based on the two-layer approach and with generalized wall functions is examined.

The overall scope of this work involves the description of the flow physics and film-cooling performance not only for the present case, but for four distinctly different classes of geometric configurations documented in companion papers. Part I examines a reference case of streamwise injection using cylindrical film holes. Part II examines the case of compound angle injection, again using cylindrical film holes. Part III examines shaped film holes with streamwise injection. Part IV examines the combination of shaped film holes and compound angle injection. As a whole, the paper documents in detail the underlying flow physics and the impact on film-cooling performance for a widely varied set of geometric configurations used in film-cooling designs.

2 Literature Review

2.1 Experimental Studies. A substantial amount of literature is available concerning experimental investigation of stream-

Contributed by the International Gas Turbine Institute and presented at the 42nd International Gas Turbine and Aeroengine Congress and Exhibition, Orlando, Florida, June 2–5, 1997. Manuscript received International Gas Turbine Institute February 1997. Paper No. 97-GT-269. Associate Technical Editor: H. A. Kidd.

wise injected film-cooling jets. One of the earlier studies was documented in Bergeles et al. (1976, 1977), which examined a single discrete jet injected normally and at a 30 deg angle to the crossflow. The authors documented jet lift-off and penetration of the crossflow boundary layer as blowing ratio increased, as well as the influence of the crossflow on the flow within the film hole itself. Andreopoulos and Rodi (1984) presented a detailed analysis of an isolated normal jet in crossflow. The paper paints a clear picture of the flowfield associated with the jet–crossflow interaction. Of particular interest is the counterrotating vortex pair found downstream of jet injection. Like Bergeles et al., the authors noted the influence of the crossflow on the flow within the film hole. Pietzryk et al. (1988, 1989, 1990) and Sinha et al. (1991) performed an experimental study on a row of discrete jets using film-hole L/D ratios representative of real film-cooling geometries. The shorter L/D ratios were found to significantly influence the flow physics and film-cooling performance. Many more examples of experimental investigations of jet–crossflow and film-cooling problems may be found in the open literature. However, regardless of the quality of the experimental work, measurements were only available at a limited number of locations, either on the surfaces or within the flowfield. In all cases, the authors were required to hypothesize about the underlying flow physics influencing the results, at least to some degree.

2.2 Computational Studies. Computational approaches to film-cooling problems suffer from their own set of difficulties. The earliest studies were limited to simplified geometries, including strictly Cartesian domains, "stair-step" representations of round film holes, and simulations confined only to the crossflow region. Early studies also used coarse grids and improper solution techniques. For example, Bergeles et al. (1978) used a "partially parabolic" scheme, which was inadequate to compute the highly complex recirculating type flow in the region of jet–crossflow interaction. As capabilities increased, it was found that much finer meshes, as well as more accurate discretization schemes, were needed to improve the accuracy of the results. Demuren (1982) showed that for identical grid meshes, the higher-order QUICK discretization scheme (Leonard, 1979) performed better than the first-order hybrid scheme (Patankar, 1980). With regard to geometry and grid generation, the recent availability of unstructured mesh solvers allows superior geometry representation and the ability to concentrate grid nodes efficiently in critical regions of the flowfield to obtain grid independence. Recently, attention has turned to the accuracy of the computational model itself, referring to the domain, model geometry, and type and location of boundary conditions in the simulation, as well as assumptions about the character of the flow (three-dimensional, compressible, turbulent, etc.). Leylek and Zerkle (1994) were the first to model the flow within the coolant supply plenum and film hole in addition to the crossflow. They found the flow upstream of the jet exit plane to be very complex, with a considerable influence on the coolant jet exit conditions. The jet exit conditions influence the subsequent downstream behavior and overall film-cooling performance. This fact was highlighted by Garg and Gaugler (1995) in a paper in which they showed that slightly different exit plane distributions in the computational simulation can result in significantly different behavior downstream. For example, heat transfer coefficient levels were shown to differ by as much as 60 percent depending on the type of exit distribution used.

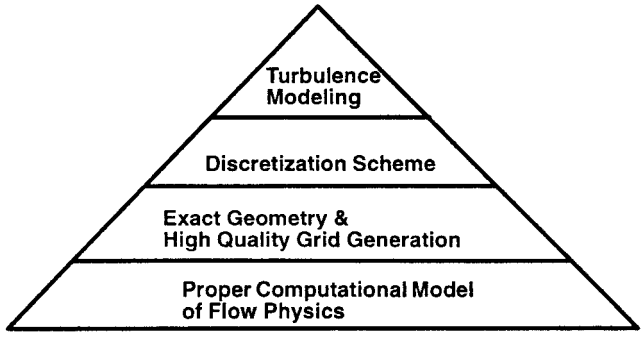

Fig. 1 Illustration of simulation hierarchy adopted for this study showing how each step builds upon the last

Very recently, a paper documented by the present authors (Walters and Leylek, 1997) presented a systematic computational methodology for this class of problems, in which each critical aspect of a simulation was addressed in the most effective manner possible. The purpose of the approach was to bring the current computational capability to a point where it is limited primarily by the turbulence treatment. Obviously, improvements to turbulence treatment for film-cooling problems is an important area of research, and computational capabilities will continue to improve as advances are made in turbulence modeling. However, even without "perfect" turbulence models, can computational results be used in conjunction with experimental data to document the key underlying physics associated with film-cooling flowfields? Also, do the CFD results have sufficiently high internal consistency to make them useful in assessing the relative performance of different film-cooling designs? This four-part paper seeks to answer these questions.

3 Computational Methodology

Walters and Leylek (1997) documented a systematic computational methodology to be used in all computational treatments of film-cooling problems. A simulation hierarchy was adopted in which each of four critical areas are addressed, and in which each step builds upon the previous step. The hierarchy is shown graphically in Fig. 1. The current results were obtained using this methodology. For further details, the reader is directed to Walters and Leylek (1997).

Nomenclature

D = film-hole diameter
DR = density ratio = ϱ_j/ϱ_∞
LE = film-hole leading edge
L/D = film-hole length-to-diameter ratio
M = blowing (or mass flux) ratio = $\varrho_j v_j/\varrho_\infty u_\infty$
T_j = coolant jet temperature
T_{aw} = adiabatic wall temperature
T_∞ = mainstream temperature
TE = film-hole trailing edge
TL = turbulence level = $(\frac{2}{3}*k)^{1/2}/u_\infty*100$
$\mathbf{V}$ = velocity vector = $(u\mathbf{i} + v\mathbf{j} + w\mathbf{k})$
k = turbulence kinetic energy
u_∞ = mainstream velocity
v_j = jet exit velocity
x = streamwise coordinate
y = vertical (away from wall) coordinate
y^+ = nondimensional distance from wall = $y*(\tau_w/\varrho_w)/\nu_w$
z = lateral coordinate
η = adiabatic effectiveness = $(T_\infty - T_{aw})/(T_\infty - T_j)$
$\bar{\eta}$ = laterally averaged adiabatic effectiveness
ϱ_j = coolant density
ϱ_∞ = mainstream density
ζ = vorticity vector = $(\zeta_x\mathbf{i} + \zeta_y\mathbf{j} + \zeta_z\mathbf{k})$

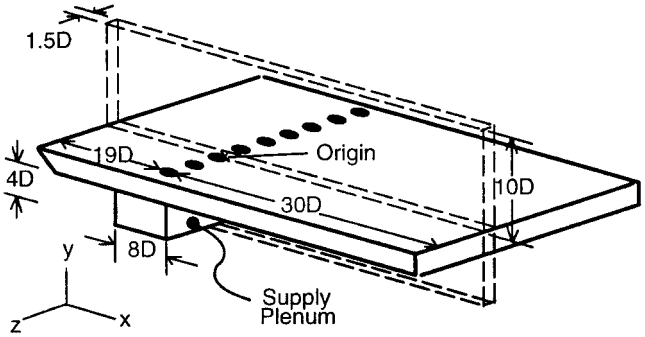

Fig. 2 Schematic of the experimental test setup, including extent of the computational domain in the *x*, *y*, and *z* directions

4 Present Contributions

This paper examines the essential flow physics of film-cooling flowfields. The results were obtained using fully elliptic Reynolds-averaged Navier–Stokes computations for the case of a row of three-dimensional round jets with streamwise injection on a flat surface. The test case examined exactly matches that documented in Walters and Leylek (1997). Specific objectives of this study are to:

- highlight all prominent flow structures and mechanisms in the supply plenum, film-hole, and crossflow regions that are associated with jet–crossflow interaction, particularly the well-known counterrotating vortex pair
- identify the source of the counterrotating vortices
- document the influence of these mechanisms on film-cooling performance
- suggest possible techniques to improve film-cooling performance
- serve as a reference case for the more complex geometries examined in the companion papers (Parts II–IV)
- demonstrate that CFD can be used to consistently resolve complex film-cooling flowfields
- highlight the differences between wall functions and a two-layer zonal model for the near-wall turbulence treatment

5 Test Case: Three-Dimensional Streamwise Injected Jet

The three-dimensional validation test case is based on the experimental work of Pietzryk et al. (1988, 1989, 1990) and Sinha et al. (1991). The authors documented flowfield and adiabatic effectiveness measurements for a single row of holes on a flat surface, with a 35 deg streamwise injection angle and a film-hole pitch-to-diameter ratio of 3. The experimental setup is shown in Fig. 2. The film-hole diameter was 12.7 mm. The row of holes was located 19 diameters (19 D) downstream of the flat plate leading edge, with measurements obtained from 1 D upstream of the film holes to 30 D downstream. The oncoming boundary layer was suctioned at the leading edge of the test surface, allowing a new boundary layer to develop upstream of the film holes. This boundary layer was experimentally determined to be fully turbulent from the leading edge onward, due to a tiny separation bubble located at the flat plate leading edge.

The coolant fluid was injected from a supply plenum located beneath the test section, as shown in Fig. 2. Density ratio was controlled by varying the temperature of the coolant while maintaining the crossflow temperature at 302 K. The authors documented that coolant mass flow rates were equal for each of the film holes across a given test section.

Two series of measurements were performed. The first, documented in Pietrzyk et al. (1988, 1989, 1990), used a length-to-diameter ratio of 3.5, with detailed measurements obtained for velocity and turbulence quantities throughout the flowfield. Density ratios of 1.0 and 2.0 were examined, with blowing ratios from 0.25 to 1.0. The second series, described in Sinha et al. (1991), used $L/D = 1.75$ and documented the downstream adiabatic effectiveness results, both along the centerline and at varying lateral locations. The density ratios examined ranged from 1.2 to 2.0, and blowing ratios ranged from 0.25 to 1.0.

6 Details of Numerical Simulation

Six different cases were simulated in the present study. In all cases, the density ratio (DR) was 2. For the geometry with $L/D = 3.5$, blowing ratios of 0.5 and 1 were examined, which correspond to two of the experimental cases. In addition, a case of $M = 2$ was examined, which does not have an experimental counterpart, but which shows the effects of significantly increased blowing ratio. In the case of $M = 1$, the simulation was repeated using the two-layer turbulence model instead of generalized wall functions, in order to document the differences between the two approaches.

6.1 Wall-Function Cases. The computational model for this case matched the experimental test case, and was identical to the model used by Leylek and Zerkle (1994) and Walters and Leylek (1997). The computation simulated a row of film holes using the assumption of flow symmetry at the film-hole centerline and at the one-half pitch line. The region of influence for a single film-hole within the row is shown in Fig. 2. The key aspect of the model was the application of the coolant boundary condition within the supply plenum, instead of in the highly complex film-hole inlet or exit regions. The computational extent in the y direction was 10 D above the test surface, which was far enough from the near-field region that a "slip condition" with zero normal gradients could be applied with confidence. Velocity at the crossflow inlet was a uniform 20 m/s, with an inlet temperature of 302 K. The plenum inlet velocity was varied in order to impose the proper blowing ratio, as was done in the experiments. For all computational cases, coolant inlet temperature was 153 K, corresponding to a density ratio of approximately 2.0. At both the crossflow and plenum inlet planes, turbulence intensity was 2 percent, and the length scale was taken as $\frac{1}{10}$ of the inlet extent in the y direction (crossflow) and x direction (plenum). All walls were adiabatic. A constant pressure condition was applied at the outlet, with all other flow variables upwinded.

The development of the computational grid mesh for the cases using wall functions was documented in Walters and Leylek (1997). The background grid was generated using the I-DEAS Solid Modeling and Finite Element Analysis software from SDRC, Inc. A subregion technique, in which the flow area was divided into several smaller volumes, was used in order to control the node placement within the domain. Examples of the surface grid indicating the refinement levels and grid quality in the vicinity of the film-hole exit and near-field region are shown in Fig. 3.

The simulations based on the wall-function approach were performed using the RAMPANT software package from Fluent, Inc. A second-order discretization scheme was used for all flow variables. For all cases, convergence was determined based on three criteria: first, a reduction in normalized residuals of at least three orders of magnitude, where a residual represented an average imbalance in a cell for each flow variable; second, by monitoring the overall imbalance of mass and energy within the domain and ensuring it was less than 0.01 percent; and third, by noting that the time-marching scheme had reached a "steady-state" condition, i.e., no flow variables were seen to change with increasing time steps. Grid independence for each case was established by first running on the background grid of approximately 125,000 cells, and then using the solution-based adaptation capability to adapt the grid based on gradients of all flow variables. Typically, two adaptations were performed, with the final meshes containing approximately 200,000 to 250,000 cells. The solution was processed on a 64 CPU Intel Paragon computer. Typically, convergence was obtained in approximately 2000 iterations on 24 processors, with a wall-clock run time of about one full day.

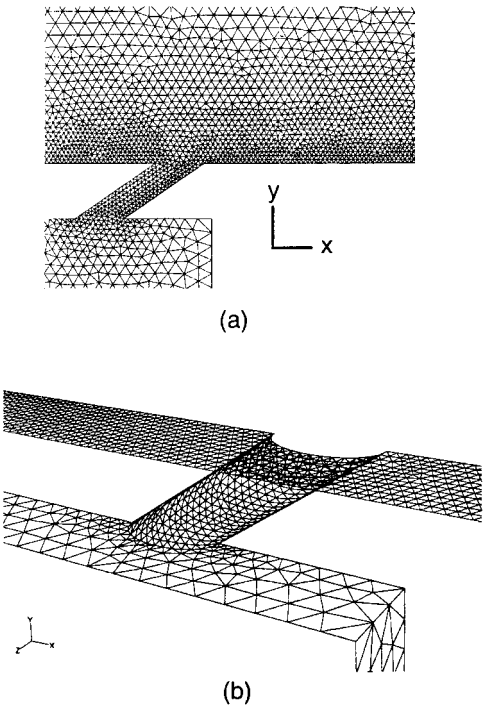

Fig. 3 Close-up of surface grid showing centerline plane (*a*) and bottom wall, film-hole, and plenum wall surfaces (*b*)

Turbulence modeling for the problem used the standard k–ϵ model of Launder and Spalding (1974). Near-wall quantities were calculated for all cases using the generalized wall functions available in RAMPANT. The combination of standard k–ϵ with wall functions represents what is currently the standard approach in complex problems. By minimizing sources of error due to computational modeling, grid generation, and discretization scheme, the performance of the standard k–ϵ model with wall functions can be determined accurately in the present simulations. Neither the turbulence models nor the wall functions were adjusted in any way to provide better agreement with experimental data.

6.2 Two-Layer Model Case. The computational model for the case using the two-layer approach was similar to that described above. In order to reduce the total number of grid cells in the entire domain to a manageable level, the domain extended only 8 D upstream of the leading edge of the film hole and 16 D downstream of the trailing edge. A boundary layer profile was applied at the inlet plane such that δ/D at the leading edge matched the experiments. The exit boundary was set as a constant-pressure condition based on the results obtained from the wall-function cases. All other aspects of the model matched the cases discussed above.

The use of the two-layer model required a different approach for grid generation than above. The initial grid was produced as a multiblock structured grid with cells concentrated near walls, within the film hole, and in the near-field region. All of the cells were placed in the active regions of the flowfield; an approach that differs from single-block structured grid generation. For the initial grid, the first layer of cells was sized so that the y^+ value in a turbulent boundary layer would be 3, resulting in a first-cell height of 0.1 mm. A uniform layer of ten cells was placed near the walls to resolve the viscous sublayer and buffer regions. The initial or background grid contained 255,912 cells. After a solution was obtained, the grid was adapted based on flowfield gradients to obtain a final grid. This study did not attempt to document the minimum number of cells needed to obtain grid independence for this case. Instead, the grid was heavily adapted to ensure that the results showed the true performance of the turbulence wall treatment. The final grid contained 618,960 cells.

The simulation was performed with the Fluent/UNS solver from Fluent, Inc., using the same second-order discretization scheme found in the RAMPANT solver. Convergence was determined based on reduction of normalized residuals three orders of magnitude and overall mass and energy imbalance within the domain of less than 0.01 percent. The solution was processed on a 4 CPU Sun SPARCserver 1000E with 1.024 Gbytes of core memory. Convergence at each grid level was typically obtained after about 1500 iterations, with a wall-clock run time on the order of one week.

Turbulence away from the walls was modeled using the standard k–ϵ equations as above. Near the wall, however, a two-layer zonal model was implemented. With this approach, the turbulent kinetic energy is computed in the viscous sublayer and buffer region using the same k equation as elsewhere. Turbulent dissipation rate, ϵ, is computed algebraically based on a prescribed length scale. The turbulent viscosity, μ_t, is given by: $\mu_t = \varrho C_\mu \sqrt{k}\, l_\mu$ where l_μ is another prescribed length scale. Both of the length scales are algebraically related to the distance from the wall. For more details of the numerics involved with the two-layer zonal model, the reader is referred to the Fluent/UNS User's Guide (1996).

7 Results and Discussion

Walters and Leylek (1997) documented many of the results from the wall-function simulations, primarily in the form of comparison with experiments for downstream adiabatic effectiveness. These comparisons showed accurate agreement with experiments, and served to validate the computational methodology which was implemented. Figure 4 shows a sample of these results, including the comparison after jet skewness—which was present in the experiments—was accounted for. Figure 4(*a*) shows centerline adiabatic effectiveness for the cases of $L/D = 1.75$, $M = 0.5$ and 1. Figure 4(*b*) shows the lateral variation of adiabatic effectiveness at $x/D = 15$ for the same cases. Note that the most significant disagreement occurs immediately downstream of the jet exit. The following sections document the physical mechanisms responsible for the surface results. The results will focus on the cases with $L/D = 3.5$, since experimental flowfield data are available for these cases only. An "inside out" presentation will be used in which each of the critical regions of the flowfield are examined separately, although the interdependence of the different regions is highlighted. Unless otherwise noted, results are from the cases that used the generalized wall functions as the near-wall treatment.

7.1 Flow in Coolant Supply Plenum and Film Hole. The coolant supply plenum acts very much like a pressurized vessel to which the film hole is attached. Velocities are extremely small except near the film-hole entrance, where the fluid accelerates and turns to enter the film hole. The complex flow within the film hole has been documented in Leylek and Zerkle (1994) and Walters and Leylek (1997). Separation and flow turning near the film-hole inlet result in a jetting region along the upstream wall as well as counterrotating secondary flow within the film hole. This separation within the film hole was first hypothesized in Pietrzyk et al. (1990). The relative strength of the jetting and secondary flow increases with increasing blowing ratio, and can have a significant impact on the jet exit conditions, as seen below.

7.2 Jet Exit Conditions. The distribution of flow variables at the jet exit is influenced by two primary mechanisms. The first is concerned with the flow within the film hole itself. The jetting and counterrotating flow serve to make higher momentum coolant fluid exit from the upstream half of the film-hole exit plane. The second mechanism is due to the interaction of the exiting jet with the crossflow. The impingement of the oncoming crossflow on the jet results in a high-pressure zone upstream of the jet leading edge (LE), while the flow turning associated with the exiting coolant results in a low-pressure region downstream of the jet trailing edge (TE). The consequent pressure gradient serves to increase the

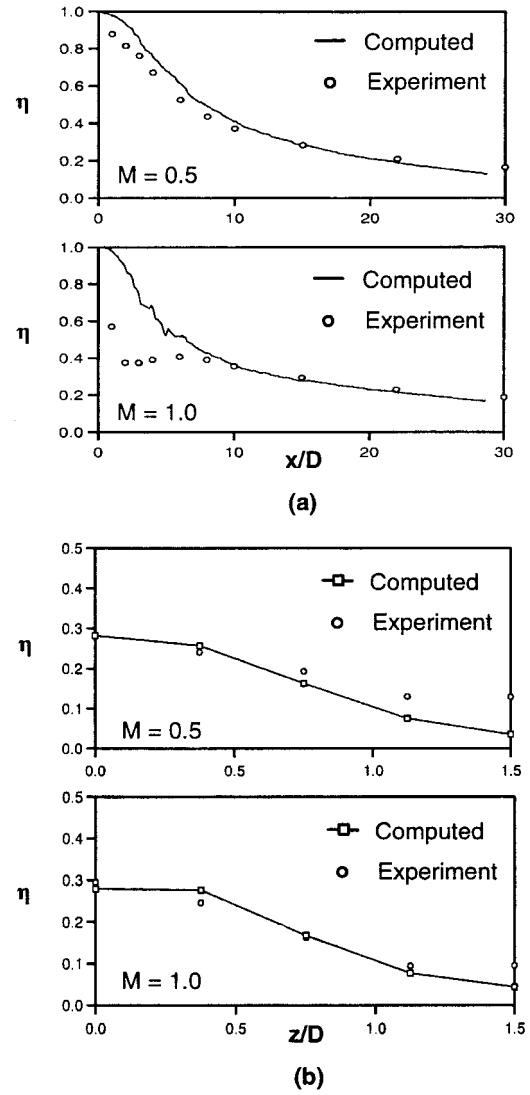

Fig. 4 Centerline adiabatic effectiveness (*a*) and lateral variation of effectiveness at *x*/*D* = 15 (*b*) show good agreement with experimental data

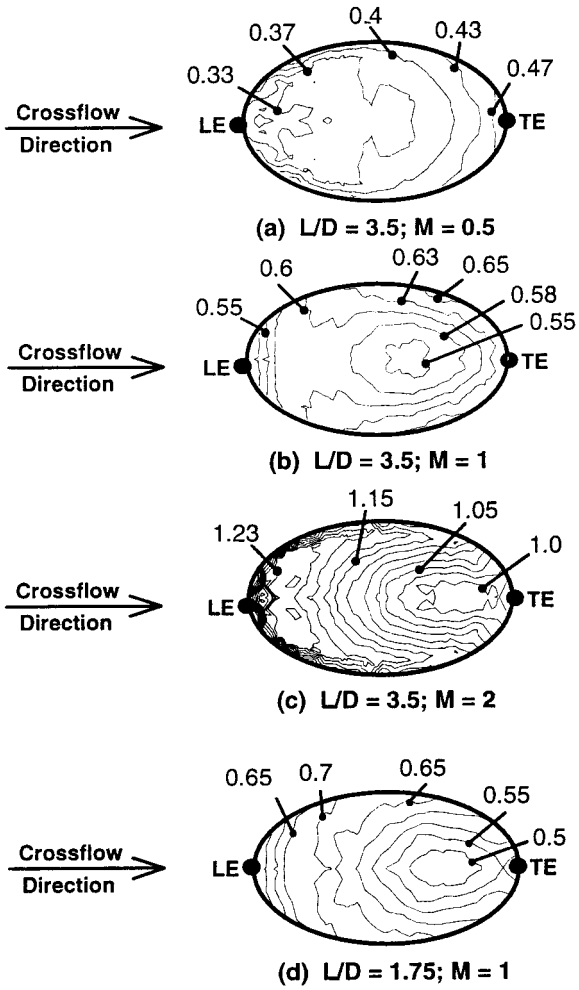

Fig. 5 Velocity magnitude contours in the jet exit plane highlight competing mechanisms that influence the jet exit conditions

momentum of the fluid exiting from the downstream portion of the jet exit. In general, the relative strength of these two mechanisms is dependent on the blowing ratio, density ratio, and geometry. For the cases considered here, it is dependent on blowing ratio and L/D ratio. As blowing ratio increases the effect of the flow in the film hole becomes more significant, pushing the flow variable distribution toward the upstream side of the jet exit. Conversely, at low blowing ratios, the influence of the flow in the film hole is less important, and variables are shifted toward the downstream of the exit. Figure 5 shows this graphically, in which the contours of normalized velocity are shown in the jet exit plane. The film-hole L/D ratio is also significant in determining the relative strength of the two mechanisms mentioned above. As L/D decreases, the effects of the separation region have less time to attenuate, and therefore exert more influence on the jet exit conditions, as shown in Fig. 5(*d*).

7.3 Near Field of Jet–Crossflow Interaction. The interaction of the exiting coolant jet with the crossflow results in an extremely complex flowfield in the immediate vicinity of the jet exit. The jet acts as a blockage to, and is turned in the downstream direction by the crossflow. Velocity vectors in the $z = 0$ centerline plane are shown in Fig. 6(*a*) for the case of $L/D = 3.5$ and $M = 1$. It is apparent that the exiting jet is almost immediately turned in the streamwise direction. Pressure contours in the centerline plane for the same case are shown in Fig. 6(*b*). The high-pressure region upstream of the exiting jet and low-pressure region downstream are apparent. Of particular significance to the flow in the near field is the formation of separate flow regions, secondary flow structure, and turbulence production. Each of these are discussed below.

When examining the near-field behavior, it is helpful to separate the effects of bulk fluid motion from the effects of diffusion. This is often difficult if only primary variables are examined—temperature, for example. The difficulty lies in delineating the different regions of the flowfield, e.g., the "dividing line" between jet and crossflow. Moussa et al. (1977) proposed using the vorticity field to describe the boundaries between the jet and the crossflow for an experimental investigation of a normal jet in crossflow. This technique, with some extension, has been used in the present study to obtain a clearer picture of the flow physics.

Pietzryk et al. (1989) documented the existence of shear layers downstream of the jet exit along the centerline plane, which represented a division between different regions in the flowfield. These regions included the crossflow above the coolant, the coolant jet, the wake region, and (for higher blowing ratios) the entrained crossflow fluid beneath the coolant. The shear layers separating each of these regions were determined experimentally and are shown in Fig. 7. The figure shows profiles of the velocity gradient $\partial u/\partial y$ in the centerline ($z = 0$) plane for $L/D = 3.5$ and $M = 0.5$ (*a*) and $M = 1$ (*b*). Note that since the velocity gradient $\partial v/\partial x$ is almost zero here, $\partial u/\partial y$ is approximately equal to the negative of the z-direction vorticity. Shear layers are represented

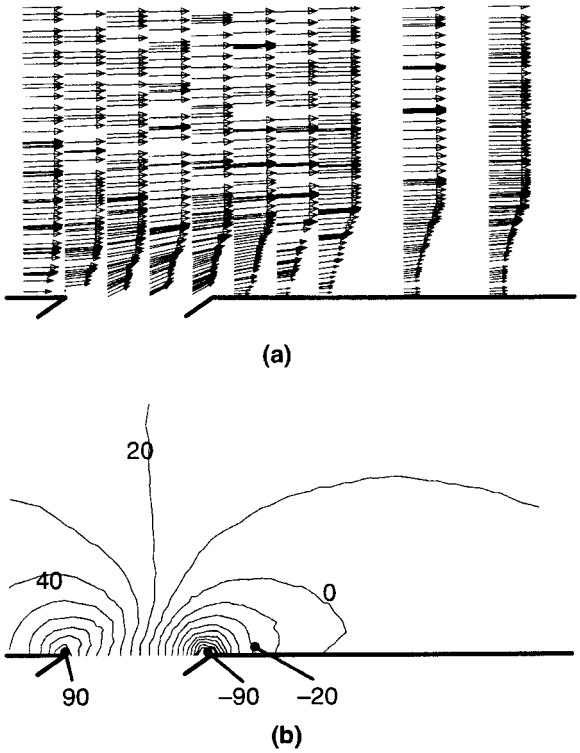

Fig. 6 Velocity vectors (*a*) and gage pressure contours in Pa (*b*) for $L/D = 3.5$ and $M = 1$ show jet bent quickly in downstream direction and pressure gradient at the jet exit

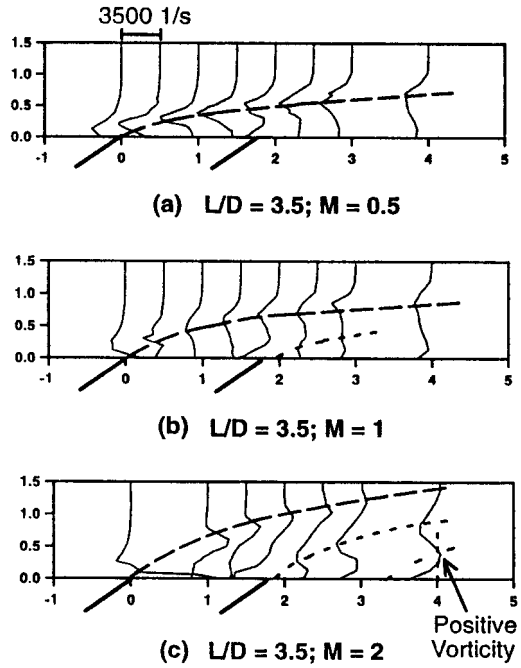

Fig. 8 Profiles of *z*-direction vorticity for three cases highlight the computed existence of those regions found experimentally and shown in Fig. 7

by peaks in the profiles. Note particularly the shear layer over the wake region (S5 in Fig. 7).

These regions were observed in the present study as well. Figure 8 shows the profiles of *z*-direction vorticity obtained computationally at several locations in the near field. The shear layers in Fig. 7 are apparent for the two higher blowing ratio cases. In addition, for the case of $M = 2$, the lift-off of the wake and the entrainment of crossfluid fluid beneath the jet is apparent by $x/D = 4$, as indicated by the positive vorticity at this location.

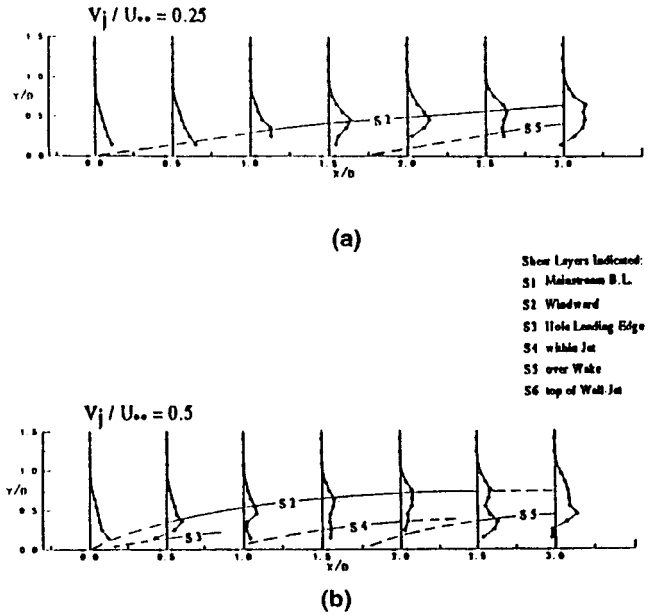

Fig. 7 Experimental profiles of velocity gradient $\partial u/\partial y$ show separate regions of flowfield downstream of jet exit along $z = 0$ centerline

Computationally, it was desired to determine exactly what causes the wake region shown in Figs. 7 and 8. Figure 9 shows the profiles of temperature gradient magnitude for the bounding cases with $M = 0.5$ and $M = 2$. The peaks in the profiles represent the dividing line between coolant and crossflow fluid along the centerline. Comparison with Fig. 8(*a*) and 8(*c*) indicates that the wake is in fact made up of coolant fluid. The reason for this is shown in Fig. 10. Here pathlines emanating from the film-hole exit plane show the fluid in the film-hole boundary layers is tucked underneath the jet core by the low-pressure zone located downstream of the trailing edge. This low-momentum fluid encounters an adverse pressure gradient (see Fig. 6(*b*)) as it moves downstream, increasing the velocity defect. While plausible, this explanation of the wake structure may not be correct. Pietrzyk et al. (1989) hypoth-

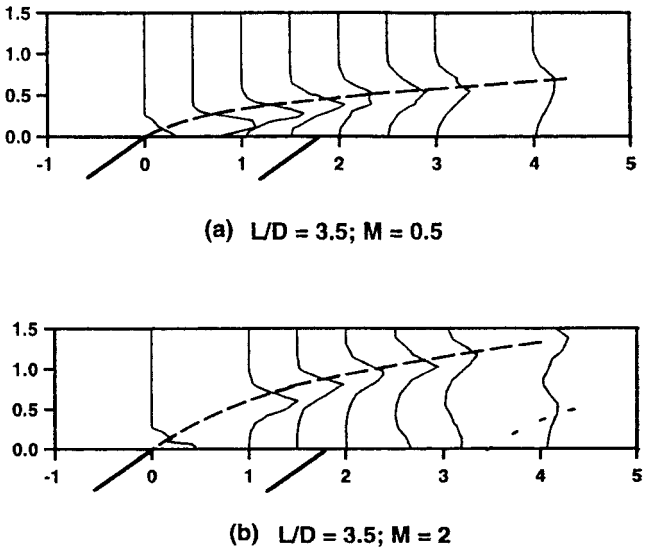

Fig. 9 Profiles of temperature gradient magnitude along the centerline show that the wake region is made up of coolant fluid

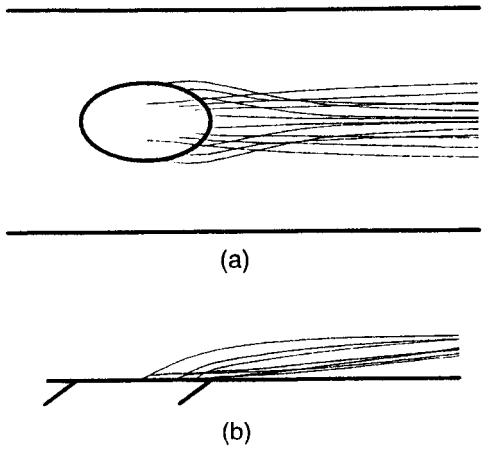

Fig. 10 Coolant path lines show the movement of the fluid in the film-hole boundary layers beneath the core coolant fluid, creating the wake region

esized the existence of a reverse flow zone immediately downstream of the trailing edge, too small to be detected with the instruments used. Similarly, it is possible that a small reverse flow zone may not be resolved with the coarser grid used with wall functions. This is examined more closely in Section 7.5 for the much finer grid, which was used in conjunction with the two-layer near-wall treatment.

As the fluid moves downstream, the coolant jet/wake is moved away from the wall along the centerline by the well-known counterrotating vortex structure. This secondary flow is shown computationally and experimentally in Fig. 11 at a downstream location $x/D = 5$ for the case of $L/D = 3.5$ and $M = 1$. As has been well documented, the strength of the counterrotating motion increases with increasing blowing ratio. The counterrotating vortices are

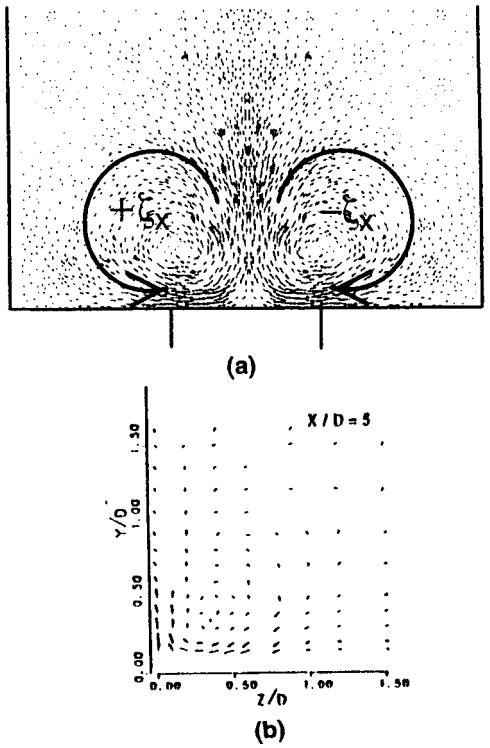

Fig. 11 Velocity vectors in a constant *x*-coordinate plane at $x/D = 5$ for $M = 1$ show counterrotating vortex structure present in computational (*a*) and experimental (*b*) results

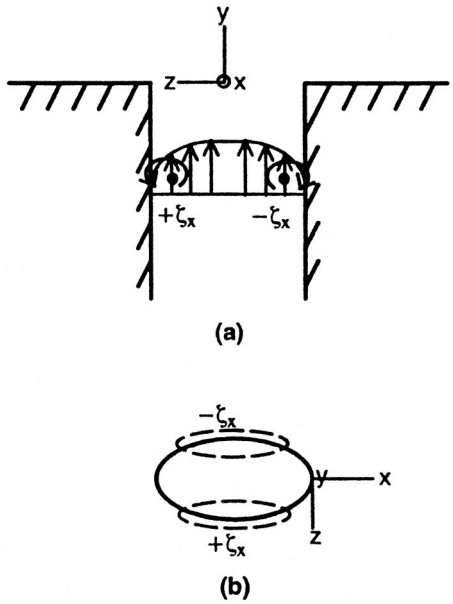

Fig. 12 Illustration of the streamwise vorticity exiting the film hole in the boundary layers

known to have a detrimental effect on the film-cooling performance. The following discussion addresses the sources of this secondary motion in terms of a vorticity analysis. Knowledge of the causes of the secondary motion can be used to reduce its impact on the film-cooling performance.

There are two contributing sources for the counterrotating vortices: the streamwise oriented vorticity contained in the film-hole boundary layers and the shearing between the jet and crossflow due to the mismatch in streamwise momentum. The vorticity exiting the film hole has been found to be more significant, and will be examined first. An illustration of the vorticity within the film-hole boundary layers is shown in Fig. 12. It is apparent that the boundary layers exiting on the lateral edges of the film hole will contain x-direction vorticity, ζ_x. This exiting vorticity can be seen in Fig. 13, which shows contours of streamwise vorticity in constant x-coordinate planes at different locations. The locations of maximum vorticity correspond to the centers of the counterrotating vortices. Downstream of injection, the vorticity "pockets" are diffused outward and realigned by the wall. Consequently, the counterrotating vortices grow larger and become less strong. For lower blowing ratios, the vorticity pockets remain close to the wall due to the low vertical momentum of the coolant fluid. The wall has a destructive effect on the streamwise vorticity, as it reorients the vorticity vector to the z direction. Correspondingly, the counterrotating vortices degrade rapidly. At higher blowing ratios, the pockets are located farther from the wall by the increased vertical momentum of the exiting coolant. The streamwise vorticity in this case is dissipated less rapidly and the counterrotating vortices are apparent much farther downstream. Although the geometry for this case is fixed, it should be noted that the distance between the vorticity pockets or vortex centers is also significant. If vorticity pockets of opposite sign are located close together, there will be a net cancellation, resulting in dissipation of the vortices. On the other hand, if the vortex centers are located far apart, the induction lift is reduced, as is the convective strength of the secondary flow at the centerline. These points are addressed in more detail in the companion paper designated Part III.

The shearing between the exiting jet and the crossflow is not a significant contributor to the counterrotating vortex formation for three reasons. First, the region where most of the jet–crossflow interaction occurs is well within the crossflow boundary layer, and so the shearing is much less strong than would occur for example in a jet exiting from a pipe far from a wall (offset jet). Second, the

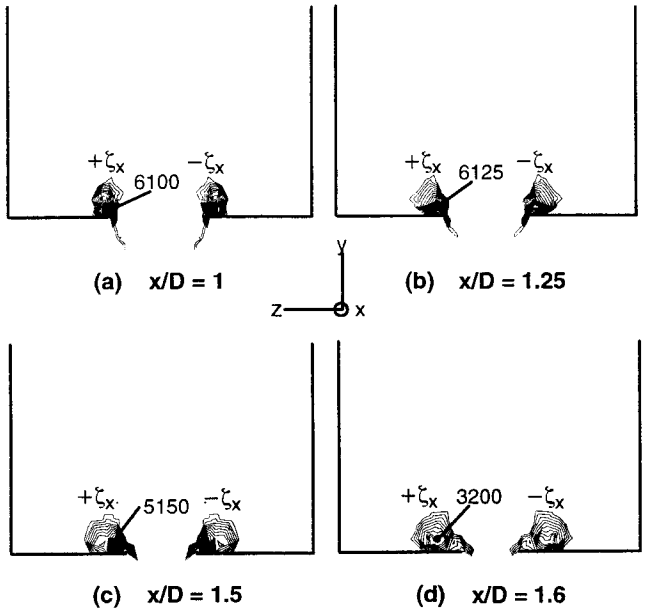

Fig. 13 Contours of streamwise (*x*-direction) vorticity show the vorticity exiting the film hole, resulting in the counterrotating structure shown in Fig. 11 above

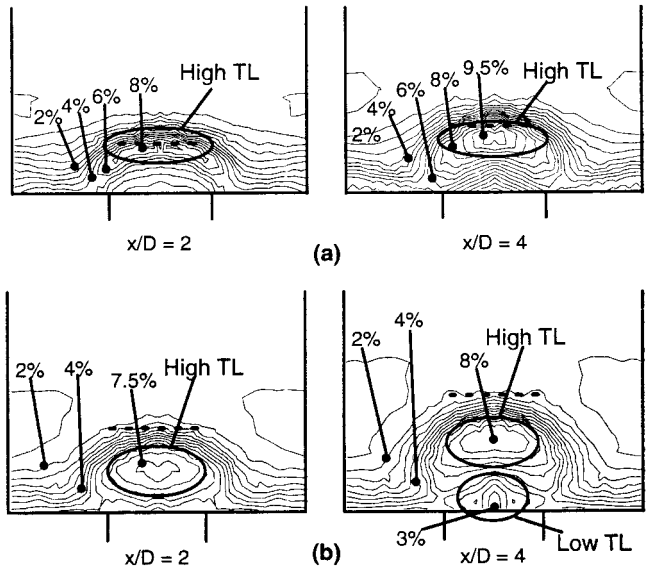

Fig. 14 Contours of turbulence level for the case of $M = 0.5$ (*a*) and $M = 1$ (*b*) at two downstream locations show the influence of two different sources of turbulence production

y-direction vorticity generated by the shearing of the jet is not significantly realigned to the *x* direction simply because the coolant exits with a shallow discharge angle (see Fig. 6(*a*)). This is very different from a normal jet case, in which significant realignment would occur due to the almost 90 deg bending of the jet after exiting the film hole. Finally, the positive *y*-direction vorticity produced at the jet–crossflow interface is counteracted by the negative *y*-direction vorticity exiting the film hole. This is most significant at higher blowing ratios, where the jet and crossflow velocities are approximately equal, and little ζ_y is in fact produced at the jet–crossflow interface.

Turbulence in the near field has a significant effect on the diffusion and dissipation of the coolant jet, as has been documented experimentally and computationally. The major source of turbulent kinetic energy varies according to the operating conditions. At low blowing ratios, the turbulence is produced primarily in the shear layer between the crossflow and the exiting jet due to the mismatch in the streamwise momentum. As blowing ratio increases, this velocity mismatch decreases and the turbulence production within the film hole becomes the dominant source. Figure 14 shows turbulence level contours (TL) in constant *x*-coordinate planes at $x/D = 2$ and 4 for the cases of $M = 0.5$ (*a*) and $M = 1$ (*b*). The location of the shear layer between the jet and crossflow is indicated with a straight dashed line. The location of maximum TL indicates the major source. For the higher blowing ratio case, the turbulence leaves the coolant jet exit plane after being generated in the separation region near the inlet plane of the film hole. Also, at higher blowing ratios, turbulence is produced in the shear layer between the wake and the jet region, resulting in a turbulent "core" within the coolant for several diameters downstream.

The mechanisms mentioned above serve to locate the coolant in the near field. Induction lift is generated when two counterrotating vortices are in close proximity to each other; therefore, the counterrotating vortex structure shown above lifts the coolant upward away from the wall. Near the test surface, lateral diffusion is opposed by convection toward the centerline. Therefore, lateral diffusion is low near the wall. Likewise, at the centerline, diffusion of the coolant downward toward the wall is opposed by upward convection, reducing the film-cooling effectiveness. Temperature contours for $M = 0.5$ and $M = 1$ are shown in Fig. 15 at downstream locations of $x/D = 2$ and $x/D = 4$. It is apparent that for lower blowing ratios the coolant remains near the wall, diffusing outward as it moves downstream. Upward lift is imperceptively low and lateral diffusion is opposed by weak secondary flow. At the higher blowing ratio, the coolant is seen to be lifted away from the wall and a "pinching" effect is visible near the wall, due to the movement of crossflow fluid toward the centerline by the relatively strong counterrotating vortices. The net result is that as more coolant is added via increasing blowing ratio, the effects of higher turbulence and, more importantly, of the stronger counterrotating vortices, decrease the effectiveness. It is apparent that the most significant improvement to film-cooling performance will involve reducing the impact of the counterrotating vortex structure. Ways of accomplishing this include: realigning or reducing the

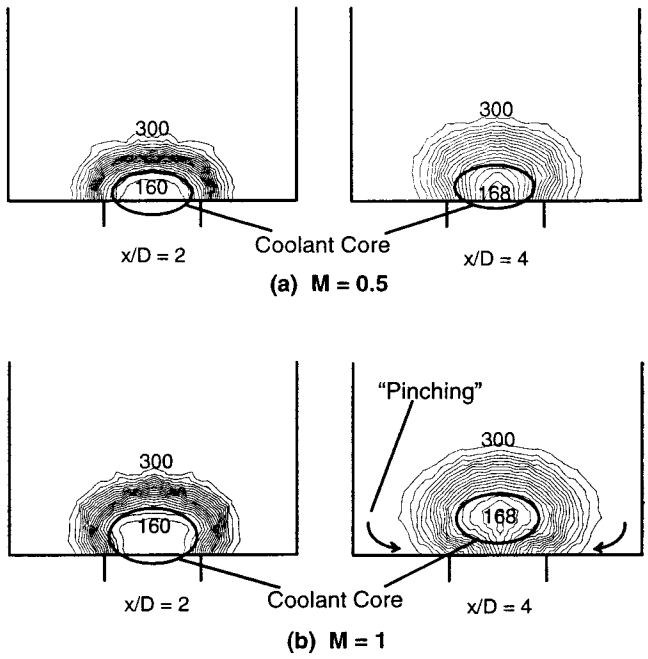

Fig. 15 Temperature contours in Kelvin for $M = 0.5$ (*a*) and $M = 1$ (*b*) at two downstream locations highlight the pinching in of the crossflow fluid and the lift-off of the coolant core due to the secondary motion

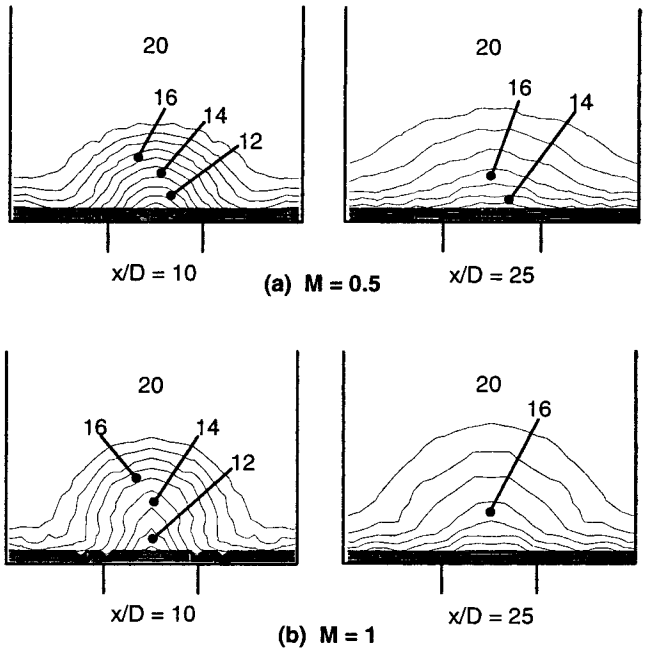

Fig. 16 Velocity contours downstream of near-field interaction show wakelike structure returning to boundary-layer-like flow

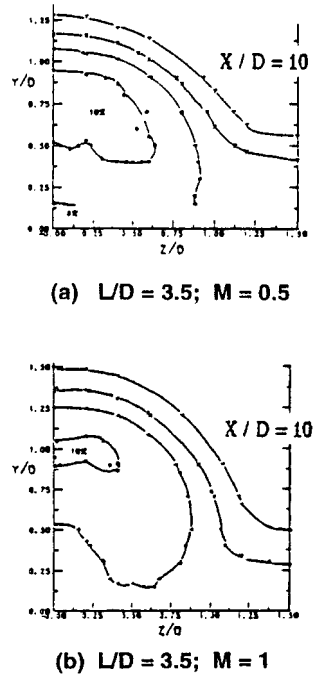

Fig. 17 Experimental velocity contours show similar structure to the computed contours in Fig. 15

strength of the vorticity field exiting the jet; locating the high-vorticity pockets close to the wall in order to dissipate them rapidly; and increasing the distance between vortex cores, reducing the induction lift and the convective strength of the secondary flow at the centerline. Each of these approaches to improving film-cooling performance are examined in Part III of this paper.

7.4 Downstream of Jet–Crossflow Interaction. As close as 5 diameters downstream, the secondary flow becomes negligible for all of the cases considered in this paper. The flow assumes an appearance much like a wake, with a momentum deficit due to the exiting coolant, and momentum, thermal energy, and turbulent energy are diffused in all directions. The location of the coolant core varies with blowing ratio, depending on where it has been deposited during the near-field interaction. Figure 16 shows the streamwise velocity (u) contours at two different downstream locations for $M = 0.5$ and $M = 1$. Comparable experimental contours are shown in Fig. 17. The wakelike behavior is apparent, and the flow moves exponentially toward a boundary layer situation in the downstream direction. Figure 18 shows the temperature contours for the same cases in the same locations. The diffusion of the coolant as it travels downstream is apparent. It is most significant to note that the downstream behavior is highly sensitive to the near-field interaction, which serves to locate the coolant at some given position away from the wall.

7.5 Two-Layer Zonal Model. Results obtained with the two-layer model differed most significantly from those obtained with wall functions in the region immediately downstream of the trailing edge. The use of the two-layer model allowed a much finer grid in this region, resulting in a better description of the flowfield. The two-layer model simulation resolved a small reverse flow zone beneath the exiting jet near the centerline. This reverse flow had been hypothesized by Pietrzyk et al. (1989). Velocity vectors along the centerline are shown in Fig. 19. The reverse flow region is comprised of slow-moving fluid in the crossflow boundary layer, which is tucked beneath the exiting jet by the low-pressure zone downstream of the trailing edge. There is a saddle point where the crossflow fluid moving toward the centerline from either side meets beneath the exiting jet. This is shown by the pathlines in Fig. 20, in which computational "massless particles" were released at locations of $x = 10$ mm and 0.1 mm from the wall. The movement of crossflow fluid beneath the exiting jet due to the pressure gradient is apparent, as is the reverse flow. Crossflow fluid not reversed by the pressure gradient is nonetheless tucked beneath the jet, entrained by the counterrotating vortices farther downstream.

The influence of the two-layer model on surface characteristics is apparent in Fig. 21, which shows temperature contours along the test surface for the same case using wall functions (a) and the two-layer model (b). The surface stays cooler for a longer distance downstream of the trailing edge when using the wall function approach. This is because the coolant has not been computed to lift

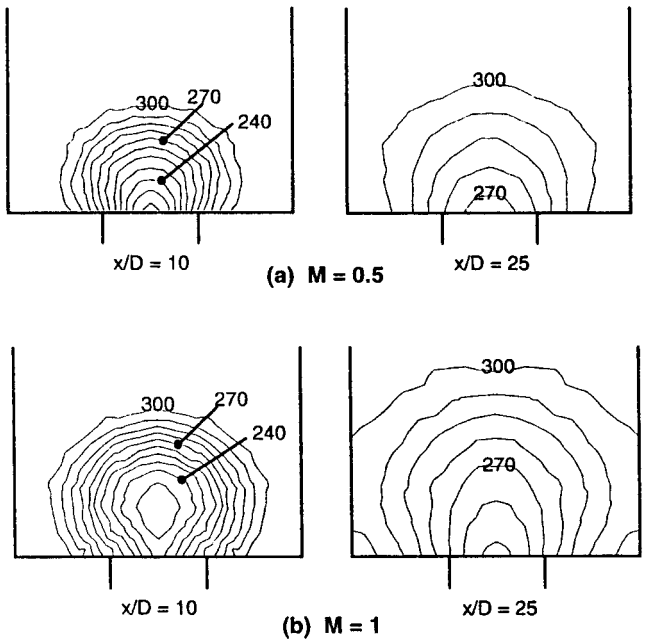

Fig. 18 Temperature contours downstream of near-field interaction show diffusion of the coolant as the jet travels downstream

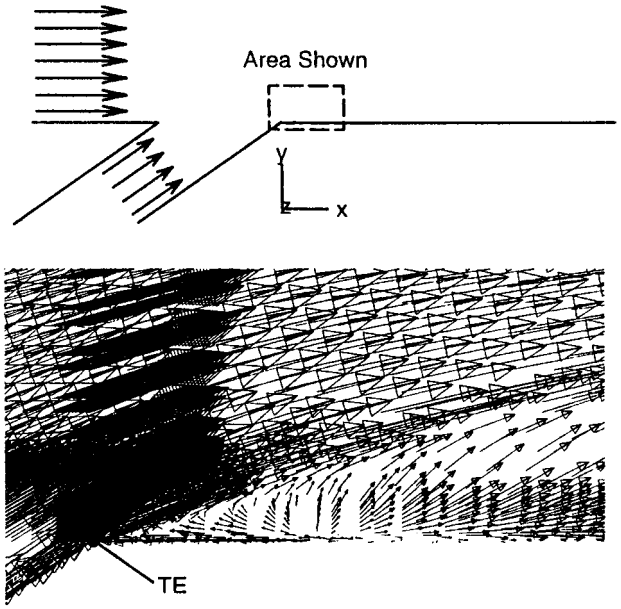

Fig. 19 Velocity vectors along the centerline for the two-layer model case show a small reverse flow zone, which was not resolved in the wall function cases

off above a reverse flow zone. For the two-layer model case, temperatures rise very fast downstream of the trailing edge since crossflow fluid has been tucked beneath the coolant jet. Note, however, that as the flow moves farther downstream, the contours become very similar. This is expected since the wall functions should perform adequately in these downstream, boundary-layer-like regions, and the flow is diffusion-dominated. The centerline plots of adiabatic effectiveness are compared in Fig. 22. Note that experimental values for adiabatic effectiveness were not available for $L/D = 3.5$, so the computed effectiveness is expected to be higher than the measured effectiveness. Again, it is noted that the major differences between the two wall treatments occur in the near field. Far field results for the two cases are very similar.

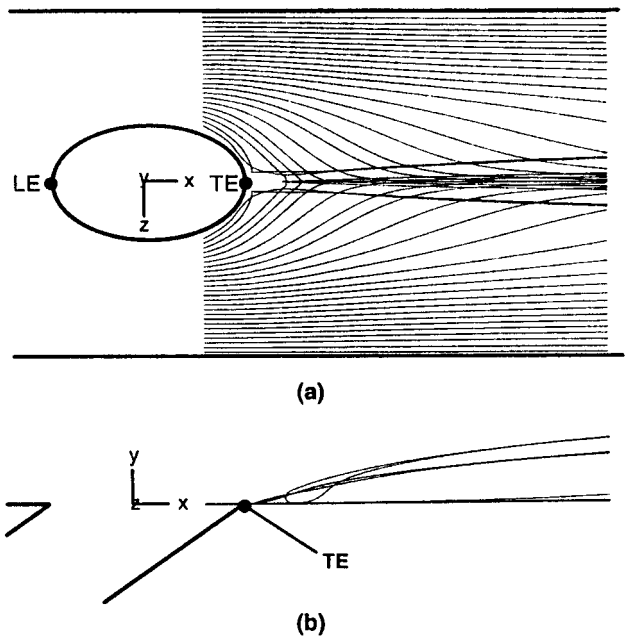

Fig. 20 Pathlines from the crossflow boundary layer top view (*a*) and side view (*b*) show saddle point and reverse flow downstream of the trailing edge

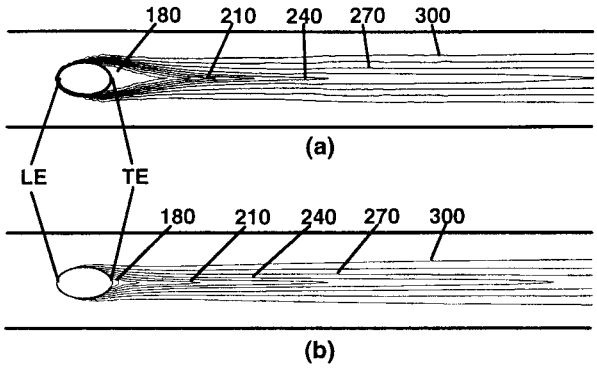

Fig. 21 Temperature contours along downstream bottom wall highlight differences between simulations performed with wall functions (*a*) and two-layer model (*b*)

8 Conclusions

Results have been presented for a systematic computational simulation of a streamwise injected, cylindrical hole film-cooling flowfield. The combination of the computed results and the previously documented experimental study of this case (Pietzryk et al., 1989) has been investigated using a vorticity-based analysis in order to draw conclusions regarding the underlying flow physics of the problem. Key conclusions include the following:

- The counterrotating secondary flow structure downstream of the jet exit is the most significant mechanism affecting the film-cooling performance in the streamwise injection cases. The dominant vorticity emanates from the film hole. Its origin is traced back to the streamwise oriented vorticity contained in the film-hole boundary layers.
- Film-cooling performance for a streamwise injected case may be significantly improved by controlling the strength of the counterrotating vortex pair. Methods may include: reducing or realigning the vorticity exiting the film hole; decreasing the vertical location of the streamwise vorticity pockets relative to the downstream wall; and increasing the distance between the vorticity pockets in order to reduce their lift and convective strength.
- The use of a two-layer wall treatment instead of wall functions significantly increases the computational intensity of the simulation. However, the two-layer model is necessary in order to resolve the recirculating flow beneath the exiting jet. Far field results from the two-layer model are almost equivalent to those found with wall functions.
- The primary flow structures downstream of jet injection include a jet region and a coolant wake region beneath the jet. The use of a two-layer zonal wall treatment allowed resolution

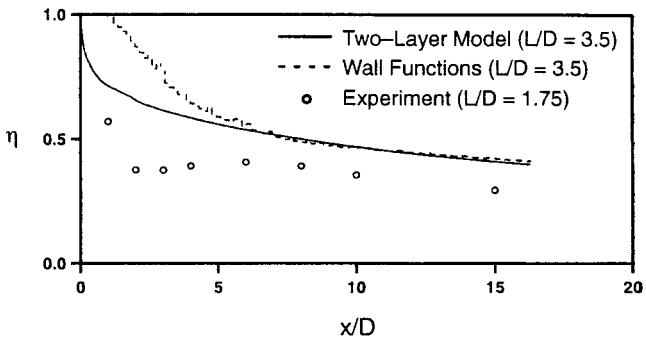

Fig. 22 Centerline plot of adiabatic effectiveness shows significant difference between the results with different wall treatments immediately downstream of the trailing edge, but similar behavior farther downstream ($M = 1$, $DR = 2$)

of a small reverse flow zone immediately downstream of the trailing edge. However, even the simulations using wall functions showed the two flow regions. This is due to the fact that the cause of the wake region, namely the low-pressure pocket downstream of the trailing edge, was resolved in all simulations.

- The inclusion of the supply plenum and film-hole regions in the computational model is critical to an accurate treatment of this class of problems. The flow in these regions is complex, and exerts considerable influence on the jet exit conditions. Existence of separation, jetting, and counterrotating vortices within the film hole has been confirmed.

Acknowledgments

This paper was prepared with the support of the U.S. Department of Energy, Morgantown Energy Technology Center, Cooperative Agreement No. DE-FC21-92MC29061. The authors would like to thank Mr. Gary Berger and Mr. Richard Baldwin of the Engineering Computer Operations at Clemson University for their assistance in all computer related matters. We would also like to thank Dr. Rick Lounsbury at Fluent, Inc., for his invaluable support with RAMPANT and Fluent/UNS.

References

Andreopoulos, J., and Rodi, W., 1984, "Experimental Investigation of Jets in a Crossflow," *Journal of Fluid Mechanics*, Vol. 138, pp. 92–127.

Bergeles, G., Gosman, A. D., and Launder, B. E., 1976, "The Near-Field Character of a Jet Discharged Normal to a Main Stream," ASME *Journal of Heat Transfer*, Vol. 107, pp. 373–378.

Bergeles, G., Gosman, A. D., and Launder, B. E., 1977, "The Near-Field Character of a Jet Discharged Through a Wall at 30° to a Mainstream," *AIAA Journal*, Vol. 14, pp. 499–504.

Bergeles, G., Gosman, A. D., and Launder, B. E., 1978, "The Turbulent Jet in a Cross Stream at Low Injection Rates: A Three-Dimensional Numerical Treatment," *Numerical Heat Transfer*, Vol. 1, pp. 217–242.

Demuren, A. O., 1982, "Numerical Calculation of Steady Three-Dimensional Turbulent Jets in Cross Flow," Rep. SFB 80/T/129, Sonderforschungsbereich 80, University of Karlsruhe, Germany.

Fluent/UNS User's Guide, 1996, Fluent Incorporated, Lebanon, NH.

Garg, V. K., and Gaugler, R. E., 1997, "Effect of Velocity and Temperature Distribution at the Hole Exit on Film Cooling of Turbine Blades," ASME JOURNAL OF TURBOMACHINERY, Vol. 119, pp. 343–351.

Launder, B. E., and Spalding, D. B., 1974, "The Numerical Computation of Turbulent Flows," *Computer Methods in Applied Mechanics and Engineering*, Vol. 3, pp. 269–289.

Leonard, B. P., 1979, "A Stable and Accurate Convection Modeling Procedure Based on Quadratic Upstream Interpolation," *Computer Methods in Applied Mechanics and Engineering*, Vol. 19, pp. 59–98.

Leylek, J. H., and Zerkle, R. D., 1994, "Discrete-Jet Film Cooling: A Comparison of Computational Results With Experiments," ASME JOURNAL OF TURBOMACHINERY, Vol. 113, pp. 358–368.

Moussa, Z. M., Trischka, J. W., and Eskinazi, S., 1977, "The Near Field in the Mixing of a Round Jet With a Cross-Stream," *Journal of Fluid Mechanics*, Vol. 80, Part 1, pp. 49–80.

Patankar, S. V., 1980, *Numerical Heat Transfer and Fluid Flow*, Hemisphere Publishing Corporation, New York.

Pietrzyk, J. R., Bogard, D. G., and Crawford, M. E., 1988, "Hydrodynamic Measurements of Jets in Crossflow for Gas Turbine Film Cooling Applications," ASME Paper No. 88-GT-194.

Pietrzyk, J. R., Bogard, D. G., and Crawford, M. E., 1989, "Experimental Study of the Interaction of Dense Jets With a Crossflow for Gas Turbine Applications," Report No. 89-1, Turbulence and Turbine Cooling Research Laboratory, Mechanical Engineering Department, The University of Texas at Austin.

Pietrzyk, J. R., Bogard, D. G., and Crawford, M. E., 1990, "Effects of Density Ratio on the Hydrodynamics of Film Cooling," ASME JOURNAL OF TURBOMACHINERY, Vol. 112, pp. 428–436.

RAMPANT User's Guide, 1996, Fluent Incorporated, Lebanon, NH.

Sinha, A. K., Bogard, D. G., and Crawford, M. E., 1991, "Film-Cooling Effectiveness Downstream of a Single Row of Holes With Variable Density Ratio," ASME JOURNAL OF TURBOMACHINERY, Vol. 113, pp. 442–449.

Walters, D. K., and Leylek, J. H., 1997, "A Systematic Computational Methodology Applied to a Three-Dimensional Film-Cooling Flowfield," ASME JOURNAL OF TURBOMACHINERY, Vol. 119, pp. 777–775.

A Detailed Analysis of Film Cooling Physics: Part II—Compound-Angle Injection With Cylindrical Holes

K. T. McGovern

J. H. Leylek

Department of Mechanical Engineering,
Clemson University,
Clemson, SC 29634

Detailed analyses of computational simulations with comparisons to experimental data were performed to identify and explain the dominant flow mechanisms responsible for film cooling performance with compound angle injection, Φ, of 45, 60, and 90 deg. A novel vorticity and momentum based approach was implemented to document how the symmetric, counterrotating vortex structure typically found in the crossflow region in streamwise injection cases, becomes asymmetric with increasing Φ. This asymmetry eventually leads to a large, single vortex system at Φ = 90 deg and fundamentally alters the interaction of the coolant jet and hot crossflow. The vortex structure dominates the film cooling performance in compound angle injection cases by enhancing the mixing of the coolant and crossflow in the near wall region, and also by enhancing the lateral spreading of the coolant. The simulations consist of fully elliptic and fully coupled solutions for field results in the supply plenum, film hole, and crossflow regions and includes surface results for adiabatic effectiveness η and heat transfer coefficient h. Realistic geometries with length-to-diameter ratio of 4.0 and pitch-to-diameter ratio of 3.0 allowed for accurate capturing of the strong three-way coupling of flow in this multiregion flowfield. The cooling configurations implemented in this study exactly matched experimental work used for validation purposes and were represented by high-quality computational grid meshes using a multiblock, unstructured grid topology. Blowing ratios of 1.25 and 1.88, and density ratio of 1.6 were used to simulate realistic operating conditions and to match the experiments used for validation. Predicted results for η and h show good agreement with experimental data.

1 Introduction

Film cooling of gas turbine stator and rotor airfoil surfaces, hub and casing endwalls has played a crucial role in maintaining the structural integrity of these hot-section components at operating temperatures in excess of the melting temperature of the alloys used. The term film-cooling refers to the use of relatively cool air extracted from the latter stages of the high-pressure compressor, which is channeled to the turbine section and is ejected into the hot flowpath through small holes in the airfoil and endwall surfaces. Ideally, this coolant air remains close to the surface to be protected and spreads quickly between the holes to form a thin film of cool air, which isolates the component from the hot combustion gases. However, the complex flow structures present at the coolant injection site often lead to lift-off or quick dilution and therefore little protection. Higher performance demands of future gas turbine designs is leading to a need for a more thorough understanding of film-cooling behavior, better databases of film-cooling performance, and truly predictive design tools. Film-cooling designs leading to increased overall effectiveness with reduced cooling air can then be implemented with more certainty.

The use of different hole geometries is one method of improving film cooling performance that has seen increased usage in the higher performance designs. Streamwise injected coolant jets through discrete holes (described in Part I) are now being turned laterally as described in the present paper (Part II), shaped (Part III), or combination of the two (Part IV) in order to extract better cooling of vital components. The purpose of this detailed four-part study is to look into these different film cooling configurations and determine the dominant physical mechanisms responsible for their performance. A row of discrete, round holes with compound angle injection is targeted in the present study for the purposes outlined above. Compound angle is implemented in modern designs to improve the spreading rate of the coolant and therefore provide more uniform coverage. However, in past studies it was found that compound angle also leads to undesirable increases in surface heat fluxes. In order to use this coolant geometry effectively, the mechanisms responsible for the contradictory surface results for adiabatic effectiveness (η) and heat transfer coefficient (h) must be fully understood so that compound angle injection can be effectively implemented in future designs with greater confidence.

Gas turbine designers are in desparate need of truly predictive design tools to test newer film-cooling concepts involving compounding, shaping, and combinations of the two for the wide range of operating conditions encountered in practice. These advanced design tools must be consistently accurate, economical, and capable of providing results with quick turnaround time. In this study, a novel implementation of computational fluid dynamics (CFD) model is validated for complex film-cooling configurations and is shown to be capable of providing reliable information regarding the relative performance of various film-cooling configurations.

2 Terminology

Due to the lack of large-scale computational studies into the flowfield physics of compound-angle injection in the open literature, standard terminology designed to help readers adjust easily to the many possible orientations of the complex film cooling configurations are nonexistent. The present authors feel the need to define some useful terminology in an effort to improve the readability of this document.

Contributed by the International Gas Turbine Institute and presented at the 42nd International Gas Turbine and Aeroengine Congress and Exhibition, Orlando, Florida, June 2–5, 1997. Manuscript received International Gas Turbine Institute February 1997. Paper No. 97-GT-270. Associate Technical Editor: H. A. Kidd.

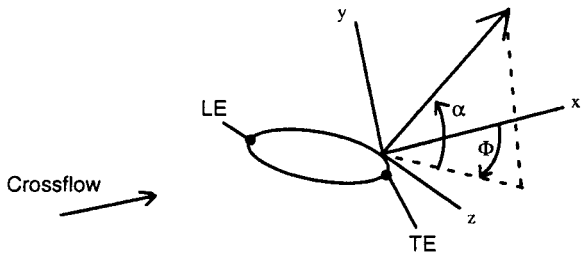

Fig. 1 Demonstration of the terminology used for compound-angle injection film cooling

Compound angle (Φ) is measured clockwise from the x–y plane as shown in Fig. 1. The film-hole leading edge (LE) and trailing edge (TE) points for the streamwise injection case are fixed relative to the elliptic breakout of cylindrical holes at the exit plane. As the film hole is rotated according to the compound angle specified, the LE and TE points rotate with it as shown in Fig. 1. LE and TE are used as constant reference points when discussing flow within the film hole and at the exit plane so that the "intended" injection of the coolant is always in the direction from the leading edge to the trailing edge. "Upstream Edge" refers to the side of the film hole upwind of the line connecting LE and TE. Similarly, the "Downstream Edge" refers to the side of the film hole downwind of the line connecting LE and TE. Typically, the hot cross-stream fluid flows streamwise (x direction) over the upstream edge and the coolant jet flows over the downstream edge on its way toward the test surface. The origin of the coordinate system is attached to the downstream most point on the film-hole breakout, as shown in Fig. 1.

3 Literature Review

The majority of compound angle studies available in the open literature are fairly new due to the recent focus on improving film-cooling designs. As cooling technology has honed in on the need to study film-cooling configurations with realistic geometries, recent companion paper studies such as:

- Schmidt et al. (1996) study of η, Sen et al. (1996) study of h,
- Ekkad et al. (1997a, b), two-paper study of η and h, and,
- Ligrani et al. (1994a, b),

have been published addressing this issue. In each of these studies surface results from select compound angle configurations were analyzed to document film cooling performance and to compare the surface results to a streamwise injection reference case. A summary of the results is included below to document the possibility that compound angle injection improves film cooling performance, and to document the need for a simultaneous examination of flowfield and surface results to explain the physical mechanisms involved.

In the study by Sen et al. (1996) and Schmidt et al. (1996), a row of film holes with $\alpha = 35$ deg and $\Phi = 60$ deg was compared to an equivalent streamwise injection ($\Phi = 0$ deg) case. Measured η results showed that the compound angle injection increased the effectiveness of the coolant. However, the heat transfer coefficient was also found to increase over the reference case. In order to combine the two results from adiabatic effectiveness and heat transfer coefficient tests to determine the ultimate effect on film-cooling performance, a heat flux reduction ratio (heat flux for a film cooled surface normalized by the heat flux for a solid surface under a simple boundary layer flow) was utilized, which combined the effects of both η and h on the film-cooling performance. It was found for the case of $\Phi = 60$ deg that an increasing M leads to an augmentation of the heat flux entering the test surface compared to boundary layer flows, and therefore that particular film cooling configuration was completely ineffective.

Studies by Ekkad et al. (1997a, b) provided surface results for $\Phi = 45$ and 90 deg orientations. Similar to the previous studies, this work also combined the two results to provide the overall effect on the heat flux into the downstream surface. A compound angle of $\Phi = 45$ deg was found to actually perform better than the streamwise injection case, while the $\Phi = 90$ deg case was found to perform relatively poorly—despite the fact that this case provided better adiabatic effectiveness results.

Ligrani et al. (1994a, b) studied a case of $\Phi = 30$ and 50.5 deg for both a single row and staggered double row of compound angle injected jets. Their study consisted of adiabatic effectiveness and Stanton number measurements to characterize the overall cooling performance. However, unlike the two previous works, they did not combine the two types of surface result.

The only investigation that attempted to address some of the mechanisms involving film cooling with compound angle injection was a study by Lee et al. (1997) who documented the velocity field, pressure losses, and surface flow visualization for a wide

Nomenclature

Cp = pressure coefficient = $p/(1/2\rho V^2)_\infty$
D = film-hole diameter
DR = density ratio = ρ_j/ρ_∞
h = heat transfer coefficient in the presence of film cooling jets = $q''/(T_{aw} - T_w)$, W/m^{2}K
h_o = heat transfer coefficient in the absence of film cooling jets (reference) = $q''_o/(T_\infty - T_w)$, W/m^{2}K
LE = leading edge of streamwise injection film hole at exit plane
L = length of film hole
L/D = length-to-diameter ratio of film hole
M = blowing (or mass flux) ratio = $(\rho V)_j/(\rho V)_\infty$
q'' = surface heat flux per unit area, W/m^2
p = static pressure, Pa
P = pitch (or lateral spacing) between film holes
P/D = pitch-to-diameter ratio of film hole
tke = turbulent kinetic energy, m^2/s^2
T = local fluid static temperature, K
TE = trailing edge of streamwise injection film hole at exit plane
TI = turbulence intensity = $(2/3*tke)^{1/2}/V*100$, percent
V = velocity magnitude, m/s
y^+ = nondimensional distance away from wall
u = streamwise (x-direction) velocity component (m/s)
v = vertical (y-direction) velocity component (m/s)
w = lateral (z-direction) velocity component (m/s)
x = streamwise direction
y = vertical direction
z = lateral direction
α = injection angle, deg
Φ = compound angle, deg
η = adiabatic effectiveness = $(T_\infty - T_{aw})/(T_\infty - T_j)$
ϱ = fluid density, kg/m^3
θ = nondimensional temperature = $(T_\infty - T)/(T_\infty - T_j)$

Subscripts

∞ = mainstream conditions at crossflow inlet plane
aw = adiabatic wall
j = conditions at coolant supply plenum inlet plane
o = conditions in the absence of film cooling
w = conditions at wall

range of compound angle holes. Their study was limited by the use of a single (or isolated) discrete hole and an unrealistic length-to-diameter ratio (L/D) of 40. In their study, velocity measurements in planes perpendicular to the crossflow path were made to document the transformation from a symmetric, counterrotating vortices encountered in $\Phi = 0$ deg to a single, large vortex structure seen in $\Phi = 90$ deg cases. In addition, surface results were used to characterize the path of the coolant and its interaction with the crossflow.

4 Outstanding Issues

It can be concluded from these studies that compound angle injection can provide better film-cooling performance, such as the case shown for $\Phi = 45$ deg by Ekkad et al. (1997a, b). In some cases, however, compound angle injection leads to such high heat transfer coefficients that it would be better to introduce no film cooling at all as in the case of $\Phi = 60$ deg and $M = 2.0$ documented by Sen et al. (1996). Clearly, there are a number of studies with contradictory observations regarding the effects of compound angles in film cooling. Although these studies provide a database of information describing the surface results, they do not document the physical mechanisms responsible for the outcome. Only a simultaneous, in-depth examination of the flowfield and surface results can provide this type of analysis to gas turbine designers. Such understanding is crucial to extending the results of the simplified flat plate studies to the more complex operating environment of gas turbines. Finally, modern computational fluid dynamics methodologies developed to enable the gas turbine designers to assess the relative performance of different compound angle configurations accurately has not at all been resolved in the open literature.

5 Present Contributions

The primary goals of this four part study are to: (*i*) uncover the dominant flowfield mechanisms responsible for the surface adiabatic effectiveness and heat transfer coefficient distributions; (*ii*) demonstrate the capability of computational fluid dynamics in providing consistently accurate results to distinguish between various film cooling configurations. The specific contributions of the present study are as follows:

- validation of a state-of-the-art computational methodology to predict η and h for compound-angle injection film cooling;
- documentation of the dominant physical mechanisms influencing the film cooling behavior with a novel use of the vorticity concept;
- description of the effects of varying the Φ angle on the dominant mechanisms and on the surface results;
- determination of the effects of blowing ratio (M) on film cooling behavior for various Φ angles;
- comparisons of the relative performance of different film cooling configurations; and
- establishment of a predictive computational design methodology.

To accomplish the stated objectives, results for compound-angle injection cases of $\Phi = 45$, 60, and 90 deg are computationally compared to a streamwise reference case ($\Phi = 0$ deg) and also to experimentally measured data obtained in-house and in the open literature. These geometries are demonstrated in Fig. 2 by a single pitch of the row of holes studied.

6 Simulation Details

The computational methodology implemented in the present research was developed and validated for studying jet–crossflow interactions as described by Butkiewicz et al. (1995), Walters et al. (1995), Hyams et al. (1996), and Walters and Leylek (1997). Consistent with those studies, the NURBS-based solid modeling

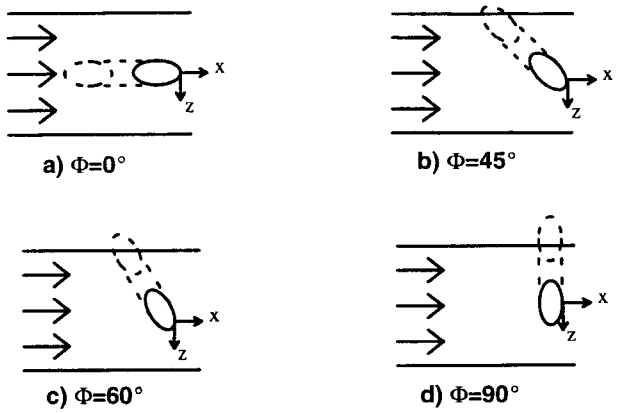

Fig. 2 Top view of a single pitch of a row of holes showing the four film cooling configurations studied

software, I-DEAS, by SDRC, Inc. was utilized to capture the geometry accurately, including the film-hole, plenum, and crossflow regions. I-DEAS was then used to generate a high-quality, high-density background grid mesh in this complex and rather large computation domain. The actual CFD analysis was performed using Fluent/UNS solver by Fluent, Inc., which is a pressure-correction based, multi-block, multigrid, unstructured/adaptive solver. The higher order linear reconstructive discretization scheme was used to reduce numerical viscosity and to better capture all gradients. Turbulence closure was attained using standard (or high Reynolds number) k–ϵ turbulence model in conjunction with the generalized wall functions. Strict convergence criteria were met in which:

- global mass and energy imbalances were brought below 0.01 percent;
- residuals normalized by inlet fluxes were brought below 0.1 percent; and
- dependent variables monitored in important areas of the flowfield were shown to not change with further iterations.

Also grid independence was established within Fluent/UNS by adapting to the highest gradient regions of the flow field and monitoring the variables to ensure that the dependent variables changed less than 5 percent at monitored locations. A hanging-node adaption procedure was used that maintained the high quality of the initial background grid. Typically, a background grid consisted of approximately 300,000 cells with the majority of the cells in the jet–crossflow interaction region. The final grid, which provided a "grid-independent" solution, contained approximately 620,000 cells with the majority of adaptions in the film-hole and the near-field regions. For more details of the computational methodology the reader is encouraged to study the reference papers published by the Clemson group cited above. The unique aspects of the present work are included below to extend the established methodology to the study of compound angle injection.

Computational Model. The computational models were constructed as the exact replicas of the experimental counterparts for all cases. Nondimensional parameters such as the lateral spacing between holes, $P/D = 3$, and the length of the film hole, $L/D = 4.0$, were consistent among all the models. Due to the symmetric nature of film cooling with a row of holes with streamwise injection ($\Phi = 0$ deg), the computational domain was reduced to a half-pitch simulation between two symmetry planes. For the compound angle cases ($\Phi > 0$ deg), a full-pitch was modeled and repeating boundary conditions were applied between holes as shown in Fig. 3. A zero normal gradient condition was imposed at $10D$ above the test surface, where it was determined to be far enough away to not affect the jet–crossflow interaction. The test section downstream of the film-hole TE was extended to $25D$

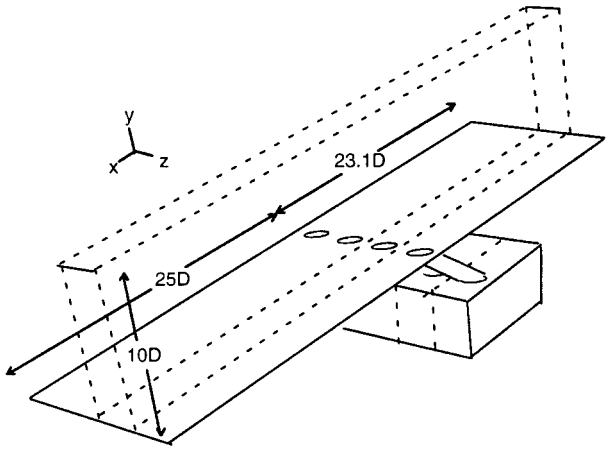

Fig. 3 Isometric view of the computational domain aft looking forward showing the extent of the domain for Φ = 60 deg

where a convective outflow (upwinding) condition was applied, which allowed the jet–crossflow interaction to be documented far downstream of the coolant exit plane. The film-hole diameter, flow conditions, and plenum geometry differed slightly between the experimental cases modeled and are described separately for each study documented below.

Φ = 0 and 60 deg. For the computational study of Φ = 0 and 60 deg cases, the geometry and operating parameters exactly matched to the experimental works of Schmidt et al. (1996). Using a hole diameter of 11.1 mm, a one-dimensional flow concept was used to set the plenum inlet velocity to achieve an average velocity of 11.75 m/s within the metering section of the film hole. The plenum dimensions in the x, z, and y directions were $9.15D$ wide by $3D$ deep by $4.57D$ high, respectively. In order to match the upstream boundary layer development of the University of Texas experiments a turbulent boundary layer was started at $23.1D$ upstream of the streamwise hole by applying a uniform velocity inlet condition there. Crossflow velocities were set to obtain the desired blowing ratio based on the film-hole nominal velocity 11.75 m/s and Re = 18,717.

Φ = 45 and 90 deg. For the compound angle configurations Φ = 45 and 90 deg, the geometry and operating parameters were modeled to correspond with experiments from Clemson University (Farmer et al., 1997). The crossflow was introduced at 300 K and with a free-stream velocity of 25 m/s. In order to match the boundary layer thickness of $0.7D$ at the film-hole LE, a $\frac{1}{7}$th law turbulent boundary layer velocity profile was applied at $10D$ upstream of the leading edge of the film hole based on actual data obtained at that location. Plenum inlet velocity was then varied to give the desired film-hole nominal velocity to set the blowing ratio using a hole diameter of 8.3 mm.

Grid Generation. The solid model of every film cooling geometry was divided into a large number of subregions within I-DEAS in order to obtain a high-quality grid as discussed in Walters and Leylek (1997). In this study, some additional steps were taken within I-DEAS in order to apply the periodic boundary conditions properly in Fluent/UNS. Regions had to be added with the stipulation that corresponding surfaces on the periodic walls matched perfectly across the film cooling passage. The "Surface Dependency" feature in I-DEAS was applied to these periodic walls to ensure that nodes and cells on these surfaces were built with the same nodal and cell distribution. (The reader is encouraged to refer to the I-DEAS users' manual for more information on this feature.)

7 Experiments Used for Validation

The computational simulations were validated by comparisons to both in-house experimental work at Clemson University and companion studies by Schmidt et al. (1996) and Sen et al. (1996) from The University of Texas at Austin. These two sources of experimental data employed two completely different measurement techniques for determining the surface results as discussed below.

7.1 In-House Experimental Work. Experiments were carried out at Clemson University to measure the adiabatic effectiveness in a 0.6 m × 0.6 m low-speed wind tunnel. The experimental setup implemented used a hue-based thermochromic liquid crystal temperature measurement method. A low-conductivity substrate material test plate was coated with a layer of liquid crystals with a temperature bandwidth between 15°C and 20°C. A real time image-capturing system was used to calibrate the liquid crystal's temperature response to the corresponding hue values. A density ratio (DR) of 1.55 was obtained through the injection of CO_2 gas into an ambient air mainstream flow. The foreign gas was injected at various temperatures below the liquid crystal bandwidth to achieve the desired hue response. $M = 1.25$ and $M = 1.88$ were obtained by varying the flow rate of the foreign gas, while the mainstream velocity was held constant at 10 m/s. The adiabatic effectiveness was calculated based on T_∞, T_j, and T_{aw} under steady state operating conditions.

7.2 Experimental Setup for Schmidt et al. (1996). The research efforts at the University of Texas modeled film cooling behavior using cryogenically cooled air ($T = 187.5$ K) injected into ambient air crossflow resulting in a $DR = 1.6$. Adiabatic effectiveness results were calculated from temperature measurements made by thermocouples imbedded in the downstream wall. For the determination of h, ambient air was used as the injectant at a $DR = 1.0$. The momentum flux ratio, $J = 0.98$ was used as a scaling parameter to combine the η results at $DR = 1.6$ and $M = 1.25$ and the h results at $DR = 1.0$ and $M = 1.0$ to calculate a Net Heat Flux Reduction (NHFR) parameter, $\text{NHFR} = 1 - h/h_o(1 - \eta\theta_\infty)$.

8 Results and Discussion

Flow in the Film Hole. The flow field developed at the entrance to the film hole was shown in Walters and Leylek (1997) to be complex and very dependent on the operating conditions. The complexities in this region are primarily due to the flowpath design. Coolant is channeled to the film hole through a plenum much larger in volume than the film hole itself, and therefore, as the coolant enters into the film hole, it is strongly accelerated. Along with this velocity increase there is excessive turning at the sharp-edged entrance to the film hole. At an injection angle of 35 deg, some of the coolant has to go through a turn of 145 deg into the film hole at the downstream side of the plenum. The inability of the coolant to negotiate this turn leads to a large three-dimensional separation along the downstream surface of the film hole. This separation region results in:

- nonuniform coolant distribution
- secondary motion within the film hole
- high-velocity gradients
- high turbulence generation.

The mechanisms discussed above are primarily dominated by the flow at the entrance to the film hole. As the film hole is rotated to provide lateral momentum to the coolant fluid in the compound-angle injection cases, the entrance region remains essentially unchanged except for the location of the separation region relative to the plenum. The flow at the entrance and throughout the majority of the film hole are unaffected by the large changes in the exit conditions brought about by the compound angle injection. One method of demonstrating this is to examine the parameters along

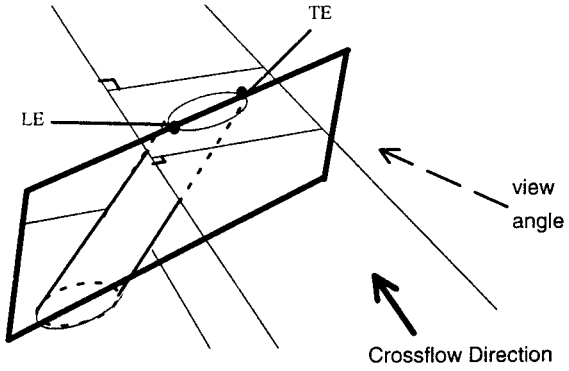

Fig. 4 Demonstration of the film-hole centerline plane for Φ = 60 deg

the film-hole centerline planes. The definition of the film-hole centerline plane is shown in Fig. 4 for Φ = 60 deg. In Fig. 5 the velocity contours along the film-hole centerline plane show the similarity of the flow between the two configurations for both the Φ = 0 and Φ = 60 deg case. Similarly, good correspondence was also found for the turbulence intensity and the secondary flow structures described for the streamwise injection case in Walters and Leylek (1997).

Exit Conditions. As the coolant approaches the exit plane of the film hole, the coolant flow deviates considerably from the streamwise injection case due to significant changes in the pressure field at the exit. The physical explanation for the pressure changes shown in Fig. 6 is given in the near-field evaluation. As the compound angle is increased the pressure field imposed at the jet exit is changed in the following three ways:

- the upstream high pressure region acts across a wider area of the film-hole breakout,
- the downstream low pressure decreases even further behind the film-hole breakout, and
- the streamwise pressure gradients increase due to a decrease in the streamwise breakout distance between the pressure extremes, as Φ is increased.

These changes in the pressure field cause higher blockage at the exit, which leads to deviations of the coolant trajectory after it leaves the film hole. The case of Φ = 45 and Φ = 60 deg resemble the *Cp* contours depicted for Φ = 90 deg.

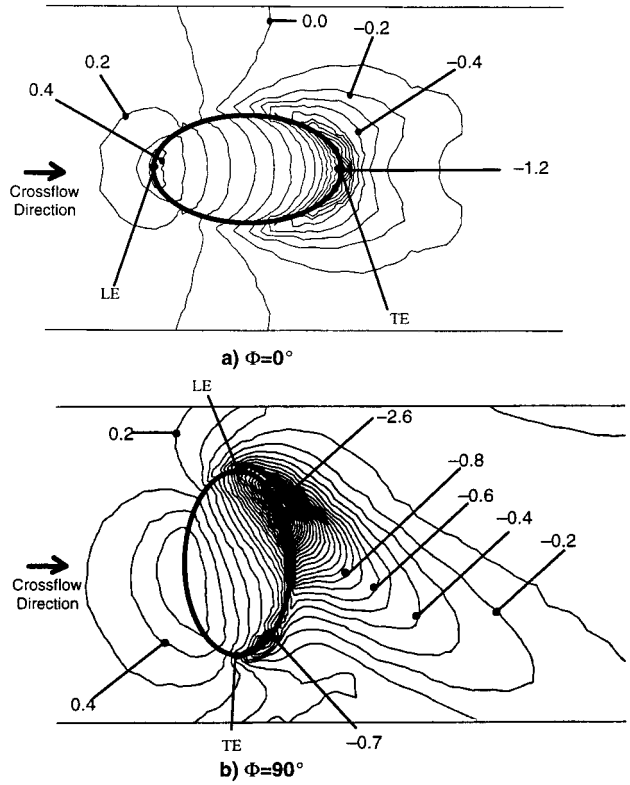

Fig. 6 *Cp* along the test surface showing increased pressure gradients between (*a*) Φ = 0 deg and (*b*) Φ = 90 deg at *M* = 1.25

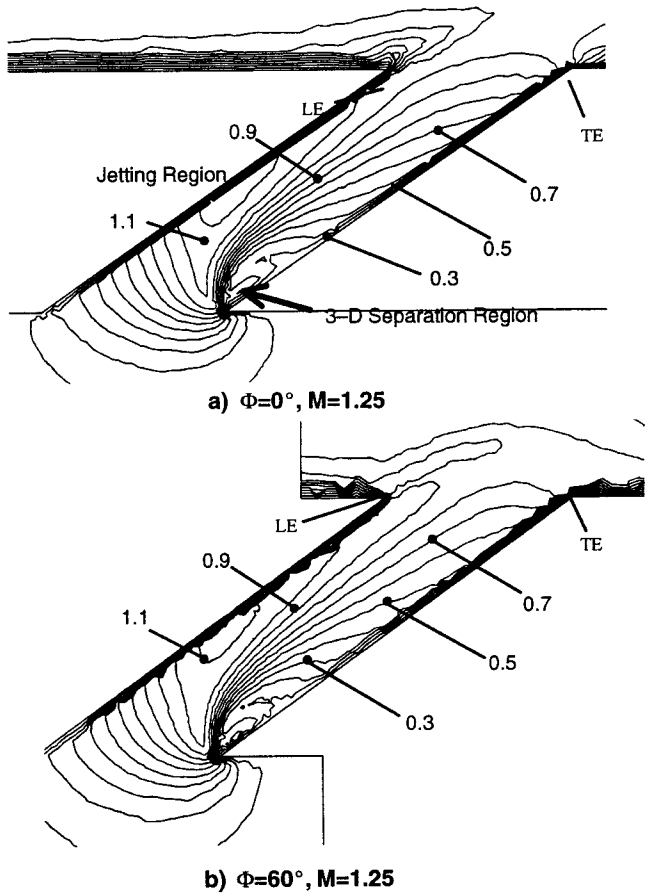

Fig. 5 Velocity magnitude normalized by U_∞ showing jetting and separation regions demonstrating very good correspondence between (*a*) the streamwise Φ = 0 deg and (*b*) the Φ = 60 deg compound-angle cases

Coolant Distribution. The coolant distribution at the exit is determined by two competing mechanisms:

- the nonuniform distribution of coolant within the film hole due to the separation region at the inlet to the film hole, and
- exit plane blockage due to pressure gradients caused by the crossflow impinging on the coolant.

As can be seen in the streamwise case in Fig. 5(*a*), the separation region at the inlet to the film hole leads to a jetting effect along the upstream edge of the wall. Due to the short $L/D = 4.0$, the relatively high-momentum jetting fluid does not completely diffuse out across the film hole and therefore is still evident even at the coolant exit plane. In Fig. 7 the effective coolant distribution at the exit is shown by contours of normalized v, or vertical velocity component. Little variation of v at the exit is seen due to the balance of the effects of high-momentum jetting fluid mentioned near the leading edge and streamwise pressure gradients due to crossflow impingement. This distribution is dependent on operating conditions as discussed in Walters and Leylek (1997).

For the same operating conditions, compound-angle film cooling can be seen to be more strongly affected by the pressure

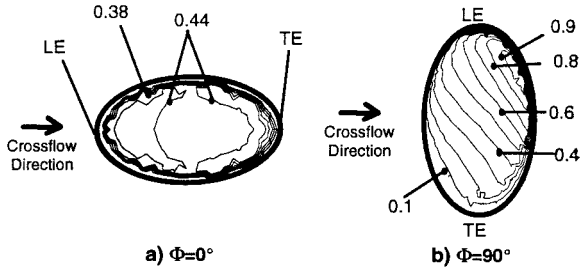

Fig. 7 v/U_∞ **for the case of** $M = 1.25$ **showing the effects of compound-angle injection on the coolant distribution at the exit for (*a*)** $\Phi = 0$ **deg, and (*b*)** $\Phi = 90$ **deg**

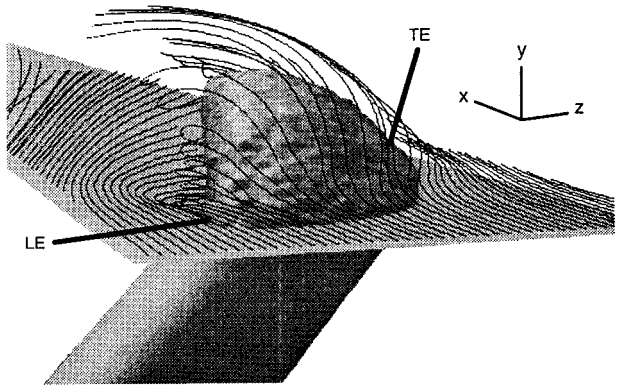

Fig. 9 Particle traces released from the crossflow boundary layer showing the complex flow around an isotherm $\Theta = 0.2$ **for** $M = 1.25$ **and** $\Phi = 60$ **deg**

gradients and blockage at the exit plane. The blockage is stronger because it acts over a larger area and therefore the coolant is forced to exit near the downstream edge of the film hole. The smaller effective exit area leads to an increase in v near the downstream edge of the hole and little coolant exiting from the upstream edge. Because of the orientation of the hole, the jetting fluid is now forced to exit along the downstream edge of the film hole near the LE point and there is no opportunity to have the balance of blockage and jetting seen in the streamwise case.

Coolant Trajectory

Compound Discharge Angle (Φ)*.* The jet trajectory is so strongly affected by the pressure distribution that very little of the fluid exited with the intended film-hole metal angle for all the cases studied. The deviation of the coolant trajectory from the compound angle of the metal is shown in Fig. 8 for the case of $\Phi = 90$ deg. The coolant compound angle trajectory at the exit ranges from 40 deg (approximately half of the metal angle) near the TE, to almost the metal angle of 85 deg at the upstream side of the LE. This trend was consistent in both computational and experimental results for all of the compound angle cases studied. The coolant near the trailing edge region exited at a very shallow compound angle due to its low momentum, which allowed it to be turned by the crossflow accelerating between the holes. This will prove to be important in explaining the results for adiabatic effectiveness and heat transfer coefficient in later sections. The area of highest compound discharge angle at the exit plane coincides with the upstream edge near the LE point. Coolant is not able to negotiate the high-pressure gradients seen and therefore flows almost parallel to the film hole exit plane toward the trailing edge.

Streamwise Discharge Angle (α)*.* The streamwise discharge angle of the coolant at the film-hole exit plane showed a similar dependence on the presence of high pressure blockage and jetting fluid regions. The low injection angles, $\alpha < 35$ deg, are all seen along the upstream edge of the film hole where blockage due to the high-pressure regions leads to low vertical momentum. However, near the downstream edge the coolant exits at $\alpha > 35$ deg where jetting fluid is being forced to exit due to the reduction in the effective exit area of the film hole by blockage.

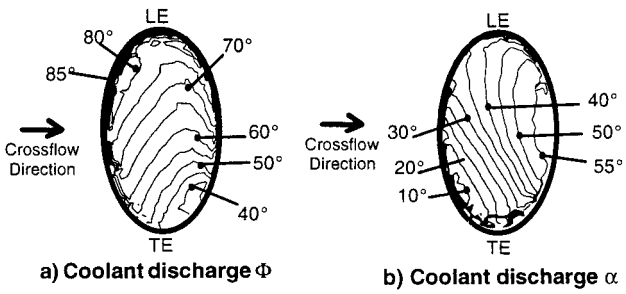

Fig. 8 Discharge angles showing the jet trajectory as it exits the film hole for the case of $\Phi = 90$ **deg,** $M = 1.25$

Near-Field Behavior. The near-field behavior of jet–crossflow interactions with compound angle injection is dominated by:

- the vorticity contained within the film-hole boundary layers;
- the vorticity generated at the interface of the coolant and the crossflow along the downstream edge near the LE point;
- the pressure field set up in the jet–crossflow interaction; and
- the turbulence generated in the shear layers between the jet and crossflow.

The vorticity sources are responsible for the strength of the secondary flow structures that degrade the coolant and cause rapid spreading downstream of the film hole. The pressure field dominates the general path taken by the crossflow and coolant as the two interact. The turbulence generated leads to a decrease in η by enhancing diffusion of the coolant toward the wall and an increase in h due to elevated turbulence near the wall. These three mechanisms will be described separately below as they relate to the nearfield behavior shown in Fig. 9 by particle traces released from the boundary layer of the oncoming crossflow flowing over an isothermal surface $\Theta = 0.2$, which characterizes the coolant path.

Effects of Vorticity. The vorticity field in compound angle injection is significantly different from the streamwise injection cases with cylindrical and shaped holes documented in the companion papers designated as Part I and Part III. For the streamwise injection cases, it was shown that the primary cause of the symmetric counterrotating vortex structures seen downstream of the jet/crossflow interaction site was the vorticity emanating from the film-hole boundary layers. In compound-angle injection, a new mechanism for streamwise vorticity appears at the interface region between the crossflow and coolant jet on the downstream side of LE. The strength of this new source increases with increasing Φ. The relative strength of the two vorticity sources is configuration dependent. With compound-angle injection, the originally symmetric counterrotating vortex structure becomes increasingly asymmetric as Φ increases and eventually turns into a single vortex at $\Phi = 90$ deg. It is the positive x-direction vorticity along the upstream edge that is inhibited by compound-angle injection. Therefore, the counterclockwise rotating leg (looking upstream) of the secondary flow structure starts shrinking with increasing Φ and collapses completely at $\Phi = 90$ deg.

In compound-angle injection, the strong side of the vortex lies along the downstream edge and the weak vortex along the upstream edge of the film-hole. The increase in the strength of the downstream edge vortex is caused by the fact that as the film hole is turned laterally at increasing Φ, the crossflow fluid flows per-

pendicular to the coolant flow direction as it negotiates over and around the leading edge side as shown in Fig. 9. Because of the good alignment of the vorticity generated at this interface and the local velocity field, this particular interaction plays a more dominant role. In addition, the crossflow fluid flows parallel to the downstream edge all the way around the film hole resulting in a coalescing of the vorticity. This vorticity generates a single large rotating vortex structure in the near field whose center lies slightly behind the exiting jet. As the coolant is turned toward the downstream and bent over, the vorticity aligns itself with the coolant path, which, as described earlier, is along a direction at half the compound angle of the metal (for the case of $M = 1.25$, $DR = 1.6$).

The weakening of the upstream edge vortex was attributed to its dependence on the vorticity emanating from the film-hole boundary layer along this surface. As the film hole is turned laterally, the effective coalescing of vorticity is reduced due to the fact that:

- the long surface of the film hole is turned toward the crossflow causing the boundary layer vorticity to get blocked by the stagnation region formed at the upstream edge; and
- the coolant trajectory is very shallow along the upstream edge of the film hole resulting in a shift in the vorticity vector direction.

As the compound angle is increased to 60 and 90 deg, the weak vortex disappears due to these mechanisms.

Effects of Pressure. As the oncoming crossflow impinges on the exiting coolant, it is forced either between the film holes or over the jets due to the large pressure rise setup along the upstream edges of the jets as shown in Fig. 6. As the compound angle is increased, the high-pressure region becomes wider and more of the crossflow is forced over the jets. Also the remaining crossflow fluid that flows between holes is forced through an effective spacing, which decreases with increasing Φ and is subjected to sharper turning angles. This high-pressure region also continues to affect the coolant fluid after it exits the film hole by quickly forcing the coolant to begin bending down toward the test surface and also toward the downstream direction. The bending of the jet as it exits the film hole leads to two low-pressure regions behind the film hole. The first of these is on the downstream side of the LE point, where the jetting fluid exits at the highest injection angle and lifts off immediately. The separating coolant jet is quickly bent over resulting in a low-pressure region under its curved streamlines. This low-pressure pocket sucks the upstream crossflow fluid right under the jet, inducing lateral momentum, which will be shown to be present even in the far-field. The second low-pressure region is near the downstream side of the TE point where the low-momentum coolant exits and is being turned toward the streamwise direction by the crossflow fluid accelerating between two adjacent film holes.

Turbulence Generation. The two major sources of turbulence are the film-hole generated turbulence and the turbulence generated in the high-velocity gradient region on the downstream edge near LE as shown in Fig. 10. In the near-field, the high-turbulence present close to the test surface is dominated by the latter due to the following two reasons:

- the turbulence in this region does not have a chance to attenuate due to its close proximity to the high-velocity gradients fueling turbulence at the jet–crossflow interface; and
- the flow from the high-turbulence region remains close to the wall due to the coolant being bent over the top of it.

Because this high turbulence lies underneath the coolant, it will aid in diffusing the coolant toward the wall to improve η. However, it will also tend to increase h in these regions as will be discussed in the surface results. Turbulence generated within the film hole is convected out and deposited in the center of the coolant core. Since

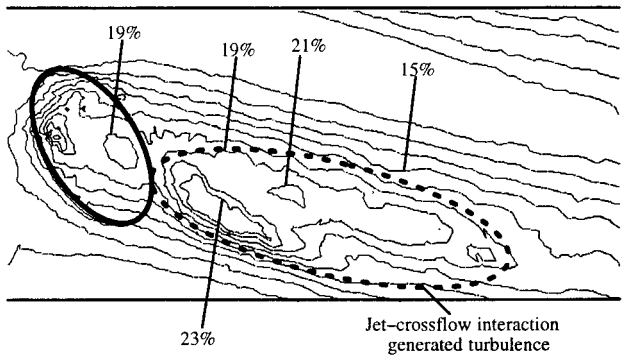

Fig. 10 Turbulence intensity on a plane $y/D = 0.2$ showing turbulence quantities exiting the film-hole as well as those generated by the jet-crossflow interaction for $M = 1.25$, $\Phi = 60$ deg

there are no shear layers to sustain it, this particular turbulence pocket quickly diffuses and dissipates throughout the core region. It only plays a small role in the surface results when it is carried toward the surface by the vortex structure.

Far-Field Behavior. The far-field behavior is dominated by the flow structures set up in the near field. In the streamwise case discussed in the companion paper (Part I), the far-field behavior is shown to be strongly dominated by a counterrotating vortex structure, which tends to lift the coolant off the surface to be protected. In compound angle cases, this counterrotating vortex becomes asymmetric and actually collapses to a single rotating vortex with significant lateral motion of coolant near the wall. The single vortex structure continues to play a role in the far field by convectively mixing the coolant and the crossflow leading to a relatively uniform lateral distribution of temperature as shown in Fig. 11. The vortex loses its strength with downstream distance and eventually the flow becomes a crossplane shear layer between the streamwise free stream and the lateral motion near the test surface, Fig. 12.

Surface Results

Adiabatic Effectiveness. The surface results examined in this paper consist of η and h distributions along the downstream test surface. The coolant distribution on the test surface shown in Fig. 13 can be characterized by three primary regions:

1 The first region is the low-momentum coolant fluid, which oozed out of the trailing edge of the film hole and remained attached. This coolant deteriorated with downstream distance by secondary flow;

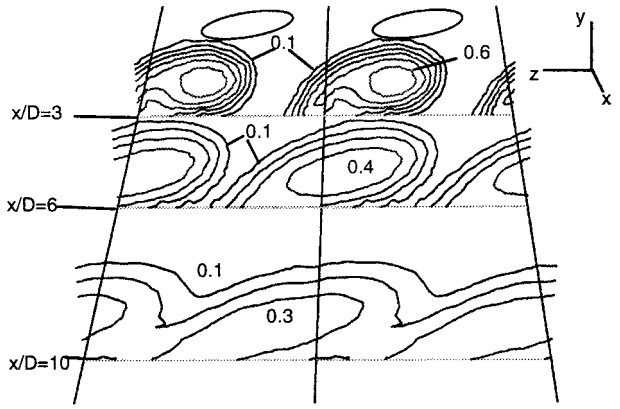

Fig. 11 Contours of θ at downstream locations showing a quick merger of coolant between holes for $\Phi = 60$ deg, $M = 1.25$

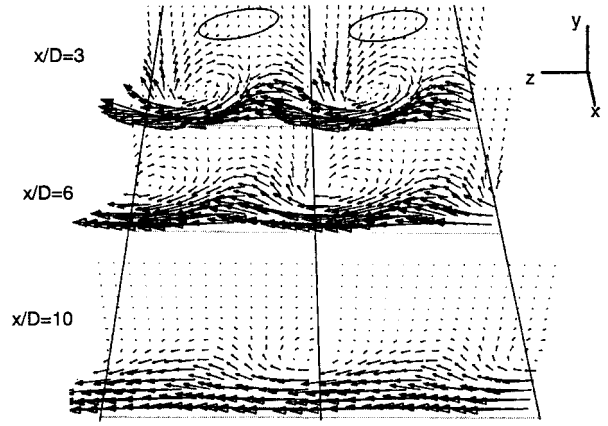

Fig. 12 Velocity vectors in crossplanes showing the demise of the vortex as it is damped to a pure lateral shear layer for $M = 1.25$, $\Phi = 60$ deg

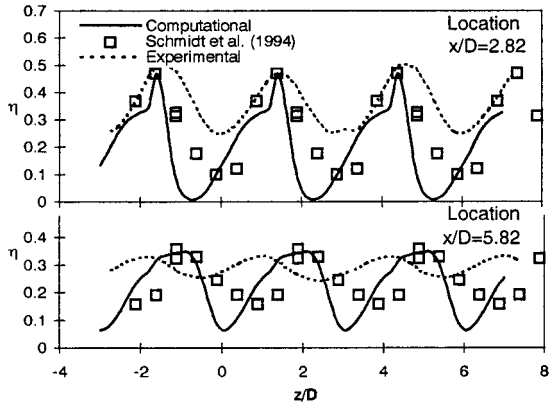

Fig. 14 Lateral distribution of η at downstream locations showing good correspondence between experiments and computations for $\Phi = 60$ deg and $M = 1.25$

2 The second region is a hot region as a result of hot crossflow fluid tucking under the coolant along the downstream edge of the film hole starting at LE; and
3 The third region is caused by the coolant core lifting off and returning to the wall downstream through diffusion and secondary flow convection.

In region 1, the trajectory setup in the near-field is roughly seen to hold with the surface results downstream. The coolant follows a path approximately half of the compound angle of the metal. These trends are shown in Fig. 14 for both the experimental and computational data with only slight deviations in magnitude and lateral motion. The computations consistently predicted lower η results between film holes in the near-field region and a higher, narrower attached region. These deviations are attributed partly to insufficient spreading in the computations and also the limited ability of creating perfectly adiabatic surfaces in experiments. It can also be seen in Fig. 14 that the lateral motion is underpredicted. The η results for the other cases studied are shown in the laterally averaged $\bar{\eta}$ in Fig. 15. Increasing the compound angle leads to a narrower attached region and therefore lower values of $\bar{\eta}$ in the near field. The compound angle had positive effects with downstream distance by causing the coolant core to be convected and diffused toward the surface more quickly, leading to an increase in $\bar{\eta}$. Increasing blowing ratio tended to cause region 1 to decrease quicker due to increased jetting effects leading to a decrease in $\bar{\eta}$ the near field, however the increase in coolant does lead to higher $\bar{\eta}$ farther downstream as the core returns to the protected surface.

Heat Transfer Coefficient. Compound-angle injection was found to alter the heat transfer coefficient result significantly. For example, turbulence at the wall is significantly increased where the crossflow accelerates underneath the coolant. This factor leads to increased h/h_o values in Fig. 16 in regions where the highest temperatures are found in Fig. 13. Validation of these results was provided by comparisons of a $DR = 1.0$, $M = 1.0$ case to the equivalent case by Sen et al. (1996) in Fig. 17 showing good correspondence. Also the laterally averaged value of h/h_o was utilized to compare the different configurations studied in Fig. 18.

9 Conclusions

Large-scale computational simulations with high-density, high-quality grid meshes were carried out for film cooling configurations with a row of cylindrical holes involving compound-angle injections at $\Phi = 45$, 60, and 90 deg. Predicted results were validated against experimental data and compared to the reference

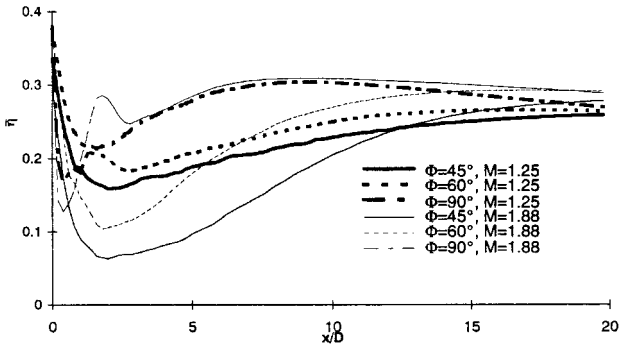

Fig. 15 Laterally averaged $\bar{\eta}$ versus downstream distance showing the effects of compound-angle injection Φ and blowing ratio

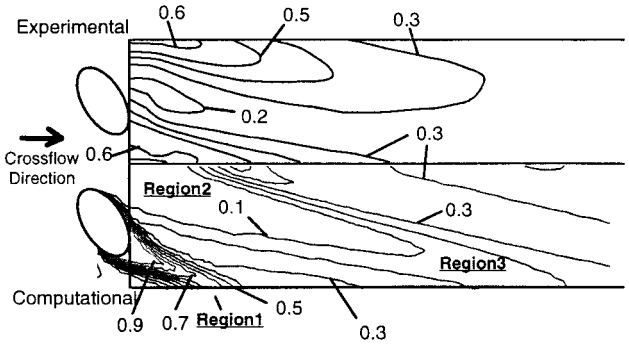

Fig. 13 Contours of η on the downstream wall showing the characteristic regions for both computations (bottom) and experiments (top) for $\Phi = 60$ deg and $M = 1.25$

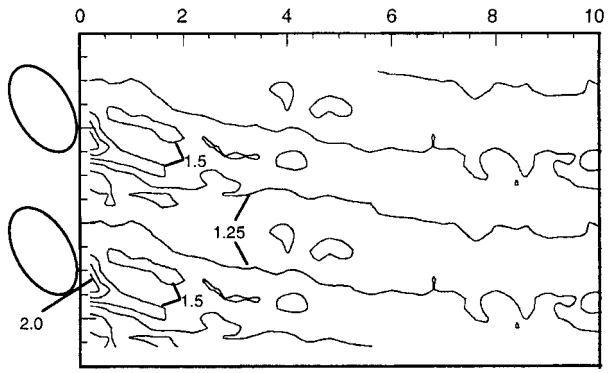

Fig. 16 Normalized heat transfer coefficient for $M = 1.25$ and $\Phi = 60$ deg

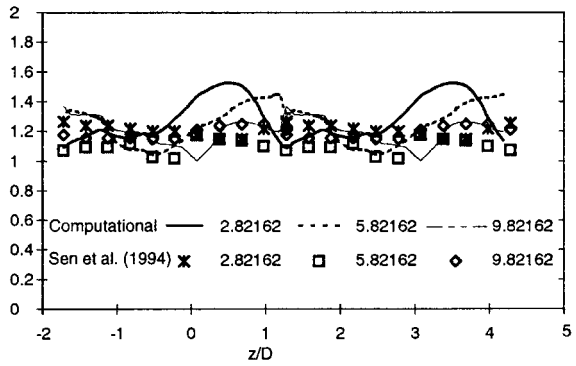

Fig. 17 Lateral distributions of heat transfer coefficient show good agreement between computationally predicted and experimentally measured data

case of streamwise injected coolant jets. The key set of conclusions drawn in this study are as follows:

- η and h distribution on the test surface is dominated by the vortex structure found downstream of the jet–crossflow interaction site;
- as Φ increases the well-known symmetric counterrotating vortex structure becomes increasingly asymmetric as one leg collapses and the other one forms a single dominant vortex at $\Phi = 90$ deg;
- the collapsing leg is associated with vorticity along the upstream edge of the film hole, which is blocked due to a large stagnation region created by the crossflow impinging on the coolant jet;
- an important second source of vorticity is found at the interface of crossflow and coolant jet along the downstream edge near the LE point. This vorticity augments the one in the film-hole boundary layer and strengthens as the compound angle increases. Relative magnitudes of the two vorticity sources is configuration dependent;
- compounding improves the lateral uniformity of the adiabatic effectiveness. At high Φ angles, the lateral distribution of η is ruler-flat within only a few diameters downstream of the row of film holes; and
- the heat transfer coefficient was found to be augmented due to the compounding effects in all the cases studied; however, there is net gain as the compound-angle injection is capable of providing a highly sought-after feature in film cooling, namely, lateral spreading and uniformity.

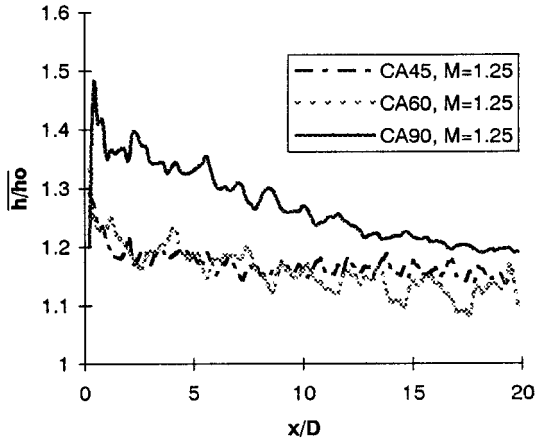

Fig. 18 Laterally averaged heat transfer coefficient results showing the effects of compound angle on the heat transfer characteristics

Acknowledgments

This paper was prepared with the support of the U.S. Department of Energy, Morgantown Energy Technology Center, Cooperative Agreement No. DE-FC21-92MC29061. The authors would like to thank Clemson University graduate students Mr. John Farmer and Mr. Dave Seager, as well as their faculty advisor Prof. James A. Liburdy, for the experimental data used in the present study. Also, special thanks are due to Mr. Gary Berger and Mr. Richard Baldwin of CNS at Clemson University and John Lane of the University of South Carolina for their assistance in computer related matters. We are also deeply indebted to Dr. Rick Lounsbury at Fluent, Inc., for his invaluable support with Fluent/UNS.

References

Butkiewicz, J., Walters, D., McGovern, K., and Leylek, J., 1995, "A Systematic Computational Methodology Applied to a Jet-in-Crossflow. Part 1: Structured Grid Approach," ASME Paper No. 95-WA/HT-2.

Ekkad, S., Zapata, D., and Han, J., 1997a, "Heat Transfer Coefficients Over a Flat Surface With Air and CO_2 Injection Through Compound Angle Holes Using a Transient Liquid Crystal Image Method," ASME JOURNAL OF TURBOMACHINERY, Vol. 119, pp. 580–586.

Ekkad, S., Zapata, D., and Han, J., 1997b, "Film Effectiveness Over a Flat Surface With Air and CO_2 Injection Through Compound Angle Holes Using a Transient Liquid Crystal Image Method," ASME JOURNAL OF TURBOMACHINERY, Vol. 119, pp. 587–593.

Farmer, J. P., Seager, D. J., and Liburdy, J. A., 1997, "The Effect of Shaping Inclined Slots on Film Cooling Effectiveness and Heat Transfer Coefficient," ASME Paper No. 97-GT-339.

Hyams, D., McGovern, K., and Leylek, J., "Effects of Geometry on Slot-Jet Film Cooling Performance," ASME Paper No. 96-GT-187.

Lee, S., Kim, Y., and Lee, J., 1997, "Flow Characteristics and Aerodynamic Losses of Film-Cooling Jets With Compound Angle Orientations," ASME JOURNAL OF TURBOMACHINERY, Vol. 119, pp. 310–319.

Ligrani, P., Wigle, J., Ciriello, S., and Jackson, S., 1994a, "Film Cooling From Holes With Compound Angle Orientations, Part I: Results Downstream of Two Staggered Rows of Holes With 3*D* Spanwise Spacing," ASME *Journal of Heat Transfer*, Vol. 116, pp. 341–352.

Ligrani, P., Wigle, J., and Jackson, S., 1994b, "Film Cooling From Holes With Compound Angle Orientations, Part II: Results Downstream of a Single Row of Holes With 6*D* Spanwise Spacing," ASME *Journal of Heat Transfer*, Vol. 116, pp. 353–362.

Fluent-UNS Users Guide, May 1996, Release 4.0, Fluent Inc., Lebanon, NH.

Schmidt, D., Sen, B., and Bogard, D., 1996, "Film Cooling With Compound Angle Holes: Adiabatic Effectiveness," ASME JOURNAL OF TURBOMACHINERY, Vol. 118, pp. 807–813.

Sen, B., Schmidt, D., and Bogard, D., 1996, "Film Cooling With Compound Angle Holes: Heat Transfer," ASME JOURNAL OF TURBOMACHINERY, Vol. 118, pp. 300–306.

Walters, D., and Leylek, J., 1997, "A Consistently Accurate Computational Methodology Applied to a Three-Dimensional Film Cooling Flowfield," ASME JOURNAL OF TURBOMACHINERY, Vol. 119, pp. 777–785.

Walters, D., McGovern, K., Butkiewicz, J., and Leylek, J., 1995, "A Systematic Computational Methodology Applied to a Jet-in-Crossflow Part 2: Unstructured/Adaptive Grid Approach," ASME Paper No. 95-WA/HT-52.

A Detailed Analysis of Film Cooling Physics: Part III—Streamwise Injection With Shaped Holes

D. G. Hyams

J. H. Leylek

Department of Mechanical Engineering,
Clemson University,
Clemson, SC 29634

The physics of the film cooling process for shaped, streamwise-injected, inclined jets is studied for blowing ratio ($M = 1.25, 1.88$), density ratio ($DR = 1.6$), and length-to-diameter ratio ($L/D = 4$) parameters typical of gas turbine operations. A previously documented computational methodology is applied for the study of five distinct film cooling configurations: (1) cylindrical film hole (reference case); (2) forward-diffused film hole; (3) laterally diffused film hole; (4) inlet shaped film hole, and (5) cusp-shaped film hole. The effect of various film hole geometries on both flow and thermal field characteristics is isolated, and the dominant mechanisms responsible for differences in these characteristics are documented. Special consideration is given to explaining crucial flow mechanisms from a vorticity point of view. It is found that vorticity analysis of the flow exiting the film hole can aid substantially in explaining the flow behavior downstream of the film hole. Results indicate that changes in the film hole shape can significantly alter the distribution of the exit-plane variables, therefore strongly affecting the downstream behavior of the film. Computational solutions of the steady, Reynolds-averaged Navier–Stokes equations are obtained using an unstructured/adaptive, fully implicit, pressure-correction solver. Turbulence closure is obtained via the high-Reynolds-number k–ϵ model with generalized wall functions. Detailed field results as well as surface phenomena involving adiabatic film effectiveness (η) and heat transfer coefficient (h) are presented. When possible, computational results are validated against corresponding experimental cases from data found in the open literature. Detailed comparisons are made between surface and field results of the film hole shapes investigated in this work; design criteria for optimizing downstream heat transfer characteristics are then suggested.

1 Introduction

An understanding of jet-in-crossflow interaction is crucial in the design of hot section components in modern gas turbine engines. The temperature of the gases entering the turbine section is typically near the melting point of the alloys used in the turbine airfoils and endwalls; to prevent these components from failing at such elevated temperatures, they are commonly film cooled to isolate the metal from the hot gases. In addition, the geometry of film cooling holes is often modified in some manner to improve cooling performance, thus allowing for better metal protection and/or a decreased coolant supply; however, these configurations are often implemented with weak understanding of flow and heat transfer characteristics in and near the film hole. This study focuses on inclined discrete jet film cooling physics and the effect of film-hole shaping on both flow and thermal field characteristics. Detailed field data, the adiabatic effectiveness, and the surface heat transfer coefficient will be used to evaluate the advantages and disadvantages of film-hole shaping. Emphasis is placed on determining, with the help of vorticity analysis, the dominant mechanisms responsible for the performance of the various film hole configurations. Specifically, the present investigation aims to examine several film-hole shapes, pinpoint the flow mechanisms responsible for determining downstream heat transfer, and suggest ways of using film hole geometry to exploit or attenuate these flow mechanisms.

Contributed by the International Gas Turbine Institute and presented at the 42nd International Gas Turbine and Aeroengine Congress and Exhibition, Orlando, Florida, June 2–5, 1997. Manuscript received International Gas Turbine Institute February 1997. Paper No. 97-GT-271. Associate Technical Editor: H. A. Kidd.

2 Literature Review

The interaction of jets in crossflow has been heavily researched both experimentally and computationally. Some relevant references applicable to cylindrical film holes are discussed in detail in Part I of this paper; only references specific to shaped film holes are discussed here.

Goldstein et al., (1974) were among the first to pioneer the use of shaped film holes for improved film cooling performance. The performance of inclined holes with a 10 deg laterally flared exit was compared with the performance of streamwise inclined cylindrical film holes, both with an L/D of 5.2 and P/D of 3 and 6. Flow visualization studies showed that with and without the mainstream flow, the shaped hole provided much better lateral coverage of the test surface and also attenuated jet liftoff. Effectiveness data confirmed the observations that the shaped film hole afforded better lateral coverage and better centerline effectiveness. In addition, the shaped film holes provided significant improvements in cooling performance at any M and DR. The authors hypothesized that the increased exit area of the shaped holes was responsible for slowing the coolant flow such that less penetration through the oncoming boundary layer and into the mainstream occurred.

Papell (1984) experimentally studied a novel shape for use in film cooling. Papell found that shaping the hole with a cusp (similar in appearance to a kidney bean) induced strong longitudinal vortex structures within the film hole; he hypothesized, with the aid of flow visualizations, that creating these vortical structures enabled the crossflow to use its energy to force the jet down to the surface, rather than itself creating the counterrotating vortices. Further, he postulated that the placement of the cusp on the leeward side (TE) forced the film hole secondary flow to rotate in a direction opposite of that traditionally observed in cylindrical

film holes. Papell offered evidence in the form of adiabatic effectiveness and film coverage data to support his findings that his cusp-shaped holes provided better film cooling performance.

Makki and Jakubowski (1986) presented downstream heat transfer results for a film hole with a trapezoidal shaped expansion. Using the downstream heat transfer coefficient versus the heat transfer coefficient of an undisturbed boundary layer, they showed that the shaped film hole consistently provided better heat transfer characteristics than simple cylindrical holes with the same metering section. Makki and Jakubowski reported that the shaped holes offered up to 23 percent better film cooling performance than the corresponding cylindrical hole. Much guesswork was applied in determining the physical mechanisms responsible for this improved film cooling performance; like Goldstein et al. (1974), the authors attributed much of the improved film cooling performance to the decreased momentum flux at the jet exit due to the diffusing shape of the trapezoidal film hole.

Schmidt et al. (1996) and Sen et al. (1996) presented two companion papers in which the effect of adding a 15 deg forward diffusing exit to a streamwise oriented film hole was investigated. Moderate M and DR typical of gas turbines were used, along with a realistic L/D of 4.0 and P/D of 3.0. They found that the exit diffused film hole demonstrated better spread of adiabatic effectiveness than the cylindrical counterpart; however, by $x/D = 15$ the expanded and round compound angle holes had essentially the same level of effectiveness. From the heat transfer coefficient standpoint, the forward-expanded hole performed poorly, presumably because of the increased interaction between the jet and mainstream. A key conclusion shown in this work was that to determine overall film cooling performance, it is crucial to obtain knowledge of both the adiabatic effectiveness and the heat transfer coefficient.

Thole et al. (1998) studied the effect of film hole geometry on the film cooling flowfield. The film hole shapes examined in this work were a cylindrical (reference) case, a hole with a laterally expanded exit, and a hole with a forward–laterally expanded exit. M and DR were unity, and external mainstream Mach number and internal coolant supply Mach number were nearly matched at approximately 0.3. Results from this study showed that by expanding the exit of the film holes, the penetration of the jet as well as the severe shear regions in the near field were significantly reduced when compared to the reference cylindrical hole. Turbulence levels, although similar in magnitude between the three cases, were found to originate from different sources; therefore, the flow characteristics were very dependent on the film hole geometry.

Haven and Kurosaka (1996) documented the effects of film hole shape on the near-field vortical structures characteristic of a jet-in-crossflow interaction. Note that the study concentrated solely on fluid mechanics (no heat transfer), and the shaped jets were injected normal to the test surface. The shapes investigated were simple two-dimensional shapes without a metering section and with equal cross-sectional area; the shapes were: (1) circular, (2) square, (3) rectangular, and (4) elliptical. Limited quantitative data were taken; rather, flow visualizations were conducted for various film hole shapes to determine the effect on downstream vortical structures. The authors proposed that the counterrotating vortices downstream of the jet exit plane had a significant influence on jet liftoff, by the mutual induction lift generated by these structures. They concluded that hole geometries that cause these vortices to form farther apart tend to inhibit jet detachment, since the lift generated by mutual induction is less. One of the principal mechanisms affecting the formation of the counterrotating vortices was the vorticity contained in the film hole sidewall boundary layers. This vorticity will be discussed in detail in the present paper.

Hyams et al. (1996) studied the effects of slot jet shaping on the heat transfer downstream of a slot jet. It was found that shaping of the slot inlet and exit provided significant gains in the film cooling performance. Flow mechanisms responsible for this behavior, such as the exit plane momentum characteristics and sources of turbulence within the film hole, were documented in detail. Both adiabatic effectiveness and heat transfer coefficient data were obtained in this study.

The effect of film hole shaping and orientation for transonic conditions was investigated by Wittig et al. (1996). Measurements and computations were performed for a cylindrical film hole, laterally expanded film hole, and a forward–laterally expanded film hole. Effectiveness data and flowfield data were only presented for the cylindrical reference case, however. Velocity field computations with a multiblock structured grid provided fair agreement with the measured results along the centerplane outside of the film hole; however, predictions within the film hole and at the film hole exit plane were (according to the authors) poor. Only one experimental visualization was presented for any shaped case; the bulk of the results discussed only the cylindrical film hole.

No detailed computational studies of three-dimensional shaped film holes exist in the open literature at this time. In addition, no

Nomenclature

AR = area ratio = $A_{\text{metering}}/A_{\text{exit-plane}}$
CUSP = cusp shaped film-hole
D = diameter of film-hole
DR = density ratio = ρ_j/ρ_∞
FDIFF = film hole with a forward diffused exit
h = heat transfer coefficient = $q''/(T_w - T_{aw})$, W/m^{2}K
ISHAP = film hole with inlet shaping
L/D = length-to-diameter ratio of film hole
LDIFF = film hole with laterally diffused exit
LE = leading edge of film-hole exit plane
M = blowing (or mass flux) ratio = $(\rho V)_j/(\rho V)_\infty$
Pr = Prandtl number
P/D = pitch-to-diameter ratio of film hole
q'' = surface heat flux per unit area, W/m^2
Re = Reynolds number
REF = cylindrical reference film-hole case
St = Stanton number
T = local fluid temperature
TE = trailing edge of film-hole exit plane
tke = tubulence kinetic energy
TL = turbulence level (in percent) = $(\frac{2}{3}*\text{tke})^{1/2}/V_\infty*100$
V = local fluid velocity magnitude = $|\vec{V}|$
$\vec{V}$ = local velocity vector = $u\hat{i} + v\hat{j} + w\hat{k}$
VR = velocity ratio = V/V_∞
x = coordinate in the streamwise direction
x_0 = unheated starting length
y = coordinate normal to the test surface
y^+ = nondimensional wall distance = $y\sqrt{\tau_w/\rho_w/\nu_w}$
z = coordinate in the lateral direction
α = coolant jet injection angle
δ = boundary layer thickness
η = adiabatic effectiveness = $(T_\infty - T_{aw})/(T_\infty - T_j)$
ν = kinematic viscosity
ρ = fluid density
$\vec{\xi}$ = total vorticity vector = $\xi_x\hat{i} + \xi_y\hat{j} + \xi_z\hat{k}$

Subscripts

∞ = mainstream conditions at crossflow inlet plane
aw = adiabatic wall
fh = condition inside film hole
j = nominal jet conditions
w = conditions at wall

systematic investigation has been conducted concerning different film hole configurations and their effect on the complex three-dimensional flow mechanisms present both inside of the film hole and in the near-field interaction.

3 Present Contributions

The primary objective of this work is to examine thoroughly the physics of a row of inclined, discrete, shaped jets in crossflow, while pinpointing the physical flowfield and heat transfer differences between a cylindrical reference case and selected shaped film holes. These three-dimensional studies include several shapes as suggested by the gas turbine industry and as chosen at the discretion of the principal investigators. Objectives of this study are to:

- determine the effect of several industry-relevant film hole shapes on downstream heat transfer;
- investigate and document the physical mechanisms responsible for changes in film cooling performance for shaped film holes, so that better designs can be achieved;
- present both adiabatic effectiveness and heat transfer coefficient downstream of shaped-hole film cooling configurations;
- demonstrate that CFD can be used to capture flow and heat transfer details accurately and dependably;
- validate a consistently accurate computational methodology and transfer this technology to the gas turbine industry;
- establish criteria for more effective design for shaped film holes.

4 Computational Methodology

The computational methodology used in this study is identical to the methodology documented in Walters and Leylek (1997) and will not be repeated here. The computational hierarchy used encompasses a proper film cooling model, an exact geometry, a high-quality, high-density computational mesh, high-order discretization schemes, and turbulence modeling that is suitable for the problem at hand. The simulations are carried out in a fully elliptic manner using an implicit, pressure-correction based, unstructured/adaptive grid Navier–Stokes solver.

5 Experimental Details

Data from the University of Texas (Schmidt et al., 1996) are used for the cylindrical and forward-diffused film holes. Schmidt et al. (1996) document adiabatic effectiveness results downstream of streamwise-injected cylindrical and forward-diffused film holes, and the experimental apparatus is detailed in that work. The film holes used in this study are injected at $\alpha = 35$ deg, and spaced at $P/D = 3$. The exact geometry of these film holes is reproduced in the computations and is shown in Fig. 1. The density ratio of these interactions was $DR = 1.6$; blowing ratios tested were $M = 1.25$ and $M = 1.88$.

6 Simulation Details

6.1 Definition of Shaped Film Holes. Five basic film hole shapes are investigated in this work. The configurations are: (1) cylindrical (REF), (2) forward diffused (FDIFF), (3) laterally diffused (LDIFF), (4) inlet shaped (ISHAP), and (5) cusp shaped (CUSP). Schematics of each of these shapes is shown in Fig. 1.

Each film hole geometry (except for the CUSP case) is simulated for two blowing ratios, and adiabatic effectiveness and heat transfer results are obtained for each. Table 1 below shows an overview of the simulations performed in the present work. Boundary condition specifics are discussed in the following section.

6.2 Modeling and Boundary Conditions. For each of the film hole shapes described in this work, the boundary conditions

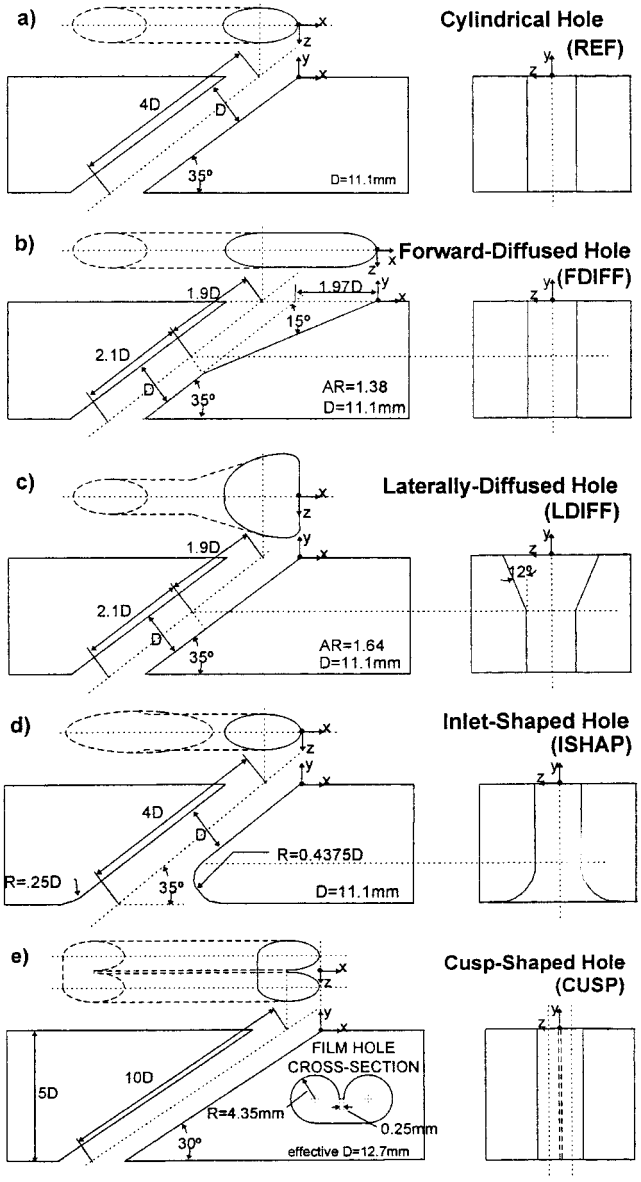

Fig. 1 Schematics of the selected film hole shapes show the geometry of each configuration in three orthogonal planes

are identical except for differences noted in the following paragraphs; a schematic of the domain and boundary conditions is shown in Fig. 2. Symmetry conditions are imposed at the longitudinal centerline of the jet, as well as at $P/D = 1.5$. These boundary conditions enforce streamwise injection of the jet and a lateral spacing of $P/D = 3$ for an infinite row of jets. Due to the height of the wind tunnel used in the experimental counterparts, a zero-normal-gradient (slip-wall) condition is applied at the top of

Table 1 Overview of the simulations performed in the present work

Film Hole Shape	M	DR	test surface
Cylindrical (REF)	1.25, 1.88	1.6	adiabatic, const. q"
Forward Diffused (FDIFF)	1.25, 1.88	1.6	adiabatic, const. q"
Laterally Diffused (LDIFF)	1.25, 1.88	1.6	adiabatic, const. q"
Inlet Shaped (ISHAP)	1.25, 1.88	1.6	adiabatic, const. q"
Cusp Shaped (CUSP)	1.25	1.08	adiabatic, const. q"

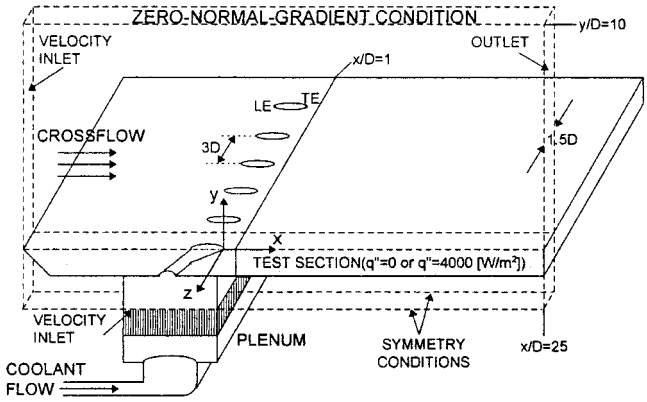

Fig. 2 A sketch of the computational domain shows the boundary condition scheme used for each shaped case

the domain. This zero-gradient wall is imposed at $y/D = 10$ for all simulations to reduce the size of the computational domain; it is found that all gradients in the y direction are negligible far before this limit is reached.

An outlet (convection) boundary condition is imposed at $x/D = 25$. The plenum inlet velocity (coolant air) is set to achieve $\mathrm{Re}_{fh} = 18{,}700$ for every case; this matches the velocity range used in Schmidt et al. (1996), and the exact velocities are documented in the following paragraphs. Various M are attained by varying the crossflow (air) inlet flux, as described below. TL at the plenum inlet is assumed to be 0.1 percent. For all cases, the length scale for each inlet was taken to be one-tenth of the inlet extent. Following the Schmidt et al. (1996) cryogenic setup, the crossflow inlet temperature is specified as 300 K, and the plenum coolant temperature is set at 187.5 K; these temperatures force $DR = 1.6$ for all cases. All walls are adiabatic, except for the test section in the active wall (heat transfer coefficient) simulations; in these cases, the wall heat flux is set to 4000 W/m^2. The heated test section starts at $x/D = 1$ for all cases.

The geometry for the REF and FDIFF cases is taken from the work of Schmidt et al. (1996); therefore, the plenum geometry and the upstream section match the experimental setup described there. This plenum is 50.8 mm high and 101.6 mm wide, and the inlet velocity is set to 0.335 m/s. A uniform velocity inlet condition is imposed at the beginning of the 237 mm upstream section, and a turbulent boundary layer is allowed to develop from this point. Turbulence intensity at the crossflow inlet is assumed to be 0.2 percent, as per the documentation of Schmidt et al. (1996).

For the LDIFF and ISHAP cases, the plenum geometry matches the geometry used in in-house experiments; this geometry is documented in Farmer et al. (1997). The plenum velocity is set to 0.2855 m/s. The upstream section is extended $10D$ prior to the upstream edge of the film holes, in accordance to the location at which velocity and turbulence intensity profiles were experimentally acquired. Experimentally measured profiles for velocity and turbulence intensity are imposed at this location. The experimentally measured $\delta/D = 0.55$ condition at the film hole is matched.

The plenum used in the Schmidt et al. (1996) experiments is also used in the CUSP case, since the actual geometry of the plenum was not specified in Papell (1984). The crossflow inlet velocity profile is constructed to match $\delta/D = 1.3$ at the film hole breakout and the inlet TL is set to 3 percent, as documented in Papell's study. Temperature at the crossflow inlet is set to 295 K, and the coolant is injected at 273 K; these temperatures set $DR = 1.08$. Since D, L/D, Re_{fh}, and DR are different from the other simulations in this work, no cross comparisons involving the CUSP case and other shaped cases are possible.

Most notable of the boundary condition and modeling differences in these simulations are the two different plenum geometries used. However, since the flow in the supply plenum is largely stagnant, differences in plenum geometry are very unlikely to affect film hole inlet-plane conditions.

6.3 Convergence. A fully implicit, pressure-correction, unstructured/adaptive grid code was used to perform all processing of the computational simulations. Figure 3 shows the ISHAP surface grid used in this study; this grid shows the typical cell quality and density of the mesh for all the computations. Preprocessing and post-processing were performed on Sun and SGI workstations, while computations were performed on a 64 CPU Intel Paragon supercomputer. Simulations were typically run using 32–56 CPUs, which required about 6 hours per 300 iterations; approximately 1500 iterations were necessary to reach a fully converged state. Convergence was established when the mass and energy imbalance in the entire computational domain was less than 0.01 percent of inlet fluxes, normalized residuals had fallen at least three orders of magnitude, and no change was observed in any field result. Grid independence was assessed by repeatedly refining the grid (based on field gradients) until no observable changes were apparent in the field results. Typical background grids started at 250,000 cells; fully converged and grid independent results were typically 400,000 cells.

7 Results

7.1 Vorticity Analysis of Film Cooling Interactions. Part I of this four-part series highlights that the most dominant mechanism in determining film cooling performance is the longitudinal vortex structure formed aft of the jet injection site. Further, it is stated that boundary layer vorticity from the film hole controls the strength of these longitudinal vortices. The physical explanations of the important flow mechanisms in the following sections rely heavily on vorticity analysis; consequently, it is necessary to define the concepts that are used to pinpoint the formation of film hole boundary layer vorticity.

Note that in all discussions of vorticity that follow, only the positive z side of the film hole is considered. Due to symmetry, the same mechanisms (but with opposite sign) occur on the negative z direction side.

For a streamwise-injected film hole, the contributors to vorticity aligned in the streamwise direction (hereafter referred to as "aligned vorticity" and with the symbol ξ_x) are illustrated in Fig. 4(a). Because of secondary motion within the film hole, the interior boundary layer travels in a helical motion. The resultant vorticity vector, shown as the dotted line in Fig. 4(a), can therefore be decomposed into a component due to throughflow that is perpendicular to the flow direction, and a component due to secondary flow that is in the direction opposite to the flow direction. The resultant of these two components is then resolved to a coordinate system aligned with the predominant crossflow direc-

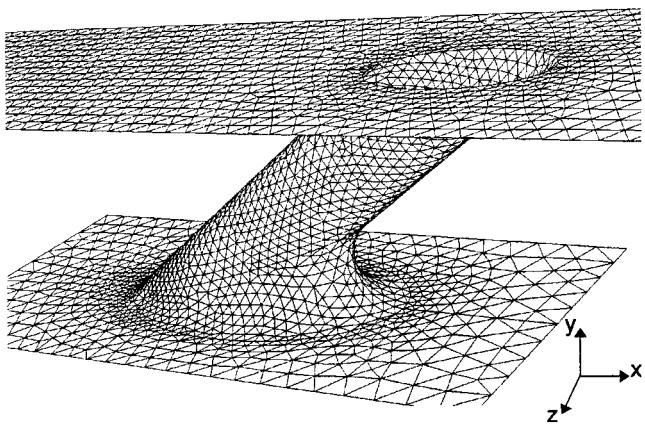

Fig. 3 A photo of the ISHAP computational grid shows typical grid quality and resolution

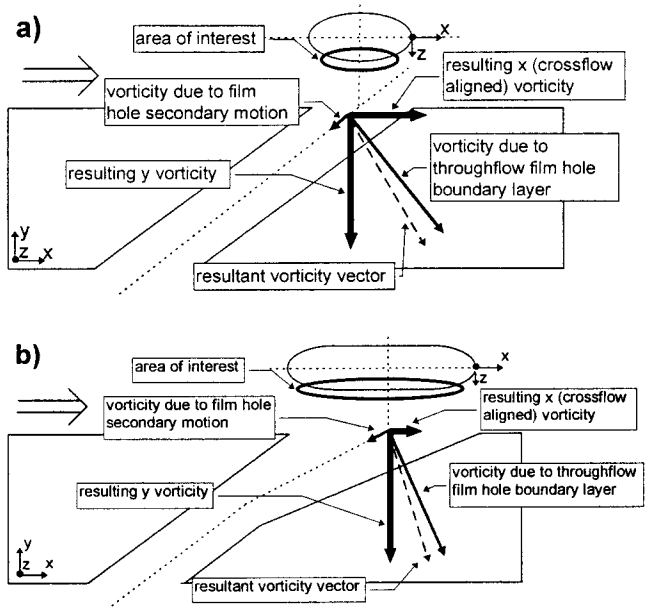

Fig. 4 Sketch of the film hole boundary layer vorticity shows the manipulation of streamwise aligned vorticity by film-hole geometry

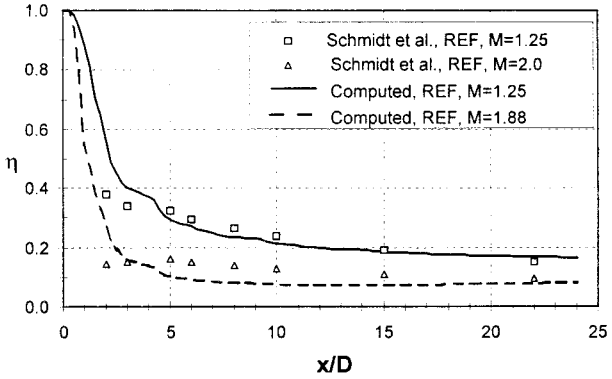

Fig. 5 A validation plot of centerline effectiveness shows good agreement between computational and experimental data

tion to determine the aligned vorticity. This aligned vorticity is denoted by ξ_x. Inspection of Fig. 4(*a*) illustrates two ways to decrease the aligned vorticity: (1) decrease the throughflow vorticity, or (2) increase the secondary vorticity.

Figure 4(*b*) illustrates the effect on the aligned vorticity as the exiting flow angle decreases. The throughflow vorticity is tilted downward, where it cannot contribute a great deal to the aligned vorticity. By the same argument, it is obvious that increasing the flow angle would not only increase the *y* momentum and penetration into the crossflow, but would also tilt the resultant sidewall vorticity vector forward; this would (detrimentally) increase the magnitude of crossflow-aligned vorticity.

7.2 Cylindrical Film Hole (REF). To form adequate comparisons and isolate mechanisms in the upcoming shaped film-hole cases, a solid well-defined reference case must be formulated. A separate reference case (an inclined cylindrical film hole) is simulated in this study to provide proper basis for comparison. The findings reported in this section are largely a summary of the work documented in Part I. Obviously, only the most relevant items and/or conclusions in this reference case are summarized here; note that the results of these separate simulations substantiate the findings of Part I of the present work. Following the reference case, separate sections identify the key mechanisms dominating the downstream heat transfer for the shaped film holes investigated in this paper.

Key conclusions from Part I include the effect of film-hole boundary layer vorticity on the downstream development of the inclined jet. The concept of explaining near-field interactions in terms of film hole boundary layer vorticity finds critical application in the area of shaped film holes. Reducing the strength of crossflow-aligned vorticity (ξ_x) exiting the film hole, and therefore the resulting counterrotating secondary structure, can prevent the liftoff of the coolant/wake structure downstream.

Figure 5 shows the computed versus measured η for the REF case at $M = 1.25$ and $M = 1.88$. Overall, the agreement between predicted and measured effectiveness is good. This lends credibility to the quality of simulations presented in the present paper. In the near field ($x/D < 3$), η is overpredicted somewhat, presumably because of a hypothesized recirculation region immediately downstream of the film-hole exit; the use of wall functions in the simulations do not allow the grid resolution necessary to capture such a phenomenon. As the jet moves downstream, the computations seem to slightly underpredict the diffusion rate of the lifted-off jet down to the test surface.

7.3 Forward-Diffused Film Hole (FDIFF). At the inlet of the FDIFF film hole, the same mechanisms are seen to exist as present in the REF case. The film-hole geometry is identical to the REF case within the metering section until the diffusing section is reached; therefore, the severe flow turning, the low-momentum zone, and jetting region are apparent as in the REF case. In fact, the consistency of the computational simulations is excellent in this area; *exactly* the same magnitude of all flow quantities for the REF and FDIFF cases are computed for the inlet and metering section of the film hole. This observation implies that the inlet development is independent of any elliptic effect by the crossflow impingement on the coolant jet, and of any effect by the diffusing section.

As the coolant flow enters the diffusing section within the FDIFF film hole, a small separation is visible on the downstream wall of the film hole; also, the entire coolant flow slows drastically as the flow area is widened. Because of the use of wall functions in these simulations, the overall extent of the separation may not be exact, and may contribute more to turbulence generation within the film hole (because of shear layers over the separation zone) than what is computed. However, it is not expected that this separation will significantly alter the distribution of the exit plane variables.

Because of the wide diffusing section, the effective *VR* of the FDIFF case is drastically lower than that of the corresponding REF case, as shown in Fig. 6(*b*). Note that the nominal $VR = 0.78$ for the $M = 1.25$ simulations. The higher-momentum jetting region is still visible on the windward side (LE) of the film hole (by examination of *VR* and α in Fig. 6(*b*) and Fig. 7(*b*), and low-momentum fluid exits from the leeward side (TE) of the film hole.

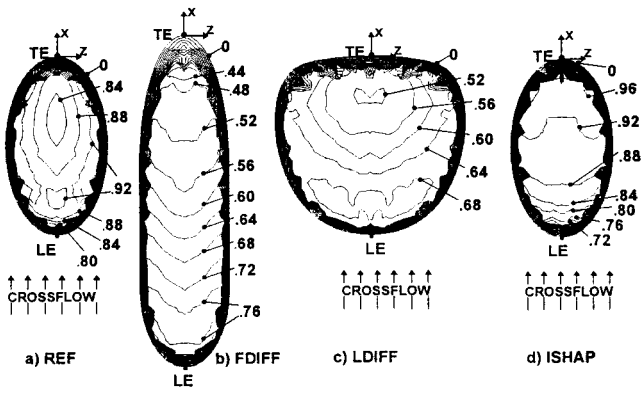

Fig. 6 A comparison of the exit plane *VR* distribution shows the low-momentum content of the diffused holes

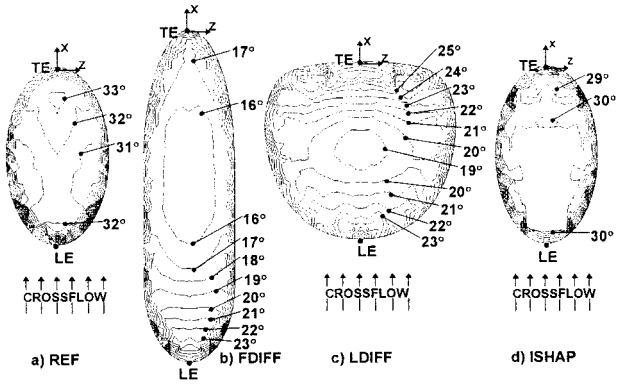

Fig. 7 Contours of the flow exit angle (α) at the exit plane show the various effective injection angles of each film hole shape

Also, as shown in Fig. 7(*b*), the flow exit angle is typically one-half that of the reference cylindrical hole; these two mechanisms contribute to an exceptionally low exit-plane *y*-momentum content of the FDIFF film hole. Although total *y*-momentum content is lower, the jetting region (comparable in magnitude to the REF case) controls the trajectory of the coolant jet. As shown in Fig. 12, the location of the jet-film interface is similar to the REF case. Note that, due to the definition of the origin in the FDIFF case (see Fig. 1(*b*)), the shear layer above the film has approximately 2*D* greater distance in which to develop. So, the jet trajectory is actually slightly below the trajectory predicted for the REF case.

Notably absent from the FDIFF case is the coolant wake observed and documented in Part I. A strong low-pressure region downstream of the TE of the film hole exit plane is absent; therefore, coolant from the film hole boundary layer is injected uniformly into the mainstream boundary layer as shown in Fig. 8(*b*). This behavior is in stark contrast to the REF case, where coolant fluid in the boundary layer is drawn toward the centerline, is slowed further by an adverse pressure gradient, and coalesces into a coolant wake that is subsequently lifted by the action of the counterrotating vortices that appear downstream of the injection site. The inward bending and lifting of the film-hole boundary layer fluid is strictly due to the action of the weak longitudinal vortices seen in the FDIFF case. The absence of a strong exit-plane pressure gradient and subsequent lack of a pronounced coolant wake is directly related to the low *y*-momentum content of the coolant exiting the FDIFF film hole.

The ξ_x levels contained within the exiting boundary layers on the lateral sides of the FDIFF film hole is much lower than the REF counterpart, as shown in Fig. 10(*b*). This difference in vorticity characteristics is due to: (1) velocity gradients along the side walls are relaxed due to decreased throughflow film-hole velocities; and (2) the shallow exit angle, especially along the side walls, afforded by the forward diffusing section. Each of these two mechanisms contributes greatly to the reduction in streamwise vorticity seen in the FDIFF case. More detail on this topic is discussed in section 8.2. Note that the length of the film-hole sidewall tends to add more ξ_x to counteract the advantages enumerated above; however, this effect, along with the constant dissipation of vorticity near the wall, is not pronounced enough to add significantly to the *x*-direction vorticity from the film hole. As a result of the much decreased ξ_x ejected and coalescing at the sides of the film hole, the strength of the downstream secondary motion (the typical counterrotating vortex pair) is decreased as shown in Fig. 11(*b*). Eliminating most of this secondary motion reduces unwanted induction lift and allows the coolant jet to retain proximity to the test surface, and also prevents the convection of entrained hot crossflow fluid underneath the coolant jet. A detailed discussion of this important phenomenon is given in section 8.2 of this paper and also in the companion paper designated as Part I.

The centerline temperature profiles in Fig. 9 show that the coolant core remains close to the wall, in contrast to the lifting apparent in the REF case. Downstream of the jet–crossflow interaction, the dominant mechanism becomes the generation of turbulence located throughout the film. Profiles of *TL* in Fig. 13 demonstrate the large difference in far-field turbulence production between the REF and FDIFF cases; this difference in behavior arises because of the large mismatch in exit velocity created by the FDIFF case; the crossflow attempts to "drag" the low-momentum jet along as it travels downstream. In the near field, *TL* is very similar; however, as the coolant film moves downstream, significant amounts of turbulence are generated throughout the film in the FDIFF case (an indication of the vertical velocity gradient can be assessed easily by the ξ_z profiles in Fig. 12). This large length-scale turbulence contributes a great deal to the diffusion rate of the crossflow energy into and across the coolant jet. Hence, the coolant is dissipated downstream not only by strong mixing at the film–crossflow interface, but also by mixing throughout the film itself.

As shown in Fig. 17, the centerline performance of the FDIFF film hole is excellent compared to the REF case; however, little spreading (and so small test plate coverage) of the temperature core exists. The underprediction of film spreading rate due to the anisotropic nature of turbulence downstream of a jet injection is a common feature of many CFD simulations; this issue is discussed in Part I. The heat transfer coefficient for the FDIFF case is consistently lower (at all x/D) than the REF case for $M = 1.25$ and $M = 1.88$.

7.4 Laterally Diffused Film Hole (LDIFF). Like the FDIFF case, the LDIFF case has identical film hole inlet-plane conditions as the reference case. The first effects of the film hole shaping are felt very close to the laterally diffusing section. No separation is seen on the sides of the 12 deg diffusing section; the flow smoothly negotiates the film hole area change and begins to slow as the area is widened. Note that Thole et al. (1998) observed high turbulence levels at the lateral sides of the film hole exit plane, which would imply separation within the 14 deg laterally diffused film hole; however, Re_{fh} in their experiments ($Re_{fh} \approx 52{,}000$) was three times higher than these simulations ($Re_{fh} \approx$

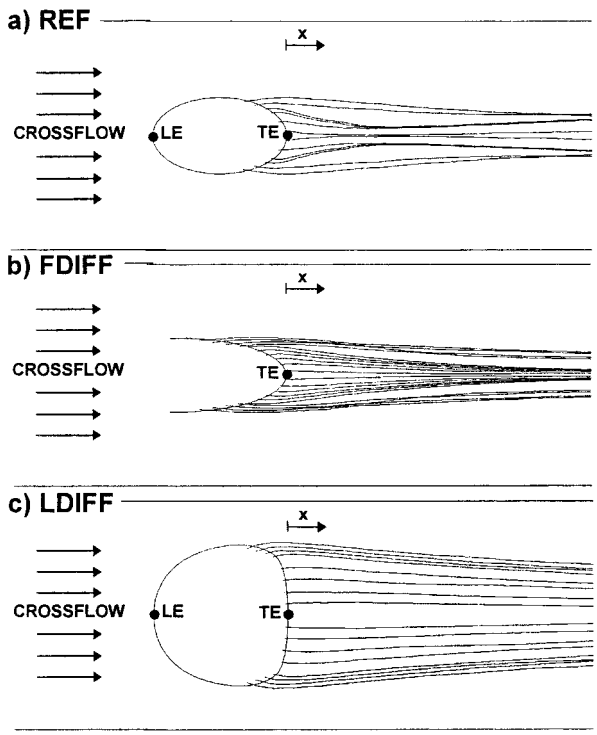

Fig. 8 Pathlines from the film-hole boundary layer show the presence or absence of a coolant wake for the REF, FDIFF, and LDIFF cases

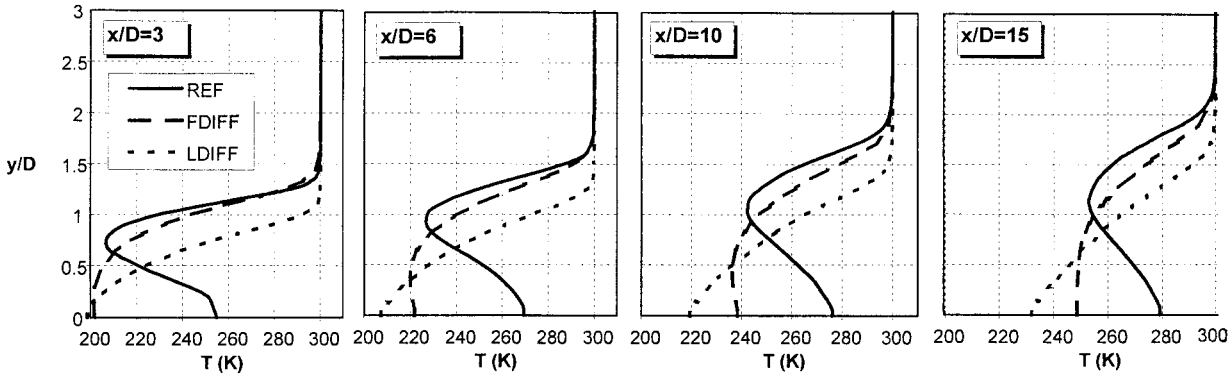

Fig. 9 Centerline temperature profiles at $x/D = 3$, $x/D = 6$, $x/D = 10$, and $x/D = 15$ for the REF, FDIFF, and LDIFF cases show the overall coolant characteristics

18,700). In addition, coolant was introduced into the film hole from a coflowing channel, which would largely eliminate the effect of the inlet separation/low-momentum zone on film hole flow characteristics. Like the FDIFF film hole, the effective *VR* at the exit plane is much smaller (Fig. 6(*c*)). The distribution of α is complex as shown in Fig. 7(*c*), but shallower than the REF case as a whole. The smallest α, near the center of the film hole, is associated with low-momentum fluid aft of the inlet separation zone; higher α is associated with the jetting region at the upstream edge and the metal angle on the downstream edge.

At the exit plane, a smoother and less severe pressure gradient exists. This again highlights that the crossflow sees a much less severe flow blockage than the REF case. Note that this condition occurs even though the LDIFF film hole presents a wider lateral area to the crossflow; the trajectory of the jet is very low, so the coolant is effectively injected into the lower-momentum crossflow boundary layer. As a result, film hole boundary layer fluid is not drawn to the centerline to form a coolant wake; rather, it is injected along the test section in the streamwise direction, as shown in Fig. 8(*c*). Notably, the coolant wake observed in Part I is not apparent in the LDIFF case; the fluid that makes up this wake is spread evenly over the test surface.

An important feature of the LDIFF film hole, as shown in Fig. 10(*c*), is the reduction afforded in streamwise-aligned vorticity. Because of the decreased velocity gradients along the walls of the film hole, the vorticity contained in the film hole boundary layer is much less in magnitude; it is also physically separated in the *z*-direction as it is deposited on the test plate. The flow angle also significantly affects the magnitude of ξ_x, as in the FDIFF case; as shown in Fig. 7(*c*), the flow direction exiting the LDIFF film hole is much less than the REF case. Obviously, the lower *x*-direction vorticity content causes the longitudinal vortices to be weakened in strength (Fig. 11(*c*)). Weak longitudinal vortices allow the film to remain firmly attached to the surface, and the film has a greater chance to spread along the surface (rather than being "pinched" as documented in Part I). In addition, since the vortices are physically separated, less induction lift (which lifts the coolant core) results from their presence. Profiles of *z* vorticity in Fig. 12 show the difference in liftoff characteristics for the REF and LDIFF cases. Positive *z* vorticities denote liftoff and the infiltration of high-momentum, high-temperature crossflow fluid underneath the coolant jet. In contrast to the coolant liftoff apparent in the REF case, the LDIFF case demonstrates lateral vorticity characteristics similar to a boundary layer, which is ideal for a film cooling application.

As the coolant moves downstream in a wakelike manner in the far-field, the behavior is much like the FDIFF case. Velocity gradients in the shear layer above the jet and throughout the film fuel turbulence in that area, augmenting the diffusion of crossflow energy into the coolant layer. This effect is much smaller in the $M = 1.88$ case, because the effective *VR* of the jet and crossflow is more closely matched.

The laterally averaged η, shown in Fig. 18, is approximately three times that of the REF case; this drastic improvement is attributed to (1) an excellent lateral coverage over the test plate as seen in Fig. 16(*c*), (2) shallow injection that is kept largely into the low-momentum crossflow boundary layer, and (3) much weaker, laterally separated longitudinal vortices to prevent crossflow entrainment and downstream coolant liftoff. Note that the slope of the LDIFF curve in Fig. 18 decreases throughout the length of the domain; this implies that the coolant is slowly dissipated by the diffusion mechanisms described in the previous paragraph. In

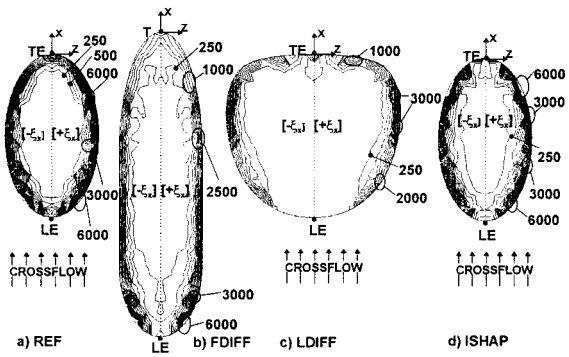

Fig. 10 The streamwise-aligned vorticity distribution at the film-hole exit plane shows the potential for generating secondary flow

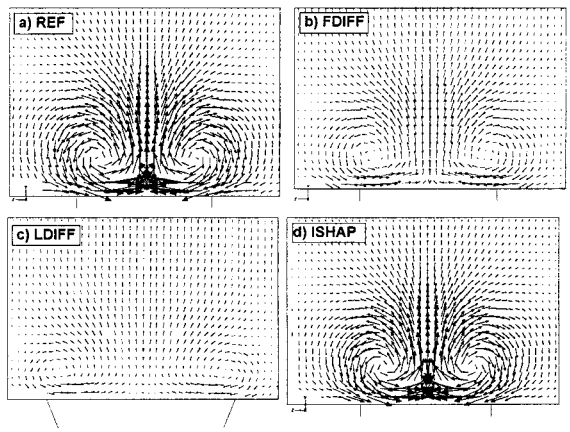

Fig. 11 A comparison of secondary flow magnitudes at $x/D = 2$ shows the near-elimination of streamwise vortices for the diffusion film holes

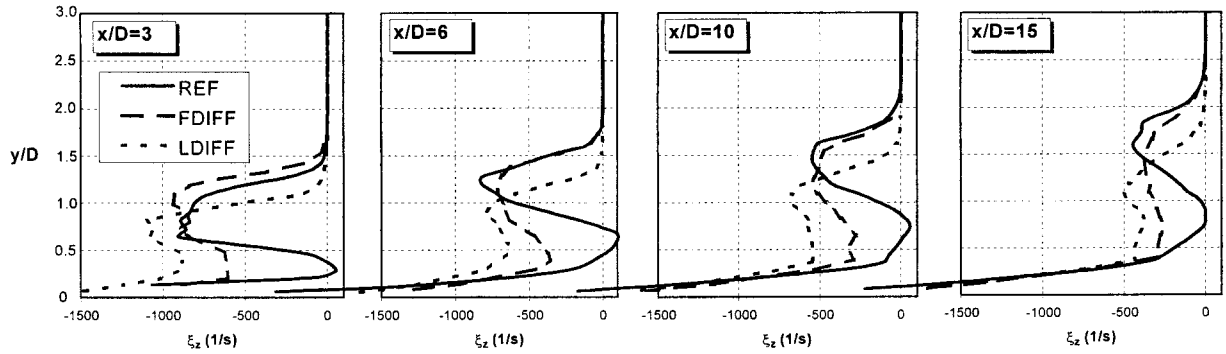

Fig. 12 Lateral (*z*) vorticity profiles delineate the film–crossflow shear layer and indicate the level of transverse velocity gradients for the REF, FDIFF, and LDIFF cases

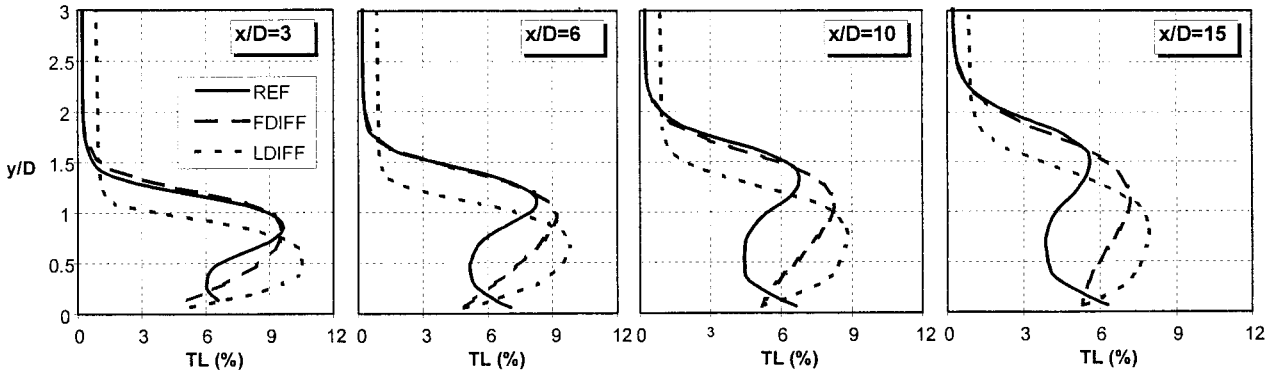

Fig. 13 Profiles of *TL* at downstream stations show the shear layer interaction between film and crossflow

contrast, the coolant jet in the REF case has already reached its lower limit by $x/D = 5$. The heat transfer coefficient for the LDIFF case is consistently higher (at all x/D) than the REF case for $M = 1.25$ and $M = 1.88$; significant differences are seen primarily in the near-field; as the jet moves downstream, only slight differences in the heat transfer coefficient are observed.

7.5 Inlet-Shaped Film Hole (ISHAP). In contrast to the previous shaped cases in which the inlet geometry is identical to the REF case, the ISHAP case demonstrates drastically different inlet flow behavior. The separation zone and the jetting region have been largely eliminated, which is the objective of this type of film-hole shaping. As a result, velocity gradients on the film-hole walls are relaxed slightly, and the throughflow velocity profile in the film hole is almost concentric. In addition, turbulence generation at the film-hole inlet is reduced to approximately two-thirds of the magnitude seen in the REF case; evidence of this is shown in Fig. 14.

Exit plane distributions of *VR*, α, and ξ_x (Fig. 6(*d*), Fig. 7(*d*), and Fig. 10(*d*), respectively) are very similar in appearance to the REF case, except for the elimination of the jetting region. Because of the elimination of high-momentum fluid on the windward side of the film hole, the crossflow is able to exert a considerable influence on the exit-plane velocity distribution. High-velocity fluid is forced to exit from the leeward side of the film hole, as the crossflow blocks the upstream side. This mechanism also contributes to intense positive and negative ξ_x at the leeward side of the film hole, in close proximity to the test surface. *TL* at the film-hole exit plane is approximately two-thirds that of the REF case, which denotes a much less viscous jet; this advantage is gained due to the elimination of turbulent production at the film hole inlet. Unfortunately, as discussed in the following paragraph, the lack of high *TL* at the film hole exit is inconsequential; for the range of *M* and *DR* studied in this work, the dominant turbulence source is due to the shear layer formed over the coolant jet.

The ISHAP case, by preventing the low-momentum/low-pressure zone at the inlet, eliminates much of the secondary motion

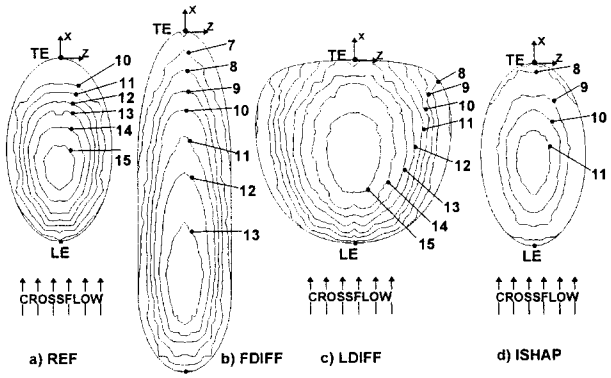

Fig. 14 A comparison of exit plane *TL* (percent) for all shapes shows the reduction of film hole turbulence by inlet shaping

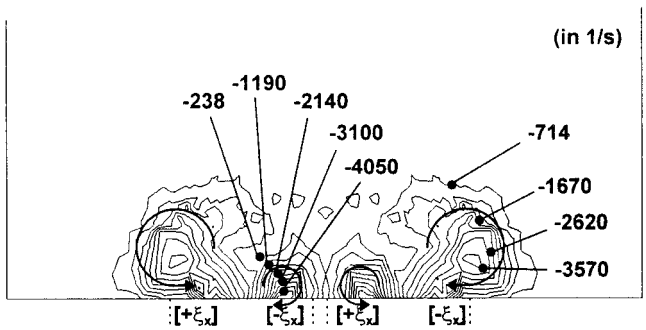

Fig. 15 Aligned vorticity contours at *x/D* = 0 for the CUSP case show the generation of an extra pair of vorticity cores at the cusp location

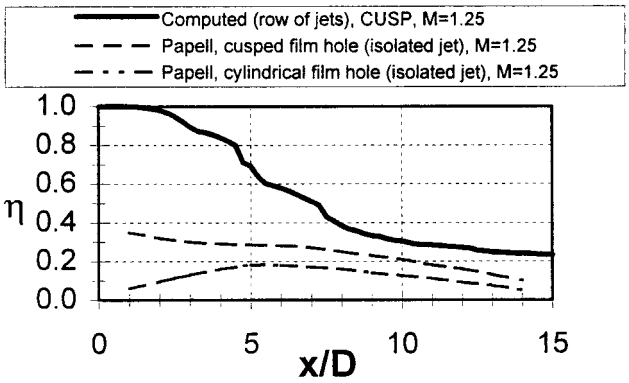

Fig. 16 A comparison of centerline effectiveness for computed (row of jets) and measured (single jet) results for the CUSP case

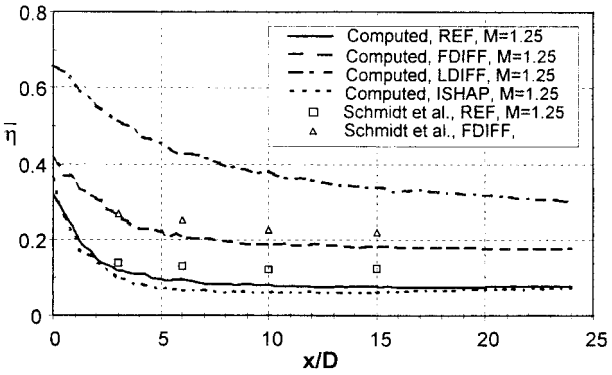

Fig. 18 A comparison between predicted and measured laterally averaged adiabatic effectiveness for various shaped hole film cooling configurations

within the film hole; the flow is purely in the throughflow direction. Since this secondary motion within the film hole creates negative streamwise-aligned vorticity (in a sense to cancel throughflow generated ξ_x; see Fig. 4(*a*)), no counteraction of the positive-aligned vorticity exists. So, the aligned vorticity advantage gained by relaxing velocity gradients near the sidewalls (by the elimination of the jetting region) is lost by this counteracting mechanism. Further details on this mechanism are given in section 8.2.

As such, the downstream behavior of the ISHAP case is almost identical to the REF case. Strong longitudinal vortices are formed, and the coolant jet lifts away from the surface. Due to less turbulent mixing in the coolant jet as it leaves the film hole, the cold temperature core is more intact in the near field; however, as the turbulence-laden film shear layer becomes the dominant mechanism, the coolant is dissipated just as in the REF case. Since the coolant has lifted away from the surface, this effect is not apparent in the surface temperature distribution.

The surface results for the ISHAP case strongly mimic the REF case, since the field in each case is very similar. For $M = 1.25$ and $M = 1.88$, the centerline and laterally averaged effectiveness match the REF case very closely. The same is true for the heat transfer coefficient; no significant differences are noted for the laterally averaged h for $M = 1.25$ or $M = 1.88$. So, the use of inlet shaping in this range of flow parameters is not useful for increasing downstream thermal protection.

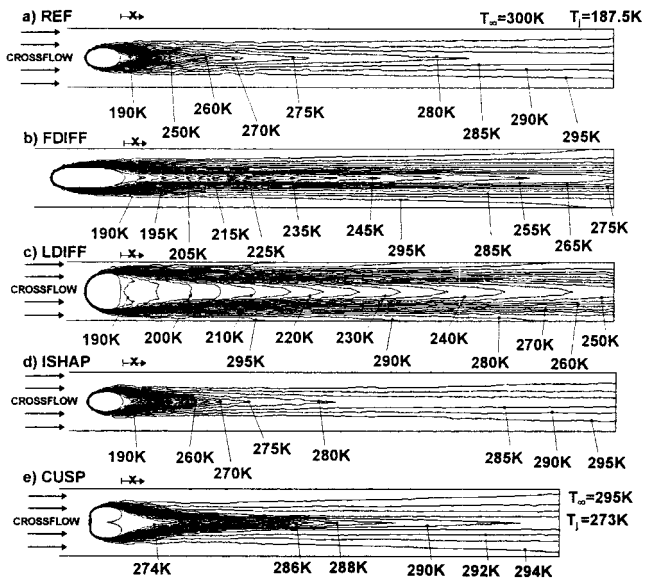

Fig. 17 A comparison of the temperature footprints on the test plate shows the distribution of coolant on the test surface for all film hole shapes

7.6 Cusp-Shaped Film Hole (CUSP). According to Papell's work, the direction of the film hole secondary motion is controlled by the orientation of the cusp-shaped film hole; this is outlined in section 2 (remember that the leeward-facing cusp-shaped hole, as shown in Fig. 1(*e*), is simulated in this work). No evidence to support Papell's conclusions concerning the direction of secondary motion within the film hole is found. Instead, it is believed that the direction of rotation is governed by the low-pressure/low-momentum zone at the entrance to the film hole near the downstream edge. Evidence from the simulations suggests that at this film hole inlet, boundary layer fluid along both the outer walls and the cusp wall is initially pumped downward toward the low-pressure zone. As the flow stabilizes downstream of the inlet, the secondary flow along the outer wall dominates that of the cusp wall; hence, the two chambers of the film hole each have a single vortex rotating in the direction away from the cusp. This direction is the same as that present in the REF case. Counterrotating structures are indeed present within the film hole chambers; however, their magnitude is approximately the same, when normalized by the throughflow, as the REF case.

At the exit plane of the CUSP film hole, the *VR* and *TL* distributions reflect the large L/D of this case. Due to the length of the film hole, inlet-generated turbulence is attenuated, and the only turbulence present at the exit plane is a weak "ring" generated by near-wall velocity gradients. Also, a thick boundary layer is present on all walls of the film hole, most notably on the straight windward section of the film hole.

Interesting vorticity characteristics are observed at the exit-plane of the CUSP film-hole. Along with the usual side-wall boundary layer vorticity observed in the other shaped film holes, the CUSP case also generates an extra pair of vorticity cores at the cusped exit, as shown in Fig. 15. This vorticity is contributed simply by the boundary layers that grow on the cusped wall. Unfortunately, this vorticity is destroyed quickly (by $x/D = 1$), since the two sides of the cusp are in close proximity; the two vorticity "pockets" emanating at each side of the cusp work to cancel one another. So, no influence is exerted on the longitudinal vortices formed as a result of the sidewall boundary layer vorticity.

Effectiveness results for the cusp-shaped film hole, shown in Fig. 16, do not agree well with data presented by Papell; however, computations are expected to overpredict the centerline effectiveness since the simulation was for a row of film-holes, whereas Papell's experimental data were taken for an isolated jet. Also note the centerline effectiveness magnitude of the reference film hole measured by Papell; although (1) *VR* is only slightly over unity and (2) $\alpha = 30$ deg is a very shallow injection angle, η shows an extremely degraded film even in the near field.

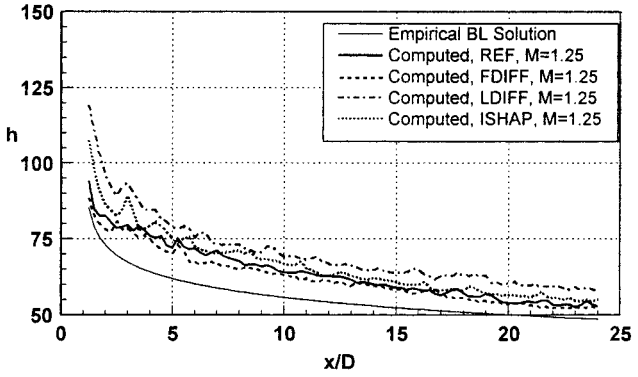

Fig. 19 Comparison of the laterally averaged heat transfer coefficient (W/m^2K) for various shaped hole configurations to an empirical correlation for a flat plate

8 Simulation Summary

8.1 Surface Results

8.1.1 Adiabatic Test Surface. The temperature footprint of each shaped hole configuration is shown in Fig. 17. It is evident that the REF and ISHAP cases are the worst performers in terms of effectiveness levels and lateral spreading, and that their behavior is almost identical. This implies, as discussed in section 7.5, that the alteration in the exit-plane distributions afforded by the ISHAP case does not have a significant impact on the film cooling performance. The FDIFF case performs very well along the centerline; however, lateral spreading characteristics of the jet, although better than the REF and ISHAP cases, are not favorable. Although the absolute values of lateral spreading are expected to be underpredicted due to the isotropic turbulence model used, strong internal consistency of the simulations enables reliable assessment of the relative performance between the different shaped cases. The LDIFF case is by far the best film cooling performer of the configurations tested in this work. The effectiveness is very high along the centerline, and lateral spreading and overall coverage of the test plate is impressive as the coolant jets appear to coalesce quickly as they move downstream. One would expect the coolant from this film hole to merge even more quickly than the simulations capture. The excellent performance of the LDIFF case is also due to its low trajectory and wide breadth; the coolant is effectively injected into the crossflow boundary layer and remains there until dissipated by diffusion mechanisms downstream. Also, no appreciable longitudinal vortices exist to lift the coolant core from the test surface. Moreover, the vortex cores are spread apart in the lateral direction, which further weakens induction lift of the coolant. The temperature footprint for the CUSP case in Fig. 17(a) shows the same characteristics as the REF case; the near field test section is cooled, but longitudinal vortices force liftoff of the jet/wake structure downstream.

A comparison of laterally averaged η is shown in Fig. 18; these effectiveness results reinforce the points given above, and show the relative performance of each film hole shape. Data for the REF and FDIFF cases also appear in Fig. 18; it is clear that the computations slightly underpredict the laterally averaged η by approximately 5 percent. This underprediction is due to the lack of lateral spreading captured by the computations, as documented in Walters and Leylek (1997). The injection widths of the REF and FDIFF cases are each only 1D wide; computations predict that the coolant is concentrated along the centerline at the expense of uncooled area between the coolant layers. Cooling performance (in terms of η) is in the same order for $M = 1.88$, but cannot be shown here due to space constraints.

8.1.2 Active Test Surface. The heat transfer coefficient for each film-hole shape is shown in Fig. 19 for $M = 1.25$. The thin line in this plot denotes the empirical unheated starting length boundary layer correlation for the heat transfer coefficient:

$$\mathrm{St} = 0.03\ \mathrm{Pr}^{-0.4}\ \mathrm{Re}_x^{-0.2}\left[1 - \left(\frac{x}{x_0}\right)^{0.9}\right]^{-1/9}$$

where St is the Stanton number, Pr is the Prandtl number, Re_x is the Reynolds number based on location, x is the distance from the start of the turbulent boundary layer, and x_0 is the unheated starting length. Each shape has a heat transfer coefficient somewhat above that of an undisturbed boundary layer. Notable differences in the h performance of the shaped film holes are only present in the near-field of the jet-crossflow interaction; downstream behavior is very similar for each case. Thus, film hole shaping tends to affect the h distribution in the immediate surroundings in the near field; far downstream, as the coolant jet travels as a wakelike structure, differences in h behavior are not significant.

For low and high M cases, the FDIFF case obtained the best (lowest) heat transfer coefficient, and the LDIFF case gave the highest h. For $M = 1.88$, all of the cases showed lower heat transfer coefficients than at $M = 1.25$. This result is simply because the crossflow velocity is lower for the high blowing ratio case. When normalized by the empirical solution above, however, the $M = 1.88$ cases exhibited slightly higher h on the test surface than the low M cases. Because the h results are very similar, the overall performance of the film cooling holes can be assessed by the adiabatic effectiveness distribution. In this regard, the LDIFF configuration has better cooling performance than the other configurations in this work; the centerline and laterally averaged effectiveness for this case is substantially higher than each other case.

8.2 Flowfield Results. For the diffusion-type film holes, the effective VR and α of the jet is lowered significantly (Figs. 6 and 7). A noticeable decrease in jet trajectory is not seen in the FDIFF case, however, since the strength of the jetting region at the exit plane is comparable to the magnitude seen in the REF case. Comparable effective VR is seen for the REF and ISHAP case; a notable difference in the ISHAP case is the elimination of the jetting region. This elimination allows the crossflow to exert considerably more influence on the jet exit velocity profiles; as shown in Fig. 6(d), the highest momentum jet fluid shifts from the windward side of the film hole to the leeward side.

TL is comparable between the REF and diffused cases; turbulence generated at the inlet plane of the film hole is the primary source of the turbulence observed at the exit-plane. The ISHAP case reduces film-hole turbulence a great deal, and might be useful in blowing parameter combinations in which film-hole turbulence dominates. For the range of M and DR studied in the present work, film-hole generated turbulence is inconsequential; mixing caused by the shear layers above the film layer is the dominant turbulent mechanism. In particular, cases in which the effective VR is lowered significantly (FDIFF and LDIFF cases) show that the coolant is dispersed by continuous turbulence generation in and throughout the film as it travels downstream in the far-field.

Clearly, the dominating mechanism determining downstream film cooling performance is the counterrotating vortex structure formed aft of the jet–crossflow interaction. The previous simulations demonstrate that the magnitude of this secondary motion is governed by the streamwise-aligned vorticity deposited from the film hole boundary layers. As such, one can conclude that the manipulation of the film-hole boundary layer shape factor and the direction of the outgoing boundary layer plays a crucial role in improving film cooling performance.

For a streamwise-injected jet, the contributors to ξ_x are illustrated in Fig. 4(a). Because of the secondary motion within the film hole, the interior boundary layer travels in a helical motion. The resultant vorticity vector, shown as the dotted line in Fig. 4(a), can therefore be decomposed into a component due to throughflow that is perpendicular to the flow direction, and a component due to

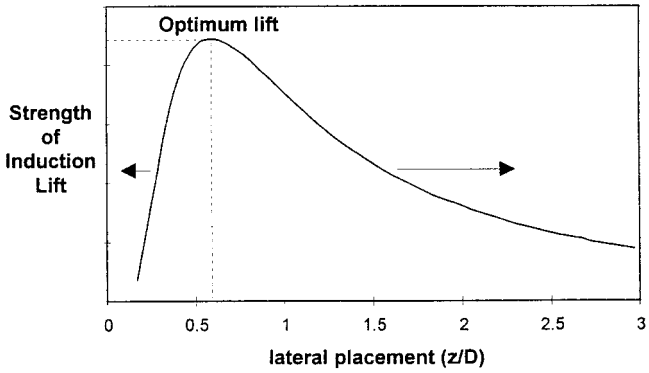

Fig. 20 A conceptual induction lift curve shows qualitatively the importance of avoiding coolant lift by the positioning of the deposited film hole boundary layer

secondary flow that is in the direction opposite to the flow direction. The resultant of these two components is then resolved to a coordinate system aligned with the predominant crossflow direction to determine ξ_x.

As evident in the simulations in this study, Fig. 4(*a*) illustrates two ways to decrease the aligned vorticity: (1) decrease the through-flow vorticity, or (2) increase the secondary vorticity. The former can be accomplished by relaxing the velocity gradient near the sidewalls of the film hole; this was illustrated in the FDIFF and LDIFF cases, and most diffusing film holes will have this characteristic. The latter can be accomplished by inducing strong secondary motion within the film hole. Papell (1984) claimed to have addressed this item with the windward cusp-shaped film hole; however, the present work was unable to substantiate his hypothesis regarding the mechanisms for any advantage gained by a cusp-shaped film hole (even though the case simulated was leeward-cusped). The idea of increasing the counterrotating motion within the film hole is promising; one could envision a case in which the secondary vorticity vector is strong enough to tilt the vorticity resultant so far as to create negative aligned vorticity at the film hole sidewalls. Such a condition would cause downstream counterrotating vortices, but in the *opposite* direction, such that the coolant is spread along the wall and negative induction lift is generated by the longitudinal vortices!

Figure 4(*b*) illustrates the effect on the aligned vorticity as the exiting flow angle decreases. The throughflow vorticity is tilted downward, where it cannot contribute a great deal to the aligned vorticity. This effect is illustrated most prominently by the FDIFF configuration. By the same argument, it is obvious that increasing the flow angle would not only increase the y-momentum and penetration into the crossflow, but would also tilt the resultant sidewall vorticity vector forward; this would (detrimentally) increase the magnitude of crossflow-aligned vorticity.

One might design a film hole configuration in which opposite-signed vorticity is generated in close proximity to the exiting sidewall boundary layers. In this case, vorticity cancellation would commence, and the aligned vorticity leading to the longitudinal vortices would be destroyed.

Last, the separation of the aligned vorticity deposited from the film hole is crucial. Induction lift generated by the longitudinal vortices can be minimized by positioning the exiting boundary layers an a suboptimal lift position. An example of this is illustrated in the LDIFF configuration. If opposite-signed vorticity is deposited in very close proximity, cancellation will occur; on the other hand, if the opposite-signed vorticity is deposited a large distance apart, induction lift is negligible. Therefore, as illustrated in Fig. 20, there must exist some "optimum lift" that must be avoided in film cooling configuration design.

9 Conclusions

A number of computational simulations are carried out for film cooling configurations involving cylindrical, forward diffused, laterally diffused, inlet shaped, and cusp shaped film holes. The key conclusions from this study are as follows:

- of the film holes tested in this work, the laterally diffused film hole provides the best coverage and highest effectiveness. The forward diffused film hole performs well along the centerline, but does not spread laterally. The cylindrical and inlet-shaped film hole perform poorly at both blowing ratios; the coolant lifts off from the test surface in these cases.
- film hole shaping can significantly affect the distribution of the exit plane variables, which determine downstream film cooling performance.
- crossflow-aligned vorticity from the film hole boundary layers, which governs the formation of detrimental longitudinal vortices, can be controlled by the geometry of the film hole. Streamwise vorticity reduction involves (1) decreasing the magnitude of the throughflow vorticity by decreasing velocity magnitude near the walls, (2) increasing the magnitude of the opposite direction vorticity by increasing the secondary motion within the film hole, or (3) changing the sense of the total vorticity vector by altering the exit flow direction.
- CFD can be used to sort the relative performance of shaped film cooling configurations and provide logic for determining the reasons for increases or decreases in film cooling performance.

Acknowledgments

This paper was prepared with the support of the U.S. Department of Energy, Morgantown Energy Technology Center, Cooperative Agreement No. DE-FC21-92MC29061. The authors would like to thank Mr. Gary Berger and Mr. Richard Baldwin of the Engineering Computer Operations at Clemson University for their assistance in all computer-related matters. Also, Mr. John Lane provided first-rate support for the Intel Paragon supercomputer used for the crunching of many simulations. We are also deeply indebted to Dr. Rick Lounsbury at Fluent, Inc. for his invaluable support for RAMPANT and Fluent/UNS.

References

Farmer, J. P., Seager, D. J., and Liburdy, J. A., 1997, "The Effect of Shaping Inclined Slots on Film Cooling Effectiveness and Heat Transfer Coefficient," ASME Paper No. 97-GT-339.

Goldstein, R., Eckert, E., and Burggraf, F., 1974, "Effects of Hole Geometry and Density on Three-Dimensional Film Cooling," *International Journal of Heat and Mass Transfer*, pp. 595–606.

Haven, B. A., and Kurosaka, M., 1996, "The Effect of Hole Geometry on Lift-Off Behavior of Coolant Jets," AIAA Paper No. AIAA 96-0618.

Hyams, D., McGovern, K., and Leylek, J., 1996, "Effects of Geometry on Slot-Jet Film Cooling Performance," ASME Paper No. 96-GT-187.

Makki, Y. H., and Jakubowski, G. S., 1986, "An Experimental Study of Film Cooling from Diffused Trapezoidal Shaped Holes," AIAA Paper No. AIAA-86-1326.

Papell, S., 1984, "Vortex Generating Flow Passage Design for Increased Film Cooling Effectiveness and Surface Coverage," ASME Paper No. 84-HT-22.

Schmidt, D., Sen, B., and Bogard, D., 1996, "Film Cooling With Compound Angle Holes: Adiabatic Effectiveness," ASME JOURNAL OF TURBOMACHINERY, Vol. 118, pp. 807–813.

Sen, B., Schmidt, D., and Bogard, D., 1996, "Film Cooling With Compound Angle Holes: Heat Transfer," ASME JOURNAL OF TURBOMACHINERY, Vol. 118, pp. 800–806.

Thole, K., Gritsch, M., Schulz, A., and Wittig, S., 1998, "Flowfield Measurements for Film-Cooling Holes With Expanded Exits," ASME JOURNAL OF TURBOMACHINERY, Vol. 120, pp. 327–336.

Walters, D., and Leylek, J., 1997, "A Systematic Computational Methodology Applied to a Three-Dimensional Film-Cooling Flowfield," ASME JOURNAL OF TURBOMACHINERY, Vol. 119, pp. 777–785.

Wittig, S., Schulz, A., Gritsch, M., and Thole, K. A., 1996, "Transonic Film-Cooling Investigations: Effects of Hole Shapes and Orientations," ASME Paper No. 96-GT-222.

A Detailed Analysis of Film Cooling Physics: Part IV—Compound-Angle Injection With Shaped Holes

R. A. Brittingham

J. H. Leylek

Department of Mechanical Engineering,
Clemson University,
Clemson, SC 29634

The flow physics of film cooling with compound-angle shaped holes is documented for realistic gas turbine parameters. For the first time in the open literature, the combined effects of compound-angle injection and hole shaping are isolated and the dominant mechanisms are examined. Results provide valuable insight into the flowfield of this class of film-cooling jets. Computational and experimental results are presented for a row of holes injected at 35 deg on a flat plate with three distinct geometric configurations: (1) streamwise injected cylindrical holes (reference case); (2) 15 deg forward-diffused holes injected at a 60 deg compound angle; and (3) 12 deg laterally diffused holes injected at a 45 deg compound angle. Detailed field and surface data, including adiabatic effectiveness (η) and heat transfer coefficient (h), of the two compound-angle shaped holes are provided and compared to: (i) the reference streamwise cylindrical case; (ii) results from Part II detailing the compound-angle flowfield for cylindrical holes; (iii) results of Part III detailing the streamwise injected shaped-hole flowfield; and (iv) experimental data. The 60 deg compound-angle forward-diffused holes provided excellent lateral coolant distribution, but suffered from crossflow ingestion at the film-hole exit plane. The 45 deg compound-angle lateral-diffused hole had much steeper lateral effectiveness variations. A previously documented and validated computational methodology was utilized. Computations were performed using a multiblock, unstructured-adaptive grid, fully implicit pressure-correction Navier–Stokes code with multigrid and underrelaxation type convergence accelerators. All simulations had fixed length-to-diameter ratio of 4.0, pitch-to-diameter ratio of 3.0, nominal density ratio of 1.55 and film-hole Reynolds number of 17,350, which allowed isolation of the combined effects of compound-angle injection and hole shaping for nominal blowing ratios of 1.25 and 1.88. The results demonstrate the ability of the prescribed computational methodology to predict accurately the complex flowfield associated with compound-angle shaped-hole film-cooling jets.

1 Introduction

In modern gas turbine engines, the temperature of the gases entering the high-pressure turbine is typically at or near the melting point of the alloys used to construct the airfoils. Film cooling is commonly used to protect these parts by isolating them from the hot crossflow. As turbine inlet temperatures rise and coolant flow rates decrease in pursuit of higher efficiency and lower emissions, film cooling is becoming increasingly important. These demands require that the most airfoil and endwall protection be extracted from each unit of coolant. As a result, film-hole geometry has received much attention. Turbine designers have turned to compound-angle holes as well as shaped holes in efforts to utilize the coolant better. One further step that has been implemented is the combination of compound-angle holes with shaped holes producing noncylindrical holes oriented away from the streamwise direction. Unfortunately, these complex configurations are often implemented with little understanding of the physical mechanisms which govern the jet/crossflow interaction. The current design procedure is empirical in nature and relies on existing databases and slow, costly destructive testing if a novel configuration is to be used. There presently exists no truly predictive capability for turbine designers to rely on. In order for significant improvements to be made in film cooling, the fundamental physics of the jet/crossflow interaction must be understood and predictive design capability must be established. This paper addresses the dominant physical mechanisms found in two compound-angle shaped-hole configurations, with special emphasis on the physics which govern jet/crossflow interactions. Detailed field and surface data, including adiabatic effectiveness (η) and heat transfer coefficient (h_f), are presented. The comparison of these results to experimental data further validates the computational methodology previously outlined by this research group.

Contributed by the International Gas Turbine Institute and presented at the 42nd International Gas Turbine and Aeroengine Congress and Exhibition, Orlando, Florida, June 2–5, 1997. Manuscript received International Gas Turbine Institute February 1997. Paper No. 97-GT-272. Associate Technical Editor: H. A. Kidd.

2 Literature Review

Most of the work documented about jet/crossflow interactions has concentrated on streamwise injected jets, with less work documented for compound-angle jets and shaped jets. The companion paper in Part I provides a detailed review of pertinent background literature of streamwise injection studies with cylindrical holes. Parts II and III provide information about compound-angle cylindrical-hole studies and streamwise injected shaped-hole studies, respectively. Consequently, this paper will simply highlight compound-angle and shaped-hole studies and focus on compound-angle shaped-hole (CASH) investigations.

2.1 Experimental Studies

2.1.1 Compound-Angle Cylindrical-Hole Studies. There are few studies documented in the open literature for compound-angle cylindrical holes with geometric and flow parameters representative of modern turbine engines. Ekkad et al. (1997a, b) and Ligrani

et al. (1994a, b) both found that $\bar{\eta}$ increases for compound-angle injection relative to streamwise injection. Lee et al. (1997) provided field data and concluded that the two symmetric counterrotating vortices seen downstream of a streamwise jet ($\Phi = 0$ deg) in crossflow gradually collapse into a single strong vortex as the compound angle increases. The reader is referred to the companion paper in Part II for further details on these studies.

2.1.2 Streamwise Injected Shaped-Hole Studies. The influence of hole geometry on film cooling for streamwise injected jets has been studied by Goldstein et al. (1974), Papell (1984), and Makki and Jakubowski (1986) for a variety of hole shapes. All three studies document significant η improvements over cylindrical holes. Haven and Kurosaka (1996) provided velocity and vorticity distributions for a number of different hole shapes. They concluded that the counterrotating vortex pair seen downstream of a streamwise jet in crossflow results from the film-hole boundary layer vorticity. Thole et al. (1998) presented flowfield data for cylindrical holes, lateral expanded holes, and forward-lateral expanded holes with $\alpha = 30$ deg and $L/D = 6$. The lateral expansion angle was 14 deg and the forward expansion angle was 15 deg. They found higher turbulence levels at the jet exit plane for the holes with expanded exits, which were attributed to hypothetical separation at the start of the expanding sections. There was no separation at the film-hole inlet as the coolant was supplied from a coflowing channel and not from a plenum. Another interesting result was the presence of a slight crossflow ingestion at the leading edge of the forward-lateral expanded hole. The reader is referred to the companion paper in Part III for more details on these studies.

2.1.3 Compound-Angle Shaped-Hole (CASH) Studies. In two recently published companion papers, Schmidt et al. (1996) and Sen et al. (1996) investigated compound-angle cylindrical film holes, streamwise injected forward-diffused film holes, and compound-angle forward-diffused film holes. For the CASH configurations, the authors utilized a single row of holes with $\alpha = 35$ deg, $\Phi = 60$ deg, $L/D = 4.0$, and $P/D = 3.0, 6.0$. The geometry included a $2.1D$ long metering section followed by a 15 deg forward diffusing section. Adiabatic effectiveness and heat transfer results were presented and compared to cylindrical compound-angle holes and cylindrical streamwise holes. No field data was provided. Tests were conducted with $DR = 1.6$ for η and $DR = 1.0$ for h_f results. Blowing ratios included $M = 0.63$, 1.25, and 1.88. Results showed that the $\Phi = 60$ deg forward-diffused holes had significantly better laterally averaged effectiveness than either the $\Phi = 0$ or 60 deg cylindrical holes at all downstream stations examined for $M = 1.25$ and $M = 1.88$ (Schmidt, 1995). Results also showed superior lateral distribution of the coolant when the $\Phi = 60$ deg forward-diffused holes were utilized, especially in the very near field. Conversely, heat transfer coefficient results showed that compound-angle holes have higher h_f/h_o values than $\Phi = 0$ deg holes. The authors cited "increased interaction between the jets and the mainstream" as the cause of the higher h_f values. To give a picture of overall performance, they defined a net heat flux reduction parameter (NHFR), which combined the effects of both h_f and spatially averaged η. Using this parameter, they determined that film-cooling performance decreased with momentum flux increase for all holes over the parameter range tested. The configuration with the best NHFR was $\Phi = 0$ deg cylindrical holes at low momentum flux ratio.

2.2 Computational Studies. There currently are no computational studies in the open literature documenting jet/crossflow interactions for compound-angle shaped holes. There are, however, some computational works in the literature which provide valuable information relevant to this study. These include:

- Bergeles et al. (1978)
- Leylek and Zerkle (1994)
- Garg and Gaugler (1995)
- Walters and Leylek (1998)

The reader is referred to Part I of this paper for an in-depth discussion of each paper. A major conclusion first drawn by Leylek and Zerkle (1994) is that to capture the physics of the jet/crossflow interaction accurately, the computational model must include the crossflow, film hole, and plenum regions. This stems from the fact that the flow is highly coupled in these three regions and arbitrary specification of the jet exit plane conditions can lead to significant errors. Building on this conclusion, a consistently accurate, predictive methodology was developed and validated in Walters and Leylek (1998). This study emphasized the importance of four issues when consistently accurate predictions are desired:

Nomenclature

CASH = compound-angle saped hole
D = diameter of film hole
DR = density ratio = (ρ_j/ρ_∞)
FDIFF60 = forward-diffused Φ = 60 deg configuration
h = heat transfer coefficient, W/m^2K
L = length of film hole
LDIFF45 = laterally-diffused Φ = 45 deg configuration
LE = leading edge of coolant jet exit plane
L/D = length-to-diameter ratio of film hole
M = mass flux (or blowing ratio) = $(\rho V)_j/(\rho V)_\infty$
O = downstream-most point of coolant jet exit plane
P = lateral distance between two adjacent film holes
P/D = pitch-to-diameter ratio of film hole
Pr = Prandtl number
REF = streamwise injected cylindrical-hole reference case
Re_x = Reynolds number based on x
St = Stanton number
T = local fluid temperature
TE = trailing edge of coolant jet exit plane
tke = turbulent kinetic energy, m^2/s^2
TL = turbulence level = $(100*(\frac{2}{3}*tke)^{0.5})/V_\infty$, percent
$\mathbf{V}$ = local fluid velocity vector
V = magnitude of local velocity vector = $|\mathbf{V}|$
VR = velocity ratio = (V_j/V_∞)
x, y, z = Cartesian coordinate system axes
y^+ = nondimensional wall distance = $y\sqrt{|(\tau_w|/\rho_w)}/\nu_w$
α = injection angle measured from the x–z plane, deg
δ = boundary layer thickness
ϵ = dissipation rate of turbulent kinetic energy, m^2/s^3
η = adiabatic effectiveness = $(T_\infty - T_{aw})/(T_\infty - T_j)$
$\bar{\eta}$ = laterally averaged adiabatic effectiveness
Θ = nondimensional fluid temperature = $(T_\infty - T)/(T_\infty - T_j)$
ν = dynamic viscosity
ξ_x = streamwise component of the vorticity vector
ρ = density
τ = shear stress
Φ = compound angle measured from the x–y plane, deg

Subscripts

∞ = mainstream conditions at crossflow inlet plane
aw = adiabatic wall
f = with film cooling
j = coolant jet conditions
o = without film cooling
w = condition at wall

- proper modeling of the flow physics
- accurate geometry capture and high quality grid generation
- higher-order discretization scheme
- appropriate turbulence closure model

The methodology outlined in Walters and Leylek (1998) was utilized in the present study.

2.3 Outstanding Issues. Presently, gas turbine designers have a limited experimental and computational database of film-cooling information to utilize in the development of the next generation of high efficiency and low emission engines. With truly predictive tools unavailable, only small perturbations from existing designs are possible with reasonable assurance of reliable results. Little of this database deals with compound-angle holes, little deals with shaped holes and even less deals with CASH. The lack of predictive capability for designs not found in the database is a serious and expensive problem for turbine designers. At the heart of these deficiencies lies a lack of understanding of the physics of three-dimensional jet/crossflow interactions. As the geometry is complicated by compounding the angle and shaping the hole, this becomes an increasing deficit. These outstanding issues can be summed up in this short list:

- lack of experimental/computational data for CASH
- lack of predictive design capability
- lack of physical understanding of governing mechanisms

3 Present Contributions

The present study attempts to address the outstanding issues outlined in the preceding section by documenting the downstream film cooling performance for two CASH geometries. These performance results can be evaluated against streamwise cylindrical (Part I), compound-angle cylindrical (Part II), and streamwise shaped (Part III) configurations presented in the companion papers to assess relative performance. The dominant physical mechanisms present in the film hole, near field, and far field of each CASH configuration are examined using momentum and vorticity concepts. This study further validates the reliable and accurate predictive design tool put forth in Walters and Leylek (1998), as well as proving that computational fluid dynamics (CFD) can be utilized to determine relative performance of different film cooling configurations with high internal consistency.

4 Computational Methodology

The methodology utilized in this study has been fully documented in Walters and Leylek (1998). To highlight, solution of the time-averaged, steady Navier–Stokes equations was achieved utilizing a multiblock, unstructured/adaptive, pressure-correction code with multigrid and underrelaxation type convergence accelerators. The standard k–ϵ model was used for turbulence closure. For near-wall treatment, the generalized wall functions available in Fluent/UNS from Fluent, Inc., were employed, with careful consideration of y^+ issues in the grid generation phase. A high-quality background grid was generated from a solid model of the domain. For an example of grid quality, see Fig. 1, which shows a histogram of the grid mesh. Note that a skewness value of 0 in this figure represents a perfect equilateral tetrahedron, and a value of 1 represents a highly skewed cell. The solution was first obtained on this relatively coarse background grid (~450,000 cells). Adaption (or refinement) was performed based on field gradients and the simulation was again converged. This process was repeated until the solution was grid independent (typically between 700,000 and 800,000 cells). Adaption was performed using the hanging-node technique available in Fluent/UNS, which preserves the high quality of the background grid upon refinement. Convergence was established using strict convergence criteria, which included <0.01 percent mass and energy imbalance in the entire domain, global normalized residual levels <0.1 percent, and no change in dependent variable (e.g., **V**, tke, ϵ) fields upon further iterations.

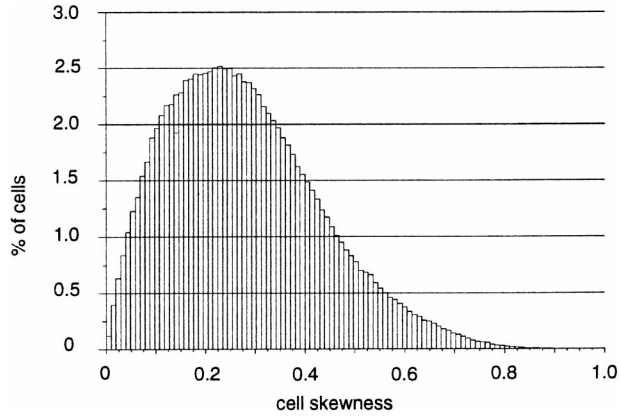

Fig. 1 Histogram of cell skewness for 450,000 cell initial grid for FDIFF60 case shows high grid quality

Grid independence was established when further refinement steps, each adding on the order of 75,000 to 100,000 cells, provided negligible change in dependent variable fields evaluated at a number of strategic locations in the flowfield. Convergence was typically achieved in 1000 to 1500 iterations. The computational simulations were primarily performed on Clemson University Advanced Computational Research Lab (ACRL) workstations, including two SGI Indigo 2 computers, an ONYX, as well as Sun Sparc 10, 1000E and ULTRA II machines. Typical central processor (cpu) times were approximately 4 to 8 minutes per iteration, depending on grid size, platform, and number of cpu's.

5 Simulation Details

5.1 Terminology. In the explanation of complex CASH flowfields, it is necessary to introduce some terminology to be used, as illustrated in Fig. 2. Included in this figure are the definitions of the leading edge (*LE*), trailing edge (*TE*) and downstream-most (*O*) points, as well as the fluid discharge angles α and Φ. The upstream and downstream edges of the film-hole breakout are also shown. The term "aft-looking-forward" will be used to designate a view from downstream of the injection site looking back upstream. This terminology will be used throughout the present paper and is consistent with the companion papers in Parts I, II, and III.

5.2 Computational Model. As outlined in the literature review, for accurate representation of the jet/crossflow interaction, it is necessary to model the crossflow, film hole, and plenum regions simultaneously. The present computational model, shown schematically in Fig. 3 for the two CASH cases, reflects this fact. The

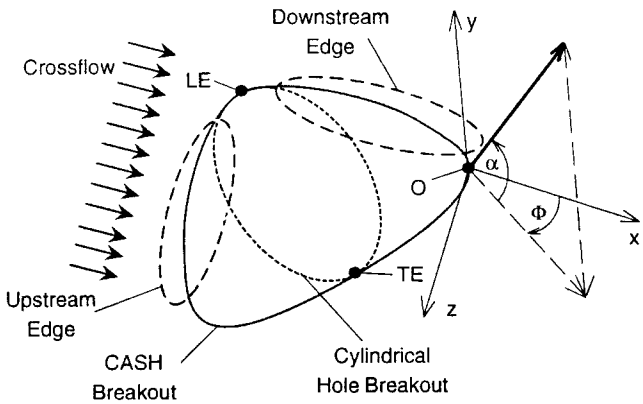

Fig. 2 Terminology definitions to be used in the present paper, consistent with the companion papers in Parts I, II, and III

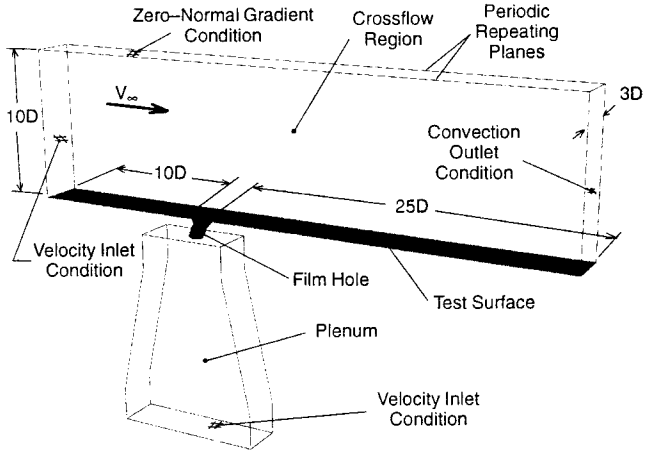

Fig. 3 Shematic of computational model utilized in the present study, showing the plenum, film hole, and crossflow regions with the domain extents and boundary conditions

coolant is supplied from a plenum through the film hole and enters the crossflow region. All simulations have $L/D = 4.0$, $P/D = 3.0$, and $\alpha = 35$ deg. The CASH models with $\Phi = 45$ and 60 deg extend laterally one full pitch between the repeating planes, as symmetry along the hole centerline and between adjacent holes is not applicable for these configurations. The origin of the coordinate system for the REF case and the LDIFF45 case is located at the downstream-most point of the film-hole breakout (point *O*). For the FDIFF60 case, due to the experimental setup that provided the validation data, the origin is located at the trailing edge of the film hole along the hole centerline (point *TE*). The location of these origins is visible in Fig. 4. Exact dimensions of the model for each case were dependent on the particular validation data used. The working fluid is air, with density governed by the Ideal Gas equation, viscosity determined by Sutherland's Law and constant specific heat.

5.3 Compound-Angle Shaped-Hole Configurations. Three film-hole configurations were studied in this work. First, a streamwise cylindrical reference case (REF) with $\alpha = 35$ deg, $L/D = 4.0$, and $P/D = 3.0$ was investigated as a baseline for comparisons. This geometry matched that of an in-house experimental study at Clemson University. Plenum dimensions and location were supplied by the Clemson team. Film hole diameter was 8.3 mm. Two CASH configurations were studied and are shown in Fig. 4. The first was a 15 deg forward-diffused hole with $\Phi = 60$ deg (FDIFF60), matching the geometry of Schmidt et al. (1996) and Sen et al. (1996). The plenum dimensions provided by the University of Texas group were used to construct the plenum for this model. The film hole had a $2.1D$ long metering section followed by a 15 deg forward-diffusing section. The metering section is measured along the film-hole centerline. Film hole diameter was 11.1 mm. The second configuration was a 12 deg lateral-diffused hole with $\Phi = 45$ deg (LDIFF45) matching the geometry of the Clemson University study. The plenum for this case matched that of the REF case. This particular film hole had a $2.1D$ long metering section, measured along the centerline, followed by a 12 deg (on each side) lateral diffusing section. The diameter of the film hole was 8.3 mm. The two CASH geometries have cylindrical compound-angle and streamwise shaped counterparts in Parts II and III, respectively, allowing comparison between the streamwise and compound-angle versions of the lateral- and forward-diffused holes.

5.4 Boundary and Test Conditions. Each geometry examined had an exact computational model representing the experimental setup that provided the validation data. Similarly, boundary conditions were matched to the experimental values. Each computational model extended $10D$ high from the test surface where a "slip" type boundary condition with zero-normal gradients was applied. An outlet convection boundary was imposed at $25D$ downstream of the origin. The computations were designed to simulate a row of holes, therefore the REF case had symmetry planes applied at the jet centerline and at the midplane between adjacent jets. For the CASH cases, repeating (or periodic) conditions were used at the midplanes between adjacent jets, yielding a full pitch domain. To implement periodic repeating planes, the surface grid must be generated on one lateral side of the domain and then mirrored onto the other surface, resulting in matching node patterns. The fluxes out of the cells on one side are then used as the inlet fluxes on the other side.

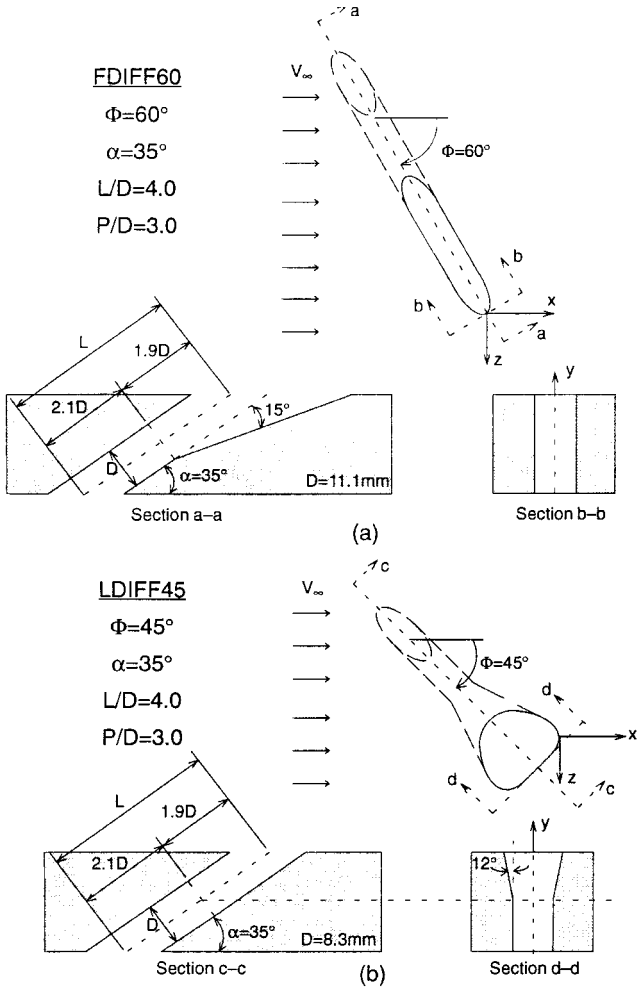

Fig. 4 Definition of (*a*) FDIFF60 and (*b*) LDIFF45 geometries investigated in the present study

At $10D$ upstream of the leading edge of the hole, **V**, tke, and ϵ profiles were applied. For the REF and LDIFF45 geometries, which matched the in-house tests, experimental velocity, turbulence intensity, and boundary layer thickness data were measured at $10D$ upstream. These were used in conjunction with the experimental δ/D at the hole of 0.55 to generate inlet plane profiles of all relevant dependent variables. For the FDIFF60 case, which matched the University of Texas data, inlet conditions were given at $23.1D$ upstream of the trailing edge of the film hole. These conditions were used in the models of Parts II and III where the computational domains extended the full $23.1D$ upstream. Inlet conditions at $10D$ for the present case were taken from fully converged, grid-independent results at $10D$ upstream of the film hole leading edge from Parts II and III, thereby eliminating $13.1D$ of the upstream computational domain. For the FDIFF60 case, δ/D

Table 1 Computational test conditions for each geometry

Geometry	Nominal M	DR	Test Surface Conditions
REF	1.25, 1.88	1.55	adiabatic, constant heat flux
FDIFF60	1.25, 1.88	1.60	adiabatic
LDIFF45	1.25, 1.88	1.55	adiabatic, constant heat flux

at the hole was 0.5. The crossflow velocity for each case was specified to achieve the desired blowing ratio. In all the results documented in the present paper, the nominal film-hole Reynolds number was held constant at 17,350 to ensure consistency of the flow between different cases. The crossflow temperature was set at $T_\infty = 300$ K in all simulations with T_j varied to set DR. The test conditions for the different geometries are summarized in Table 1.

6 Results

6.1 Validation. The computational methodology used in this study has undergone extensive validation. This is well documented in Walters and Leylek (1998). Additional validation has been put forth in Part II for compound-angle cylindrical holes and Part III for streamwise shaped holes. Furthermore, internal consistency of results between the authors of this four-part paper for similar geometries is excellent. The surface results for the REF case are provided for validation and comparison purposes. The reader is referred to Part I for a detailed discussion of the flowfield for this geometry.

For all surface result comparison plots in Section 6.1, continuous lines are used for computational results at $M = 1.25$ (comp $M = 1.25$), dashed lines represent the Clemson University experimental data (exp), solid symbols represent the University of Texas data (Schmidt et al.) and connected hollow symbols are used for computational results at the higher blowing ratio (comp $M = 1.88$). All experimental data shown are for $M = 1.25$. The $M = 1.88$ computational data are shown simply to display the trends for the higher blowing ratio and is not discussed. Agreement for the $M = 1.88$ computational data is similar to that of the $M = 1.25$ data. It should be noted that the experimental method used by Farmer et al. (1997), thermochromic liquid crystals, yielded very dense data sets which are therefore displayed as dashed lines. Schmidt et al. (1996) used thermocouples at a finite number of locations, consequently their data are displayed as discrete points.

Figure 5(a) shows a three-way comparison of centerline η for the REF case at $M = 1.25$. Note that $DR = 1.55$ for the Clemson University experimental data and $DR = 1.60$ for the Schmidt et al. (1996) data. The results show good agreement between the two experimental data sets and the computational data except in the near-field region for $x/D \leq 3$. As was discussed in the companion paper, Part I, a two-layer model can be used in the place of wall-functions to more accurately capture this near-field behavior. Along the centerline, it is common for computations to overpredict η somewhat due to the use of isotropic eddy viscosity models. The turbulence field resulting from a jet/crossflow interaction is known to be highly anisotropic, therefore the use of an isotropic eddy viscosity model will yield less lateral diffusion and spreading. One would expect centerline η for computations to be above experimental data for a configuration such as the REF case. By the same argument, lateral slices (constant x/D planes) should show lower lateral spreading in the computational results, as is the case in Fig. 5(b, c). Similar lateral trends are seen in Fig. 5(b, c), with good agreement of magnitudes.

Figure 5 demonstrates that results from the present simulations are consistent with experiments and also with previous computational results (see Part I, Walters and Leylek (1998)) for a streamwise cylindrical hole. Three-way comparisons are also possible for the FDIFF60 case. Figure 6(a) shows good agreement between both experimental data sets and the present computations for η at $M = 1.25$. Especially impressive is the agreement of experimental and computational data in the near field. As x/D increases, experimental data should generally be below computational data for $\bar{\eta}$ due to thermal gains (conduction, radiation) which cannot be totally eliminated for experiments but are identically zero for computations. Neither experimental group attempted to correct for radiation or through-the-metal conduction. These corrections would have pushed experimental $\bar{\eta}$ values up. Even with these possible sources of errors, agreement is very good for such a complex geometry. Lateral η distributions are shown for this configuration at $x/D = 3$ and 15 in Fig. 6(b, c), respectively. The trends and magnitudes of lateral η distribution are very consistent between experimental and computational data at $x/D = 3$ in Fig. 6(b). This is excellent agreement in the near field. In the far field, Fig. 6(c), the trends are again similar, but computational η now lies $\sim$0.1 above experiments, possibly due to error sources previously mentioned. Surface results will be examined in more detail in Section 7.1.

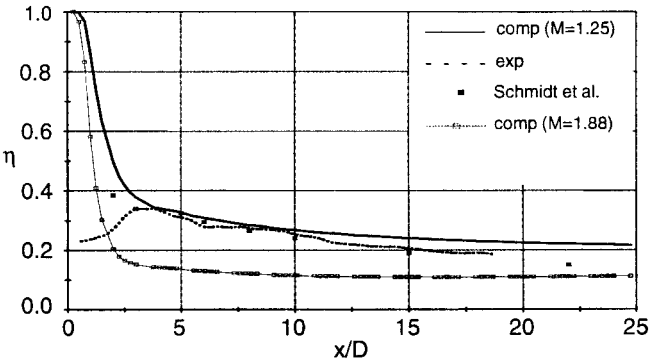

Fig. 5(a) Centerline ($z/D = 0$) adiabatic effectiveness comparison for REF case at $M = 1.25$ demonstrates the consistency of experiments and computations

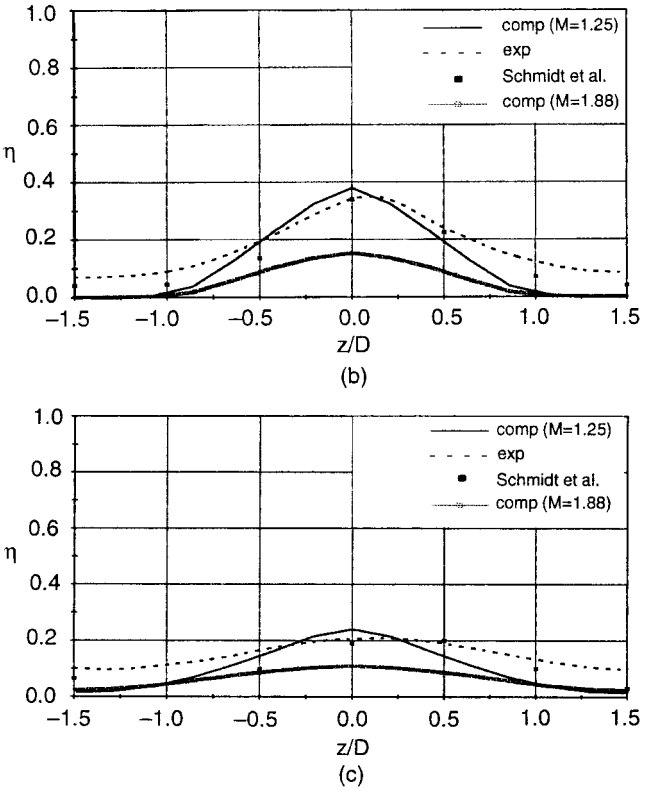

Fig. 5(b, c) Lateral adiabatic effectiveness distributions for REF case at (b) $x/D = 3$ and (c) $x/D = 15$, $M = 1.25$, show good agreement with experimental data in the near and far fields

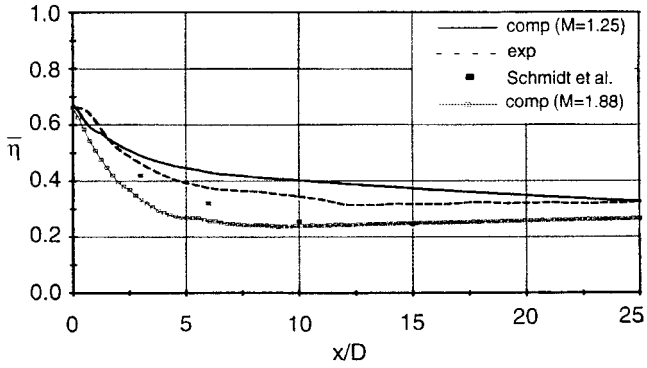

Fig. 6(*a*) Lateral averaged adiabatic effectiveness comparison for FDIFF60 case at $M = 1.25$ demonstrates excellent agreement in the near field

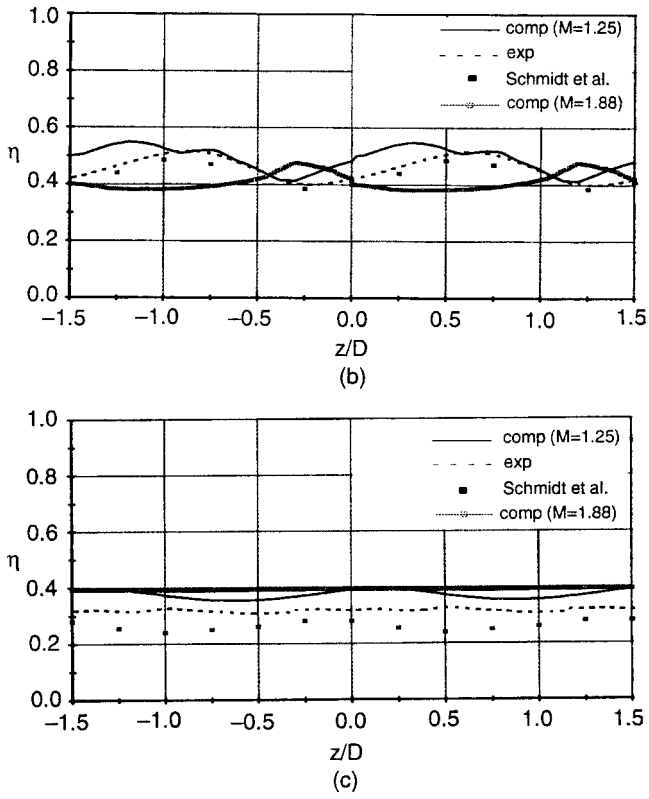

Fig. 6(*b*, *c*) Lateral adiabatic effectiveness distributions for FDIFF60 case at (*b*) $x/D = 3$ and (*c*) $x/d = 15$, $M = 1.25$, shows consistent agreement between experiments and computations

6.2 Cylindrical Reference Case (REF). Forward of this point, many figures will have three parts, with each part corresponding to a different geometric configuration. In these figures, part (*a*) shows results for the REF case with the results for the FDIFF60 and LDIFF45 cases in parts (*b*) and (*c*), respectively. The three are shown together for comparison purposes, noting that the LDIFF45 configuration is not discussed until Section 6.4.

The reference case has been thoroughly documented in the companion paper in Part I. The geometry was repeated as part of this study to ensure consistency between investigators and simulations compared in the present paper. Only a few important aspects of the flow will be highlighted. The flow enters the film hole from the plenum. Since a shallow injection angle is used ($\alpha =$ 35 deg), the flow cannot negotiate the sharp corner on the downstream side of the film hole entrance, causing a low pressure pocket and a three-dimensional recirculation region at this location. The remainder of the flow accelerates around this region toward the upstream side of the hole, causing a jetting region of high-momentum fluid. These effects combine to set up the counterrotating secondary flow found within the film hole, as well as the nonuniform jet exit conditions.

As the jet exits the film hole, it encounters the crossflow, which impinges on it and redirects it downstream. This interaction is characterized by a high-pressure stagnation region at the leading edge and a low-pressure region at the trailing edge of the film-hole exit plane. The low-pressure region at *TE* draws the low-momentum coolant boundary layer fluid exiting the film hole, setting up the wake region immediately downstream of the jet exit. The strong vorticity in the jet boundary layer as it exits the hole, coupled with the much weaker vorticity generated by the shearing between the jet and crossflow, set up the counterrotating vortex pair commonly seen downstream of a streamwise jet injection site. Three undesirable effects of the vortex pair are typically encountered. First, the direction of rotation is such that hot crossflow fluid is entrained underneath the jet on the surface. Second, the vortex pair creates lift by mutual induction, thereby causing the coolant core to move away from the wall. Third, the turbulence generated promotes rapid coolant jet mixing. Well downstream of injection, the flow returns to a boundary layer type flow.

6.3 $\Phi = 60$ deg Forward-Diffused Film Hole (FDIFF60). The film hole entrance region for the FDIFF60 case is very similar to the REF case. Separation is seen at the entrance with jetting fluid going around this region along the upstream wall. As shown in Part II, normalized velocity contours for compound-angle holes agree well with streamwise holes for matching hole shapes. This was substantiated by results from the present study. Pressure and turbulence fields at the hole entrance region also appear to be unaffected by the compound-angle orientation. The only difference from the REF case detected in the entrance region for the FDIFF60 configuration is a slight asymmetry of the counterrotating secondary flow in the film hole. Once the start of the diffusing section is reached, the flow ceases to be nearly identical to the REF case. Similarities with the streamwise shaped case are present in the vicinity of the diffusing section onset, but the crossflow influence is more drastic in compound-angle geometries and the similarities with the streamwise forward-diffused case stop well before the exit plane is reached.

At the start of the 15 deg diffusing section in the film hole, a recirculation region is captured along the lower surface of the hole. The magnitude of the recirculation is much less than at the entrance to the film hole, but this elongated separation area extends about half the length of the diffusing section. Recirculation velocities in this region are on the order of 0.02 percent of V_∞. A small amount of turbulence is generated in the shear layer around this recirculation region, which adds to the high turbulence generated at the film hole inlet. The diffusing section is designed to slow the jet fluid, however the jetting fluid is not greatly affected by the forward diffusion. The fluid most affected is in the lower half of the film hole, adjacent to the area change, which was already at low momentum levels. The low-momentum region produced at the inlet to the film hole grows in size as the diffusing section starts while the jetting fluid stays primarily unaffected along the upstream wall.

The effects of separation and jetting at the film-hole inlet, film-hole diffusion and the interaction with the crossflow provide highly nonuniform exit-plane conditions. It was shown in Part II that injecting at a compound angle had a drastic effect on exit-plane conditions. Part III detailed the complex effects of hole shaping at the exit plane. The reader is cautioned that simple superposition of these effects *does not* apply. Similarities in the FDIFF60 case do exist with both the $\Phi = 60$ deg cylindrical case and the $\Phi = 0$ deg forward-diffused case, but some mechanisms present in this geometry are not found in either of the other two. This is evident at the exit plane, as will now be discussed.

As the crossflow approaches the FDIFF60 holes, it has no line-of-sight between adjacent film holes, as the lateral projected

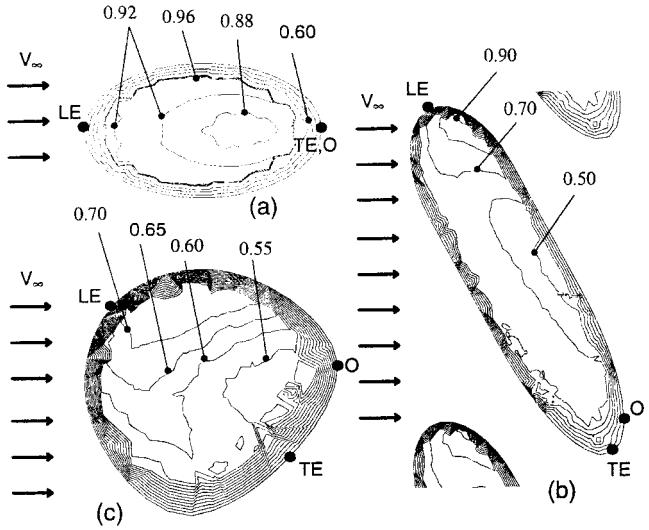

Fig. 7 Exit-plane *VR* contours for the (*a*) REF, (*b*) FDIFF60, and (*c*) LDIFF45 cases (*M* = 1.25) show increased complexity for CASH geometries

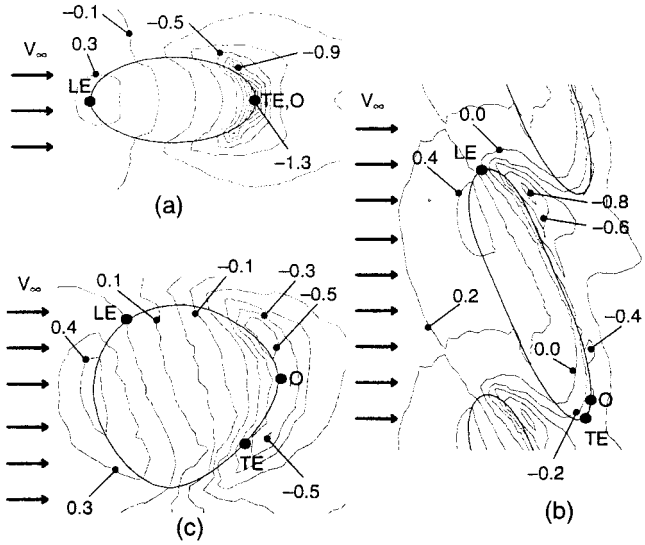

Fig. 9 Exit-plane pressure coefficient contours for the (*a*) REF, (*b*) FDIFF60, and (*c*) LDIFF45 cases (*M* = 1.25) show the high-pressure stagnation region on the upstream edge and the low-pressure region on the downstream edge

width is $3.3D$ with $P/D = 3.0$. With no low-resistance path for the crossflow to follow between the jets, this interaction of jet and crossflow leads to a significant blockage of the jet. If the crossflow did not exist, the core of the jetting fluid would exit adjacent to point *LE* and the low-momentum fluid adjacent to point *TE*. An effect of the crossflow on the jet is seen as the core of the jetting fluid exits slightly downstream of point *LE*, as shown by the location of the high *VR* region in Fig. 7(*b*) and high α in Fig. 8(*b*). The lower momentum fluid is more drastically affected by the impact with the crossflow. This is evident in Fig. 8(*b*), where an area of negative α indicates complete blockage of the jet by the crossflow and actual *crossflow ingestion* into the film hole! Negative *y*-velocity components exist in this area. Thole et al. (1998) measured slight crossflow ingestion for a streamwise forward-lateral expanded hole. Although the geometries are quite different, the need for a priori performance knowledge of a new film-hole design is already indicated. No recirculation of crossflow is present at this location. The negative *y*-velocities are produced by a small vortex located over this region with clockwise rotation when viewed aft-looking-forward. This "ingestion vortex" will be discussed in more detail shortly. Note that in the FDIFF60 case in Fig. 9(*b*), the pressure coefficient in the region of ingestion is ~0.2. This is not a high value, but in the presence of the velocity vectors with very small *y*-components found here, this slightly elevated pressure may aid the ingestion process. The low-momentum fluid that would have exited adjacent to point *TE* has been forced to the downstream edge of the film hole, beyond point *O*. Most of the coolant exits from the area of the hole downstream of a line connecting points *LE* and *O*.

The extreme nonuniformity of exit plane conditions is visible in Fig. 8(*b*) for discharge α and Fig. 10(*b*) for discharge Φ as compared to the REF case in Figs. 8(*a*) and 10(*a*). Note that α is computed relative to the *x*–*z* plane and Φ is measured relative to the *x*–*y* plane. For the FDIFF60 metal angles of $\alpha = 35$ deg and $\Phi = 60$ deg, wide variations are seen as α ranges from 0 to 40 deg and Φ ranges from 25 to 45 deg. These exit-plane conditions play a major factor in determining downstream performance, therefore the suggestion of Leylek and Zerkle (1994) that crossflow, film hole, and plenum regions be simultaneously modeled is substantiated by the nonuniform jet exit conditions.

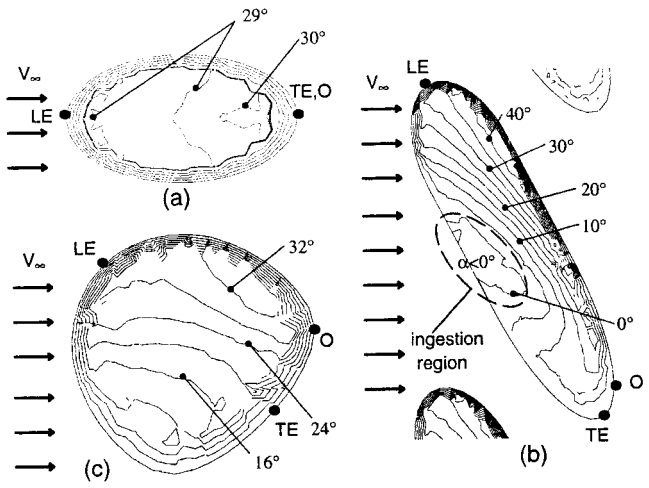

Fig. 8 Exit-plane discharge α contours for the (*a*) REF, (*b*) FDIFF60, and (*c*) LDIFF45 cases (*M* = 1.25) show the impact of the crossflow on jet trajectory, with actual crossflow ingestion in the FDIFF60 case

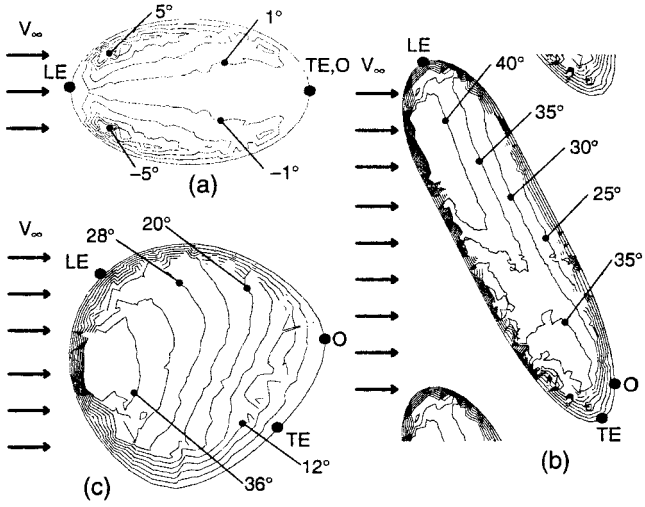

Fig. 10 Exit-plane discharge Φ contours for the (*a*) REF, (*b*) FDIFF60, and (*c*) LDIFF45 cases (*M* = 1.25) show wide variations in Φ over the exit plane for CASH configurations

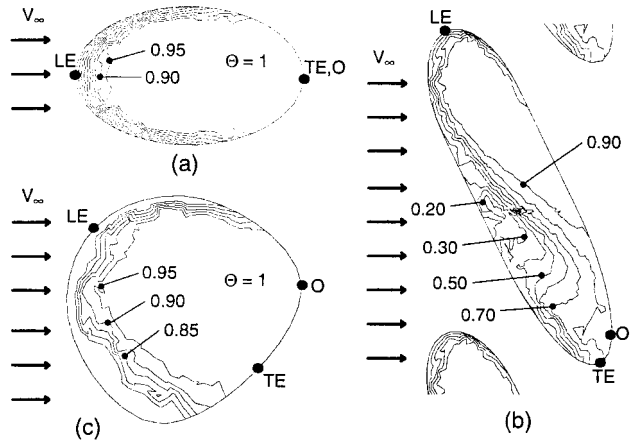

Fig. 11 Exit-plane discharge Θ contours for the (*a*) REF, (*b*) FDIFF60, and (*c*) LDIFF45 cases (*M* = 1.25) show the shielding of the low-momentum fluid from the crossflow by the high-momentum jetting fluid in the REF and LDIFF45 cases

The exit-plane temperature distribution is shown in Fig. 11(*b*). In the REF case, the strong jetting fluid lies between the crossflow and the low-momentum fluid at the exit plane, shielding the low-momentum fluid from impact with the crossflow. This effect of this shielding can be seen in Fig. 11(*a*), as the Θ distribution for the REF case is fairly uniform. For the FDIFF60 case shown in Fig. 10(*b*), the low-momentum fluid is no longer shielded from the crossflow, leaving it essentially "out in the open." This slower moving low-momentum fluid exiting from the *TE* part of the hole is significantly affected by thermal diffusion of the crossflow as the nondimensional temperature, Θ, is less than 0.8 over about half of the exit plane.

The *TL* distribution for the FDIFF60 case on a *y–z* plane located at point *O* is shown in Fig. 12(*b*). Contours of *TL* in the film hole and around the jet exit allow the origin of the high *TL* to be tracked. The source of the highest *TL* seen in Fig. 12(*b*) is the turbulence produced at the film-hole inlet. The *TL* of the jet fluid is slightly higher in the FDIFF60 case than the REF case as seen in Figs. 12(*b*) and 12(*a*), due to the small amount of turbulence

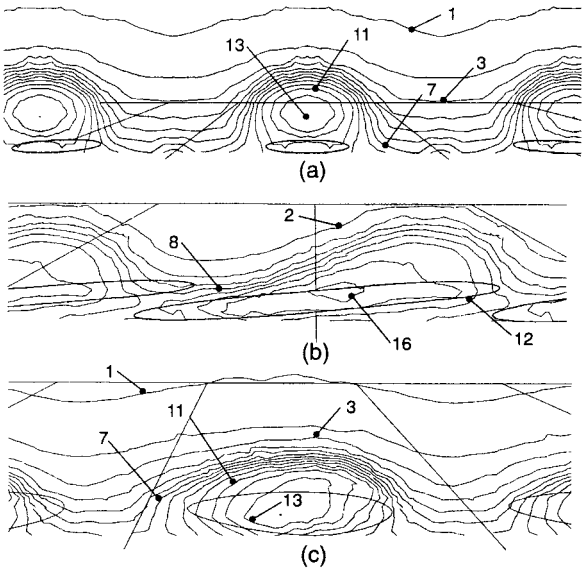

Fig. 12 Aft-looking-forward view of *TL* contours (percent) on a *y–z* plane at point *O* for the (*a*) REF, (*b*) FDIFF60, and (*c*) LDIFF45 cases (*M* = 1.25) show similar turbulence fields for all cases, with a slight increase for the FDIFF60 case due to separation at the start of the film hole diffusing section

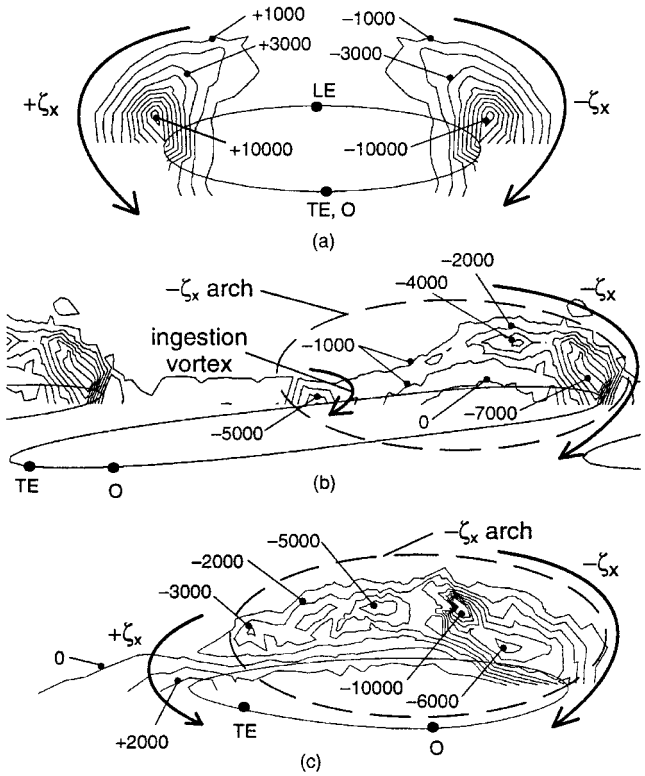

Fig. 13 Aft-looking-forward view of *x*-vorticity contours on a *y–z* plane located over the hole for the (*a*) REF, (*b*) FDIFF60, and (*c*) LDIFF45 cases (*M* = 1.25) show the negative ζ_x arch seen in the two CASH cases and the ingestion vortex vorticity for the FDIFF60 case

generated by the recirculation region at the start of the diffusing section. Recall that Thole et al. (1998) measured higher turbulence levels at the exit of expanded holes, attributed to hypothetical separation at the start of the expanding sections. Of note is the fact that the velocity gradients between the jet and crossflow, while still a source of turbulence, do not generate the high levels of turbulence produced at the film hole inlet. These velocity gradients do, however, help to sustain the turbulence as the jet travels downstream. These velocity gradients are more severe in these two CASH configurations than in the REF case, therefore higher turbulence levels are seen downstream in the FDIFF60 and LDIFF45 cases.

It was discussed in Part I that the counterrotating vortex structure seen downstream of injection results primarily from the vorticity in the film-hole boundary layer. In Part III, the strength of this secondary flow was shown to vary with hole shaping, as exit conditions were changed. As shown in Lee et al. (1997) and discussed in Part II, as Φ is increased, one side of the symmetric vortex pair collapses and the other strengthens due to: (1) blockage of the exiting hole boundary layer by the crossflow along the upstream edge and (2) shear between the crossflow and jet. The *x*-direction vorticity, ξ_x, for all cases is shown in Fig. 13 for *y–z* planes located at points midway between *LE* and *TE* for the REF and LDIFF45 case but slightly farther upstream at $x/D = -1.5$ for the FDIFF60 case. The thin boundary layer of the jetting fluid exiting near point *LE* in the FDIFF60 case has strong negative ξ_x (contour level −7000 in Fig. 12(*b*)). The surviving half of the downstream counterrotating pair originates near the wall just downstream of point *LE* due to this $-\xi_x$, as was the case for Φ = 60 deg cylindrical configuration. By examining the jet trajectory across the hole (Figs. 8, 10), a shear layer is distinguished between the jet (moving at α and Φ) and crossflow (moving at α = ~0 deg and Φ = ~0 deg), which has a negative ξ_x component. Near point *LE*, this vorticity serves to strengthen the vorticity generated in the film-hole boundary layer.

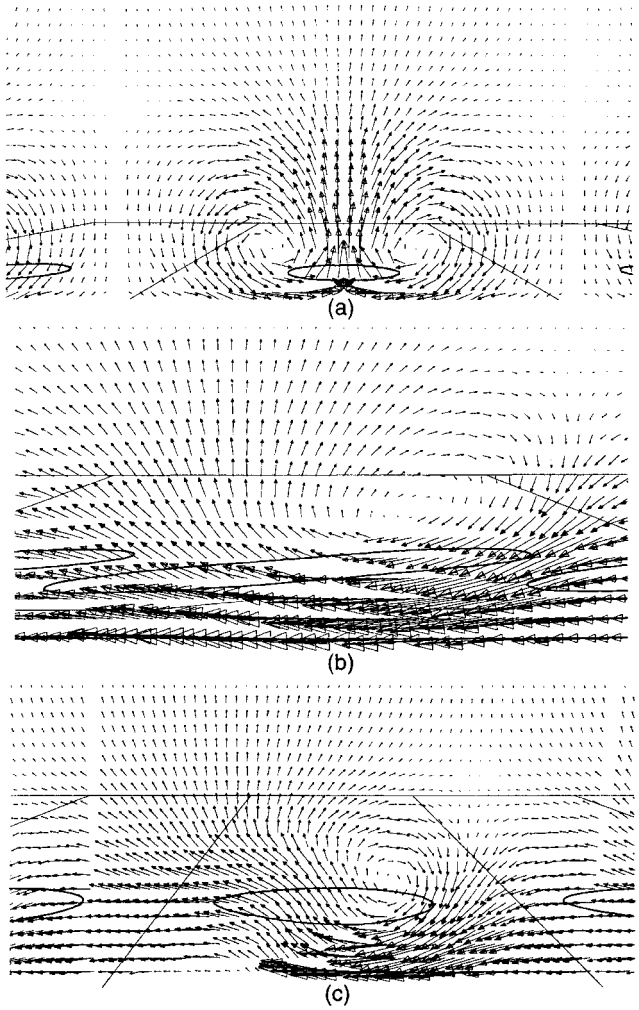

Fig. 14 Aft-looking-forward view of in-plane velocity vectors on a *y–z* plane at *x/D* = 2 for the (*a*) REF, (*b*) FDIFF60, and (*c*) LDIFF45 cases (*M* = 1.25) show the collapse of one half of the downstream vortex pair (scale equal on all parts)

At the ingestion region laterally across the hole from point *LE*, along the upstream edge, $+\xi_x$ would be expected due to the jet boundary layer, however, the total ξ_x is negative there for two main reasons. First, the film hole boundary layer is blocked by the crossflow, as shown in Fig. 8(*b*), and therefore the $+\xi_x$ from the jet boundary layer is small. Second, shear between the jet and crossflow produces $-\xi_x$ components, which dominate in this region for this case. The $-\xi_x$ produced in the jet/crossflow shear layer is evident in Fig. 13(*b*) by the $-\xi_x$ "arch" located across the hole. It is this $-\xi_x$ along the upstream edge that sets up the ingestion vortex, which is located over the hole and responsible for the crossflow ingestion. This vortex causes the crossflow in the ingestion area to follow a helical pattern as it dips down into the hole ($\alpha < 0$ deg region in Fig. 8(*b*)) and then back up and out of the hole as it rides over the low momentum fluid exiting along the downstream edge. The crossflow ingestion, coupled with the lack of shielding for the low-momentum fluid allowing greater thermal diffusion down into the film hole, causes the metal temperature along the upstream wall of the hole and the area around point *TE* to be much higher than the jet temperature, with η as low as 0.8 along the wall of the hole. With $-\xi_x$ due to jet/crossflow shear and boundary layer blockage by the crossflow prevailing over the area around point *TE*, insufficient $+\xi_x$ is present to establish the second vortex commonly seen downstream in streamwise injection. This is consistent with the $\Phi = 60$ deg cylindrical case, and is evident in Fig. 14(*b*) from the secondary fluid motion present in plane at $x/D = 2$. The ingestion vortex is weak when compared to the vortex in Fig. 14(*b*) and is not a factor downstream of the hole, although causing very harmful crossflow. It is not noticeable at $x/D = 2$.

Despite the fact that the crossflow does not have a line-of-sight through the row of holes, it does turn and accelerate between adjacent holes, due to: (1) deflection by the jet exiting from the *TE* area of the neighboring hole, (2) low pressure along the downstream edge of the jet, and (3) action of the strong vortex. The pressure field at the exit plane is shown in Fig. 9(*b*) as the pressure coefficient, which is normalized by the crossflow velocity. The crossflow tucks in under the jetting fluid and is spread laterally across the test surface by the secondary vortex, evident from the vectors in Fig. 14(*b*) and the pathlines in Fig. 15(*a*), where a surface of constant $T = 205$ K is shown exiting the hole ($T_j = 187.5$ K). The jetting fluid can be seen slightly lifting off as the crossflow goes underneath. This jetting fluid is immediately caught in the strong vortex and mixes quickly, adding to the uniformity of downstream coverage.

The flow in the far field away from the wall is simply in the streamwise direction. As the wall is approached, the flow is directed at increasing Φ, with the velocity very near the wall at $\Phi = 11$ deg for $x/D = 20$. For fluid above $y/D = 1.5$, the lateral velocity component is less than 1 percent of V_∞.

6.4 Φ = 45 deg Laterally Diffused Film Hole (LDIFF45). As in the FDIFF60 configuration, the flow in the film hole prior to the diffusing section in the LDIFF45 case is very similar to the REF case. Again, a slight asymmetry of the secondary vortical structure in the film hole entrance region is noted. It does not appear that this asymmetry significantly affects the exit plane distributions or downstream performance.

The diffusing section in the LDIFF45 has a much greater impact on the high momentum jetting fluid than the diffusing section in the FDIFF60 case. In the FDIFF60 case, the diffusing area was on the bottom of the hole adjacent to the low-momentum fluid. In the LDIFF45 hole, the sides are diffused adjacent to the jetting fluid, which is therefore directly affected. Note that 15 deg of forward diffusing were seen in the FDIFF60 case, resulting in an exit plane

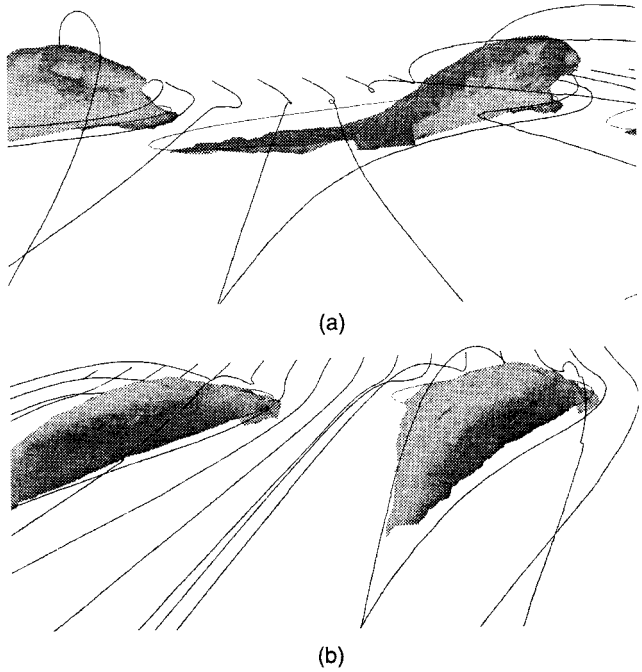

Fig. 15 Aft-looking-forward view of pathlines around a constant *T* = 205 K surface for the (*a*) FDIFF60 and (*b*) LDIFF45 cases (*M* = 1.25) demonstrate the complex flowfield for both CASH configurations

to metering cross section area ratio of 4.15. In the LDIFF45 case, 2×12 deg $= 24$ deg of lateral diffusing are present, but the resulting area ratio is only 3.31. The lateral diffused hole, while having a smaller exit plane to metering cross section area ratio, is more successful in lowering the exit velocity ratio, as shown in Fig. 7(*c*). The highest exit-plane *VR* in the LDIFF45 case was ~0.75 (Fig. 7(*c*)), but it was ~0.90 in the FDIFF60 case (Fig. 7(*b*)). This suggests that the location of area change is as important as the magnitude of the area change for effective diffusion of the coolant jet in the film hole.

As in the streamwise lateral-diffused case, no recirculation is seen at the start of the diffusing section in the LDIFF45 film hole. This is in contrast to the separation regions from the lateral-expanded holes of Thole et al. (1998) which they hypothesized from elevated exit-plane turbulence levels. A few differences between the work of Thole et al. (1998) and the present paper must be acknowledged to view this contrast in the proper light. The nominal film-hole Reynolds number is about three times higher in the work of Thole et al. (1998) than in the present investigation (~52,000 versus 17,350, respectively). The nature of the flow in the film hole is quite different, as a co-flowing coolant channel was used by Thole et al. (1998) and a plenum in the present investigation. The large separation region at the inlet to the film hole seen with a plenum would not exist for a co-flowing coolant geometry. The higher turbulence generated at the film-hole inlet through the use of a plenum could suppress separation at the start of the diffusing section by high-momentum diffusion. Also, with the low-momentum region created by separation at the film-hole inlet, the flow is much less uniform across the film hole. The effective area that the higher momentum fluid occupies at a given cross section is thus reduced by the low-momentum region in the present work, forcing the higher momentum fluid to reside along the wall. These differences demonstrate the complex nature of the flow in film-cooling configurations and the need for predictive design capability.

As no separation is seen at the start of the diffusing section, no turbulence is generated there. This is visible from the consistent *TL* levels in Figs. 12(*a, c*) for the REF and LDIFF45 cases, respectively. Compare these levels to the slightly elevated *TL* levels in the FDIFF60 case in Fig. 12(*b*), which did have separation in the diffusing section. As in the FDIFF60 case, the turbulence levels downstream are higher for the LDIFF45 case than the REF case due to the larger velocity gradients between the jet and crossflow.

Relative to the FDIFF60 case, the crossflow sees less of an obstruction as it approaches the LDIFF45 holes. One major difference to be noted between the two geometries is that in the LDIFF45 case, the crossflow does not have a line-of-sight between adjacent holes. The pressure field, shown in Fig. 9, shows less severe pressure gradients in both CASH cases relative to the REF case, with the smallest gradients in the LDIFF45 geometry in Fig. 9(*c*). The high-pressure stagnation region at the upstream wall provides some blockage of the jet, causing the core of the jetting fluid to exit slightly downstream of point *LE*. This is evident from the *VR* contours at the exit plane, shown in Fig. 7(*c*). Blockage of the jet by the crossflow also affects the low-momentum fluid in the *TE* region of the film hole, causing it to exit downstream of point *TE*. No crossflow ingestion is present in the LDIFF45 case. The exit plane distributions of α and Φ are seen in Figs. 8(*c*) and 10(*c*). Again, wide and complex variations in coolant discharge angles are seen across the hole. In the LDIFF45 case, the jet follows a lower trajectory as it exits the hole than the FDIFF60 case. This is discernible from the α distributions (Fig. 8(*c*)) and *VR* distributions (Fig. 7(*c*)) as well as the pathlines shown in Fig. 15(*b*) around a constant $T = 205$ K surface ($T_j = 193.55$ K).

Figures 11(*b, c*) show that the temperature distribution at the hole is much more uniform for the LDIFF45 case than the FDIFF60 case, as more shielding of low-momentum fluid from the crossflow is present due to the smaller fluid Φ and the hole shape. The exit-plane temperature is thus much higher in the *TE* area for the LDIFF45 case than the FDIFF60. This, coupled with no crossflow ingestion, cause adiabatic effectiveness values of near unity over most of the LDIFF45 hole wall.

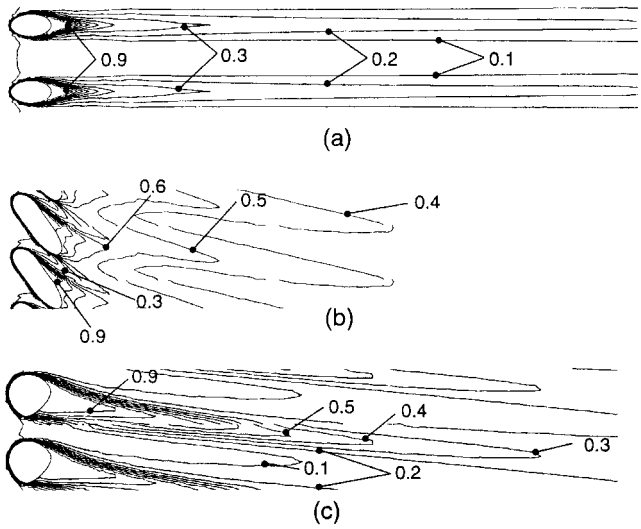

Fig. 16 Adiabatic effectiveness footprints for the (*a*) REF, (*b*) FDIFF60, and (*c*) LDIFF45 cases ($M = 1.25$) show the excellent lateral distribution for the FDIFF60 case but wide variations for the REF and LDIFF45 cases

Similarities are present with the FDIFF60 case in the vorticity field presented in Fig. 13(*b*). As shown in the FDIFF60 case, strong $-\xi_x$ is present in the *LE* region due to the film-hole boundary layer and the jet/crossflow shear layer. In the LDIFF45 case shown in Fig. 13(*c*), the $-\xi_x$ arch is again seen over the film hole delineating the jet/crossflow shear layer. In this case, the film-hole boundary layer on the upstream edge is not completely blocked off, as it was in the FDIFF60 case. Positive ξ_x is thus seen exiting the film hole in the area around and just upstream of point *TE* in Fig. 13(*c*). The jet/crossflow shear layer is still present, but the α, Φ, and *VR* distributions at the exit plane yield vorticity vectors that are oriented such that their negative *x*-components are smaller than in the FDIFF60 case. This effect, coupled with stronger $+\xi_x$ from the exiting boundary layer (less blockage by the crossflow), produces small positive total ξ_x in the *TE* region. This $+\xi_x$ is barely strong enough to set up the second half of the downstream vortex pair. This is consistent with the $\Phi = 45$ deg cylindrical case presented in Part II, where this half of the downstream vortex pair was present but small. This vortex is weak and dissipates quickly, as seen from the velocity vectors at $x/D = 2$ in Fig. 14(*c*).

The far field behavior is similar to that of the FDIFF60 case, although less uniform in the lateral direction. At $x/D = 20$, the flow angle near the wall is $\Phi = 7$ deg. For $y/D > 1.5$, the lateral velocity component is less than 1 percent of V_∞, consistent with the FDIFF60 case.

7 Simulation Overview

7.1 Surface Results

7.1.1 Adiabatic Effectiveness. Adiabatic effectiveness footprints for the REF, FDIFF60, and LDIFF45 cases are shown in Fig. 16(*a, b, c*), respectively for $M = 1.25$. It is readily apparent that adding a compound angle helps to spread the coolant. This was shown in detail in Part II. Note the quick coalescence of neighboring jets in the FDIFF60 case in Fig. 16(*b*), remembering that the crossflow had no line-of-sight between adjacent holes. The uniformity of coverage is excellent in the FDIFF60 case compared to the REF (Fig. 16(*a*)) and LDIFF45 (Fig. 16(*c*)) cases. Notice in the LDIFF45 case that large sections between the holes do not see any coolant for the first few diameters downstream of injection.

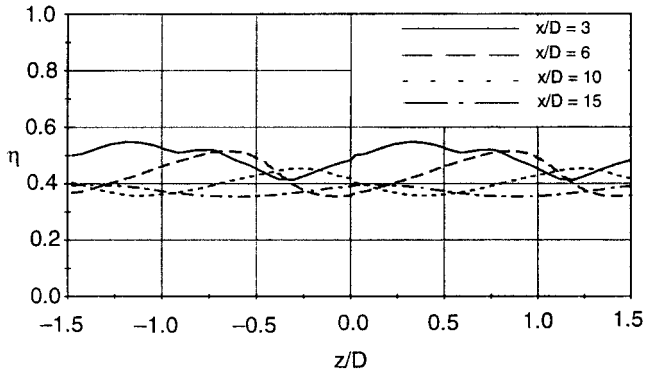

Fig. 17 Lateral adiabatic effectiveness distribution for the FDIFF60 case for $M = 1.25$ shows consistent coolant coverage across the pitch

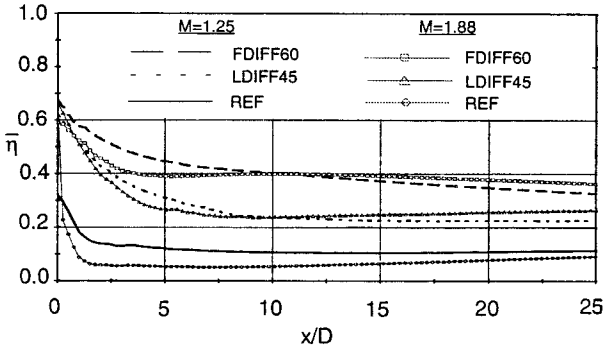

Fig. 19 Lateral averaged adiabatic effectiveness comparison of the REF, FDIFF60, and LDIFF45 cases shows the superior downstream performance of the FDIFF60 configuration

The lateral variations of η for various x/D stations are shown in Fig. 17 for the FDIFF60 case and Fig. 18 for the LDIFF45 case for $M = 1.25$. The wide variation in η across the test surface seen in the LDIFF45 configuration, but not in the FDIFF60, causes large thermal gradients and would be detrimental to the useful life of the metal blade. This variation results from the crossflow adjacent to the test surface being able to easily flow between the holes. To alleviate this problem common to discrete hole injection, CASH film cooling configurations can be designed with projected lateral hole widths wider than the P/D, thus somewhat mimicking the performance of a slot jet. The spanwise uniformity of η even at $x/D = 3$ for the FDIFF60 case is remarkable when compared with the large variation for the LDIFF45 case.

Lateral averaged η distribution for all three shapes are compared in Fig. 19, again showing the superior downstream performance of the FDIFF60 configuration for both blowing ratios. It was shown in Part II that $\Phi = 45$ deg cylindrical holes performed better than $\Phi = 60$ deg holes and in Part III that the $\Phi = 0$ deg lateral-diffused hole had better performance than the $\Phi = 0$ deg forward-diffused case. Upon combination, it is evident that superposition does not apply as the $\Phi = 45$ deg lateral-diffused case had poorer downstream performance than the $\Phi = 60$ deg forward-diffused case. Clearly, the mechanisms governing film cooling performance are nonlinear in nature.

7.1.2 Heat Transfer Coefficient. Improving η is important in film cooling, but the heat transfer coefficient must also be taken into account. To normalize h_f, an empirical relation for turbulent boundary layer flow with unheated starting length was used to determine the Stanton number and thus the heat transfer coefficient h_o:

$$\mathrm{St} = 0.03\ \mathrm{Pr}^{-0.4}\ \mathrm{Re}_x^{-0.2}\left[1 - \left(\frac{x_o}{x}\right)^{0.9}\right]^{-1/9} \quad (1)$$

x_o = unheated starting length

Results of laterally averaged heat transfer coefficients for the REF and LDIFF45 case are shown in Fig. 20 normalized by the turbulent boundary layer solution. The centerline h_f/h_o data of Sen et al. (1996) for a geometry similar (different plenum) to the REF case with similar flow conditions is shown for validation ($M = 1.0$ and $DR = 1.0$). The trends of h_f/h_o for the simulations reported in the present paper are consistent with those reported in Sen et al. (1996).

The more complex interaction of the LDIFF45 case produced higher h_f/h_o values than were seen in the REF case. Recall that the turbulence levels downstream were higher for the LDIFF45 configuration than the REF case due to the larger velocity gradients between the jet and crossflow. This turbulence promotes mixing of the jet and crossflow and augments heat transfer. These heat transfer coefficient trends are consistent with the h_f/h_o values reported for compound-angle cylindrical holes in Part II and for streamwise injected shaped holes in Part III. Heat transfer coefficient increased with increasing M, which is consistent with the results presented in the Literature Review section.

7.2 Flowfield Results. Compound-angle injection was found to alter the flow slightly in the film hole relative to the streamwise REF case, by producing a small asymmetry of the secondary counterrotating motion. Film-hole diffusion was found to produce separation at the start of the diffusing section for a 15 deg forward diffusion, but not for a 12 deg lateral diffusion. Lateral diffusion was shown to be more effective in lowering the exit plane VR due to the proximity of the jetting fluid relative to the area change. Hole shaping greatly lowered pressure gradients in the area of the breakout relative to cylindrical holes at the same compound angle for the two shapes investigated. Complex exit-

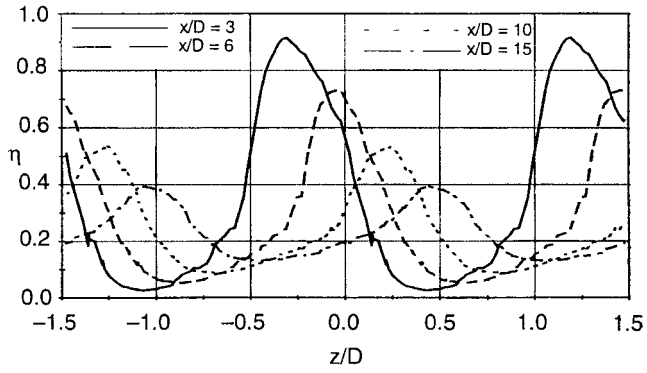

Fig. 18 Lateral adiabatic effectiveness distribution for the LDIFF45 case for $M = 1.25$ shows wide variations in coolant coverage across the pitch

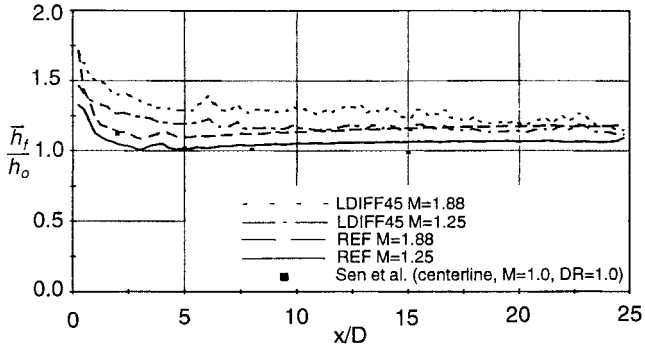

Fig. 20 Lateral averaged heat transfer coefficients for the REF and LDIFF45 cases show an increase in heat transfer coefficient with the increased geometric complexity for both blowing ratios

plane and near-field flow was demonstrated for both CASH configurations. Blockage by the crossflow exhibited significant influence on the exiting jet fluid, especially away from the *LE*, which is adjacent to the strongest jetting fluid. This blockage effect was so pronounced on the upstream edge of the FDIFF60 case that crossflow ingestion occurred. Streamwise aligned vorticity (ξ_x) in the region of the jet exit was determined to greatly affect the downstream performance by the creation of secondary vortical structures. The existence, strength, location, and direction of rotation of these vortices are governed by the vorticity field set up primarily by film hole boundary layers and jet/crossflow shear layers. This vorticity field is geometric configuration and flowfield parameter dependent. Far field behavior is that of a shear layer flow, with increasing lateral velocity component as the wall is approached.

8 Summary and Discussion

Results have been presented and flowfields discussed for cylindrical streamwise and compound-angle holes as well as shaped streamwise and compound-angle holes in the companion papers designated as Parts I through IV. The streamwise cylindrical case in Part I was used to explore basic flow structures found in the film hole and in the region of jet and crossflow interaction. The origination of the crossflow counterrotating vortices was examined and shown to be due to the streamwise aligned vorticity of the film hole boundary layers. Adding a compound angle to cylindrical holes was shown in Part II to significantly alter the flowfield at the exit plane and downstream. Highly nonuniform exit conditions were shown, as well as extreme pressure and velocity gradients near the hole. The streamwise aligned vorticity of the hole boundary layer was shown to be augmented by the jet/crossflow shear layer vorticity on the *LE* side of the hole and hindered by the same on the *TE* side. This effect plus the boundary layer blockage on the upstream edge of the hole was determined to be the cause of the collapse of one half of the downstream vortex pair. Lateral η distribution and coolant jet coalescence was shown to improve upon adding a compound angle.

As hole shaping was added in Part III, flow in the film hole and at the exit plane was again complex. It was determined that the strength of the downstream counterrotating vortices can be weakened by proper hole shaping. Another important conclusion was that the lift produced by the interaction of the two vortices could be hindered by spreading them apart. Compound-angle shaped holes (CASH) were shown in Part IV to be nonlinear combinations of compound-angle holes and shaped holes. Similarities in the film-hole flowfields with both compound-angle holes and shaped holes were shown for various film-hole locations, although structures appear in some CASH configurations that do not appear in either the compound-angle or shaped counterparts, e.g., crossflow ingestion. Exit-plane coolant velocity, temperature, and discharge-angle distributions were shown to be highly nonuniform and complex. As in the compound-angle cylindrical case, streamwise aligned film-hole boundary layer and jet/crossflow shear layer vorticity are both major factors in downstream secondary flow motion and film-cooling performance. Which mechanism dominates is dependent on the geometric configuration and flowfield parameters. Jet coalescence and lateral coolant distribution were found to improve over the compound-angle cylindrical case, but remained very dependent on film hole geometry. Crossflow line-of-sight between adjacent holes was shown to significantly affect the lateral coolant distributions.

As a quick comparison of the four types of geometries examined, the optimum $\overline{\eta}$ performer from each group is shown in Fig. 21. It is evident that film-hole geometry plays a major factor in determining downstream performance, and is a valid arena for further study.

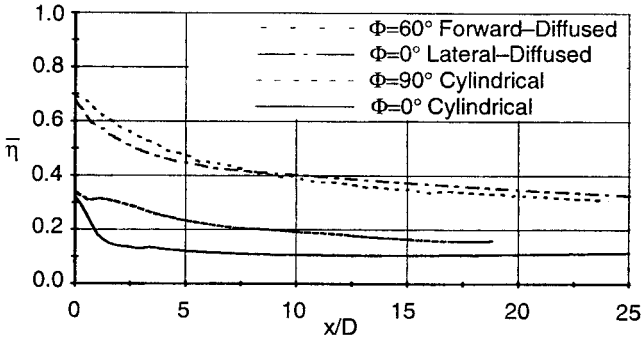

Fig. 21 Lateral averaged adiabatic effectiveness comparison for different geometry types at $M = 1.25$ highlights the effects of compound-angle injection and hole shaping

9 Conclusions

Results have been presented for two CASH film-cooling configurations investigated at geometric and flowfield parameters typically seen in modern gas turbines. The good agreement between computational and experimental results demonstrates the quality of the simulations documented in the present paper. Important conclusions drawn from this work include:

- Superposition of effects for compound-angle cylindrical holes and streamwise shaped holes do not necessarily apply to CASH holes.
- The flow in the film hole prior to shaping is mostly unaffected by the compound angle.
- The flow in the film hole once the shaped area has been reached is similar to streamwise shaped counterparts until the effects of the crossflow are felt as the exit-plane is approached.
- The coolant jet exit-plane conditions are highly nonuniform due to film-hole flow history effects and blockage by the crossflow.
- The vorticity field at the jet-exit is due primarily to film hole boundary layers and the jet/crossflow shear layer. This field determines the existence, strength, direction of rotation, and location of secondary vortical structures, and is configuration dependent.
- Certain combinations of geometry and flow parameters have been shown to lead to crossflow ingestion into the film hole.
- CASH can be designed to eliminate crossflow line-of-sight between adjacent holes, and thus somewhat mimic slot-jet performance.
- A true physical understanding of the flowfield is necessary to suggest design improvements.
- CFD can be used to accurately compare the relative performance of CASH film-cooling configurations.

Acknowledgments

This paper was prepared with the support of the U. S. Department of Energy, Morgantown Energy Technology Center, Cooperative Agreement No. DE-FC21-92MC29061. The authors would like to thank Clemson University graduate students Mr. John Farmer and Mr. Dave Seager, as well as their advisor Prof. James Liburdy for valuable, as yet unpublished, experimental surface data and another graduate student, Mr. Phillip Berger, for velocity inlet profiles. Also deserving of special recognition are Mr. Gary Berger and Mr. Richard Baldwin of the Computer and Network Services at Clemson University for their assistance in all computer-related matters. We are also deeply indebted to Dr. Rick Lounsbury at Fluent, Inc., for his invaluable support for RAMPANT and Fluent/UNS.

References

Ekkad, S., Zapata, D., and Han, J., 1997a, "Heat Transfer Coefficients Over a Flat Surface With Air and CO_2 Injection Through Compound Angle Holes Using a Transient Liquid Crystal Image Method," ASME JOURNAL OF TURBOMACHINERY, Vol. 119, pp. 580–586.

Ekkad, S., Zapata, D., and Han, J., 1997a, "Film Effectiveness Over a Flat Surface With Air and CO_2 Injection Through Compound Angle Holes Using a Transient Liquid Crystal Image Method," ASME JOURNAL OF TURBOMACHINERY, Vol. 119, pp. 587–593.

Farmer, J., Seager, D., and Liburdy, J., 1997, "The Effect of Shaping Inclined Slots on Film Cooling Effectiveness and Heat Transfer Coefficient," ASME Paper No. 97-GT-339.

Goldstein, R., Eckert, E., and Burggraf, F., 1974, "Effects of Hole Geometry and Density on Three-Dimensional Film Cooling," *International Journal of Heat and Mass Transfer*, Vol. 17, pp. 595–606.

Haven, B., and Kurosaka, M., 1996, "The Effect of Hole Geometry on Lift-Off Behavior of Coolant Jets," AIAA Paper No. AIAA 96-0618.

Lee, S., Kim, Y., and Lee, J., 1997, "Flow Characteristics and Aerodynamic Losses of Film-Cooling Jets With Compound Angle Orientations," ASME JOURNAL OF TURBOMACHINERY, Vol. 119, pp. 310–319.

Leylek, J., and Zerkle, R., 1994, "Discrete-Jet Film Cooling: A Comparison of Computational Results With Experiments," ASME JOURNAL OF TURBOMACHINERY, Vol. 116, pp. 358–368.

Ligrani, P., Wigle, J., Ciriello, S., and Jackson, S., 1994a, "Film-Cooling From Holes With Compound Angle Orientations: Part 1—Results Downstream of Two Staggered Rows of Holes With 3*d* Spanwise Spacing," ASME *Journal of Heat Transfer*, Vol. 116, pp. 341–352.

Ligrani, P., Wigle, J., and Jackson, S., 1994b, "Film-Cooling From Holes With Compound Angle Orientations: Part 2—Results Downstream of a Single Row of Holes With 6d Spanwise Spacing," ASME *Journal of Heat Transfer*, Vol. 116, pp. 353–362.

Makki, Y. H., and Jakubowski, G. S., 1986, "An Experimental Study of Film Cooling From Diffused Trapezoidal Shaped Holes," AIAA Paper No. AIAA-86-1326.

Papell, S., 1984, "Vortex Generating Flow Passage Design for Increased Film Cooling Effectiveness and Surface Coverage," ASME Paper No. 84-HT-22.

Schmidt, D., 1995, "Effects of Injection Hole Geometry, Surface Roughness, and Freestream Condition on Film Cooling," Ph.D. Dissertation, University of Texas at Austin.

Schmidt, D., Sen, B., and Bogard, D., 1996, "Film Cooling With Compound Angle Holes: Adiabatic Effectiveness," ASME JOURNAL OF TURBOMACHINERY, Vol. 118, pp. 807–813.

Sen, B., Schmidt, D., and Bogard, D., 1996, "Film Cooling with Compound Angle Holes: Heat Transfer," ASME JOURNAL OF TURBOMACHINERY, Vol. 118, pp. 800–806.

Thole, K., Gritsch, M., Schulz, A., and Wittig, S., 1998, "Flowfield Measurements for Film-Cooling Holes With Expanded Exits," ASME JOURNAL OF TURBOMACHINERY, Vol. 120, pp. 327–336.

Walters, D., and Leylek, J., 1998, "A Systematic Computational Methodology Applied to a Three-Dimensional Film-Cooling Flowfield," ASME JOURNAL OF TURBOMACHINERY, Vol. 120, pp. 777–785.

Effect of Internal Coolant Crossflow Orientation on the Discharge Coefficient of Shaped Film-Cooling Holes

M. Gritsch[1]

C. Saumweber

A. Schulz

S. Wittig

E. Sharp[2]

Lehrstuhl und Institut für Thermische Strömungsmaschinen, Universität Karlsruhe (T.H.), Kaiserstr. 12, 76128 Karlsruhe, Germany

Discharge coefficients of three film-cooling hole geometries are presented over a wide range of engine like conditions. The hole geometries comprise a cylindrical hole and two holes with a diffuser-shaped exit portion (a fanshaped and a laidback fanshaped hole). For all three hole geometries the hole axis was inclined 30 deg with respect to the direction of the external (hot gas) flow. The flow conditions considered were the hot gas crossflow Mach number (up to 0.6), the coolant crossflow Mach number (up to 0.6) and the pressure ratio across the hole (up to 2). The effect of internal crossflow approach direction, perpendicular or parallel to the main flow direction, is particularly addressed in the present study. Comparison is made of the results for a parallel and perpendicular orientation, showing that the coolant crossflow orientation has a strong impact on the discharge behavior of the different hole geometries. The discharge coefficients were found to strongly depend on both hole geometry and crossflow conditions. Furthermore, the effects of internal and external crossflow on the discharge coefficients were described by means of correlations used to derive a predicting scheme for discharge coefficients. A comparison between predictions and measurements reveals the capability of the method proposed.

Introduction

Discharge coefficients are a means to quantify the throughflow losses of film-cooling holes. Since the cooling performance depends strongly on the flow rate ejected through the hole, the knowledge of the discharge coefficient is crucial for a reliable design of the cooling system. Discharge coefficients are known to depend on many geometric and aerodynamic parameters, such as hole geometry and the pressure ratio across the hole, as well as internal and external crossflow conditions.

Recently, Hay and Lampard (1998) gave a comprehensive review of published discharge coefficient data. The main geometric parameters include hole inclination angle (Hay et al., 1983), hole orientation angle (Hay et al., 1994a), hole length (Burd and Simon, 1999), and hole entry or exit radiusing (Hay and Spencer, 1992; Hay et al., 1994b).

Recent attention has been given to holes with a diffuser-shaped expansion at the hole exit portion, since these configurations are known for improving the thermal protection of the airfoil (e.g., Gritsch et al., 1998a, d; Thole et al., 1998). Discharge coefficients of holes with expanded exits were studied by Hay and Lampard (1995) and Gritsch et al. (1998b). They found elevated discharge coefficients as compared to cylindrical holes due to pressure recovery in the expanded portion of the hole.

The effect of external crossflow was addressed by several studies (Hay et al., 1983; Rowbury et al., 1997). Generally, the external crossflow tends to impede the jet exiting the hole, resulting in lower discharge coefficients as compared to the zero crossflow case. For some flow configurations, however, higher discharge coefficients may occur due to the fact that the crossflow effectively draws up the jet flow.

The effect of internal crossflow has received less attention. Hay et al. (1983) were the only researchers investigating discharge coefficients experimentally with coolant crossflow approaching perpendicular to the main flow. They identified additional losses occurring due to the strong turn of the flow entering the hole.

The present study focuses on discharge coefficients of cylindrical and noncylindrical holes with an internal crossflow approaching perpendicular to the main flow direction. A correlation-based predicting scheme developed by Gritsch et al. (1998c) for cylindrical holes with internal crossflow parallel to the main flow is extended for use for holes with an expanded exit portion and internal crossflow perpendicular to the main flow.

Experimental Apparatus

The present investigation was carried out in a continuous flow wind tunnel at the Institut für Thermische Strömungsmaschinen (ITS), Karlsruhe, Germany. The film-cooling test rig consists of a primary loop representing the external flow and a secondary loop representing the internal flow of an airfoil. The primary and secondary loops were oriented perpendicular to each other, providing flow conditions typically found in turbine blades (Fig. 1). A more detailed description of the experimental facility is given by Wittig et al. (1996).

The tests were carried out using a single, scaled-up film-cooling hole with an inclination angle of 30 deg. In total, three hole geometries were tested (Fig. 2). These were a cylindrical hole and two holes with expanded exit portions (fan-shaped hole and laid-back fan-shaped hole). The diameter of the cylindrical hole and the diameter of the cylindrical inlet portion of both expanded holes was 10 mm. Both expanded holes show a lateral expansion angle of 14 deg resulting in a hole width of 30 mm at the hole exit. The radii of the "corners" depend on the radius of the tool used; which corresponds to the radius of the cylindrical inlet portion. The laid-back fan-shaped hole had an additional forward expansion of 15 deg resulting in a hole length of 40 mm at the hole exit. The

[1] Present address: ABB Corporate Research Ltd., 5405 Baden-Dättwil, Switzerland.

[2] Present address: Dept. of Mech. Eng., Purdue University, West Lafayette, IN 47907-1288.

Contributed by the International Gas Turbine Institute and presented at the 44th International Gas Turbine and Aeroengine Congress and Exhibition, Indianapolis, Indiana, June 7–10, 1999. Manuscript received by the International Gas Turbine Institute February 1999. Paper No. 98-GT-40. Review Chair: D. C. Wisler.

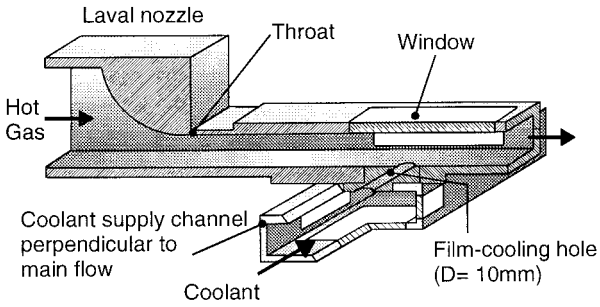

Fig. 1 Film-cooling test section

exit-to-entry area ratio of the fan-shaped and the laid-back fan-shaped hole were 3.0 and 3.1, respectively. The length-to-diameter ratio L/D is 6 for all holes. Entry and exit of the holes were sharp edged. The interior surfaces were aerodynamically smooth. The discharge coefficient C_D is defined as the ratio of actual and ideal mass flow rate through the hole.

The ideal mass flow rate is calculated assuming an isentropic, one-dimensional expansion from the total pressure in the secondary loop to the static pressure in the primary loop:

$$C_D = \frac{\dot{m}}{p_{tc}\left(\frac{p_m}{p_{tc}}\right)^{(\kappa+1)/2\kappa}\sqrt{\frac{2\kappa}{(\kappa-1)RT_{tc}}\left(\left(\frac{P_{tc}}{p_m}\right)^{(\kappa-1)/\kappa}-1\right)}\frac{\pi}{4}D^2} \tag{1}$$

For the expanded hole geometries, the discharge coefficient was based on the area of the metering section of the hole. This makes it more convenient to evaluate the effect of expanding the hole exit since the discharge coefficients can be directly compared to those of the cylindrical holes.

The total pressure and temperature of the coolant were measured $1D$ upstream of the hole inlet with a probe located $2D$ off channel centerline. The static pressure in the mainstream was measured at the side wall $10D$ upstream of the hole exit.

Each hole geometry was tested for a matrix of three internal Mach numbers (Ma_c = 0, 0.3, and 0.6) and three external Mach numbers (Ma_m = 0, 0.3, and 0.6) over a range of pressure ratios p_{tc}/p_m = 1 to 2.25. Moreover, each hole geometry was tested at four pressure ratios p_{tc}/p_m = 1.1, 1.2, 1.4, and 1.6 over a range of internal Mach numbers Ma_c = 0 to 0.6 with no external crossflow applied (Ma_m = 0).

The complete set of the operating conditions of the test rig is given in Table 1. Preliminary tests performed by Gritsch et al. (1998c) showed that the effect of coolant-to-mainflow-temperature ratio on the discharge coefficient is negligible. For a fixed pressure ratio, the temperature ratio was varied from 0.54 to 1 and no measurable effect on the discharge coefficient was found as long as the crossflow Mach numbers were matched. The measurements presented in this paper have therefore been conducted with a mainflow temperature equal to the coolant flow temperature of 290 K.

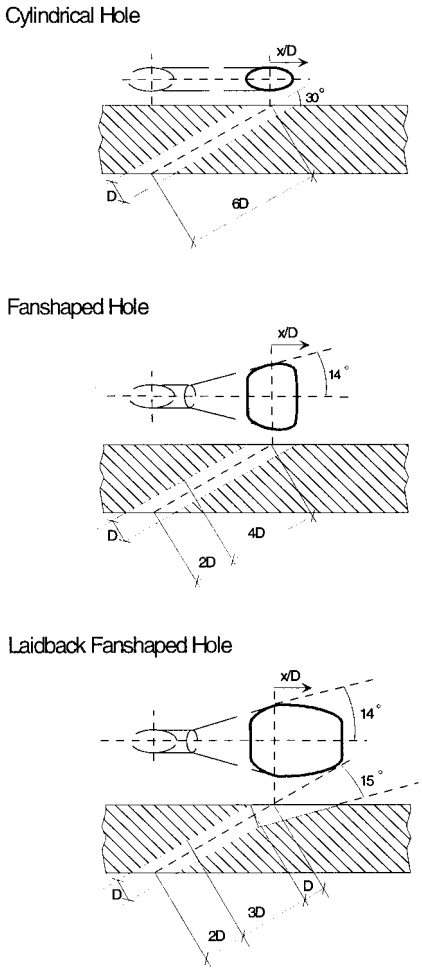

Fig. 2 Hole geometries tested

Estimates of Accuracy

Uncertainties were estimated following the procedure given by Kline and McClintock (1953). The uncertainty in the values of C_D primarily resulted from the uncertainty in measuring the actual flow rate through the film-cooling hole and the uncertainty in determining the ideal flow rate. Due to the fact that the secondary loop was designed as a closed loop, the actual flow rate could be measured for all flow cases directly by measuring the flow rate supplied to the closed loop using a standard orifice, which leads to a maximum uncertainty of 2.5 percent except for very low mass

Nomenclature

b = channel width
C_D = discharge coefficient
D = film-cooling hole diameter
h = channel height
I = jet-to-crossflow momentum flux ratio
L = film-cooling hole length measured along the centerline
Ma = Mach number
$\dot{m}$ = mass flow rate through film-cooling hole
p = static pressure
p_t = total pressure
R = gas constant
Re_D = Reynolds number based on hole diameter
T_t = total temperature
Tu = turbulence intensity
κ = ratio of specific heats

Subscripts

c = internal flow conditions
m = external flow conditions
$noCr$ = no crossflow at hole entry and exit
$extCr$ = with crossflow at hole exit
$intCr$ = with crossflow at hole entry
$h,1$ = hole entry conditions
$h,2$ = hole exit conditions

Table 1 Operating conditions

Internal pressure	p_{tc}	<2 Bars
Internal temperature	T_{tc}	290 K
Pressure ratio	p_{tc}/p_m	1...2.25
Temperature ratio	T_{tc}/T_{tm}	1
Internal Mach number	Ma_c	0...0.6
External Mach number	Ma_m	0...0.6
Internal Reynolds number	Re_{Dc}	$<2.5\cdot10^5$
External Reynolds number	Re_{Dm}	$<1.5\cdot10^5$
Internal turbulence intensity	Tu_c	<1%
External turbulence intensity	Tu_m	<1.5%

flow rates. Provision was made to avoid even tiny leakage in the secondary loop as described by Wittig et al. (1996). The uncertainty in determining the ideal flow rate was calculated to be much less than 2 percent except for very low pressure ratios. Overall, the uncertainty in the values of C_D was found to be less than 2 percent in most of the cases considered, increasing up to 4.5 percent for very low pressure ratios and mass flow rates.

Results and Discussion

Constant Crossflow Mach Number Tests. For the first series of tests the internal ("coolant") as well as the external ("hot gas") Mach number were kept constant while the pressure ratio p_{tc}/p_m was varied from 1 to 2. Figure 3 shows the results for the cylindrical hole.

From a first glance it can be seen that the effect of external Mach number is weak as compared to the internal Mach number and the pressure ratio, which are the factors dominating the behavior of the discharge coefficient for all operating conditions. In the absence of crossflow on either side of the film-cooling hole, there is only a weak dependence of the discharge coefficient on pressure ratio with a slight increase of about 10 percent when the pressure ratio is raised from 1 to 2. This effect does not occur for incompressible flows (Lichtarowicz et al., 1965) and is believed to be due to a pressure ratio effect on the cross sectional area of the vena contracta. It has been reported by others previously (e.g., Jackson, 1963).

For zero internal crossflow, a slight impact of external Mach number on the discharge coefficient was found, which becomes more pronounced for pressure ratios below 1.4, with the highest C_D values at a given pressure ratio associated with the case of no external crossflow and the lowest associated with that of maximum external crossflow.

The effect of external Mach number changes if internal crossflow is present. For an internal crossflow Mach number of $Ma_c = 0.3$, the highest discharge coefficients occur for an external Mach number of $Ma_m = 0.3$. In case of $Ma_c = 0.6$, the highest C_D values were found for the highest external Mach number whereas the lowest discharge coefficients correspond to the case of no external crossflow. The same trends have been observed by Rowbury et al. (1997) who termed this phenomenon "crossover effect." The extent of the crossover effect depends on internal and external crossflow conditions as well as on the orientation of the hole with respect to the crossflows on either side. As already reported by Rowbury et al. (1997), there should be two competing effects responsible for the crossover effect: The first effect is a reduction in static pressure in certain regions of the hole exit due to local acceleration of the mainstream flow, which tends to increase the mass flow through the hole. This acceleration is caused by the exiting coolant and the corresponding blockage of the mainstream path similar to the flow around a cylindrical obstacle. The second effect is the "pinching" of the coolant jet by the external crossflow, which causes the mass flow to decrease. Obviously the crossover effect is favored by the perpendicular orientation of coolant crossflow with respect to the hot gas flow since the data of Gritsch et al. (1998b), taken for the same geometries and operating conditions but parallel orientation of internal and external crossflow, do not exhibit any crossover tendencies.

In Figs. 4 and 5 the results for the shaped holes are presented. These curves exhibit similar trends as compared to the cylindrical hole, but the effect of external Mach number appears to be even

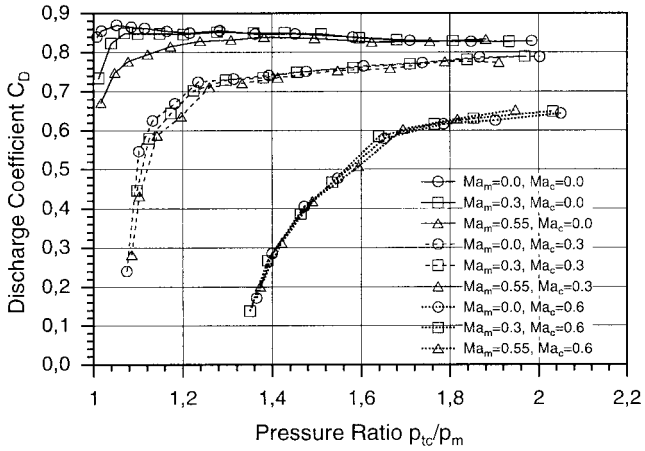

Fig. 4 Fan-shaped hole, discharge coefficient C_D versus pressure ratio p_{tc}/p_m

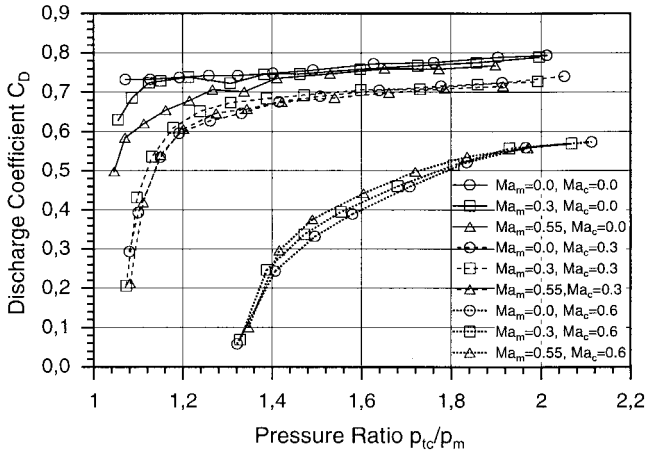

Fig. 3 Cylindrical hole, discharge coefficient C_D versus pressure ratio p_{tc}/p_m

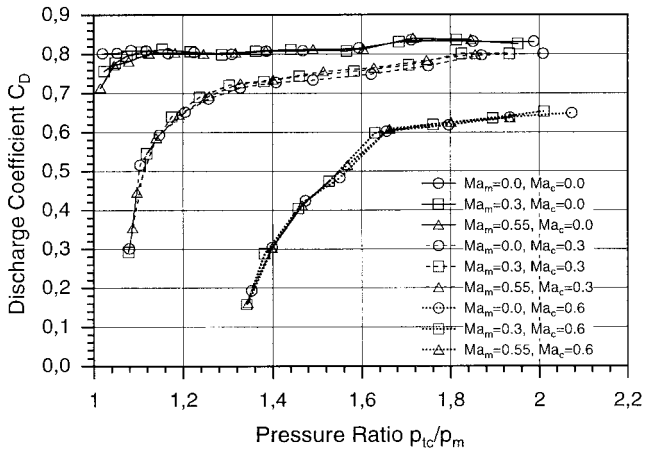

Fig. 5 Laid-back fan-shaped hole, discharge coefficient C_D versus pressure ratio p_{tc}/p_m

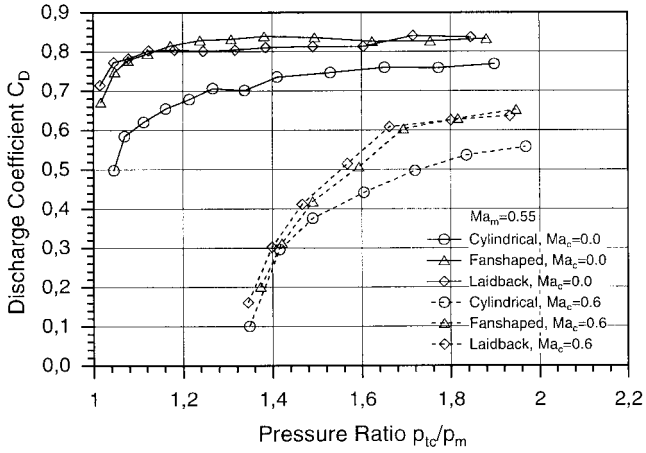

Fig. 6 Discharge coefficient C_D versus pressure ratio p_{tc}/p_m, effect of hole shape

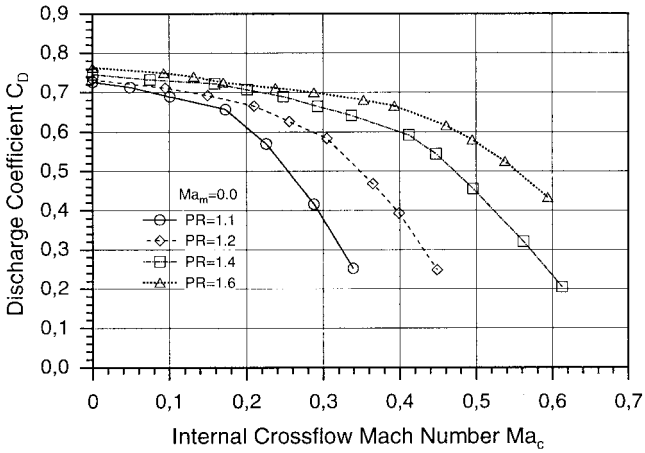

Fig. 7 Cylindrical hole, discharge coefficient C_D versus internal crossflow Mach number Ma_c

further reduced, a feature desirable for the designer. Particularly for the laid-back fan-shaped hole, there is almost no effect of external Mach number discernible. As highlighted before, the crossover phenomenon and the impact of external Mach number in general depends on the blockage of the main stream path. This blockage is less severe for the shaped holes due to decreased exit momentum and smaller exit angles (see, e.g., Hyams and Leylek 2000) and therefore the influence of external Mach number is decreased.

Likewise, in the absence of internal crossflow, the shaped holes show smaller variations with pressure ratio. If no external or internal crossflow is present, the discharge coefficients of the shaped holes are almost unaffected by the pressure ratio, indicating that the flow through the holes is choked even for low pressure ratios. Overall, the values of the discharge coefficients of the shaped holes are significantly increased in comparison to the cylindrical holes.

Figure 6 shows a comparison of the different hole geometries for an external Mach number of 0.55 and internal Mach numbers of 0 and 0.6, respectively. It appears that in terms of discharge coefficients an additional layback has hardly any influence since the C_D values of the shaped holes are always very similar and larger than the discharge coefficients of the cylindrical holes. This is consistent with the findings of Hay and Lampard (1995) and Gritsch et al. (1998b). However, as indicated by Gritsch et al. (1998a) the laid-back fan-shaped hole provides an improved lateral spread of the coolant as compared to the fan-shaped hole and correspondingly yields increased lateral averaged film-cooling effectiveness values, especially at high blowing ratios.

Constant Pressure Ratio Tests. In a second series of tests, the internal Mach number Ma_c was varied between 0 and 0.6 for a given constant pressure ratio without external crossflow applied. The results of these tests are presented in Figs. 7–9.

For a perpendicular orientation of coolant crossflow with respect to the hole axis, an increased coolant crossflow Mach number yields increased losses and therefore lower discharge coefficients. This effect is more pronounced for lower pressure ratios.

From the curves in Figs. 7–9, it can be clearly seen that the effect of internal crossflow Mach number is huge and must be taken into account in any case in order to design a particular film cooling configuration properly. The influence of pressure ratio becomes more important as the internal Mach number is raised. It is interesting to note that the shape of the C_D versus Ma_c curves for the shaped holes looks similar for a given pressure ratio and quite different from the curves of the cylindrical hole. For the cylindrical hole the curvature in C_D versus Ma_c never changes, whereas the corresponding curves of the shaped holes change their curvature twice. This effect is more pronounced for lower pressure ratios. There appears to be a limiting internal crossflow Mach number above which the shaped and the cylindrical holes show a similar characteristic. For low pressure ratios the diffuser section of the shaped holes yields to significant higher discharge coefficients (in comparison with the cylindrical holes) only if also the internal crossflow Mach number is small.

Effect of Coolant Crossflow Orientation. Figure 10 shows the effect of different internal coolant crossflow orientations with

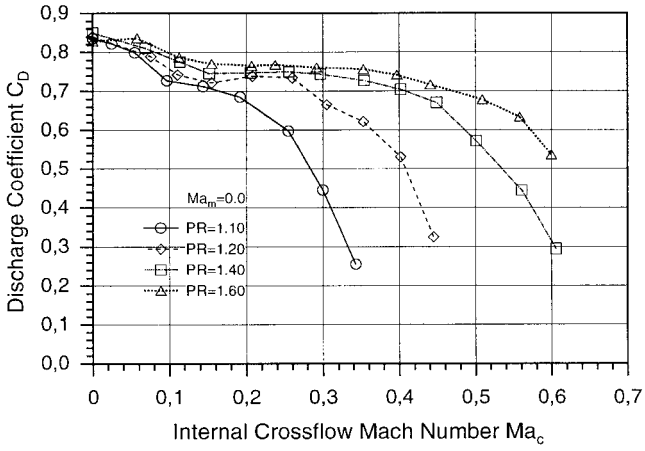

Fig. 8 Fan-shaped hole, discharge coefficient C_D versus internal crossflow Mach number Ma_c

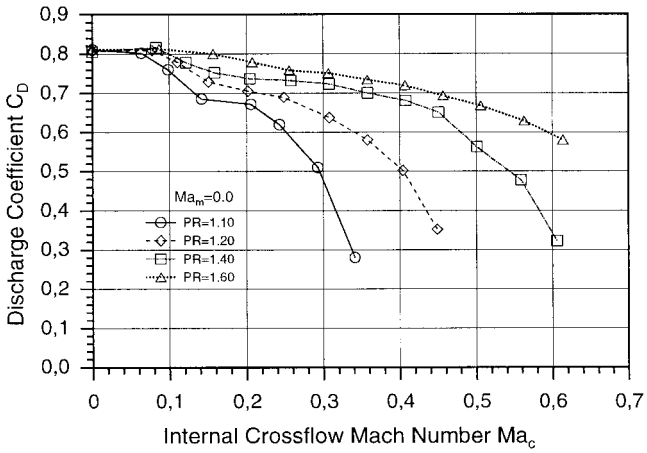

Fig. 9 Laid-back fan-shaped hole, discharge coefficient C_D versus internal crossflow Mach number Ma_c

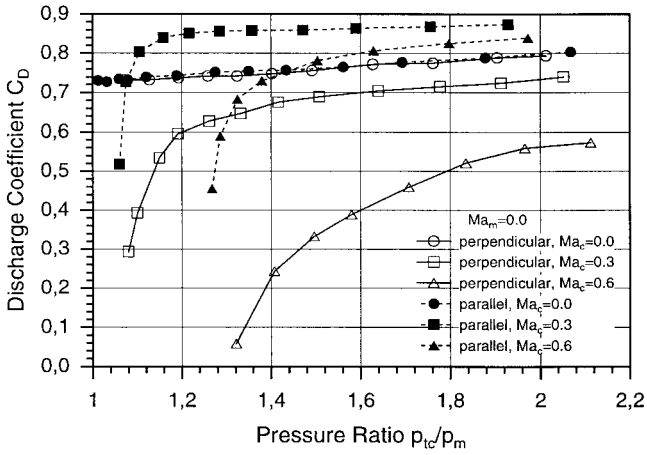

Fig. 10 Cylindrical hole, discharge coefficient C_D versus pressure ratio p_{tc}/p_m, effect of coolant crossflow orientation

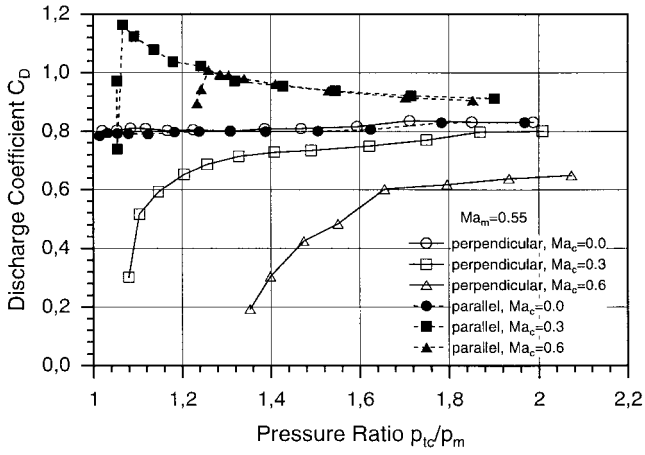

Fig. 11 Laid-back fan-shaped hole, discharge coefficient C_D versus pressure ratio p_{tc}/p_m, effect of coolant crossflow orientation

respect to the external main flow direction for the cylindrical hole without external crossflow. As expected, there is no influence of the coolant channel orientation if no crossflow on either side of the hole is present with the two lines for the same operating conditions but different coolant crossflow orientations collapsing to a single curve, indicating the quality and repeatability of the measurements. For the parallel orientation of the coolant channel and a given pressure ratio, an internal Mach number exists for which maximum discharge coefficients occur, as pointed out by Gritsch et al. (1998b). In case of a perpendicular coolant crossflow orientation, no such optimum internal Mach number exists since an increase of internal Mach number always results in decreased discharge coefficients, consistent with the findings of Hay et al. (1983). This fact can be explained by the existence of a separation region at the entry of the film-cooling hole with size and location strongly depending on internal crossflow conditions (Thole et al., 1997). In the case of parallel coolant crossflow orientation with no internal crossflow, the separation region occurs at the downstream (with respect to the external crossflow) edge of the cooling hole. If the internal Mach number is increased, a velocity component in the direction of the hole axis is present and the size of the aforementioned separation region will decrease. A second separation zone will form at the upstream edge of the hole. For high internal Mach numbers, the separation region will be found at the upstream edge only, its size increasing with internal Mach number. Somewhere between those two extremes, zero and high internal crossflow Mach number, there is a medium Mach number for which the overall size of the separation regions is at a minimum, resulting in minimum losses and maximum discharge coefficients.

In case of a perpendicular orientation of coolant crossflow and hole axis, no velocity component of the internal crossflow in the direction of the hole axis exists and the coolant has to turn 90 deg to enter the hole. A separation zone at the upstream edge of the hole is therefore always present and increases in size with the internal Mach number, resulting in increased pressure losses at the hole entry and therefore decreased discharge coefficients (compare Figs. 7–9).

In Fig. 11 the effect of coolant crossflow orientation on the discharge coefficient of laid-back fan-shaped holes is presented. As for the cylindrical hole, no external crossflow was present for this series of tests. In the absence of internal and external crossflow, the coolant channel orientation again does not play a role and the overall tendencies are similar to the corresponding curves of the cylindrical holes. Although for the parallel coolant crossflow orientation there is an internal Mach number for a given pressure ratio at which the discharge coefficient is at a maximum, no such maximum exists for perpendicular coolant crossflow orientation and an increase in internal Mach number will always lead to reduced discharge coefficients, consistent to the results of the numerical studies of Kohli and Thole (1997, 1998). As compared to the cylindrical hole, however, a much larger dependence on coolant crossflow orientation was found for the laid-back fan-shaped hole. Although not shown in this paper, the corresponding plots of the fan-shaped hole are quite similar to those of the laidback fanshaped holes as could be expected from the aforementioned results.

Prediction and Validation

For the flow through a hole with crossflow on both sides, pressure losses occur at the hole entry, inside the hole, and at the hole exit. Based on the suggestion given by Sasaki et al. (1976) and Tillman and Jen (1984) that these pressure losses could be taken into account independently, Gritsch et al. (1998c) derived an empirical approach for predicting discharge coefficients of film cooling holes with internal crossflow parallel to the external crossflow. This method has been adopted in the present work and extended for use with holes having an expanded exit portion and internal crossflow perpendicular to the main flow. By doing so, it was intended to systematize the different loss mechanisms and to evaluate the potential of correlations, which offer the advantage of an easy implementation in existing design tools and little computational effort as compared to CFD.

Without crossflow on either side of the hole, the discharge coefficient depends only on the pressure ratio (see, e.g., Fig. 3) and a correlation $C_{DnoCR} = f(p_{tc}/p_m)$ seems to be reasonable. This function yields a baseline discharge coefficient for which additional losses due to crossflows must be taken into account.

It was shown that for perpendicular coolant crossflow orientation, the internal crossflow increases the losses at the hole entry side, which strongly depend on both the internal Mach number and pressure ratio. To separate the different loss mechanisms, the data sets taken without external crossflow were plotted versus the jet-to-internal crossflow momentum flux ratio as given by

$$I_{jet/intCr} = \frac{(\kappa \cdot p \cdot \mathrm{Ma}^2)_{h,1}}{(\kappa \cdot p \cdot \mathrm{Ma}^2)_C} \tag{2}$$

with

$$\mathrm{Ma}_{h,1} = \frac{\dot{m}}{\frac{\pi}{4} D^2 \cdot p_{h,1}} \sqrt{\frac{R \cdot T_{h,1}}{\kappa}} \tag{3}$$

For the $\mathrm{Ma}_c = 0.0$ case, $I_{jet/intCr}$ is not defined. Therefore a fixed value of

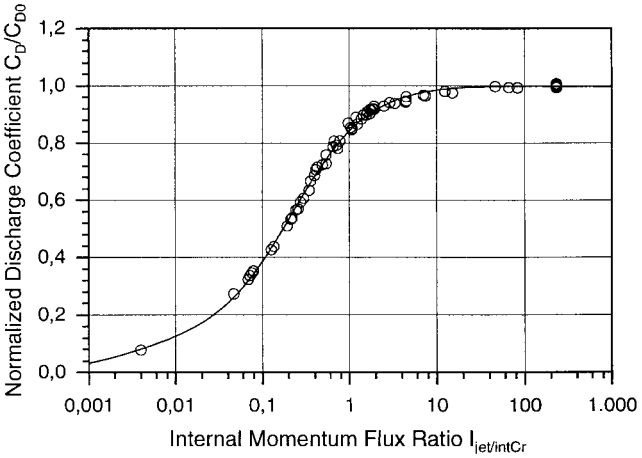

Fig. 12 Cylindrical hole, normalized discharge coefficient versus jet-to-internal crossflow momentum flux ratio

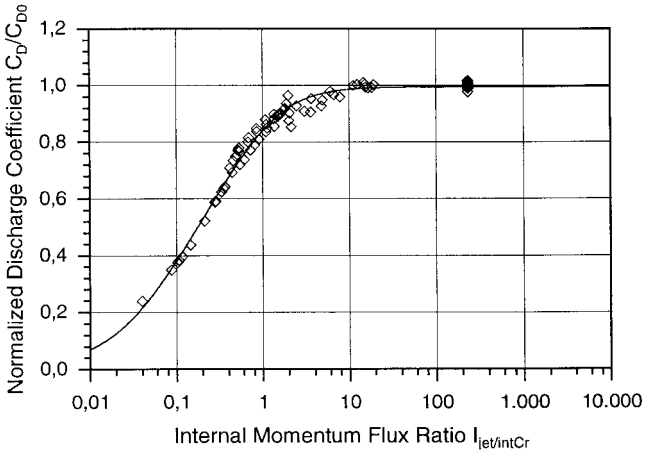

Fig. 14 Laid-back fan-shaped hole, normalized discharge coefficient versus jet-to-internal crossflow momentum flux ratio

$$I_{jet/intCr} = \left[\frac{(b \cdot h)_C}{(\pi/4)D^2}\right]^2 \quad (4)$$

is used to represent the momentum flux ratio for this case, which is covered by the correlation as well.

It was found that there is a common trend with some scatter, which obviously results from the baseline pressure losses inside the hole still included in the measured discharge coefficients (see Gritsch et al., 1998c). Therefore, in order to eliminate the contributions of the baseline pressure losses inside the hole, the discharge coefficient was normalized by the baseline discharge coefficient at the same pressure ratio and plotted versus the internal momentum flux ratio, as shown in Figs. 12–14. It is discernible that the normalized discharge coefficients collapse to a single curve. Correlating these data by a least-squares curve fit gives a function $C_{DintCr}/C_{DnoCr} = f(I_{jet/intCr})$ that represents the additional losses due to the presence of an internal crossflow, as also shown in Figs. 12–14. As can be seen from these figures, the discharge coefficients increase monotonically with internal momentum flux ratio $I_{jet/intCr}$, which has an impact over a broad range. Only for momentum flux ratios larger than 100 are the discharge coefficients unaffected by the entry side coolant crossflow, regardless of the geometry considered.

The same procedure could also be applied to evaluate the additional losses due to external crossflow (see Gritsch et al., 1998c). As shown in the foregoing sections, however, the effect of external Mach number is very weak (see Figs. 3–5) in the perpendicular coolant crossflow orientation case and may therefore be neglected here.

After considering the impacts of baseline hole flow and hole entry crossflow separately, the discharge coefficient of any flow situation can be predicted using the following calculation scheme:

$$C_D\left(\frac{p_{tc}}{p_m};\, I_{jet/intCr}\right) = C_{DnoCr}\left(\frac{p_{tc}}{p_m}\right) * \frac{C_{DintCr}}{C_{DnoCr}}\,(I_{jet/intCr}) \quad (5)$$

Due to the need for a mass flow rate to determine the momentum flux ratio terms, an iterative calculation of the discharge coefficient is necessary with the baseline C_D value serving as a good starting point. Total pressures, total temperatures, and crossflow Mach numbers at hole entry and exit side have to be entered to describe the flow configuration.

For the purpose of validation, the predicted discharge coefficients were compared to data sets with crossflows on both sides of the film-cooling holes which were not used to derive the correlations. The good agreement between calculated and measured data, see Figs. 15–17, clearly demonstrates the capabilities of the method proposed.

Conclusions

A study was performed to acquire discharge coefficients of cylindrical holes and holes with expanded exits with special atten-

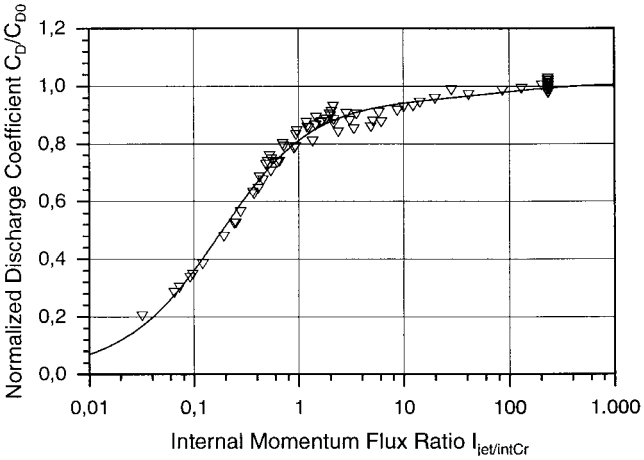

Fig. 13 Fan-shaped hole, normalized discharge coefficient versus jet-to-internal crossflow momentum flux ratio

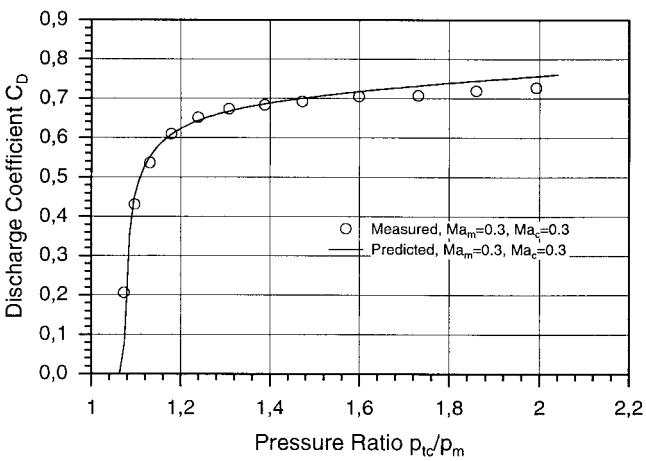

Fig. 15 Cylindrical hole, comparison of measured and predicted discharge coefficients

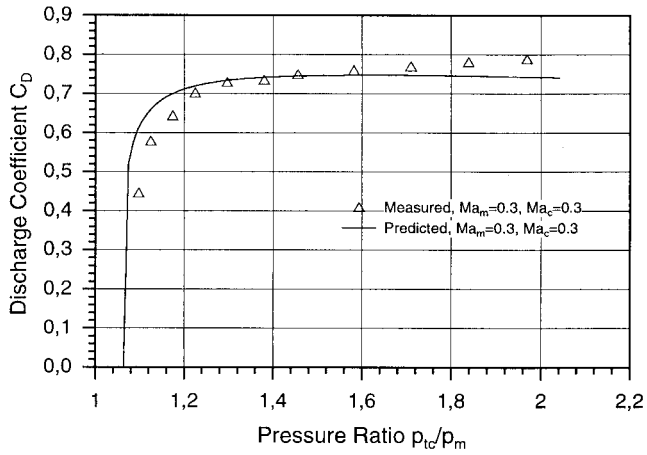

Fig. 16 Fan-shaped hole, comparison of measured and predicted discharge coefficients

tion paid to coolant crossflow orientation. The hole inlet crossflow Mach numbers, hole exit crossflow Mach numbers, and pressure ratios across the hole have been varied over a wide range of engine-like conditions. Furthermore, an empirical method for predicting discharge coefficients has been applied and extended successfully. The following conclusions can be drawn:

- Discharge coefficients are not only strongly dependent on the flow conditions applied (i.e., internal Mach numbers, pressure ratio, external Mach numbers), but also on the coolant crossflow orientation.
- With the same crossflow conditions applied, the discharge coefficients of the shaped holes are in general higher than those of the cylindrical holes.
- In terms of discharge coefficients, the performance of fan-shaped holes is almost unaffected by an additional lay-back.
- For perpendicular orientation of internal (coolant) and external (hot gas) crossflow, the discharge coefficient is decreased with increasing internal Mach number.
- For perpendicular orientation of internal and external crossflow, the discharge coefficients of shaped holes are almost independent of external Mach number, a feature desirable for the designer. For cylindrical holes the effect of external Mach number is weak and additionally depends on pressure ratio and the internal Mach number applied.

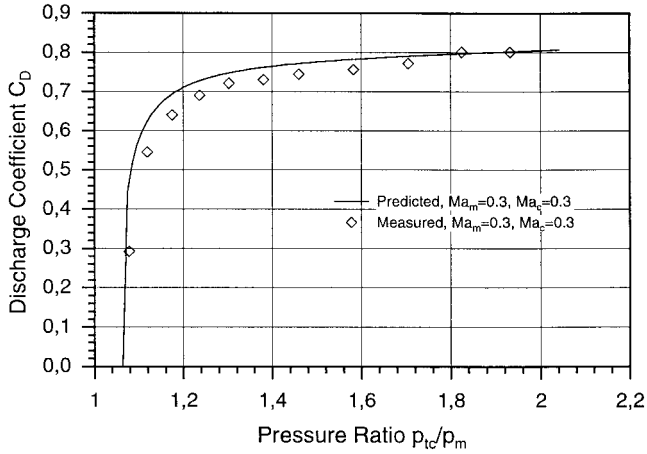

Fig. 17 Laid-back fan-shaped hole, comparison of measured and predicted discharge coefficients

Acknowledgments

This study was partly funded by the European Union through a grant by the Brite Euram program "Turbine Aero-Thermal External Flows" under Contract No. BRPR-CT97-0519. Mr. Sharp would also like to express his appreciation to Prof. Wittig and the Universität Karlsruhe for financial support during the research period.

References

Burd, S. W., and Simon, T. W., 1999, "Measurements of Discharge Coefficients in Film-Cooling," ASME JOURNAL OF TURBOMACHINERY, Vol. 121, pp. 243–248.

Gritsch, M., Schulz, A., and Wittig, S., 1998a, "Adiabatic Wall Effectiveness Measurements of Film-Cooling Holes With Expanded Exits," ASME JOURNAL OF TURBOMACHINERY, Vol. 120, pp. 568–574.

Gritsch, M., Schulz, A., and Wittig, S., 1998b, "Discharge Coefficient Measurements of Film-Cooling Holes With Expanded Exits," ASME JOURNAL OF TURBOMACHINERY, Vol. 120, pp. 560–567.

Gritsch, M., Schulz, A., and Wittig, S., 1998c, "Method of Correlating Discharge Coefficients of Film-Cooling Holes," *AIAA Journal*, Vol. 36, pp. 976–980.

Gritsch, M., Schulz, A., and Wittig, S., 1998d, "Heat Transfer Coefficient Measurements of Film-Cooling Holes With Expanded Exits," ASME Paper No. 98-GT-28.

Hay, N., Henshall, S. E., and Manning, A., 1994a, "Discharge Coefficients of Holes Angled to the Flow Direction," ASME JOURNAL OF TURBOMACHINERY, Vol. 116, pp. 92–96.

Hay, N., Lampard, D., and Benmansour, S., 1983, "Effect of Crossflows on the Discharge Coefficient of Film Cooling Holes," ASME *Journal of Engineering for Power*, Vol. 105, pp. 243–248.

Hay, N., and Lampard, D., 1995, "The Discharge Coefficient of Flared Film Cooling Holes," ASME Paper No. 95-GT-15.

Hay, N., and Lampard, D., 1998, "Discharge Coefficient of Turbine Cooling Holes: A Review," ASME JOURNAL OF TURBOMACHINERY, Vol. 120, pp. 314–319.

Hay, N., Lampard, D., and Khaldi, A., 1994b, "The Coefficient of Discharge of 30° Inclined Film Cooling Holes With Rounded Entries or Exits," ASME Paper No. 94-GT-180.

Hay, N., and Spencer, A., 1992, "Discharge Coefficients of Cooling Holes With Radiused and Chamfered Inlets," ASME JOURNAL OF TURBOMACHINERY, Vol. 114, pp. 701–706.

Hyams, D. G., and Leylek, J. H., 2000, "A Detailed Analysis of Film Cooling Physics: Part III—Streamwise Injection With Shaped Holes," ASME JOURNAL OF TURBOMACHINERY, Vol. 122, this issue, pp. 122–132.

Jackson, R. A., 1963, "The Compressible Discharge of Air Through Small Thick Plate Orifices," *Applied Scientific Research*, Vol. A13, pp. 241–248.

Kline, S., and McClintock, F., 1953, "Describing Uncertainties in Single-Sample Experiments," *Mechanical Engineering*, Vol. 75, pp. 3–8.

Kohli, A., and Thole, K. A., 1997, "A CFD Investigation on the Effect of Entrance Flow Conditions in Discrete Film-Cooling Holes," *Proc. 32nd ASME National Heat Transfer Conference*, Vol. 12, pp. 223–232.

Kohli, A., and Thole, K. A., 1998, "Entrance Effects on Diffused Film-Cooling Holes," ASME Paper No. 98-GT-402.

Lichtarowicz, A., Duggins, R. K., and Markland, E., 1965, "Discharge Coefficients for Incompressible Non-cavitating Flow Through Long Orifices," *Journal Mechanical Engineering Science*, Vol. 7, pp. 210–219.

Rowbury, D. A., Oldfield, M. L. G., and Lock, G. D., 1997, "Engine Representative Discharge Coefficients Measured in an Annular Nozzle Guide Vane Cascade," ASME Paper No. 97-GT-99.

Sasaki, M., Takahara, K., Sakata, K., and Kumagai, T., 1976, "Study on Film Cooling of Turbine Blades," *Bulletin of the JSME*, Vol. 19, pp. 1344–1352.

Thole, K. A., Gritsch, M., Schulz, A., and Wittig, S., 1997, "Effect of a Crossflow at the Entrance to a Film-Cooling Hole," ASME *Journal of Fluids Engineering*, Vol. 119, pp. 533–541.

Thole, K. A., Gritsch, M., Schulz, A., and Wittig, S., 1998, "Flowfield Measurements for Film-Cooling Holes with Expanded Exits," ASME JOURNAL OF TURBOMACHINERY, Vol. 120, pp. 327–336.

Tillman, E. S., and Jen, H. F., 1984, "Cooling Airflow Studies at the Leading Edge of a Film-Cooled Airfoil," ASME *Journal of Engineering for Gas Turbines and Power*, Vol. 106, pp. 214–221.

Wittig, S., Schulz, A., Gritsch, M., and Thole, K. A., 1996, "Transonic Film-Cooling Investigations: Effects of Hole Shapes and Orientations," ASME Paper No. 96-GT-222.

Effects of Orientation Angles on Film Cooling Over a Flat Plate: Boundary Layer Temperature Distributions and Adiabatic Film Cooling Effectiveness

In Sung Jung

Joon Sik Lee

Turbo and Power Machinery Research Center,
Department of Mechanical Engineering,
Seoul National University,
Seoul 151-742, Korea

Presented are experimental results describing the effects of orientation angle of film cooling holes on boundary layer temperature distributions and film cooling effectiveness. Film flow data were obtained from a row of five film cooling holes on a flat test plate. The inclination angle of the hole was fixed at 35 deg and four orientation angles of 0, 30, 60, and 90 deg were investigated. The velocity ratios surveyed were 0.5, 1.0, and 2.0. The boundary layer temperature distributions were measured at three downstream locations using 1 μm platinum wire. Detailed adiabatic film cooling effectiveness distributions were measured using thermochromic liquid crystal. Results show that the increased lateral momentum in the case of large orientation angle injection strongly affects boundary layer temperature distributions. Temperature distribution characteristics are, in general, explained in the context of the interactions between injectant and free-stream fluid and between injectants issuing from adjacent holes. The adiabatic film cooling effectiveness distributions are discussed in connection with the boundary layer temperature distributions. Spanwise-averaged effectiveness distributions and space-averaged effectiveness distributions are also presented with respect to the velocity ratios and the orientation angles.

Introduction

Film cooling is commonly used to prevent turbine blades from thermal failure caused by operation in a high-temperature environment. The injected coolant from film holes forms a thin thermal insulation layer to protect the blade surface from the hot gas flow. The film cooling efficiency is dependent mainly upon blade geometry, coolant injection geometry, free-stream flow characteristics, coolant to free-stream flow velocity ratio, and coolant to approaching gas temperature ratio (Art and Bourguignon, 1990).

While there is a large body of existing literature on film cooling, most of the work focuses primarily on simple angle configuration. Compound angle injection, however, is more often used for gas turbine blade cooling. A recent study (Ligrani et al., 1992) has also suggested that compound angle injection provides increased adiabatic effectiveness and greater lateral spreading of the coolant than simple angle injection.

The compound angle injection hole has two injection angles, as shown in Fig. 1(*c*). The inclination angle (α) is defined as the angle between the injection vector and its projection on the x–z plane, whereas the orientation angle (β) is defined as the angle between the streamwise direction and the projection of the injection vector on the x–z plane. In the compound angle orientation system, the coolant is injected with a spanwise momentum, which provides more uniform film coverage.

Goldstein et al. (1970) described the effectiveness characteristics with lateral injection. The effectivenesses following single hole of the inclination angle of 15 and 35 deg were investigated. They reported that the effect of lateral injection is to widen the temperature field and decrease the peak effectiveness for the blowing ratio of 0.5. For the higher blowing ratios, however, the lateral injection increases both the width of the temperature field and the peak film cooling effectiveness. It is only recently that the compound angle injection has received attention again. Mehendale and Han (1992) studied the influence of high mainstream turbulence on leading edge film cooling effectiveness and heat transfer coefficient. The orientation angle was 90 deg and the results indicated that the film effectiveness decreases with increasing blowing ratio, but the opposite was true for the heat transfer coefficient.

Honami et al. (1994) described the behavior of the injected jet over a flat surface with 90 deg orientation angle holes. They measured streamwise mean velocity, boundary layer temperature fields, and effectiveness distributions using liquid crystal. Their results show that 90 deg orientation angle injection forms an asymmetric structure with a large-scale vortex motion on one side caused by the interaction with the mainstream. In addition, they concluded that the asymmetry is promoted with increased mass flux ratio, resulting in low film cooling effectiveness.

Schmidt et al. (1996) measured the film cooling effectiveness using a single row of inclined holes, which injected high-density, cryogenically cooled air. They reported that 60 deg orientation angle injection at a high momentum flux ratio results in higher effectiveness values than streamwise-directed holes. The forward expansion hole with compound angle orientation showed significantly improved effectiveness.

Ekkad et al. (1997) provided effectiveness results for two different density ratios. The adopted orientation angles were 0, 45, and 90 deg. Using the transient liquid crystal technique, they reported that compound angle injection produces higher film effectiveness than simple angle injection for both density ratios. They concluded that the highest effectiveness was obtained at a mass flux ratio of 1.0 for compound angle injection.

Lee et al. (1997) visualized near-hole surface flow patterns, and measured three-dimensional velocity field with orientation angle

Contributed by the International Gas Turbine Institute and presented at the 44th International Gas Turbine and Aeroengine Congress and Exhibition, Indianapolis, Indiana, June 7–10, 1999. Manuscript received by the International Gas Turbine Institute February 1999. Paper No. 99-GT-143. Review Chair: D. C. Wisler.

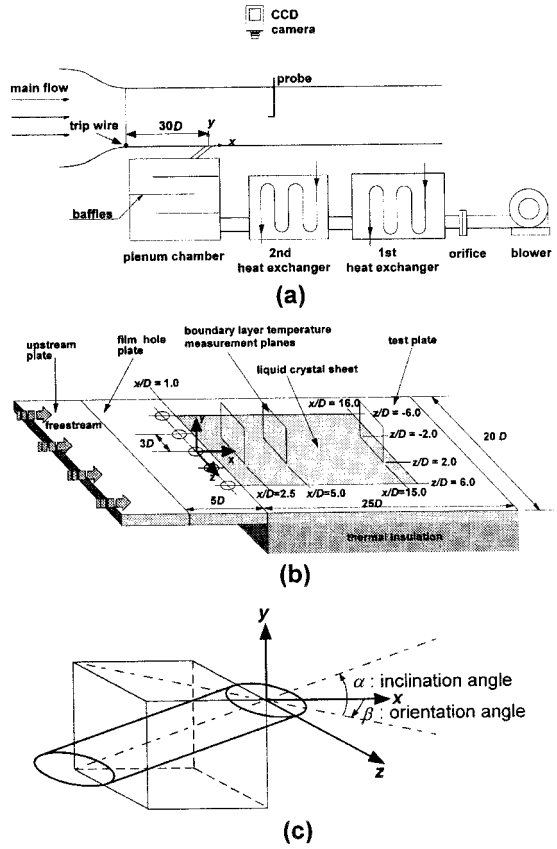

Fig. 1 Experimental setup and film hole configuration

variations ranging from 0 to 90 deg. They proposed a near-wall flow model based on the surface flow visualizations. It has also been found from the flow measurements that with a small orientation angle of 15 deg, a pair of counterrotating vortices joins to form a single strong vortex, and the aerodynamic loss field is related closely to the secondary flow. A recent paper by Kaszeta et al. (1998) presents detailed mean velocity fields, turbulence intensity fields, and Reynolds stress distributions with lateral injection (β = 90 deg) in comparison with simple angle injection. They showed that the lateral injection results in a wider spreading of the injection jet flow than the streamwise injection counterpart.

These studies, in general, show that the compound angle injection configuration provides significantly improved effectiveness compared to simple angle configuration. The understanding and knowledge of orientation angle effects on film cooling are, however, still fragmentary. In this study, film cooling from holes with orientation angles of 0, 30, 60, and 90 deg are investigated at a fixed inclination angle of 35 deg. The velocity ratios are 0.5, 1.0, and 2.0. Adiabatic film cooling effectiveness distributions are measured using thermochromic liquid crystal. The liquid crystal technique is used due to its high spatial resolution, which gives detailed effectiveness distributions downstream of the injection holes. The boundary layer temperature distributions are also measured and discussed in relation with the effectiveness distributions.

Experimental Apparatus and Procedures

A schematic of the wind tunnel and the injectant supply system is shown in Fig. 1(*a*). The wind tunnel is an open-circuit and subsonic one, with a 6.25 to 1 contraction ratio nozzle and an exit cross section of 0.4 × 0.28 m. The nozzle leads to the test section, which is a rectangular duct 3.0 m long. Holes and a slot are located in the upper plate of the test section for probing. At a free-stream velocity of 10 m/s, flow at the test section inlet shows excellent spatial uniformity with spanwise velocity variations less than 0.3 percent, and a turbulence level less than 0.2 percent. A boundary layer trip wire of 1.8 mm diameter is located on the test plate just downstream of the nozzle exit. The air, used as the injectant, first flows through an orifice followed by two heat exchangers that control the injectant air temperature. The air is then ducted to a plenum chamber and discharged through the injection holes.

Experiments were conducted at the fixed free-stream mean velocity of 10 m/s. The injection hole diameter (D) is 20 mm and its length is 4 D. The Reynolds number ($\mathrm{Re}_X = U_\infty X/\nu$) based on the distance between the trip wire and the hole center is 383,000. The boundary layer thickness (based on 0.99 U_∞) at the hole center location is 0.91 D, while the displacement thickness is 0.14 D and the momentum thickness is 0.10 D. The ratio of the displacement thickness to the momentum thickness, i.e., the shape factor of the boundary layer, is 1.4, which is the typical value of a fully developed turbulent boundary layer. The velocity ratio (VR) is the ratio of the injectant mean velocity to free-stream mean velocity. The velocity ratio values are 0.5, 1.0, and 2.0. The corresponding injectant Reynolds numbers ($\mathrm{Re}_D = U_c D/\nu$) are 6400, 12,700, and 25,400, respectively. In the measurements of the boundary layer temperature distribution and the adiabatic film cooling effectiveness, the free-stream temperature is fixed at 20°C, while the injectant is heated to 40°C. The density ratio of injectant to free-stream due to the heating is 0.93. Thus, the momentum ratio values are 0.23, 0.93, and 3.72 for velocity ratios of 0.5, 1.0, and 2.0, respectively.

The film hole plates (see Fig. 1(*b*)) are prepared for each orientation angle of 0, 30, 60, and 90 deg. The direction of the orientation angle is in the $+z$ direction as described in Fig. 1(*c*). In each film hole plate, a row of five holes is located 30 D downstream of the trip wire. The hole spacing between the hole centers is 3 D. As described in Fig. 1(*b*), the bottom plate of the duct consists of an upstream plate, a film hole plate, and a test plate. The test plate starts at x/D = 1.0. To prevent the adiabatic wall temperature elevation near the downstream edge of the holes, the injection holes were machined in the injection plate, not in the measurement plate. Polystyrene was foamed in the triangular gap

Nomenclature

D = film hole diameter
I = injectant momentum to free-stream momentum ratio = $\rho_c U_c^2/\rho_\infty U_\infty^2$
Re_D = injectant Reynolds number = $U_c D/\nu$
Re_X = free-stream Reynolds number = $U_\infty X/\nu$
T = temperature
U = velocity
X = distance from leading edge of the test plate to film hole center
VR = injectant velocity to free-stream velocity ratio = U_c/U_∞
x, y, z = streamwise, normal, and spanwise coordinates
α = inclination angle
β = orientation angle
η = local adiabatic film cooling effectiveness
Θ = boundary layer dimensionless temperature = $(T - T_\infty)/(T_c - T_\infty)$
ν = kinematic viscosity

Subscripts and Superscripts

$\bar{}$ = spanwise-averaged
$\bar{\bar{}}$ = space-averaged
aw = adiabatic
c = plenum chamber (or coolant)
s = simple angle injection
w = wall
∞ = free-stream

between the injection plate and the measurement plate. The foamed polystyrene in the gap works as a thermal barrier that minimizes the conduction from the injection holes to the measurement plate.

To measure the temperature distribution on the entire surface downstream of the injection holes, a thermochromic liquid crystal (TLC) sheet is used. The TLC sheet covers the test plate from $x/D = 1.0$ to $x/D = 16.0$, and from $z/D = -6.0$ to $z/D = 6.0$. The TLC sheet consists of 110-μm-thick polyester film, TLC coating, black paint, and adhesive layer. The total thickness of the sheet is 240 μm. A 12.7-mm-thick polycarbonate plate is attached just beneath the TLC sheet. Formed polystyrene of 50 mm in thickness is used for insulation. A CCD camera is used to capture TLC color images, which is aligned perpendicular to the TLC sheet 1.2 m away. Two 150 W halogen lamps are used to illuminate the TLC sheet.

There are various TLC techniques used for temperature measurements. Among many techniques, the steady-state, hue-capturing method is adopted in this study. The liquid crystal used to measure effectiveness distributions has a color changing temperature range from 20°C to 30°C. Since the bandwidth of the TLC sheet is wide, the sheet can map the entire isothermal pattern of a surface from a single image. The robust TLC color-temperature response calibration, however, is necessary for high-accuracy measurements. It is known that the perceived color of a TLC depends on the lighting/viewing arrangement, the spectrum of the primary illuminant and background light, and the optical properties of the measurement path as well as temperature (Farina et al., 1994). When temperature is measured with the TLC, extra care is taken to fix all the conditions identical with the calibration to avoid the color variation problem.

The TLC calibration has been conducted using an apparatus consisting of a 600 mm $\times$ 50 mm $\times$ 20 mm copper bar equipped with 10 thermocouples, a hot water chamber and a cool water chamber at the opposite ends of the copper bar, and the thermal insulation blocks. T-type thermocouples calibrated with a precision platinum resistance thermometer are embedded into the surface of the copper bar. This arrangement allows an entire TLC hue–temperature calibration curve to be computed from a single image. The hue–temperature calibration is fitted to a sixth-order polynomial. The calibration uncertainty is estimated to be 0.17°C and the standard deviation is 0.083°C with a confidence level of 95 percent. As the temperature reading is going on, TLC color is captured continuously and averaged to produce a single color image. The color information, which is calculated from the image at each axial location, is related to temperature using the curve fit coefficient of the temperature distribution polynomial.

The free-stream and the injectant temperatures are measured with T-type thermocouples that are calibrated in a constant temperature bath with a precision platinum resistance thermometer. The traverse system consisted of x–y–z directional linear traverse systems. The probe, which is attached to the linear guide, is traversed by rotation of the screw driven by the stepping motor. The resolutions of the traverse system are 20 μm in the x and z directions and 10 μm in the y direction.

The boundary layer temperature distribution can be utilized to draw information on injectant behavior and has a close relation with effectiveness distribution at the wall. A 1-μm-dia cold wire probe driven by a constant current anemometer is used to measure the temperature distributions. The calibrations of the cold wire system are performed using a platinum resistance thermometer. The temperature readings are time-averaged. The boundary layer temperature distribution is described in terms of dimensionless temperature, which is defined as

$$\Theta = \frac{T - T_\infty}{T_c - T_\infty} \tag{1}$$

The measurement of boundary layer temperature distribution is taken at the three y–z planes at $x/D = 2.5$, 5.0, and 10.0, with $-2.0 \le z/D \le 2.0$ as shown in Fig. 1(b). In the y and z directions, temperatures are measured every 0.2 D.

The adiabatic film cooling effectiveness is defined as

$$\eta = \frac{T_{aw} - T_\infty}{T_c - T_\infty} \tag{2}$$

where T_{aw} denotes the adiabatic wall temperature measured using the liquid crystal.

The uncertainty of the adiabatic wall temperature can be caused by the following contributors: inaccurate calibration of the liquid crystal sheet, reading inaccuracy of the hue value, aerodynamic heating, and conduction and radiation losses. The uncertainty analysis is evaluated on 20 to 1 odds (95 percent confidence level). All the uncertainty values are evaluated from the method of single-sample experiments proposed by Kline and McClintock (1953). The uncertainty of the dimensionless boundary layer temperature is 6.4 percent at the typical Θ value of 0.25, and that of the adiabatic film cooling effectiveness is 6.8 percent at a typical η value of 0.2. The uncertainty value of the dimensionless boundary layer temperature is getting larger as the difference between the free-stream and the boundary layer temperatures becomes smaller. For example, the uncertainty value is 4.4 percent at $\Theta = 0.5$, but it increases up to 28.8 percent at $\Theta = 0.05$. The same is true for the uncertainty value of the adiabatic film cooling effectiveness that the uncertainty value increases as the difference between the free-stream and the adiabatic wall temperatures decreases. The uncertainty value is 2.5 percent at $\eta = 0.5$ but 29.5 percent at $\eta = 0.05$.

Results and Discussion

Boundary Layer Temperature Distribution. In the boundary layer temperature measurement, the injectant is heated, while all other components in the wind tunnel test section are maintained at the free-stream temperature. Higher magnitudes of the dimensionless temperature thus indicate greater concentration of injectant, and clear indications of the protection provided by the injectant.

Figure 2 shows dimensionless boundary layer temperature distributions at $VR = 0.5$ ($I = 0.23$). Because of the relatively small vertical component of injectant momentum, the injectant is located very close to the wall. Due to the spanwise component of injectant momentum in the compound angle injection, the injectant trajectory is shifted in the positive z direction. As expected, it is clearly seen that the shifting is getting larger with increasing orientation angle. Note that in all cases, the injectant is issued at $z/D = 0$.

As the orientation angle increases, the boundary layer temperature distribution shows some distinctively different features from that of simple angle injection. First, the symmetric temperature distribution in the case of simple angle injection changes to an asymmetric shape. The asymmetry is amplified as the orientation angle increases. According to Lee et al. (1997) and Kaszeta et al. (1998), the asymmetry in temperature distribution is due to the transformation of a pair of counterrotating vortices in the case of simple angle injection to a single strong vortex in compound angle injection. The shape of the isotherms for compound angle injection implies that the downwash region of the single vortex is located at the negative z side of the injectant, while the upwash region of the single vortex is located at the positive z side of the injectant.

Another important change incurred by compound angle injection is that regions of higher temperature or higher injectant concentration between the holes (near the region of $z/D = \pm 1.5$) are observed. As β increases, the injectant spreads in the spanwise direction so that the regions between holes are covered with the injectant, while such regions are not protected in simple angle injection. The transport of the injectant fluid in the positive z direction caused by the secondary flow developing near the wall (Kaszeta et al., 1998) also increases the protection. Another feature of compound angle injection is that the temperature gradient in the

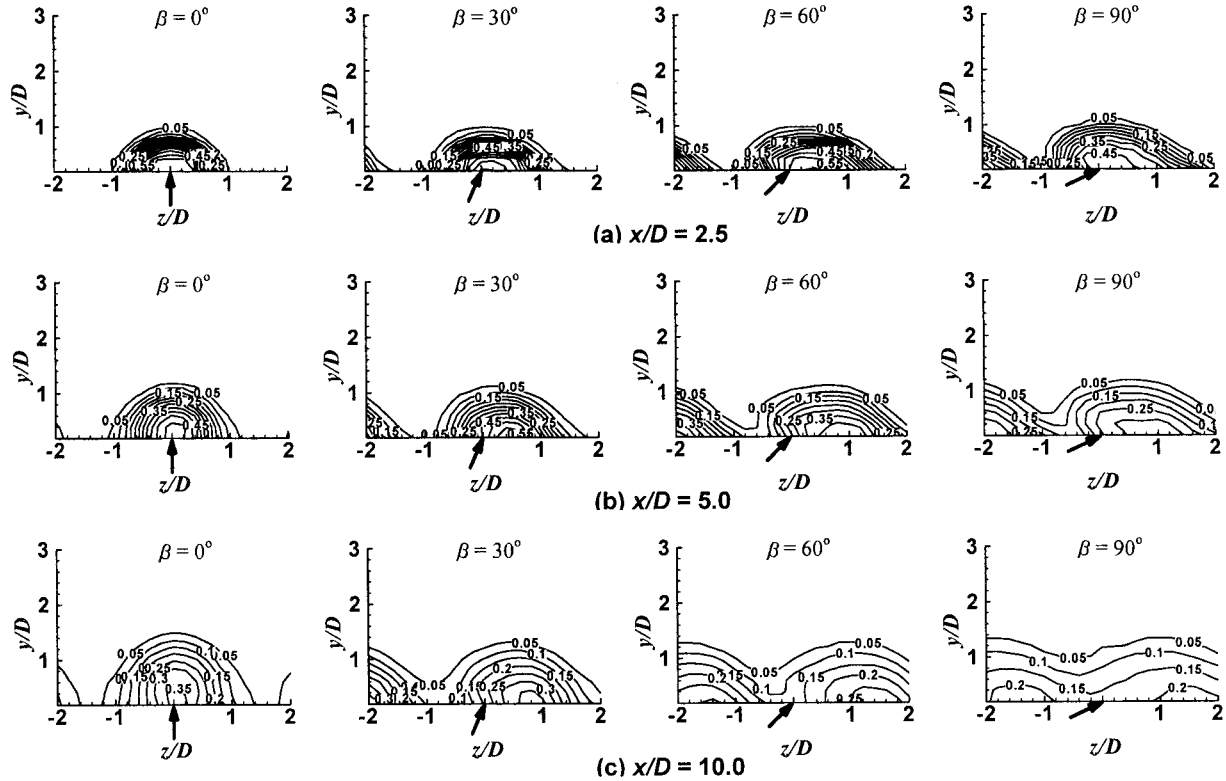

Fig. 2 Boundary layer temperature (Θ) distributions for *VR* = 0.5

vertical direction decreases with the orientation angle at the same x/D locations. This is because the strong secondary flow with large orientation angle entrains free-stream fluid, which intensifies the mixing between the injectant and free-stream fluid. The mixing caused by entrainment is evident from the decrease in the maximum temperature with large orientation angle.

Figure 3 shows the boundary layer temperature distributions at a higher velocity ratio of $VR = 1.0$ ($I = 0.93$). Since the vertical

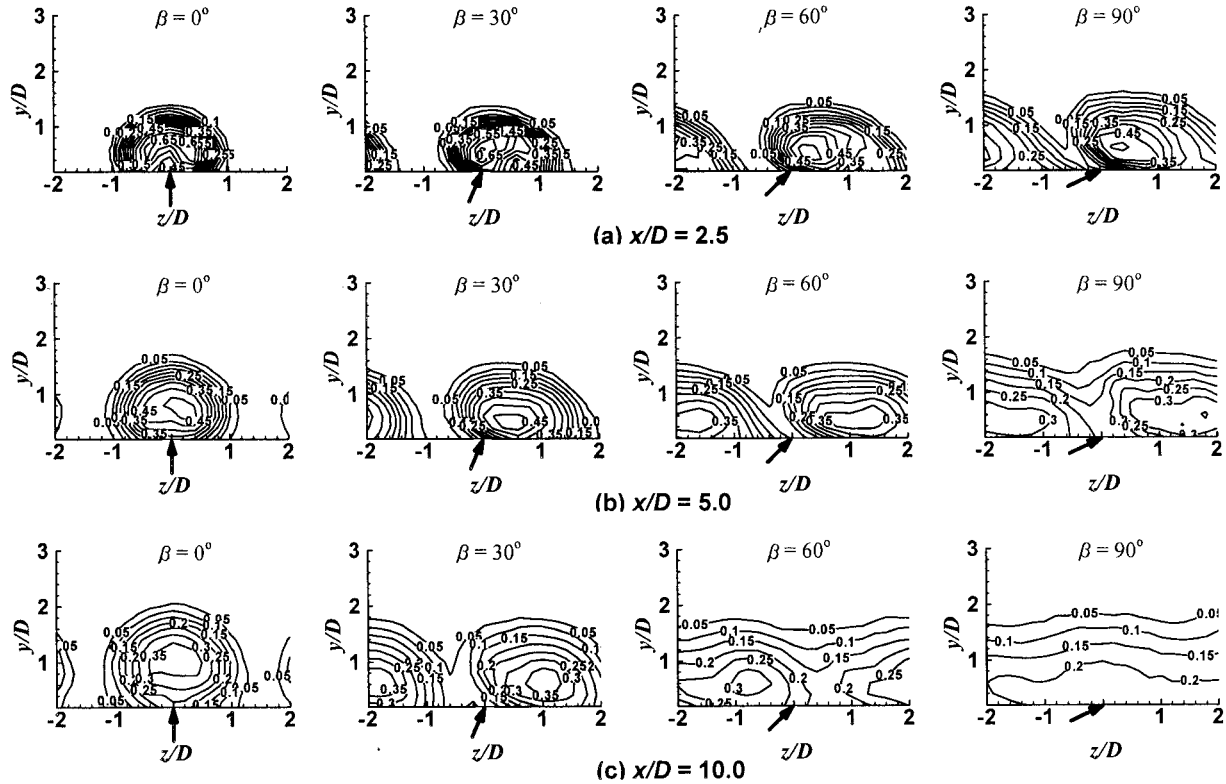

Fig. 3 Boundary layer temperature (Θ) distributions for *VR* = 1.0

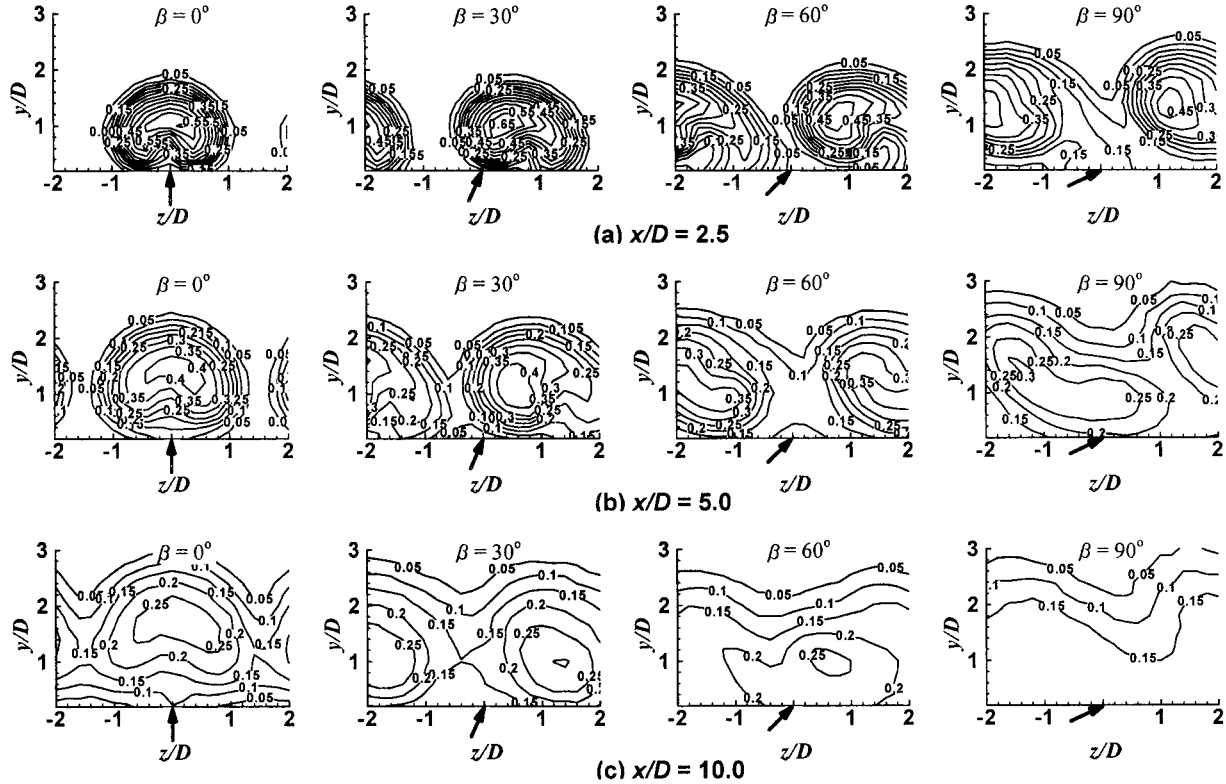

Fig. 4 Boundary layer temperature (Θ) distributions for *VR* = 2.0

momentum increases to 0.93 with the velocity ratio, the injectant starts to lift off from the wall so that the maximum temperature regions are completely detached from the wall. In addition to the lift-off, the injectant moves more in the *z* direction than at the velocity ratio of 0.5 because of the increased spanwise momentum. The distortion of the kidney-shaped isotherms in the case of simple angle injection by the single vortex in compound angle injection is more evident compared to those at the velocity ratio of 0.5. The regions between holes are still unprotected and the temperature near the wall decreases compared to the temperature in simple angle injection for the velocity ratio of 0.5 due to the lift-off. As the orientation angle increases, however, the regions between the

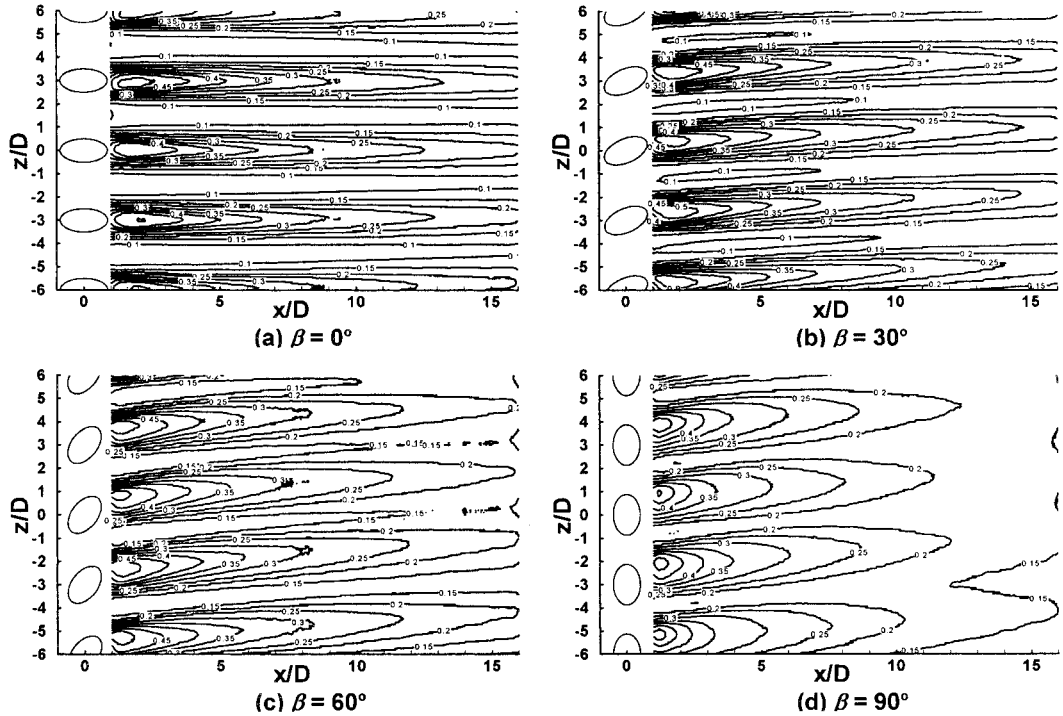

Fig. 5 Adiabatic film cooling effectiveness (η) distributions for *VR* = 0.5

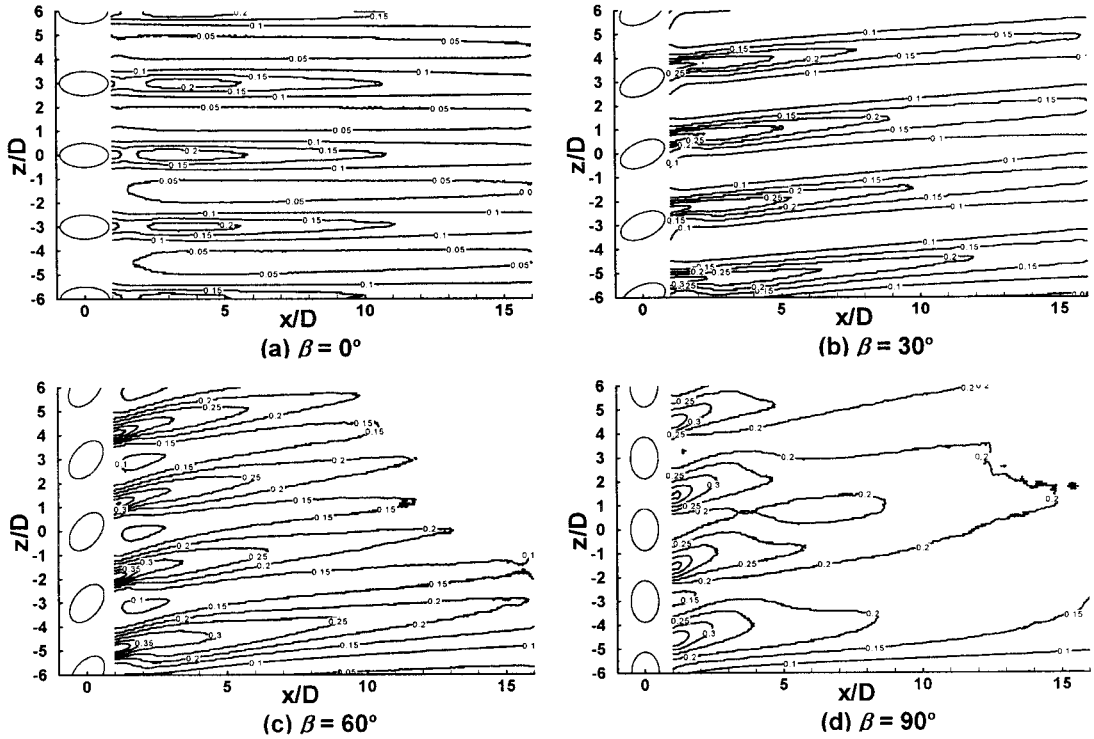

Fig. 6 Adiabatic film cooling effectiveness (η) distributions for $VR = 1.0$

holes are well covered with injectant and the interactions between the neighboring injectants become more active compared to $VR = 0.5$. This is due to the decrease in the distance between the neighboring injectants, and the intensified z-directional flow by the strong vortical motion of the high velocity ratio of 1.0. In particular, the temperature distribution for $\beta = 90$ deg at $x/D = 10.0$ is nearly uniform in the spanwise direction.

The boundary layer temperature distributions for the velocity ratio of 2.0 ($I = 3.72$) are shown in Fig. 4. As can be seen in near-hole temperature distributions (Fig. 4(a)), the injectant completely separates from the wall. At the velocity ratio of 2.0, the isotherms are expanded in the y direction as well as in the z direction. This is because the intensified vortical motion at the relatively higher velocity ratio entrains the free-stream fluid more

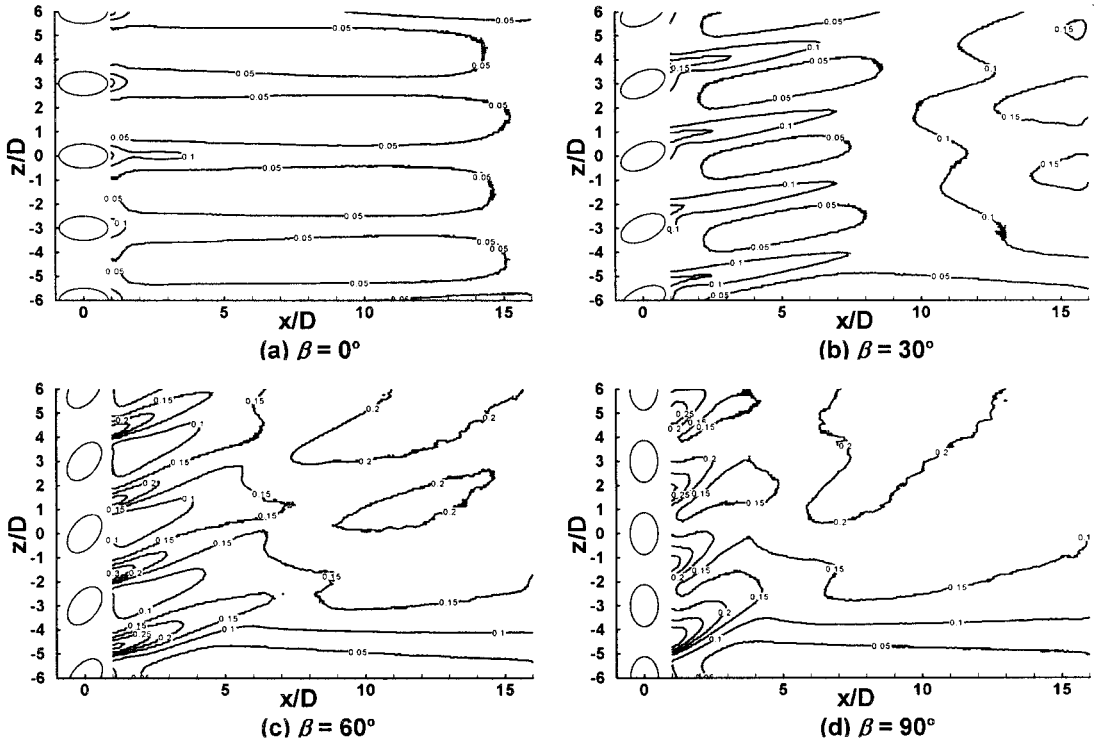

Fig. 7 Adiabatic film cooling effectiveness (η) distributions for $VR = 2.0$

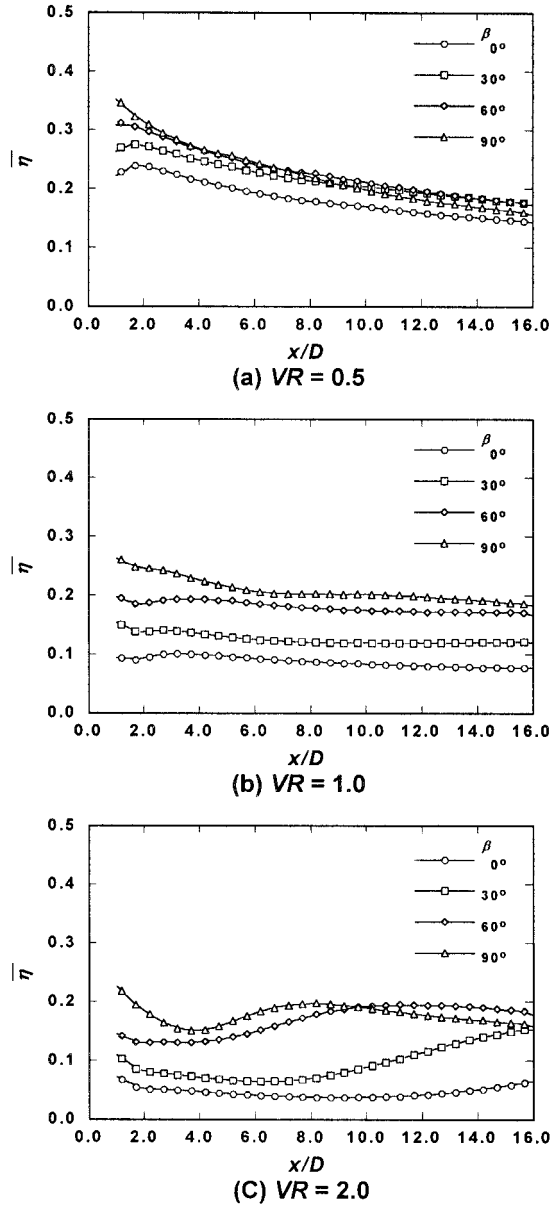

Fig. 8 Spanwise-averaged effectiveness distributions

vigorously, thus enhancing the mixing between injectant and free-stream fluid. The mixing is enhanced more at large orientation angle and high velocity ratio. Particularly, at $x/D = 5.0$ and 10.0, the temperature near the wall increases as the orientation angle increases. With larger values of β, the entrained free-stream fluid is mixed with the neighboring injectant before being transported to the wall due to the enhanced z-directional flow. The free-stream fluid entrained by strong vortical motion, however, is transported directly to the wall without mixing in simple angle injection.

Adiabatic Film Cooling Effectiveness Distributions. The film cooling effectiveness distributions at $VR = 0.5$ ($I = 0.23$) are shown in Fig. 5. The effectiveness values are larger compared to those at other velocity ratios. The high effectiveness level results from the attachment of the injectant to the wall as shown in the boundary layer temperature distribution (Fig. 2). As the orientation angle increases from 0 deg, the symmetric characteristic with respect to the hole center becomes asymmetric. Additionally, the region of high effectiveness moves in the positive z direction with the flow in compound angle injection. In simple angle injection, there are regions between holes where the effectiveness is low and the high effectiveness regions are narrow (Fig. 5(a)). As the orientation angle increases, however, the effectiveness between holes increases so that the effectiveness distribution in the spanwise direction becomes uniform (Fig. 5(b), (c), and (d)).

When the velocity ratio increases to 1.0 ($I = 0.93$), the injectant starts to separate from the wall due to high momentum of the injectant. The separation and the entrainment of the free-stream fluid to the wall by a pair of counterrotating vortices result in lower effectiveness than that at the velocity ratio of 0.5, as shown in Fig. 6. In compound angle injection, however, the protection is better than in simple angle injection as shown in Fig. 6(b), (c), and (d). One of the reasons is the decrease of the regions exposed to free stream due to the decrease in the distance between the neighboring injectants in compound angle injection. With high values of β, the entrained free stream fluid is mixed with the neighboring injectant before being transported to the wall due to the decrease in the distance between injectants and the enhanced z-directional flow of the vortex. The entrained free-stream fluid is transported directly to the wall without mixing in simple angle injection.

The film cooling effectiveness distributions at the velocity ratio of 2.0 ($I = 3.72$) are shown in Fig. 7. The effectiveness is generally low because the injectant separates completely from the wall due to the high vertical momentum. The effectiveness level near the injection holes is high, and then as the injectant moves downstream, the level decreases. The effectiveness, however, increases again as the injectant moves further downstream. In addition to the increase, the region shows a small spanwise variation of the effectiveness. The increase has a close relationship with the interaction between the neighboring injectants. It is evident from the boundary layer temperature distribution that as β increases, the coalescence of the injectant starts in the more upstream region. The coalescence is attributed to the temperature increase near the wall (Fig. 4). The effectiveness distribution at the velocity ratio of 2.0 also shows that as β increases, the increase in the effectiveness starts much further upstream.

Since the periodicity of effectiveness distribution breaks in the

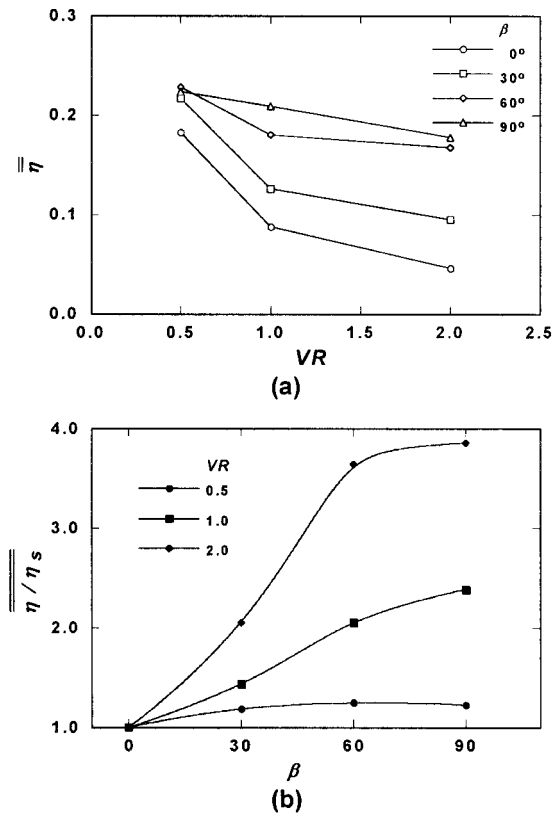

Fig. 9 Space-averaged effectiveness distributions

region of $x/D \leq -2.0$ at the velocity ratio of 2.0 with 90 deg orientation angle (Fig. 7(*d*)), spanwise-averaged effectivenesses were determined by integrating the measured effectiveness and dividing it by the span of $-1.5 \leq z/D \leq 4.5$. The results are shown in Fig. 8. In case of the velocity ratio of 0.5 ($I = 0.23$), the spanwise-averaged effectiveness decreases with x/D (Fig. 8(*a*)). The spanwise-averaged effectivenesses for three compound angle injections are nearly the same except in the hole region, while the spanwise-averaged effectiveness of simple angle injection shows a relatively low level. At the velocity ratio of 1.0 ($I = 0.93$), spanwise-averaged effectiveness increases with the orientation angle (Fig. 8(*b*)). The decrease with x/D is smaller than that of the simple angle injection. Figure 8(*c*) shows the increase of spanwise-averaged effectiveness at the velocity ratio of 2.0 ($I = 3.72$). The data show that the starting location of the increase moves upstream as the orientation angle increases.

The effect of the four orientation angles and the three velocity ratios on adiabatic film cooling effectiveness, the space-averaged effectivenesses, are compared in Fig. 9. The space-averaged effectivenesses are determined by averaging the effectiveness in the region of $-1.5 \leq z/D \leq 4.5$ and $1.0 \leq x/D \leq 16.0$. As shown in Fig. 9(*a*), higher velocity ratios result in lower space-averaged effectivenesses regardless of the orientation angles. As the orientation angle increases, however, the decrement in the space-averaged effectiveness with respect to *VR* decreases. For example, the space-averaged effectiveness is 0.18 at $VR = 0.5$ in the case of simple angle injection, and it decreases to 0.05 at $VR = 2.0$. However, in the case of $\beta = 90$ deg, the space-averaged effectiveness is 0.22 at $VR = 0.5$, and it decreases to 0.17 at $VR = 2.0$.

The space-averaged values were normalized with the space-averaged effectiveness of simple angle injection ($\overline{\overline{\eta_s}}$) and shown in Fig. 9(*b*) to investigate the effect of orientation angle on space-averaged effectiveness. The increase in space-averaged effectiveness is small at the velocity ratio of 0.5, but the increase is large at the velocity ratio of 1.0. The increase is most significant at the velocity ratio of 2.0.

Conclusions

The effects of orientation angles and velocity ratios on boundary layer temperature distribution and adiabatic film cooling effectiveness were experimentally studied. The investigated orientation angles are 0, 30, 60, and 90 deg. The velocity ratios adopted are 0.5, 1.0, and 2.0. The boundary layer temperature distributions were measured with the heated injectant. The adiabatic film cooling effectivenesses were measured in detail using thermochromic liquid crystal. From the results, some important observations are noticed and summarized below.

1 As the orientation angle increases, the enhanced vortex entrains free-stream fluid more strongly, thus augmenting the mixing between free-stream fluid and injectant. The mixing spreads the injectant concentration, and lowers the injectant maximum temperature. This observation is true for all velocity ratios investigated.

2 At velocity ratios of 1.0 and 2.0, the injectant vortical motion transports the neighboring injectant as well as the free-stream fluid to the wall. The transported injectant results in the high fluid temperature near the wall. This is more significant with increasing orientation angle.

3 Adiabatic film cooling effectiveness distributions are influenced by the interaction between the neighboring injectants in the boundary layer. As the orientation angle increases, more uniform and higher effectiveness distributions are obtained because of the coalescence of injectants.

4 The effects of orientation angles vary depending on the velocity ratios. While the increase in space-averaged effectiveness with orientation angle is small at the velocity ratio of 0.5, the increase with orientation angle is significant at the velocity ratio of 2.0.

References

Arts, T., and Bourguignon, A. E., 1990, "Behavior of a Coolant Film With Two Rows of Holes Along the Pressure Side of a High-Pressure Nozzle Guide Vane," ASME JOURNAL OF TURBOMACHINERY, Vol. 112, pp. 512–521.

Ekkad, S. V., Zapata, D., and Han, J. C., 1997, "Film Effectiveness Over a Flat Surface With Air and CO_2 Injection Through Compound Angle Holes Using a Transient Liquid Crystal Image Method," ASME JOURNAL OF TURBOMACHINERY, Vol. 119, pp. 587–593.

Farina, D. J., Hacker, J. M., Moffat, R. J., and Eaton, J. K., 1994, "Illuminant Invariant Calibration of Thermochromic Liquid Crystals," *Experimental Thermal and Fluid Science*, Vol. 9, pp. 1–12.

Goldstein, R. J., Eckert, E. R. G., Eriksen, V. L., and Ramsey, J. W., 1970, "Film Cooling Following Injection Through Inclined Circular Tubes," *Israel Journal of Technology*, Vol. 8, No. 1–2, pp. 145–154.

Honami, S., Shizawa, T., and Uchiyama, A., 1994, "Behavior of the Laterally Injected Jet in Film Cooling: Measurements of Surface Temperature and Velocity/Temperature Field Within the Jet," ASME JOURNAL OF TURBOMACHINERY, Vol. 116, pp. 106–112.

Kaszeta, R. W., Simon, T. W., Oke, R. A., and Burd, S. W., 1998, "Flow Measurements in Film Cooling Flows With Lateral Injection," ASME Paper No. 98-GT-54.

Kline, S. J., and McClintock, F. A., 1953, "Describing Uncertainties in Single Sample Experiments," *Mechanical Engineering*, Vol. 75, Jan., pp. 3–8.

Lee, S. W., Kim, Y. B., and Lee, J. S., 1997, "Flow Characteristics and Aerodynamic Losses of Film-Cooling Jets With Compound Angle Orientations," ASME JOURNAL OF TURBOMACHINERY, Vol. 119, pp. 310–319.

Ligrani, P. M., Ciriello, S., and Bishop, D. T., 1992, "Heat Transfer, Adiabatic Effectiveness, and Injectant Distributions Downstream of a Single Row and Two Staggered Rows of Compound Angle Film-Cooling Holes," ASME JOURNAL OF TURBOMACHINERY, Vol. 114, pp. 687–700.

Mehendale, A. B., and Han, J. C., 1992, "Influence of High Mainstream Turbulence on Leading Edge Film Cooling Heat Transfer," ASME JOURNAL OF TURBOMACHINERY, Vol. 114, pp. 707–715.

Schmidt, D. L., Sen, B., and Bogard, D. G., 1996, "Film Cooling With Compound Angle Holes: Adiabatic Effectiveness," ASME JOURNAL OF TURBOMACHINERY, Vol. 118, pp. 807–813.

Experimental Study of Showerhead Cooling on a Cylinder Comparing Several Configurations Using Cylindrical and Shaped Holes

H. Reiss

A. Bölcs

Swiss Federal Institute of Technology, Lausanne, Switzerland

Film cooling and heat transfer measurements on a cylinder model have been conducted using the transient thermochromic liquid crystal technique. Three showerhead cooling configurations adapted to leading edge film cooling of gas turbine blades were directly compared: "classical" cylindrical holes versus two types of shaped hole exits. The experiments were carried out in a free jet test facility at two different flow conditions, Mach numbers M = 0.14 and M = 0.26, yielding Reynolds numbers based on the cylinder diameter of 8.6e4 and 1.55e5, respectively. All experiments were done at a mainstream turbulence level of Tu = 7 percent with an integral length scale of $L_x = 9.1$ mm (M = 0.14), or $L_x = 10.5$ mm (M = 0.26), respectively. Foreign gas injection (CO_2) was used, yielding an engine–near density ratio of 1.6, with blowing ratios ranging from 0.6 to 1.5. Detailed experimental results are shown, including surface distributions of film cooling effectiveness and local heat transfer coefficients. Additionally, heat transfer and heat load augmentation due to injection with respect to the uncooled cylinder are reported. For a given cooling gas consumption, the laid-back shaped hole exits lead to a clear enhancement of the cooling performance compared to cylindrical exits, whereas laterally expanded holes give only slight performance enhancement.

Introduction

The further enhancement of the specific power output and thermal efficiency of modern gas turbines goes along with continuously increasing turbine inlet temperatures over recent years. Due to operation temperatures that largely exceed the allowable material temperatures, extensive cooling of the first stage(s) of the turbine is necessary in order to ensure high reliability of the "hot" components, and to achieve long life cycles of the blading. Currently, internal cooling via convection and impingement is combined with extensive external cooling via film cooling. For the correct thermal design of turbine components, detailed knowledge of heat transfer rates and metal temperatures is required. Today, however, high uncertainties for the local heat transfer persist, yielding even higher uncertainties for the local material temperatures. Therefore, it is still difficult to determine the optimum thermal design. This situation can be improved by providing accurate heat transfer data—gathered with numerical tools, or experimentally—for realistic, "near-engine" cooling situations.

One of the focal points of cooling research is the optimization of film cooling schemes, aimed at maximizing the external cooling effects with a minimum coolant gas consumption. This can be achieved, for example, by finding the optimum configuration of injection holes. In this context, the use of sophisticated hole arrangements with "shaped" exits—rather than simple cylindrical holes—has to be mentioned as a very promising option. In fact, considerable improvement of cooling performance has been reported by several researchers for simplified situations.

Previous Work on Shaped Holes. Several experimental studies on flat plate film cooling with shaped holes can be found in the literature, generally indicating a positive effect of shaped holes on the cooling performance.

Goldstein et al. (1973) carried out measurements on a flat plate equipped with a single cooling hole, and compared a cylindrical hole exit to a conically widened one. Increased cooling effectiveness was detected for widened hole exits in both downstream and lateral directions. It was reasoned that the reduced momentum of the jet due to hole expansion toward the exit reduces the jet's tendency to detach from the model surface, thus reducing penetration of the coolant into the boundary layer. As a result, less mixing and better coverage occur.

Wittig et al. (1996) tested a single cooling hole with inclination in the flow direction on a large-scale model at trans- and supersonic flow conditions. A cylindrical hole was compared with two kinds of shaped holes: laterally expanded, and laid back and laterally expanded. It was reported that the tendency of jet lift-off is lowered by inclining injection holes into flow direction, or shaping hole exits to obtain "smoother" injection. Also here, this was attributed to a reduced momentum of the injected secondary fluid due to a diffuser effect of the widened exits.

Other studies investigated an entire cooling row instead of individual holes, also indicating positive effect of diffuser-shaped exits (Beeck et al., 1993; Giebert et al., 1997; Bittlinger et al., 1994).

These studies have been done on various model geometries and cooling configurations. However, a direct quantitative comparison between the different hole shapes is difficult since often the configurations differ not only in exit shape, but also other geometric parameters (number of injection rows, hole spacing, orientation, exit shape, etc.). Moreover, a mismatch of other experimental parameters such as flow conditions may make direct comparisons impossible. For high curvature situations such as on the leading edge, or the pressure or suction sides of turbine blades, not much data on shaped holes in combination with several rows of injection holes has been published, to the knowledge of the authors. It is

Contributed by the International Gas Turbine Institute and presented at the 44th International Gas Turbine and Aeroengine Congress and Exhibition, Indianapolis, Indiana, June 7–10, 1999. Manuscript received by the International Gas Turbine Institute February 1999. Paper No. 99-GT-123. Review Chair: D. C. Wisler.

therefore hard to draw conclusions from the literature data on the actual benefit of shaped holes for leading edge cooling.

Present Study. The objective of the present study is to explore the potential improvement of film cooling with shaped holes for the leading edge region. In particular, it is of interest to investigate the combined effect of high surface curvature, stagnation point flow with a very thin boundary layer and high flow acceleration, and the interaction of several rows of cooling holes as they are currently found in gas turbines. Another aim of this study is to provide an experimental data set allowing the direct comparison of several injection schemes for a complex and realistic situation, which might be useful for both gas turbine design and code validation.

Experimental Setup

Free Jet Test Facility. The experiments were carried out in a free jet test facility, using a rapid exposure mechanism for a cylinder model, which has been used in a previous study by Hoffs et al. (1997). The cylinder model can be pivoted into the free jet flow, as shown in Fig. 1. It is mounted on a base plate with micrometrical angle adjustment, allowing for precise orientation of the showerhead with respect to the main flow. A turbulence grid is attached to the free jet exit, creating near-engine turbulence intensity values at the cylinder leading edge of about $Tu = 7$ percent, with a nondimensional integral length scale of $L_x/D = 0.30$ percent (M = 0.14) or $L_x/D = 0.35$ (M = 0.26). Turbulence quantities were measured with hot-wire anemometry. The free jet exit has a diameter of 5 cylinder diameters D. The exchangeable showerhead section has a length of $2D$. Once in measurement position, the cylinder leading edge is located at a distance of $5D$ downstream of the turbulence grid. The preconditioned coolant gas is supplied to the plenum chamber of the test section via insulated tubings. CO_2 is used as coolant gas, yielding a density ratio of $DR \approx 1.6$. The model surface is viewed with a miniature CCD camera situated next to the free jet exit. Halogen light sources and fiber optics are used for illumination. The flow around the cylinder test section is essentially two dimensional, which was verified with hot wire and aerodynamic probe measurements.

Instrumentation. The cylinder carrying the test specimen is depicted in Fig. 2. A series of pressure taps are arranged in the circumferential direction, adjacent to the showerhead insert. To measure the initial temperature to which the model is preconditioned, six thermocouples are embedded in the Perspex test section at various locations. The cut-out on the right-hand side of Fig. 2 shows the orientation of the showerhead in the main flow (thin radial lines indicate positions of pressure taps). The model surface is coated with a thin layer of commercial narrow-band thermochromic liquid crystals. These are sprayed on prior to each series of experiments, and subsequently polished for repeatable

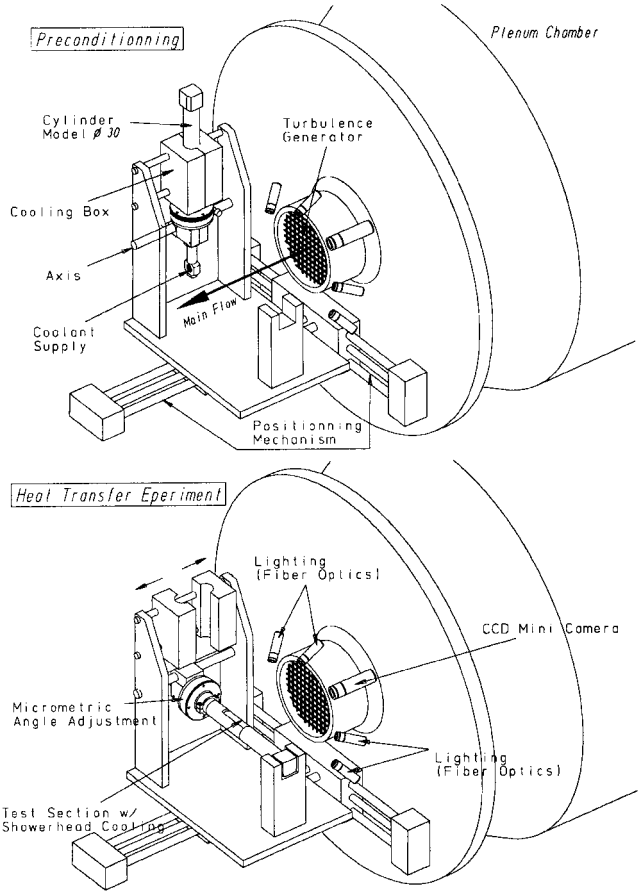

Fig. 1 Free jet test facility with pivot mechanism for cylinder model

Nomenclature

A = surface area, m^2
c_p = specific heat at constant pressure, J/kgK
d = leading edge, diameter, hole diameter, mm
D = cylinder diameter, mm
DR = coolant-to-gas density ratio = ρ_c/ρ_g
G = bulk blowing ratio = $u_c\rho_c/u_g\rho_g$
I = bulk momentum flux ratio = $u_c^2\rho_c/u_g^2\rho_g$
L = cooling hole length, m/s
L_x = longitudinal integral lengthscale, m
M = Mach number = $u/(\kappa RT)^{0.5}$
Nu_D = Nusselt number = $\alpha D/\lambda$
n = summation index
p = pressure, Pa; pitch, mm
Q = heat flux, W
q = specific heat flux, W/m^2
R = ideal gas constant, J/kg/K
Re_D = Reynolds number $(uD)/v$
R_a, R_z, R_t = surface roughness parameters (DIN4768), μm
r_0 = recovery factor
T = temperature, K
t = time, s
Tu = turbulence intensity, percent
u = velocity, m/s
x = model depth, m
α = local heat transfer coefficient, $W/(m^2K)$
β = spanwise inclination angle, deg
γ = surface angle, exit location angle, deg
η = film cooling effectiveness
κ = isentropic coefficient = c_p/c_v
λ = thermal conductivity, J/mK
Λ = thermal diffusivity = $\lambda/(\rho c_p)$, m^2/s
ρ = density, kg/m^3
τ = summation index
μ = dynamic viscosity, Ns/m^2
ν = kinematic viscosity, m^2/s
Φ = overall effectiveness
φ = streamwise inclination angle, deg

Subscripts

aw = adiabatic wall
c = coolant
f = film cooling
g = mainstream gas
i = initial
r = recovery
s = static conditions, surface
t = total conditions
0 = reference, cooling hole base

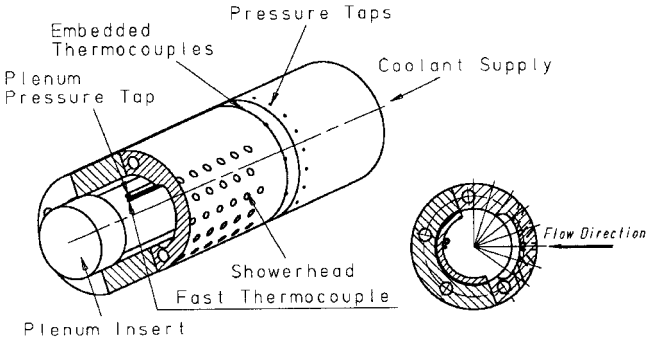

Fig. 2 Cylinder model instrumentation

and smooth surface quality. Typically, surface roughnesses of $R_z = 9 \pm 1.5\ \mu$m, $R_a = 2.4 \pm 0.5\ \mu$m, and $R_t = 15 \pm 2.7\ \mu$m are achieved.

Data Analysis. The local heat flux onto a film-cooled surface can be written as

$$q = \alpha_f (T_{aw} - T_w) \tag{1}$$

where the driving temperature difference for the definition of α_f is the adiabatic wall temperature T_{aw} (which is the effective gas temperature at the wall) minus the surface temperature of the model. T_{aw} is unknown and depends on the temperatures of the mainstream and the injected coolant gas, and on the mixing between jets and main flow. It can be written in dimensionless form as the film cooling effectiveness

$$\eta = \frac{T_{aw} - T_{rg}}{T_{tc} - T_{tg}} \tag{2}$$

expressing how closely T_{aw} approaches the coolant injection temperature. Both unknowns α_f and η are functions of the aerodynamic flow field alone and do not depend on the actual choice of the temperature values, as long as constant gas properties are supposed (Vedula and Metzger, 1991).

The data analysis is based on the theory of one-dimensional transient heat conduction into a semi-infinite solid. The governing differential equation for the temperature evolution of the solid is

$$\frac{\partial^2 T}{\partial x^2} = \frac{1}{\Lambda} \frac{\partial T}{\partial t} \tag{3}$$

with the initial condition $T(x, t)|_{t=0} = T_i$. It is supposed that, during an experiment, a heat pulse enters only a short distance into the model compared to its wall thickness, i.e., the model interior remains at initial temperature T_i at all times, and the temperature gradient $\partial T/\partial x$ is zero. This is formally expressed as the boundary condition for Eq. (3) as $\lim_{x\to\infty} T(x, t) = T_i$. At the surface a convective boundary condition is imposed:

$$-\lambda \left.\frac{\partial T(x, t)}{\partial x}\right|_{x=0} = \alpha_f (T_{aw} - T(x, t))|_{x=0} \tag{4}$$

Equation (4) represents an instantaneous step change of the effective fluid temperature along the model surface from T_i to T_{aw}. In reality, a true step change for the mainstream temperature can be closely approximated by rapid exposure of the preconditioned model to the flow (Hoffs et al., 1997). However, this is not the case for T_{aw} since the coolant injection temperature varies gradually during a transient experiment due to internal heat exchange, which occurs in the supply tubings, the plenum, and particularly in the cooling holes inside the pre-conditioned model. Thus, the adiabatic wall temperature becomes a function of time. This is accounted for by approximating the measured coolant injection temperature with a power series of typically fourth to fifth order as

$$T_{tc}(t) = \sum_{n=0}^{N} A_n \frac{t^n}{\Gamma(n+1)} \tag{4}$$

Employing this transient coolant temperature, the Laplace transform method yields an analytical solution for the temperature evolution at $x = 0$, as previously described by Drost et al. (1997):

$$T_w - T_i = (T_{rg} - \eta T_{tg} - T_i)[1 - e^{\beta^2}\,\mathrm{erfc}(\beta)] - \eta \sum_{n=0}^{N} \left\{ A_n \left(\frac{\kappa}{\alpha_f}\right)^{2n} [e^{\beta^2}\,\mathrm{erfc}(\beta) - \sum_{\tau=0}^{2n} ((-2\beta)^\tau i^\tau\,\mathrm{erfc}(0))] \right\} \tag{5}$$

with $\kappa = \lambda/\sqrt{\Lambda} = \sqrt{\rho\lambda c_p}$ and $\beta = \alpha_f\sqrt{t}/\kappa$.

Equation (5) contains the two unknowns α_f and η. In order to solve for α_f and η, a multiple-regression analysis is applied: Six to eight transient experiments are conducted at identical aerodynamic and thermal conditions but with varying coolant temperatures. The actual coolant temperature evolution at the hole exit, which is calculated based on measurements of the coolant total conditions in the plenum chamber, is shown on the left-hand side of Fig. 3. The corresponding (calculated) wall temperature rise for a given surface position is indicated on the right-hand side of Fig. 3. Since a single layer of narrow band liquid crystals is used, one "event" can be detected per chosen hue value and test, that is when the surface point passes the corresponding liquid crystal temperature T_{LC}. A least-square fit of Eq. (5) is applied to the ensemble of points $(t, T_w = T_{LC})_i$ yielding both unknowns α_f and η.

This "overdetermined" approach results in smaller uncertainties, compared to those obtained using the minimum of only two experiments. Taking into account the existing measurement uncertainties, the error on the heat transfer coefficient is about 6 percent, and on the film cooling effectiveness 4 percent (for $\eta = 0.3$) to 10 percent (for $\eta = 0.1$). Varying the injection temperature over a range of 30 K causes variations of the density ratio and blowing ratio, and momentum ratio of the order of 8 percent over an ensemble of tests.

Image Processing. The color play of the liquid crystals is captured with a miniature CCD camera, that views the upper side of the test section, covering surface angles γ from roughly -10 to 90 deg. The RGB image signal is analyzed with a special image processing computer based on the hue capturing technique, which consists of a real-time conversion of the RGB signal into a hue-saturation-intensity signal and then filtering out all but a specified range of hue values, which yields a considerable reduction of the data. Typically two narrow color bands (green and cyan) were chosen, which were calibrated individually. For the specific liquid crystals used, the temperatures of appearance of these two colors were approximately 0.5°C apart. The reduced image sequence is then stored and transferred to a workstation for later data processing. This consists of a coordinate transformation from the image coordinates of the camera into model surface coordinates using a

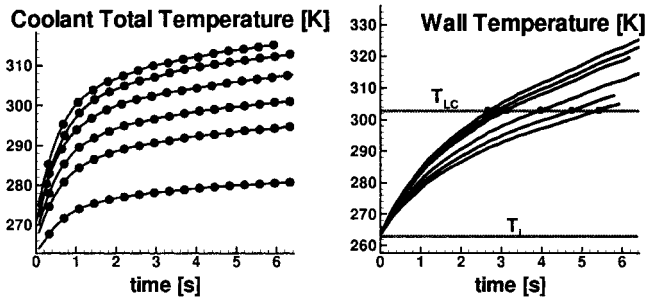

Fig. 3 Variation of coolant and wall temperatures for a test ensemble

reference grid, followed by separating the liquid crystal events at given position and their respective time of appearance. In order to reduce the influence of the noise of the image signal on the data evaluation, a number of pixels are treated together, subdividing the model surface into a regular grid with user-defined resolution. Typically, 200 × 300 cells were used, yielding a spatial resolution of roughly 15 data points over a surface distance corresponding to one hole diameter d.

The color events are detected using an averaging procedure in both time and space: A hue signal needs to appear at a surface position as well as neighboring positions, over a number of consecutive images in order to be considered as an event.

The type of crystals used in this study showed a good accuracy of the temperature calibration the order of ±0.15°C for a given hue value. The influence of view angle or irregular illumination, which is important for wide-band liquid crystals, can be neglected.

Experimental Procedure. The test facility runs at steady-state conditions. The mainstream temperature is adjusted to 60–65°C. Prior to the heat transfer tests, the cylinder model is preconditioned to an initial temperature of about −15°C using a cooling box that encloses the cylinder model (see Fig. 1). The initial temperature of the test insert is monitored using several thermocouples, as illustrated in Fig. 2. The coolant temperature is set via cooling and heating devices and heat exchangers. In order to achieve the desired variation of injection temperature, it is necessary to precondition the coolant supply tubings. Thus the coolant flow is readily established prior to the test start, up to the actual orifice to the plenum chamber where it is bypassed around the showerhead section, into the ambient air. At the actual start of a transient experiment, the cylinder is released from the cooling box and rapidly pivoted into its measuring position in the flow. An automatic valve switches on the coolant gas from the bypass to the plenum in the cylinder. A programmable control device regulates the flow rate during the test in order to limit flow rate fluctuations, which might occur during switching over from bypass to cooling mode; additionally the actual flow rate is continuously measured with a laminar flow element. The transient total temperature in the plenum is measured with fine fast-response thermocouples residing in the plenum center, and the coolant total pressure is acquired with a pressure tap (see also Fig. 2).

Subsequently during data processing the effective coolant temperature at the exit location is determined via an isentropic calculation, based on the measured total conditions in the plenum and the static pressure at the hole exit. The latter is interpolated from pressure tap measurements on the cylinder surface. The error on the coolant exit temperature due to internal heat exchange depends strongly on the actual coolant temperature of the respective test. A worst case estimation has been done using a numerical simulation of the transient heat exchange in the near-hole region, yielding an error of less then 0.5°C, which is considered negligible.

Table 1 Test matrix for showerhead experiments

Main Stream				Film Cooling	
M [-]	Re_d [-]	Tu [%]	L_x [mm]	G_{CO2} [-]	I_{CO2} [-]
0.14	8.6e4	7%	9.1	0.6	0.21
				1.0	0.60
				1.3	1.02
				1.5	1.35
0.26	1.55e5	7%	10.5	0.6	0.21
				1.0	0.60
				1.3	1.02
				1.5	1.35

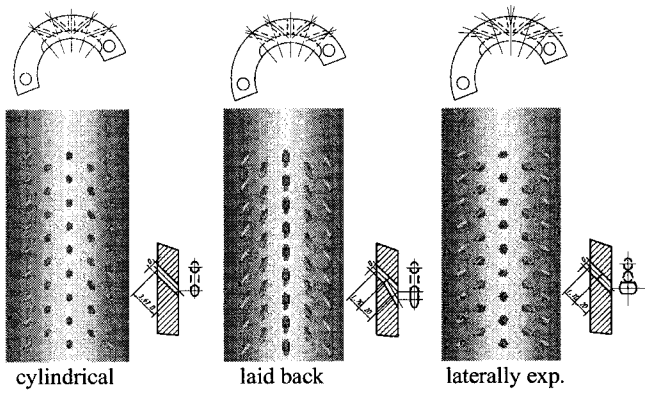

Fig. 4 Overview of showerhead geometries

Test Conditions. An overview of the test conditions that were measured in this study is given in Table 1. All measurements were carried out at the nominal angle of attack of 0 deg, i.e., the flow was symmetric with respect to the showerhead arrangement. The temperature ratio between mainstream and secondary fluid varied from $T_g/T_c = 1.0$ to 1.2, depending on the actual coolant injection temperature of the individual test. Both the blowing and momentum flux ratios are given as bulk quantities, i.e., they are averaged for the entire showerhead. Inevitable variations of the local coolant flow rate through individual cooling rows result from the circumferential pressure distribution around the cylinder. The flow splits among the different rows could not be assessed experimentally. They can be estimated based on the measured driving pressure ratio $p_{plen}/p_{s,exit}$. However, the calculation of the mass flow distribution is sensitive to slight variations of the pressure ratio. This is especially true for small blowing ratios, for which $p_{plen}/p_{s,exit}$ is very close to unity and the quantity being injected through the middle row is low. Given the existing measurement uncertainty on the pressure ratio, the following coolant distribution has to be considered as approximately: 12 ± 5 percent of the total coolant mass flow was injected at the 0 deg position, 18 ± 5 percent through each of the rows at ±20 deg, and 26 ± 5 percent at ±40 deg, with slight variations depending on the blowing ratio. Potential differences between the cylindrical and hole shapes could not be resolved.

The hot gas ingestion into the showerhead through the middle row was checked by monitoring the pressure ratio p_{plen}/p_{tot}. Additionally, the temperature transients in the plenum were checked for steep temperature peaks occurring at model insertion, which are a clear indicator of any hot gas ingestion. For bulk blowing ratios G greater than 0.5, no hot gas ingestion was detected.

To allow direct comparison, both G and I refer to the "inner" hole surface A_o which is the same for all three showerhead models, rather than to the actual exit surface A.

Showerhead Geometries

The geometries for this study were specially designed for the leading edge region, using some of the features of shaped holes that were already used by Gritsch et al. (1998). However, particular design constraints for film cooling of a gas turbine leading edge have to be respected, such as limited space, relatively small wall thickness, and constraints in terms of possible hole orientations. Therefore, the hole types reported in literature for flat plate situations were modified and specifically adapted for the showerhead arrangement. The resulting design is a compromise between feasibility of manufacture and complexity. Figure 4 shows the three showerhead configurations.

The "basic" showerhead configuration (Fig. 4, left) consists of five staggered rows of cylindrical holes with a diameter ratio of $d/D = 0.05$. They are arranged symmetrically with respect to the free jet flow, at circumferential positions 0, ±20, and ±40 deg,

and a hole spacing of $p/d = 3.7$ in the "spanwise" direction. The holes of all five rows are oriented by 45 deg toward the cylinder axis (i.e., perpendicular to the main flow), whereas the holes of all neighboring rows are additionally inclined by 30 deg in the circumferential direction (i.e., toward the local main flow direction).

The "laid-back" configuration (Fig. 4, center) uses the same hole arrangement, but the exits are opened by 15 deg in the direction of the hole inclination, over a depth of two hole diameters. This increased the effective surface area of the hole exits by a factor of 3.5 compared to cylindrical holes.

The third configuration (Fig. 4, right) has hole exits that are shaped laterally outward, in a sense perpendicular to the hole inclination. This is done on both sides for the center row by an angle of ± 10 deg, and by 15 deg for the neighboring rows only on one side, in the direction of main flow. The exit surface area for this configuration is increased by a factor of 1.8 with respect to the cylindrical holes.

Results and Discussion

The data are presented in the form of contour plots showing the surface distribution on a portion of the model, as well as in the form of spanwise-averaged quantities as a function of surface angle. The contours are instructive and allow a qualitative interpretation, since they effectively illustrate the characteristics of the formation of the cooling film, in terms of the behavior of the individual jets (lift-off, re-attachment, trajectory, etc.), and the interaction between the different cooling rows. This is needed for understanding the highly three-dimensional physical effects involved in showerhead cooling. The plots contain about 160×250 data points, corresponding to a spatial resolution of approximately $\frac{1}{15}$ hole diameter d. However, in regions of high efficiencies such as in the streaks downstream of a cooling hole, the data were relatively noisy, which is due to the nature of the liquid crystal signal at these points: The signal appears very fast for high coolant injection temperatures, which yields high uncertainties with regards to time. In contrast, for very low injection temperatures, it may not appear at all during a transient test, i.e., the rise of the surface temperature is too slow, and the surface does not heat up to the liquid crystal temperature, yielding partly irregular spacing of the data points. This was accounted for when deriving the spanwise-averaged curves by interpolating the zones of missing data. The spanwise-averaged results are used for quantitative discussion, and meaningful comparison of the cooling performance among the cooling configurations.

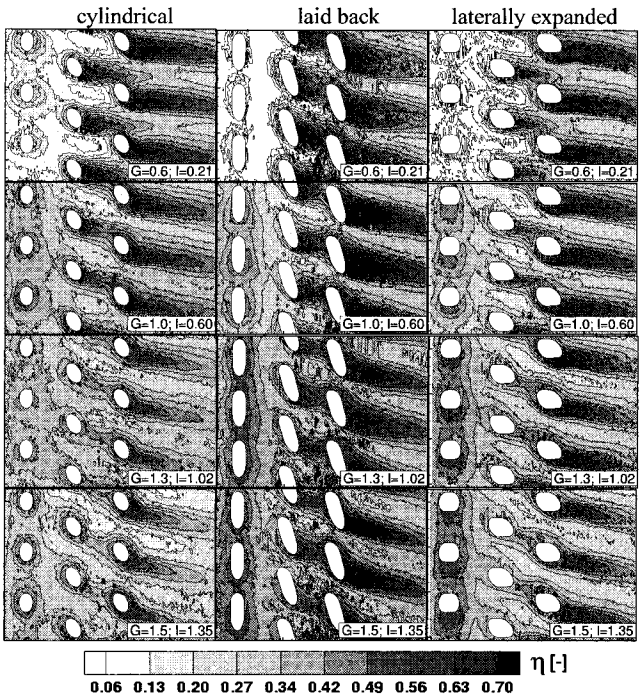

Fig. 5 Detailed film cooling effectiveness at low Mach number (M = 0.14; Re_D = 8.6e4)

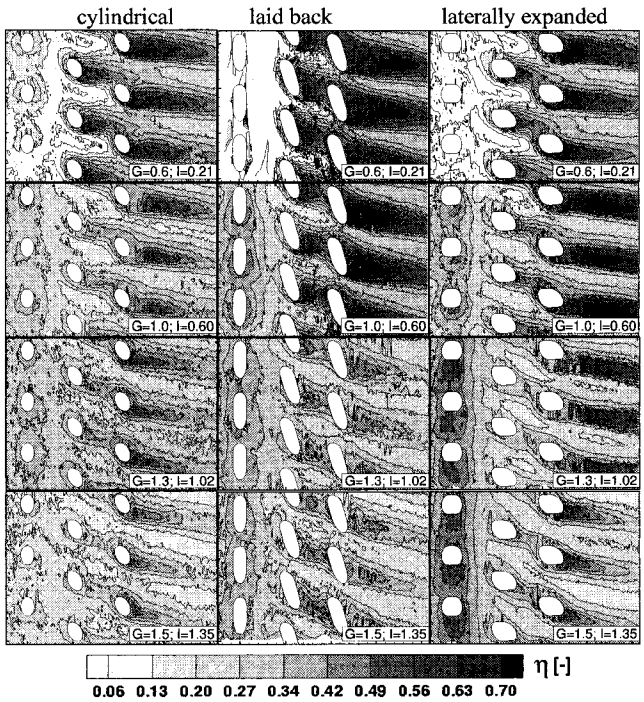

Fig. 6 Detailed film cooling effectiveness at high Mach number (M = 0.26; Re_D = 1.55e5)

Film Cooling Effectiveness. Detailed results of film cooling effectiveness are presented in Fig. 5 for the low Mach number case, and in Fig. 6 for the high Mach number case. Each of the figures contains 12 individual graphs, arranged in three columns for the cylindrical, laid back, and laterally expanded holes from left to right, and in four lines for the blowing ratios $G = 0.6$, 1.0, 1.3, and 1.5 from top to bottom. The graphs represent an unwrapped section of the model surface covering surface angles from approximately -10 to 80 deg along the horizontal axis, and a spanwise distance corresponding to four axial hole spacings along the vertical axis. The cooling rows at 0, 20, and 40 deg can be seen from left to right; they are subsequently referred to as row "1" (stagnation line), "2" (20 deg), and "3" (40 deg). The main flow direction is toward the right. The hole exits for the respective cooling configuration are added to the graphs (in true shape, size, and position) to illustrate the actual proportions of the showerhead. The spanwise inclination of the cooling holes by 45 deg is pointing downward in the graphs, and the coolant supply to the plenum comes from the top. High efficiencies are indicated as black, and low as white. The corresponding spanwise-averaged film cooling effectiveness $\bar{\eta}$ is shown in Figs. 7 and 8.

Generally, good periodicity of the contours in the spanwise direction can be stated, indicating a regular flow through the cooling pattern. Also, good symmetry in the circumferential direction is obvious around the injection row 1 on the left, confirming the correct adjustment of the showerhead with respect to the main flow direction. The effect of three-dimensional conduction in proximity of the exits is apparent, stemming from internal heat transfer in the cooling holes. The strength of this effect depends on the direction and the exit shape. Since the data analysis is based on one-dimensional heat conduction equation, the data in these zones are not valid, and may therefore not be considered for a quantitative discussion.

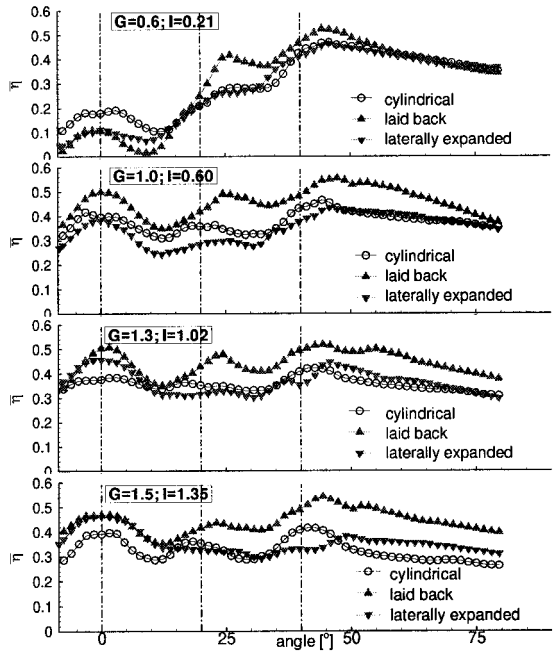

Fig. 7 Spanwise-averaged film cooling effectiveness at low Mach number ($M = 0.14$; $Re_D = 8.6e4$)

The coolant mass flow through the holes varies from one row to another, because of the pressure distribution around the cylinder surface. This can clearly be seen by pronounced streaks of high efficiency behind row 3, which are less distinct or missing at rows 2 and 1. It can also be seen that the jet trajectory is sensitive to the blowing ratio: For a low blowing ratio of $G = 0.6$, the respective streaks are almost aligned with the main flow direction, whereas they deviate more and more for higher blowing. This is due to the compound angle orientation of the holes and plays an important role for the formation of the cooling film. Good staggering of the jet trajectories results for low coolant injection, yielding good lateral coverage just downstream of the showerhead, whereas the jet trajectories "merge" for higher blowing. At $G = 1.5$, the streaks from row 2 fall right onto the exits of row 3.

For the *cylindrical holes at low Mach number*, it can be seen that the streaks of rows 2 and 3 are the biggest at $G = 0.6$, and get smaller as the blowing ratio increases. This effect is known in the literature as jet lift-off, i.e., the coolant gas starts to leave the boundary layer with the increasing momentum of the jet, up to the extreme of an entire loss of the coolant to the main flow, with no cooling effect at all. Along the stagnation line, however, no traces of discrete jets can be distinguished, but rather smeared zones of generally increased effectiveness. The flow situation for injection at stagnation point is considerably different from the other injection stations further downstream. The boundary layer is very thin, mainstream velocity is low, and the injection velocity has no component aligned with the main flow. Clearly, the direction of the coolant is highly sensitive to the slightest change of the main flow direction. The effectiveness contours indicate a rather homogeneous distribution of the coolant, and it is proposed that rather than forming distinct jets with defined zones of film coverage, the coolant is injected through the boundary layer, mixes well with the main fluid, and then falls back onto the model surface. Only for cases with very high injection mass flow is the coolant lost into the mainstream. At a low blowing ratio of $G = 0.6$, the spanwise-averaged effectiveness is gradually building up from relatively low values of 0.2 at the leading edge to a maximum of 0.5 at 45 deg, and subsequently running out to a level of 0.4 toward higher angles. Local maxima can be seen behind each cooling row. For the higher blowing ratios, the curve is much flatter, on an overall level of about 0.3.

Laid back holes exhibit generally much broader streaks than cylindrical holes, i.e., better coverage of the surface with the coolant film. Except for the stagnation region, the spanwise-averaged effectiveness is higher as indicated in Fig. 7, giving peak values as high as 0.5 behind the third cooling row.

The *laterally expanded holes* show effectiveness values on approximately the same level as the cylindrical holes. For higher blowing, they become clearly superior, and the streaks of the third cooling row diminish less rapidly than for the cylindrical holes. This indicates that the jet lift-off is delayed for the laterally expanded holes.

Another phenomenon that is opposed to the described jet lift-off can be seen in the contour plots in Figs. 5 and 6: The jets of rows 3 are well attached to the surface at low blowing, then coverage behind the holes improves as coolant gas injection increases, and for further increased blowing, the jets start to detach with subsequent re-attachment a little further downstream. This "drift" of the point of maximum coolant efficiency can most clearly be seen for the laterally expanded holes at low Mach number in Fig. 5. One would expect complete jet detachment at even higher blowing ratios than 1.5. For the cylindrical holes at high Mach number, and even more pronounced for the laterally expanded holes at high Mach number (Fig. 6), an inversion of the tendency can be stated for high blowing: At low blowing ratios they start out with the above described behavior (beginning jet detachment and re-attachment), but for higher blowing ratios, a sudden shift of the maximum of the streaks back to the hole occurs, combined with a further decrease in the level of effectiveness further downstream. The following explanation is proposed: This "inversion" of the tendency of the jet to detach occurs at high blowing ratios, when the jet trajectories become highly curved, i.e., the jets of row 2 impinge right onto the jets of row 3. This may have the effect of bending down the cooling jets of row 3 toward the surface, yielding a jet inclination that is stronger than what would correspond to the hole geometry and injection velocity. Since the coolant still has high momentum, a good portion of it leaves the boundary layer a little further downstream. The results are a relatively high effectiveness directly behind the holes, but subsequent loss of the coolant to the main flow. The streaks start directly behind the exit openings and are very short.

A similar effect of favorable interaction between cooling rows

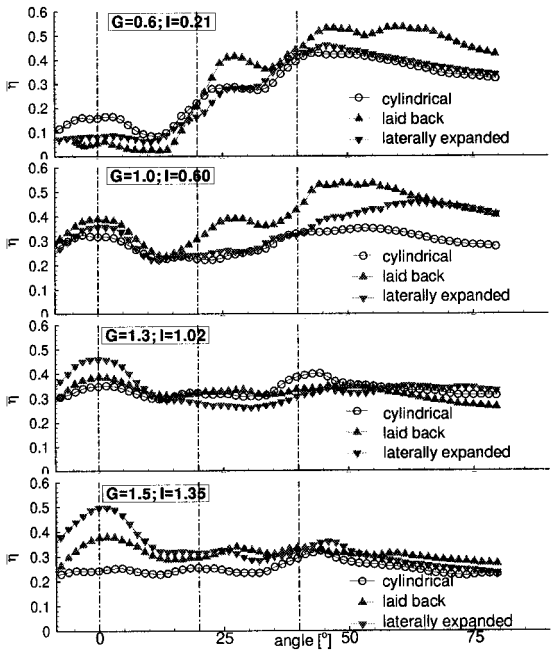

Fig. 8 Spanwise-averaged film cooling effectiveness at high Mach number ($M = 0.26$; $Re_D = 1.55e5$)

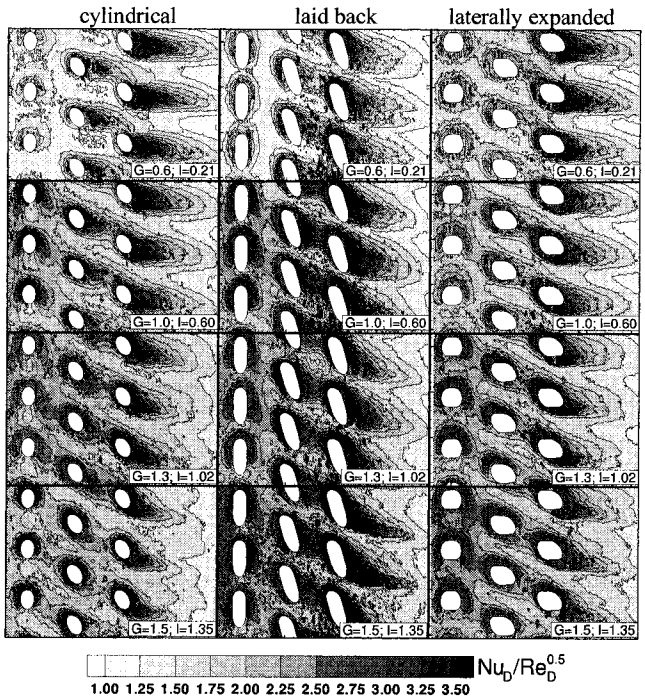

Fig. 9 Detailed heat transfer at low Mach number (M = 0.14; Re_D = 8.6e4)

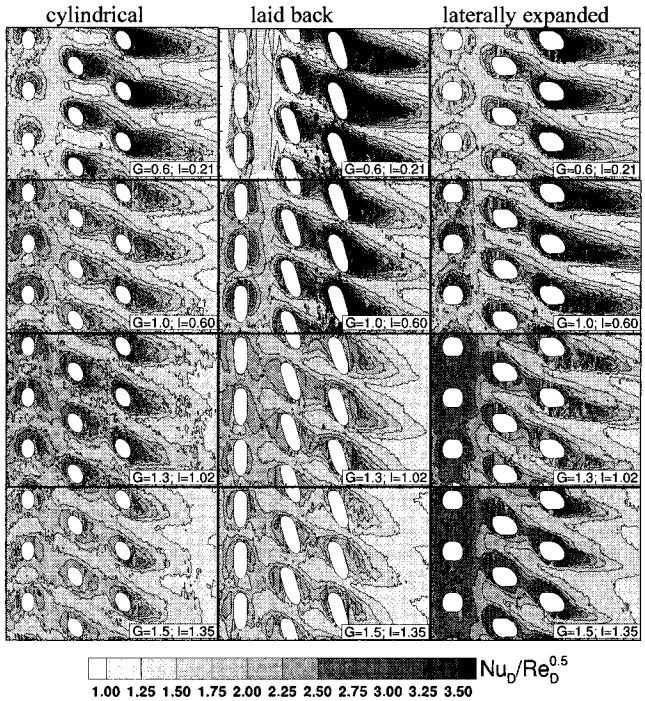

Fig. 10 Detailed heat transfer at high Mach number (M = 0.26; Re_D = 1.55e5)

has also been reported by Drost and Bölcs (1999), who investigated a double row injection arrangement on the suction side of a turbine blade. The onset of the inversion effect depends on the main flow conditions and the hole geometry. It occurs at $G = 1.3$ for the cylindrical holes, and at $G = 1.5$ for laterally expanded holes.

Effect of Mach Number. The measurements indicate that film cooling effectiveness is slightly lower for the high Mach number case. In general, the streaks of high effectiveness behind the exits in Fig. 6 are smaller than in Fig. 5, and the onset of flow separation occurs earlier (i.e., at smaller blowing ratios). The following explanation is proposed: Even though, at constant momentum flux ratio between free stream and coolant, higher momentum flow has the tendency of stronger jet deflection due to higher main fluid momentum close to the wall (an effect reported by Mehendale and Han, 1993), a smaller quantity of coolant remains in the boundary layer, since the latter is considerably thinner. Despite the fact that the jet trajectory may be slightly flatter at higher flow conditions, the jet penetration relative to the boundary layer thickness is stronger, and a bigger portion of the coolant gas is lost to the free stream. This explanation is applicable as long as direct "injection" into the boundary layer is the dominant mechanism for the presence of coolant gas close to the wall, rather than lateral diffusion of coolant from a jet that is only traversing the boundary layer. Which mechanism is predominant may be completely different from one injection geometry to another. All cooling configurations used in this study have injection that is partly aligned with the flow direction due to the hole orientation, i.e., "direct" injection may play the most important role, and consequently the film effectiveness decreases with increasing Mach number.

Local Heat Transfer. Detailed surface distributions of nondimensionalized heat transfer $Nu_D/Re_D^{0.5}$ are given in Fig. 9 for the low Mach number case, and in Fig. 10 for the high Mach number case. The corresponding spanwise-averaged data are shown in Figs. 11 and 12. It is apparent in the contour plots that zones of high cooling efficiency behind the holes also have high local heat transfer coefficients. Peak values of up to 3.5 occur for some cases. Around the hole exits, zones of increased heat transfer correspond to regions that are affected by three-dimensional conduction from the holes, as described before in the discussion of cooling effectiveness results. Looking at the spanwise-averaged $Nu_D/Re_D^{0.5}$ in Figs. 11 or 12, the overall level of the curves for angles up to 45 deg is about $Nu_D/Re_D^{0.5}$ = 2–2.5, with strong fluctuations around the injection openings. A detailed quantitative discussion of spanwise averaged heat transfer results within the showerhead (i.e., surface angles < 45 deg) is not done here, since interpretation of the small differences is difficult, in particular due to the high uncertainty in the near hole regions. Downstream of the actual

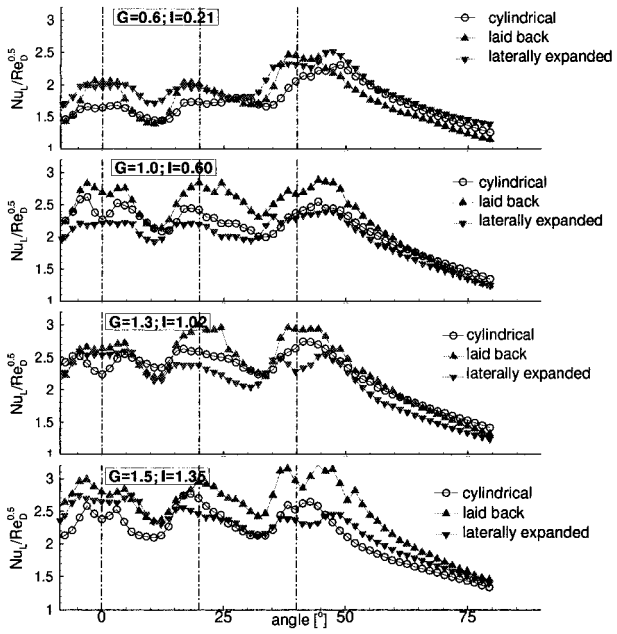

Fig. 11 Spanwise-averaged heat transfer at low Mach number (M = 0.14; Re_D = 8.6e4)

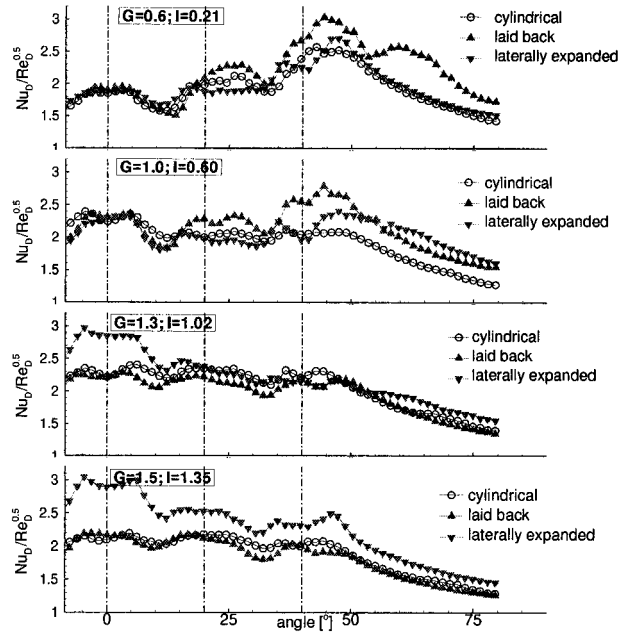

Fig. 12 Spanwise-averaged heat transfer at high Mach number (M = 0.26; Re_D = 1.55e5)

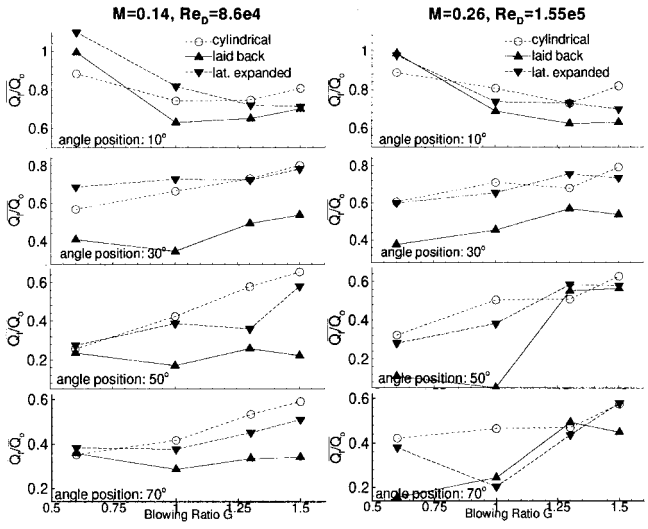

Fig. 13 Comparison of cooling schemes: spanwise averaged heat flux ratio at discrete surface positions

showerhead ($\gamma > 45$ deg) the differences between the three cooling configurations are rather small at low Mach number, compared to pronounced differences in cooling effectiveness. Only for the $G = 1.5$ the heat transfer is clearly staggered, being the highest for laid back holes, followed by laterally expanded and cylindrical holes. Maximum values of $Nu_D/Re_D^{0.5} = 2.5$–2.8 occur at 50 deg, running out to very similar values of $Nu_D/Re_D^{0.5} = 1$ at $\gamma = 80$ deg. At high Mach number, distinct differences in heat transfer occur at $G = 0.6$ and 1.0, but less pronounced at $G = 1.3$ and $G = 1.5$. Generally, laterally expanded and laid back holes show higher values.

Cooling Performance. An evaluation of the cooling performance cannot be done solely on the basis of the cooling effectiveness, or the heat transfer, since film cooling involves two adverse effects: reduced effective fluid temperature at the wall on one hand, but also strong mixing and associated increased local heat transfer on the other hand. Therefore, the cooling configurations are compared in terms of the local heat flux ratio Q_f/Q_0, which relates the local heat flux of the cooled model with an uncooled case, which allows the evaluation of the actual benefit of the film cooling, according to Mehendale et al. (1994)

$$\frac{Q_f}{Q_0} = \frac{\alpha_f}{\alpha_0}\left(1 - \frac{\eta}{\Phi}\right) \tag{6}$$

with the overall cooling effectiveness ϕ defined as

$$\Phi = \frac{T_w - T_g}{T_c - T_g} = 0.5 - 0.7 \tag{7}$$

In reality, ϕ varies over the surface, depending on the main flow conditions, cooling parameters, etc., and this distribution is not known. For this study, one representative value of $\phi = 0.6$ was chosen in order to have an indicator of cooling performance. Figure 13 shows the spanwise-averaged heat flux ratio $\overline{Q_f/Q_0}$ at four discrete angular positions: 10, 30, 50, and 70 deg. The first three locations were chosen to be far enough from the hole exits to avoid three-dimensional conduction effects, and close enough to a respective cooling row to show the influence of only this cooling station, aiming to discuss separately the individual cooling rows. The graphs on the left-hand side contain results for the low Mach number case, and on the right-hand side for the high Mach number case. The last position at $\gamma = 70$ deg is far downstream of the showerhead. For completeness, Fig. 14 contains the corresponding spanwise-averaged effectiveness.

It is observed that at $\gamma = 10$ deg, the heat flux can be reduced by the greatest amount for intermediate blowing ratio with cylindrical and laid back holes, whereas a continuous decrease of the heat flux ratio is seen for laterally expanded holes. The laid back holes at $G = 1.0$ perform best where the heat flux is actually reduced to 65 percent with respect to the uncooled case.

Behind row 2, at $\gamma = 30$ deg, laid back holes perform clearly better, with a minimum value of down to 0.35 at $G = 1.0$, compared to 0.55 or 0.7 for cylindrical and laterally expanded holes, which occur at low blowing values of $G = 0.6$.

Behind row 4, at $\gamma = 50$ deg, heat flux ratio is similar for all three hole types at $G = 0.6$, but cooling performance gets worse when increasing G for cylindrical and laterally expanded holes. Only the laid back type stays at very low levels of $\overline{Q_f/Q_0} = 0.2$.

Far downstream of the showerhead, at $\gamma = 70$ deg, the behavior is comparable to the 50 deg station, but with more regularly staggered heat flux ratio when increasing coolant injection.

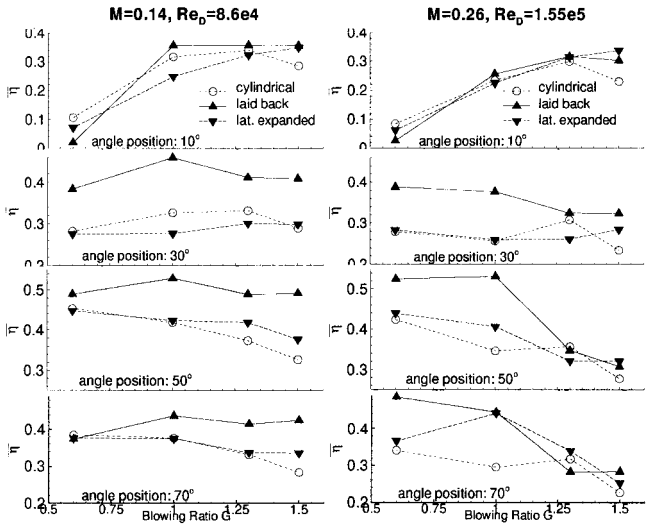

Fig. 14 Comparison of cooling schemes: spanwise averaged film cooling effectiveness at discrete surface positions

Generally, there are two adverse phenomena that are apparent:

1 *Higher cooling effectiveness associated with reduced heat flux,* as can be seen at an angular position of 10 deg (plots on top of Figs. 13 and 14). This may be explained with the presence of more coolant in proximity of the wall, without introducing excessive additional mixing, hence only little rise of the heat transfer coefficient. In that case, the effect of the reduced fluid temperature is predominant and the heat flux is lower.
2 *High cooling effectiveness combined with stagnating or even rising heat flux,* as it is the case at an angular position of 50 deg (third line of plots in Figs. 13 and 14). Here, the introduction of more coolant into the boundary layer seems to cause considerable additional mixing, associated with strongly increased heat transfer coefficients. In that case, the mixing effect is dominant to the point that it outweighs the favorable effect of the lower fluid temperature at the wall. This results in increased heat flux.

Which one of these two effects is dominant depends on the local injection situation.

Conclusions

Heat transfer and film cooling experiments were performed on a cylinder model comparing three cooling configurations in showerhead arrangement, at two free-stream flow conditions, $M = 0.14$ and 0.26, at an elevated turbulence intensity of $Tu = 7$ percent. The cooling configurations consist of five-row arrangements of cylindrical holes with both streamwise compound angle and orientation, and three different exit shapes.

Detailed film cooling efficiency and local heat transfer were presented, and the performance of the cooling schemes was compared in terms of heat load ratio with respect to an uncooled cylinder. The complex character of the formation of cooling films was shown, which is essentially governed by the jet lift-off tendency at high coolant injection rates at downstream positions, whereas right at the stagnation point film formation functions very differently. For some cases, an effect of attachment of jets by upstream cooling rows was found, illustrating the importance of the interaction of individual cooling rows for showerhead cooling.

It was found that holes with laid back type widened exits clearly enhance the overall cooling performance of the showerhead, compared to classical cylindrical holes. This was primarily associated with better lateral spread of the individual cooling jets, and with a considerably reduced tendency of jet detachment at higher blowing due to the diffuser effect. Laterally expanded holes performed better than cylindrical holes, but not as well as laid back shaped holes.

Acknowledgments

This study was done within the Brite/EuRam 4th framework, and was funded by the Swiss government. The authors would like to thank all partners of the Brite/Euram 4th framework for their permission for publication.

References

Beeck, A., Fottner, L., Benz, E., and Wittig, S., 1993, "The aerodynamic effect of coolant ejection in the leading edge region of a film cooled turbine blade," *Heat Transfer and Cooling in Gas Turbines,* Vol. AGARD-CP-527, Paper 35.

Bittlinger, G., Schulz, A., and Wittig, S., 1994, "Film cooling effectiveness and heat transfer coefficients for slot injection at high blowing ratios," ASME Paper No. 94-GT-182.

Drost, U., and Bölcs, A., 1999, "Investigation of Detailed Film Cooling Effectiveness and Heat Transfer Distributions on a Gas Turbine Airfoil," ASME JOURNAL OF TURBOMACHINERY, Vol. 121, pp. 233–232.

Drost, U., Bölcs, A., and Hoffs, A., 1997, "Utilization of the Transient Liquid Crystal Technique for Film Cooling Effectiveness and Heat Transfer Investigations on a Flat Plate and a Turbine Airfoil," ASME Paper No. 97-GT-26.

Giebert, D., Gritsch, M., Schulz, A., and Wittig, S., 1997, "Film-Cooling Holes With Expanded Exits: A Comparison of Computational Results With Experiments," ASME Paper No. 97-GT-163.

Goldstein, R. J., and Eckert, E. R. G., 1973, "Effects of hole geometry and density on three-dimensional film cooling," *Journal of Heat and Mass Transfer,* Vol. 17, pp. 595–607.

Gritsch, M., Schulz, A., and Wittig, S., 1998, "Adiabatic Wall Effectiveness Measurements of Film-Cooling Holes With Expanded Exits," ASME JOURNAL OF TURBOMACHINERY, Vol. 120, pp. 549–556.

Hoffs, A., Drost, U., and Bölcs, A., 1997, "An Investigation of Effectiveness and Heat Transfer on a Showerhead-Cooled Cylinder," ASME Paper No. 97-GT-69.

Mehendale, A. B., and Han, J.-C., 1993, "Reynolds number effect on leading edge film effectiveness and heat transfer coefficient," *Int. Journal of Heat and Mass Transfer,* Vol. 36, No. 15, pp. 3723–3730.

Mehendale, A. B., Ou, S., Han, J.-C., and Lee, C. P., 1994, "Unsteady Wake over linear turbine blade cascade with air and CO_2 film injection: Part II—Effect on film effectiveness and heat transfer distributions," ASME JOURNAL OF TURBOMACHINERY, Vol. 116, pp. 730–737.

Vedula, R. J., and Metzger, D. E., 1991, "A method for the simultaneous determination of local effectiveness and heat transfer distributions in three-temperature convection situations," ASME Paper No. 91-GT-345.

Wittig, S., Schulz, A., Gritsch, M., and Thole, K. A., 1996, "Transonic Film-Cooling Investigations: the Effects of Hole Shapes and Orientations," ASME Paper No. 96-GT-222.

An Infrared Technique for Evaluating Turbine Airfoil Cooling Designs

P. C. Sweeney
Rolls-Royce Allison,
Indianapolis, IN 46206

J. F. Rhodes
Allison Advanced Development Company,
Indianapolis, IN 46206

An experimental approach is used to evaluate turbine airfoil cooling designs for advanced gas turbine engine applications by incorporating double-wall film-cooled design features into large-scale flat plate specimens. An infrared (IR) imaging system is used to make detailed, two-dimensional steady-state measurements of flat plate surface temperature with spatial resolution on the order of 0.4 mm. The technique employs a cooled zinc selenide window transparent to infrared radiation and calibrates the IR temperature readings to reference thermocouples embedded in each specimen, yielding a surface temperature measurement accuracy of ±4°C. With minimal thermocouple installation required, the flat plate/IR approach is cost effective, essentially nonintrusive, and produces abundant results quickly. Design concepts can proceed from art to part to data in a manner consistent with aggressive development schedules. The infrared technique is demonstrated here by considering the effect of film hole injection angle for a staggered array of film cooling holes integrated with a highly effective internal cooling pattern. Heated free stream air and room temperature cooling air are used to produce a nominal temperature ratio of 2 over a range of blowing ratios from 0.7 to 1.5. Results were obtained at hole angles of 90 and 30 deg for two different hole spacings and are presented in terms of overall cooling effectiveness.

Introduction

The demands of tomorrow's increasingly aggressive gas turbine engine cycles continue to drive the evolution of advanced hot section cooling designs. The objectives of increased cycle efficiencies, higher engine thrust-to-weight ratio, and extended component life require improved turbine cooling designs that use less cooling air more effectively. Today, however, these long-standing goals are accompanied by the challenge of designing cooled turbine components that can also be manufactured more affordably. Simplified double-wall film-cooled designs, based on the highly effective Lamilloy® quasi-transpiration cooling concept, are currently under development to meet these needs for the next generation of military and commercial gas turbine applications.

Modern experimental techniques play an important role in this development process, both in preliminary design concept screening and as an important source of validation data for heat transfer design analysis tools (Moon and Glezer, 1996). The present paper describes an experimental approach that combines rapid prototyping of easily tested large-scale flat plate specimens with a highly productive infrared (IR) temperature measurement technique. This approach is used to assess the relative cooling performance of several design concepts in a cost-effective and timely manner, and to identify the most promising combinations of various internal cooling features and film hole geometries. This paper emphasizes the details and benefits of the IR measurement technique and reports the effect of film hole injection angle demonstrated by this technique for a baseline design geometry.

A relatively small number of investigators have used infrared imaging techniques (also referred to as "quantitative infrared thermography") in the past several years to measure flat plate surface temperatures in film cooling experiments. However, the benefits and practical details of implementing this technique have not been universally emphasized in the film cooling literature.

Contributed by the International Gas Turbine Institute and presented at the 44th International Gas Turbine and Aeroengine Congress and Exhibition, Indianapolis, Indiana, June 7–10, 1999. Manuscript received by the International Gas Turbine Institute February 1999. Paper No. 99-GT-142. Review Chair: D. C. Wisler.

Scherer et al. (1991) measured surface temperature distribution on a constant heat flux surface using an AGEMA Thermovision 870 camera with a spectral range of 2 to 5 μm. The camera viewed the test surface through a 240 mm diameter CaF_2 window, yielding an image of 140 pixels square with a spatial resolution of 3 pixels per mm. Martiny et al. (1995) measured the adiabatic effectiveness of an effusion-cooled test surface by viewing through a sapphire window with an infrared camera. The free stream-to-coolant temperature ratio was 1.7 at a free stream temperature of 272°C. The model and spectral range of the camera were not specified, but the image array size was also 140 × 140 pixels. Wittig et al. (1996) investigated shaped hole film cooling heat transfer and adiabatic effectiveness in transonic flow using a sapphire window and the same AGEMA 870 camera. Martiny et al. (1997a) continued with the same technique and equipment to investigate the heat transfer and adiabatic effectiveness of a single wall jet. All but one of these investigations used the inherent two-dimensional advantage of the IR imaging technique to present informative contour plots of temperature, adiabatic effectiveness, and/or heat transfer distributions.

Sen et al. (1996) measured film cooling heat transfer for compound angle holes using an Inframetrics infrared imaging system. In a related work, Schmidt et al. (1996) investigated adiabatic effectiveness of compound angle holes using cryogenically cooled cooling air to produce a free stream-to-coolant temperature ratio of 1.6. No mention was made of an IR technique. However, Schmidt et al. (1996a, b) did discuss the infrared technique used to measure surface temperatures in investigations of surface roughness and free-stream turbulence on heat transfer and adiabatic effectiveness, and further specified the camera model as an Inframetrics 600L. The free stream-to-coolant temperature ratio for these two studies was 2.0, produced using cryogenically cooled cooling air. No details were given about how optical access to the test surface was achieved. Unfortunately, none of these four works presented data in the form of the two-dimensional contour plots made possible by IR imaging techniques.

Reilly (1996) and co-workers measured the overall cooling effectiveness of full coverage (or "multi-hole") film cooled panels using an

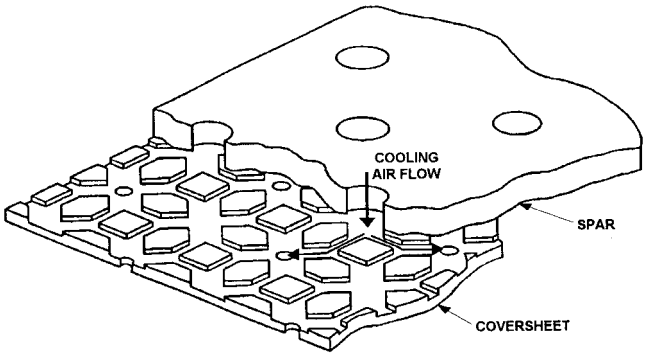

Fig. 1 Lamilloy® snowflake design

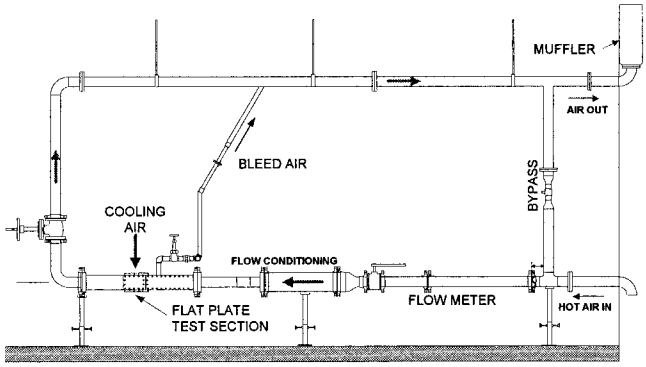

Fig. 2 The flat plate rig uses electrically heated air to simulate the proper free stream-to-coolant temperature ratio

Inframetrics 525 camera with a spectral range of 8 to 12 μm. The test surface was viewed through a zinc selenide window, transparent to infrared radiation in the 8 to 12 μm range. Data are presented as span-averaged overall effectiveness versus streamwise location on the panel.

The infrared imaging techniques described in the studies cited above all have several features in common. In each case, the test surface was painted with a high-emissivity flat black paint. In each case, the required optical access to the test surface was achieved by installing some type of IR-transmissive window in a wall of the flow channel. And, in each case, the infrared temperature measurements were calibrated to thermocouples embedded in or attached to the metallic test surface, under actual operating conditions. This procedure not only corrects for the emissivity of the flat black paint and the transmissivity of the viewing window, but also accounts for the peculiarities of the overall radiative environment unique to a particular setup.

The present study builds on the IR techniques described above to investigate the overall cooling effectiveness of a Lamilloy "snowflake" cooling design applied to a flat plate specimen. The snowflake design is illustrated in Fig. 1. Data from this specimen are used as a baseline for comparison to new designs that reduce the quantity and complexity of hole patterns and internal features, making them less costly to manufacture. The data are also useful for improving the predictive capabilities of the in-house Lamilloy design optimization system (LAMILOPT), as new design features depart from the better-understood aspects of the designs in current use.

Overall effectiveness, $(T_g - T_s)/(T_g - T_c)$, is an appropriate measure of cooling performance for the highly coupled combination of internal impingement, through-the-wall conduction, and full-coverage film cooling found in double-wall film-cooled designs such as Lamilloy. Martiny et al. (1997b) analytically demonstrated the coupled nature of heat transfer in an effusion cooled combustor wall and presented results in terms of overall cooling effectiveness. Furthermore, the two-dimensional imaging capability of the IR technique provides quantitative information about the relative effects of internal convection, internal conduction, and film cooling on the net surface temperature of the specimen. The terms overall effectiveness and effectiveness will be used interchangeably throughout this report.

Facility and Instrumentation. Flat plate cooling performance was measured using an existing flat plate heat transfer facility (see Fig. 2) modified to provide optical access for two-dimensional infrared (IR) measurement of specimen surface temperatures. Overall cooling effectiveness, η, is calculated directly from measured steady-state values of specimen surface temperature, free stream temperature, and cooling air temperature. The flat plate facility uses electrically heated air at a nominal temperature of 427°C and cooling air at 45–95°C to produce a free stream-to-coolant temperature ratio in the range 1.9–2.2, and a free stream Reynolds number (Re_L) ranging from 1.0×10^6 to 1.8×10^6, representative of actual engine conditions. The boundary layer is removed immediately upstream of the flat plate specimen by venting the air through a perforated plate. A trip strip is installed between the perforated plate and the leading edge of the specimen to ensure a fully turbulent boundary layer over the specimen surface. Boundary layer bleed flow, cooling air flow, and free stream hot air flow are measured with ASME orifice tube flow meters. Free-stream flow rate is also calculated from a total pressure rake and static pressure wall taps 30 cm upstream of the flat plate leading edge. Free stream air temperature is measured by a five-element shielded thermocouple rake spanning the center of the flow channel height 28 cm upstream of the leading edge of the specimen. Uncertainty in the precision of the hot gas temperature measurement is estimated at 5°C. Cooling air temperature is measured by a six-element rake of closed-tip thermocouple wires positioned inside the cooling air plenum approximately 25 mm upstream of the back side of the specimen. An uncertainty in the precision of the cooling air temperature measurement of 10°C was estimated by calculating the worst case standard deviation of the six thermocouple readings.

Specimen Design and Preparation. Martiny et al. (1997b) have shown, in an analytical parametric study, that the ratio of

Nomenclature

D = film (hot side) hole diameter
G_c^* = dimensionless coolant mass flux
L = specimen length
Ma = Mach number
Nu = Nusselt number
P = static pressure
P_t = total pressure
Pr = Prandtl number
Re = Reynolds number
S = diagonal hole spacing
St = Stanton number
T = temperature
X = streamwise location
Y = spanwise location
W = mass flow rate
α = film hole injection angle
η = overall effectiveness = $(T_g - T_s)/(T_g - T_c)$
Δ = measurement uncertainty

Subscripts

b = boundary layer bleed
g = free stream
c = coolant, upstream of test specimen
L = having specimen length L as characteristic dimension
s = specimen surface

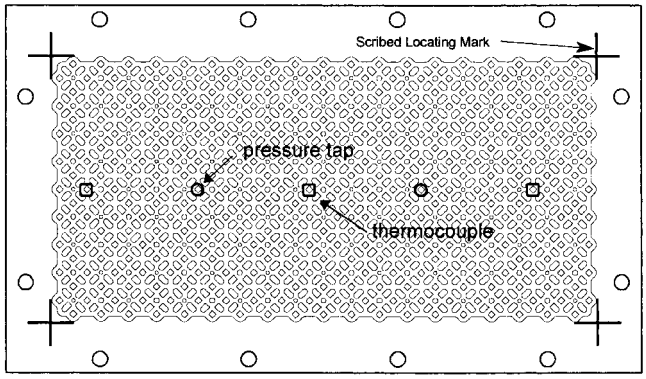

Fig. 3 Specimen preparation involves installing instrumentation and scribing locating marks

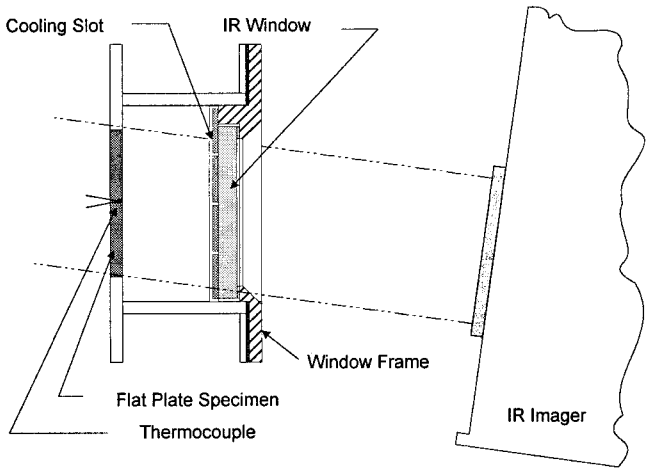

Fig. 4 A film of air is used to cool the ZnSe window

convective to conductive heat transfer (Biot number) in an effusion cooled panel has a strong influence on overall cooling effectiveness. To the extent that convection and conduction are even more strongly coupled in a typical Lamilloy design, it is very important that an experimental approach achieve reasonable Biot number similitude. Because the experiment is run at temperatures and pressures significantly below actual engine conditions, the convective heat transfer in the test specimen is approximately three times lower than in the engine. The thermal conductivity of 6-4 titanium is about 2.5 times lower than the cast nickel-base superalloys typically used in turbine airfoil applications, and three times lower than wrought cobalt-based materials. Therefore, selecting 6-4 titanium for the specimen material produces an experimental Biot number that is from 83 to 100 percent of the actual engine conditions. Applying the worst case (83 percent) discrepancy to the results of Martiny et al. (1997b) yields an uncertainty in overall effectiveness of about 3 percent. Titanium has the added benefits of being easy to machine and easy to join by welding or brazing processes.

The flat plate specimens used in this study are approximately three times larger than actual engine scale and have overall dimensions of 17.8 cm long by 10.2 cm wide by 0.64 cm thick. Specimens were fabricated by machining internal cooling passages and impingement holes in a thick spar sheet (cold side) and film holes in a thinner cover sheet (hot side), and furnace brazing the two halves together. The portion of the specimen that contains the cooling features is roughly 15 cm by 7.6 cm, leaving a solid perimeter 2.5 cm wide for mounting the plate to the coolant plenum. After brazing, each plate was ultrasonically inspected for bond integrity and flow tested to detect any blocked holes or passages. As shown in Fig. 3, three closed-tip thermocouples and two static pressure taps were inserted into holes drilled through the center of internal pedestals (normal to the plate surface), and laser welded around their perimeter at the plate surface to create good thermal contact with the plate material.

After instrumentation, the specimen surface was painted with heat-resistant flat black paint and allowed to dry for no less than 12 hours before curing the paint by baking the plate at 260°C for 1 hour. The curing step produces a finish that will remain uniform regardless of subsequent temperature variations encountered in the actual testing process. Considerable effort was involved in selecting a paint that satisfied this requirement. Locating marks are scribed on the painted surface near the four corners of each plate to indicate the perimeter of the internal cooling passages, as illustrated in Fig. 3.

Measurement Technique. A Thermal Image Processor (TIP) system from Bales Scientific Inc. was used to make high-resolution two-dimensional infrared measurements of specimen temperatures in the flat plate rig. The TIP system yields direct pixel-by-pixel temperature measurements without the difficulty of recording a video image, grabbing frames, or converting gray scale levels to temperature values in separate processes. The TIP system uses a HgCdTe detector cooled by liquid nitrogen and has a spectral range of 10 to 12 μm. The Bales TIP system uses two internal blackbody temperature references, no-drift circuitry, and a specialized factory calibration procedure to achieve a minimum detectable temperature difference of 0.1°C.

The flat plate rig is oriented with the test surface in a vertical position, which allows the IR imager to be placed conveniently on a horizontal surface adjacent to the rig. The distance between the front face of the camera and the specimen surface is approximately 25 cm. A radiation barrier with an opening for the viewing aperture is placed between the rig and the imager to shield the body of the unit from the heat of the flow channel. The resulting image size for this arrangement was generally 360 by 180 pixels, with a spatial resolution of 0.4 mm per pixel. An integrated computer system stores recorded images on the system hard drive.

Optical access for IR measurement of flat plate specimen surface temperatures is provided by a 8.9 cm wide, 16.5 cm long, 0.95 cm thick zinc selenide window installed in the flow channel wall opposite the specimen surface, as shown in Fig. 4. The window is coated with a broad band anti-reflective coating to maximize infrared transmission in the 10–12 μm wavelength range. The IR imager was tilted slightly, as shown in Fig. 4, to avoid reflection of the cryogenic detector off the window and back into the camera, creating an artificial "cold spot" on the specimen image.

Because the maximum service temperature of the coated window material is 200°C, as recommended by the manufacturer, the inside surface of the window is cooled with a film of air injected at room temperature. Although Reilly (1996) successfully used an uncoated zinc selenide window at a hot gas temperature of 315°C without cooling, the transmissivity of uncoated zinc selenide is on the order of 0.6, compared to 0.95 for a coated window. Slot film cooling correlations by Ballal and Lefebvre (1972, 1973) and Stollery and El-Ehwany (1967) were used to determine the appropriate slot height, slot lip thickness, and coolant flow rate range required to cool the window adequately using room temperature air. Preliminary experiments using an instrumented stainless steel plate in place of the window (with thermal conductivity very close to that of zinc selenide) verified that the window slot cooling design would keep the window surface below its maximum operating temperature of 200°C. The left-most surface of the cooling slot shown in Fig. 4 (closest to the specimen) is flush with the upstream wall of the flow channel. The cooling slot streamwise exit plane just overlaps the upstream edge of the viewing window, holding the window in place against the exterior window frame.

Accurate infrared surface temperature measurements were achieved by calibrating temperature readings from the IR imager with thermocouples installed in a flat plate calibration specimen

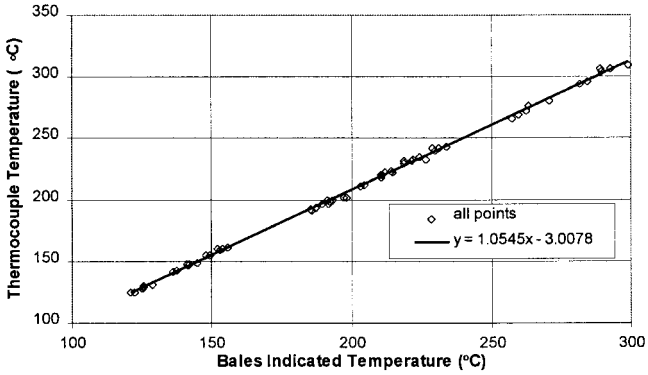

Fig. 5 The IR temperature calibration has an uncertainty of less than 4°C

prior to testing actual specimens. The calibration plate was fabricated from copper alloy 101 and thermocouples were embedded in lengthwise slots along the back surface of the plate to minimize conduction losses through the thermocouple leads. A row of 3.2-mm-dia angled holes was drilled at the downstream end of the plate to discharge cooling flow from the back side of the plate. The surface of the plate exposed to the hot air flow was painted with heat resistant flat black paint.

Steady-state calibration data were acquired over a range of plate temperatures from 100 to 315°C at free stream gas temperatures of 200, 315, and 427°C. The plate temperature was varied at each hot gas temperature by adjusting the cooling air flow over the back surface of the plate. Each data point was acquired by recording simultaneous readings from the infrared imager and calibration plate thermocouples. Figure 5 shows the actual metal temperature of the copper calibration plate as measured by the embedded thermocouples plotted versus the Bales TIP-indicated temperature. Based on the least-squares linear fit of the data points, the maximum uncertainty in this calibration is less than 4°C.

The combined influence of surface, coolant, and free-stream temperature measurement uncertainties on the error in the overall effectiveness measurement was calculated using the method of error propagation described by Dieck (1992). The results of this analysis are shown in Fig. 6 as a function of overall effectiveness level. Figure 6 shows that the uncertainty in effectiveness decreases as the free stream-to-coolant temperature ratio increases from 1.9 to 2.2 (increasing the free stream-to-coolant temperature difference from 332 to 382°C). Furthermore, Fig. 6 illustrates that increasing free stream temperature from the value of 327°C used by Wittig et al. (1996) to the value of 427°C used in the current study also decreases uncertainty.

The infrared temperature measurement technique has several advantages over the traditional thermocouple approach to surface

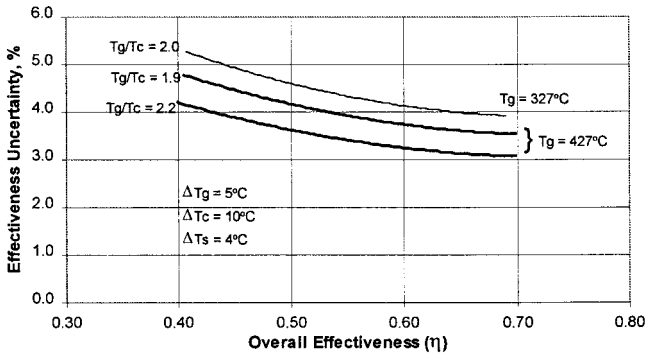

Fig. 6 Increasing free stream-to-coolant temperature difference reduces uncertainty of effectiveness measurement

Table 1 The test matrix evaluates the effect of coolant flow and Re_L on overall effectiveness

T_g/T_c (±0.15)	Ma_g (±0.005)	Re_L (±0.02 x 10^6)	P_c/P_{tg} (±0.01)
2	0.5	1.0 x 10^6	0.90, 0.95, 1.00, 1.05, 1.10
2	0.5	1.5 x 10^6	0.90, 0.95, 1.00, 1.05, 1.10
2	0.5	1.8 x 10^6	0.90, 0.95, 1.00, 1.05, 1.10

temperature measurement. An obvious advantage is the full coverage two-dimensional temperature image with pixel size spatial resolution, eliminating all but two or three thermocouples from each specimen. This reduces instrumentation costs and speeds specimen preparation and installation time, while increasing the quantity of temperature data by three orders of magnitude. Another benefit of this technique is the improved accuracy of the IR technique over embedded thermocouples when a careful temperature calibration is performed to relate infrared temperature readings to actual metal temperature. The thin coversheet associated with typical Lamilloy designs makes it difficult to embed even the smallest thermocouple leads in grooves along the hot surface of the plate. In past experiments, the only alternative has been a "through-the-wall" thermocouple installation prone to conduction errors. Both thermocouple techniques alter the heat conduction path through the specimen to some extent. The IR technique is completely nonintrusive in this respect, and requires only a coat of heat-resistant flat black paint.

Experimental Procedure. The overall cooling effectiveness of each flat plate specimen was measured over the range of free stream and coolant flow conditions shown in Table 1. The variability allowed in setting each of the run conditions is shown in parenthesis below the column headings. Furthermore, the free stream temperature was allowed to vary from the target value of 427°C (at $Re_L = 1.0 \times 10^6$ and $Re_L = 1.5 \times 10^6$) to 400°C (at $Re_L = 1.8 \times 10^6$), as long as the parameters in Table 1 were held to the stated tolerances. Cooling air flow was varied by adjusting the coolant-static-to-free stream-total pressure ratio over a range typical of actual engine conditions. The range of pressure ratios listed in Table 1 corresponds to blowing ratios from approximately 0.7 to 1.5. Decreasing the cooling air flow rate typically resulted in a small rise in cooling air temperature, causing the nominal free stream-to-coolant temperature ratio to vary by as much as ±7 percent. This variation was considered sufficiently small that additional measures to control cooling air temperature were not pursued.

The test matrix shown in Table 1 is designed to assess the effect of coolant flow rate and free stream Reynolds number on cooling effectiveness for each flat plate specimen. Acquiring each data point involved adjusting the run conditions as required, and then recording readings simultaneously from the TIP system and the PC-based data acquisition system. Data recorded with the PC system (air temperatures, flow rates, pressures) were averaged over a three-minute period, while IR image data recorded once every 2 seconds with the TIP system (two-dimensional surface temperatures) were averaged over a one-minute period, as shown in Fig. 7. (Averaging the IR data over the entire three-minute period would have resulted in excessive data file size.)

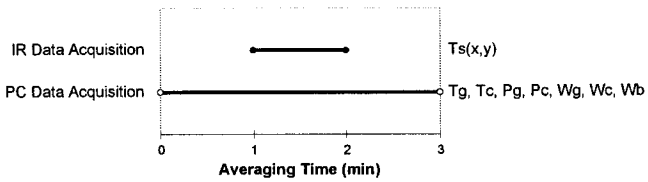

Fig. 7 Infrared surface temperatures and rig flow conditions are recorded simultaneously

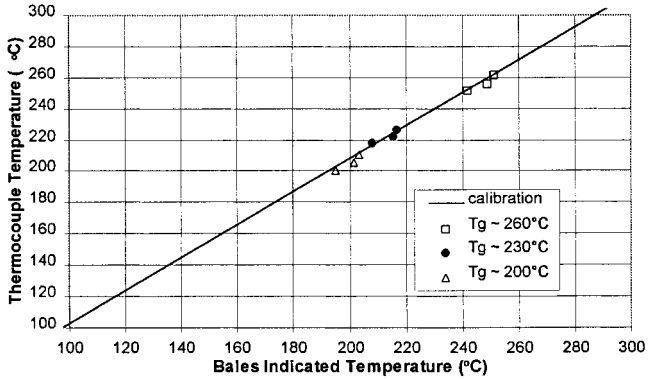

Fig. 8 Calibration checks for each specimen with no cooling flow ensure temperature measurement accuracy (specimen 1 is shown here)

Before starting the test matrix for a particular specimen, the size and position of the IR image displayed on the TIP system computer monitor was adjusted to match the portion of the specimen inside the scribed locating marks. This step defines the surface area for which temperatures will be recorded by the TIP system and establishes a spatial reference between the recorded IR temperature data and the specimen plate internal geometry. The size and position of the IR image were not changed as data acquisition progressed through the test matrix. The registration uncertainty between recorded image and actual plate features is estimated at 1.6 mm.

In addition to the 15 test matrix data points for each specimen, three IR calibration check points were also recorded for each flat plate specimen, using the three thermocouples installed in each of the specimen plates. Because these thermocouples are inserted through highly cooled internal pedestals normal to the plate surface, this installation is quite vulnerable to conduction errors through the thermocouple lead. Therefore, measurements from these thermocouples were considered valid only when the specimen was at thermal equilibrium with no cooling air flowing through the plate. Three of these no-coolant-flow "calibration check" data points were recorded for each specimen—two at the beginning of the test matrix, one at the end—at hot gas temperatures of 200, 260, and 230°C, respectively. In all cases, the calibration check points fell soundly on the line generated from the copper calibration plate, as shown in Fig. 8, ensuring the accuracy of the entire set of two-dimensional IR images recorded for a particular specimen. The calibration check is useful for identifying changes in the temperature calibration that may have been caused by degradation of the zinc selenide window or specimen paint finish over the duration of a test. However, after more than 50 hours of run time, no problems have been encountered with the durability of the zinc selenide window or paint finish.

Results

The results that can be obtained using the infrared technique and experimental procedure described above are demonstrated here by considering the effect of film hole injection angle for a staggered array of film cooling holes integrated with a highly effective internal cooling pattern. Overall cooling effectiveness results were obtained at hole angles of 90 and 30 deg for two different hole spacings, as summarized in Table 2. Specimen geometry is illustrated in Fig. 9. Note that impingement hole spacing is identical to but offset from the film holes.

Table 2 Summary of test specimen geometry

Specimen Number	Hole Spacing (S/D)	Film Hole Angle (α)
1	10.5	90°
2	10.5	30°
3	14.8	90°
4	14.8	30°

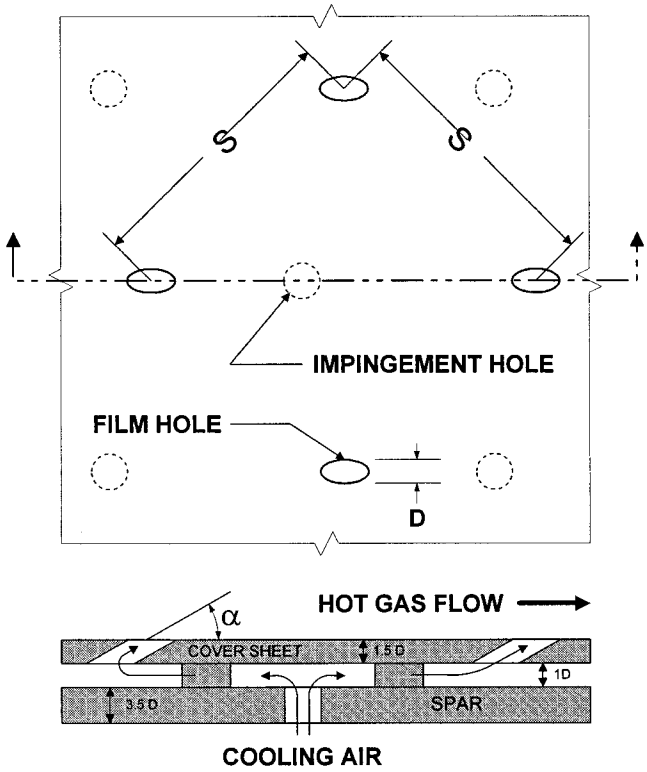

Fig. 9 Lamilloy hole geometry consists of staggered arrays of impingement and film holes.

Data Reduction. The two-dimensional surface temperature data recorded with the TIP system infrared imager for each flat plate specimen is combined with the corresponding free stream air and cooling air temperatures to calculate overall cooling effectiveness and is displayed as a two-dimensional contour plot, as shown in Fig. 10. The corners of the contour plot correspond to the locator marks scribed on the specimen plate and the edges of the plot correspond to the perimeter of the internal cooling pattern machined into the plate (see Fig. 3). The distance from the boundary layer trip to the upstream edge of the contour plot ($X/D = 0$) is $20D$. The regions of lower effectiveness around the edges of the plate can be attributed to heat conduction from the uncooled perimeter of the specimen.

For the purposes of making more quantitative comparisons of cooling performance among specimens, the two-dimensional ef-

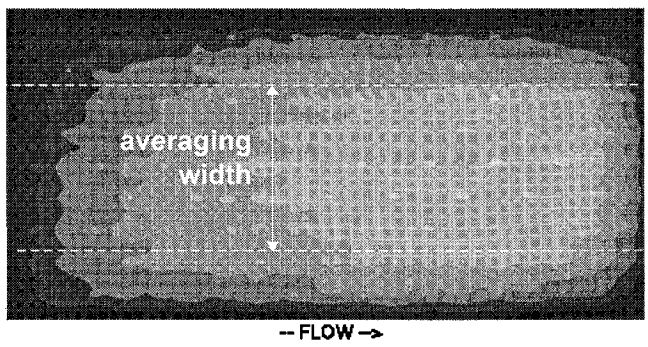

Fig. 10 A two-dimensional contour plot is useful for associating cooling performance with specific cooling design features

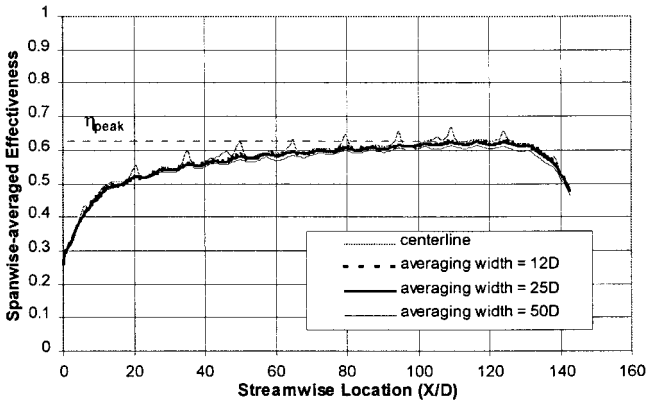

Fig. 11 Spanwise-averaged effectiveness values were independent of averaging width for all specimens tested

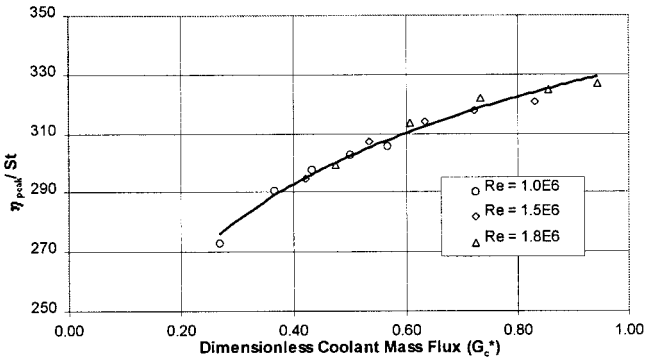

Fig. 13 Overall effectiveness is independent of Re_L when normalized by Stanton number

fectiveness data shown in Fig. 10 is used to calculate a spanwise-averaged effectiveness at one pixel increments in the streamwise direction. To eliminate the edge effects evident at the top and bottom of the contour plots, effectiveness values were averaged across a strip 24 hole diameters wide along the center of the plate rather than across the entire span. The width of the spanwise strip over which the data are averaged had a negligible influence on the averaged value for strip widths of 12, 24, and 48 hole diameters, as shown in Fig. 11.

Also shown in Fig. 11 is the local cooling effectiveness along the streamwise centerline of the plate (averaged over 1.5 hole diameters). The sharp periodic effectiveness peaks in the centerline curve indicate local areas of reduced surface temperature, as the IR imager "sees" into the 90 deg hot side holes to the cold side of the specimen plate. The two smaller peaks at $X/D \sim 45$ and $X/D \sim 105$ are pressure taps. The dashed line indicating the peak effectiveness value in Fig. 11 pertains to the spanwise-averaged data.

The peak spanwise-averaged effectiveness can be determined at each point in the test matrix, and plotted as a function of cooling air flow rate, as illustrated in Fig. 12 for specimen 1. This format allows comparison of various specimen designs on the basis of cooling air requirements. Coolant mass flux is presented in dimensionless terms to protect proprietary design information. The apparent influence of free-stream Reynolds number (Re_L) on overall effectiveness illustrated in Fig. 12 is, more appropriately, the influence of convective heat flux to the specimen surface from the free stream flow. For fully turbulent flow over a flat plate, Re_L is related to Stanton number by the expression:

$$St \equiv Nu_L/(Re_L\ Pr) = 0.0296\ Re_L^{-1/5}\ Pr^{-2/3} \qquad (1)$$

Normalizing the overall cooling effectiveness values in Fig. 12 by the turbulent flat plate Stanton number renders the data independent of Re_L, as shown in Fig. 13. Therefore, subsequent presentation of overall effectiveness data will be for the $Re_L = 1.5 \times 10^6$ case only.

Comparison. Span-averaged peak effectiveness levels of the four specimens tested in this investigation are plotted as a function of dimensionless cooling air flow rate and compared in Fig. 14. Presenting cooling performance data in this format readily identifies superior cooling designs and allows data points recorded at similar cooling air flow rates to be grouped together, as indicated by the dashed oval drawn on the plot. Grouping data points in this manner allows further comparison of various specimen design features at "constant" G_c^* using the contour plot and spanwise-averaged formats.

Comparison of the four specimen designs on the basis of spanwise-averaged peak effectiveness begins with the two baseline specimens, 1 and 3, indicated by the open symbols in Fig. 14. These curves indicate the cooling performance levels of the well-established Lamilloy "snowflake" design. Changing hot side hole angle from 90 deg in specimens 1 and 3 to 30 deg in specimens 2 and 4 produces improvement in cooling performance by enhancing hot side film coverage, as indicated by the solid symbols in Fig. 14. The improvement with 30 deg film holes is more pronounced for the smaller hole spacing ($S/D = 10.5$).

Baseline: Effect of Hole Spacing. Contour plots of overall cooling effectiveness for baseline specimens 1 and 3 are shown in Figs. 15(*a*) and 16(*a*), respectively. For each specimen, a drawing of the pedestal/hole pattern is shown directly beside each contour plot to associate design features with cooling performance. For example, the small round dots shown in a lighter color in Fig. 15(*a*) correspond to the hot side hole locations on specimen 1 illustrated in Fig. 15(*b*). The larger round dots of a slightly darker shade in Fig. 16(*a*) correspond to the cold side hole locations in

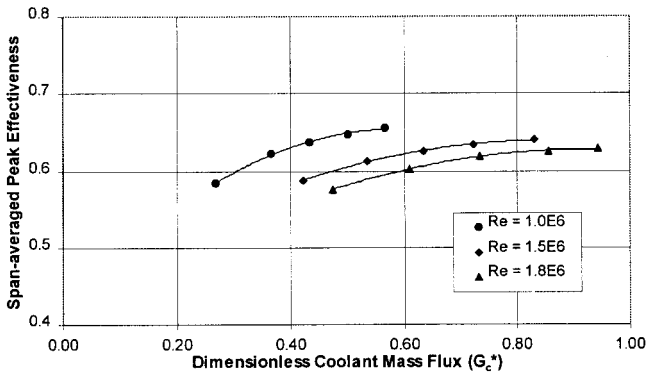

Fig. 12 The test matrix yields span-averaged peak effectiveness data at three free stream Reynolds numbers

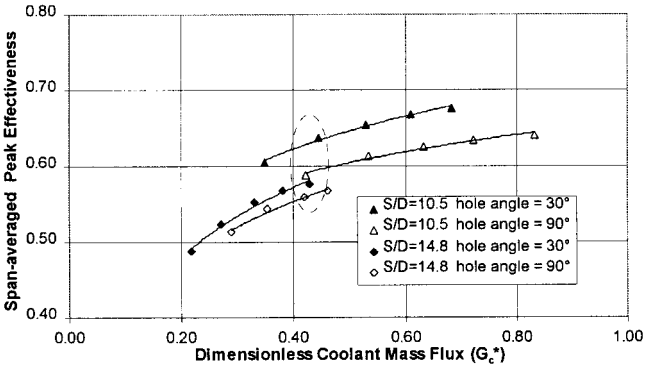

Fig. 14 A film hole angle of 30 deg improves cooling performance by enhancing hot side film coverage

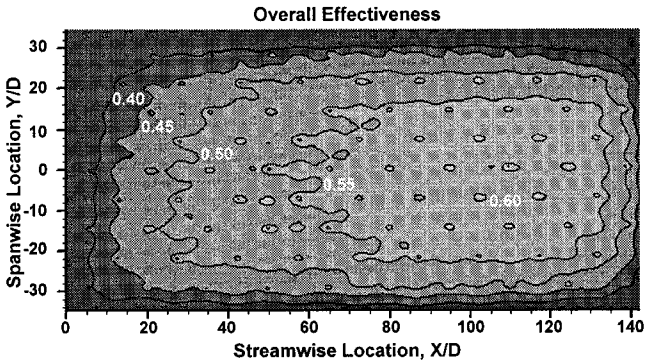

Fig. 15(*a*) Small dot-shaped areas of high effectiveness correspond to film hole locations

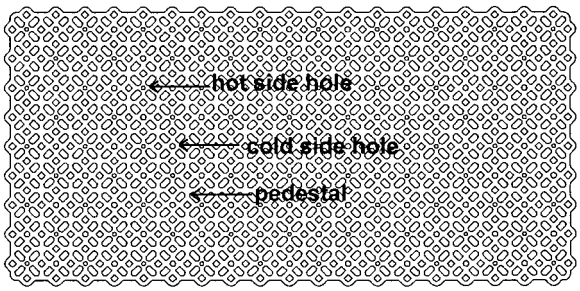

Fig. 15(*b*) Specimen 1 has film hole spacing of *S*/*D* = 10.5 and injection angle of 90 deg

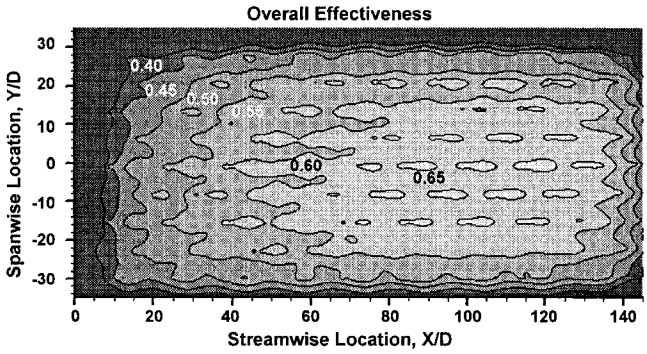

Fig. 17(*a*) Hole injection angle of 30 deg enhances cooling film build-up

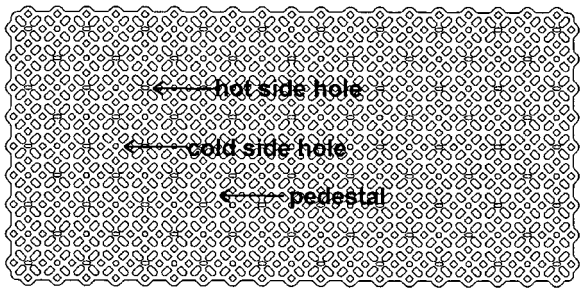

Fig. 17(*b*) Specimen 2 has film hole spacing of *S*/*D* = 10.5 and injection angle of 30 deg

specimen 3 and demonstrate the strong effect of impingement on overall cooling performance. As with specimen 1, the smaller dots in Fig. 16(*a*) indicate hot side or film holes. Comparison of Figs. 15(*a*) and 16(*a*) reveals that impingement zones are not as pronounced for specimen 1 because the closer spacing of the cold side holes produces a more uniform hot side metal temperature than the more sparsely spaced holes in the design of specimen 3. As expected, the effectiveness of the $S/D = 10.5$ hole spacing is significantly higher than the more sparse array of holes.

Effect of Angled Holes. Contour plots of overall cooling effectiveness for Lamilloy snowflake specimens 2 and 4 are shown in Figs. 17(*a*) and 18(*a*), respectively. The pedestal/hole pattern is shown directly below each contour plot. Comparing these plots to Figs. 15(*a*) and 16(*a*) illustrates the influence of 30 deg angled hot

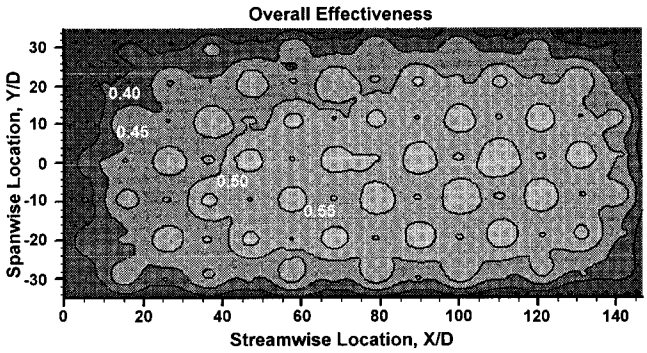

Fig. 16(*a*) Large dot-shaped areas of high effectiveness correspond to impingement hole locations

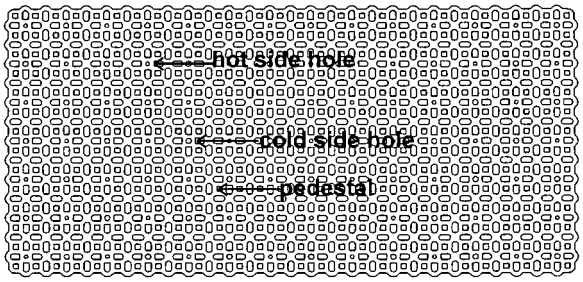

Fig. 16(*b*) Specimen 3 has film hole spacing of *S*/*D* = 14.8 and injection angle of 90 deg

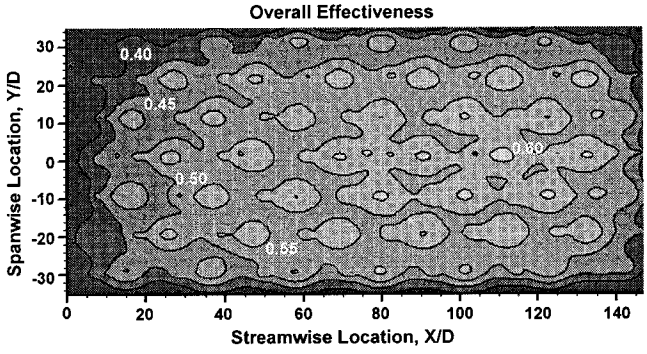

Fig. 18(*a*) Film coverage from angled holes augments effectiveness of impingement regions immediately downstream of film holes

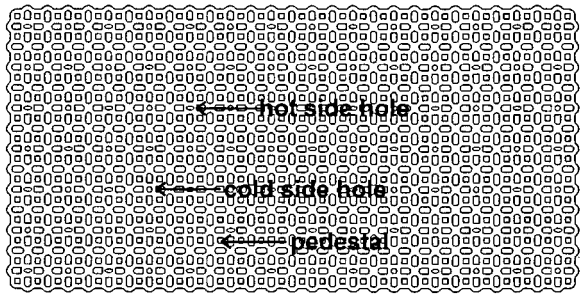

Fig. 18(*b*) Specimen 4 has film hole spacing of *S*/*D* = 14.8 and injection angle of 30 deg

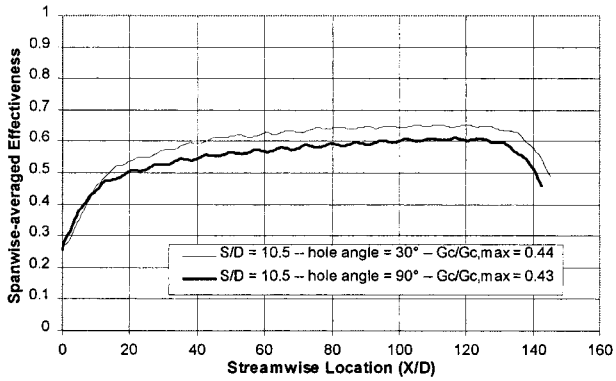

Fig. 19 Angled holes improve effectiveness by 10 percent for *S/D* = 10.5

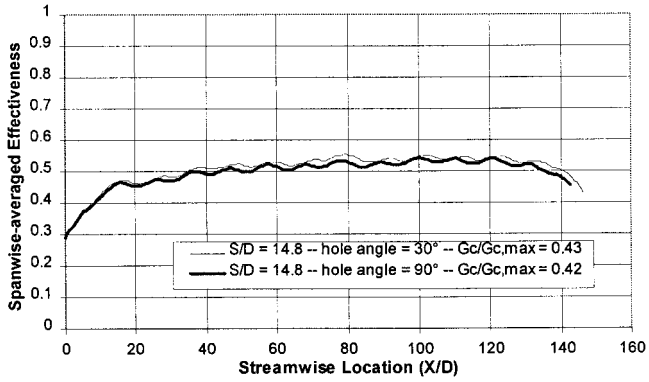

Fig. 20 Angled holes produce minimal improvement in effectiveness for *S/D* = 14.8

side holes on overall effectiveness. Improvement in the overall effectiveness level is most evident for specimens 1 and 2, where the closely spaced hot side holes enhance the development of full film coverage on the hot surface. While the angled holes also improve film coverage on the more sparse hot side hole pattern of specimens 3 and 4, the effect remains more localized. The contour plot in Fig. 18(*a*) also shows that film cooling from an angled hot side hole, positioned directly upstream of a cold side hole, enhances the overall effectiveness of the impingement zone produced by the cold side hole.

The quantitative influence of angled hot side holes on overall effectiveness level is more clearly demonstrated in Figs. 19 and 20, which plot spanwise-averaged effectiveness as a function of streamwise location for the $S/D = 10.5$ and 14.8 hole spacings, respectively. For the $S/D = 10.5$ designs, Fig. 19 shows that an overall effectiveness of 0.6 with normal hot side holes increases to 0.65 with 30 deg angled holes in the region $100 < X/D < 120$. However, angled holes for the $S/D = 14.8$ design produce negligible improvement, as shown in Fig. 20.

Conclusions

- An experimental approach that combines the application of double-wall film-cooled design concepts to flat plate specimens with an accurate, high-resolution IR temperature measurement technique is a cost effective way to identify promising designs in a timely manner, while gaining insight into the relative contribution of various design features to overall cooling performance.
- The elevated temperature of the free-stream flow and large coolant-to-free-stream temperature difference not only simulates the proper coolant-to-free-stream density ratio, but significantly reduces experimental uncertainty in the overall effectiveness derived from the measured temperature data. Good Biot number similitude between engine hardware and flat plate specimens was achieved by selecting 6-4 titanium alloy for the specimen material.
- Film holes angled at 30 deg improved the spanwise-averaged effectiveness of the normal hole Lamilloy snowflake design by approximately 10 percent, for the $S/D = 10.5$ hole spacing. However, film holes angled at 30 deg did not significantly influence the spanwise-averaged effectiveness of the normal hole design for the $S/D = 14.8$ hole spacing.

Acknowledgments

The authors are grateful to Dr. Nirm Nirmalan for his technical advice on many aspects of this endeavor and to Jim Loebig for his suggestions on optical access for infrared thermography. The authors would also like to thank Jim Golay and Dan Carr for their assistance in preparing test specimens and installing them in the experimental facility. The authors also wish to acknowledge Charles Stevens of Wright Laboratory for his encouragement to publish this information.

References

Ballal, D. R., and Lefebvre, A. H., 1972, "A Proposed Method for Calculating Film-Cooled Wall Temperatures in Gas Turbine Combustion Chambers," ASME Paper No. 72-WA/HT-24.

Ballal, D. R., and Lefebvre, A. H., 1973, "Film-Cooling Effectiveness in the Near Slot Region," ASME *Journal of Heat Transfer*, Vol. 95, pp. 265–266.

Dieck, R. H., 1992, *Measurement Uncertainty Methods and Applications*, Instrument Society of America, pp. 91–112.

Martiny, M., Schulz, A., and Wittig, S., 1995, "Full-Coverage Film Cooling Investigations: Adiabatic Wall Temperatures and Flow Visualization," ASME Paper No. 95-WA/HT-4.

Martiny, M., Schulz, A., Wittig, S., and Dilzer, M., 1997a, "Influence of a Mixing-Jet on Film Cooling," ASME Paper No. 97-GT-247.

Martiny, M., Schulz, A., and Wittig, S., 1997b, "Mathematical Model Describing the Coupled Heat Transfer in Effusion Cooled Combustor Walls," ASME Paper No. 97-GT-329.

Moon, H. K., and Glezer, B., 1996, "Application of Advanced Experimental Techniques in the Development of a Cooled Turbine Nozzle," ASME Paper No. 96-GT-233.

Reilly, R. S., 1996, "Advanced Film Cooling Rig Development and Test Results," NASA Contractor Report #204136, Aug., limited distribution.

Scherer, V., Wittig, S., Morad, K., and Mikhael, N., 1991, "Jets in a Crossflow: Effects of Hole Spacing to Diameter Ratio on the Spatial Distribution of Heat Transfer," ASME Paper No. 91-GT-356.

Schmidt, D. L., Sen, B., and Bogard, D. G., 1996, "Film Cooling With Compound Angle Holes: Adiabatic Effectiveness," ASME JOURNAL OF TURBOMACHINERY, Vol. 118, pp. 807–813.

Schmidt, D. L., Sen, B., and Bogard, D. G., 1996a, "Effects of Surface Roughness on Film Cooling," ASME Paper No. 96-GT-299.

Schmidt, D. L., and Bogard, D. G., 1996b, "Effects of Free-Stream Turbulence and Surface Roughness on Film Cooling," ASME Paper No. 96-GT-462.

Sen, B., Schmidt, D. L., and Bogard, D. G., 1996, "Film Cooling With Compound Angle Holes: Heat Transfer," ASME JOURNAL OF TURBOMACHINERY, Vol. 118, pp. 800–806.

Stollery, J. L., and El-Ehwany, A. A. M., 1967, "On the Use of a Boundary Layer Model for Correlating Film-Cooling Data," *Int. J. Heat and Mass Transfer*, Vol. 10, pp. 101–105.

Wittig, S., Schulz, A., Gritsch, M., and Thole, K. A., 1996, "Transonic Film-Cooling Investigations: Effects of Hole Shapes and Orientations," ASME Paper No. 96-GT-222.

Measurement of Eddy Diffusivity of Momentum in Film Cooling Flows With Streamwise Injection

R. W. Kaszeta

T. W. Simon

Heat Transfer Laboratory,
University of Minnesota,
Minneapolis, MN 55455

Measurements of mean velocity and turbulent shear stress are presented for the mixing region of a film cooling situation in which the coolant is streamwise injected with an injection angle of 35 deg. Measurements are performed using triple-sensor anemometry so that all three instantaneous velocity components are documented. The free-stream turbulence intensity level is 12 percent, the ratio of the integral length scale to injection hole diameter is 4.0, the coolant-to-mainstream momentum flux ratio is 1.0, and the density ratio is unity. From these measurements, values for the eddy diffusivities of momentum in the lateral and wall-normal directions are calculated. Additionally, calculated values of the ratio of eddy diffusivity in the spanwise direction to eddy diffusivity in the wall-normal direction are presented, which provide documentation of the anisotropy of turbulent transport in this film cooling flow.

Introduction

Film cooling is commonly used to prevent distress in and failure of gas turbine engine airfoils, which would result from excessive operating temperatures. With film cooling, cool air is bled from the compressor, ducted to the internal chambers of the turbine airfoils, and discharged through small holes in the airfoil walls. This air provides a thin, cool, insulating blanket along the external surface of the airfoil. The cooling effectiveness is dependent upon the approach flow characteristics (including velocity distributions, turbulence intensity distribution, and turbulence length scale), the film cooling flow characteristics, and the blade and film cooling hole geometries.

Much effort has been spent simulating film cooling flows computationally. Most calculations are usually done with a gradient diffusion model where the turbulent diffusion is proportional to the mean strain rate. The proportionality is the eddy diffusivity, ϵ. For most calculations, the eddy diffusivity of momentum for wall-normal transport, $\epsilon_{M,y}$, is calculated from models developed from data taken in two-dimensional boundary layers. The lateral diffusivity term, $\epsilon_{M,z}$, used with $\partial\bar{u}/\partial z$ to compute lateral turbulent transport, is simply assigned to be the same. The presence of discrete jets in a film cooling boundary layer creates a flow that is three dimensional in nature, thus requiring accurate modeling of the eddy diffusivity of momentum in both the wall-normal and spanwise directions, $\epsilon_{M,y}$ and $\epsilon_{M,z}$, respectively. Experimental measurement of eddy diffusivity of heat and mass by Quarmby and Quirk (1974) showed that the ratio of magnitudes of the diffusivities in the radial and circumferential directions in a tube ranged greatly, with values close to unity near the pipe center and as high as 100 as the wall was approached.

Numerically investigating film cooling flows, Sathyamurthy and Patankar (1992) found that the assumption of isotropic turbulent eddy viscosity (through use of a standard k–ϵ model) produced unsatisfactory predictions of coolant film lateral spreading. Leylek and Zerkle (1994) agree. Sathyamurthy and Patankar attempted to provide more accurate predictions of film cooling lateral jet spreading by adopting the model of boundary layer anisotropy developed by Bergeles et al. (1978), which is based upon an approximate linear fit of the Quarmby and Quark measurements in a fully turbulent pipe flow:

$$\frac{\epsilon_{M,z}}{\epsilon_{M,y}} = 1 + \left[3.5\left(1 - \frac{y}{\delta} \right) \right] \tag{1}$$

where δ is the boundary layer thickness. Similar success with the Bergeles et al. model for anisotropy of eddy diffusivity was reported by Xu et al. (1990).

In order to develop computational film cooling models further, experimental measurements of eddy diffusivity of momentum in both the lateral and wall-normal directions must be made. Wang et al. (1996) presented measurements of $\epsilon_{M,z}$ and $\epsilon_{M,y}$ taken with a row of streamwise-oriented film cooling holes of long development length ($L/D = 7.0$) under high (12 percent) free-stream turbulence intensity conditions. Their eddy diffusivity ratios, $\epsilon_{M,z}/\epsilon_{M,y}$, ranged from 3.0 to upward of 15.0. However, Wang et al. provided measurements in the vicinity of only one spanwise location, $z/D = 0.75$. Furthermore, their spatial resolution is now considered to be a bit coarse for such measurements. Thus, it is desirable to investigate the magnitudes of eddy diffusivities more fully in streamwise injection film cooling flows.

Present Study

The present study focuses on measurements of turbulent shear stresses in film cooling flows where the coolant is injected inline with the freestream flow, with an injection angle, β, of 35 deg. Such measurements are taken on y–z planes at two streamwise locations downstream of the film cooling holes. The measured distributions of mean velocity and turbulent shear stresses are used to calculate values of the eddy diffusivities of momentum in both the lateral and wall-normal directions. The objective of this research is to provide experimental documentation of the anisotropy of eddy diffusivity of momentum in film cooling flows, as well as to provide support for computational modeling of these flows. The film cooling mixing region is investigated with a high free-stream turbulence intensity (~12 percent) and a single row of 11 film cooling supply holes of short entry length, $L/D = 2.3$, and lateral pitch to diameter ratio, P/D, of 3.0, representative of actual turbines. For all the experimental cases, ambient air was used for both the mainstream and coolant injection flows, resulting in a density

Contributed by the International Gas Turbine Institute and presented at the 44th International Gas Turbine and Aeroengine Congress and Exhibition, Indianapolis, Indiana, June 7–10, 1999. Manuscript received by the International Gas Turbine Institute February 1999. Paper No. 99-GT-37. Review Chair: D. C. Wisler.

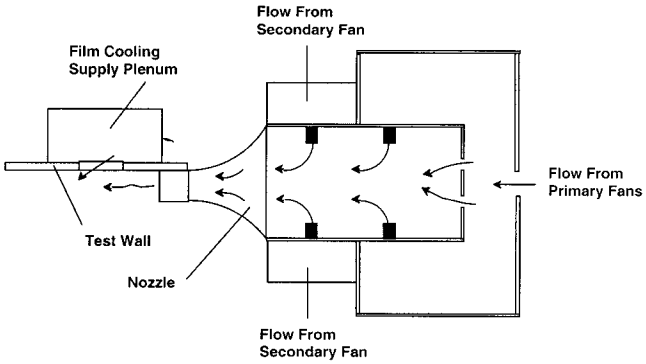

Fig. 1 Test section

ratio of unity. This density ratio is not representative of actual film cooling flows. However, it has been shown that some flow characteristics, like jet penetration, of the film cooling flow collapse, somewhat, when momentum flux ratios match (Forth and Jones, 1986).

Experimental Configuration

Wind Tunnel. The free-stream flow is a wall jet, supplied by a high-turbulence blown-type wind tunnel facility. The facility is described in detail by Wang et al. (1996). The measured free-stream turbulence at the 68.6 cm × 12.7 cm nozzle exit is nearly isotropic with a free-stream turbulence intensity (FSTI) of approximately 12.3 percent and a decay rate, $\partial(\text{FSTI})/\partial(x/D)$ of approximately 0.12 percent, yielding a FSTI of approximately 11 percent at the injection location. The FSTI level is characteristic of flows exiting the combustor stages of actual gas turbine engines (Goebel et al., 1993). The exit-plane turbulence intensity and mean velocity are uniform to within 2 percent of their mean values. The integral length scale ℓ in the free stream above the holes (calculated from a u' power spectrum) is approximately 7.7 cm ($\ell/D \approx 4$).

Test Facility. The test facility (Fig. 1) consists of an upstream plate (25.4 cm × 68.6 cm), a film cooling test plate (15.2 cm × 68.6 cm), a downstream plate (91 cm × 68.6 cm), and the film coolant supply system. The film cooling plates and the film cooling geometry are shown in Fig. 2.

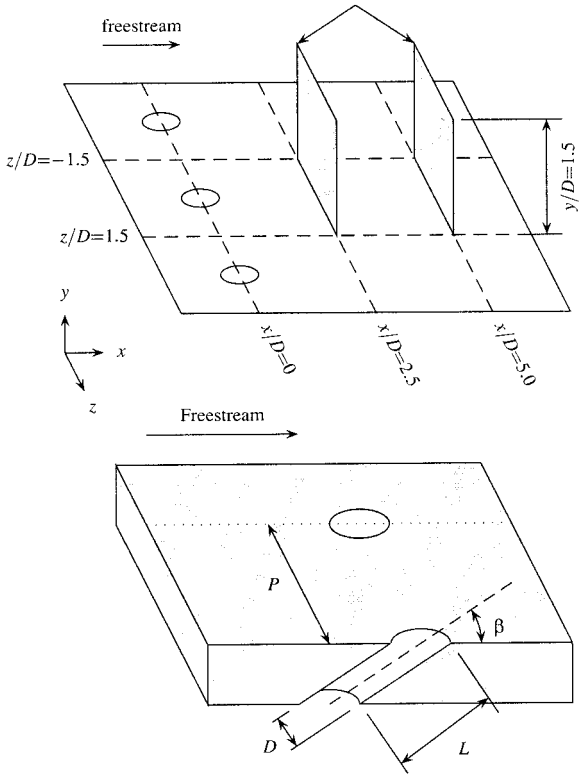

Fig. 2 Measurement planes and film cooling geometry

The upstream and downstream plates are fabricated of 9.53 mm thick cast acrylic. The test plate, fabricated from a 2.54-cm-thick silicon phenolic laminate plate, has a single column of eleven streamwise-oriented film cooling holes distributed uniformly across the plate. The film cooling holes, 1.9 cm in diameter, are spaced 3D apart. These dimensionless parameters are representative of film cooling designs in modern airfoils.

Nomenclature

D = film cooling hole diameter
DR = density ratio of coolant to mainstream flow = ρ_c/ρ_0
FSTI = free-stream turbulence intensity
I = momentum flux ratio of coolant to mainstream = $\rho_c U_c^2/\rho_0 U_0^2$
L = film cooling delivery length
ℓ = integral length scale of turbulence
M = coolant-to-mainstream mass flux ratio = $\rho_c U_c/\rho_0 U_0$
P = lateral distance between film cooling holes
Re_θ = Reynolds number based on U_0 and θ
Re_D = Reynolds number based on hole diameter and bulk coolant velocity
St_D = Stanton number based on free-stream velocity, frequency, and hole diameter = fD/U_0
u = streamwise component of velocity
U_0 = time-averaged free-stream velocity
U_c = bulk coolant velocity
$\overline{u'v'}$, $\overline{u'w'}$ = Reynolds turbulent shear stresses
v = wall-normal component of velocity
VR = coolant-to-mainstream velocity ratio = U_c/U_0
w = spanwise component of velocity
x = streamwise distance from center of hole
y = normal distance from wall surface
z = spanwise distance from center of hole
β = film cooling inclination angle
δ = hydrodynamic boundary layer thickness (99 percent)
δ^* = displacement thickness
$\epsilon_{M,y}$ = eddy diffusivity of momentum in y direction = $-\overline{u'v'}/(\partial\bar{u}/\partial y)$
$\epsilon_{M,z}$ = eddy diffusivity of momentum in z direction = $-\overline{u'w'}/(\partial\bar{u}/\partial z)$
θ = momentum thickness
θ_w = approach angle of flow to triple-sensor probe
ρ = density

Subscripts and Superscripts

$-$ = time-averaged
$'$ = instantaneous values of velocity fluctuation
0 = free-stream flow
c = coolant flow

Serving as a boundary layer trip, a 1.6 mm × 13 mm × 68.6 cm square-edged rectangular polycarbonate strip is attached to the upstream plate, with its upstream edge located 21.1 cm upstream of the hole centers. In all the experiments, the mainstream flow velocity is maintained at a nominal value of $U_0 = 11.0$ m/s, and the coolant velocity is set to achieve a momentum flux ratio, I, of 1.0 ($\mathrm{Re}_D \sim 13{,}000$). The approach flow conditions at $x/D = -4.0$ are $\delta/D = 1.10$, $\delta^*/D = 0.094$, $\theta/D = 0.073$, and $\mathrm{Re}_\theta = 960$ (details of these measurements are given in Burd et al., 1998). The coolant flow is supplied by a fan through a metering section having two laminar flow meters and through a large, unrestricted supply plenum.

Instrumentation. A triple-sensor hot-film probe (TSI Model 1299BM-20) was used to obtain velocity, turbulence intensity, and turbulent shear stress measurements. The hot-film sensors on this probe have a diameter of 50.8 μm, and an active sensing length of 1.016 mm (approximately $\frac{1}{20}$ the diameter of the film cooling holes). Due to its triple-sensor construction, the probe spatially averages over a spherical volume of approximately 2 mm in diameter. The probe was driven using TSI IFA 100 anemometer bridges. A total of 262,144 (2^{18}) data points were taken at 5 kHz for a total sampling time of 52.4 seconds. The hot-film voltages were recorded using an IOTech ADC 488/8SA A/D converter controlled via a GPIB interface. An automated GPIB-controlled, two-axis traversing system (0.025 mm resolution) was used to control the probe positioning in the wall-normal and spanwise directions. Movement in the streamwise direction was accomplished with a manual traverse.

Experimental Procedure. The data used in this paper were originally collected as part of an investigation into streamwise- and lateral-injection film cooling velocity fields, presented in Kaszeta et al. (1998). Triple-sensor profiles of the mean velocities, rms velocity fluctuation, and turbulent shear stress amplitudes were taken on y–z planes, with $\Delta z = 0.3175$ cm ($\Delta z/D = 0.167$) and y varying near-logarithmically from $y = 0.3175$ cm (as close as the triple-sensor probe mount could be placed to the wall) to $y = 2.86$ cm (in the free-stream flow).

Prior to data collection, the high-turbulence wind tunnel was activated to allow the mainstream flow to come to steady state. Next, the triple-sensor probe was aligned with the free-stream flow (with the coolant flow turned off). Then the film cooling flow was activated. After a sufficient warmup time, data collection was initiated.

During data collection, care was taken that the approach angle, θ_w, between the approach flow velocity vector and the sensor axis did not exceed 35 deg. It was previously determined (Russ and Simon, 1990) that this was the threshold angle of attack for the probe. Beyond this, instantaneous flow reversal over one or more of the three sensing films was sufficiently frequent that incorrect flow measurements resulted. The long data collection times of these profiles required careful monitoring of the flow temperatures. First-order corrections of the triple-sensor response due to small changes in room temperature were made.

Calculation of Eddy Diffusivity of Momentum. The eddy diffusivities of momentum in the spanwise and wall-normal directions are calculated as the turbulent shear stress divided by the local streamwise velocity gradient:

$$\epsilon_{M,z} = -\overline{u'w'}/(\partial \bar{u}/\partial z) \tag{2}$$

$$\epsilon_{M,y} = -\overline{u'v'}/(\partial \bar{u}/\partial y) \tag{3}$$

Since the velocity gradients approach zero at many locations in the flow, we can expect large variations in the calculated values of $\epsilon_{M,z}$ and $\epsilon_{M,y}$. Also, to achieve reasonable accuracy when calculating these values, it is necessary to calculate the local velocity gradient as accurately as possible. Our procedure for calculating the eddy diffusivities is as follows:

1 The local values of $\partial \bar{u}/\partial y$ and $\partial \bar{u}/\partial z$ over the entire y–z profile are calculated from fitted smooth splines using MATLAB (MathWorks, Inc.). This results in fairly accurate estimations of $\partial \bar{u}/\partial y$ and $\partial \bar{u}/\partial z$, with overall uncertainties of about 12 percent.
2 The eddy diffusivities are calculated using (2) and (3). Regions of the flow in which small streamwise velocity gradients result in large (>30 percent) calculated uncertainties in diffusivity values are discarded.
3 The ratio of eddy diffusivities, $\epsilon_{M,z}/\epsilon_{M,y}$, is calculated for all points at which both $\epsilon_{M,z}$ and $\epsilon_{M,y}$ are available. Again, points at which the calculated uncertainties exceed 30 percent are discarded.

Experimental Uncertainty. The uncertainties involved in triple-sensor measurements are difficult to assess. They result from changes in fluid properties between calibration and measurement, near-wall effects, alignment errors, and sensor drift. In order to estimate the magnitudes of the uncertainties in the triple-sensor measurements and verify that the triple-sensor probe can accurately measure velocity and shear stress quantities, the probe was used to measure turbulent shear stress and velocity profiles in a turbulent pipe flow and the data were compared to the published data of Laufer (1953). They compared within 5 percent. Additionally, the film cooling data for in-line injection collected in this study were compared with data taken on the same facility with a single-wire probe (Burd et al., 1998) with nearly identical results. From these experiences it was concluded that the errors present in the velocity and rms fluctuation measurements are on the same order as those of the single-wire sensor, 5–7 percent, while errors in the turbulent shear stresses are larger, on the order of 8–10 percent. As mentioned previously, due to the uncertainties in both the shear stresses and calculated velocity gradients, as well as the low value of velocity gradients at many locations in the flow, the uncertainty in value for the eddy diffusivities can grow to be quite large (upward of 60 percent). However, our analysis procedure discards values of eddy diffusivity with calculated uncertainties greater than 30 percent. Uncertainty in the total coolant mass flow rate is 2.3 percent. All uncertainties are expressed with 95 percent confidence.

Cases Studied. Profiles of mean velocities and turbulent shear stresses were taken at the two y–z planes shown in Fig. 2, $x/D = 2.5$ and $x/D = 5$, y ranging from $y/D = 0.2$ to $y/D = 1.5$, and z ranging from $z/D = -1.5$ to $z/D = 1.5$. Measurements were taken about the middle of the eleven holes. Due to the large size of the triple-sensor probe, very near-wall data ($y/D < 0.2$) were not collected.

Experimental Results

Figures 3(a) and 3(b) show distributions of normalized streamwise velocity, $\bar{u}/U_0$, and secondary fluid motion at $x/D = 2.5$ with $I = 1.0$. While the boundary conditions of the flow are symmetric, the profiles show a slight asymmetry. Such asymmetry is expected to have minimal effect on the results present herein. It has been observed in many streamwise film cooling studies (for example, a similar asymmetry is shown by Kohli and Bogard, 1997). Due to the high blowing rate and near-hole location, this case shows the highest streamwise velocity gradients of all the cases and, thus, the lowest values of uncertainty when calculating $\epsilon_{M,z}$ and $\epsilon_{M,y}$. Therefore, the analysis of eddy diffusivities of momentum focuses on this case. Examining Fig. 3(a), we can see that the coolant flow acts as a blockage, which produces a region of decreased streamwise velocity directly downstream of the cooling holes. Examining Fig. 3(b), we can see a matched pair of "kidney vortices" common to streamwise-injected film cooling flows.

Figures 4(a) and 4(b) show the turbulent shear stress $\overline{u'w'}$ and its associated mean strain rate, $\partial \bar{u}/\partial z$, which characterize turbulent transport in the spanwise direction. Examining both figures, one can see similar features in the two distributions. However, it is

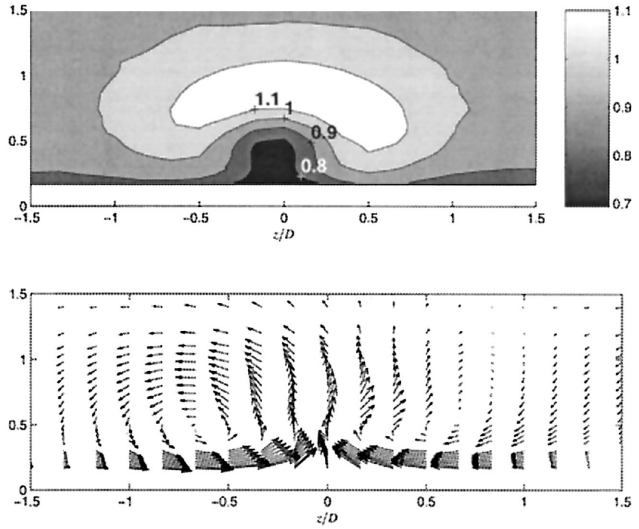

Fig. 3 Mean velocity distribution $\bar{u}/U_0$ (a), $\bar{v}$, $\bar{w}$ (b) versus y/D at $x/D = 2.5$ with $I = 1.0$

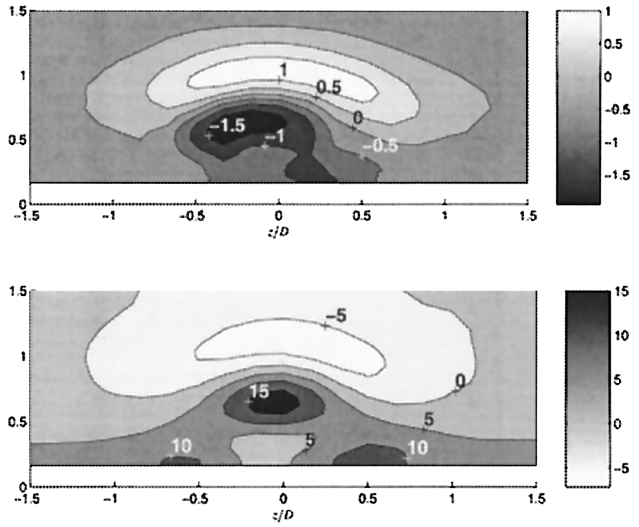

Fig. 5 Turbulent shear stress $\overline{u'v'}$ [m^2/s^2] (a) and associated gradient $\partial\bar{u}/\partial y$ [s^{-1}] (b), versus y/D at $x/D = 2.5$ with $I = 1.0$

important to note some differences—the outer pockets of high turbulent shear stress seen at $z/D = \pm 0.6$ have much weaker velocity gradient counterparts than the inner pockets of shear stress at $z/D = \pm 0.3$. Also, there are two regions of high shear stress magnitude near the wall ($y/D = 0.25$, $z/D = \pm 0.2$) that have no visible counterparts in the $\partial\bar{u}/\partial z$ distribution. Therefore, we can expect some significant variations in the calculated value of $\epsilon_{M,z}$ at different regions of the y–z plane.

Figures 5(a) and 5(b) show the turbulent shear stress $\overline{u'v'}$ and its associated mean strain rate, $\partial\bar{u}/\partial y$, which characterize turbulent transport in the wall-normal direction. Again, each region of high shear stress is generally accompanied by a region of high velocity gradient. However, opposite of the shear stress in the spanwise direction, we see near-wall regions of high velocity gradient ($y/D = 0.25$, $z/D = \pm 0.6$) with no associated regions of high shear stress. Thus, like $\epsilon_{M,z}$, we can expect to see significant variations in $\epsilon_{M,y}$ over the entire y–z plane.

Using these data, $\epsilon_{M,z}$ (Fig. 6) and $\epsilon_{M,y}$ (Fig. 7) were calculated. Examining $\epsilon_{M,z}$ (Fig. 6), we can see a number of interesting features. First, over much of the measured field, $\epsilon_{M,z}$ is fairly constant, ranging in value from 0.2 m^2/s to 0.4 m^2/s. However, in the region of the film cooling jet periphery, for example at $z/D = \pm 0.5$ and $y/D = 0.25$ (corresponding with the region in which we previously observed a poor qualitative agreement between the distributions in $\partial\bar{u}/\partial z$ and $\overline{u'w'}$), there are regions of the flow in which $\epsilon_{M,z}$ is negative, which means that at those locations the local lateral turbulent transport of streamwise momentum is actually opposite in direction to that of the velocity gradient. A reasonable explanation for these observed negative eddy diffusivities is that the flow behind the emerging film cooling jet contains coherent unsteadiness. Eckert (1987) noted cross-transport of energy by boundary work in similar, coherent, unsteady flows, leading to energy transfer against the thermal gradient. Such boundary work leads to momentum transfer against local gradients as well. Eckert notes that local streamline curvature and unsteadiness are prerequisites for such transport. Additional examples of such "negative viscosity" are presented by Starr (1968). With respect to this flowfield, vortex shedding from turbulent jets in crossflow is well documented. For example, McMahon et al. (1971) showed that a wall-normal turbulent jet in crossflow sheds vortices in the same manner as does flow past a solid, normal, circular cylinder. Spectral measurements taken in the jet region in our facility under the

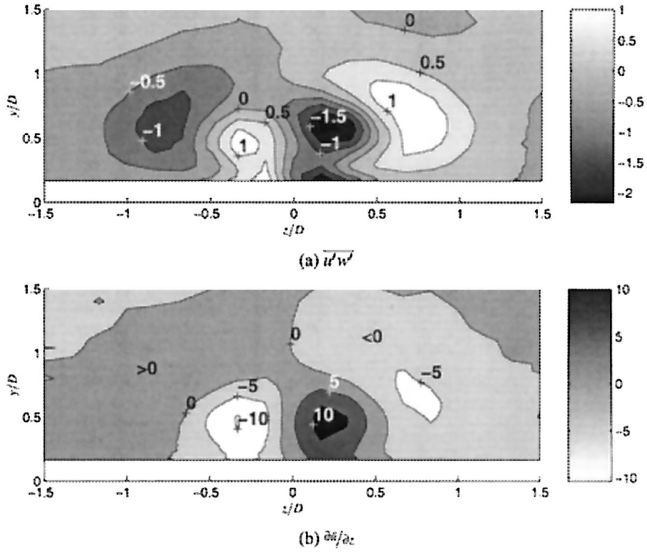

Fig. 4 Turbulent shear stress $\overline{u'w'}$ [m^2/s^2] and associated gradient $\partial\bar{u}/\partial z$ [s^{-1}] at $x/D = 2.5$ with $I = 1.0$

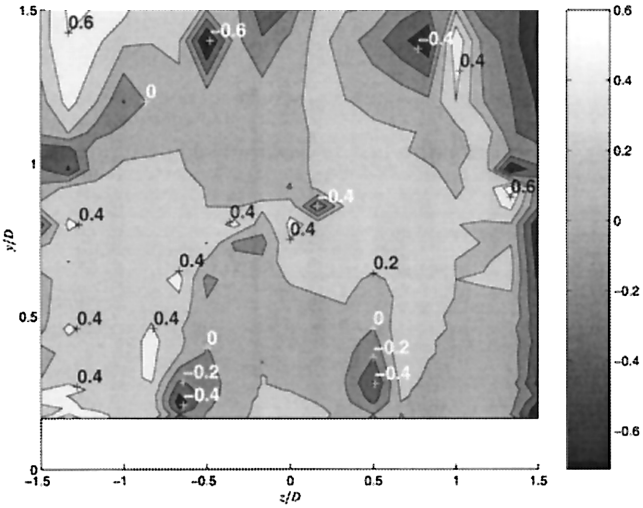

Fig. 6 Eddy diffusivity of momentum in the z direction, $\epsilon_{M,z}$ [m^2/s], at $x/D = 2.5$ with $I = 1.0$

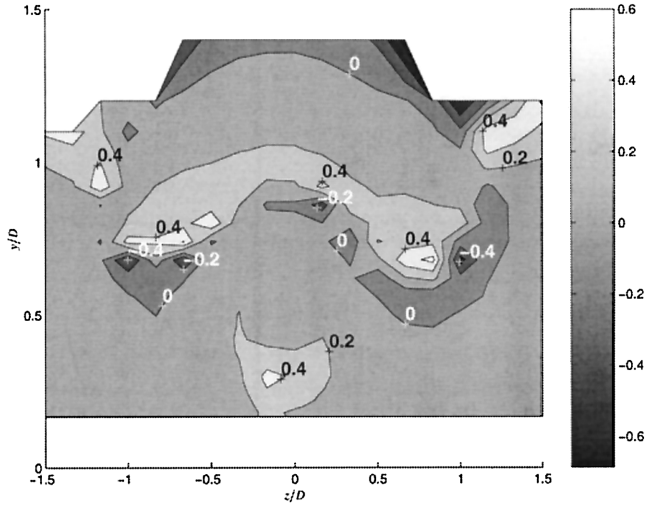

Fig. 7 Eddy diffusivity of momentum in the *y* direction, $\epsilon_{M,y}$ [m^2/s], at $x/D = 2.5$ with $I = 1.0$

same flow conditions (Burd and Simon, 1999) show a localized frequency peak suggestive of a coherent structure, such as vortex shedding. This peak occurred at a Strouhal number based on hole diameter and free-stream velocity, St_D, of 0.06 (for comparison, a rigid cylinder of the jet diameter in crossflow of the free-stream velocity sheds vortices at $St_D = 0.21$). Note that in Fig. 6, most regions of negative diffusivity are accompanied by neighboring regions of higher than average diffusivity (for example, the region of $\epsilon_{M,z} = +0.4$ m^2/s located at $z/D = 0$ and $y/D = 0.75$ has an adjacent region of $\epsilon_{M,z} = -0.4$ m^2/s located at $z/D = 0.125$ and $y/D = 0.8$, a similar pairing can be seen near $z/D = -0.75$ and $y/D = 0.25$), suggesting that in these regions the transport of streamwise momentum is enhanced by the coherent unsteadiness of adjacent flow.

Examining Fig. 7, we see a similar range of values for wall-normal diffusivity as seen for the lateral direction transport. Much of the flow-field is fairly constant, ranging in value from 0.2 m^2/s to 0.4 m^2/s. However, like $\epsilon_{M,z}$, we still see localized regions of negative $\epsilon_{M,y}$ around the periphery of the film cooling jet.

Figure 8 show the ratio of eddy diffusivities, $\epsilon_{M,z}/\epsilon_{M,y}$. In the region near the jet core ($y/D \sim 0.85$, $-0.5 \leq z/D \leq 0.5$), the ratio has, generally, a positive value in the range 1.5–4.0, clearly showing anisotropic behavior. Within the region of strongest lateral shear (see Fig. 4(*b*), $y/D \sim 0.4$, $z/D \sim 0.25$) we see these curious zones of negative $\epsilon_{M,z}/\epsilon_{M,y}$, attributable to the negative values of $\epsilon_{M,z}$. At the edge of the jet ($0.75 < z/D < 1.0$, $y/D < 0.5$), where the jet flow is mixing with the free-stream flow and it is presumed that the mixing eddy sizes are larger than in the region of strongest lateral shear, $\epsilon_{M,z}/\epsilon_{M,y}$ values range from 1.0−4.0, again indicating strong anisotropy. Measured values reported by Wang et al. (1996) for approximately this same region and in the same case, but at $x/D = 5.0$, are near 7.0. With the benefit of observing the steep gradients in this area (see marked region in via Fig. 8), we suspect this difference in values is due to errors in Wang et al.'s calculation of gradients. The values of $\partial\bar{u}/\partial z$ reported by Wang et al. were calculated using finite differences between two y profiles with spacing $\Delta z/D = 0.333$, which appears to be too large a spacing to accurately calculate the local gradients. This results in calculated gradients that are too small, and, thus, larger calculated values of $\epsilon_{M,z}$ and $\epsilon_{M,z}/\epsilon_{M,y}$. To ensure that the present study used a sufficiently small $\Delta z/D$, preliminary data were collected using $\Delta z/D = 0.0833$ instead of $\Delta z/D = 0.167$, and no significant change in the calculated gradients occurred, so it was concluded that a $\Delta z/D = 0.167$ was sufficient.

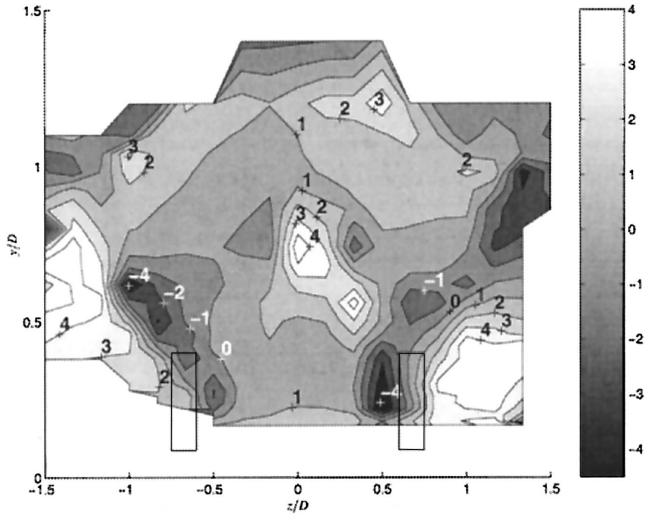

Fig. 8 Ratio of eddy diffusivities, $\epsilon_{M,z}/\epsilon_{M,y}$, at $x/D = 2.5$ with $I = 1.0$

In computation, anisotropy has traditionally been incorporated by a linear rise in $\epsilon_{M,z}/\epsilon_{M,y}$ from 1.0 to a maximum value of $\epsilon_{M,z}/\epsilon_{M,y} = 4.5$ as the wall is approached, as proposed by Bergeles et al. (1978). Recall that this model was based on two-dimensional (non-film cooled) turbulent pipe flow data. Xu et al. (1990) and Sathyamurthy and Patankar (1992) show that this model improves the accuracy of the cooling jet lateral spreading rate. However, our current results support the use of an anisotropic transport correction in the general range of values given by the Bergeles et al. model, but do not support this particular distribution. Our results indicate that the flow field is far more complex than the Bergeles et al. model would imply.

Concluding Remarks

The results represent detailed documentation of the turbulent transport properties present in a film cooling mixing region with streamwise-oriented injection. These results provide useful insight into the nature of turbulent transport present in these flows, and also provide experimental measurements of $\epsilon_{M,z}$ and $\epsilon_{M,y}$ which may be useful to computational researchers. From these results, a number of conclusions can be made:

1 Due to the presence of structured unsteadiness in the mixing region, negative eddy diffusivities are calculated around the periphery of the jet. These negative values suggest that future investigations into turbulent transport in these flows to account for both the structured and turbulent characteristics of the flow are needed.
2 Eddy transport is somewhat larger in the lateral direction than in the wall-normal direction, and, thus, isotropic turbulence modeling should not be applied. Over a large portion of the measured region, the eddy diffusivity ratio, $\epsilon_{M,z}/\epsilon_{M,y}$, is larger than unity, lying in the range 1.5–2.5. However, these values are considerably smaller than those previously reported for this flow by Wang et al. (1996).
3 While computational work incorporating the Bergeles model of anisotropy has shown some success, our results show that the anisotropy of turbulent transport in this flow is too complex to be represented with such a simple model.

Acknowledgments

This work is part of a combined study of film cooling with lateral injection and short delivery holes sponsored by the Department of Energy and NASA-Lewis Research Center, respectively. The DOE project is managed by Dr. Daniel Fant of the South Carolina Energy R&D Center and the NASA study Project Monitor is Douglas Thurman. Additional support in the form of a

graduate fellowship was provided by the National Science Foundation Fellowship program.

References

Bergeles, G., Gosman, A. D., and Launder, B. E., 1978, "The Turbulent Jet in a Cross Stream at Low Injection Rates: A Three-Dimensional Numerical Treatment," *Numerical Heat Transfer*, Vol. 1, pp. 217–242.

Burd, S. W., Kaszeta, R. W., and Simon, T. W., 1998, "Measurements in Film Cooling Flows: Hole *L*/*D* and Turbulence Intensity Effects," ASME JOURNAL OF TURBOMACHINERY, Vol. 120, pp. 791–798.

Burd, S. W., and Simon, T. W., 1999, "Turbulence Spectra and Length Scales Measured in Film Coolant Flows Emerging From Discrete Holes," ASME JOURNAL OF TURBOMACHINERY, Vol. 121, pp. 551–557.

Eckert, E. R. G., 1987, "Cross Transport of Energy in Fluid Streams," *Wärme Stoff*, Vol. 21, pp. 73–81.

Forth, C. J. P., and Jones, T. V., 1986, "Scaling Parameters in Film Cooling," *Proc. 8th Intl. Heat Transfer Conference*, Vol. 3, pp. 1271–1276.

Goebel, S. G., Abuaf, N., Lovett, J. A., and Lee, C.-P., 1993, "Measurements of Combustor Velocity and Turbulence Profiles," ASME Paper No. 93-GT-228.

Kaszeta, R. W., Simon, T. W., Oke, R. A., and Burd, S. W., 1998, "Flow Measurements in Film Cooling Flows With Lateral Injection," ASME Paper No. 98-GT-54.

Kohli, A., and Bogard, D. G., 1997, "Adiabatic Effectiveness, Thermal Fields, and Velocity Fields for Film Cooling With Large Angle Injection," ASME JOURNAL OF TURBOMACHINERY, Vol. 119, pp. 352–358.

Laufer, J., 1953, "The Structure of Turbulence in Fully-Developed Pipe Flows," NACA Report 1174.

Leylek, J. H., and Zerkle, R. D., 1994, "Discrete-Jet Film Cooling: A Comparison of Computational Results With Experiments," ASME JOURNAL OF TURBOMACHINERY, Vol. 116, pp. 358–368.

McMahon, H. M., Hester, D. D., and Palfery, J. G., 1971, "Vortex Shedding from a Turbulent Jet in a Cross-Wind," *Journal of Fluid Mechanics*, Vol. 48, No. 1, pp. 73–80.

Quarmby, A., and Quirk, R., 1974, "Axisymmetric and Non-Axisymmetric Turbulent Diffusion in a Plain Circular Tube at High Schmidt Number," *Intl. Journal Heat Mass Transfer*, Vol. 17, pp. 143–174.

Russ, S., and Simon, T. W., 1990, "Signal Processing Using the Orthogonal Triple-Wire Equations," *Flow Lines*, the TSI quarterly magazine, Winter.

Sathyamurthy, P., and Patankar, S. V., 1992, "Film Cooling Studies Using a Three-Dimensional Parabolic Procedure," University of Minnesota Supercomputer Institute Research Report 92/44.

Starr, V. P., 1968, *Physics of Negative Viscosity Phenomena*, McGraw-Hill.

Wang, L., Tsang, H., Simon, T. W., and Eckert, E. R. G., 1996, "Measurements of a Mean Flow and Eddy Transport Over a Film Cooling Surface," in: *Proc. 31st National Heat Transfer Conference*, Vol. 5, ASME HTD-Vol. 327, pp. 71–79.

Xu, J. Z., Ko, S. Y., Chen, S. J., and Tsou, F. K., 1990, "Computer Simulation of Film-Cooling With Coolants From One and Two Rows of Holes," ASME Paper No. 90-WA/HT-7.

Journal of Turbomachinery

Technical Brief

A Two-Dimensional Numerical Investigation of Transient Heat Flux Gage Performance in Short-Duration Facilities

J. Kim,[1] H. Sakamoto,[2] and M. G. Dunn[3]

Introduction

Thin-film heat-flux gages have been used for the past fifty years in short-duration facilities (test times typically on the order of one to ten milliseconds) to measure local heat flux in a wide variety of high-energy flow situations. These gages consist of a thin platinum strip (typically 1×10^{-8} m thick) bonded to a substrate material of low thermal diffusivity, e.g., Pyrex glass. The substrate, which can be contoured to almost any desired shape (e.g., strip inserts, leading-edge inserts, buttons, etc.) is then embedded into the surface of a component of interest such as a turbine blade. A photograph of a button gage embedded in turbine blade is shown in Fig. 1. The heat-flux gage is operated in a constant-current circuit (typically 1 mA to avoid excessive heating) from which the film temperature history during the experiment is deduced using a temperature coefficient of resistance calibration for that particular gage. The heat flux that must have produced the inferred temperature history of the substrate surface is then calculated using a one-dimensional, time-dependent heat conduction approximation as described in Seymour (1987).

The reason for using a low-thermal-diffusivity substrate is to "hold the heat at the surface," i.e., the gage is usually embedded in a metal component whose thermal diffusivity is so high that the surface temperature increases by a very small amount during the duration of the experiment. Use of the substrate material leads to increases in surface temperature that are typically on the order of five degrees Kelvin or larger, and the resulting improvement in signal-to-noise ratio is an important factor in the success of these devices. The surface temperature increase of the insulating substrate may complicate the interpretation of the data, however. If one elects to use a button-type heat-flux gage instead of the contoured strip, then there exists a temperature difference between the surface of the insulating substrate and the surrounding metal, which has come to be known as a "heat-island." The heat flux to the gage is different from that to the adjoining metal by some amount that depends upon many parameters, and it is the latter flux that is desired.

This note reports the results of a simplified numerical investigation of the potential heat-island effect for a button-type gage placed in a metal substrate, and is designed to obtain an estimate of the magnitude of the deviations from the ideal calculated values that might be expected when using these gages. A two-dimensional simulation of a strip gage embedded in a flat plate normal to the flow direction was performed since a fully three-dimensional simulation would have taken prohibitively long given the available resources. Details of the two-dimensional simulations are given in the next section. The numerical results are compared with published experimental results (Dunn et al., 1997) for which heat-flux measurements were made for button-type and continuous strip-type gages (for which there is no "heat island") inserted in a three-dimensional turbine vane just ahead of a downstream rotor, and simultaneously exposed to identical flow conditions with the turbine stage operating at design-corrected conditions.

Problem Formulation

A transient, elliptic, conjugate two-dimensional heat transfer simulation of the problem was performed using the commercially available CFD code FLUENT. For simplicity, the three-dimensional circular inserts were modeled as two-dimensional strips normal to the flow direction. Three geometries were studied. The first geometry (Fig. 2(*a*)) consisted of two Pyrex strips embedded in a steel flat plate (no bonding agent is present) exposed to a gas stream at elevated temperature and pressure. The second geometry (Fig. 2(*b*)), which represents the physically more realistic case, included modeling of the bonding agent (epoxy) that is used to hold the substrate in the steel. The third geometry was similar to the first, except the length of Pyrex ahead of the platinum sensing element was increased. The substrate was chosen to be sufficiently thick so that the heat wave did not reach the bottom surface during the calculation time. Fluid acceleration along the length of the channel was negligible. A 300×60 weighted grid was chosen. Transient calculations of the wall temperature and wall heat transfer coefficients along the wall were obtained from 0 to 26 ms with a time step of 1 ms. Nominal inlet conditions are given in Table 1, and bracket the experimental conditions at the turbine inlet (Dunn et al., 1997). A summary of the cases that were run is shown in Table 1, while the assumed properties of steel, Pyrex, and epoxy are summarized in Table 2. Additional details regarding the numerical calculations are given in Kim et al. (1996).

[1] University of Maryland, Dept. of Mechanical Engineering, College Park, MD 20742.
[2] University of Minnesota, Dept. of Mechanical Engineering, Minneapolis, MN 55455.
[3] The Ohio State University, Department of Aerospace Engineering, Columbus, OH 43210.

Contributed by the International Gas Turbine Institute of The American Society of Mechanical Engineers. Manuscript received by the International Gas Turbine Institute January 1, 1999; revised version received June 1, 1999. Associate Technical Editor: T. H. Okiishi.

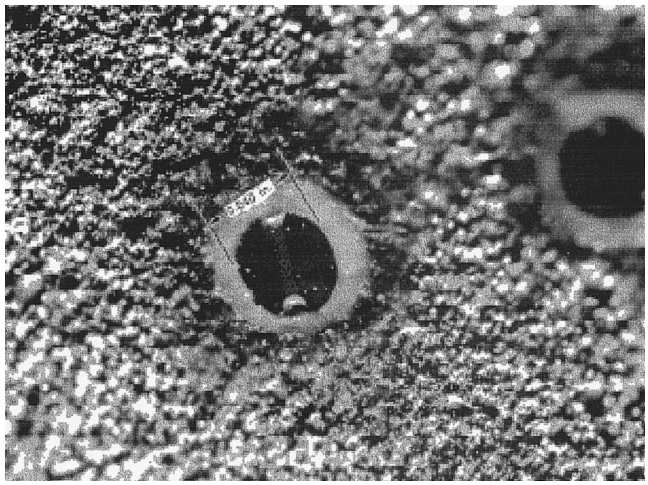

Fig. 1 Photograph of a button-type gage embedded in a turbine blade. The gage is about 1 mm in diameter, and is held in the blade using epoxy (white material surrounding the gage).

Dimensional Analysis

A dimensional analysis was performed to determine the relevant problem parameters. Consider the case where a thin-film gage painted on a Pyrex substrate is embedded flush with the surface of a steel plate, as shown in Fig. 2(*a*). The deviation of the heat transfer coefficient data at the center of the insert from the ideal case of no insert is defined as

$$\text{percent deviation} = \frac{h_{\text{calc}} - h_{\text{strip}}}{h_{\text{calc}}} \times 100 \tag{1}$$

where h_{calc} is obtained from the solution for a wall of uniform material and h_{strip} is the heat transfer coefficient indicated by the gage. The percent deviation can be expressed as a function of the following quantities:

$$\text{percent deviation} = f[T_{gl} - T_w,\ T_\infty - T_w,\ h,\ t,\ u_\infty,\ a,\ x,\ \rho_{gl},\ c_{p,gl},\ k_{gl},\ \rho_{st},\ c_{p,st}k_{st},\ \rho_{fl},\ c_{p,fl},\ k_{fl},\ \mu_{fl}] \tag{2}$$

where the subscripts stand for gl = Pyrex, st = steel, fl = fluid, and w = wall. Many of the resulting groups can be eliminated if it is assumed that the following are constant: steel temperature (it increases very little during the time of interest), gage width, free-stream velocity, properties of the steel and Pyrex, and the fluid properties. The numerical results showed that the nondimensional Pyrex surface temperature could be written in terms of two other groups as

$$\left(\frac{T_{gl} - T_w}{T_\infty - T_w}\right) = f\left(\frac{ha}{k_{gl}},\ \frac{\alpha_{gl}t}{a^2}\right) \tag{3}$$

The percent deviation was also found to be fairly independent on the location of the gage on the plate, and can therefore be described by an equation consisting of three groups:

$$\text{percent deviation} = f\left[\frac{ha}{k_{gl}},\ \frac{\alpha_{gl}t}{a^2},\ \frac{\rho_{fl}}{\rho_{gl}}\right] \tag{4}$$

If epoxy is present, additional terms must be added to account for the width of the epoxy and for the epoxy properties.

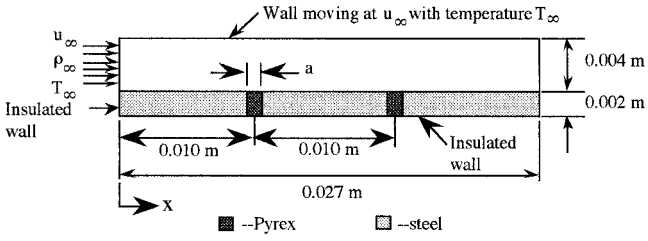

Fig. 2(*a*) Flow domain for Pyrex/steel case

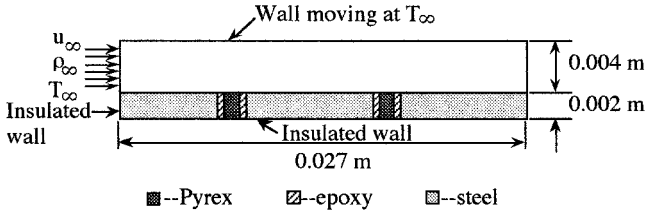

Fig. 2(*b*) Flow domain for Epoxy/Pyrex/steel case

Table 1 Flow conditions for the numerical simulations. Other problem parameters are: (1) free-stream velocity u_∞ = 70.6 m/s, (2) plate length = 0.027 m, and (3) properties of air taken at 550 K. The effective Reynolds number was changed in the calculations by specifying different gas density values as was done in the experiment of Dunn et al. (1997).

Case	Laminar/ Turbulent	Fluid Density (kg/m^3)	Epoxy	Gauge Width, a (mm)
1	Laminar	2.1	No	1.0
2	Laminar	4.0	No	1.0
3	Laminar	10.0	No	1.0
4	Laminar	20.0	No	1.0
5	Laminar	50.0	No	1.0
6	Laminar	2.1	Yes	1.0
7	Laminar	4.0	Yes	1.0
8	Laminar	4.0	No	1.5
9	Turbulent	2.1	No	1.0
10	Turbulent	4.0	No	1.0
11	Turbulent	10.0	No	1.0
12	Turbulent	20.0	No	1.0
13	Turbulent	50.0	No	1.0
14	Turbulent	4.0	Yes	1.0
15	Turbulent	4.0	No	1.5

Results

Verification of Numerical Results. Three checks were made on the calculations using the above-described grid and specifying the entire wall to be a uniform material: (1) Steady-state cases run using laminar and turbulent flow (k–ϵ model) were found to be well within 5 percent of the correlations for all cases. (2) An unsteady case run to obtain time-dependent temperature profiles assuming a wall of uniform composition (Pyrex), uniform initial temperature, and a step change in wall temperature for $t > 0$ agreed with the analytical semi-infinite solid solution to within 2 percent. (3) A case simulating flow over a plate with an unheated starting length agreed with the correlation given in Kay and Crawford (1993) within 3 percent.

Table 2 Material properties used in the simulations

Material	ρ (kg/m^3)	k (W/m-K)	C_p (J/kg-K)
Steel	7833	54	465
Pyrex	2210	1.09	836
Epoxy	1400	0.238	300

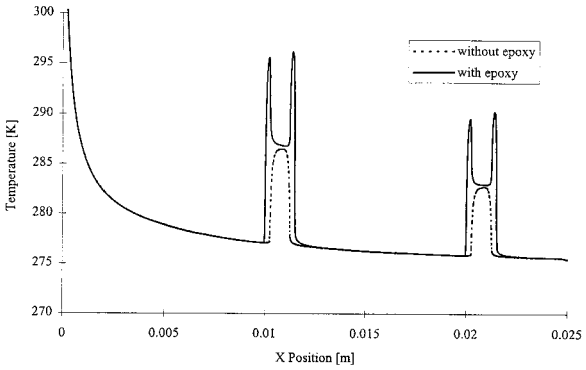

Fig. 3(*a*) Typical variation in wall temperature for cases with and without epoxy

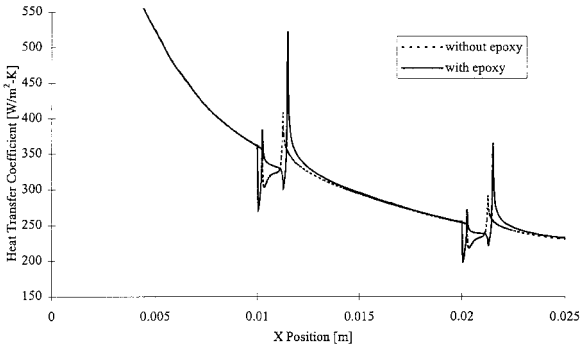

Fig. 3(*b*) Typical variation in wall heat transfer coefficient for cases with and without epoxy

Results for Pyrex/Steel Surface. Typical variations in the wall temperature and heat transfer coefficient with wall and gas conduction are seen in Figs. 3(*a, b*). Results were obtained for $t =$ 10, 20, and 25 ms after flow arrival at the gage location. In the experiment, the gages are read at a time corresponding to establishment of the design stage pressure ratio being achieved. For a small turbine, this time may be as little as 10 ms, but for a large machine a time after flow arrival of 15 ms to 20 ms is a safe time to anticipate design flow conditions. It is desirable to read the heat-flux gages as early as possible, because the percent deviations were observed to increase with time and those for turbulent flow were seen to be larger than those for laminar flow.

An equation that describes the numerical results to within 2 percent is given by

$$\text{percent deviation} = \left\{0.605 + 297\left(\frac{\alpha_{gl}t}{a^2}\right) + \left[314 + 39400\left(\frac{\alpha_{gl}t}{a^2}\right)\right]\left(\frac{\rho_{fl}}{\rho_{gl}}\right)\right\} + \left\{4.17 + 380\left(\frac{\alpha_{gl}t}{a^2}\right) - \left[101 + 4160\left(\frac{\alpha_{gl}t}{a^2}\right)\right]\left(\frac{\rho_{fl}}{\rho_{gl}}\right)\right\}\left(\frac{ha}{k_{gl}}\right) \quad (5)$$

This equation was used to predict the percent deviations for the experimental conditions of Dunn et al. (1997), with the understanding that the experimental data were obtained on a three-dimensional turbine airfoil in a compressible flow. The percent deviations for the flow conditions given in Table 3 at a time of 20 ms (the time at which the gages are typically read for this machine) was found to be 11.8 and 16.1 percent for the low and high Reynolds number cases, respectively. This is considerably larger than the 5–10 percent uncertainty ascribed to the experimental data. However, a significant portion of this discrepancy can be shown to be due to not incorporating in the calculation model the epoxy used to hold the gages in the component.

Table 3 Flow conditions for Dunn et al. (1997)

	Low Re Case	High Re Case
Maximum Heat Transfer Coefficient (W/m^2-K)	895	1390
Inlet Density (kg/m^3)	2.6	3.6
Inlet Temperature (K)	571	601
Gauge Width, a (mm)	1.0	1.0

Results for Pyrex/Steel/Epoxy Surface. Calculations were performed with epoxy of width 0.25 mm (value measured from Fig. 1) inserted upstream and downstream of the Pyrex gages. Typical variations in wall temperature and heat transfer coefficient for a case with epoxy are shown in Figs. 3(*a, b*). Figure 3(*a*) shows that the epoxy heats up more than the Pyrex, with the epoxy downstream of the Pyrex heating up more than the epoxy upstream of the Pyrex, as expected. Figure 3(*b*) shows that the heat transfer coefficient decreases sharply upon encountering the epoxy to a level even lower than that encountered with the Pyrex only, since the epoxy is at a higher temperature than the Pyrex. At the center of the gage, however, the heat transfer coefficient has rebounded to a value significantly higher than that corresponding to the steel/Pyrex case, resulting in a significantly lower percent deviation.

The calculations indicated that the percent deviations for all the laminar flow cases with epoxy were about 65 percent of the values without epoxy. The turbulent cases with epoxy showed that reductions in percent deviations were slightly dependent on the density ratio, and fairly independent of time and position on the plate. The percent deviations for the turbulent cases decreased by approximately 66 to 83 percent for flow densities of 4.0–20 kg/m^3, respectively. Based on these results, the maximum percent deviation for the high Reynolds number case of Dunn et al. (1997) is expected to decrease by about 66 percent from 16.1 to 10.6 percent. The 10.6 percent value is consistent with the observed upper limit on the experimental uncertainty of 10 percent. The maximum expected percent deviation for the low Reynolds number case when epoxy is included is well within the experimental scatter.

Effect of Pyrex Length. Strip inserts similar to those used in Dunn et al. (1997) would have a substantial increase in the length of Pyrex ahead of the gages (orders of magnitude greater than the example used here). Increasing the length of Pyrex ahead of the platinum sensing element decreases the percent deviation since the flow has more time to adjust to the new boundary condition. To quantify this effect, a case was run using a gage 1.5 mm wide rather than the nominal gage width of 1.0 mm (no epoxy was included in this simulation). The flow was considered to be turbulent with a density of 4.0 kg/m^3. The percent deviation for the wider gage decreased by 25 percent from that calculated for the shorter length of Pyrex.

Conclusions

A two-dimensional model of the button-type gage geometry yields heat transfer coefficients that are within approximately 10 percent of the value calculated in the absence of the button for the range of parameters studied here and for the flow conditions of the experimental data to which these calculations are compared. Modeling of the epoxy surrounding the gage is crucial to obtaining accurate results. Smaller values of percent deviations can easily be obtained by reading the gages at the

earliest time for which the design stage pressure ratio is established, or by increasing the length of the Pyrex substrate ahead of the thin-film gage.

References

Dunn, M. G., Kim, J., and Rae, W. J., 1997, "Investigation of the Heat-Island Effect for Heat-Flux Measurements in Short-Duration Facilities," ASME JOURNAL OF TURBOMACHINERY, Vol. 119, pp. 753–760.

Kays, W. M., and Crawford, M. E., 1993, *Convective Heat and Mass Transfer*, 3rd ed., McGraw-Hill.

Kim, J., Ross, R., and Dunn, M. G., 1996, "Numerical Investigation of the Heat-Island Effect for Button-Type, Transient, Heat-Flux Gauge Measurements," *Proc. ASME National Heat Transfer Conference*, Houston, TX, ASME HTD-Vol. 327, Vol. 5, pp. 33–39.

Seymour, P. J., 1987, "Techniques for Numerical Evaluation of Unsteady Heat Flux From Thin Film Gauges," MS Thesis, State University of New York at Buffalo.